

ABSTRACT

LIN, CHIAO-WEN. Characterization of the Solute Dynamics Signature of an Agricultural Coastal Plain Stream, North Carolina, USA. (Under the direction of Dr. François Birgand).

The context of this research is the quantification of water quality benefits of stream restoration. This common mitigation practice has not received widespread acceptance, in part because of the lack of concordant evidence of its benefits, and magnitude thereof, on stream water quality. The reasons might be that the benefits are too small to be measurable, and/or that the uncertainties on the quantification methods are just too large to detect benefits. The only variable on which we have control are the quantification methods and their uncertainties. To document the water quality benefits of stream restoration, North Carolina Department of Transportation, North Carolina Forest Service and North Carolina State University have collaborated to conduct a pilot study where new monitoring techniques have been applied to minimize quantification uncertainties. We chose to take nutrients loads as the indicator of the bulk effect of restoration on water quality. In this work, it is necessary to report the characterization of the solute dynamics and calculate indicators of water quality benefits. For this, flow and water quality were monitored on a 'continuous' basis during the 16-month pre-restoration period in the Claridge Canal, a coastal plain stream to be restored in Goldsboro, North Carolina.

The results indicated that it was possible to calculate the concentrations of a suite of water quality parameters every 15-min combining absorbance spectra from *in situ* ultraviolet-visual (UV-Vis) spectrophotometers, with water quality rating curves developed from Partial Least Squares Regressions (PLSR). We were able to construct robust water quality rating curves to measure nitrate (NO₃-N), Total Dissolved Nitrogen (TDN), Total Kjeldahl Nitrogen (TKN), Dissolved Organic Carbon (DOC), and Total Phosphorus (TP)

concentrations, using the absorbance data as index data. The method did not work well for ammonium ($\text{NH}_4\text{-N}$) and phosphate ($\text{PO}_4\text{-P}$), although this might have come from less than ideal calibration point pools. It was found that turbidity-based rating curves were better suited to calculate Total Suspended Solid (TSS) concentrations and loads.

Then, this research quantified the uncertainties on annual cumulative loads associated with the data generated by UV-Vis spectrophotometers. For this, we used bootstrap, random and stratified sample subsets from the original dataset and applied PLSR on these subsets to estimate the uncertainties on annual loads. The bootstrap resampling results demonstrated that uncertainties on annual loads associated with the application of UV-Vis spectrophotometers were much lower than those typically obtained from infrequent sampling, and could be within $\pm 5\%$ measuring error for nitrate, TDN, TKN, DOC and TSS; and approximately $\pm 10\%$ for TP. It was found that to obtain robust rating curves that would lead to precise and unbiased cumulative annual loads, it is desirable to stratify calibration concentrations.

At last, the unique flow and concentration datasets were used to characterize nutrients and material dynamics in the events and seasonal scales in this coastal plain watershed. In this research, a unique pattern of concentration troughs and peaks was found during flow peaks. Unlike most upland watersheds, the summer dynamics have highlighted the unique role of the near-stream zone, which in the flat coastal plain watersheds tend to be drier than the rest of the soil profile. We were able to associate events scales with seasonal variations. As a result, the role of stream denitrification and the release of DOC due to diagenetic processes were shown during warmer months.

© Copyright 2017 Chiao-Wen Lin

All Rights Reserved

Characterization of the Solute Dynamics Signature of an Agricultural Coastal Plain Stream,
North Carolina, USA.

by
Chiao-Wen Lin

A dissertation submitted to the Graduate Faculty of
North Carolina State University
in partial fulfillment of the
requirements for the degree of
Doctor of Philosophy

Biological and Agricultural Engineering

Raleigh, North Carolina

2017

APPROVED BY:

Dr. François Birgand
Committee Chair

Dr. Matthew Polizzotto
Minor Representative

Dr. Marcelo Ardón Sayão
External Member

Dr. Michael R. Burchell

Dr. William F. Hunt

DEDICATION

I dedicate this work to my family who gave me endless love and support.

BIOGRAPHY

Chiao-Wen Lin was born on July 22, 1986 to Tong-Fa Lin and Huei-Ying Lai. She grew up with her parents and younger brother in Taichung, Taiwan. During her childhood, her parents educated her with much patience and encouragement which formed her with an open-minded personality. Chiao-Wen and her family enjoyed outdoor activities including hiking and sightseeing; from these experiences, she was impressed by the breadth and beauty of natural environment and inspired to study in greater depth.

After Chiao-Wen graduated from Mingdao High School, she enrolled in Hydraulic and Ocean Engineering at National Cheng Kung University. In 2008, she received the bachelor degree, and she discovered a great desire to immerse herself even deeper in the fields of ecological engineering and water resources. Then, she worked with Dr. Wen-Lian Chang for the master degree in Bioenvironmental Systems Engineering in National Taiwan University during 2008- 2010. For her master research, she focused on the application of waste oyster shell as wastewater purification material in constructed wetlands.

In 2011, she received a scholarship to study abroad which was awarded by the Ministry of Education in Taiwan. In August, 2012, she came to Raleigh, North Carolina to pursue a doctorate degree under the direction of Dr. François Birgand in Biological and Agricultural Engineering at North Carolina State University. She worked on characterizing solute dynamics with continuous water quality and hydrology monitoring in an agricultural coastal plain stream.

ACKNOWLEDGMENTS

Pursuing a doctorate degree is like climbing a magnificent mountain. I would never have reached the summit without support in past five years.

I would like to thank my advisor, Dr. François Birgand for his confidence in my abilities and for instructing me in various aspects of my Ph.D., including experiment design, figure plotting, data interpretation, and scientific writing. His support and encouragement stimulated my potential ability to reach the goal. I want to thank my committee members: Dr. Marcelo Ardón Sayão, Dr. Matthew Polizzotto, Dr. Michael Burchell, and Dr. William Hunt who helped me to enhance the quality of the dissertation, to summarize the “big picture” perspectives of the research, and gave me other helpful suggestions.

I am thankful for Dr. Nicole Bowen and Elizabeth Allen, who not only helped with research-related work but also introduced me to American culture. I appreciate many aspects of assistance and support from the faculty, fellow students, and friends in the Biological and Agricultural Engineering Department at North Carolina State University: Dr. John Classen, Dr. Garey Fox, Dr. Barbara Doll, Dr. Kyle Aveni-Deforge, Dr. Randall Etheridge, Dr. Troy Gilmore, Dr. Yo-Jin Shiau, Heather Austin, Sherry Li, Bryan Maxwell, Danielle Winter, Cyrus Belenky, Wenlong Liu, Yu Liu, Sheida Moin, Taylor Carter, Erin Bennett, Magdlena Rabiipour, Kathleen Bell, and Mason Marriner.

I want to thank Rachel Huie and Hiroshi Tajiri from the Environmental Analysis Test Service Lab; Jenny James and Linda Mackenzie from the Center for Applied Aquatic Ecology; and Guillermo Ramirez from the Environmental and Agricultural Testing Service at North Carolina State University for helping me to analyze water and sediment samples. I

would like to thank Dr. Diana Oviedo Vargas and Dr. Wayne Yuan who guided me in the extracellular coenzyme activity experiment.

I would like to thank North Carolina Department of Transportation for funding this research and the Ministry of Education in Taiwan for providing the scholarship for the first two years.

I am thankful for all the people who told me “Best of luck” and helped me during these five years. I appreciate all the challenges and difficulties which made me stronger. Last but not least, I want to thank my parents and my younger brother, Cheng-Sheng Lin, in Taiwan, who always give me unconditional support and encouragement to help me have the confidence to complete my doctorate degree.

TABLE OF CONTENTS

LIST OF TABLES	x
LIST OF FIGURES	xii
Chapter 1: Introduction	1
1.1 Research Motivation	1
1.2 Research Questions	3
1.3 Objectives	4
1.4 References	6
Chapter 2: Application of ultraviolet-visual spectrophotometers and water quality rating curves to monitor concentrations and loads on a continuous basis in an agricultural coastal plain stream	9
2.1 Introduction	9
Water quality benefits of stream restoration not well quantified	9
Application and calibration of Ultraviolet-visual spectrophotometers	13
Hypotheses and objectives	14
2.2 Methods	15
Site description	15
Background	16
Flow measurements	17
Water sample collection and measurements	19
Installation of the monitoring system	19
Equipment maintenance	21
Laboratory analyses	21
Cumulative load calculations	23
Calibration methods for concentrations from spectral data	23
Methods for correcting erroneous data and filling missing data	25
2.3 Results and Discussion	29
Developing index velocity ratings to calculate flow	29
Degradation sample study results	31
Discrete sample results	35
Global Calibration versus discrete sample results	36
PLSR calibration fitting procedure	39

It is possible to create water quality rating curves for most parameters tested.....	44
TSS Predictions from PLSR and turbidity.....	65
PLSR calibration vs Global Calibration vs Local Calibration on load estimations.....	68
Discussion: can nutrient concentrations and loads be measured reliably with water quality rating curves?	70
Beyond water quality rating curves: additional local concentration corrections	72
Results for filling missing flow data.....	77
Results for filling missing nitrate concentration data	80
Challenges and maintenance for the application of UV-Vis spectrophotometers in situ	86
2.4 Conclusions.....	87
2.5 Acknowledgements.....	88
2.6 References.....	89
Chapter 3: Uncertainties assessment for continuous and infrequent sampling in measuring nutrient loads with the application of UV-Visual spectrophotometers in an agricultural coastal plain stream.....	97
3.1 Introduction.....	97
A revolution at play in water quality monitoring thanks to in situ probes	97
Research questions and hypotheses	99
Objectives	100
3.2 Methods.....	101
Research context and site description	101
Flow measurements	102
Water sample collection and measurements	103
Laboratory analysis.....	104
Calibration methods for concentrations from spectral data	105
Uncertainties on concentrations and annual loads	107
Resampling the existing calibration points.....	108
Uncertainties estimation on annual loads as hydrological indicator with resampling..	110
Uncertainties estimation on annual loads as hydrological indicator with infrequent sampling.....	111
Obtaining 12-month of the spectral data.....	113
3.3 Results and Discussion	113
Redundant potential in the annual spectral data	113

Reference calibrations and loads	115
Uncertainties estimations for three resampling methods and infrequent sampling	123
3.4 Conclusions.....	138
3.5 Acknowledgements.....	141
3.6 References.....	141
Chapter 4: High resolution hydrochemical dynamics to reveal biogeochemical processes in an agricultural coastal plain watershed	147
4.1 Introduction.....	147
Objectives	149
4.2 Methods.....	150
Site description.....	150
Flow measurement	153
Water samples collections and measurements	154
Laboratory analysis.....	155
Cumulative loads, annual and seasonal flow-weighted concentration calculations	155
Hysteresis index (HI) calculation for concentration and flow rate and statistical analysis	157
4.3 Results and Discussion	160
Typical coastal plain concentration and load levels	160
General dilution and concentration effects during storm events in the Claridge Canal	163
Hysteresis index analyses confirm differences in lags between flow and concentration peaks and troughs.....	167
Proposed mechanisms to explain event scale concentration patterns	174
Odd DOC concentration and load patterns at the MD reveal exchanges with the Little River.....	177
Double-mass curves reveal season scale dynamics drivers for NO ₃ -N and DOC exports	179
4.4 Conclusions.....	184
4.5 Acknowledgements.....	186
4.6 References.....	186
Chapter 5: General Conclusion	194
Ability to create water quality rating curves for UV-Vis spectrophotometers	196
Reduce errors on measuring loads with using UV-Vis spectrophotometers and the most robust sampling method for affordable number of calibration points	197

Costs comparisons between continuous monitoring and stream restoration projects ..	199
Biogeochemical process in an agricultural coastal plain watershed.....	201
Comparisons of nutrient dynamics between lowland coastal plain watershed and other watersheds.....	202
5.2 References.....	206
APPENDICES	210
Appendix A:	211
A.1 The GIS sources for Figure 1.1	211
Appendix B: Uncertainties estimations for annual loads for different stream solutes with bootstrap sampling.....	212
Appendix C: Uncertainties estimations for annual loads for different stream solutes with random subset sampling.....	226
Appendix D: Uncertainties estimations for annual loads for different stream solutes with stratified sampling.....	266
Appendix E: Uncertainties estimations for annual loads for different stream solutes with infrequent sampling	293
Appendix F: Hysteresis Graphs for NO ₃ -N and DOC.....	384
F.1 Hysteresis plots at UP station	384
F.2 Hysteresis plots at MD station.....	402
F.3 Hysteresis plots at DN station.....	420
Appendix G: Summary of Hysteresis Index.....	438
Appendix H: Tracer Experiment	439
H.1 Introduction.....	439
H.2 Methods.....	439
H.3 Preliminary Results and Data Analysis.....	443
H.4 References	447
Appendix I: Extracellular coenzyme activity experiment	449
I.1 Introduction	449
I.2 Methods	450
I.3 Preliminary Results and Data Analysis	453
I.4 References	458

LIST OF TABLES

Table 2.1 Summary of the degradation samples results	33
Table 2.2 Summary of the laboratory analyses for discrete samples (Units: mg/L; concentrations with significant ‘degradation’ not included)	36
Table 2.3 Summary of linear regressions between Global Calibration and discrete samples results for NO ₃ -N and DOC among the three monitoring stations	38
Table 2.4 Summary of PLSR calibration for NO ₃ -N, NH ₄ -N, TDN, TKN, DOC TP, and PO ₄ -P at the three stations (UP, MD, DN) (Units for RMSE: mg/L).....	48
Table 2.5 Summary of PLSR calibration for TSS at the three stations (UP, MD, DN)	50
Table 2.6 Differences in nitrate and DOC loads computed using concentrations from the PAR files, those predicted using PLSR, from local calibration.....	69
Table 2.7 Summary of NO ₃ -N cumulative loads for Manual method and Semi-Automatic method.....	85
Table 3.1 Methods applied to calculate the annual loads in this research (Adapted from Johnes, 2007; Birgand et al., 2010; Cassidy and Jordan, 2011)	112
Table 3.2 Summary of the laboratory analysis, PLSR predicted results and reference annual loads for NO ₃ -N, TDN, TKN, DOC TP, and TSS at UP and DN	117
Table 3.3 Uncertainty estimation for NO ₃ -N annual loads (e_{avg} and e_5 to e_{95} ; presented in the percentage as relative difference of the reference loads) for four sampling methods (bootstrap, random subset, stratified and infrequent sampling) with different number of samples and sampling intervals	126
Table 3.4 Uncertainty estimation for TDN annual loads (e_{avg} and e_5 to e_{95} ; presented in the percentage as relative difference of the reference loads) for four sampling methods (bootstrap, random subset, stratified and infrequent sampling) with different number of samples and sampling intervals	127
Table 3.5 Uncertainty estimation for TKN annual loads (e_{avg} and e_5 to e_{95} ; presented in the percentage as relative difference of the reference loads) for three sampling methods (bootstrap, random subset and infrequent sampling) with different number of samples and sampling intervals	128
Table 3.6 Uncertainty estimation for DOC annual loads (e_{avg} and e_5 to e_{95} ; presented in the percentage as relative difference of the reference loads) for four sampling methods (bootstrap, random subset, stratified and infrequent sampling) with different number of samples and sampling intervals	129
Table 3.7 Uncertainty estimation for TP annual loads (e_{avg} and e_5 to e_{95} ; presented in the percentage as relative difference of the reference loads) for three sampling methods (bootstrap, random subset and infrequent sampling) with different number of samples and sampling intervals	130

Table 3.8 Uncertainty estimation for TSS annual loads with PLSR prediction (e_{avg} and e_5 to e_{95} ; presented in the percentage as relative difference of the reference loads) for three sampling methods (bootstrap, random subset and infrequent sampling) with different number of samples and sampling intervals	131
Table 3.9 Uncertainty estimation for TSS annual loads with Turbidity prediction (e_{avg} and e_5 to e_{95} ; presented in the percentage as relative difference of the reference loads) for three sampling methods (bootstrap, random subset and infrequent sampling) with different number of samples and sampling intervals	132
Table 3.10 Summary of calculated uncertainties for all parameters, stations and method leading to lowest uncertainty	136
Table 4.1 The length of tributaries in the Clairidge Canal	152
Table 4.2 Vegetation cover, land use, and soil properties in the studied watersheds	153
Table 4.3 Summary of Hysteresis Indices and trajectory directions (C: Clockwise, AC: Anti-Clockwise) for observed storm events for NO_3-N and DOC in the Claridge Canal (NA: concentration data not applicable; the storm with bold font and star symbol is used for estimating the spatial effects).....	171
Table 4.4 Flow-weighted concentrations of NO_3-N and DOC (mg/L) for different phases during entire monitoring period (2013-12-12 to 2015-03-18) at UP station	181
Table 5.1 Costs analysis for the stream restoration projects (Unit: \$/ft.)	201
Table 5.2 Summary of nitrate and DOC dynamics for the Claridge Canal and other research	205
Table G.1 Summary of number of storm events with trajectory direction (C: Clockwise, AC: Anti-Clockwise) for NO_3-N and DOC in different seasons in the Claridge Canal	438
Table G.2 Summary of number of mutual storm events with trajectory direction (C: Clockwise, AC: Anti-Clockwise) for NO_3-N and DOC at the three stations in the Claridge Canal (n = 22 for each station).....	438
Table H.1. The installment of monitoring equipment at the injection site and nine monitoring stations	442
Table H.2 Nutrient uptake parameters at Station C in the Claridge Canal	444
Table I.1 Ecoenzymes, relative fluorescent model substrate, and biological function in this study	453

LIST OF FIGURES

Figure 2.1 Three monitoring stations along the Claridge Canal in Goldsboro, North Carolina (I: Contributing watershed area for UP station; I and II: Contributing watershed area for MD station; I, II, and III: Contributing watershed area for DN station)	16
Figure 2.2 Schematic of a trapezoidal flume cross-section, showing the Doppler velocity meter, the virtual vertical column and the location of the manual velocity measurement points (marked as +; Modified from Birgand, 2000).....	18
Figure 2.3 Schematic of the elements of the water quality monitoring system (not in the scale; numbers detailed in text; Modified from Etheridge et al., (2013)).....	20
Figure 2.4 An example of flow results at UP (blue line), MD (red line), DN (green line) from February 20 to March 10 in 2015.	26
Figure 2.5 Manual mean velocity versus Doppler sensor velocity at the three stations. (a) UP; (b) MD; (c) DN.....	30
Figure 2.6 The linear regression relationship between Global Calibration and Discrete Samples for NO ₃ -N at UP. (Black solid line: 1 to 1 line; Black dash line: Regression line) .	37
Figure 2.7 The linear regression relationship between Global Calibration and Discrete Samples for DOC at UP. (Black solid line: 1 to 1 line; Black dash line: Regression line)	38
Figure 2.8 RMSEP (mg/L) and number of components from PLSR output for NO ₃ -N at UP in spring and summer.....	40
Figure 2.9 Regression relationships between lab measured NO ₃ -N and PLSR predicted NO ₃ -N from PLSR calibrations at UP in spring and summer with 4 and 9 components. (a) 4 components; (b) 9 components.	41
Figure 2.10 Continuous NO ₃ -N concentrations from PLSR calibration with 4 components (black line), NO ₃ -N concentrations from Discrete Samples (red dots), Flow rate (blue line) at UP on July 30-August 7 in 2014.....	42
Figure 2.11 Continuous NO ₃ -N concentrations from PLSR calibration with 9 components (black line), NO ₃ -N concentrations from Discrete Samples (red dots), Flow rate (blue line) at UP on July 30-August 7 in 2014.....	43
Figure 2.12 Regression relationships between measured NO ₃ -N and predicted NO ₃ -N from PLSR calibrations. (a) UP in spring and summer; (b) UP in fall and winter; (c) MD in spring and summer; (d) MD in fall and winter; (e) DN in spring and summer; (f) DN in fall and winter.	51
Figure 2.13 Regression relationships between measured NH ₄ -N and predicted NH ₄ -N from PLSR calibrations. (a) UP in spring and summer; (b) UP in fall and winter; (c) MD in spring and summer; (d) MD in fall and winter; (e) DN in spring and summer; (f) DN in fall and winter.	53

Figure 2.14 Regression relationships between measured TDN and predicted TDN from PLSR calibrations. (a) UP in spring and summer; (b) UP in fall and winter; (c) MD in spring and summer; (d) MD in fall and winter; (e) DN in spring and summer; (f) DN in fall and winter. 55

Figure 2.15 Regression relationships between measured TKN and predicted TKN from PLSR calibrations. (a) UP in spring and summer; (b) UP in fall and winter; (c) MD in spring and summer; (d) MD in fall and winter; (e) DN in spring and summer; (f) DN in fall and winter. 57

Figure 2.16 Regression relationships between measured DOC and predicted DOC from PLSR calibrations. (a) UP in spring and summer; (b) UP in fall and winter; (c) MD in spring and summer; (d) MD in fall and winter; (e) DN in spring and summer; (f) DN in fall and winter. 59

Figure 2.17 Regression relationships between measured TP and predicted TP from PLSR calibrations. (a) UP in spring and summer; (b) UP in fall and winter; (c) MD in spring and summer; (d) MD in fall and winter; (e) DN in spring and summer; (f) DN in fall and winter. 61

Figure 2.18 Regression relationships between measured PO₄-P and predicted PO₄-P from PLSR calibrations. (a) UP in spring and summer; (b) UP in fall and winter; (c) MD in spring and summer; (d) MD in fall and winter; (e) DN in spring and summer; (f) DN in fall and winter. 63

Figure 2.19 Regression relationships between measured TSS and predicted TSS from PLSR calibrations. (a) UP; (b) MD; (c) DN..... 65

Figure 2.20 The regression relationship for TSS concentrations from discrete samples and turbidity prediction at the three stations. (a) UP; (b) MD; (c) DN. 67

Figure 2.21 An example of “stray” data points because of biofouling. Continuous NO₃-N concentrations from PLSR calibration (black line), NO₃-N concentrations from Discrete Samples (red dots), Flow rate (blue line), and Field visit date (gray vertical line) at UP on February 5-20 in 2014..... 74

Figure 2.22 Continuous NO₃-N concentrations from PLSR calibration with correction by using AQUARIUS software (black line), NO₃-N concentrations from Discrete Samples (red dots), Flow rate (blue line), and Field visit date (gray vertical line) at UP on February 5-20 in 2014..... 75

Figure 2.23 An example of noisy points because of malfunctioning of the monitoring system. Continuous NO₃-N concentrations from PLSR calibration (black line), NO₃-N concentrations from Discrete Samples (red dots), Flow rate (blue line), and Field visit date (gray vertical line) at UP on April 18-25 in 2014..... 76

Figure 2.24 Continuous NO₃-N concentrations from PLSR calibration after removing of noisy points by using AQUARIUS software (black line), NO₃-N concentrations from

Discrete Samples (red dots), Flow rate (blue line), and Field visit date (gray vertical line) at UP on April 18-25 in 2014.....	77
Figure 2.25 An example of missing flow data because of malfunctioning for the monitoring system. Continuous flow rate at UP (blue line) and MD (red line) from November 23 to December 3 in 2014.....	78
Figure 2.26 The regression relationship for flow between UP and MD on November 23-26 in 2014.....	79
Figure 2.27 Continuous flow (blue solid line) at UP, predicted flow (blue dashed line) at UP, and continuous flow (red line) at MD from November 23 to December 3 in 2014.	79
Figure 2.28 An example of missing concentration data because of malfunctioning for the monitoring system. Continuous NO ₃ -N concentrations from PLSR calibration (black line), NO ₃ -N concentrations from Discrete Samples (red dots), Flow rate (blue line), and Field visit date (gray vertical line) at UP on February 12-26 in 2014.	82
Figure 2.29 Continuous NO ₃ -N concentrations from PLSR calibration (solid black line), continuous NO ₃ -N concentrations by using Manual method to fill the missing data (dashed black line), NO ₃ -N concentrations from Discrete Samples (red dots), Flow rate (blue line), and Field visit date (gray vertical line) at UP on February 12-26 in 2014.	83
Figure 2.30 The regression relationship between flow rate and NO ₃ -N at UP on February 12-15.....	84
Figure 2.31 Continuous NO ₃ -N concentrations from PLSR calibration (solid black line), continuous NO ₃ -N concentrations by using Semi-Automatic method to fill the missing data (dashed black line), NO ₃ -N concentrations from Discrete Samples (red dots), Flow rate (blue line), and Field visit date (gray vertical line) at UP on February 12-26 in 2014.	85
Figure 3.1 Three monitoring stations along the Claridge Canal in Goldsboro, North Carolina (I: Contributing watershed area for UP station; I and II: Contributing watershed area for MD station; I, II, and III: Contributing watershed area for DN station)	102
Figure 3.2 The source of annual spectral data including with (w/) and without (w/o) storm events presented in percentage at UP (Original: the initial spectral data; Patch from different years: the missing spectral data was filled from the same months in different years; Redundant: the missing spectral data was filled from different months).	114
Figure 3.3 The source of annual spectral data including with (w/) and without (w/o) storm events presented in percentage at DN (Original: the initial spectral data; Patch from different years: the missing spectral data was filled from the same months in different years; Redundant: the missing spectral data was filled from different months).	115
Figure 3.4: Regression relationship between measured and predicted NO ₃ -N (A and D), TDN (B and E), TKN (C and F) using PLSR calibration with original calibration points at UP (top row) and DN (bottom row).	119

Figure 3.5: Regression relationship between measured and predicted DOC (A and D), TP (B and E), TSS (C and F) using PLSR calibration with original calibration points at UP (top row) and DN (bottom row).	120
Figure 3.6: Regression relationship between measured and predicted TSS using Turbidity predictions with original calibration points at UP (A) and DN (B).	121
Figure 3.7 Cumulative probability of occurrence for NO ₃ -N, TDN and TKN concentrations at UP station.....	121
Figure 3.8 Cumulative probability of occurrence for NO ₃ -N, TDN and TKN concentrations at DN station	122
Figure 3.9 Cumulative probability of occurrence for DOC concentrations at UP and DN stations	122
Figure 3.10 Cumulative probability of occurrence for TP concentrations at UP and DN stations	123
Figure 3.11 Cumulative probability of occurrence for TSS concentrations at UP and DN stations	123
Figure 3.12: Distribution of uncertainties of annual loads for nitrate (top row; A and B) and DOC (bottom row; C and D) corresponding to 24 stratified (left column; A and C) and random (B and D) samples used to create the calibrations	125
Figure 4.1 Three monitoring stations along the Claridge Canal in Goldsboro, North Carolina (I: Contributing watershed area for UP station; I and II: Contributing watershed area for MD station; I, II, and III: Contributing watershed area for DN station)	152
Figure 4.2 Example of the C vs Q relationship during an event (not to scale) to demonstrate the calculation for hysteresis index for a clockwise loop (Black circle: The normalized observed concentrations [$C_{i, normalized}$] as a function of normalized flow rate [$Q_{i, normalized}$], red diamond: the calculated concentrations with the linear interpolation between two observed points for the rising limb [$C_{j, RL}$] and the falling limb [$C_{j, FL}$])	160
Figure 4.3 NO ₃ -N Cumulative loads (kg/ha) over entire monitoring period (2013-12-12 to 2015-03-18) at all stations in the Claridge Canal	162
Figure 4.4 DOC Cumulative loads (kg/ha) over entire monitoring period (2013-12-12 to 2015-03-18) at all stations in the Claridge Canal	163
Figure 4.5 Continuous and discrete NO ₃ -N and DOC with flow rate from January 10 to January 20 at UP in winter 2014.....	164
Figure 4.6 Continuous and discrete NO ₃ -N and DOC with flow rate from July 14 to August 08 at UP in summer 2014.....	165
Figure 4.7 Hysteresis patterns observed for nitrate (A and B) and DOC (C and D) showing clockwise (A and D) and anticlockwise patterns (B and C) for events #4 (2013-12-17) and #14 (2014-02-25) at the UP station.....	168

Figure 4.8 Characterization of hydrodynamic C-Q patterns during events. Positive/negative HI suggest clock/anticlockwise patterns, and positive/negative slope suggest concentration/dilution effects..... 169

Figure 4.9 Hypothetical hydraulic and nutrient export functioning in the artificially drained soils of the coastal plain during an event (Left: nitrate: pink line; DOC: brown line; flow: blue line. Right: water table: dark blue lines; organic horizon of soil: brown; near stream zone: beige. Number in green circles represent the change of the water table in order during a storm event) 175

Figure 4.10 Continuous and discrete of NO₃-N with flow rate from August 11 to August 22 in 2014 at UP and DN..... 178

Figure 4.11 Continuous and discrete of DOC with flow rate from August 11 to August 22 in 2014 at UP and DN..... 179

Figure 4.12 Cumulative loads (kg/ha) of NO₃-N and DOC as a function of cumulative flow volumes over entire monitoring period (2013-12-12 to 2015-03-18) with 5 phases at UP station (The vertical lines labeled as season represented the beginning date of the certain season.)..... 180

Figure 4.13 Percentage of differences for flow-weighted concentrations between each phase and the entire monitoring period (2013-12-12 to 2015-03-18) for NO₃-N and DOC at UP station (0% represents there is no difference for flow-weighted concentration between each phase and the entire monitoring period) 182

Figure B.1 Distribution of uncertainties estimation presented in the percentage as relative difference of reference annual load expressed as histogram for NO₃-N (uncertainties with the bias [e_{avg} , red solid line or e_{50} , black dash line] and precision [e_5 and e_{95} , blue dash lines, are precision limits of 5th and 95th percentiles, respectively) with bootstrap (BS) sampling at UP. 212

Figure B.2 Distribution of uncertainties estimation presented in the percentage as relative difference of reference annual load expressed as histogram for NO₃-N (uncertainties with the bias [e_{avg} , red solid line or e_{50} , black dash line] and precision [e_5 and e_{95} , blue dash lines, are precision limits of 5th and 95th percentiles, respectively) with bootstrap (BS) sampling at DN. 213

Figure B.3 Distribution of uncertainties estimation presented in the percentage as relative difference of reference annual load expressed as histogram for TDN (uncertainties with the bias [e_{avg} , red solid line or e_{50} , black dash line] and precision [e_5 and e_{95} , blue dash lines, are precision limits of 5th and 95th percentiles, respectively) with bootstrap (BS) sampling at UP. 214

Figure B.4 Distribution of uncertainties estimation presented in the percentage as relative difference of reference annual load expressed as histogram for TDN (uncertainties with the bias [e_{avg} , red solid line or e_{50} , black dash line] and precision [e_5 and e_{95} , blue dash lines, are

precision limits of 5 th and 95 th percentiles, respectively) with bootstrap (BS) sampling at TDN.	215
Figure B.5 Distribution of uncertainties estimation presented in the percentage as relative difference of reference annual load expressed as histogram for TKN (uncertainties with the bias [e_{avg} , red solid line or e_{50} , black dash line] and precision [e_5 and e_{95} , blue dash lines, are precision limits of 5 th and 95 th percentiles, respectively) with bootstrap (BS) sampling at UP.	216
Figure B.6 Distribution of uncertainties estimation presented in the percentage as relative difference of reference annual load expressed as histogram for TKN (uncertainties with the bias [e_{avg} , red solid line or e_{50} , black dash line] and precision [e_5 and e_{95} , blue dash lines, are precision limits of 5 th and 95 th percentiles, respectively) with bootstrap (BS) sampling at DN.	217
Figure B.7 Distribution of uncertainties estimation presented in the percentage as relative difference of reference annual load expressed as histogram for DOC (uncertainties with the bias [e_{avg} , red solid line or e_{50} , black dash line] and precision [e_5 and e_{95} , blue dash lines, are precision limits of 5 th and 95 th percentiles, respectively) with bootstrap (BS) sampling at UP..	218
Figure B.8 Distribution of uncertainties estimation presented in the percentage as relative difference of reference annual load expressed as histogram for DOC (uncertainties with the bias [e_{avg} , red solid line or e_{50} , black dash line] and precision [e_5 and e_{95} , blue dash lines, are precision limits of 5 th and 95 th percentiles, respectively) with bootstrap (BS) sampling at DN.	219
Figure B.9 Distribution of uncertainties estimation presented in the percentage as relative difference of reference annual load expressed as histogram for TP (uncertainties with the bias [e_{avg} , red solid line or e_{50} , black dash line] and precision [e_5 and e_{95} , blue dash lines, are precision limits of 5 th and 95 th percentiles, respectively) with bootstrap (BS) sampling at UP.	220
Figure B.10 Distribution of uncertainties estimation presented in the percentage as relative difference of reference annual load expressed as histogram for TP (uncertainties with the bias [e_{avg} , red solid line or e_{50} , black dash line] and precision [e_5 and e_{95} , blue dash lines, are precision limits of 5 th and 95 th percentiles, respectively) with bootstrap (BS) sampling at DN.	221
Figure B.11 Distribution of uncertainties estimation presented in the percentage as relative difference of reference annual load expressed as histogram for TSS with PLSR prediction (uncertainties with the bias [e_{avg} , red solid line or e_{50} , black dash line] and precision [e_5 and e_{95} , blue dash lines, are precision limits of 5 th and 95 th percentiles, respectively) with bootstrap (BS) sampling at UP.	222
Figure B.12 Distribution of uncertainties estimation presented in the percentage as relative difference of reference annual load expressed as histogram for TSS with PLSR prediction (uncertainties with the bias [e_{avg} , red solid line or e_{50} , black dash line] and precision [e_5 and	

e ₉₅ , blue dash lines, are precision limits of 5 th and 95 th percentiles, respectively) with bootstrap (BS) sampling at DN.....	223
Figure B.13 Distribution of uncertainties estimation presented in the percentage as relative difference of reference annual load expressed as histogram for TSS with Turbidity prediction (uncertainties with the bias [e _{avg} , red solid line or e ₅₀ , black dash line] and precision [e ₅ and e ₉₅ , blue dash lines, are precision limits of 5 th and 95 th percentiles, respectively) with bootstrap (BS) sampling at UP.	224
Figure B.14 Distribution of uncertainties estimation presented in the percentage as relative difference of reference annual load expressed as histogram for TSS with Turbidity prediction (uncertainties with the bias [e _{avg} , red solid line or e ₅₀ , black dash line] and precision [e ₅ and e ₉₅ , blue dash lines, are precision limits of 5 th and 95 th percentiles, respectively) with bootstrap (BS) sampling at DN.....	225
Figure C.1 Distribution of uncertainties estimation presented in the percentage as relative difference of reference annual load expressed as histogram for NO ₃ -N (uncertainties with the bias [e _{avg} , red solid line or e ₅₀ , black dash line] and precision [e ₅ and e ₉₅ , blue dash lines, are precision limits of 5 th and 95 th percentiles, respectively) with random (RD) subset sampling (n = 12) at UP.....	226
Figure C.2 Distribution of uncertainties estimation presented in the percentage as relative difference of reference annual load expressed as histogram for NO ₃ -N (uncertainties with the bias [e _{avg} , red solid line or e ₅₀ , black dash line] and precision [e ₅ and e ₉₅ , blue dash lines, are precision limits of 5 th and 95 th percentiles, respectively) with random (RD) subset sampling (n = 12) at DN.....	227
Figure C.3 Distribution of uncertainties estimation presented in the percentage as relative difference of reference annual load expressed as histogram for NO ₃ -N (uncertainties with the bias [e _{avg} , red solid line or e ₅₀ , black dash line] and precision [e ₅ and e ₉₅ , blue dash lines, are precision limits of 5 th and 95 th percentiles, respectively) with random (RD) subset sampling (n = 24) at UP.....	228
Figure C.4 Distribution of uncertainties estimation presented in the percentage as relative difference of reference annual load expressed as histogram for NO ₃ -N (uncertainties with the bias [e _{avg} , red solid line or e ₅₀ , black dash line] and precision [e ₅ and e ₉₅ , blue dash lines, are precision limits of 5 th and 95 th percentiles, respectively) with random (RD) subset sampling (n = 24) at DN.....	229
Figure C.5 Distribution of uncertainties estimation presented in the percentage as relative difference of reference annual load expressed as histogram for NO ₃ -N (uncertainties with the bias [e _{avg} , red solid line or e ₅₀ , black dash line] and precision [e ₅ and e ₉₅ , blue dash lines, are precision limits of 5 th and 95 th percentiles, respectively) with random (RD) subset sampling (n = 52) at UP.....	230
Figure C.6 Distribution of uncertainties estimation presented in the percentage as relative difference of reference annual load expressed as histogram for NO ₃ -N (uncertainties with the bias [e _{avg} , red solid line or e ₅₀ , black dash line] and precision [e ₅ and e ₉₅ , blue dash lines, are	

precision limits of 5th and 95th percentiles, respectively) with random (RD) subset sampling (n = 52) at DN. 231

Figure C.7 Distribution of uncertainties estimation presented in the percentage as relative difference of reference annual load expressed as histogram for TDN (uncertainties with the bias [e_{avg} , red solid line or e_{50} , black dash line] and precision [e_5 and e_{95} , blue dash lines, are precision limits of 5th and 95th percentiles, respectively) with random (RD) subset sampling (n = 12) at UP. 232

Figure C.8 Distribution of uncertainties estimation presented in the percentage as relative difference of reference annual load expressed as histogram for TDN (uncertainties with the bias [e_{avg} , red solid line or e_{50} , black dash line] and precision [e_5 and e_{95} , blue dash lines, are precision limits of 5th and 95th percentiles, respectively) with random (RD) subset sampling (n = 24) at UP. 233

Figure C.9 Distribution of uncertainties estimation presented in the percentage as relative difference of reference annual load expressed as histogram for TDN (uncertainties with the bias [e_{avg} , red solid line or e_{50} , black dash line] and precision [e_5 and e_{95} , blue dash lines, are precision limits of 5th and 95th percentiles, respectively) with random (RD) subset sampling (n = 52) at UP. 234

Figure C.10 Distribution of uncertainties estimation presented in the percentage as relative difference of reference annual load expressed as histogram for TDN (uncertainties with the bias [e_{avg} , red solid line or e_{50} , black dash line] and precision [e_5 and e_{95} , blue dash lines, are precision limits of 5th and 95th percentiles, respectively) with random (RD) subset sampling (n = 12) at DN. 235

Figure C.11 Distribution of uncertainties estimation presented in the percentage as relative difference of reference annual load expressed as histogram for TDN (uncertainties with the bias [e_{avg} , red solid line or e_{50} , black dash line] and precision [e_5 and e_{95} , blue dash lines, are precision limits of 5th and 95th percentiles, respectively) with random (RD) subset sampling (n = 24) at DN. 236

Figure C.12 Distribution of uncertainties estimation presented in the percentage as relative difference of reference annual load expressed as histogram for TDN (uncertainties with the bias [e_{avg} , red solid line or e_{50} , black dash line] and precision [e_5 and e_{95} , blue dash lines, are precision limits of 5th and 95th percentiles, respectively) with random (RD) subset sampling (n = 52) at DN. 237

Figure C.13 Distribution of uncertainties estimation presented in the percentage as relative difference of reference annual load expressed as histogram for TKN (uncertainties with the bias [e_{avg} , red solid line or e_{50} , black dash line] and precision [e_5 and e_{95} , blue dash lines, are precision limits of 5th and 95th percentiles, respectively) with random (RD) subset sampling (n = 12) at UP. 238

Figure C.14 Distribution of uncertainties estimation presented in the percentage as relative difference of reference annual load expressed as histogram for TKN (uncertainties with the bias [e_{avg} , red solid line or e_{50} , black dash line] and precision [e_5 and e_{95} , blue dash lines, are

precision limits of 5 th and 95 th percentiles, respectively) with random (RD) subset sampling (n = 24) at UP.....	239
Figure C.15 Distribution of uncertainties estimation presented in the percentage as relative difference of reference annual load expressed as histogram for TKN (uncertainties with the bias [e_{avg} , red solid line or e_{50} , black dash line] and precision [e_5 and e_{95} , blue dash lines, are precision limits of 5 th and 95 th percentiles, respectively) with random (RD) subset sampling (n = 52) at UP.....	240
Figure C.16 Distribution of uncertainties estimation presented in the percentage as relative difference of reference annual load expressed as histogram for TKN (uncertainties with the bias [e_{avg} , red solid line or e_{50} , black dash line] and precision [e_5 and e_{95} , blue dash lines, are precision limits of 5 th and 95 th percentiles, respectively) with random (RD) subset sampling (n = 12) at DN.....	241
Figure C.17 Distribution of uncertainties estimation presented in the percentage as relative difference of reference annual load expressed as histogram for TKN (uncertainties with the bias [e_{avg} , red solid line or e_{50} , black dash line] and precision [e_5 and e_{95} , blue dash lines, are precision limits of 5 th and 95 th percentiles, respectively) with random (RD) subset sampling (n = 24) at DN.....	242
Figure C.18 Distribution of uncertainties estimation presented in the percentage as relative difference of reference annual load expressed as histogram for TKN (uncertainties with the bias [e_{avg} , red solid line or e_{50} , black dash line] and precision [e_5 and e_{95} , blue dash lines, are precision limits of 5 th and 95 th percentiles, respectively) with random (RD) subset sampling (n = 52) at DN.....	243
Figure C.19 Distribution of uncertainties estimation presented in the percentage as relative difference of reference annual load expressed as histogram for DOC (uncertainties with the bias [e_{avg} , red solid line or e_{50} , black dash line] and precision [e_5 and e_{95} , blue dash lines, are precision limits of 5 th and 95 th percentiles, respectively) with random (RD) subset sampling (n = 12) at UP.....	244
Figure C.20 Distribution of uncertainties estimation presented in the percentage as relative difference of reference annual load expressed as histogram for DOC (uncertainties with the bias [e_{avg} , red solid line or e_{50} , black dash line] and precision [e_5 and e_{95} , blue dash lines, are precision limits of 5 th and 95 th percentiles, respectively) with random (RD) subset sampling (n = 24) at UP.....	245
Figure C.21 Distribution of uncertainties estimation presented in the percentage as relative difference of reference annual load expressed as histogram for DOC (uncertainties with the bias [e_{avg} , red solid line or e_{50} , black dash line] and precision [e_5 and e_{95} , blue dash lines, are precision limits of 5 th and 95 th percentiles, respectively) with random (RD) subset sampling (n = 52) at UP.....	246
Figure C.22 Distribution of uncertainties estimation presented in the percentage as relative difference of reference annual load expressed as histogram for DOC (uncertainties with the bias [e_{avg} , red solid line or e_{50} , black dash line] and precision [e_5 and e_{95} , blue dash lines, are	

precision limits of 5 th and 95 th percentiles, respectively) with random (RD) subset sampling (n = 12) at DN.....	247
Figure C.23 Distribution of uncertainties estimation presented in the percentage as relative difference of reference annual load expressed as histogram for DOC (uncertainties with the bias [e_{avg} , red solid line or e_{50} , black dash line] and precision [e_5 and e_{95} , blue dash lines, are precision limits of 5 th and 95 th percentiles, respectively) with random (RD) subset sampling (n = 24) at DN.....	248
Figure C.24 Distribution of uncertainties estimation presented in the percentage as relative difference of reference annual load expressed as histogram for DOC (uncertainties with the bias [e_{avg} , red solid line or e_{50} , black dash line] and precision [e_5 and e_{95} , blue dash lines, are precision limits of 5 th and 95 th percentiles, respectively) with random (RD) subset sampling (n = 52) at DN.....	249
Figure C.25 Distribution of uncertainties estimation presented in the percentage as relative difference of reference annual load expressed as histogram for TP (uncertainties with the bias [e_{avg} , red solid line or e_{50} , black dash line] and precision [e_5 and e_{95} , blue dash lines, are precision limits of 5 th and 95 th percentiles, respectively) with random (RD) subset sampling (n = 12) at UP.....	250
Figure C.26 Distribution of uncertainties estimation presented in the percentage as relative difference of reference annual load expressed as histogram for TP (uncertainties with the bias [e_{avg} , red solid line or e_{50} , black dash line] and precision [e_5 and e_{95} , blue dash lines, are precision limits of 5 th and 95 th percentiles, respectively) with random (RD) subset sampling (n = 24) at UP.....	251
Figure C.27 Distribution of uncertainties estimation presented in the percentage as relative difference of reference annual load expressed as histogram for TP (uncertainties with the bias [e_{avg} , red solid line or e_{50} , black dash line] and precision [e_5 and e_{95} , blue dash lines, are precision limits of 5 th and 95 th percentiles, respectively) with random (RD) subset sampling (n = 52) at UP.....	252
Figure C.28 Distribution of uncertainties estimation presented in the percentage as relative difference of reference annual load expressed as histogram for TP (uncertainties with the bias [e_{avg} , red solid line or e_{50} , black dash line] and precision [e_5 and e_{95} , blue dash lines, are precision limits of 5 th and 95 th percentiles, respectively) with random (RD) subset sampling (n = 12) at DN.....	253
Figure C.29 Distribution of uncertainties estimation presented in the percentage as relative difference of reference annual load expressed as histogram for TP (uncertainties with the bias [e_{avg} , red solid line or e_{50} , black dash line] and precision [e_5 and e_{95} , blue dash lines, are precision limits of 5 th and 95 th percentiles, respectively) with random (RD) subset sampling (n = 24) at DN.....	254
Figure C.30 Distribution of uncertainties estimation presented in the percentage as relative difference of reference annual load expressed as histogram for TP (uncertainties with the bias [e_{avg} , red solid line or e_{50} , black dash line] and precision [e_5 and e_{95} , blue dash lines, are	

precision limits of 5th and 95th percentiles, respectively) with random (RD) subset sampling (n = 52) at DN. 255

Figure C.31 Distribution of uncertainties estimation presented in the percentage as relative difference of reference annual load expressed as histogram for TSS with PLSR prediction (uncertainties with the bias [e_{avg} , red solid line or e_{50} , black dash line] and precision [e_5 and e_{95} , blue dash lines, are precision limits of 5th and 95th percentiles, respectively) with random (RD) subset sampling (n = 12) at UP. 256

Figure C.32 Distribution of uncertainties estimation presented in the percentage as relative difference of reference annual load expressed as histogram for TSS with PLSR prediction (uncertainties with the bias [e_{avg} , red solid line or e_{50} , black dash line] and precision [e_5 and e_{95} , blue dash lines, are precision limits of 5th and 95th percentiles, respectively) with random (RD) subset sampling (n = 24) at UP. 257

Figure C.33 Distribution of uncertainties estimation presented in the percentage as relative difference of reference annual load expressed as histogram for TSS with PLSR prediction (uncertainties with the bias [e_{avg} , red solid line or e_{50} , black dash line] and precision [e_5 and e_{95} , blue dash lines, are precision limits of 5th and 95th percentiles, respectively) with random (RD) subset sampling (n = 52) at UP. 258

Figure C.34 Distribution of uncertainties estimation presented in the percentage as relative difference of reference annual load expressed as histogram for TSS with PLSR prediction (uncertainties with the bias [e_{avg} , red solid line or e_{50} , black dash line] and precision [e_5 and e_{95} , blue dash lines, are precision limits of 5th and 95th percentiles, respectively) with random (RD) subset sampling (n = 12) at DN. 259

Figure C.35 Distribution of uncertainties estimation presented in the percentage as relative difference of reference annual load expressed as histogram for TSS with PLSR prediction (uncertainties with the bias [e_{avg} , red solid line or e_{50} , black dash line] and precision [e_5 and e_{95} , blue dash lines, are precision limits of 5th and 95th percentiles, respectively) with random (RD) subset sampling (n = 24) at DN. 260

Figure C.36 Distribution of uncertainties estimation presented in the percentage as relative difference of reference annual load expressed as histogram for TSS with Turbidity prediction (uncertainties with the bias [e_{avg} , red solid line or e_{50} , black dash line] and precision [e_5 and e_{95} , blue dash lines, are precision limits of 5th and 95th percentiles, respectively) with random (RD) subset sampling (n = 12) at UP. 261

Figure C.37 Distribution of uncertainties estimation presented in the percentage as relative difference of reference annual load expressed as histogram for TSS with Turbidity prediction (uncertainties with the bias [e_{avg} , red solid line or e_{50} , black dash line] and precision [e_5 and e_{95} , blue dash lines, are precision limits of 5th and 95th percentiles, respectively) with random (RD) subset sampling (n = 24) at UP. 262

Figure C.38 Distribution of uncertainties estimation presented in the percentage as relative difference of reference annual load expressed as histogram for TSS with Turbidity prediction (uncertainties with the bias [e_{avg} , red solid line or e_{50} , black dash line] and precision [e_5 and

e_{95} , blue dash lines, are precision limits of 5th and 95th percentiles, respectively) with random (RD) subset sampling (n = 52) at UP..... 263

Figure C.39 Distribution of uncertainties estimation presented in the percentage as relative difference of reference annual load expressed as histogram for TSS with Turbidity prediction (uncertainties with the bias [e_{avg} , red solid line or e_{50} , black dash line] and precision [e_5 and e_{95} , blue dash lines, are precision limits of 5th and 95th percentiles, respectively) with random (RD) subset sampling (n = 12) at DN. 264

Figure C.40 Distribution of uncertainties estimation presented in the percentage as relative difference of reference annual load expressed as histogram for TSS with Turbidity prediction (uncertainties with the bias [e_{avg} , red solid line or e_{50} , black dash line] and precision [e_5 and e_{95} , blue dash lines, are precision limits of 5th and 95th percentiles, respectively) with random (RD) subset sampling (n = 24) at DN. 265

Figure D.1 Distribution of uncertainties estimation presented in the percentage as relative difference of reference annual load expressed as histogram for NO₃-N (uncertainties with the bias [e_{avg} , red solid line or e_{50} , black dash line] and precision [e_5 and e_{95} , blue dash lines, are precision limits of 5th and 95th percentiles, respectively) with stratified sampling (2B, n = 12) at UP..... 266

Figure D.2 Distribution of uncertainties estimation presented in the percentage as relative difference of reference annual load expressed as histogram for NO₃-N (uncertainties with the bias [e_{avg} , red solid line or e_{50} , black dash line] and precision [e_5 and e_{95} , blue dash lines, are precision limits of 5th and 95th percentiles, respectively) with stratified sampling (2B, n = 12) at DN. 267

Figure D.3 Distribution of uncertainties estimation presented in the percentage as relative difference of reference annual load expressed as histogram for NO₃-N (uncertainties with the bias [e_{avg} , red solid line or e_{50} , black dash line] and precision [e_5 and e_{95} , blue dash lines, are precision limits of 5th and 95th percentiles, respectively) with stratified sampling (2B, n = 24) at UP..... 268

Figure D.4 Distribution of uncertainties estimation presented in the percentage as relative difference of reference annual load expressed as histogram for NO₃-N (uncertainties with the bias [e_{avg} , red solid line or e_{50} , black dash line] and precision [e_5 and e_{95} , blue dash lines, are precision limits of 5th and 95th percentiles, respectively) with stratified sampling (2B, n = 24) at DN. 269

Figure D.5 Distribution of uncertainties estimation presented in the percentage as relative difference of reference annual load expressed as histogram for NO₃-N (uncertainties with the bias [e_{avg} , red solid line or e_{50} , black dash line] and precision [e_5 and e_{95} , blue dash lines, are precision limits of 5th and 95th percentiles, respectively) with stratified sampling (2B, n = 30) at UP..... 270

Figure D.6 Distribution of uncertainties estimation presented in the percentage as relative difference of reference annual load expressed as histogram for NO₃-N (uncertainties with the bias [e_{avg} , red solid line or e_{50} , black dash line] and precision [e_5 and e_{95} , blue dash lines, are

precision limits of 5th and 95th percentiles, respectively) with stratified sampling (3B, n = 30) at UP..... 271

Figure D.7 Distribution of uncertainties estimation presented in the percentage as relative difference of reference annual load expressed as histogram for NO₃-N (uncertainties with the bias [e_{avg} , red solid line or e_{50} , black dash line] and precision [e_5 and e_{95} , blue dash lines, are precision limits of 5th and 95th percentiles, respectively) with stratified sampling (5B, n = 30) at UP..... 272

Figure D.8 Distribution of uncertainties estimation presented in the percentage as relative difference of reference annual load expressed as histogram for NO₃-N (uncertainties with the bias [e_{avg} , red solid line or e_{50} , black dash line] and precision [e_5 and e_{95} , blue dash lines, are precision limits of 5th and 95th percentiles, respectively) with stratified sampling (2B, n = 30) at DN..... 273

Figure D.9 Distribution of uncertainties estimation presented in the percentage as relative difference of reference annual load expressed as histogram for NO₃-N (uncertainties with the bias [e_{avg} , red solid line or e_{50} , black dash line] and precision [e_5 and e_{95} , blue dash lines, are precision limits of 5th and 95th percentiles, respectively) with stratified sampling (2B, n = 52) at UP..... 274

Figure D.10 Distribution of uncertainties estimation presented in the percentage as relative difference of reference annual load expressed as histogram for NO₃-N (uncertainties with the bias [e_{avg} , red solid line or e_{50} , black dash line] and precision [e_5 and e_{95} , blue dash lines, are precision limits of 5th and 95th percentiles, respectively) with stratified sampling (2B, n = 52) at DN..... 275

Figure D.11 Distribution of uncertainties estimation presented in the percentage as relative difference of reference annual load expressed as histogram for NO₃-N (uncertainties with the bias [e_{avg} , red solid line or e_{50} , black dash line] and precision [e_5 and e_{95} , blue dash lines, are precision limits of 5th and 95th percentiles, respectively) with stratified sampling (3B, n = 30) at DN..... 276

Figure D.12 Distribution of uncertainties estimation presented in the percentage as relative difference of reference annual load expressed as histogram for TDN (uncertainties with the bias [e_{avg} , red solid line or e_{50} , black dash line] and precision [e_5 and e_{95} , blue dash lines, are precision limits of 5th and 95th percentiles, respectively) with stratified sampling (2B, n = 12) at UP..... 277

Figure D.13 Distribution of uncertainties estimation presented in the percentage as relative difference of reference annual load expressed as histogram for TDN (uncertainties with the bias [e_{avg} , red solid line or e_{50} , black dash line] and precision [e_5 and e_{95} , blue dash lines, are precision limits of 5th and 95th percentiles, respectively) with stratified sampling (2B, n = 24) at UP..... 278

Figure D.14 Distribution of uncertainties estimation presented in the percentage as relative difference of reference annual load expressed as histogram for TDN (uncertainties with the bias [e_{avg} , red solid line or e_{50} , black dash line] and precision [e_5 and e_{95} , blue dash lines, are

precision limits of 5 th and 95 th percentiles, respectively) with stratified sampling (2B, n = 30) at UP.....	279
Figure D.15 Distribution of uncertainties estimation presented in the percentage as relative difference of reference annual load expressed as histogram for TDN (uncertainties with the bias [e_{avg} , red solid line or e_{50} , black dash line] and precision [e_5 and e_{95} , blue dash lines, are precision limits of 5 th and 95 th percentiles, respectively) with stratified sampling (2B, n = 52) at UP.....	280
Figure D.16 Distribution of uncertainties estimation presented in the percentage as relative difference of reference annual load expressed as histogram for TDN (uncertainties with the bias [e_{avg} , red solid line or e_{50} , black dash line] and precision [e_5 and e_{95} , blue dash lines, are precision limits of 5 th and 95 th percentiles, respectively) with stratified sampling (3B, n = 30) at UP.....	281
Figure D.17 Distribution of uncertainties estimation presented in the percentage as relative difference of reference annual load expressed as histogram for TDN (uncertainties with the bias [e_{avg} , red solid line or e_{50} , black dash line] and precision [e_5 and e_{95} , blue dash lines, are precision limits of 5 th and 95 th percentiles, respectively) with stratified sampling (5B, n = 30) at UP.....	282
Figure D.18 Distribution of uncertainties estimation presented in the percentage as relative difference of reference annual load expressed as histogram for TDN (uncertainties with the bias [e_{avg} , red solid line or e_{50} , black dash line] and precision [e_5 and e_{95} , blue dash lines, are precision limits of 5 th and 95 th percentiles, respectively) with stratified sampling (2B, n = 12) at DN.....	283
Figure D.19 Distribution of uncertainties estimation presented in the percentage as relative difference of reference annual load expressed as histogram for TDN (uncertainties with the bias [e_{avg} , red solid line or e_{50} , black dash line] and precision [e_5 and e_{95} , blue dash lines, are precision limits of 5 th and 95 th percentiles, respectively) with stratified sampling (2B, n = 24) at DN.....	284
Figure D.20 Distribution of uncertainties estimation presented in the percentage as relative difference of reference annual load expressed as histogram for TDN (uncertainties with the bias [e_{avg} , red solid line or e_{50} , black dash line] and precision [e_5 and e_{95} , blue dash lines, are precision limits of 5 th and 95 th percentiles, respectively) with stratified sampling (2B, n = 30) at DN.....	285
Figure D.21 Distribution of uncertainties estimation presented in the percentage as relative difference of reference annual load expressed as histogram for TDN (uncertainties with the bias [e_{avg} , red solid line or e_{50} , black dash line] and precision [e_5 and e_{95} , blue dash lines, are precision limits of 5 th and 95 th percentiles, respectively) with stratified sampling (2B, n = 52) at DN.....	286
Figure D.22 Distribution of uncertainties estimation presented in the percentage as relative difference of reference annual load expressed as histogram for TDN (uncertainties with the bias [e_{avg} , red solid line or e_{50} , black dash line] and precision [e_5 and e_{95} , blue dash lines, are	

precision limits of 5 th and 95 th percentiles, respectively) with stratified sampling (3B, n = 30) at DN.....	287
Figure D.23 Distribution of uncertainties estimation presented in the percentage as relative difference of reference annual load expressed as histogram for TDN (uncertainties with the bias [e_{avg} , red solid line or e_{50} , black dash line] and precision [e_5 and e_{95} , blue dash lines, are precision limits of 5 th and 95 th percentiles, respectively) with stratified sampling (5B, n = 30) at DN.....	288
Figure D.24 Distribution of uncertainties estimation presented in the percentage as relative difference of reference annual load expressed as histogram for DOC (uncertainties with the bias [e_{avg} , red solid line or e_{50} , black dash line] and precision [e_5 and e_{95} , blue dash lines, are precision limits of 5 th and 95 th percentiles, respectively) with stratified sampling (2B, n = 12) at UP.....	289
Figure D.25 Distribution of uncertainties estimation presented in the percentage as relative difference of reference annual load expressed as histogram for DOC (uncertainties with the bias [e_{avg} , red solid line or e_{50} , black dash line] and precision [e_5 and e_{95} , blue dash lines, are precision limits of 5 th and 95 th percentiles, respectively) with stratified sampling (2B, n = 24) at UP.....	290
Figure D.26 Distribution of uncertainties estimation presented in the percentage as relative difference of reference annual load expressed as histogram for DOC (uncertainties with the bias [e_{avg} , red solid line or e_{50} , black dash line] and precision [e_5 and e_{95} , blue dash lines, are precision limits of 5 th and 95 th percentiles, respectively) with stratified sampling (2B, n = 12) at DN.....	291
Figure D.27 Distribution of uncertainties estimation presented in the percentage as relative difference of reference annual load expressed as histogram for DOC (uncertainties with the bias [e_{avg} , red solid line or e_{50} , black dash line] and precision [e_5 and e_{95} , blue dash lines, are precision limits of 5 th and 95 th percentiles, respectively) with stratified sampling (2B, n = 24) at DN.....	292
Figure E.1 Comparison of uncertainties (e %) with the bias (e_{avg} or e_{50}) and precision (e_5 and e_{95} are precision limits of 5 th and 95 th percentiles, respectively) for NO ₃ -N load estimations as the function of sampling intervals with the algorithms (M5 and M6) at UP.....	293
Figure E.2 Comparison of uncertainties (e %) with the bias (e_{avg} or e_{50}) and precision (e_5 and e_{95} are precision limits of 5 th and 95 th percentiles, respectively) for NO ₃ -N load estimations as the function of sampling intervals with the algorithms (M5 and M6) at DN.....	293
Figure E.3 Comparison of uncertainties (e %) with the bias (e_{avg} or e_{50}) and precision (e_5 and e_{95} are precision limits of 5 th and 95 th percentiles, respectively) for TDN load estimations as the function of sampling intervals with the algorithms (M5 and M6) at UP.....	294
Figure E.4 Comparison of uncertainties (e %) with the bias (e_{avg} or e_{50}) and precision (e_5 and e_{95} are precision limits of 5 th and 95 th percentiles, respectively) for TDN load estimations as the function of sampling intervals with the algorithms (M5 and M6) at DN.....	294

Figure E.5 Comparison of uncertainties (e %) with the bias (e_{avg} or e_{50}) and precision (e_5 and e_{95} are precision limits of 5th and 95th percentiles, respectively) for TKN load estimations as the function of sampling intervals with the algorithms (M5 and M6) at UP 295

Figure E.6 Comparison of uncertainties (e %) with the bias (e_{avg} or e_{50}) and precision (e_5 and e_{95} are precision limits of 5th and 95th percentiles, respectively) for TKN load estimations as the function of sampling intervals with the algorithms (M5 and M6) at DN 295

Figure E.7 Comparison of uncertainties (e %) with the bias (e_{avg} or e_{50}) and precision (e_5 and e_{95} are precision limits of 5th and 95th percentiles, respectively) for DOC load estimations as the function of sampling intervals with the algorithms (M5 and M6) at UP 296

Figure E.8 Comparison of uncertainties (e %) with the bias (e_{avg} or e_{50}) and precision (e_5 and e_{95} are precision limits of 5th and 95th percentiles, respectively) for DOC load estimations as the function of sampling intervals with the algorithms (M5 and M6) at DN 296

Figure E.9 Comparison of uncertainties (e %) with the bias (e_{avg} or e_{50}) and precision (e_5 and e_{95} are precision limits of 5th and 95th percentiles, respectively) for TP load estimations as the function of sampling intervals with the algorithms (M5 and M6) at UP 297

Figure E.10 Comparison of uncertainties (e %) with the bias (e_{avg} or e_{50}) and precision (e_5 and e_{95} are precision limits of 5th and 95th percentiles, respectively) for TP load estimations as the function of sampling intervals with the algorithms (M5 and M6) at DN 297

Figure E.11 Comparison of uncertainties (e %) with the bias (e_{avg} or e_{50}) and precision (e_5 and e_{95} are precision limits of 5th and 95th percentiles, respectively) for TSS load estimations as the function of sampling intervals with the algorithms (M5 and M6) with PLSR prediction at UP 298

Figure E.12 Comparison of uncertainties (e %) with the bias (e_{avg} or e_{50}) and precision (e_5 and e_{95} are precision limits of 5th and 95th percentiles, respectively) for TSS load estimations as the function of sampling intervals with the algorithms (M5 and M6) with PLSR prediction at DN 298

Figure E.13 Comparison of uncertainties (e %) with the bias (e_{avg} or e_{50}) and precision (e_5 and e_{95} are precision limits of 5th and 95th percentiles, respectively) for TSS load estimations as the function of sampling intervals with the algorithms (M5 and M6) with Turbidity prediction at UP 299

Figure E.14 Comparison of uncertainties (e %) with the bias (e_{avg} or e_{50}) and precision (e_5 and e_{95} are precision limits of 5th and 95th percentiles, respectively) for TSS load estimations as the function of sampling intervals with the algorithms (M5 and M6) with Turbidity prediction at DN 299

Figure E.15 Distribution of uncertainties estimation presented in the percentage as relative difference of reference annual load expressed as histogram for NO₃-N (uncertainties with the bias [e_{avg} , red solid line or e_{50} , black dash line] and precision [e_5 and e_{95} , blue dash lines, are precision limits of 5th and 95th percentiles, respectively) with infrequent sampling (M5, weekly) at UP 300

Figure E.16 Distribution of uncertainties estimation presented in the percentage as relative difference of reference annual load expressed as histogram for NO₃-N (uncertainties with the bias [e_{avg} , red solid line or e_{50} , black dash line] and precision [e_5 and e_{95} , blue dash lines, are precision limits of 5th and 95th percentiles, respectively) with infrequent sampling (M6, weekly) at UP..... 301

Figure E.17 Distribution of uncertainties estimation presented in the percentage as relative difference of reference annual load expressed as histogram for NO₃-N (uncertainties with the bias [e_{avg} , red solid line or e_{50} , black dash line] and precision [e_5 and e_{95} , blue dash lines, are precision limits of 5th and 95th percentiles, respectively) with infrequent sampling (M5, biweekly) at UP..... 302

Figure E.18 Distribution of uncertainties estimation presented in the percentage as relative difference of reference annual load expressed as histogram for NO₃-N (uncertainties with the bias [e_{avg} , red solid line or e_{50} , black dash line] and precision [e_5 and e_{95} , blue dash lines, are precision limits of 5th and 95th percentiles, respectively) with infrequent sampling (M6, biweekly) at UP..... 303

Figure E.19 Distribution of uncertainties estimation presented in the percentage as relative difference of reference annual load expressed as histogram for NO₃-N (uncertainties with the bias [e_{avg} , red solid line or e_{50} , black dash line] and precision [e_5 and e_{95} , blue dash lines, are precision limits of 5th and 95th percentiles, respectively) with infrequent sampling (M5, monthly) at UP..... 304

Figure E.20 Distribution of uncertainties estimation presented in the percentage as relative difference of reference annual load expressed as histogram for NO₃-N (uncertainties with the bias [e_{avg} , red solid line or e_{50} , black dash line] and precision [e_5 and e_{95} , blue dash lines, are precision limits of 5th and 95th percentiles, respectively) with infrequent sampling (M6, monthly) at UP..... 305

Figure E.21 Distribution of uncertainties estimation presented in the percentage as relative difference of reference annual load expressed as histogram for NO₃-N (uncertainties with the bias [e_{avg} , red solid line or e_{50} , black dash line] and precision [e_5 and e_{95} , blue dash lines, are precision limits of 5th and 95th percentiles, respectively) with infrequent sampling (M5, weekly) at DN..... 306

Figure E.22 Distribution of uncertainties estimation presented in the percentage as relative difference of reference annual load expressed as histogram for NO₃-N (uncertainties with the bias [e_{avg} , red solid line or e_{50} , black dash line] and precision [e_5 and e_{95} , blue dash lines, are precision limits of 5th and 95th percentiles, respectively) with infrequent sampling (M6, weekly) at DN..... 307

Figure E.23 Distribution of uncertainties estimation presented in the percentage as relative difference of reference annual load expressed as histogram for NO₃-N (uncertainties with the bias [e_{avg} , red solid line or e_{50} , black dash line] and precision [e_5 and e_{95} , blue dash lines, are precision limits of 5th and 95th percentiles, respectively) with infrequent sampling (M5, biweekly) at DN..... 308

Figure E.24 Distribution of uncertainties estimation presented in the percentage as relative difference of reference annual load expressed as histogram for NO₃-N (uncertainties with the bias [e_{avg} , red solid line or e_{50} , black dash line] and precision [e_5 and e_{95} , blue dash lines, are precision limits of 5th and 95th percentiles, respectively) with infrequent sampling (M6, biweekly) at DN..... 309

Figure E.25 Distribution of uncertainties estimation presented in the percentage as relative difference of reference annual load expressed as histogram for NO₃-N (uncertainties with the bias [e_{avg} , red solid line or e_{50} , black dash line] and precision [e_5 and e_{95} , blue dash lines, are precision limits of 5th and 95th percentiles, respectively) with infrequent sampling (M5, monthly) at DN. 310

Figure E.26 Distribution of uncertainties estimation presented in the percentage as relative difference of reference annual load expressed as histogram for NO₃-N (uncertainties with the bias [e_{avg} , red solid line or e_{50} , black dash line] and precision [e_5 and e_{95} , blue dash lines, are precision limits of 5th and 95th percentiles, respectively) with infrequent sampling (M6, monthly) at DN. 311

Figure E.27 Distribution of uncertainties estimation presented in the percentage as relative difference of reference annual load expressed as histogram for TDN (uncertainties with the bias [e_{avg} , red solid line or e_{50} , black dash line] and precision [e_5 and e_{95} , blue dash lines, are precision limits of 5th and 95th percentiles, respectively) with infrequent sampling (M5, weekly) at UP..... 312

Figure E.28 Distribution of uncertainties estimation presented in the percentage as relative difference of reference annual load expressed as histogram for TDN (uncertainties with the bias [e_{avg} , red solid line or e_{50} , black dash line] and precision [e_5 and e_{95} , blue dash lines, are precision limits of 5th and 95th percentiles, respectively) with infrequent sampling (M6, weekly) at UP..... 313

Figure E.29 Distribution of uncertainties estimation presented in the percentage as relative difference of reference annual load expressed as histogram for TDN (uncertainties with the bias [e_{avg} , red solid line or e_{50} , black dash line] and precision [e_5 and e_{95} , blue dash lines, are precision limits of 5th and 95th percentiles, respectively) with infrequent sampling (M5, biweekly) at UP..... 314

Figure E.30 Distribution of uncertainties estimation presented in the percentage as relative difference of reference annual load expressed as histogram for TDN (uncertainties with the bias [e_{avg} , red solid line or e_{50} , black dash line] and precision [e_5 and e_{95} , blue dash lines, are precision limits of 5th and 95th percentiles, respectively) with infrequent sampling (M6, biweekly) at UP..... 315

Figure E.31 Distribution of uncertainties estimation presented in the percentage as relative difference of reference annual load expressed as histogram for TDN (uncertainties with the bias [e_{avg} , red solid line or e_{50} , black dash line] and precision [e_5 and e_{95} , blue dash lines, are precision limits of 5th and 95th percentiles, respectively) with infrequent sampling (M5, monthly) at UP..... 316

Figure E.32 Distribution of uncertainties estimation presented in the percentage as relative difference of reference annual load expressed as histogram for TDN (uncertainties with the bias [e_{avg} , red solid line or e_{50} , black dash line] and precision [e_5 and e_{95} , blue dash lines, are precision limits of 5th and 95th percentiles, respectively) with infrequent sampling (M6, monthly) at UP. 317

Figure E.33 Distribution of uncertainties estimation presented in the percentage as relative difference of reference annual load expressed as histogram for TDN (uncertainties with the bias [e_{avg} , red solid line or e_{50} , black dash line] and precision [e_5 and e_{95} , blue dash lines, are precision limits of 5th and 95th percentiles, respectively) with infrequent sampling (M5, weekly) at DN. 318

Figure E.34 Distribution of uncertainties estimation presented in the percentage as relative difference of reference annual load expressed as histogram for TDN (uncertainties with the bias [e_{avg} , red solid line or e_{50} , black dash line] and precision [e_5 and e_{95} , blue dash lines, are precision limits of 5th and 95th percentiles, respectively) with infrequent sampling (M6, weekly) at DN. 319

Figure E.35 Distribution of uncertainties estimation presented in the percentage as relative difference of reference annual load expressed as histogram for TDN (uncertainties with the bias [e_{avg} , red solid line or e_{50} , black dash line] and precision [e_5 and e_{95} , blue dash lines, are precision limits of 5th and 95th percentiles, respectively) with infrequent sampling (M5, biweekly) at DN. 320

Figure E.36 Distribution of uncertainties estimation presented in the percentage as relative difference of reference annual load expressed as histogram for TDN (uncertainties with the bias [e_{avg} , red solid line or e_{50} , black dash line] and precision [e_5 and e_{95} , blue dash lines, are precision limits of 5th and 95th percentiles, respectively) with infrequent sampling (M6, biweekly) at DN. 321

Figure E.37 Distribution of uncertainties estimation presented in the percentage as relative difference of reference annual load expressed as histogram for TDN (uncertainties with the bias [e_{avg} , red solid line or e_{50} , black dash line] and precision [e_5 and e_{95} , blue dash lines, are precision limits of 5th and 95th percentiles, respectively) with infrequent sampling (M5, monthly) at DN. 322

Figure E.38 Distribution of uncertainties estimation presented in the percentage as relative difference of reference annual load expressed as histogram for TDN (uncertainties with the bias [e_{avg} , red solid line or e_{50} , black dash line] and precision [e_5 and e_{95} , blue dash lines, are precision limits of 5th and 95th percentiles, respectively) with infrequent sampling (M6, monthly) at DN. 323

Figure E.39 Distribution of uncertainties estimation presented in the percentage as relative difference of reference annual load expressed as histogram for TKN (uncertainties with the bias [e_{avg} , red solid line or e_{50} , black dash line] and precision [e_5 and e_{95} , blue dash lines, are precision limits of 5th and 95th percentiles, respectively) with infrequent sampling (M5, weekly) at UP. 324

Figure E.40 Distribution of uncertainties estimation presented in the percentage as relative difference of reference annual load expressed as histogram for TKN (uncertainties with the bias [e_{avg} , red solid line or e_{50} , black dash line] and precision [e_5 and e_{95} , blue dash lines, are precision limits of 5th and 95th percentiles, respectively) with infrequent sampling (M6, weekly) at UP..... 325

Figure E.41 Distribution of uncertainties estimation presented in the percentage as relative difference of reference annual load expressed as histogram for TKN (uncertainties with the bias [e_{avg} , red solid line or e_{50} , black dash line] and precision [e_5 and e_{95} , blue dash lines, are precision limits of 5th and 95th percentiles, respectively) with infrequent sampling (M5, biweekly) at UP..... 326

Figure E.42 Distribution of uncertainties estimation presented in the percentage as relative difference of reference annual load expressed as histogram for TKN (uncertainties with the bias [e_{avg} , red solid line or e_{50} , black dash line] and precision [e_5 and e_{95} , blue dash lines, are precision limits of 5th and 95th percentiles, respectively) with infrequent sampling (M6, biweekly) at UP..... 327

Figure E.43 Distribution of uncertainties estimation presented in the percentage as relative difference of reference annual load expressed as histogram for TKN (uncertainties with the bias [e_{avg} , red solid line or e_{50} , black dash line] and precision [e_5 and e_{95} , blue dash lines, are precision limits of 5th and 95th percentiles, respectively) with infrequent sampling (M5, monthly) at UP..... 328

Figure E.44 Distribution of uncertainties estimation presented in the percentage as relative difference of reference annual load expressed as histogram for TKN (uncertainties with the bias [e_{avg} , red solid line or e_{50} , black dash line] and precision [e_5 and e_{95} , blue dash lines, are precision limits of 5th and 95th percentiles, respectively) with infrequent sampling (M6, monthly) at UP..... 329

Figure E.45 Distribution of uncertainties estimation presented in the percentage as relative difference of reference annual load expressed as histogram for TKN (uncertainties with the bias [e_{avg} , red solid line or e_{50} , black dash line] and precision [e_5 and e_{95} , blue dash lines, are precision limits of 5th and 95th percentiles, respectively) with infrequent sampling (M5, weekly) at DN..... 330

Figure E.46 Distribution of uncertainties estimation presented in the percentage as relative difference of reference annual load expressed as histogram for TKN (uncertainties with the bias [e_{avg} , red solid line or e_{50} , black dash line] and precision [e_5 and e_{95} , blue dash lines, are precision limits of 5th and 95th percentiles, respectively) with infrequent sampling (M6, weekly) at DN..... 331

Figure E.47 Distribution of uncertainties estimation presented in the percentage as relative difference of reference annual load expressed as histogram for TKN (uncertainties with the bias [e_{avg} , red solid line or e_{50} , black dash line] and precision [e_5 and e_{95} , blue dash lines, are precision limits of 5th and 95th percentiles, respectively) with infrequent sampling (M5, biweekly) at DN..... 332

Figure E.48 Distribution of uncertainties estimation presented in the percentage as relative difference of reference annual load expressed as histogram for TKN (uncertainties with the bias [e_{avg} , red solid line or e_{50} , black dash line] and precision [e_5 and e_{95} , blue dash lines, are precision limits of 5th and 95th percentiles, respectively) with infrequent sampling (M6, biweekly) at DN..... 333

Figure E.49 Distribution of uncertainties estimation presented in the percentage as relative difference of reference annual load expressed as histogram for TKN (uncertainties with the bias [e_{avg} , red solid line or e_{50} , black dash line] and precision [e_5 and e_{95} , blue dash lines, are precision limits of 5th and 95th percentiles, respectively) with infrequent sampling (M5, monthly) at DN. 334

Figure E.50 Distribution of uncertainties estimation presented in the percentage as relative difference of reference annual load expressed as histogram for TKN (uncertainties with the bias [e_{avg} , red solid line or e_{50} , black dash line] and precision [e_5 and e_{95} , blue dash lines, are precision limits of 5th and 95th percentiles, respectively) with infrequent sampling (M6, monthly) at DN. 335

Figure E.51 Distribution of uncertainties estimation presented in the percentage as relative difference of reference annual load expressed as histogram for DOC (uncertainties with the bias [e_{avg} , red solid line or e_{50} , black dash line] and precision [e_5 and e_{95} , blue dash lines, are precision limits of 5th and 95th percentiles, respectively) with infrequent sampling (M5, weekly) at UP..... 336

Figure E.52 Distribution of uncertainties estimation presented in the percentage as relative difference of reference annual load expressed as histogram for DOC (uncertainties with the bias [e_{avg} , red solid line or e_{50} , black dash line] and precision [e_5 and e_{95} , blue dash lines, are precision limits of 5th and 95th percentiles, respectively) with infrequent sampling (M6, weekly) at UP..... 337

Figure E.53 Distribution of uncertainties estimation presented in the percentage as relative difference of reference annual load expressed as histogram for DOC (uncertainties with the bias [e_{avg} , red solid line or e_{50} , black dash line] and precision [e_5 and e_{95} , blue dash lines, are precision limits of 5th and 95th percentiles, respectively) with infrequent sampling (M5, biweekly) at UP..... 338

Figure E.54 Distribution of uncertainties estimation presented in the percentage as relative difference of reference annual load expressed as histogram for DOC (uncertainties with the bias [e_{avg} , red solid line or e_{50} , black dash line] and precision [e_5 and e_{95} , blue dash lines, are precision limits of 5th and 95th percentiles, respectively) with infrequent sampling (M6, biweekly) at UP..... 339

Figure E.55 Distribution of uncertainties estimation presented in the percentage as relative difference of reference annual load expressed as histogram for DOC (uncertainties with the bias [e_{avg} , red solid line or e_{50} , black dash line] and precision [e_5 and e_{95} , blue dash lines, are precision limits of 5th and 95th percentiles, respectively) with infrequent sampling (M5, monthly) at UP..... 340

Figure E.56 Distribution of uncertainties estimation presented in the percentage as relative difference of reference annual load expressed as histogram for DOC (uncertainties with the bias [e_{avg} , red solid line or e_{50} , black dash line] and precision [e_5 and e_{95} , blue dash lines, are precision limits of 5th and 95th percentiles, respectively) with infrequent sampling (M6, monthly) at UP..... 341

Figure E.57 Distribution of uncertainties estimation presented in the percentage as relative difference of reference annual load expressed as histogram for DOC (uncertainties with the bias [e_{avg} , red solid line or e_{50} , black dash line] and precision [e_5 and e_{95} , blue dash lines, are precision limits of 5th and 95th percentiles, respectively) with infrequent sampling (M5, weekly) at DN..... 342

Figure E.58 Distribution of uncertainties estimation presented in the percentage as relative difference of reference annual load expressed as histogram for DOC (uncertainties with the bias [e_{avg} , red solid line or e_{50} , black dash line] and precision [e_5 and e_{95} , blue dash lines, are precision limits of 5th and 95th percentiles, respectively) with infrequent sampling (M6, weekly) at DN..... 343

Figure E.59 Distribution of uncertainties estimation presented in the percentage as relative difference of reference annual load expressed as histogram for DOC (uncertainties with the bias [e_{avg} , red solid line or e_{50} , black dash line] and precision [e_5 and e_{95} , blue dash lines, are precision limits of 5th and 95th percentiles, respectively) with infrequent sampling (M5, biweekly) at DN..... 344

Figure E.60 Distribution of uncertainties estimation presented in the percentage as relative difference of reference annual load expressed as histogram for DOC (uncertainties with the bias [e_{avg} , red solid line or e_{50} , black dash line] and precision [e_5 and e_{95} , blue dash lines, are precision limits of 5th and 95th percentiles, respectively) with infrequent sampling (M6, biweekly) at DN..... 345

Figure E.61 Distribution of uncertainties estimation presented in the percentage as relative difference of reference annual load expressed as histogram for DOC (uncertainties with the bias [e_{avg} , red solid line or e_{50} , black dash line] and precision [e_5 and e_{95} , blue dash lines, are precision limits of 5th and 95th percentiles, respectively) with infrequent sampling (M5, monthly) at DN..... 346

Figure E.62 Distribution of uncertainties estimation presented in the percentage as relative difference of reference annual load expressed as histogram for DOC (uncertainties with the bias [e_{avg} , red solid line or e_{50} , black dash line] and precision [e_5 and e_{95} , blue dash lines, are precision limits of 5th and 95th percentiles, respectively) with infrequent sampling (M6, monthly) at DN..... 347

Figure E.63 Distribution of uncertainties estimation presented in the percentage as relative difference of reference annual load expressed as histogram for TP (uncertainties with the bias [e_{avg} , red solid line or e_{50} , black dash line] and precision [e_5 and e_{95} , blue dash lines, are precision limits of 5th and 95th percentiles, respectively) with infrequent sampling (M5, weekly) at UP..... 348

Figure E.64 Distribution of uncertainties estimation presented in the percentage as relative difference of reference annual load expressed as histogram for TP (uncertainties with the bias [e_{avg} , red solid line or e_{50} , black dash line] and precision [e_5 and e_{95} , blue dash lines, are precision limits of 5th and 95th percentiles, respectively) with infrequent sampling (M6, weekly) at UP..... 349

Figure E.65 Distribution of uncertainties estimation presented in the percentage as relative difference of reference annual load expressed as histogram for TP (uncertainties with the bias [e_{avg} , red solid line or e_{50} , black dash line] and precision [e_5 and e_{95} , blue dash lines, are precision limits of 5th and 95th percentiles, respectively) with infrequent sampling (M5, biweekly) at UP..... 350

Figure E.66 Distribution of uncertainties estimation presented in the percentage as relative difference of reference annual load expressed as histogram for TP (uncertainties with the bias [e_{avg} , red solid line or e_{50} , black dash line] and precision [e_5 and e_{95} , blue dash lines, are precision limits of 5th and 95th percentiles, respectively) with infrequent sampling (M6, biweekly) at UP..... 351

Figure E.67 Distribution of uncertainties estimation presented in the percentage as relative difference of reference annual load expressed as histogram for TP (uncertainties with the bias [e_{avg} , red solid line or e_{50} , black dash line] and precision [e_5 and e_{95} , blue dash lines, are precision limits of 5th and 95th percentiles, respectively) with infrequent sampling (M5, monthly) at UP..... 352

Figure E.68 Distribution of uncertainties estimation presented in the percentage as relative difference of reference annual load expressed as histogram for TP (uncertainties with the bias [e_{avg} , red solid line or e_{50} , black dash line] and precision [e_5 and e_{95} , blue dash lines, are precision limits of 5th and 95th percentiles, respectively) with infrequent sampling (M6, monthly) at UP..... 353

Figure E.69 Distribution of uncertainties estimation presented in the percentage as relative difference of reference annual load expressed as histogram for TP (uncertainties with the bias [e_{avg} , red solid line or e_{50} , black dash line] and precision [e_5 and e_{95} , blue dash lines, are precision limits of 5th and 95th percentiles, respectively) with infrequent sampling (M5, weekly) at DN..... 354

Figure E.70 Distribution of uncertainties estimation presented in the percentage as relative difference of reference annual load expressed as histogram for TP (uncertainties with the bias [e_{avg} , red solid line or e_{50} , black dash line] and precision [e_5 and e_{95} , blue dash lines, are precision limits of 5th and 95th percentiles, respectively) with infrequent sampling (M6, weekly) at DN..... 355

Figure E.71 Distribution of uncertainties estimation presented in the percentage as relative difference of reference annual load expressed as histogram for TP (uncertainties with the bias [e_{avg} , red solid line or e_{50} , black dash line] and precision [e_5 and e_{95} , blue dash lines, are precision limits of 5th and 95th percentiles, respectively) with infrequent sampling (M5, biweekly) at DN..... 356

Figure E.72 Distribution of uncertainties estimation presented in the percentage as relative difference of reference annual load expressed as histogram for TP (uncertainties with the bias [e_{avg} , red solid line or e_{50} , black dash line] and precision [e_5 and e_{95} , blue dash lines, are precision limits of 5th and 95th percentiles, respectively) with infrequent sampling (M6, biweekly) at DN..... 357

Figure E.73 Distribution of uncertainties estimation presented in the percentage as relative difference of reference annual load expressed as histogram for TP (uncertainties with the bias [e_{avg} , red solid line or e_{50} , black dash line] and precision [e_5 and e_{95} , blue dash lines, are precision limits of 5th and 95th percentiles, respectively) with infrequent sampling (M5, monthly) at DN. 358

Figure E.74 Distribution of uncertainties estimation presented in the percentage as relative difference of reference annual load expressed as histogram for TP (uncertainties with the bias [e_{avg} , red solid line or e_{50} , black dash line] and precision [e_5 and e_{95} , blue dash lines, are precision limits of 5th and 95th percentiles, respectively) with infrequent sampling (M6, monthly) at DN. 359

Figure E.75 Distribution of uncertainties estimation presented in the percentage as relative difference of reference annual load expressed as histogram for TSS with PLSR prediction (uncertainties with the bias [e_{avg} , red solid line or e_{50} , black dash line] and precision [e_5 and e_{95} , blue dash lines, are precision limits of 5th and 95th percentiles, respectively) with infrequent sampling (M5, weekly) at UP..... 360

Figure E.76 Distribution of uncertainties estimation presented in the percentage as relative difference of reference annual load expressed as histogram for TSS with PLSR prediction (uncertainties with the bias [e_{avg} , red solid line or e_{50} , black dash line] and precision [e_5 and e_{95} , blue dash lines, are precision limits of 5th and 95th percentiles, respectively) with infrequent sampling (M6, weekly) at UP..... 361

Figure E.77 Distribution of uncertainties estimation presented in the percentage as relative difference of reference annual load expressed as histogram for TSS with PLSR prediction (uncertainties with the bias [e_{avg} , red solid line or e_{50} , black dash line] and precision [e_5 and e_{95} , blue dash lines, are precision limits of 5th and 95th percentiles, respectively) with infrequent sampling (M5, biweekly) at UP..... 362

Figure E.78 Distribution of uncertainties estimation presented in the percentage as relative difference of reference annual load expressed as histogram for TSS with PLSR prediction (uncertainties with the bias [e_{avg} , red solid line or e_{50} , black dash line] and precision [e_5 and e_{95} , blue dash lines, are precision limits of 5th and 95th percentiles, respectively) with infrequent sampling (M6, biweekly) at UP..... 363

Figure E.79 Distribution of uncertainties estimation presented in the percentage as relative difference of reference annual load expressed as histogram for TSS with PLSR prediction (uncertainties with the bias [e_{avg} , red solid line or e_{50} , black dash line] and precision [e_5 and e_{95} , blue dash lines, are precision limits of 5th and 95th percentiles, respectively) with infrequent sampling (M5, monthly) at UP..... 364

Figure E.80 Distribution of uncertainties estimation presented in the percentage as relative difference of reference annual load expressed as histogram for TSS with PLSR prediction (uncertainties with the bias [e_{avg} , red solid line or e_{50} , black dash line] and precision [e_5 and e_{95} , blue dash lines, are precision limits of 5th and 95th percentiles, respectively) with infrequent sampling (M6, monthly) at UP..... 365

Figure E.81 Distribution of uncertainties estimation presented in the percentage as relative difference of reference annual load expressed as histogram for TSS with PLSR prediction (uncertainties with the bias [e_{avg} , red solid line or e_{50} , black dash line] and precision [e_5 and e_{95} , blue dash lines, are precision limits of 5th and 95th percentiles, respectively) with infrequent sampling (M5, weekly) at DN..... 366

Figure E.82 Distribution of uncertainties estimation presented in the percentage as relative difference of reference annual load expressed as histogram for TSS with PLSR prediction (uncertainties with the bias [e_{avg} , red solid line or e_{50} , black dash line] and precision [e_5 and e_{95} , blue dash lines, are precision limits of 5th and 95th percentiles, respectively) with infrequent sampling (M6, weekly) at DN..... 367

Figure E.83 Distribution of uncertainties estimation presented in the percentage as relative difference of reference annual load expressed as histogram for TSS with PLSR prediction (uncertainties with the bias [e_{avg} , red solid line or e_{50} , black dash line] and precision [e_5 and e_{95} , blue dash lines, are precision limits of 5th and 95th percentiles, respectively) with infrequent sampling (M5, biweekly) at DN..... 368

Figure E.84 Distribution of uncertainties estimation presented in the percentage as relative difference of reference annual load expressed as histogram for TSS with PLSR prediction (uncertainties with the bias [e_{avg} , red solid line or e_{50} , black dash line] and precision [e_5 and e_{95} , blue dash lines, are precision limits of 5th and 95th percentiles, respectively) with infrequent sampling (M6, biweekly) at DN..... 369

Figure E.85 Distribution of uncertainties estimation presented in the percentage as relative difference of reference annual load expressed as histogram for TSS with PLSR prediction (uncertainties with the bias [e_{avg} , red solid line or e_{50} , black dash line] and precision [e_5 and e_{95} , blue dash lines, are precision limits of 5th and 95th percentiles, respectively) with infrequent sampling (M5, monthly) at DN..... 370

Figure E.86 Distribution of uncertainties estimation presented in the percentage as relative difference of reference annual load expressed as histogram for TSS with PLSR prediction (uncertainties with the bias [e_{avg} , red solid line or e_{50} , black dash line] and precision [e_5 and e_{95} , blue dash lines, are precision limits of 5th and 95th percentiles, respectively) with infrequent sampling (M6, monthly) at DN..... 371

Figure E.87 Distribution of uncertainties estimation presented in the percentage as relative difference of reference annual load expressed as histogram for TSS with Turbidity prediction (uncertainties with the bias [e_{avg} , red solid line or e_{50} , black dash line] and precision [e_5 and e_{95} , blue dash lines, are precision limits of 5th and 95th percentiles, respectively) with infrequent sampling (M5, weekly) at UP..... 372

Figure E.88 Distribution of uncertainties estimation presented in the percentage as relative difference of reference annual load expressed as histogram for TSS with Turbidity prediction (uncertainties with the bias [e_{avg} , red solid line or e_{50} , black dash line] and precision [e_5 and e_{95} , blue dash lines, are precision limits of 5th and 95th percentiles, respectively) with infrequent sampling (M6, weekly) at UP..... 373

Figure E.89 Distribution of uncertainties estimation presented in the percentage as relative difference of reference annual load expressed as histogram for TSS with Turbidity prediction (uncertainties with the bias [e_{avg} , red solid line or e_{50} , black dash line] and precision [e_5 and e_{95} , blue dash lines, are precision limits of 5th and 95th percentiles, respectively) with infrequent sampling (M5, biweekly) at UP..... 374

Figure E.90 Distribution of uncertainties estimation presented in the percentage as relative difference of reference annual load expressed as histogram for TSS with Turbidity prediction (uncertainties with the bias [e_{avg} , red solid line or e_{50} , black dash line] and precision [e_5 and e_{95} , blue dash lines, are precision limits of 5th and 95th percentiles, respectively) with infrequent sampling (M6, biweekly) at UP..... 375

Figure E.91 Distribution of uncertainties estimation presented in the percentage as relative difference of reference annual load expressed as histogram for TSS with Turbidity prediction (uncertainties with the bias [e_{avg} , red solid line or e_{50} , black dash line] and precision [e_5 and e_{95} , blue dash lines, are precision limits of 5th and 95th percentiles, respectively) with infrequent sampling (M5, monthly) at UP..... 376

Figure E.92 Distribution of uncertainties estimation presented in the percentage as relative difference of reference annual load expressed as histogram for TSS with Turbidity prediction (uncertainties with the bias [e_{avg} , red solid line or e_{50} , black dash line] and precision [e_5 and e_{95} , blue dash lines, are precision limits of 5th and 95th percentiles, respectively) with infrequent sampling (M6, monthly) at UP..... 377

Figure E.93 Distribution of uncertainties estimation presented in the percentage as relative difference of reference annual load expressed as histogram for TSS with Turbidity prediction (uncertainties with the bias [e_{avg} , red solid line or e_{50} , black dash line] and precision [e_5 and e_{95} , blue dash lines, are precision limits of 5th and 95th percentiles, respectively) with infrequent sampling (M5, weekly) at DN..... 378

Figure E.94 Distribution of uncertainties estimation presented in the percentage as relative difference of reference annual load expressed as histogram for TSS with Turbidity prediction (uncertainties with the bias [e_{avg} , red solid line or e_{50} , black dash line] and precision [e_5 and e_{95} , blue dash lines, are precision limits of 5th and 95th percentiles, respectively) with infrequent sampling (M6, weekly) at DN..... 379

Figure E.95 Distribution of uncertainties estimation presented in the percentage as relative difference of reference annual load expressed as histogram for TSS with Turbidity prediction (uncertainties with the bias [e_{avg} , red solid line or e_{50} , black dash line] and precision [e_5 and e_{95} , blue dash lines, are precision limits of 5th and 95th percentiles, respectively) with infrequent sampling (M5, biweekly) at DN..... 380

Figure E.96 Distribution of uncertainties estimation presented in the percentage as relative difference of reference annual load expressed as histogram for TSS with Turbidity prediction (uncertainties with the bias [e_{avg} , red solid line or e_{50} , black dash line] and precision [e_5 and e_{95} , blue dash lines, are precision limits of 5 th and 95 th percentiles, respectively) with infrequent sampling (M6, biweekly) at DN.....	381
Figure E.97 Distribution of uncertainties estimation presented in the percentage as relative difference of reference annual load expressed as histogram for TSS with Turbidity prediction (uncertainties with the bias [e_{avg} , red solid line or e_{50} , black dash line] and precision [e_5 and e_{95} , blue dash lines, are precision limits of 5 th and 95 th percentiles, respectively) with infrequent sampling (M5, monthly) at DN.	382
Figure E.98 Distribution of uncertainties estimation presented in the percentage as relative difference of reference annual load expressed as histogram for TSS with Turbidity prediction (uncertainties with the bias [e_{avg} , red solid line or e_{50} , black dash line] and precision [e_5 and e_{95} , blue dash lines, are precision limits of 5 th and 95 th percentiles, respectively) with infrequent sampling (M6, monthly) at DN.	383
Figure F.1 Hysteresis plots for NO ₃ -N at UP	384
Figure F.2 Hysteresis plots for DOC at UP	393
Figure F.3 Hysteresis plots for NO ₃ -N at MD	402
Figure F.4 Hysteresis plots for DOC at MD	411
Figure F.5 Hysteresis plots for NO ₃ -N at DN.....	420
Figure F.6 Hysteresis plots for DOC at DN.....	429
Figure H.1 The injection site and 9 monitoring stations for tracer study along the Claridge Canal in Goldsboro, North Carolina	440
Figure H.2 The concentration of NO ₃ -N breakthrough curves (continuous results: raw data from UV-Vis spectrophotometer manufacturer calibration, discrete results: laboratory analysis) at Station B, C, E, G, and I at the Claridge Canal before restoration period.....	444
Figure H.3 The relationship for S_w and NO ₃ -N	445
Figure H.4 The relationship for V_F and NO ₃ -N.....	446
Figure H.5 The relationship for U and NO ₃ -N	447
Figure I.1 The concept of EEA experiment for laboratory analysis	452
Figure I.2 Preliminary results for the relationship between ln GLU and ln AP	454
Figure I.3 Ecoenzymes activities for ln(BG) and ln(AP) as an indicator of C: P acquisition (Note: 1. The EEA unit is nmol h ⁻¹ g SOM ⁻¹ which is the same unit with Sinsabaugh et al., (2008). 2. The p-value for the slope as statistically significant relationship is 0.004309<0.05 for the linear regression.)	456

Figure I.4 Ecoenzymes activities for $\ln(\text{BG})$ and $\ln(\text{NAG}+\text{LAP})$ as an indicator of C: N acquisition (Note: 1. The EEA unit is $\text{nmol h}^{-1} \text{g SOM}^{-1}$ which is the same unit with Sinsabaugh et al., (2008). 2. The p-value for the slope as statistically significant relationship is $0.154 > 0.05$ for the linear regression.) 457

Figure I.5 The relationship for ecenzymes activities for the ratio of $\ln(\text{BG}) : \ln(\text{NAG}+\text{LAP})$, as an indicator of C: N acquisition and the ratio of $\ln(\text{BG}) : \ln(\text{AP})$ as an indicator of C: P acquisition. (Note: The p-value for the slope as statistically significant relationship is $0.151 > 0.05$ for the linear regression.) 458

Chapter 1: Introduction

1.1 Research Motivation

In 2005, there were 37,099 stream restoration projects implemented in the United States, and the top goals of restoration included improving water quality, developing or enhancing riparian zones, creating/improving instream habitat, facilitating fish passage, and stabilizing stream banks (Bernhardt et al. 2005). However, lack of available data complicated making a robust assessment for success or failure of stream restoration projects (e.g., Pander and Geist, 2013; Bennett et al., 2011). In most cases, the stream restoration effects have been estimated, after restoration, by comparison between the restored and nearby ‘reference’ reaches (e.g., Colangelo, 2014; Daniluk et al., 2013; Howson et al., 2009), which can only add to the uncertainty of the estimation process. It is hypothesized that comparing pre- and post-restoration for the same stream removes this type of uncertainty from the evaluation method and is the preferred approach to assess restoration success.

One would like to be able to claim that for this or that type of restoration, water quality has been improved by ‘x%’, e.g., 50% of nitrogen was removed in streams (Craig et al., 2008; Galloway et al., 2004). In the expression ‘x% of water quality benefit’, the notion of integration over time is embedded. For very practical reasons, a common approach to estimate water quality benefits has been to compare the discrete sample concentrations and corresponding instantaneous loads over short and discontinuous periods of time.

In summary, the concept of water quality benefits of stream restoration inherently refers to a concept of integral or cumulative effect. However, one has historically had access only

to points in time, i.e., discrete flow and concentration values, corresponding, by mathematical analogy, to the derivative functions necessary to calculate the integral, or the water quality benefit. Numerous authors have shown that the uncertainty on material loads associated with infrequent sampling can be such that it is likely that the effects of stream restoration are confounded within the measurement uncertainty (e.g., Skarbøvik and Roseth, 2015; Skarbøvik et al., 2012; Cassidy and Jordan, 2011; Henjum et al., 2010; Birgand et al., 2010; Brauer et al., 2009).

New available continuous water quality sensors give access for the first time to the full dynamics of concentrations, or when combined with continuous flow measurements, the derivative functions needed to calculate the cumulative load, which information is necessary to have a chance to evaluate water quality benefits of stream restoration. The recent availability of continuous optical sensors, ultraviolet-visual spectrophotometers, for water quality has opened the possibility to obtain high frequency water quality data which can reveal concentration dynamics that were not available until now (e.g., Langergraber et al., 2003; Rieger et al., 2006, Etheridge et al., 2013).

However, these instruments are relatively new and a very limited return on experience is currently available for guidance. As a result, it is unclear whether these field spectrophotometers can be used for the conditions in the agricultural coastal plain streams, and what kind of performance one should expect. Etheridge et al. (2014, 2015) have shown that these instruments are subject to optical fouling, but these results were obtained in a tidal salt marsh, hence in very different conditions. The same authors have shown that it was possible to use the spectrophotometers to measure concentrations of parameters not known to

absorb light. Etheridge et al. (2015) have essentially proposed to create water quality rating curves where the spectrophotometer absorbance data are used as index data from which concentrations of a suite of parameters can be calculated using a rating curve, itself generated using Partial Least Squares Regression (PLSR) statistical methods.

To fill in the voids in the literature on the water quality benefits of stream restoration, North Carolina Department of Transportation (NC DOT), North Carolina Forest Service (NCFS) and North Carolina State University (NCSU) have partnered together to conduct a pilot study. The general approach to quantify the water quality benefits pursued consists in quantifying the changes in the stream solutes and material signatures of the “same” stream from before to after restoration using continuous water quality and hydrology monitoring.

1.2 Research Questions

This research attempted to answer the following questions. The first question associated with the continuous water quality data is: Can one use *in situ* ultraviolet-visual (UV-vis) spectrophotometers to measure water quality on a continuous basis in an agricultural coastal plain stream? The corollary question becomes: for what parameter and what does it take to obtain continuous data? The answers to these very important questions are necessary to enrich guidance in the use of these instruments and create water quality rating curves to interpret the absorbance data (Chapter 2).

The second question is: What are the uncertainties of concentrations and loads associated with data generated by the spectrophotometers? It is expected that the uncertainty on annual loads be much lower than when calculated from infrequent samples. The corollary questions

become: How do the uncertainties associated with the instruments compare with those associated with infrequent sampling on the annual load indicator? The answers related to the second question are to quantify the uncertainties associated with the spectrophotometers itself and compare the uncertainties for estimating annual loads with infrequent sampling (Chapter 3).

The third research question is addressed as follows: What does continuous water quality information (e.g., flow, nutrient concentration and loads) reveal about biogeochemical processes at the short term (e.g., storm events) and seasonal scales in a coastal plain predominantly agricultural watershed? Can the information obtained be used to infer in-stream processes? The answers to the above questions are to characterize the nutrient dynamics from the continuous water quality information with seasonal effects and during the storm events (Chapter 4).

1.3 Objectives

To address the research questions, the Claridge Canal due to be restored in Goldsboro, NC was monitored for water quality and hydrology at high-frequency during the pre-restoration period. Chapter 2 presents the application of ultraviolet-visual spectrophotometers to monitor water quality on a continuous basis at three stations along the Claridge Canal for 16 months. The objectives of Chapter 2 are: (1) to evaluate the possibility of creating water quality rating curves using UV-Vis spectrophotometers to measure nitrate ($\text{NO}_3\text{-N}$), ammonium ($\text{NH}_4\text{-N}$), total dissolved nitrogen (TDN), Total Kjeldahl Nitrogen (TKN), dissolved organic carbon (DOC), phosphate ($\text{PO}_4\text{-P}$), total phosphorus (TP) and total

suspended solids (TSS) in an agricultural coastal plain stream; (2) Report the potential challenges involved, and propose methods to obtain gap free time series and best results.

Chapter 3 assesses the level of uncertainties associated with the use of this technology and how these compare to uncertainties induced by infrequent sampling on nutrient loads and concentrations. The objectives of Chapter 3 are addressed as follows: (1) evaluate the uncertainties on concentration values and annual loads calculated by the ‘global calibration’ provided by the manufacturer, and calculated using PLSR depending upon the number and the distribution of the calibration points used; (2) compare these uncertainties to those that would be induced by infrequent sampling on estimating annual loads with best load algorithm methods; (3) provide guidance to users to minimize uncertainties and maximize the potential of their UV-Vis spectrophotometers.

In Chapter 4, the high frequency information is used to draw the temporal facet of the stream solutes signature of these reaches. The dynamics of nutrient exports from the storm to the seasonal scales are particularly characterized. The objectives of Chapter 4 are: (1) use cumulative load indicators to detect the seasonal trends in the generation and export of nitrate and DOC in these watersheds; (2) classify the relationships and use existing tools quantifying the hysteresis loops between nutrient concentrations (nitrate and DOC) and discharge during storm events to reveal soil and in-stream processes in these watersheds; (3) report peculiar patterns of water exchanges that might occur within the floodplain between the main river and secondary artificial streams.

1.4 References

- Bennett, S. J., Simon, A., Castro, J. M., Atkinson, J. F., Bronner, C. E., Blersch, S. S., Rabideau, A. J. 2011. The evolving science of stream restoration. *Stream Restoration in Dynamic Fluvial Systems: Scientific Approaches, Analyses, and Tools* Geophysical Monograph Series 194, Published in 2011 by the American Geophysical Union.
- Bernhardt, E. S., Palmer, M. A., Allan, J. D., Alexander, G., Barnas, K., Brooks, S., Carr, J., Clayton, S., Dahm, C., Follstad-Shah, J., Galat, D., Gloss, S., Goodwin, P., Hart, D., Hassett, B., Jenkinson, R., Katz, S., Kondolf, G. M., Lake, P. S., Lave, R., Meyer, J. L., O'Donnell, T. K., Pagano, L., Powell, B., Sudduth, E. 2005. Synthesizing U.S. river restoration efforts. *Science*, 308: 636-637.
- Birgand F., Faucheux, C., Gruau, G., Augeard, B., Moatar, F., Bordenave, P. 2010. Uncertainties in assessing annual nitrate load and concentration indicators: Part 1. Impact of sampling frequency and load estimation algorithms. *Trans. ASABE*, 53(2): 437-446.
- Brauer N., O'Geen, A. T., Dahlgren, R. A. 2009. Temporal variability in water quality of agricultural tailwaters: implications for water quality monitoring. *Agr Water Manage*, 96: 1001-1009.
- Cassidy, R. and Jordan, P. 2011. Limitations of instantaneous water quality sampling in surface-water catchments: comparison with near-continuous phosphorus time-series data. *J Hydrol*, 405: 18-193.
- Colangelo, D. J., 2014. Interim response of dissolved oxygen to reestablished flow in the Kissimmee River, Florida, U.S.A. *Restoration Ecology*, 22: 376-387.
- Craig, L. S., Palmer, M. A., Richardson, D. C., Filoso, S., Bernhardt, E. S., Bledsoe, B. P., Doyle, M. W., Groffman, P. M., Hassett, B. A., Kaushal, S. S., Mayer, P. M., Smith, S. M. 2008. Stream restoration strategies for reducing river nitrogen loads. *Frontiers in Ecology and the Environment*, 6(10): 529–538.

- Daniluk, T. L., Lautz, L. K., Gordon, R. P., Endreny, T. A., 2013. Surface water-groundwater interaction at restored streams and associated reference reaches. *Hydrology Process*, 27: 3730-3746.
- Etheridge, J. R., 2013. Quantifying the water quality benefits of a constructed brackish marsh and tidal stream system using continuous water quality and flow monitoring. In: Ph.D. Dissertation. North Carolina State University, Raleigh, NC.
- Etheridge, J. R., Birgand, F., Burchell, M. R. 2015. Quantifying nutrient and suspended solids fluxes in a constructed tidal marsh following rainfall: The value of capturing the rapid changes in flow and concentrations. *Ecological Engineering*, 78: 41-52.
- Etheridge, J. R., Birgand, F., Osborne, J. A., Osburn, C. L., Burchell, M. R., Irving, J. 2014. Using *in situ* ultraviolet–visual spectroscopy to measure nitrogen, carbon, phosphorus, and suspended solids concentrations at a high frequency in a brackish tidal marsh. *Limnol. Oceanogr. Methods*, 12: 10-22.
- Galloway, J. N., Dentener, F. J., Capone, D. G., Boyer, E. W., Howarth, R. W., Seitzinger, S. P., Asner, G. P., Cleveland, C. C., Green, P. A., Holland, E. A., Karl, D. M., Michaels A. F., Porter, J. H., Townsend A. R., Vöösmary, C. J. 2004. Nitrogen cycles: past, present, and future. *Biogeochemistry* 70: 153-226.
- Henjum, M. B., Hozalski, R. M., Wennen, C. R., Arnold, W.A., Novak, P. J. 2010. Correlations between *in situ* sensor measurements and trace organic pollutants in urban streams. *J Environ Monitor*, 12: 225-233.
- Howson, T. J., Robson, B. J., Mitchell, B. D., 2009. Fish assemblage response to rehabilitation of a sand-slugged lowland river. *River. Research Applications*, 25: 1251-1267.
- Langergraber, G., Fleischmann, N., Hofstädter, F. 2003. A multivariate calibration procedure for UV/VIS spectrometric quantification of organic matter and nitrate in wastewater. *Water Sci. Technol.*, 47(2): 63-71.

- Pander, J. and Geist, J. 2013. Ecological indicators for stream restoration success. *Ecological Indicators*, 30: 106-118.
- Rieger, L., Langergraber, G., Siegrist, H. 2006. Uncertainties of spectral *in situ* measurements in wastewater using different calibration approaches. *Water Sci. Technol.*, 53: 187-198.
- Skarbøvik, E. and Roseth, R. 2015. Use of sensor data for turbidity, pH and conductivity as an alternative to conventional water quality monitoring in four Norwegian case studies. *Acta Agriculturae Scandinavica, Section B- Soil & Plant Science*, 65(1): 63-73.
- Skarbøvik, E., Stålnacke, P., Bogen, J., Bønsnes, T. E. 2012. Impact of sampling frequency on mean concentrations and estimated loads of suspended sediment in a Norwegian river: implications for water management. *Sci Total Environ*, 433: 462-471.

Chapter 2: Application of ultraviolet-visual spectrophotometers and water quality rating curves to monitor concentrations and loads on a continuous basis in an agricultural coastal plain stream

2.1 Introduction

Water quality benefits of stream restoration not well quantified

Over the last decade, the United States has spent annually an estimated 1 billion dollars or more to restore degraded streams and rivers (Bernhardt et al., 2005; Fischenich, 2011).

However, lack of available data has complicated making a robust assessment for success or failure of stream restoration projects (e.g., Pander and Geist, 2013; Bennett et al., 2011).

Among the projects that have actually been monitored, rare are those for which pre-restoration data are available. Palmer et al. (2005) showed that only 4% of all restoration projects investigated the pre-restoration status. In most cases, the stream restoration effects are estimated, after restoration, by comparison between the restored and nearby ‘reference’ reaches (e.g., Colangelo, 2014; Daniluk et al., 2013; Howson et al., 2009), which can only add to the uncertainty of the estimation process. It is hypothesized that comparing pre- and post-restoration for the same stream removes this type of uncertainty from the evaluation method and is the preferred approach to assess restoration success.

Still, comparing pre- and post-restoration stages does imply that there be robust enough methods to characterize and compare each phase. Some indicators such as stream bank stability or macroinvertebrate and fish populations inherently integrate over time the effect of the pulsation nature of the physical, and biochemical conditions in streams. These indicators

are thus theoretically robust to indicate significant differences between pre- and post-restoration. In many cases, the population of these indicators is large enough to run statistical tests, which reinforces the significance of the difference between pre- and post-restoration. Not surprisingly, there seems to be a relative consensus in the literature about the effects of, and the reasons for, stream restoration practices on these integrative indicators (e.g., Hughes, 2016; Davis et al., 2015; Obolewski et al., 2014; Steinberger and Whol, 2013, Antón et al., 2010; Howson et al., 2009).

Interestingly, although water quality improvement is one of top goals for stream restoration, there seems to be little consensus in the literature on whether stream restoration provides water quality benefits (e.g., Bernhardt et al., 2005; Craig et al., 2008; Alexander and Allan, 2006; Castillo et al., 2016; Daigneault et al., 2017; Eshleman and Sabo, 2016). One would like to be able to claim that for this or that type of restoration, water quality has been improved by ‘x%’, e.g., 50% of nitrogen was removed in streams (Craig et al., 2008; Galloway et al., 2004). In the expression ‘x% water quality benefit’, the notion of integration over time is embedded. In other words, the concept of water quality benefit also implies an integration, in the mathematical sense of the word.

For very practical reasons, a common approach to estimate water quality benefits has been to compare the discrete sample concentrations and corresponding instantaneous loads over short and discontinuous periods of time of restored vs. unrestored stream reaches. Using the mathematical analogy, discrete concentrations and load values correspond to the derivative values needed to calculate the integral or overall water quality benefits. For the

similar hydrological conditions, it seems fair to say that significantly lower concentrations in a restored reach imply a significant water quality benefit.

It is then tempting to calculate the magnitude of the water quality benefits as the average concentration or load difference, and to conclude that the lack of significant difference between discrete concentration values necessarily equates to no significant water quality benefit. This would apply for conditions for which flow and concentrations are rather stable with time. However, streams have an inherent pulsation nature when in very short times flow rates can be multiplied by sometimes several orders of magnitude, concentrations by several folds, such that concentrations values during high flows weigh more in the total load than those during low flows.

Very much like an integral value can be obtained from an infinite number of derivative functions, water quality benefits can result from very different hydrographs and chemographs, which individual value cannot be fully comparable, e.g., from one stream to another. This suggests that there may be cases for which the average concentration difference between restored and unrestored streams may not equate the overall integrated water quality effect. There may also be cases where there is in fact a cumulative water quality benefit; although no significant difference in discrete concentration values can be statistically calculated.

In summary, it is believed that the concept of water quality benefits of stream restoration often refers to a concept of integral or cumulative effect. However, one has historically had access only to points in time, i.e., discrete flow and concentration values, corresponding to

the derivative functions necessary to calculate the integral. Numerous authors have shown that the uncertainty on material loads associated with infrequent sampling can be such that it is likely that the effects of stream restoration are confounded within the measurement uncertainty (e.g., Skarbøvik and Roseth, 2015; Skarbøvik et al., 2012; Cassidy and Jordan, 2011; Henjum et al., 2010; Birgand et al., 2010; Brauer et al., 2009).

New available continuous water quality sensors give access for the first time to the full dynamics of concentrations, or when combined with continuous flow measurements, the derivative functions needed to calculate the cumulative load, which information is necessary to have a chance to evaluate water quality benefits of stream restoration.

The number of articles reporting the use of continuous sensors to calculate nutrient loads and balance is increasing. Etheridge et al. (2015) have used such instruments to calculate the nutrient balance from loads in and out of a restored tidal marsh in North Carolina, capturing the extreme concentration dynamics associated with the tides and rainfall events. Continuous sensors are now used in agricultural watersheds to quantify the phosphorus and nitrate ($\text{NO}_3\text{-N}$) concentrations and flow relationships in a rural river with high-frequency monitoring (Bowes et al., 2015), to monitor suspended solids (SS), total phosphorus (TP) and phosphate ($\text{PO}_4\text{-P}$) (Skarbøvik and Roseth, 2015), or to estimate hydro-chemical dynamics and primary production in an urban catchment (Halliday et al., 2015). In all cases, these instruments seem to be particularly fit to address all ‘flashy’ systems such as agricultural catchments (Cassidy and Jordan, 2011).

Application and calibration of Ultraviolet-visual spectrophotometers

Field Ultraviolet-visual (UV-Vis) spectrophotometers are among the new sensors able to monitor water quality at high frequency in real time. UV-Vis spectrophotometers measure the absorbance of light from the UV to the visible range through water. The Beer-Lambert law suggests that for light absorbing constituents, absorbance of the light by water is generally correlated with concentrations in the water. It is well known that nitrate ($\text{NO}_3\text{-N}$), dissolved organic carbon (DOC), and total suspended solids (TSS), respectively absorb light in the 220-230 nm range (Crumpton et al., 1992; Suzuki and Kuroda, 1987), between 250 and 300 nm (e.g., Rochelle-Newall and Fisher, 2002; Saraceno et al., 2009; Fichot and Benner, 2011), and in the visible range (e.g., Rieger et al., 2006; Torres and Bertrand-Krajewski, 2008).

These instruments are equipped with proprietary algorithms to calculate concentrations from the absorbance data. These algorithms are sometimes referred to as ‘global calibration’ as they aim to best fit most situations. However, there is clear evidence that local calibrations improve measurements (Langergraber et al., 2003; Rieger et al., 2006; Torres and Bertrand-Krajewski, 2008). All manufacturers provide a way to adjust the embedded ‘global calibration’ to better fit local conditions. However, the same previous authors have used Partial Least Squares Regression (PLSR) to directly calibrate absorbance values measured by UV-Vis spectrophotometers to obtain best results. Etheridge et al. (2014, 2015) and Birgand et al. (2016) used the same regression method and were able to correlate absorbance to many parameters, including some not known to absorb light (nitrate, organic nitrogen [ON],

dissolved organic carbon [DOC], total suspended solids [TSS], bromide, phosphate, total phosphorus [TP], salinity, Fe, or Silica). They suggested that the method evaluated a co-variability of light absorbance with concentrations.

Hypotheses and objectives

The hypothesis is that UV-Vis spectrophotometers can be used to measure water quality at high frequency in an agricultural coastal plain stream over long periods of time. It is hypothesized that the absorbance spectra can be used as index data to create ‘water quality rating curves’ where the calibration functions are based on Partial Least Squares Regression (PLSR). It is hypothesized that water quality rating curves can also be created for parameters not known to absorb light. In addition, it is hypothesized, particularly to fill missing data gaps, that it is possible to establish a robust method to process the high-frequency absorbance data into robust concentration time series. Thus, it is hypothesized that it is possible to obtain long-term full record of flow and concentration data at a high frequency, which is a prerequisite to calculate cumulative loads, which it is believed to be robust indicators of water quality benefits.

The objectives of this research are: (1) to evaluate the possibility of creating water quality rating curves using UV-Vis spectrophotometers to measure nitrate ($\text{NO}_3\text{-N}$), ammonium ($\text{NH}_4\text{-N}$), total dissolved nitrogen (TDN), Total Kjeldahl Nitrogen (TKN), dissolved organic carbon (DOC), phosphate ($\text{PO}_4\text{-P}$), total phosphorus (TP) and total suspended solids (TSS) in an agricultural coastal plain stream; (2) report the potential challenges involved, and propose methods to obtain gap free time series and best results.

2.2 Methods

Site description

The research site is an agricultural coastal plain stream reach 2,200 m in length, thereafter referenced as the Claridge Canal, in Goldsboro, North Carolina (35.42° N, 78.02° W). This reach was slated to be restored from 2015 to 2016 for 12 months starting in autumn to offset the construction of Highway US70 Bypass. Three monitoring stations were installed as Upstream Station (UP), Middle Stream Station (MD, located 1,390 m from UP), and Downstream Station (DN, located 807 m from MD) for a total length of 2,197 m of the study reach (Figure 2.1, details in Appendix A.1). The drainage areas at UP, MD, and DN are 236 ha, 414 ha, 573 ha, respectively. The average slope of the stream was 1.93%.

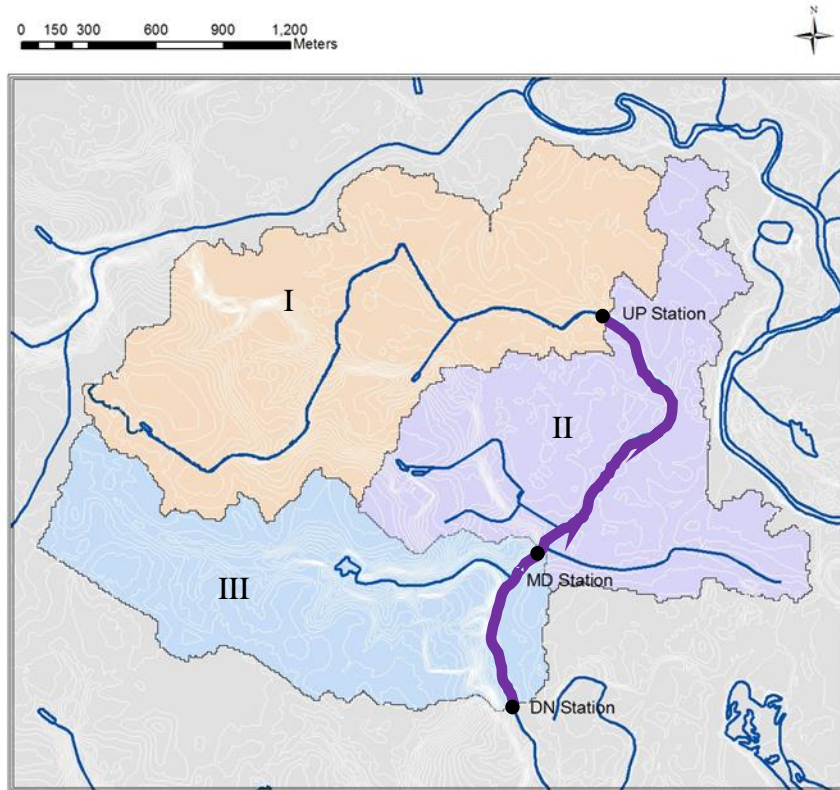


Figure 2.1

Three monitoring stations along the Claridge Canal in Goldsboro, North Carolina (I: Contributing watershed area for UP station; I and II: Contributing watershed area for MD station; I, II, and III: Contributing watershed area for DN station)

Background

One of the indicators chosen to assess the water quality benefits of this stream restoration uses cumulative nutrient loads as a basis. It is hypothesized that the bulk water quality effect can be assessed by the magnitude of the inflection of the correlation between cumulative loads of MD vs UP, and DN vs UP, between before and after restoration. For this, continuous, gap free flow and concentration data are necessary at all three stations at the

same time. The continuous monitoring of hydrology and water quality reported in this manuscript took place from December 2013 to March 2015.

Flow measurements

Because of the low gradient of the stream, variable downstream control conditions can create large hysteresis in the stage-discharge relationships at the event and seasonal scales (e.g., Birgand et al., 2013). Stage measurements alone are thus insufficient to calculate discharge. To solve this problem, stage and velocity were measured using Doppler velocity meters (SonTek IQ Doppler meter, San Diego, CA, USA) installed in wooden trapezoidal flumes. The trapezoidal flumes (details in Etheridge et al., 2013, and Birgand et al., 2005) funnel water unto a structure of known and stable geometries. The discharge (flow) rate (Q) is calculated as the product of cross-sectional average velocity (V) with the cross-sectional area (A) (Equation 1).

$$Q = V \times A \quad \text{(Equation 1)}$$

The cross-sectional area is calculated using measured stages and the known dimensions of the flumes. The cross-sectional average velocity V is calculated using the index velocity rating (Morlock et al., 2002; Birgand et al., 2005; ISO 15769, 2010). An index velocity rating was established between the Sontek velocity data and the cross-section average velocities obtained during manual gauging.

Manual gauging was performed using the velocity area method (ISO 748, 1997) every field visit, except in non-wadable conditions. For that, the cross-section of the flume was

divided into several vertical columns, marked by PVC strips were installed along the sides and on the bottom of the flume to mark the center of each column (Figure 2.2). The point velocity, measured using a portable velocity meter (Marsh-McBirney, Frederick, MD, USA; resolution 1 cm/s), in each column at 40 percent of the depth was taken as the column mean velocity (Figure 2.2). The manual mean velocity (V_m) was eventually calculated from dividing the overall flow rate, i.e., the sum of flow in each column, by the total cross-sectional area of the flume. The dimensions of the flumes at the three stations were measured using a total station after the flumes were installed. The index velocity from the Sontek used to derive the velocity rating corresponded to the average of instantaneous measurements 1-3 hours before and after each manual gauging.

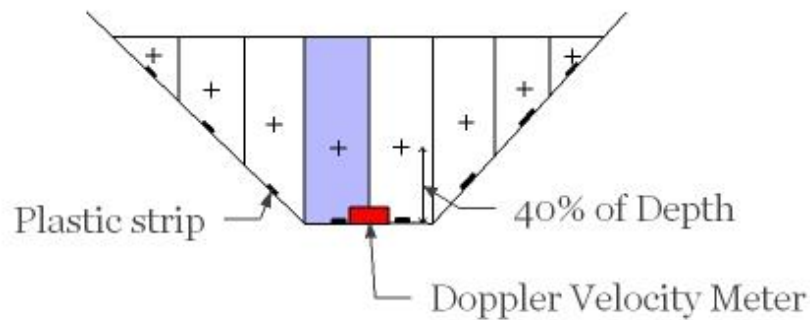


Figure 2.2

Schematic of a trapezoidal flume cross-section, showing the Doppler velocity meter, the virtual vertical column and the location of the manual velocity measurement points (marked as +; Modified from Birgand, 2000).

Water sample collection and measurements

Water quality at each station was monitored using a UV-Vis spectrophotometer (spectro::lyser model, s::can), a multi-parameter sonde (Eureka Manta 2), and an automatic discrete sampler (ISCO 6712). The UV-Vis spectrophotometer measured the absorbance of light between 220 to 750 nm for 5 and 35 mm path lengths. Thanks to the embedded Global Calibration from the manufacturer the instrument provided turbidity (NTU), nitrate ($\text{NO}_3\text{-N}$; mg/L), DOC (mg/L), and total organic carbon (TOC; mg/L) measurements every 15 minutes. At the same time interval, the Manta sonde measured Temperature ($^{\circ}\text{C}$), pH, conductivity ($\mu\text{S}/\text{cm}$), turbidity (NTU), and colored dissolved organic matter (CDOM; $\mu\text{g}/\text{L}$). The automatic discrete sampler took discrete water samples, up to 1 L every 12 hours (12 am and 12 pm). All field instruments were serviced on a biweekly basis.

Installation of the monitoring system

Although the water quality sensors are designed to be immersed, previous studies have shown that the reduced conditions surmised to exist in coastal plain streams may result in large chemical and biological fouling of the instruments (Etheridge et al., 2013). To limit the magnitude of fouling, the method developed by Etheridge et al., (2013) was applied, i.e., to shorten the time of exposure of the instruments to water (Figure 2.3). In synchrony with the 15-minutes sensor measurement intervals, a micro controller (equipped with Arduino Uno Board; www.arduino.cc) (4) triggered a peristaltic pump (3) to draw stream water (1) to the multi-parameter sonde (5) and to the UV-Vis spectrophotometer (7), both of which fitted

with flow through cells. The spectrophotometer was installed in a container (6) to avoid ambient light disturbance. After the sensors took their measurements, water was purged out of the measurement cells through a drain valve (8) under the spectrophotometer, and using the peristaltic pump (3) in a reverse mode back to the stream. The micro controller then sent a signal to a windshield washer pump (10) and valve (11) to rinse the optics the UV-Vis spectrophotometer (7) using tap water stored in a container (9) and resupplied during field visits. At 12 am and 12 pm every day, the discrete sampler (2) sampled up to ~900ml of water from the stream into the 24 bottles available.

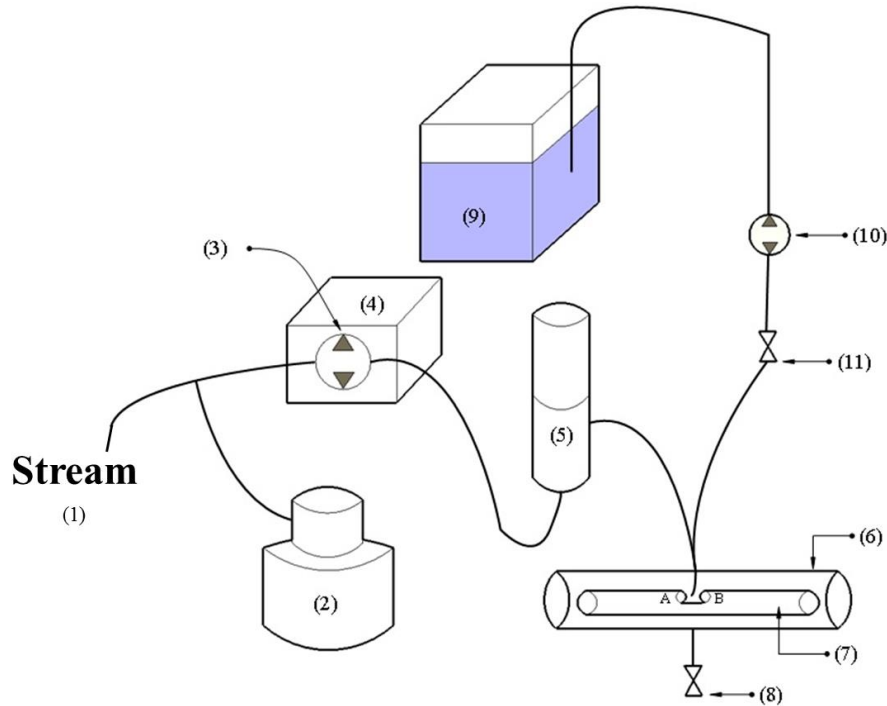


Figure 2.3

Schematic of the elements of the water quality monitoring system (not in the scale; numbers detailed in text; Modified from Etheridge et al., (2013))

Equipment maintenance

Biweekly field visits included flow and water quality data download, as well as other maintenance. The flumes and Doppler velocity meters were cleaned using brushes to remove sand, which was brought after storm events and clean algae that grew at certain times of the year. Because of bio- and chemical fouling on instruments and optics in particular (Flemming, 2011; Etheridge et al., 2014; Whelan and Regan, 2006), a cleaning procedure was applied onto the UV-Vis spectrophotometer and multi-parameter sonde based on that developed by Etheridge et al., (2014). For the UV-Vis spectrophotometers, cotton swabs soaked in 2% hydrochloric acid (HCl) were applied to the optic lens for 2-3 minutes. Then, the lenses were rinsed with deionized water and dried with a cloth. This procedure was repeated until the absorbance spectrum values in air and deionized water measurements were ‘flat’ and within 10 m^{-1} , i.e., similar to the original instrument setting. For the multi-parameter sonde, a detergent and toothbrush were used to clean the sensors except for CDOM sensor. CDOM sensor was cleaned with 2% HCl, a cotton swab and deionized water; the pH reference solution for pH sensor was changed every 2 months. The sensors in multi-parameter sonde were calibrated with standard solutions every 2-3 months.

Laboratory analyses

For each field visit, the discrete water samples were stored on ice and transported to the laboratory for analysis. The selections of the discrete samples for laboratory analysis depended on the initial water quality results from UV-Vis spectrophotometer and the flow

events, i.e., the samples taken during flow events when concentrations change rapidly were preferentially selected.

The original 900 ml discrete samples were split into several aliquots for analyses. 500 mL were transferred for TSS analysis (Standard Method 2540 D; Rice et al., 1997), and 150 mL were acidified with sulfuric acid for TKN (Standard Method 4500 N Org D; Rice et al., 2012) and TP analyses (Standard Method 4500 P F; Rice et al., 2012). The residual of the volume was filtered (pore size of 0.22 μm ; EMD Millipore Sterivex Sterile Pressure-Driven Devices, Darmstadt, Germany). Filtered solutions of 14 mL were transferred and acidified with sulfuric acid in 15 mL-centrifuge tubes for DOC (Standard Method 5310 B; Greenberg et al., 2005) and TDN analysis (adapted by Standard Method 5310 B; Greenberg et al., 2005). Another 14 mL of filtered solutions without adding sulfuric acid were transferred in 15 mL-centrifuge tubes for $\text{NO}_3\text{-N}$ (The Cadmium Reduction Method; Eaton et al., 1995), $\text{NH}_4\text{-N}$ (Salicylate Method; Eaton et al., 1995) and $\text{PO}_4\text{-P}$ analyses (Ascorbic Acid Method; Eaton et al., 1995). $\text{NO}_3\text{-N}$, $\text{NH}_4\text{-N}$, TDN, $\text{PO}_4\text{-P}$, and DOC were analyzed at the Environmental and Agricultural Testing Service; TP and TKN were analyzed at the Center for Applied Aquatic Ecology; and TSS was analyzed at the Environmental Analysis Test Service Lab at North Carolina State University.

The acid or other preservation agents were not added to unrefrigerated samples in the field. A sample degradation study was applied instead. For this, two grab samples were collected at the same time. One was labeled “Fresh”, immediately put on ice and brought back to the laboratory for analysis, and the other one was labeled “Degraded”, left in the

sampler until the next field visit, when it was retrieved and analyzed following the procedure described above (TSS not analyzed).

Cumulative load calculations

The water quality indicator sought in this manuscript is cumulative load (L), which is the integral over a given time (t) of instantaneous loads calculated as the product of solute concentration (C) with flow rate (Q ; Equation 2). In reality, a good estimator of this integral is the summation of instantaneous 15-min loads calculated from the 15-min flow (Q_i) and concentration (C_i) data (Equation 3), where K is the unit adjustment factor and N is the number of 15 min intervals in t .

$$L = \int_0^t C(t)Q(t)dt \quad \text{(Equation 2)}$$

$$L \approx K \sum_{i=1}^{i=N} C_i Q_i \quad \text{(Equation 3)}$$

Calibration methods for concentrations from spectral data

The ‘Global Calibration’ is the default algorithm embedded in the Spectro::lyser instrument to calculate concentrations *in situ* from the absorbance spectra. Nitrate, DOC, TOC concentrations, and turbidity values are thus calculated and saved in an output PARAMeter file, referred to as the PAR file. The results from the PAR files were compared to those of the discrete sample concentrations.

PLSR as a regression model was used to correlate concentrations from the discrete samples to the spectral data (from UV-Vis spectrophotometers) measured at the same time. Then, the PLSR model was applied to predict 15 min concentrations from the 15-min spectral data. PLSR essentially decreases the hundreds of wavelengths of spectral data to a smaller number of principal component vectors to obtain highest correlation with water quality concentrations (Etheridge et al., 2013). This statistical technique is well suited for data in which the explanatory variables are highly auto correlated, as are absorbance values from sequential wavelengths (Mevik et al., 2011).

The procedures for PLSR calibration were described in Etheridge et al. (2013) and Langergraber et al. (2003), using the pls package (Mevik et al., 2011) in the R software (R Core Team, 2016). Briefly, this package takes 90% of the points to create a calibration model and cross validates on the remaining 10%, and calculates indicators such as Root Mean-Square Error of Prediction (RMSEP) and R^2 for a given number of components. The model was initially run for 20 components. The optimum number of PLSR components for each analysis was chosen as the lowest number of components for which the RMSEP was at or near its minimum value.

It is hypothesized just as Etheridge et al. (2013) did, that this method essentially quantifies the co-variability of the ‘color matrix’ of the water with concentrations. It is hypothesized that this co-variability has no theoretical reason to hold for all seasons and all hydrological conditions. Thus, several models where in one all points were used, and in others where seasonal models were derived.

Methods for correcting erroneous data and filling missing data

Human errors and equipment failure invariably result in obvious errors and gaps in flow and/or concentration data in the field. Since both signals correspond to the derivative functions necessary to calculate the cumulative loads, it is essential to be able to find solutions to correct for erroneous and fill in missing data.

Handling of missing and erroneous flow data

The accumulations of sand/leaves in the flumes and the growth of algae on the Doppler sensors could disturb the measured signal of Doppler velocity meters and induced noisy measurements and outliers. After removing the ‘spikes’ or obviously unreliable data points, the flow dataset was corrected by applying the moving average velocity method (details in Birgand, 2000) in Microsoft Excel to smooth and mitigate the spikes of measurements.

From the long-term observations on flow data, there were similar patterns and trends for the flow in both non-storm and storm event conditions between the three monitoring stations in the Claridge Canal (Figure 2.4). As a result, flow rates from one station could be reliably predicted from those of the other stations, using simple linear regressions around the missing data periods. To obtain the best results, with consideration of the distances between the three stations, the predicted flow at one station was derived from the nearest station with available flow data. All the filling work was accomplished in Microsoft Excel.

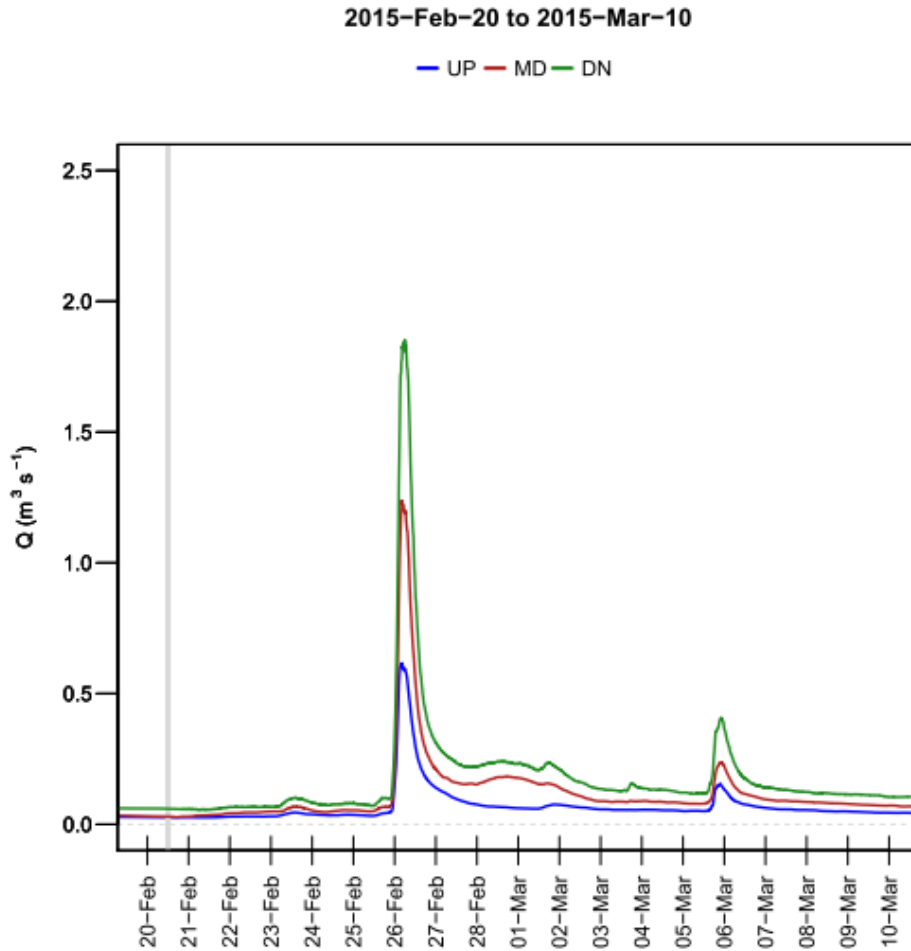


Figure 2.4 An example of flow results at UP (blue line), MD (red line), DN (green line) from February 20 to March 10 in 2015.

Handling of missing and erroneous concentration data

The antifouling system described above has the advantage of potentially reducing the magnitude of fouling but the disadvantage of increasing the probability of failure because of all the moving mechanical parts involved and increased power consumption. It was observed that infrequent power outages, tubing disconnection, etc. that prevented the pumping of water

to the instrument to function properly, and induced missing data (e.g., total power outage), air measurements (power available for the water quality probes to function properly but water did not get pumped to the instrument, hence the measurements correspond to absorbance in air) or ‘noisy’ points (large spikes in the data series). Even with the antifouling system, fouling on optic surface on UV-Vis spectrophotometers was observed. Although the PLSR calibration did correct for most of the fouling (details below), concentration ‘drifts’ away from the discrete sample results was observed.

To handle this, a sequence of data pre- and post-treatments was devised, using the AQUARIUS software (Aquatic Informatics Inc., 2009) as the main tool. The tools in the software included “Data Pre-Processing”, which could combine or separate different sets of data; “Data Correction”, which could remove outliers and drift the multiple points in a certain period.

First, ‘workable’ data time series were created after stripping missing, air and ‘noisy’ data. The discrete samples that were considered fell within the workable data times for use in the PLSR calibration. Second, two approaches were developed to fill the missing concentration data: a ‘Manual method’ and a ‘Semi-Automatic method’. For Manual method, the default method was to generate 15-min dataset by linear interpolation between consecutive discrete sample concentrations. However, during hydrological events, this did not necessarily represent well the concentration peaks and troughs generally observed when spectral data were available. For this, additional discrete data points were added to the series,

which values were ‘borrowed’ from the adjacent storm events used as references, and linearly interpolated between all points to obtain 15-min concentration series.

The Manual method, although easy to apply, is subjective. To assess its uncertainty, the more robust Semi-Automatic method was applied. For this, using Microsoft Excel, ‘local’ rating curves and regression equations between concentrations and flow rates from adjacent periods were derived (including storm events and baseflow), and predicted concentrations from flow values. The relative uncertainties of the two methods were assessed by calculating the difference in cumulative loads for both methods.

During the entire monitoring period (16 months), there were only 7 days (February 14-20 in 2015), for which the monitoring systems were frozen and malfunctioned at all three stations simultaneously because of the adverse weather; thus, all the flow and water quality results (including continuous and discrete) were missing for this short time period.

Records from the two nearby weather stations, Finch's Station North Carolina (<http://www.raws.dri.edu/cgi-bin/rawMAIN.pl?laNFIN>) and Seymour Johnson Air Force Base weather station (<https://www.wunderground.com/us/nc/seymour-johnson-air-force-base>), suggest that during this period, there were no significant precipitation events that would have generated significant flow changes (compared with the other rainfall events from January to March in 2015). As a result, the missing flow and water quality data were filled by linearly interpolating between the last data point of February 14 and the first data point of February 20 with 15-min interval.

2.3 Results and Discussion

Developing index velocity ratings to calculate flow

From regression equations shown in Figure 2.5, the cross-section average velocities were equal to 97.57% ($R^2 = 0.9858$), 93.02% ($R^2 = 0.9889$) and 98.91% ($R^2 = 0.9838$) of the Doppler sensor velocities at UP, MD and DN, respectively. In other words, the Sontek sensors tended to overestimate velocities by 2.5%, 7.0%, and 1.0%, the cross-section average velocities, justifying the need for correction and harmonization among stations. The continuous velocity values which measured by the Doppler meters were multiply by the slope values from regression equations in Figure 2.5 to obtain the velocity values multiplied by the cross-sectional area to calculate flow.

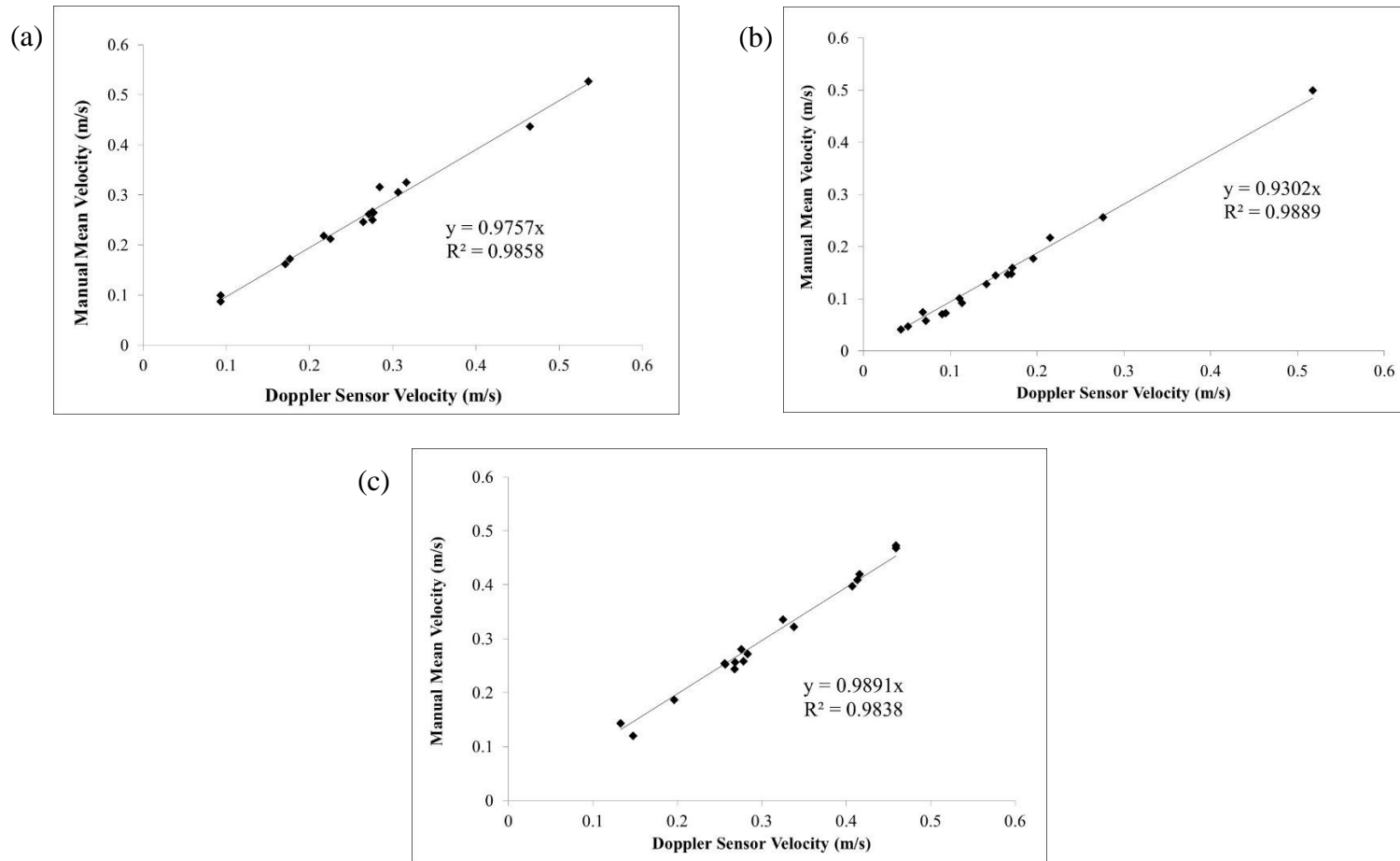


Figure 2.5

Manual mean velocity versus Doppler sensor velocity at the three stations. (a) UP; (b) MD; (c) DN.

Degradation sample study results

The main processes which affect the integrity of water samples include contamination, physical (temperature, volatilization, sorption, and degassing), chemical (precipitation and oxidation), and biological (Duncan et al., 2007). The same authors indicate that oxidation would reduce the concentrations of bulk organic parameters, as well as plankton feeding on organic matter in the water samples. As a result, it was expected that the seasonal variations would affect the degradation rate in discrete samples between the field trips especially in spring and summer since the temperature and bioavailability were higher in spring and summer.

A paired t-test was applied to evaluate the differences between the “Fresh” and “Degraded” samples for each water quality parameter ($\text{NO}_3\text{-N}$, $\text{NH}_4\text{-N}$, TDN, TKN, DOC, TP, and $\text{PO}_4\text{-P}$) at the three stations for two-time periods: spring-summer, and fall-winter (The dates of each season were separated based on spring equinox, summer solstice, fall equinox, and winter solstice of the monitoring years.). The results of degradation samples are summarized in Table 2.1 which included mean concentrations, standard deviation, percentage differences of mean concentrations between “Fresh” and “Degraded” samples, and the results of paired t-test with the p-values for $\text{NO}_3\text{-N}$, $\text{NH}_4\text{-N}$, TDN, TKN, DOC, TP, and $\text{PO}_4\text{-P}$ among the three stations. There were several significant differences ($\alpha=0.05$) between “Fresh” and “Degraded” samples in spring and summer, including $\text{NO}_3\text{-N}$ and $\text{NH}_4\text{-N}$ at MD and DN, TKN and TP at the three stations, and DOC at MD. There were no

significant differences ($\alpha=0.05$) between “Fresh” and “Degraded” samples for each water quality parameter at the three stations during the fall and winter period.

The consequence of this analysis is that when there was a significant difference ($\alpha=0.05$) between ‘fresh’ and ‘degraded’ samples for the water quality parameters in spring and summer (Table 2.1), only the discrete samples collected within 48 hours prior to the field date were used to improve the quality of PLSR calibration (suggested by Etheridge et al., 2013). All the discrete samples collected in fall and winter were used in the PLSR calibration, as no significant degradation was found at these times.

Table 2.1
Summary of the degradation samples results

Station		NO ₃ -N	NH ₄ -N	TDN	TKN	DOC	TP	PO ₄ -P
Spring and summer (03/21//2014-09/22/2014)								
UP	Mean± Standard deviation for Fresh samples (mg/L)	2.83±0.71	0.09±0.06	3.46±0.68	0.56±0.20	5.45±2.08	0.06±0.07	0.021 ±0.030
	Mean± Standard deviation for Degraded samples (mg/L)	2.95±0.66	0.07±0.04	3.50±0.69	0.49±0.16	5.22±1.83	0.05±0.06	0.017 ±0.032
	% differences of mean	+4	-27	+1	-13	-4	-27	-15
	p-value	0.198	0.080	0.455	0.027*	0.248	0.022*	0.098
MD	Mean± Standard deviation for Fresh samples (mg/L)	2.01±0.60	0.18±0.13	2.62±0.67	0.85±0.37	6.63±1.75	0.11±0.07	0.017 ±0.018
	Mean± Standard deviation for Degraded samples (mg/L)	2.14±0.59	0.09±0.14	2.65±0.67	0.55±0.14	5.73±1.38	0.08±0.05	0.017 ±0.021
	% differences of mean	+6.7	-46	+1.1	-35	-14	-34	0
	p-value	0.004*	0.011*	0.504	0.005*	3.68 x 10 ⁻⁵ *	0.004*	0.978
DN	Mean± Standard deviation for Fresh samples (mg/L)	1.93±0.57	0.20±0.12	2.55±0.66	0.86±0.32	6.02±1.33	0.10±0.09	0.014 ±0.01
	Mean± Standard deviation for Degraded samples (mg/L)	2.09±0.56	0.12±0.14	2.59±0.70	0.69±0.35	5.87±1.45	0.08±0.08	0.013 ±0.01
	% differences of mean	+8	-43	+2	-19	-2	-14	-5
	p-value	0.001*	0.015*	0.389	0.005*	0.26	9.5 x 10 ⁻⁴ *	0.669

Table 2.1 Continued

Station		NO ₃ -N	NH ₄ -N	TDN	TKN	DOC	TP	PO ₄ -P
Fall and winter (12/11/2013-03/20/2014, 09/23/2014-03/11/2015)								
UP	Mean± Standard deviation for Fresh samples (mg/L)	3.49±0.68	0.058±0.037	4.06±0.84	0.43±0.12	4.88±1.61	0.032 ±0.025	0.009 ±0.007
	Mean± Standard deviation for Degraded samples (mg/L)	3.48±0.07	0.057±0.023	4.08±0.90	0.42±0.11	4.45±1.48	0.030 ±0.028	0.008 ±0.007
	% differences of mean	-0.1	-1	0.4	-2	-9	-7	-9
	p-value	0.843	0.894	0.834	0.509	0.077	0.223	0.649
MD	Mean± Standard deviation for Fresh samples (mg/L)	2.92±0.86	0.06±0.04	3.50±0.93	0.502±0.15	5.45±1.94	0.05 ±0.05	0.010 ±0.007
	Mean± Standard deviation for Degraded samples (mg/L)	2.91±0.85	0.07±0.05	3.44±0.96	0.496±0.14	5.34±1.88	0.03 ±0.02	0.014 ±0.020
	% differences of mean	-0.4	+6	-1.7	-1	-2	-29	+38
	p-value	0.685	0.263	0.345	0.731	0.445	0.099	0.398
DN	Mean± Standard deviation for Fresh samples (mg/L)	2.76±0.67	0.070±0.05	3.25±0.74	0.518±0.14	5.59±1.79	0.049 ±0.03	0.013 ±0.01
	Mean± Standard deviation for Degraded samples (mg/L)	2.76±0.68	0.069±0.05	3.30±0.75	0.522±0.15	5.46±1.72	0.051 ±0.03	0.011 ±0.01
	% differences of mean	0	-2	+1	+1	-2	+4	-14
	p-value	0.781	0.784	0.293	0.870	0.446	0.613	0.286

(Note: *Significance at $\alpha=0.05$; % differences of mean with positive symbol: mean concentrations for Fresh samples are higher than Degraded samples; and vice versa.)

Discrete sample results

The laboratory analysis for discrete samples applied to PLSR calibrations are summarized in Table 2.2 which included the number of samples, mean concentrations, standard deviation, minimum concentrations, and maximum concentrations for $\text{NO}_3\text{-N}$, $\text{NH}_4\text{-N}$, TDN, TKN, DOC, TP, $\text{PO}_4\text{-P}$, and TSS among the three stations. In addition, the number of samples of $\text{NH}_4\text{-N}$ are less than the other parameters since the $\text{NH}_4\text{-N}$ concentrations are lower than the detection limit (0.1 mg/L) for most discrete samples (Table 2.2).

Table 2.2

Summary of the laboratory analyses for discrete samples (Units: mg/L; concentrations with significant ‘degradation’ not included)

	NO ₃ -N	NH ₄ -N	TDN	TKN	DOC	TP	PO ₄ -P	TSS
UP								
No. samples	230	67	228	218	213	216	138	212
Mean± Standard deviation	2.98±0.61	0.19±0.16	3.50±0.63	0.61±0.29	5.03±1.60	0.09±0.15	0.02±0.03	16.46±32.74
Minimum	1.0	0.10	1.8	0.28	2.6	0.01	0.01	0.33
Maximum	4.2	1.2	4.8	2.2	13.4	1.3	0.36	367
MD								
No. samples	102	79	101	98	102	58	54	81
Mean± Standard deviation	2.60±0.59	0.14±0.06	3.16±0.54	0.65±0.25	6.10±2.12	0.08±0.05	0.01±0.02	21.51±31.47
Minimum	1.1	0.10	1.7	0.3	3.0	0.02	0.01	2.0
Maximum	3.6	0.41	4.1	1.3	12.5	0.25	0.14	218
DN								
No. samples	176	72	176	161	193	159	130	166
Mean± Standard deviation	2.41±0.50	0.20±0.12	2.96±0.52	0.71±0.27	6.14±1.88	0.11±0.10	0.02±0.01	23.74±29.70
Minimum	0.8	0.10	1.5	0.3	3.7	0.02	0.01	1.0
Maximum	3.4	0.85	4.0	1.9	14.7	0.65	0.10	250

(Note: The detection limit is 0.1 mg/L for NO₃-N, NH₄-N, TDN, and DOC; 0.28 mg/L for TKN; 0.01 mg/L for TP and PO₄-P; no detection limit for TSS.)

Global Calibration versus discrete sample results

The global calibration that came with the instrument was used directly without local calibration and compared with discrete concentrations. The results show significant linear correlations between the discrete and the raw instrument values, but show large departure from the one to one line (Figure 2.6 and Figure 2.7; Table 2.3). For instance, the global calibration underpredicted nitrate concentrations and over predicted DOC concentrations at

UP station (Figure 2.6 and Figure 2.7). Additionally, the RMSE of each regression are equivalent to 10% to 25% of the absolute concentrations.

This justifies the need to find methods to create local calibration that can correct for slope, intercept and RMSE; hence the PLSR approach suggested by Torres and Bertrand-Krajewski (2008), Rieger et al., (2006), Langergraber et al. (2003), and Etheridge et al. (2014, 2015) to improve predictions for water quality concentrations.

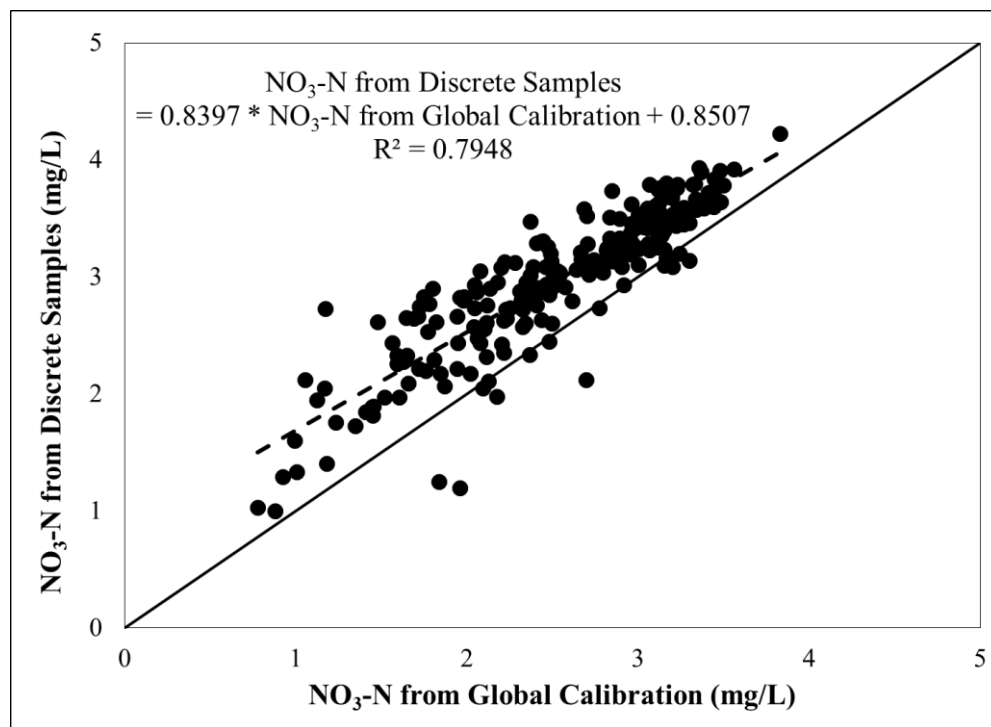


Figure 2.6

The linear regression relationship between Global Calibration and Discrete Samples for NO₃-N at UP. (Black solid line: 1 to 1 line; Black dash line: Regression line)

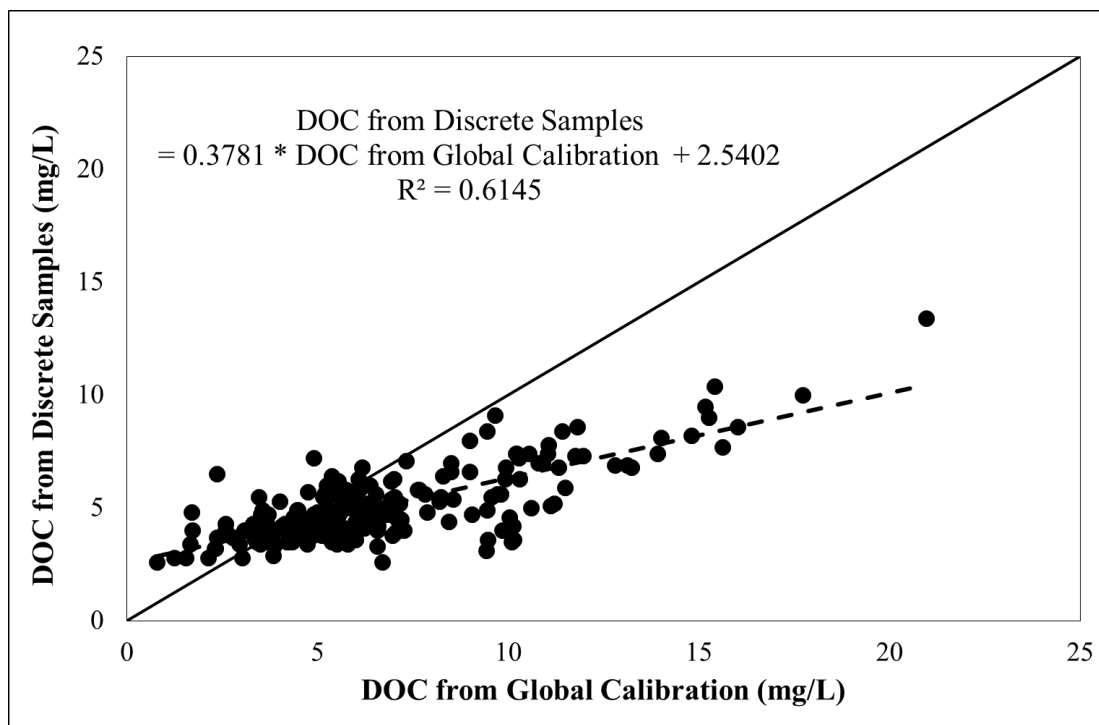


Figure 2.7

The linear regression relationship between Global Calibration and Discrete Samples for DOC at UP. (Black solid line: 1 to 1 line; Black dash line: Regression line)

Table 2.3

Summary of linear regressions between Global Calibration and discrete samples results for NO₃-N and DOC among the three monitoring stations

Station	NO ₃ -N				DOC			
	No. Observations	Regression Equation	R ²	RMSE	No. Observations	Regression Equation	R ²	RMSE
UP	230	Y = 0.8397 X + 0.8507	0.79	0.53	213	Y = 0.3781 X + 2.5402	0.61	2.78
MD	93	Y = 0.7438 X + 0.6002	0.87	0.27	91	Y = 0.6975 X + 1.7408	0.72	1.00
DN	154	Y = 0.5547 X + 0.9488	0.73	0.46	167	Y = 0.5577 X + 1.9064	0.65	1.56

(Note: 1. Y = Discrete Samples Results, and X = Global Calibration.)

PLSR calibration fitting procedure

The first item in the PLSR calibration is to define the number of components. As described in the methods section, the optimum number of components was determined as the lowest value for which the RMSEP values are at or near the minimum. In Figure 2.8, the RMSEP plots for NO₃-N at UP in spring and summer shows a breakpoint at 3 components as values decreased sharply from 0 component to 3 components. There is a first local minimum at 4 components while the overall minimum is at 9 components. Etheridge et al. (2013) suggested to use the number of components with the overall lowest RMSEP value to predict the water quality concentrations. The PLSR package in R (Mevik et al., 2011) shows that with 4 components, 99.98% of the variance is already explained and that 100% of the variance is explained with more components. However, with 9 components R² (0.97) is higher than with 4 components (R² = 0.93; Figure 2.9).

The penalty with using the first local minimum (4 components) is that the R² suggests that some concentrations might not be predicted as well as they would with 9 components. However, the gain becomes unclear by adding components as 100% of the variance is predicted with 5 components and above. The consequences appear rather clearly when plotting the concentration time series. The continuous NO₃-N concentrations with 4 components (Figure 2.10) are smoother than the results with 9 components (Figure 2.11). The physical reasons cannot be found that concentrations have such ‘noise’ while the flow data does not. It is suggested that with 9 components, the regression is ‘overfitting’; thus 4 components is the optimal number of components in this particular case.

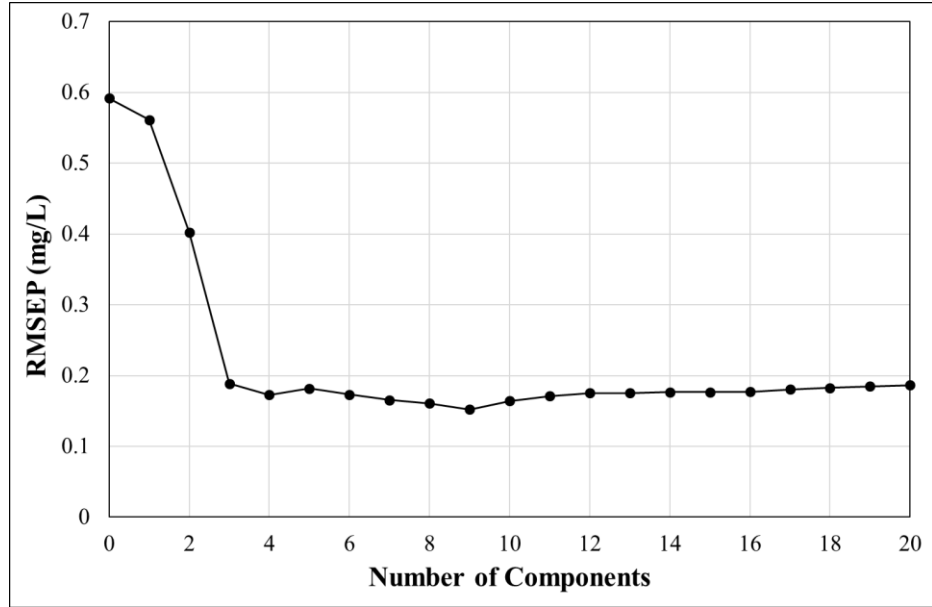


Figure 2.8

RMSEP (mg/L) and number of components from PLSR output for NO₃-N at UP in spring and summer.

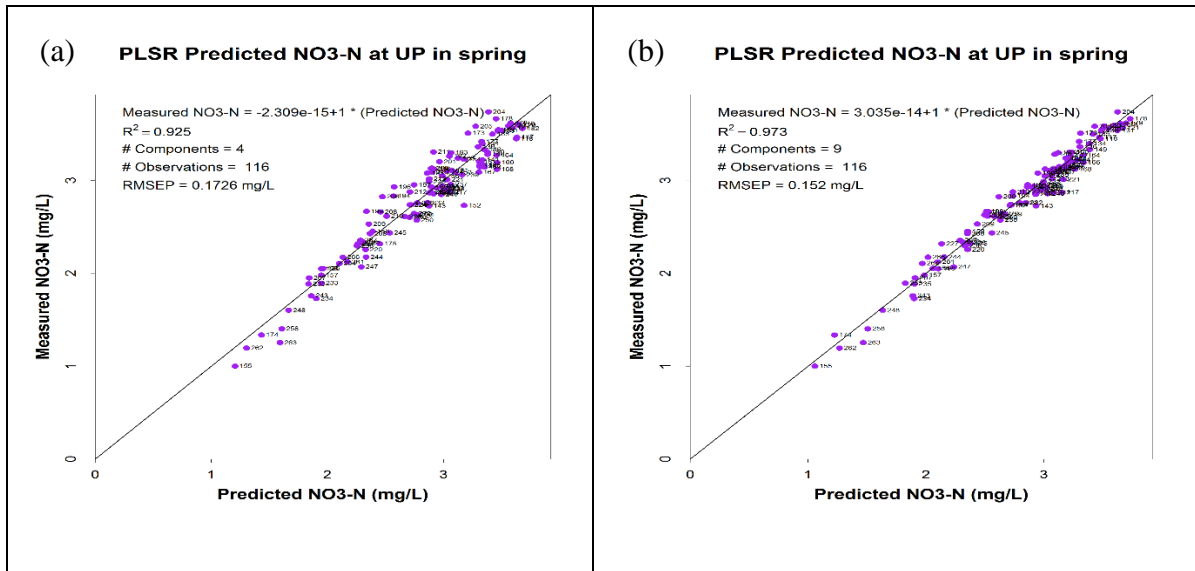


Figure 2.9

Regression relationships between lab measured NO₃-N and PLSR predicted NO₃-N from PLSR calibrations at UP in spring and summer with 4 and 9 components. (a) 4 components; (b) 9 components.

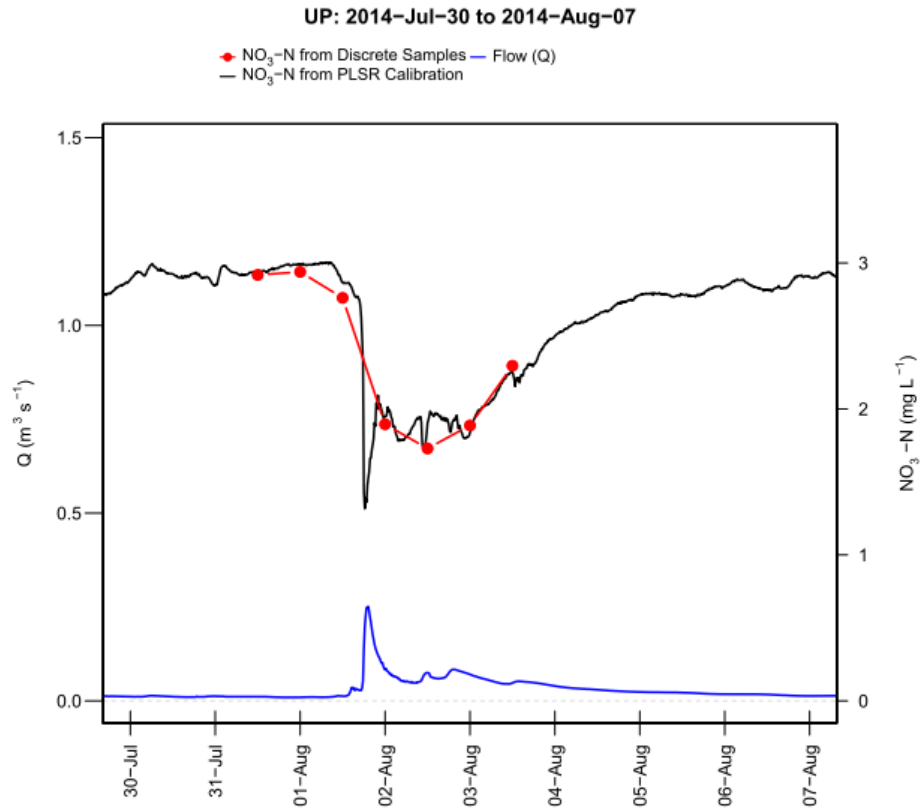


Figure 2.10

Continuous NO₃-N concentrations from PLSR calibration with 4 components (black line), NO₃-N concentrations from Discrete Samples (red dots), Flow rate (blue line) at UP on July 30-August 7 in 2014.

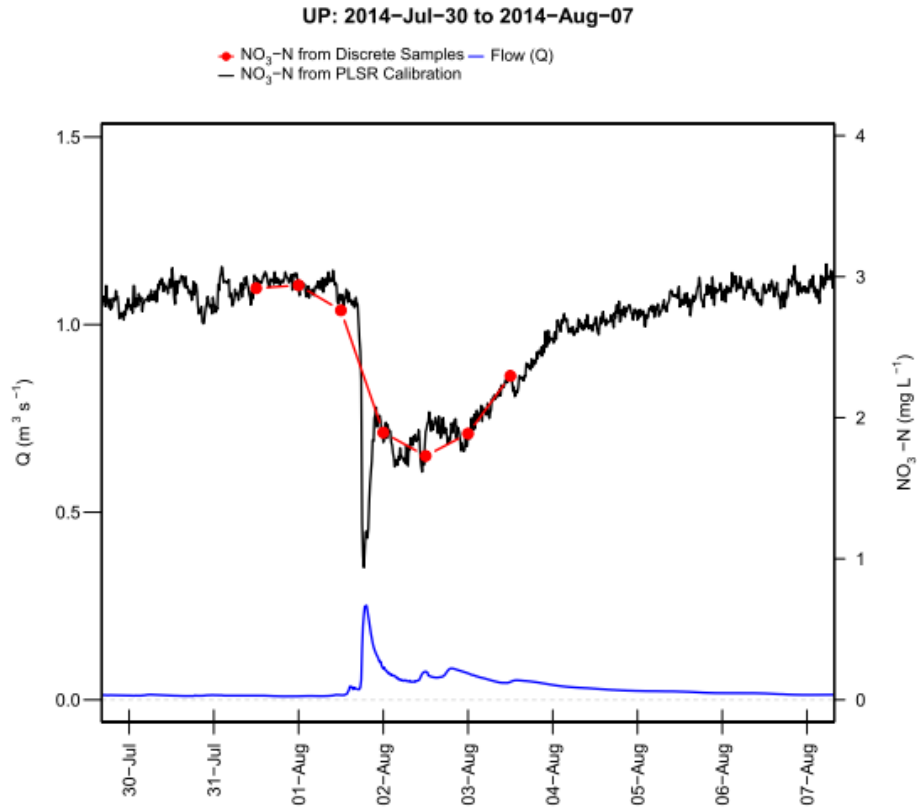


Figure 2.11

Continuous NO₃-N concentrations from PLSR calibration with 9 components (black line), NO₃-N concentrations from Discrete Samples (red dots), Flow rate (blue line) at UP on July 30-August 7 in 2014.

For each parameter and each calibration period, the optimum number of components was chosen as the least number of components above which the percentage of the variance did not increase significantly and for which R^2 values were acceptable.

The calibration process revealed apparent ‘outliers’ that were detected in an iterative process. From the regression plots, such as those in Figure 2.9, there were times when some points appeared astray from the general trend. Thus, the data points were identified and plotted in context in flow and concentration time series plots (such as those in Figure 2.10

and Figure 2.11). These corresponded to points where: (1) the S::CAN records showed unreliable data appearing as sudden ‘jumps’ possibly associated with air bubbles or air measurements associated with malfunctioning of the pumping system; (2) during rapidly changing concentrations, small asynchrony between the S::CAN measurements and the discrete sampling could have caused concentration differences; (3) the concentrations from the lab appeared out of trend with flow and concentration trends. The identified outliers were taken out; then, new regressions and concentration time series were created. This iterative process was used until there were no objective reasons (described above) to take points out of the regressions.

It is possible to create water quality rating curves for most parameters tested

The number of observations (discrete samples), final number of components for prediction, R^2 , RMSE, and Nash Sutcliffe Efficiency (NSE) values predicted from PLSR calibrations for $\text{NO}_3\text{-N}$, $\text{NH}_4\text{-N}$, TDN, TKN, DOC, TP, $\text{PO}_4\text{-P}$, and TSS at the three stations are summarized in Table 2.4, Table 2.5 and Figure 2.12 to Figure 2.19. (Note: RMSEP values in Figure 2.12 to 19 corresponded to the selected number of component for PLSR calibration itself, and RMSE in Table 2.4 and Table 2.5 denoted the root mean square error between observed and predicted concentrations.) The discrete samples were not separated by seasons for TSS with the application of PLSR calibration because there was no degradation study for TSS. To calculate the NSE, the fiteval software was used (Ritter and Muñoz-Carpena, 2013). This software evaluates the goodness of fit of a model compared to observed data. Ritter and Muñoz-Carpena (2013), after review of the literature, suggest that models

are generally considered valid when NSE are greater than 0.65 (max = 1). However, the same authors point out that the NSE values calculated for a particular set of modeled vs. observed values are dependent upon the points used to evaluate the model goodness. To provide a more robust assessment of the model performance 'fiteval' uses bootstrapping techniques to provide an empirical distribution of the RMSE and NSE values. Ritter and Muñoz-Carpena (2013) suggest that the 0.10 significance level to estimate whether a model can be considered valid or not. Practically, a model is considered valid when 90% or more of the NSE values in the empirical distribution are above 0.65. In Table 2.4 and Table 2.5, the NSE average value, the percentage of the time the model is unsatisfactory, and whether the model can be considered valid (when unsatisfactory more than 10% of possibilities) are presented.

Out of the 42 PLS regressions for the 7 parameters tested, 3 stations and 2 major climatic periods (fall-winter and spring-summer), only 2 showed poor correlations ($R^2 < 0.17$; $NSE < 0.17$) between the lab and the predicted concentrations, for NH_4-N , while all others had R^2 greater than 0.71. However, using the fiteval software and the 0.1 significance criterion, 9 of the PLS regressions cannot be validated as more than 10% of the empirical NSE values are below 0.65. Because PLS is a regression model, the R^2 and NSE values are equal (Table 2.4 and Table 2.5).

Among the parameters known to absorb light (nitrate, DOC, and TSS), nitrate had the highest significant PLS regressions with R^2 and NSE between 0.93 and 0.98 for 4-5 components, and RMSE included between 0.07 and 0.16 mg N/L. The RMSE values are within 5-10% of the measurement range (1 to 4 mg N/L). The calibrations for DOC were

second best with R^2 and NSE between 0.91 and 0.93, for 4-5 components, except for the UP station in the winter-fall ($R^2 = 0.85$ for 7 components). The RMSE were generally higher, however, ranging between 0.52 and 0.58 mg C/L, which would be around 10% error of the measured range (4-14 mg C/L). The results for TSS are discussed further below.

All other parameters are not known to have specific absorbance wavelengths or represent a large variety of molecules and matter. Nonetheless, highly significant correlations were obtained between absorbance and their concentrations. It was found that the rating curves for TDN to be the most consistent with R^2 and NSE included between 0.85 and 0.94 for 4-5 components, and RMSE included between 0.13 and 0.23, i.e., between 5%-10% of the measurement range. It was found that highly significant correlations and robust models for TP showing R^2 and NSE between 0.92 and 0.97 for 4-7 components and RMSE between 0.02 and 0.03 mg P/L, for the UP and DN stations. The RMSE represent much higher percentages of the measured range (20% to 30%) but the absolute values are of the same order of those expected from lab analysis errors. For the MD station, the correlations are not as strong, but are valid ($0.81 < R^2 < 0.88$).

Despite apparently significant correlations for all $\text{PO}_4\text{-P}$ regressions (2/3 of the regressions showing R^2 between 0.92 and 0.95), the regressions for the fall and winter periods for the UP and MD appear unsatisfactory according to the 0.1 significance criterion on the NSE distribution (the other period for the MD station is barely satisfactory). These regressions had the lowest number of points, which makes them less robust.

The significance for the TKN regressions as shown by the R^2 (between 0.80 and 0.87, one at 0.71) is a bit lower than for the previous parameters, although slightly, for 4-5 components. The PLSR model for MD in the fall-winter is invalidated by the NSE 0.1 significance criterion, however. The RMSE found are relatively high as they range between 0.12 and 0.13 mg N/L corresponding to 15% to 30% of the measurement range. The absolute values for the RMSE are in the order of the errors expected on the lab analyses for TKN, however.

Although the regressions appear highly significant (R^2 between 0.71 and 0.97) for $\text{NH}_4\text{-N}$, only one PLSR model (MD in the spring) is validated. In this particular case, and contrary to the other regressions, the concentrations for the calibration points are relatively stratified along the calibration range.

Table 2.4

Summary of PLSR calibration for NO₃-N, NH₄-N, TDN, TKN, DOC TP, and PO₄-P at the three stations (UP, MD, DN) (Units for RMSE: mg/L)

	NO ₃ -N	NH ₄ -N	TDN	TKN	DOC	TP	PO ₄ -P
UP in spring and summer							
No. Observations	116	43	116	103	85	104	106
No. PLSR Components	4	4	4	4	4	4	4
R ²	0.93	0.17	0.88	0.87	0.91	0.95	0.94
RMSE	0.16	0.15	0.21	0.10	0.52	0.03	0.005
NSE (% unsatif.)	0.93 (0%)	0.17 100%)* *	0.88 (0%)	0.87 (0%)	0.91 (0%)	0.95 (0%)	0.94 (7.4%)
UP in fall and winter							
No. Observations	114	24	112	115	128	112	32
No. PLSR Components	4	5	5	4	7	7	4
R ²	0.94	0.97	0.89	0.87	0.85	0.97	0.88
RMSE	0.14	0.03	0.21	0.11	0.58	0.02	0.02
NSE (% unsatif.)	0.94 (0%)	0.97 (15%)* *	0.89 (0%)	0.87 (0.1%)	0.85 (0%)	0.97 (0%)	0.88 (33%)**
MD in spring and summer							
No. Observations	43	25	43	40	44	34	33
No. PLSR Components	4	4	5	4	5	3	5
R ²	0.98	0.80	0.92	0.87	0.92	0.88	0.92
RMSE	0.07	0.03	0.14	0.08	0.58	0.01	0.001
NSE (% unsatif.)	0.98 (0%)	0.80 (2%)	0.92 (0%)	0.87 (0%)	0.92 (0%)	0.88 (0.1%)	0.92 (9.4%)

Table 2.4 Continued

	NO₃-N	NH₄-N	TDN	TKN	DOC	TP	PO₄-P
MD in fall and winter							
No. Observations	59	54	58	58	58	24	21
No. PLSR Components	4	4	4	4	4	3	3
R ²	0.95	0.75	0.94	0.71	0.93	0.81	0.74
RMSE	0.12	0.02	0.13	0.13	0.55	0.03	0.01
NSE (% unsatif.)	0.95 (0%)	0.75 (35%)* *	0.94 (0%)	0.71 (22%)**	0.93 (0%)	0.81 (8.8%)	0.74 (29%)**
DN in spring and summer							
No. Observations	66	39	66	61	88	61	62
No. PLSR Components	4	4	4	4	5	4	4
R ²	0.93	0.10	0.85	0.80	0.91	0.95	0.94
RMSE	0.13	0.07	0.23	0.12	0.58	0.03	0.68
NSE (% unsatif.)	0.93 (0%)	0.10 (100%) **	0.85 (0%)	0.80 (5.2%)	0.91 (0%)	0.95 (0%)	0.94 (0%)
DN in fall and winter							
No. Observations	110	33	110	100	105	98	68
No. PLSR Components	5	5	5	5	5	5	6
R ²	0.93	0.71	0.85	0.84	0.92	0.97	0.95
RMSE	0.12	0.09	0.19	0.10	0.52	0.02	0.003
NSE (% unsatif.)	0.93 (0%)	0.71 (39%)* *	0.85 (0.1%)	0.84 (2.7%)	0.92 (0%)	0.97 (0%)	0.95 (1%)

** : model considered invalid

Table 2.5

Summary of PLSR calibration for TSS at the three stations (UP, MD, DN)

	UP	MD	DN
No. Observations	212	81	166
No. PLSR Components	3	4	6
R ²	0.94	0.68	0.94
RMSE	8.239	17.675	7.411
NSE (% unsatif.)	0.94 (0.1%)	0.68 (39%)**	0.94 (0%)

** : model considered invalid

Figure 2.12

Regression relationships between measured NO₃-N and predicted NO₃-N from PLSR calibrations. (a) UP in spring and summer; (b) UP in fall and winter; (c) MD in spring and summer; (d) MD in fall and winter; (e) DN in spring and summer; (f) DN in fall and winter.

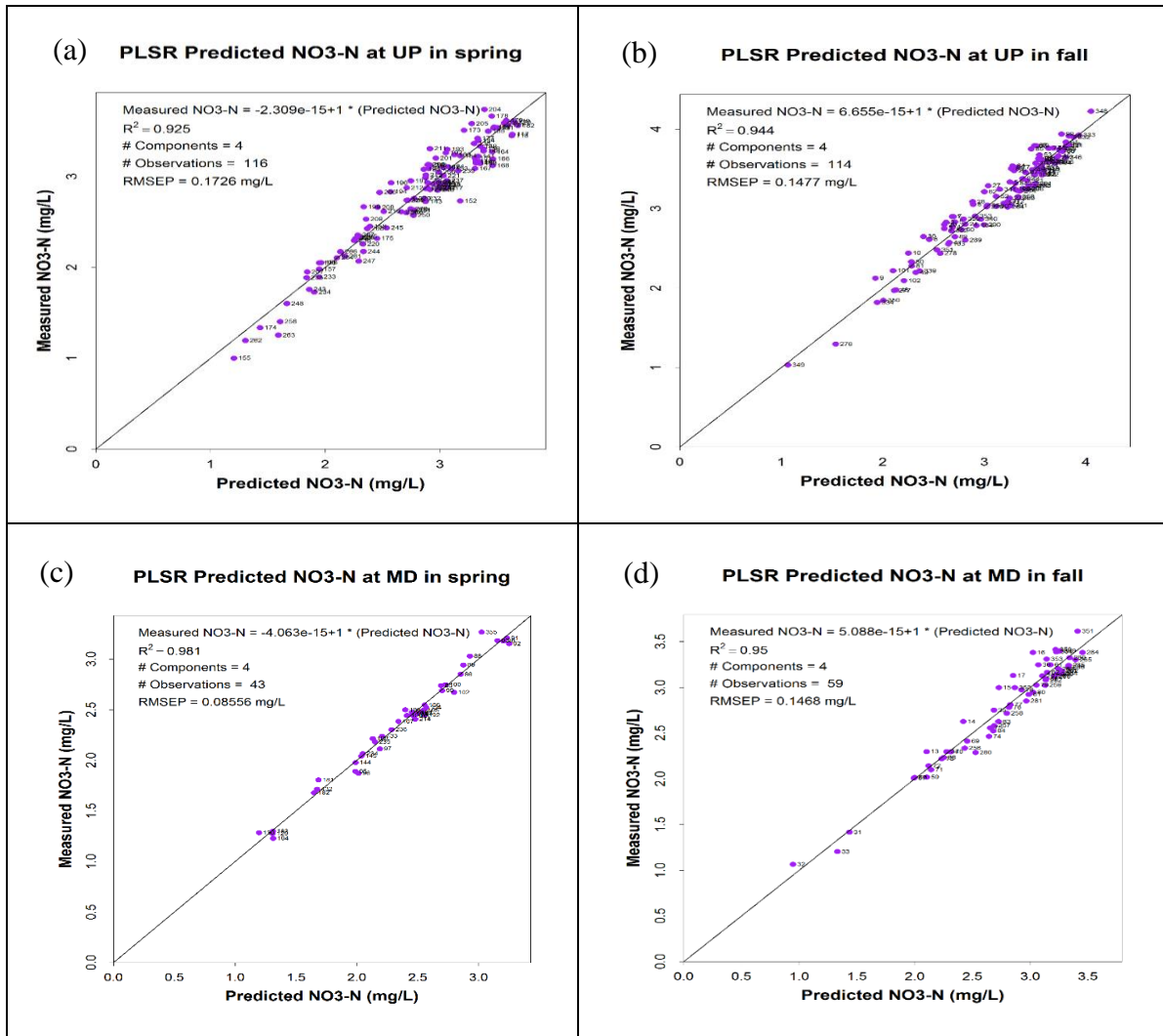


Figure 2.12 Continued

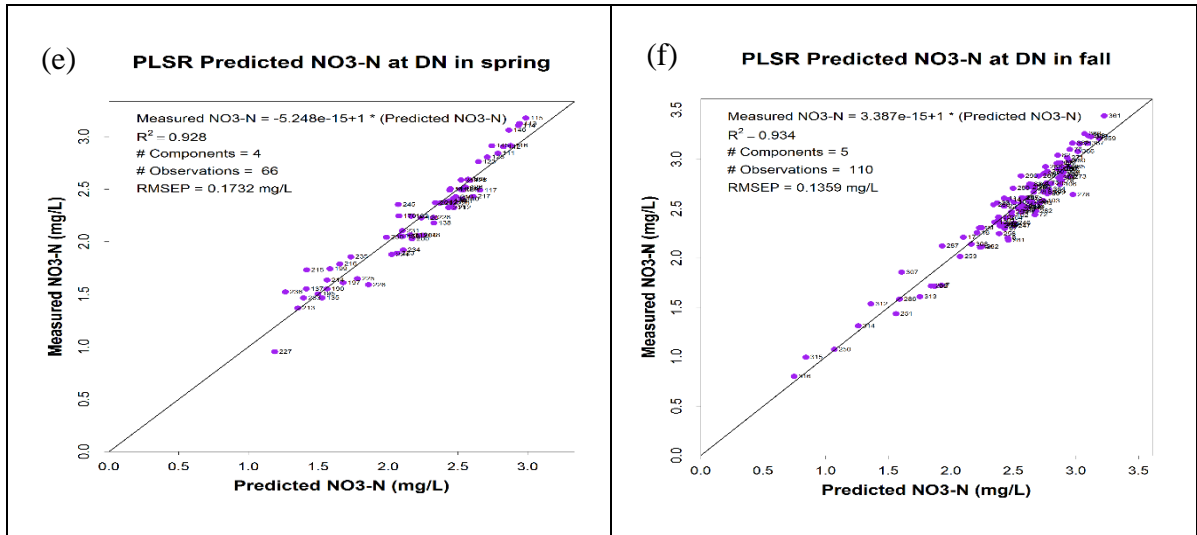


Figure 2.13

Regression relationships between measured NH₄-N and predicted NH₄-N from PLSR calibrations. (a) UP in spring and summer; (b) UP in fall and winter; (c) MD in spring and summer; (d) MD in fall and winter; (e) DN in spring and summer; (f) DN in fall and winter.

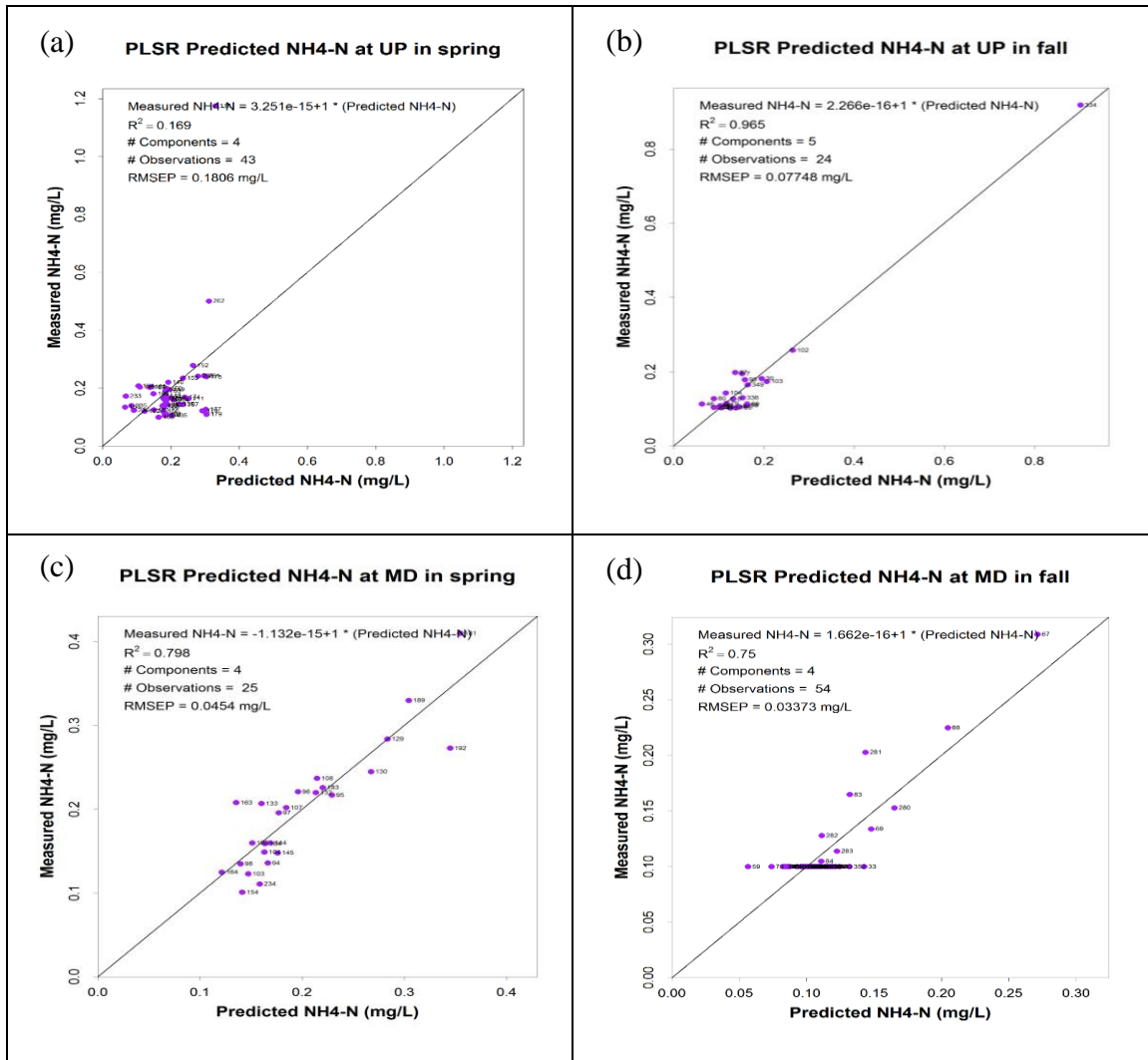


Figure 2.13 Continued

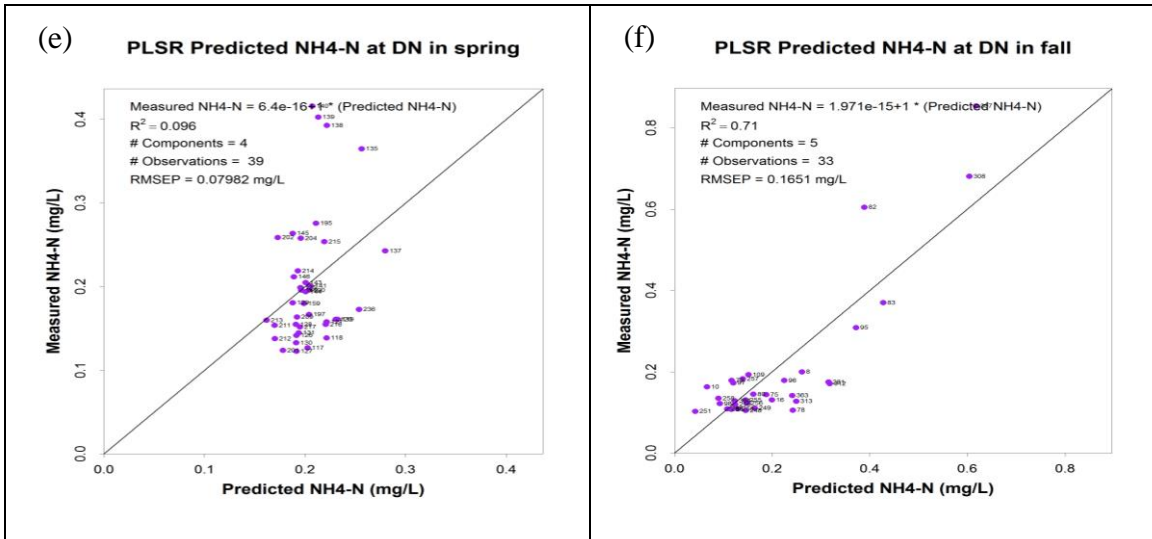


Figure 2.14

Regression relationships between measured TDN and predicted TDN from PLSR calibrations. (a) UP in spring and summer; (b) UP in fall and winter; (c) MD in spring and summer; (d) MD in fall and winter; (e) DN in spring and summer; (f) DN in fall and winter.

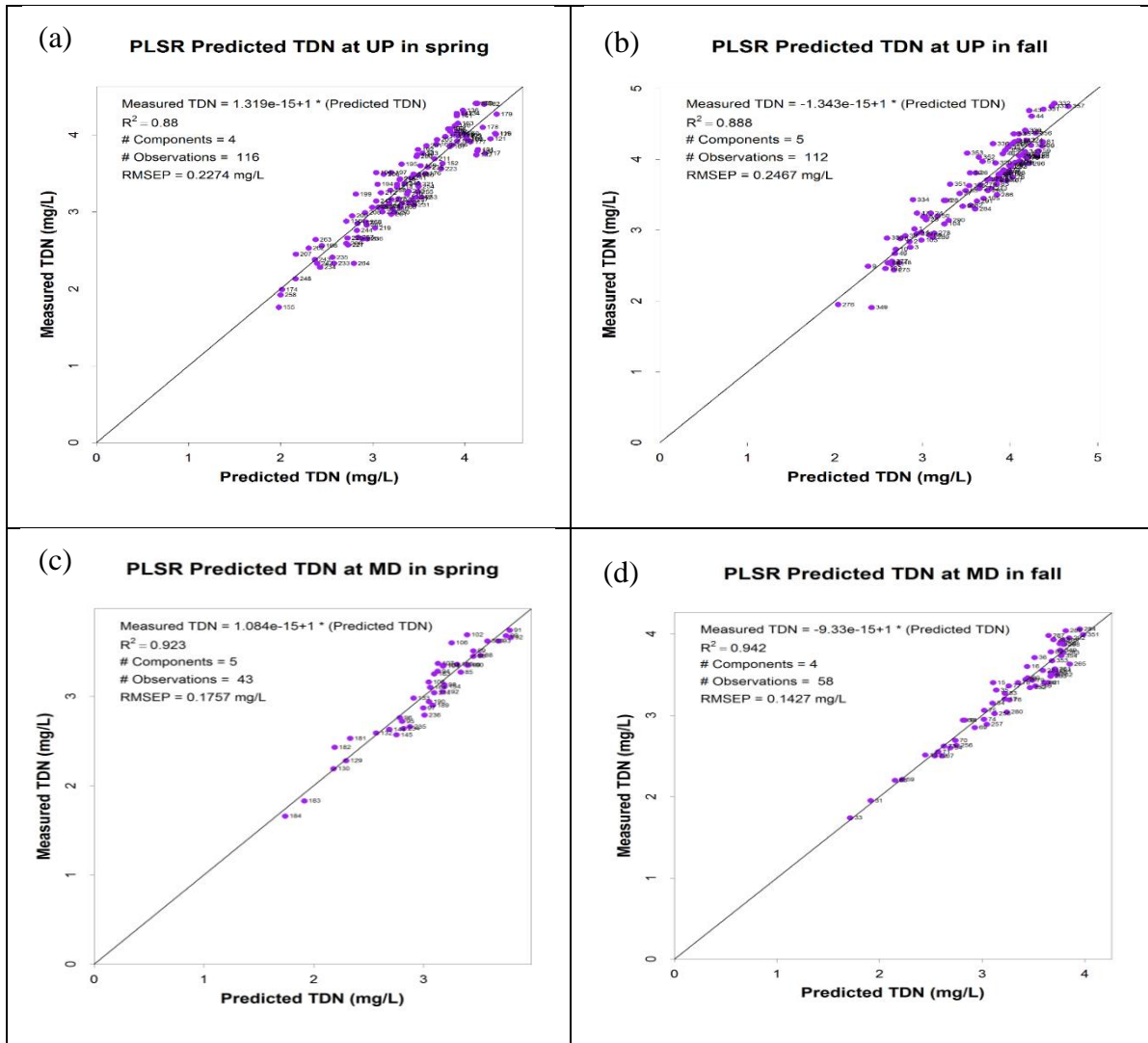


Figure 2.14 Continued

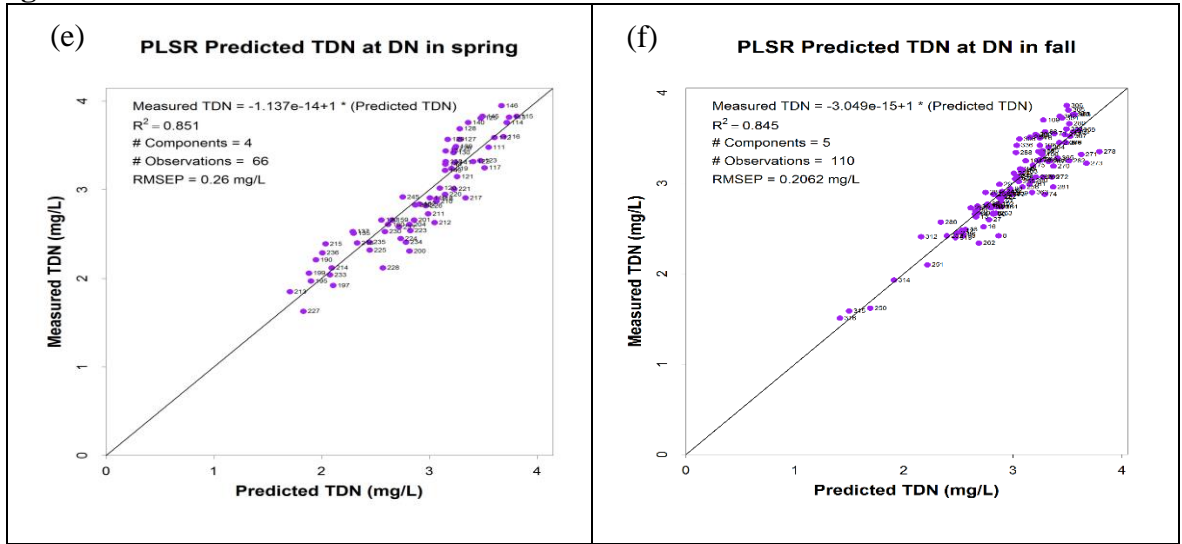


Figure 2.15

Regression relationships between measured TKN and predicted TKN from PLSR calibrations. (a) UP in spring and summer; (b) UP in fall and winter; (c) MD in spring and summer; (d) MD in fall and winter; (e) DN in spring and summer; (f) DN in fall and winter.

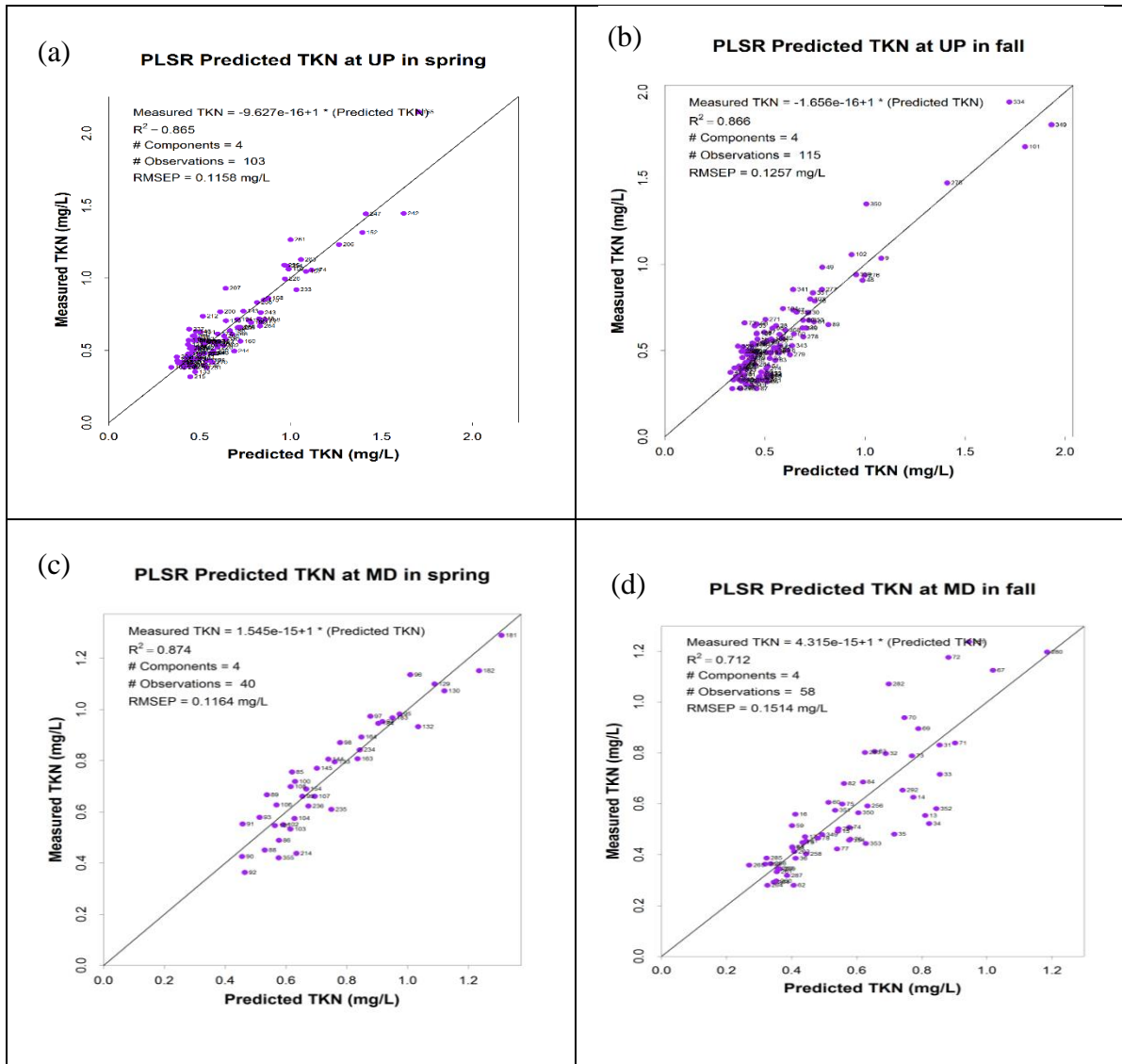


Figure 2.15 Continued

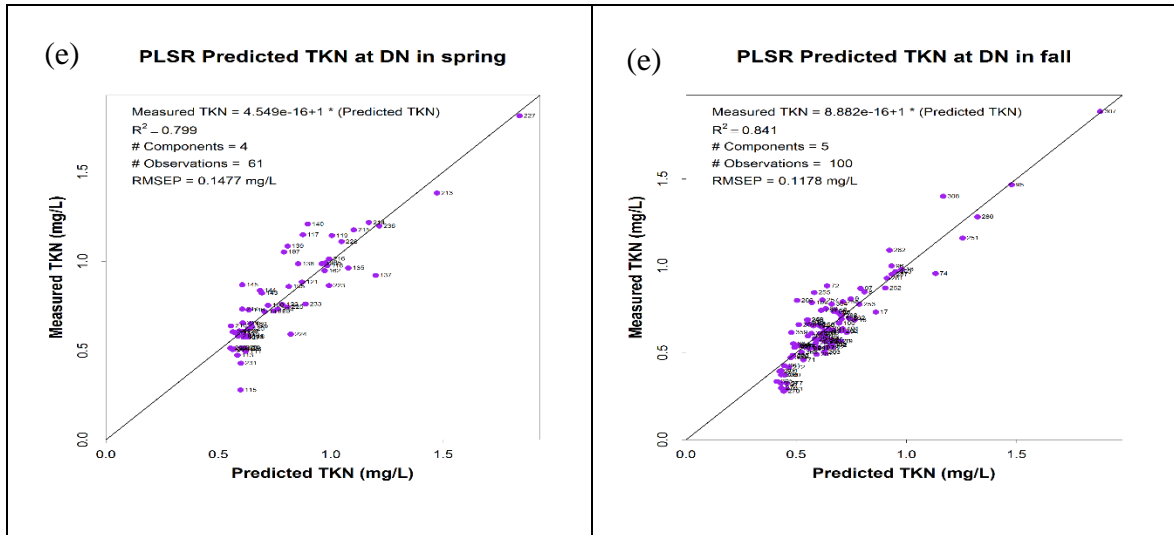


Figure 2.16

Regression relationships between measured DOC and predicted DOC from PLSR calibrations. (a) UP in spring and summer; (b) UP in fall and winter; (c) MD in spring and summer; (d) MD in fall and winter; (e) DN in spring and summer; (f) DN in fall and winter.

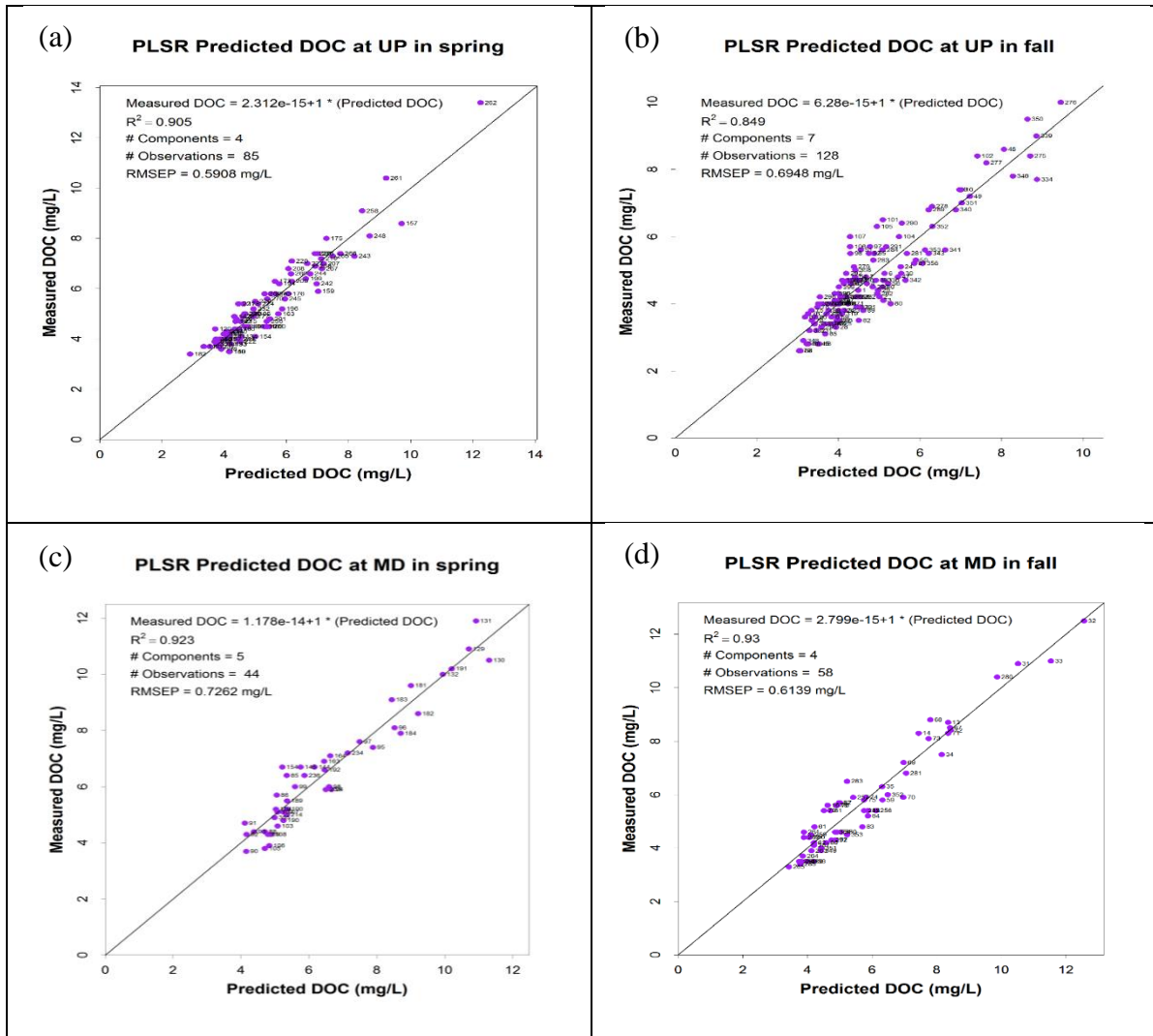


Figure 2.16 Continued

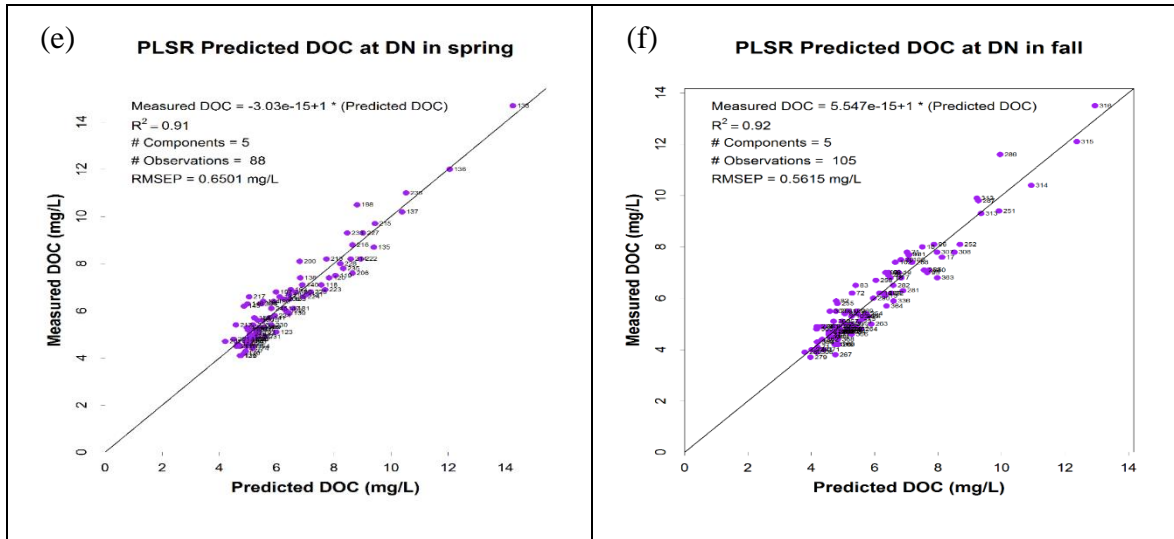


Figure 2.17

Regression relationships between measured TP and predicted TP from PLSR calibrations. (a) UP in spring and summer; (b) UP in fall and winter; (c) MD in spring and summer; (d) MD in fall and winter; (e) DN in spring and summer; (f) DN in fall and winter.

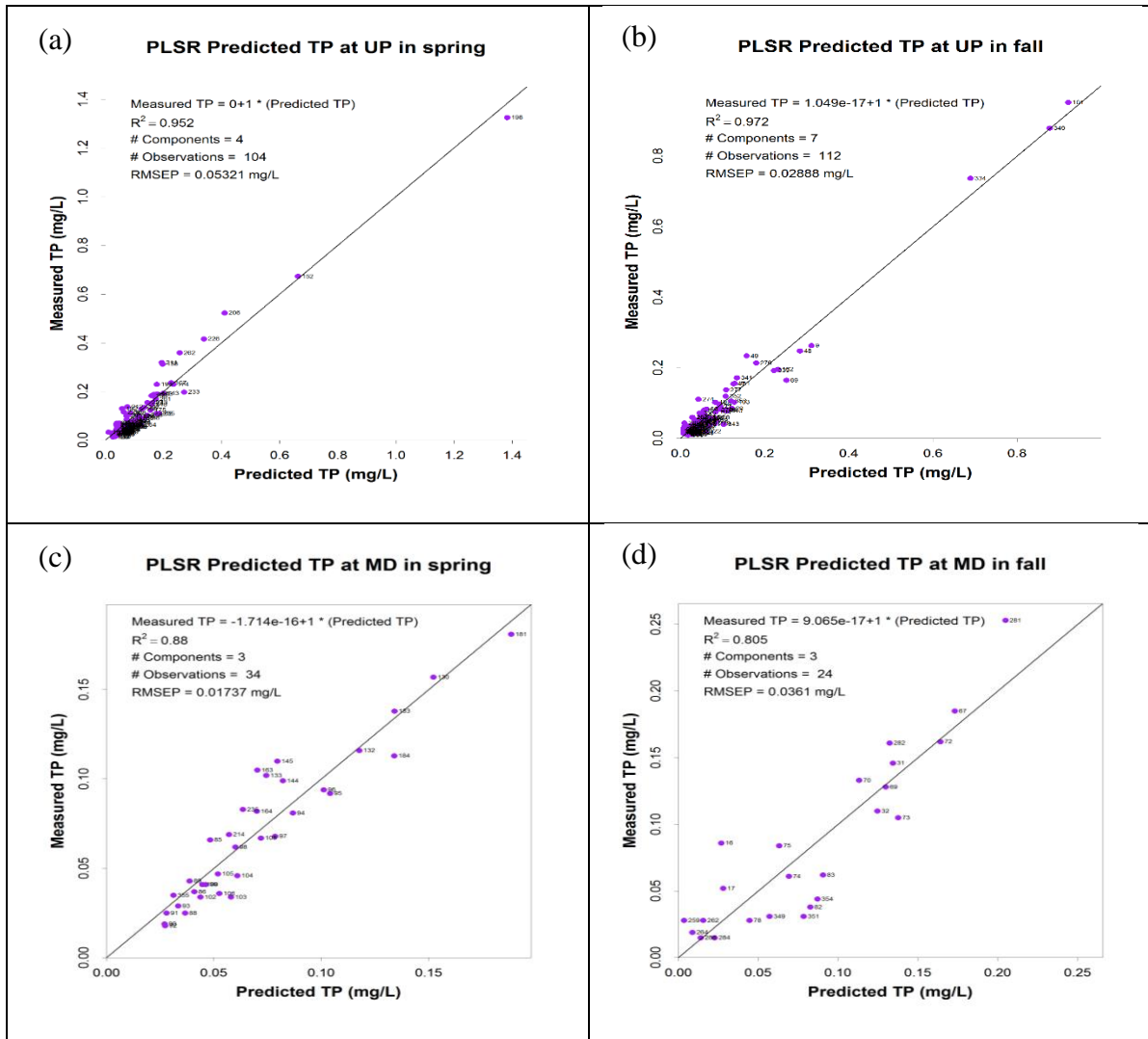


Figure 2.17 Continued

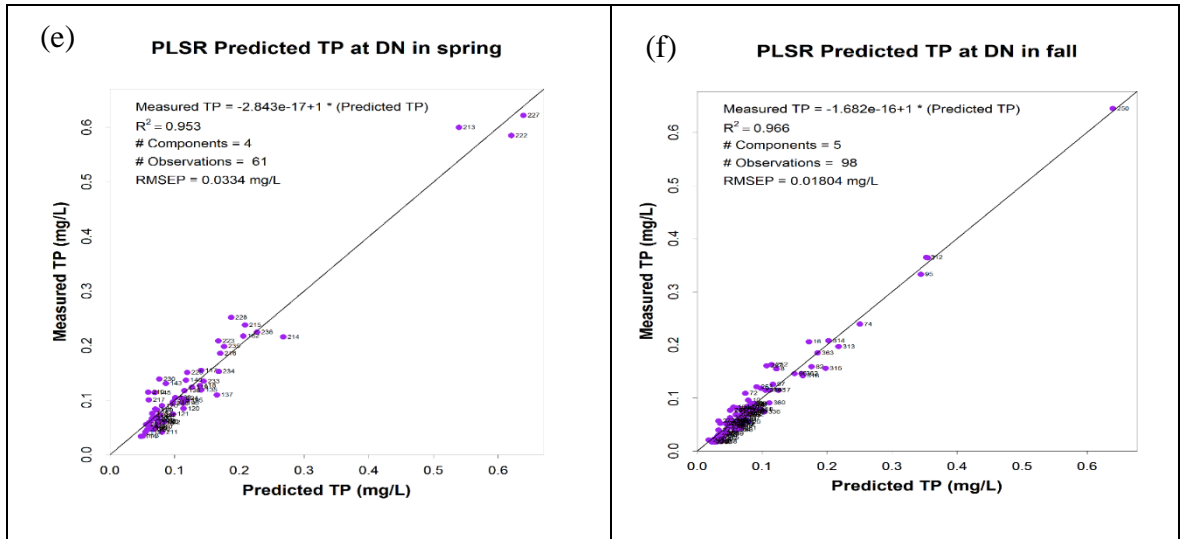


Figure 2.18

Regression relationships between measured PO₄-P and predicted PO₄-P from PLSR calibrations. (a) UP in spring and summer; (b) UP in fall and winter; (c) MD in spring and summer; (d) MD in fall and winter; (e) DN in spring and summer; (f) DN in fall and winter.

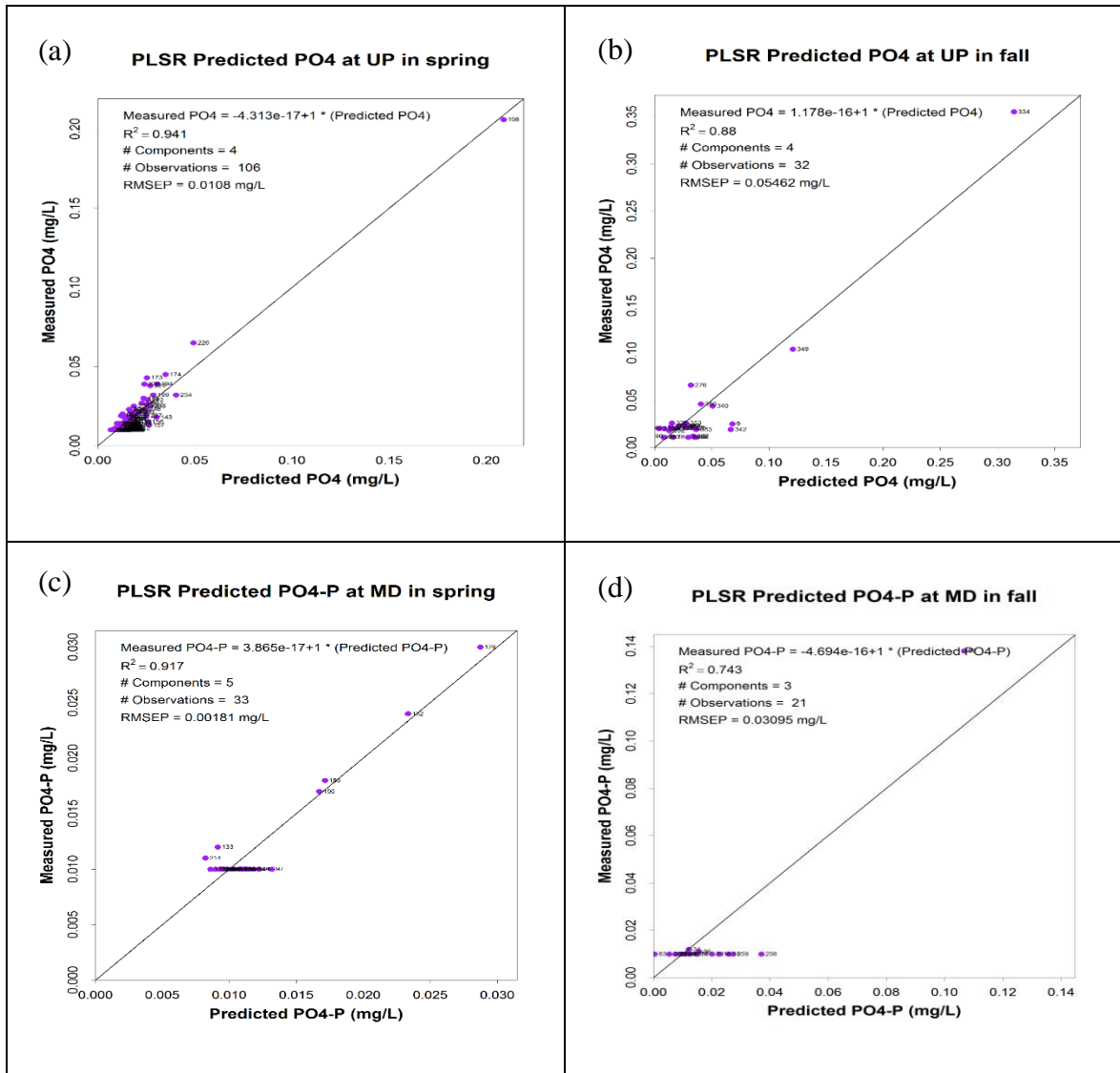
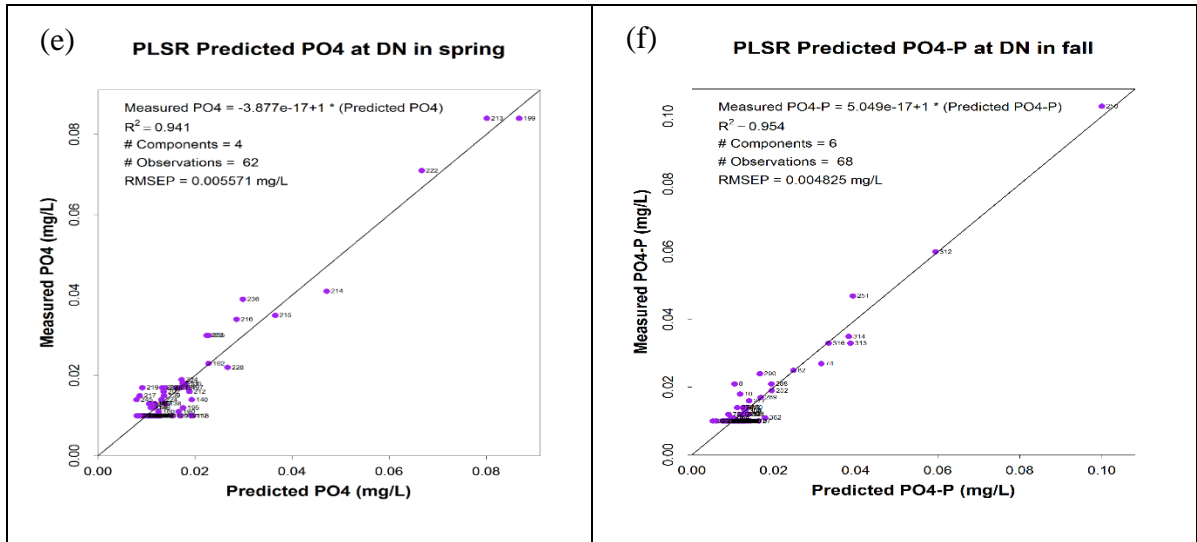


Figure 2.18 Continued



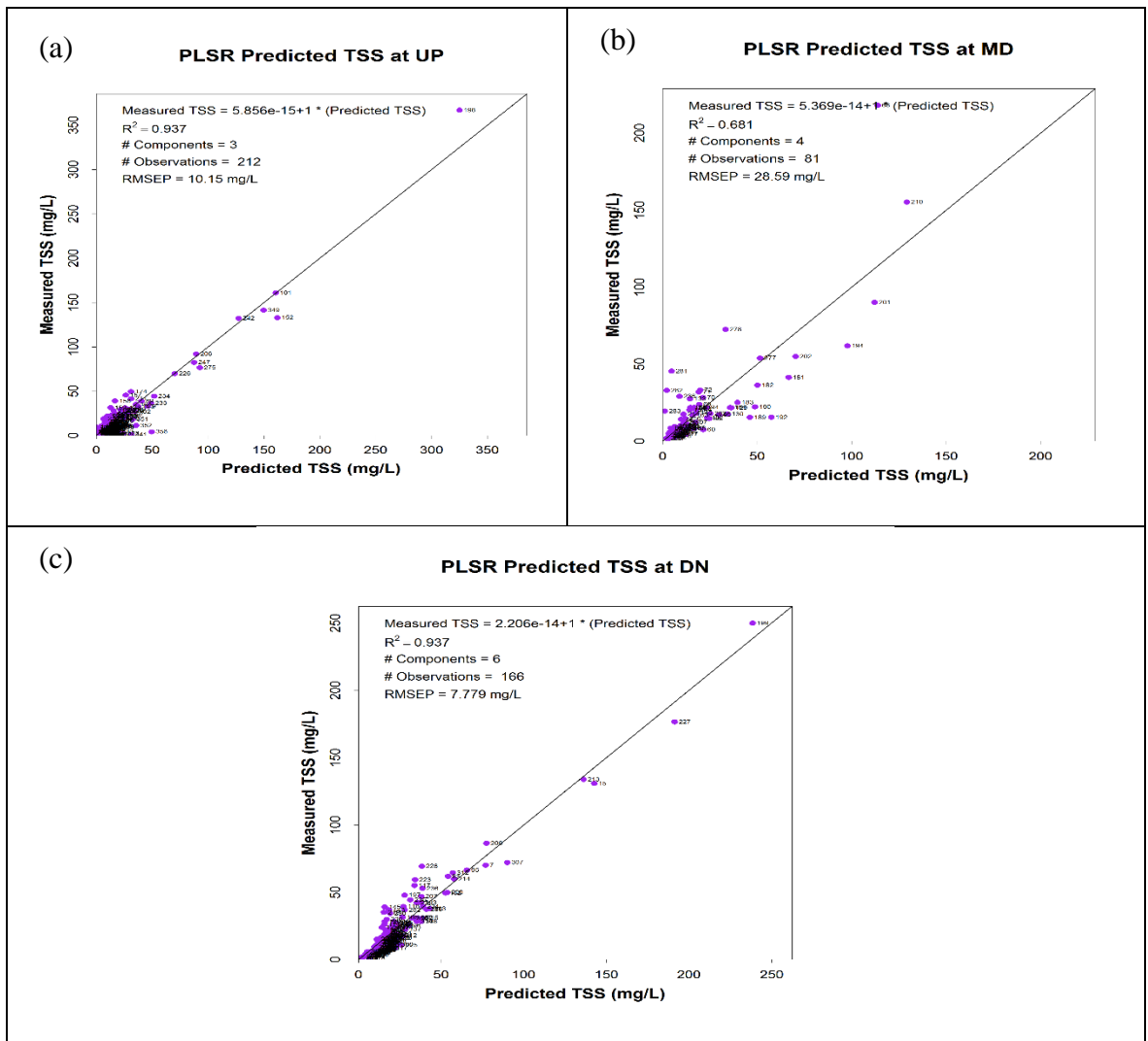


Figure 2.19

Regression relationships between measured TSS and predicted TSS from PLSR calibrations. (a) UP; (b) MD; (c) DN.

TSS Predictions from PLSR and turbidity

The PLSR method was applied to predict TSS concentrations and it was found that highly significant correlations and robust models for the UP and DN stations ($R^2 = 0.94$, RMSE is

about 8 mg/L) but not so for the MD station ($R^2=0.68$, RMSE = 18 mg/L), which model appears invalid using the 0.1 criterion for NSE. The better results for the UP and DN stations appear related, again, to the few high concentration values 5 to 10 times the median concentrations.

Thanks to the turbidity values provided by the S::CAN spectrophotometers stored in the “PAR file”, it is possible to calculate TSS concentrations from turbidity values, has been shown in the past (Birgand et al., 2005; Skarbøvik and Roseth, 2015; Ramos et al., 2015; and Gippel, 1995). The highly significant correlations between turbidity values and TSS were obtained (R^2 greater than 0.96, Figure 2.20). The RMSE from turbidity predictions are 4, 5, 6 mg/L at the UP, MD and DN stations, respectively.

The two methods to calculate TSS concentrations have comparatively high significant correlations. One way to compare their performance is to compare the TSS loads that can be calculated over periods for which absorbance data was available. The TSS cumulative loads calculated from PLSR and turbidity calibrations show very similar results at the UP station, i.e 224 and 223 kg/ha, respectively. However, loads computed with the PLSR calibrations at the MD and DN stations overestimate by about 30% those predicted using turbidity (MD: 340 vs 262 kg/ha, 29.6% difference; DN: 544.4 vs 405.2 kg/ha; 34% difference). These results are discussed below.

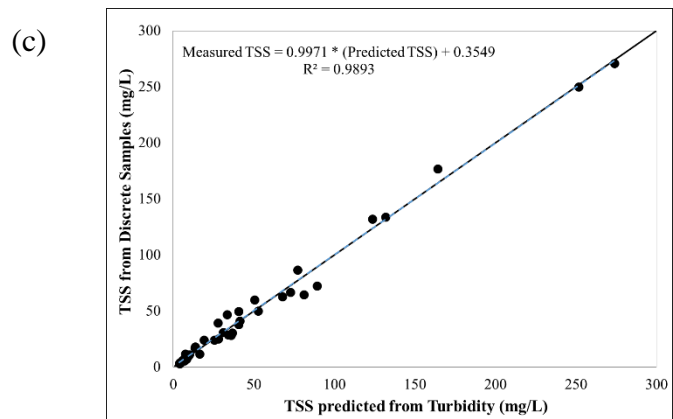
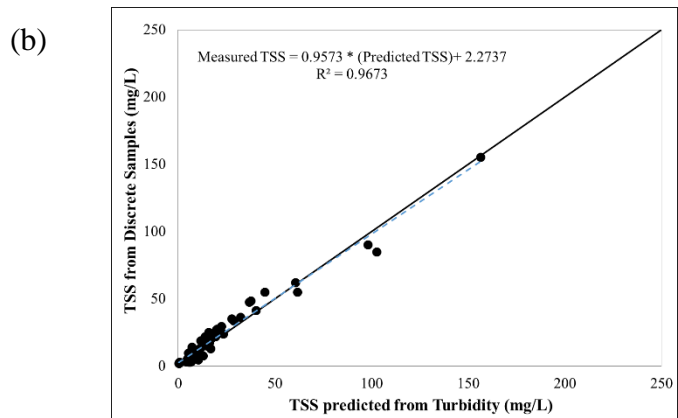
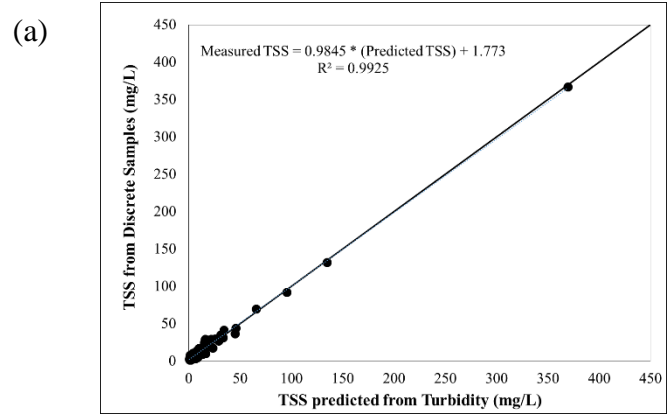


Figure 2.20

The regression relationship for TSS concentrations from discrete samples and turbidity prediction at the three stations. (a) UP; (b) MD; (c) DN.

PLSR calibration vs Global Calibration vs Local Calibration on load estimations

Results for nitrate and DOC have shown that the concentration values given directly by the instruments (in the PAR file) did not fit well with the lab values. However, it has been shown that there was a significant relationship between the PAR and the lab values (Table 2.6). It has also been shown that the PLSR were able to predict lab concentrations well (concentrations on the 1:1 line, RMSE at about 0.06 to 0.08 mg/L for nitrate and about 0.29 to 0.44 for DOC). Using the significant correlations between the PAR and the lab concentrations, it is possible to 'correct' the PAR concentrations using the regression equations in Table 2.3, and essentially make a 'local calibration'. The RMSE for such local calibrations are about 2 to 10 times those of PLSR (Table 2.3).

For nitrate and DOC, it is thus interesting to compare the consequences of these different approaches on computed loads. In other words, although the local calibrations do not appear as good on the concentration measurements, the higher errors on concentrations might cancel each other's out and provide robust load estimations. (Note: The calculated cumulative loads for nitrate and DOC in this section did not include the corrections of missing data).

Not surprisingly, there were large absolute differences (5 to 37%) between the computed load values using the PAR vs the PLSR predicted concentrations (Table 2.6). However, expectedly, loads computed using the local calibrations yielded much lower differences with the loads computed with the PLSR method. The relative errors were larger for DOC (-3% to -17%) than for nitrate (+2% to -7%), and almost always relatively underestimated using the local calibration.

Table 2.6

Differences in nitrate and DOC loads computed using concentrations from the PAR files, those predicted using PLSR, from local calibration

		Loads (kg/ha)			Relative Percentage difference with PLSR computed loads		
		UP	MD	DN	UP	MD	DN
Nitrate	PLSR	19.6	13.4	15.1	-	-	-
	PAR	16.8	10.1	15.8	-14%	-25%	+5%
	Local Calib	19.9	12.4	14.4	+2%	-7%	-5%
DOC	PLSR	38.5	30.4	37.5	-	-	-
	PAR	52.8	24.5	41.6	+37%	-19%	+11%
	Local Calib	37.2	25.2	34.6	-3%	-17%	-8%

Discussion: can nutrient concentrations and loads be measured reliably with water quality rating curves?

The use of PLSR with UV-vis spectro::photometers had been reported in waste water (Torres, and Bertrand-Krajewski, 2008), in a tidal marsh (Etheridge et al., 2013; 2014), and in a lake (Birgand et al., 2016). This study shows an application in the more standard setting of monitoring stations in streams and rivers. This research coined the concept of water quality rating curves by analogy to other rating curves often used in hydrology, such as stage-discharge relationships.

The results indicated that in an agricultural stream of the coastal plain, it was possible to establish significant and robust correlations between light absorbance data and concentrations for many parameters of interest for the N, P, and C cycles. However, it was unable to establish valid correlations between absorbance and $\text{NH}_4\text{-N}$ and $\text{PO}_4\text{-P}$ for most of the time and stations. The PLSR for TKN at the MD, which appeared significant, was invalidated using the fiteval software. For $\text{PO}_4\text{-P}$, the three regressions that had the highest significance and appeared robust, had about twice as many calibration points, compared to the three other regressions that were either barely valid or invalid. The number of calibration points, stratified along the calibration range might explain the difference between these regressions.

The one PLSR model that appeared significant for $\text{NH}_4\text{-N}$ also had calibration points relatively stratified compared to the other regressions. For the latter, the regressions were obtained with most points at or near the detection limit and very few points (1 to 3) at concentrations 5-10 times the median, which made them not robust as shown with the fiteval

software. This does suggest, however, that it might not be impossible to obtain rating curves for $\text{NH}_4\text{-N}$ and $\text{PO}_4\text{-P}$ as well, as long as there be stratified concentrations along the calibration range.

Calibrations for TKN, although valid in most cases, appear less robust than for other parameters (except $\text{NH}_4\text{-N}$ and $\text{PO}_4\text{-P}$). This might be due to the mix of particulate and dissolved matter that make TKN and that the PLS regressions are trying to predict. The consequences of regression significance on the load uncertainties are studied in Chapter 3.

The results for TSS predictions using PLSR as a rating method or turbidity as index data, point out another extremely important point and potential risk when using water quality rating curves. After review of the concentration time series, the large overestimations of the TSS loads at the MD and DN stations using PLSR compared to the turbidity based predictions, are associated with concentration peaks at or near flow peaks, which predictions are outside the calibration ranges.

The first consequence of this observation is that it is very important, for all parameters, to try to capture the largest concentration range during calibration, and identify the concentrations predicted outside the calibration range. Ideally, this should correspond to a minimum percentage of the time. For parameters that exhibit a concentration effect, the concentrations tend to peak during flow peaks, which makes their ‘capture’ or sampling difficult, and their incorporation in the calibration pool, because these events are rare by definition. The errors associated with extrapolating outside the calibration range are particularly amplified because they are associated with the flow peaks. The consequences of predictions outside the calibration range are inherently less problematic for parameters that

exhibit ‘dilution effects’ during events, such as nitrate for the studied watersheds (see Chapter 3 and 4).

The second consequence for TSS specifically, is that some of the concentration peaks predicted with the PLSR appear unrealistically high (>1000 mg/L). For turbidity values, less than 500 NTU, it is generally accepted that the TSS and turbidity increase linearly. For higher values (>500 NTU), the turbidity concentrations do not increase linearly with TSS anymore as some of the particles are in the shadows of others that have already absorbed light. It is thus likely that the predictions of TSS concentrations outside the calibration range using turbidity as index data are underestimated, yet bounded. In the end, there seems to be too much risk with the PLSR predicted TSS loads and turbidity predicted loads are the preferred choice.

Beyond water quality rating curves: additional local concentration corrections

Most of the time, PLSR could reliably predict continuous water quality concentrations and fit well with the discrete samples results, even though some fouling was observed after two weeks most of the time. This suggests that the PLSR did correct for most of the fouling. Nonetheless, the time series revealed that just before and/or just after field servicing and optics cleaning, the predicted concentrations appeared offset compared to the lab values. This coincides with PLSR ability to correct for fouling, as on average it corrects well but might ‘not correct enough’ just before field servicing, and ‘too much’ just after servicing. The concentration predictions from PLSR thus appeared as an artifact of the method, correcting manually using the AQUARIUS software was applied.

For example, in Figure 2.21, the NO₃-N continuous concentrations from PLSR calibration were about 0.3 ~ 0.5 mg/l lower than the discrete NO₃-N (in orange frame) during four days (February 15-18), which were before the field service date (February 18). With the tools in AQUARIUS software, the data points of the continuous NO₃-N concentrations (in orange frame) were drifted closer to the discrete NO₃-N concentrations to compensate for this PLSR artifact (Figure 2.22).

The AQUARIUS software was also used to correct for noisy points and missing data in the continuous water quality results during part of monitoring periods (e.g., power outage and abrasions of tubing; Figure 2.23 and Figure 2.24). Overall, the AQUARIUS software was a useful tool to correct and obtain better continuous datasets.

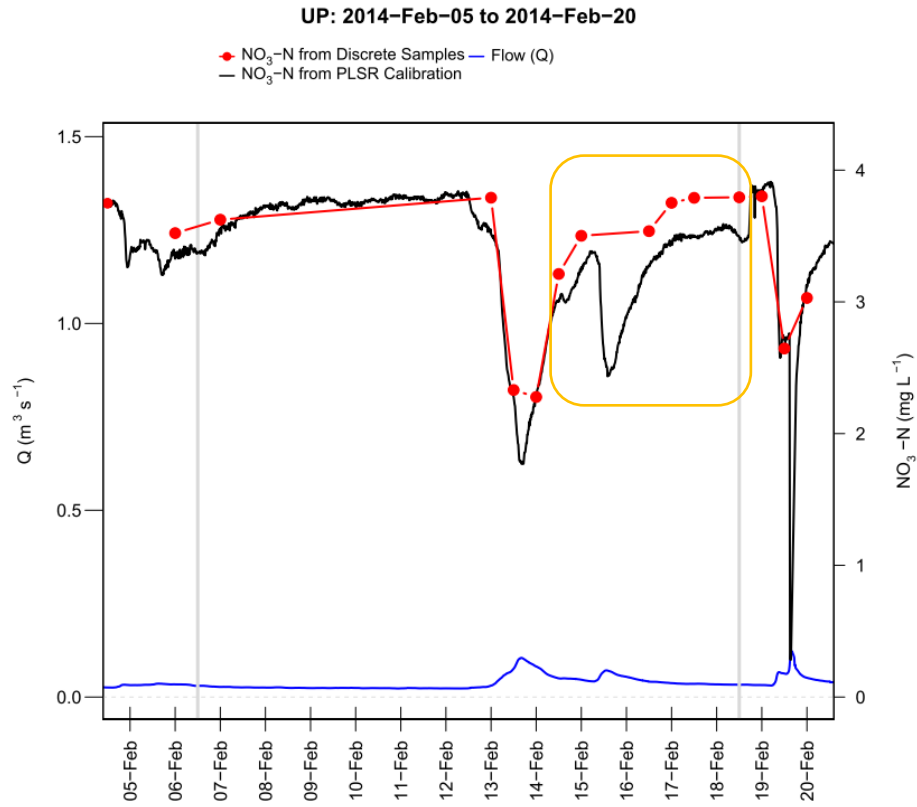


Figure 2.21

An example of “stray” data points because of biofouling. Continuous NO₃-N concentrations from PLSR calibration (black line), NO₃-N concentrations from Discrete Samples (red dots), Flow rate (blue line), and Field visit date (gray vertical line) at UP on February 5-20 in 2014.

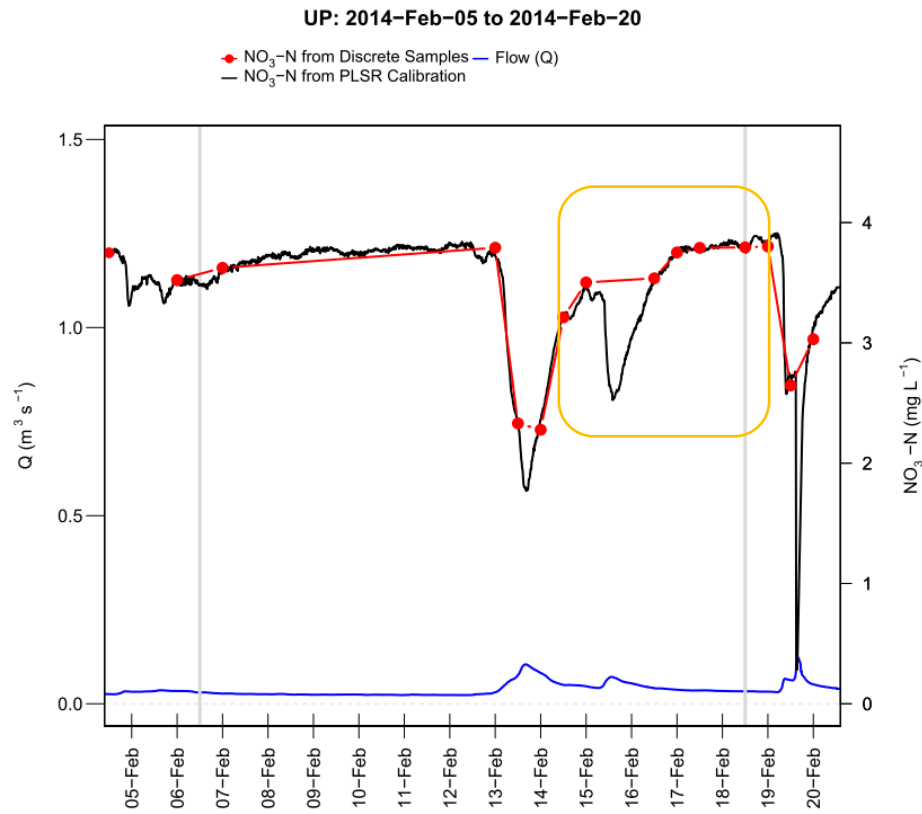


Figure 2.22

Continuous NO₃-N concentrations from PLSR calibration with correction by using AQUARIUS software (black line), NO₃-N concentrations from Discrete Samples (red dots), Flow rate (blue line), and Field visit date (gray vertical line) at UP on February 5-20 in 2014.

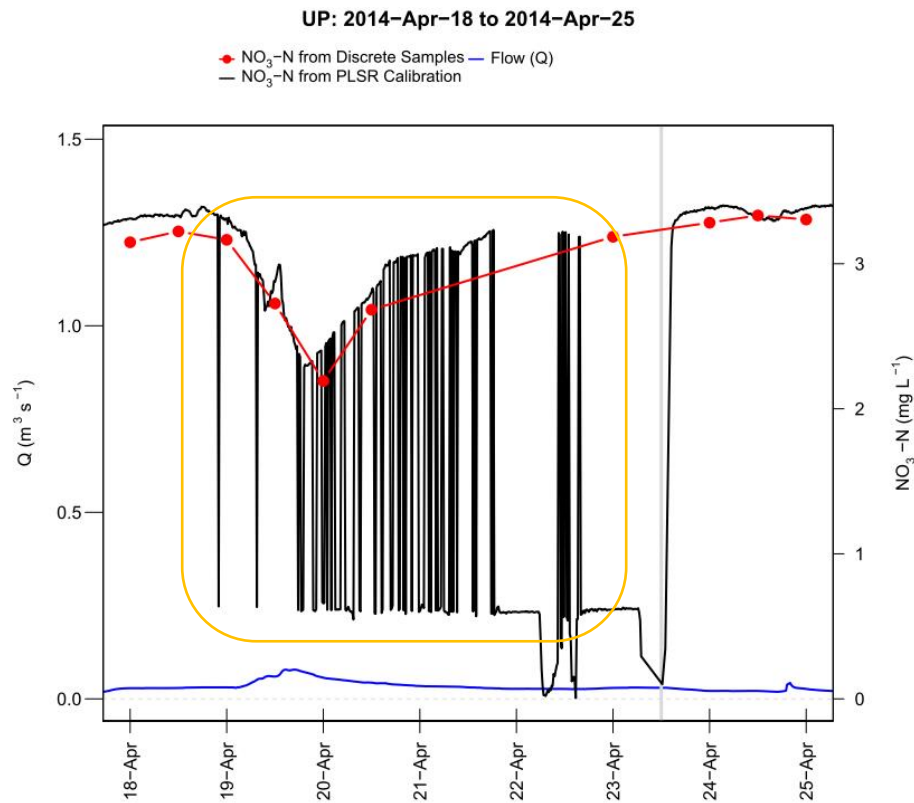


Figure 2.23

An example of noisy points because of malfunctioning of the monitoring system.
Continuous NO₃-N concentrations from PLSR calibration (black line), NO₃-N concentrations from Discrete Samples (red dots), Flow rate (blue line), and Field visit date (gray vertical line) at UP on April 18-25 in 2014.

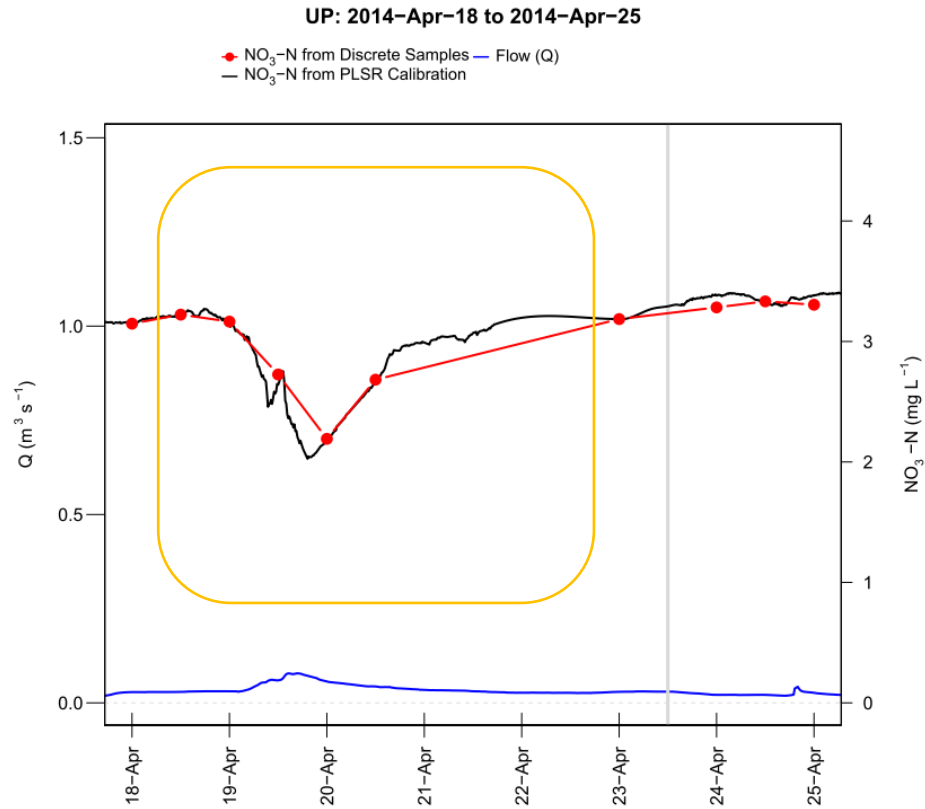


Figure 2.24

Continuous NO₃-N concentrations from PLSR calibration after removing of noisy points by using AQUARIUS software (black line), NO₃-N concentrations from Discrete Samples (red dots), Flow rate (blue line), and Field visit date (gray vertical line) at UP on April 18-25 in 2014.

Results for filling missing flow data

To compensate the loss of flow data, regression relationships among the monitoring stations were developed to fill the gap. Figure 2.25 demonstrated the continuous flow at UP and MD during the storm events from November 23 to December 3 in 2014; however, the flow data at UP was missing after November 26 (in orange frame).

Thus, the flow at MD was correlated with UP on November 23-26 (in green frame in Figure 2.25) and the regression relationship was generated (Figure 2.26). The R^2 value ($R^2 = 0.9345$) from the regression equation represented that it had high correlation for flow between UP and MD. As a result, by using the regression equation in Figure 2.26, the missing flow at UP was predicted from the flow at MD (Figure 2.27). This filling technique was applied to fill all flow data gaps.

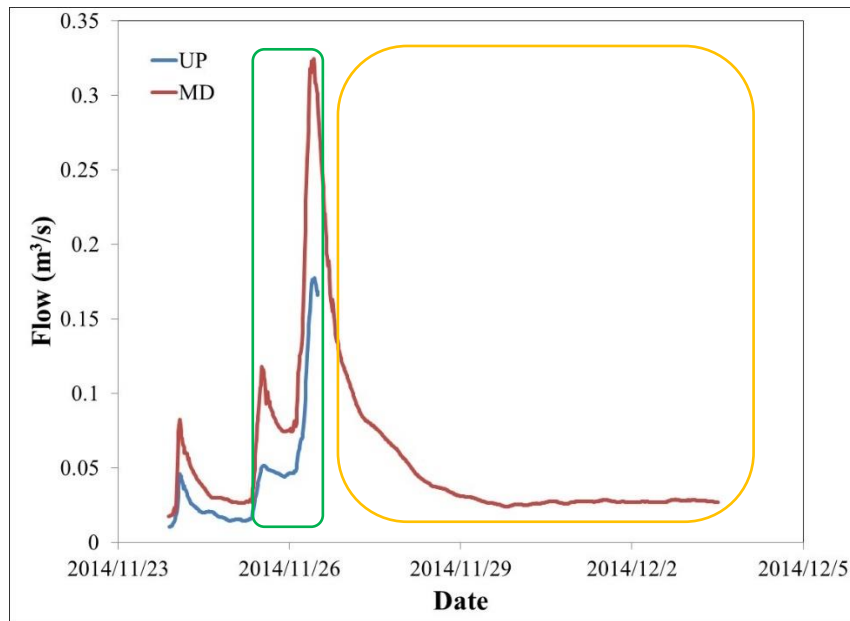


Figure 2.25

An example of missing flow data because of malfunctioning for the monitoring system.

Continuous flow rate at UP (blue line) and MD (red line) from November 23 to

December 3 in 2014.

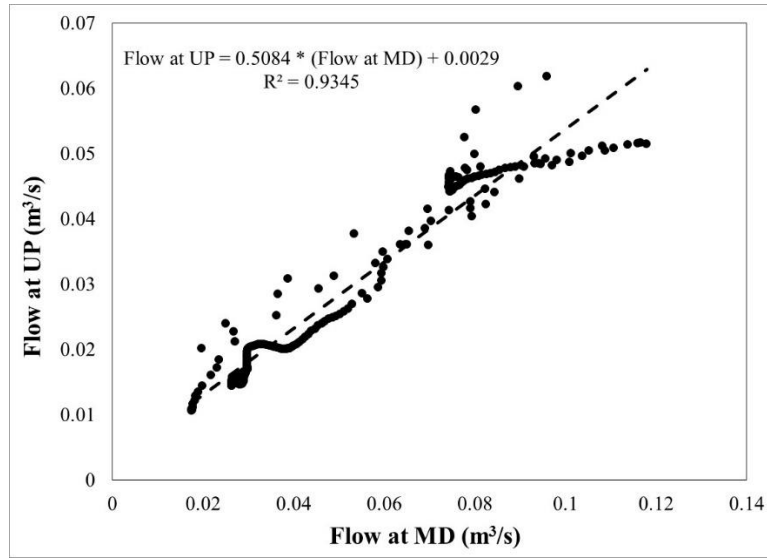


Figure 2.26

The regression relationship for flow between UP and MD on November 23-26 in 2014.

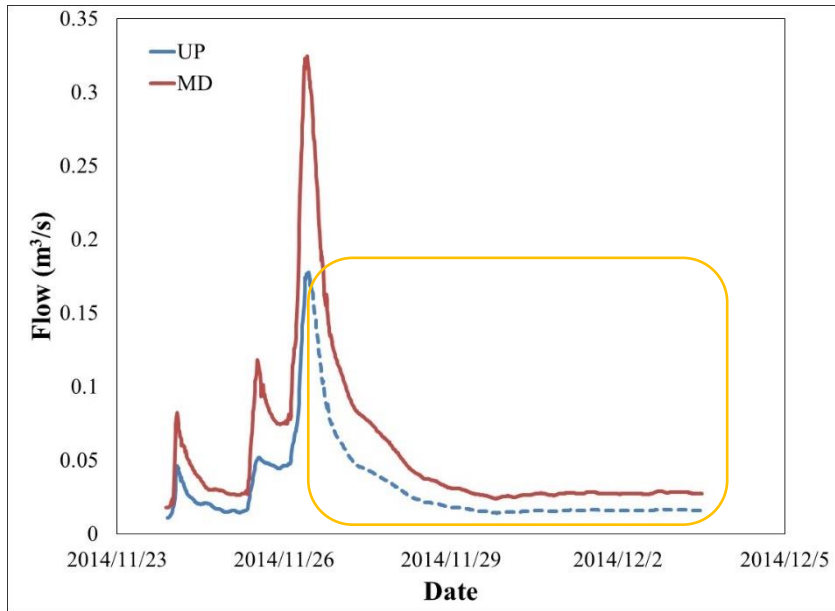


Figure 2.27

Continuous flow (blue solid line) at UP, predicted flow (blue dashed line) at UP, and continuous flow (red line) at MD from November 23 to December 3 in 2014.

Results for filling missing nitrate concentration data

As discussed previously, the monitoring system did not always function properly during several periods. The percentages of properly functioning period for the monitoring systems were 60.7, 54.4, and 64.0% at UP, MD, and DN respectively and most of periods with gap were not synchronous for the three stations. A total of three methods were compared to fill in the data. The first ‘do nothing’ method consisted in linearly interpolating between continuous discrete samples, regardless of the changes of flow. The second, the ‘Manual method’ consisted, during events, in considering the likely changes of concentrations associated with flow changes, by adding concentration points just before an event and at the flow peaks, using ‘visual expertise’ using adjacent events as guides. Although fast, the Manual method is highly subjective. The third ‘Semi-Automatic method’ took the subjectivity out of the manual method by creating regression relationships between flow rates and water quality concentrations from adjacent/similar storm events.

In Figure 2.28, there was missing data, which caused the gap (was represented as straight line in orange frame) in the continuous results on February 20-25 in 2014. Figure 2.29 shows the results of filling the missing data with a dashed line (in orange frame) based on the concentrations values from discrete samples. In addition, the missing peak/trough concentrations values during the storm events were ‘manually’ predicted from adjacent/similar storm events.

With the application of the regression equation for the storm event (in green frame) on February 12-15 in 2014 (Figure 2.30), the missing continuous $\text{NO}_3\text{-N}$ concentrations in

Figure 2.29 could be predicted from the flow rate values. Figure 2.31 demonstrated the predicted NO₃-N concentrations by using Semi-Automatic method for the missing values February 20-25 in 2014. Nevertheless, the disadvantage of Semi-Automatic method is that several predicted results astray from the discrete samples results.

After filling the missing data with the two methods, the NO₃-N cumulative loads were calculated during the entire monitored period for the three methods (Table 2.7). The NO₃-N cumulative loads for 'Manual', 'do nothing', and Semi-Automatic methods added up to 19.6, 19.7 and 19.3 kg/ha at UP; 15.6, 15.8, and 14.9 kg/ha at MD; 16.5, 16.9, and 16.6 kg/ha at DN (Table 2.7). It was expected that the 'do nothing' method would yield slightly higher load values as the linear interpolation tends to 'cut' through the concentration troughs during flow peaks, which tends to overestimate loads. The fact that the 'Manual' and 'Semi-automatic' methods yield lower values within 2% of each other (but for the MD station with the semi-automatic method) suggests that data filling is a minor source of error. However the -4.2% difference between the Manual and the Semi-automatic method suggests that it is possible that the semi-automatic method underestimate concentrations during high flow rates. Thus, Manual method was used to fill the gap for the other parameters (e.g., DOC and TSS).

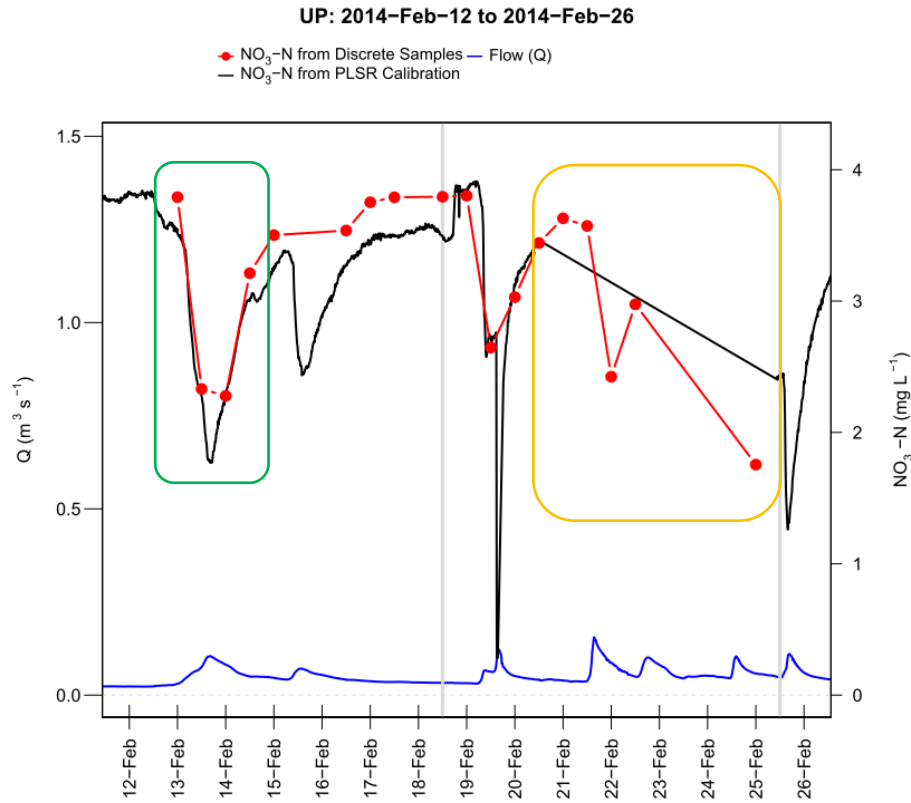


Figure 2.28

An example of missing concentration data because of malfunctioning for the monitoring system. Continuous NO₃-N concentrations from PLSR calibration (black line), NO₃-N concentrations from Discrete Samples (red dots), Flow rate (blue line), and Field visit date (gray vertical line) at UP on February 12-26 in 2014.

UP: 2014-Feb-12 to 2014-Feb-26

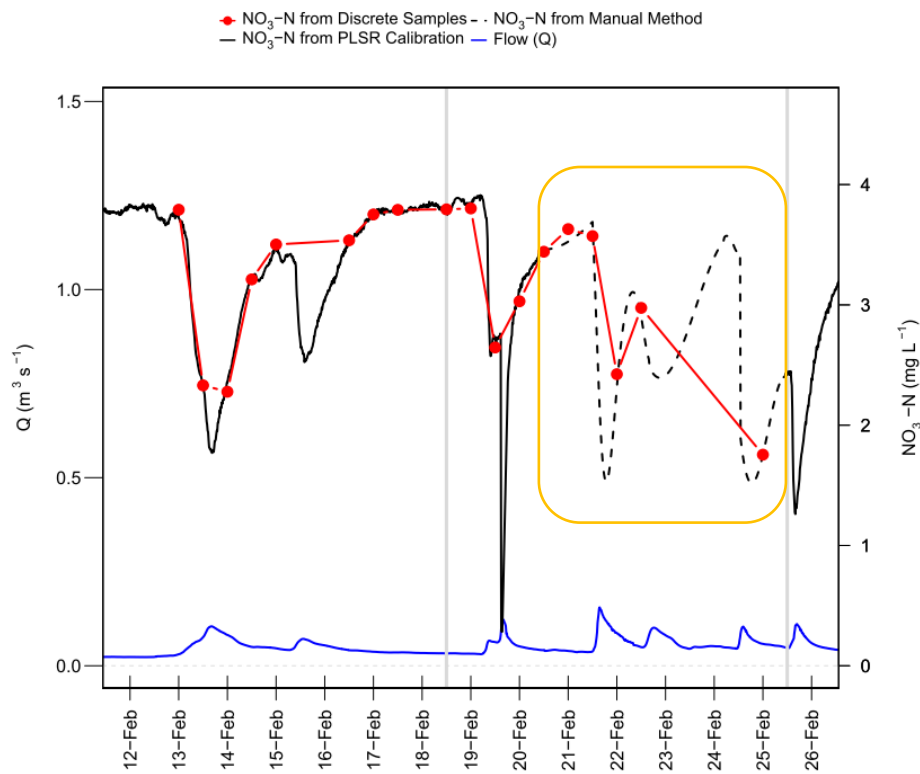


Figure 2.29

Continuous $\text{NO}_3\text{-N}$ concentrations from PLSR calibration (solid black line), continuous $\text{NO}_3\text{-N}$ concentrations by using Manual method to fill the missing data (dashed black line), $\text{NO}_3\text{-N}$ concentrations from Discrete Samples (red dots), Flow rate (blue line), and Field visit date (gray vertical line) at UP on February 12-26 in 2014.

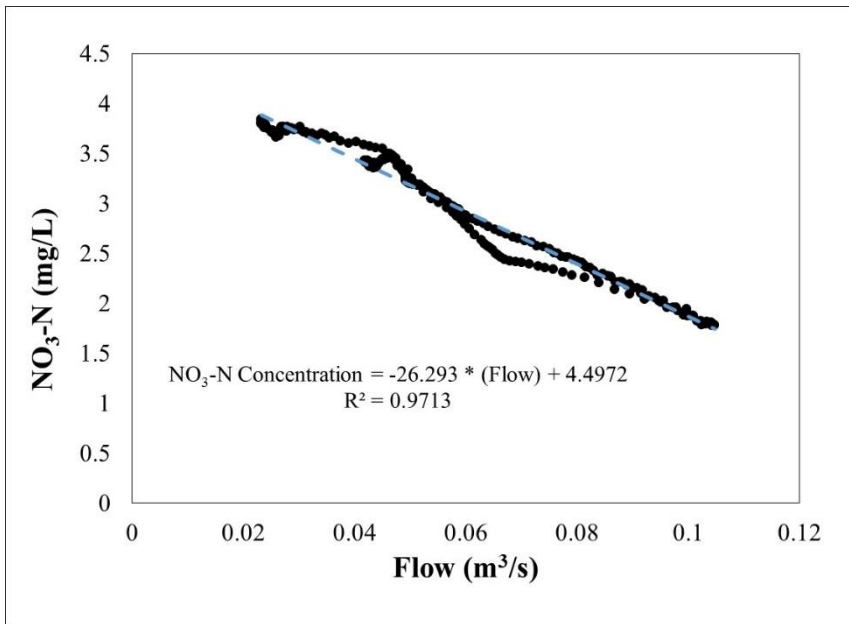
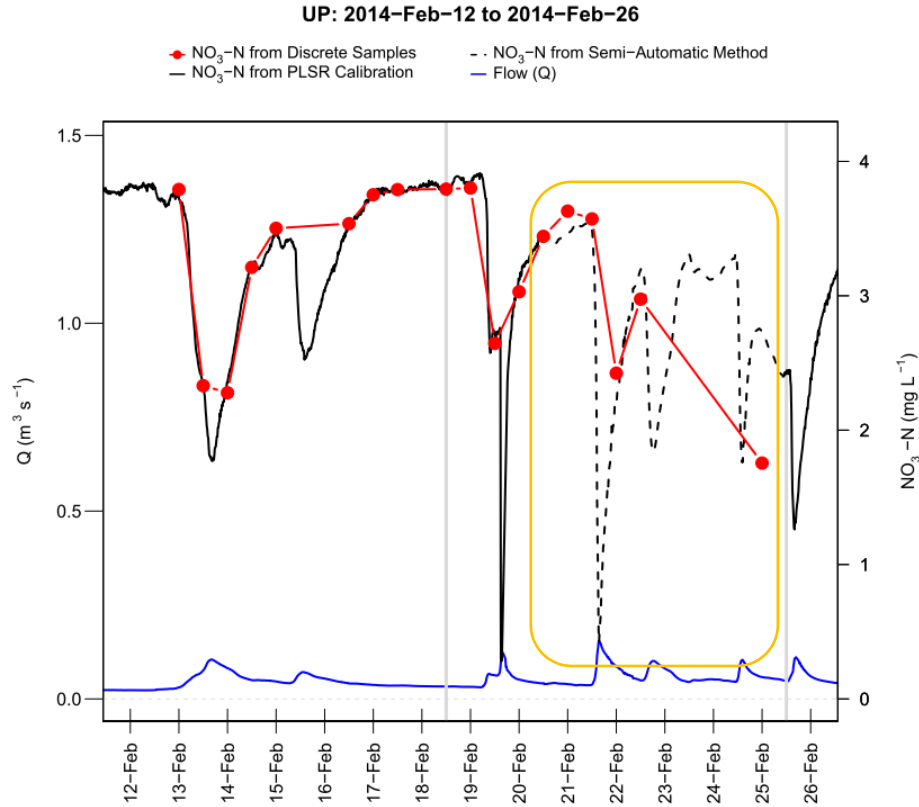


Figure 2.30

The regression relationship between flow rate and NO₃-N at UP on February 12-15.



Continuous NO₃-N concentrations from PLSR calibration (solid black line), continuous NO₃-N concentrations by using Semi-Automatic method to fill the missing data (dashed black line), NO₃-N concentrations from Discrete Samples (red dots), Flow rate (blue line), and Field visit date (gray vertical line) at UP on February 12-26 in 2014.

Table 2.7

Summary of NO₃-N cumulative loads for Manual method and Semi-Automatic method

Station	Manual Method		% Absolute difference between A and B	NO ₃ -N cumulative loads for Semi-Automatic Method (C)	% Absolute difference between A and C
	NO ₃ -N cumulative loads with Manual Method (A)	NO ₃ -N cumulative loads the 'do nothing' method (B)			
UP	19.6	19.7	+0.7%	19.3	+1.2%
MD	15.6	15.8	+1.7%	14.9	-4.2%
DN	16.5	16.9	+2.4%	16.6	+0.5%

Challenges and maintenance for the application of UV-Vis spectrophotometers *in situ*

There are several main challenges associated with obtaining high-frequency water quality and hydrology data continuously, and keeping the monitoring system (UV-Vis spectrophotometers, multi-parameter sonde and flow meter) working properly *in situ* including: (1) biofouling on optics surface, (2) sufficient power supply, (3) heat supply in adverse weather, (4) animal effects and equipment maintenance. The details were addressed as following: (1) Biofouling on optics surface, as mentioned in “Materials: Equipment maintenance” section, biofouling would affect the measurements quality of UV-Vis spectrophotometers, therefore, with 2% HCl was applied. (2) Sufficient power supply: adequate power was required for the several electronic instruments (ex: UV-Vis spectrophotometers, flow meter, multi-parameter sonde, and discrete sampler) installed at monitoring stations. To meet this need, rechargeable batteries and solar panel boards were set up at each monitoring station. (3) Heat supply in adverse weather: in winter, the water would freeze in the tubes if the temperature was below 0°C and affect the transportation of water in tubes, thus preventing water quality measurements by UV-Vis spectrophotometers. It has been suggested to use tube insulation to cover tubes. Furthermore, Skarbøvik and Roseth (2015) suggest applying a heating cable or heating lamp in-situ. (4) Animal effects and equipment maintenances: There were several animals (e.g., mice and turtles) that bit the cables, wires, and tubes, hence, the applications of hard covers to protect the cables, wires and tubes were necessary. Additionally, changing the pump tubing was necessary since the

tubing would wear out within a month. Overall, the maintenance of the monitoring stations *in situ* was essential to ensure that the measuring equipment would collect high quality data.

2.4 Conclusions

The effects of stream restoration on e.g., bank erosion, habitat, or macroinvertebrate communities seem to be relatively well established. In these examples, the indicators used are ‘integrative indicators’ as they integrate over time the effect of the pulsation nature of streams and the effect of restoration. There has been no equivalent consensus on the effects of stream restoration on water quality for at least two main reasons: either because they are very small and/or because the methods used until now were not robust enough and were not integrated over long continuous periods of time the nutrient fluxes.

One way to address the water quality impact of restoration is to provide methods to obtain reliable integrative water quality indicators, e.g., nutrient and material loads. The arrival of continuous water quality sensors to obtain concentration values on a continuous basis provides a solution to what had remained an obstacle until now. UV-Vis spectrophotometers were used to create water quality rating curves to obtain concentration data on a high frequency basis to calculate robust N, P, C, and material fluxes. It has been shown that in an agricultural stream of the coastal plain of North Carolina, it was possible to construct robust water quality rating curves to measure nitrate, TDN, TKN, DOC, and TP, using the absorbance data as index data and PLSR as a rating method. It has also been shown that this method did not work well for $\text{NH}_4\text{-N}$ and $\text{PO}_4\text{-P}$, although it is possible that optimal calibration point pools were not obtained. The results suggest that to obtain robust water

quality rating curves, it is necessary to have as large as possible a calibration concentration range, where calibration concentrations are as stratified as possible. Extrapolating beyond the calibration range is inherently risky and may result in errors, and in the case of parameters that exhibit concentration effect during events, large overestimation was observed for TSS prediction by using PLSR. For TSS, it is suggested to use the more conservative turbidity based method.

It has also been shown that the concentrations calculated by the algorithms embedded on the instruments are not reliable without local calibration, but after calibration, can yield more acceptable results for nitrate and DOC. However, the PLSR rating seems to be more robust, is not technically over complicated and can be applied to other parameters. The uncertainties induced by the combination of absorbance data and water quality rating curves is explored in Chapter 3. To obtain fully continuous nutrient flux data, it is necessary to provide methods to fill the gaps. This research demonstrated that acceptable methods were developed to fill missing flow and concentration data.

2.5 Acknowledgements

The funding for this research was supported by the North Carolina Department of Transportation, grant number 2013-37.

2.6 References

- Alexander, G. G. and Allan, J. D. 2006. Stream restoration in the Upper Midwest, USA. *Restoration Ecology*, 14(4): 595–604.
- Antón, A., Elosegí, A., García-Arberas, L., Díez, J., Rallo, A. 2010. Restoration of dead wood in Basque stream channels: effects on brown trout population. *Ecology of Freshwater Fish*, 20: 461-471.
- Aquatic Informatics Inc. 2009. Aquarius Hydrologic Workstation Software. 200–322. Water St., Vancouver, B.C. V6B 1B6, Canada. info@aquaticinformatics.com.
- Bennett, S. J., Simon, A., Castro, J. M., Atkinson, J. F., Bronner, C. E., Blersch, S. S., Rabideau, A. J. 2011. The evolving science of stream restoration. *Stream Restoration in Dynamic Fluvial Systems: Scientific Approaches, Analyses, and Tools* Geophysical Monograph Series 194, Published in 2011 by the American Geophysical Union.
- Bernhardt, E. S., Palmer, M. A., Allan, J. D., Alexander, G., Barnas, K., Brooks, S., Carr, J., Clayton, S., Dahm, C., Follstad-Shah, J., Galat, D., Gloss, S., Goodwin, P., Hart, D., Hassett, B., Jenkinson, R., Katz, S., Kondolf, G. M., Lake, P. S., Lave, R., Meyer, J. L., O'Donnell, T. K., Pagano, L., Powell, B., Sudduth, E. 2005. Synthesizing U.S. river restoration efforts. *Science*, 308: 636-637.
- Birgand F., Faucheux, C., Gruau, G., Augeard, B., Moatar, F., Bordenave, P. 2010. Uncertainties in assessing annual nitrate load and concentration indicators: Part 1. Impact of sampling frequency and load estimation algorithms. *Trans. ASABE*, 53(2): 437-446.
- Birgand, F. 2000. Quantification and modeling of in-stream processes in agricultural canals of the lower coastal plain. In: Ph.D. Dissertation. North Carolina State University, Raleigh, NC.

- Birgand, F., Aveni-Deforge, K., Smith, B., Maxwell, B., Horstman, M., Gerling, A. B., Carey, C. C. 2016. First report of a novel multiplexer pumping system coupled to a water quality probe to collect high temporal frequency *in situ* water chemistry measurements at multiple sites. *Limnol. Oceanogr. Methods*. doi:10.1002/lom3.10122.
- Birgand, F., Benoist, J.-C., Novince, E., Gilliet, N., Saint-Cast, P., Le Saos, E. 2005. Guide d'application de la technique du Doppler continu pour une section calibrée en bois, *Ingénierie-EAT*, 41: 77-82.
- Birgand, F., Lellouche, G., Appelboom, T.W. 2013. Measuring flow in non-ideal conditions for short-term projects: Uncertainties associated with the use of stage-discharge rating curves. *J. Hydrol.*, 50(3): 186-195.
- Bowes, M. J., Jarvie, H. P., Halliday, S. J., Skeffington, R. A., Wade, A. J., Loewenthal, M., Gozzard, E., Newman, J. R., Palmer-Felgate, E. J. 2015. Characterizing phosphorus and nitrate inputs to a rural river using high-frequency concentration–flow relationships. *Science of the Total Environment*, 511: 608-620.
- Brauer N., O'Geen, A. T., Dahlgren, R. A. 2009. Temporal variability in water quality of agricultural tailwaters: implications for water quality monitoring. *Agr Water Manage*, 96: 1001-1009.
- Cassidy, R. and Jordan, P. 2011. Limitations of instantaneous water quality sampling in surface-water catchments: comparison with near-continuous phosphorus time-series data. *J Hydrol*, 405:18-193.
- Castillo, D., Kaplan, D., Mossa, J. 2016. A Synthesis of Stream Restoration Efforts in Florida (USA): Florida Stream Restoration. *River Research and Applications*, 32(7): 1555–1565.
- Colangelo, D. J., 2014. Interim Response of Dissolved Oxygen to Reestablished Flow in the Kissimmee River, Florida, U.S.A. *Restoration Ecology*, 22: 376-387.

- Craig, L. S., Palmer, M. A., Richardson, D. C., Filoso, S., Bernhardt, E. S., Bledsoe, B. P., Doyle, M. W., Groffman, P. M., Hassett, B. A., Kaushal, S. S., Mayer, P. M., Smith, S. M. 2008. Stream restoration strategies for reducing river nitrogen loads. *Frontiers in Ecology and the Environment*, 6(10): 529–538.
- Crumpton, W. G., Isenhardt, T. M., Mitchell, P. D. 1992. Nitrate and organic N analyses with second-derivative spectroscopy. *Limnol. Oceanogr.*, 37: 907-913.
- Daigneault, A. J., Eppink, F. V., Lee, W. G. 2017. A national riparian restoration programme in New Zealand: Is it value for money? *Journal of Environmental Management*, 187: 166–177.
- Daniluk, T. L., Lautz, L. K., Gordon, R. P., Endreny, T. A., 2013. Surface water-groundwater interaction at restored streams and associated reference reaches. *Hydrology Process*, 27: 3730-3746.
- Davis, R. T., Tank, J. L., Mahl, U. H., Winikoff, S.G., Roley, S. S. 2015. The influence of two-stage ditches with constructed floodplains on water column nutrients and sediments in agricultural streams. *Journal of the American Water Resources Association (JAWRA)*, 51(4): 941-955.
- Duncan, D., Harvey, F., Walker, M. and Australian Water Quality. 2007. EPA Guidelines: Regulatory monitoring and testing- Water and wastewater sampling. Environment Protection Authority in Australia.
- Eaton, A. D., Clesceri, L. S., Greensberg, A. E. 1995. Standard methods for the examination of water and wastewater, 19th ed. American Public Health Association.
- Eshleman, K. N. and Sabo, R. D. (2016). Declining nitrate-N yields in the Upper Potomac River Basin: What is really driving progress under the Chesapeake Bay restoration? *Atmospheric Environment*, 146: 280–289.

- Etheridge, J. R., 2013. Quantifying the water quality benefits of a constructed brackish marsh and tidal stream system using continuous water quality and flow monitoring. In: Ph.D. Dissertation. North Carolina State University, Raleigh, NC.
- Etheridge, J. R., Birgand, F., Burchell, M. R. 2015. Quantifying nutrient and suspended solids fluxes in a constructed tidal marsh following rainfall: The value of capturing the rapid changes in flow and concentrations. *Ecological Engineering*, 78: 41-52.
- Etheridge, J. R., Birgand, F., Burchell, M.R., Smith, B. T. 2013. Addressing the fouling of *in situ* ultraviolet–visual spectrometers used to continuously monitor water quality in brackish tidal marsh waters. *J. Environ. Qual*, 42: 1896–1901.
- Etheridge, J. R., Birgand, F., Osborne, J. A., Osburn, C. L., Burchell, M. R., Irving, J. 2014. Using *in situ* ultraviolet–visual spectroscopy to measure nitrogen, carbon, phosphorus, and suspended solids concentrations at a high frequency in a brackish tidal marsh. *Limnol. Oceanogr. Methods*, 12: 10-22.
- Fichot, C. G. and Benner, R. 2011. A novel method to estimate DOC concentrations from CDOM absorption coefficients in coastal waters. *Geophys. Res. Lett.* 38: L03610 doi:10.1029/2010GL046152.
- Fischenich, J. C. 2011. Stream restoration benefits. *Stream Restoration in Dynamic Fluvial Systems: Scientific Approaches, Analyses, and Tools Geophysical Monograph Series 194*, Published in 2011 by the American Geophysical Union.
- Flemming, H.-C. 2011. Microbial biofouling: Unsolved problems, insufficient approaches, and possible solutions. In: H.C. Flemming, J. Wingender, and U. Szewzyk, editors, *Biofilm highlights*. Springer, New York. 81–109.
- Galloway, J. N., Dentener, F. J., Capone, D. G., Boyer, E. W., Howarth, R. W., Seitzinger, S. P., Asner, G. P., Cleveland, C. C., Green, P. A., Holland, E. A., Karl, D. M., Michaels A. F., Porter, J. H., Townsend A. R., Vöösmary, C. J. 2004. Nitrogen cycles: past, present, and future. *Biogeochemistry* 70: 153-226.

- Gippel, G. J. 1995. Potential of turbidity monitoring for measuring the transport of suspended solids in streams. *Hydrol Process.*, 9:83-97.
- Greenberg, A. E., Clesceri, L. S., Eaton, A. D. 2005. Standard methods for the examination of water and wastewater, 25th ed. American Public Health Association; American Water Works Association; Water Environment Federation. American Public Health Association, Washington, D.C.
- Halliday, S. J., Skeffington, R. A., Wade, A. J., Bowes, M. J., Gozzard, E., Newman, J. R., Loewenthal, M., Palmer-Felgate, E. J., Jarvie, J. P. 2015. High-frequency water quality monitoring in an urban catchment: hydrochemical dynamics, primary production and implications for the Water Framework Directive. *Hydrological Process*, 29: 3388-3407.
- Henjum, M. B., Hozalski, R. M., Wennen, C. R., Arnold, W.A., Novak, P. J. 2010. Correlations between *in situ* sensor measurements and trace organic pollutants in urban streams. *J Environ Monitor*, 12: 225-233.
- Howson, T. J., Robson, B. J., Mitchell, B. D., 2009. Fish assemblage response to rehabilitation of a sand-slugged lowland river. *River. Research Applications*, 25: 1251-1267.
- Hughes, A. O. 2016. Riparian management and stream bank erosion in New Zealand. *New Zealand Journal of Marine and Freshwater Research*, 50(2), 277-290.
- ISO 15769. 2010. Hydrometry - Guidelines for the application of acoustic velocity meters using the Doppler and echo correlation methods.
- ISO 748. 1997. Measurement of liquid flow in open channel - velocity-area methods.
- Langergraber, G., Fleischmann, N., Hofstädter, F. 2003. A multivariate calibration procedure for UV/VIS spectrometric quantification of organic matter and nitrate in wastewater. *Water Sci. Technol.*, 47(2): 63-71.

- Mevik, B., Wehrens, R., and Liland, K. H. 2015. pls: Partial least squares and principal component regression. R package 2.4-3. <http://CRAN.R-project.org/package=pls>.
- Morlock, S. E., Nguyen, H. T., Ross, J. H. 2002. Feasibility of Acoustic Doppler Velocity Meters for the Production of Discharge Records from US Geological Survey Streamflow-Gaging Stations. US Geological Survey. Water-Resources Investigations Report 01-4157.
- Obolewski, K., Glińska-Lewczuk, K., Strzelczak, A., Burandt, P. 2014. Effects of a Floodplain Lake Restoration on Macroinvertebrate Assemblages- A Case Study of the Lowland River (The Słupia River, N Poland). *Polish Journal of Ecology* 62(3): 557-573.
- Palmer, M. A., E. S. Bernhardt, J. D. Allan, P. S. Lake, G. Alexander, S. Brooks, J. Carr, S. Clayton, C. N. Dahm, J. Follstad Shah, D. L. Galat, S. G. Loss, P. Goodwin, D. D. Hart, B. Hassett, R. Jenkinson, G. M. Kondolf, R. Lave, J. L. Meyer, T. K. O'Donnell, L. Pagano and E. Sudduth. 2005. Standards for Ecologically Successful River Restoration. *Journal of Applied Ecology*, 42: 208-217.
- Pander, J. and Geist, J. 2013. Ecological indicators for stream restoration success. *Ecological Indicators*, 30: 106-118.
- R Core Team. 2016. R: A language and environment for Statistical Computing. <http://www.R-project.org>.
- Ramos, T. B., Gonçalves, M. C., Branco, M. A., Brito, D., Rodrigues, S., Sánchez-Pérez, J.-M., Sauvage, S., Prazeres, Â., Martins, J. C., Fernandes, M. L., Pires, F. P. 2015. Sediment and nutrient dynamics during storm events in the Enxoé temporary river, southern Portugal. *Catena*, 127: 177-190.

- Rice, E. W., Baird, R. B., Eaton, A. D., Clesceri, L. S. 1997. Standard methods for the examination of water and wastewater: 2540 Solids, 22nd ed. American Public Health Association; American Water Works Association; Water Environment Federation. American Public Health Association, Washington, D.C.
- Rice, E. W., Baird, R. B., Eaton, A. D., Clesceri, L. S. 2012. Standard methods for the examination of water and wastewater, 22nd ed. American Public Health Association; American Water Works Association; Water Environment Federation. American Public Health Association, Washington, D.C.
- Rieger, L., Langergraber, G., Siegrist, H. 2006. Uncertainties of spectral *in situ* measurements in wastewater using different calibration approaches. *Water Sci. Technol.*, 53: 187-198.
- Ritter, A. and R. Muñoz-Carpena. 2013. Predictive ability of hydrological models: objective assessment of goodness-of-fit with statistical significance. *J. of Hydrology* 480(1): 33-45.
- Rochelle-Newall, E. and Fisher, T. 2002. Chromophoric dissolved organic matter and dissolved organic carbon in Chesapeake Bay. *Mar. Chem.*, 77:23-41.
- Saraceno, J. F., Pellerin, B. A., Downing, B. D., Boss, E., Bachand, P. A., Bergamaschi, B. A. 2009. High-frequency *in situ* optical measurements during a storm event: Assessing relationships between dissolved organic matter, sediment concentrations, and hydrologic processes. *J. Geophys. Res.* 114: G00F09, doi:10.1029/2009JG000989.
- Skarbøvik, E. and Roseth, R. 2015. Use of sensor data for turbidity, pH and conductivity as an alternative to conventional water quality monitoring in four Norwegian case studies. *Acta Agriculturae Scandinavica, Section B- Soil & Plant Science*, 65(1): 63-73.

- Skarbøvik, E., Stålnacke, P., Bogen, J., Bønsnes, T. E. 2012. Impact of sampling frequency on mean concentrations and estimated loads of suspended sediment in a Norwegian river: implications for water management. *Sci Total Environ*, 433: 462-471.
- Steinberger, N. and Whol, E. 2013. Impacts to water quality and fish habitat associated with maintaining natural channels for flood control. *Environmental Management*, 31(6): 724–740.
- StreamStats from USGS. http://streamstatsags.cr.usgs.gov/v3_beta/viewer.htm?stabbr=NC
- Suzuki, N. and Kuroda, R. 1987. Direct simultaneous determination of nitrate and nitrite by ultraviolet second-derivative spectrophotometry. *Analyst*, 112: 1077-1079.
- Torres, A. and Bertrand-Krajewski, J.-L. 2008. Partial Least Squares local calibration of a UV–visible spectrometer used for *in situ* measurements of COD and TSS concentrations in urban drainage systems. *Water Sci. Technol*, 57: 581-588.
- Wayne County, NC. <http://www.waynegov.com/page/214>.
- Whelan, A., and Regan, F. 2006. Antifouling strategies for marine and riverine sensors. *J. Environ. Monit*, 8: 880-886.

Chapter 3: Uncertainties assessment for continuous and infrequent sampling in measuring nutrient loads with the application of UV-Visual spectrophotometers in an agricultural coastal plain stream

3.1 Introduction

A revolution at play in water quality monitoring thanks to *in situ* probes

Much of the hydrological science and engineering current knowledge results from decades of continuous flow observations at multiple stations across the landscape. While flow has been acquired on a continuous basis for decades, water quality information has been, and still is in most stations, obtained from very infrequent samples (e.g., monthly to weekly in best cases). Not surprisingly, this very partial and incomplete information has created enormous knowledge gaps between hydrology and watershed biogeochemistry, generating, among many things, large uncertainties in mass flux estimations (e.g., Birgand et al. 2010, 2011a, 2011b; Jones et al., 2012; Moatar and Meybeck. 2007), and possibly erroneous conclusions on the processes at play (e.g., Etheridge et al., 2015).

The recent mass installation of *in situ* high frequency water quality sensors appears as a ‘revolution’ (Rode et al., 2016; Blaen et al., 2016) as it provides an unprecedented ability to capture water quality dynamics on par with those of flow in real-time, opening the possibility to quantify better resolutions of nutrient dynamics in watersheds (Glasgow et al., 2004).

There is a fast increasing number of articles that have reported the use of water quality sensors in tidal marshes since 2010 (Etheridge et al., 2013, 2014, 2015), rural (Bowes et al., 2015; Skarbøvik and Roseth, 2015; Cassidy and Jordan, 2011), and urban catchments (Halliday et al., 2015).

In particular, new *in situ* Ultraviolet to Visible (UV-Vis) spectrophotometers, which measure the absorbance of light from the ultraviolet to the visible range through water, offer the capacity to measure multiple parameters at the minute time scale. Nitrate (NO₃-N), dissolved organic carbon (DOC), and total suspended solids (TSS), are known to respectively absorb light in the 220-230 nm range (Crumpton et al., 1992; Suzuki and Kuroda, 1987), in the 250-360 nm range (e.g., Rochelle-Newall and Fisher, 2002; Saraceno et al., 2009; Fichot and Benner, 2011; Grayson and Holden, 2016), and in the visible range (e.g., Rieger et al., 2006; Torres and Bertrand-Krajewski, 2008).

Concentrations are calculated from proprietary algorithms embedded in the instruments sometimes referred to as ‘global calibrations’. Several authors have proposed to establish local calibrations to calculate concentrations from the raw absorbance signal (Langergraber et al., 2003; Rieger et al., 2006; Torres and Bertrand-Krajewski, 2008) to obtain better fits with concentrations. Among these, several studies have applied Partial Least Squares Regression (PLSR) statistical technique to directly calibrate absorbance values measured by UV-Vis spectrophotometers (Langergraber et al., 2003; Rieger et al., 2006; Torres and Bertrand-Krajewski, 2008; Etheridge et al., 2014; Birgand et al., 2016; Lepot et al., 2016).

Among the very interesting applications of PLSR is that it seems possible to obtain good calibrations with parameters not known to absorb light such as organic nitrogen, (ON), bromide (Br⁻), phosphate (PO₄-P), total phosphorus (TP), iron and silica (Etheridge et al., 2014; 2015; Birgand et al., 2016; Chapter 2). It has been proposed the concept of ‘water quality rating curves’, where absorbance spectra are used as ‘index data’ (*sensu* Morlock et al., 2002) and PLSR corresponds to the ‘rating method’. It has been shown that water quality

rating might be used for parameters not known to absorb light, because it is hypothesized that in many watersheds, there might be covariability of the ‘color matrix’ of the water with concentrations (Birgand et al., 2016).

Research questions and hypotheses

Measured, or rather predicted concentrations are thus fraught with uncertainty directly linked to the residuals associated with the regressions found. Like in all calibrations, the values and robustness of the regressions depend on the number and the distribution of calibration points, which may vary from parameter to parameter, and from station to station. Additionally, despite cleaning systems and techniques, the optics of these instruments, tend to foul due to metal oxide precipitation and/or the growth of biological and microbial agents over time (e.g., Whelan and Regan, 2006; Flemming, 2011; Etheridge et al., 2013; this report).

By estimating residuals, the PLSR approach can be directly used to calculate the uncertainty associated with these continuous water quality instruments, which does not appear to have been done before. Rieger et al. (2006) and Langergraber et al. (2003) suggested the calibration points cover the entire prediction range and be distributed equally. More calibration points may suggest more robust rating curves, but the number of points must remain small enough not to add to the already high investment and maintenance costs. The research questions become: (1) what kind of uncertainty should one expect on concentration and load values from continuous water quality instruments? (2) Can one develop guidance on how to minimize uncertainty with the use of these instruments using an

affordable number of calibration points? (3) How do uncertainties associated with the UV-Vis sensors compare with those associated with infrequent sampling on the annual load indicator?

Objectives

The objective of this article is to report the uncertainties that one might expect using UV-Vis instruments in streams and rivers on concentration and load values for nitrate (NO₃-N), total dissolved nitrogen (TDN), Total Kjeldahl Nitrogen (TKN), dissolved organic carbon (DOC), total phosphorus (TP), and total suspended solids (TSS). *In situ* UV-Vis spectrophotometers and continuous monitoring of hydrology were applied at two stations in the upper coastal plain of North Carolina, USA.

As a result, the objectives of the research were addressed as follows: (1) evaluate the uncertainties on concentration values and annual loads calculated by the ‘global calibration’ provided by the manufacturer, and calculated using PLSR depending upon the number and the distribution of the calibration points used; (2) compare these uncertainties to those that would be induced by infrequent sampling on estimating annual loads with best load algorithm methods; (3) provide guidance to users to minimize uncertainties and maximize the potential of their UV-Vis spectrophotometers.

3.2 Methods

Research context and site description

The research site, referred to the Claridge Canal, is a 2.2 km long reach within an agricultural coastal plain drainage canal in Goldsboro, North Carolina (35.42° N, 78.02° W). The canal that was dug within, and against the western edge of, the Little River floodplain to provide drainage for agricultural and farming in the floodplain. The overall project aims to quantify the water quality benefits of a stream restoration by comparing nutrient export dynamics, before, during, and after restoration of the 2.2 km study reach. The article reports data obtained during the before restoration phase from December 2013 to March 2015. For the project, the monitoring sites include the Upstream Station (UP) located just upstream the reach, the Middle Stream Station (MD, located 1,390 m from UP), and the Downstream Station (DN, located 807 m from MD) for a total length of 2,197 m of the study reach. The land uses in the watershed are 70% agriculture, 20% forests or woodlands, and 10% correspond to suburban areas with impervious areas corresponding to roads and roofs. The watershed areas at UP, MD, and DN add up to 236 ha, 414 ha, 573 ha, respectively (Figure 2.1). About half of the contributing area at the DN station corresponds to the flat floodplain and the other half is located in the sandy rolling hillslope typical landscape of the upper coastal plain. The average slope of the stream was 1.93%.

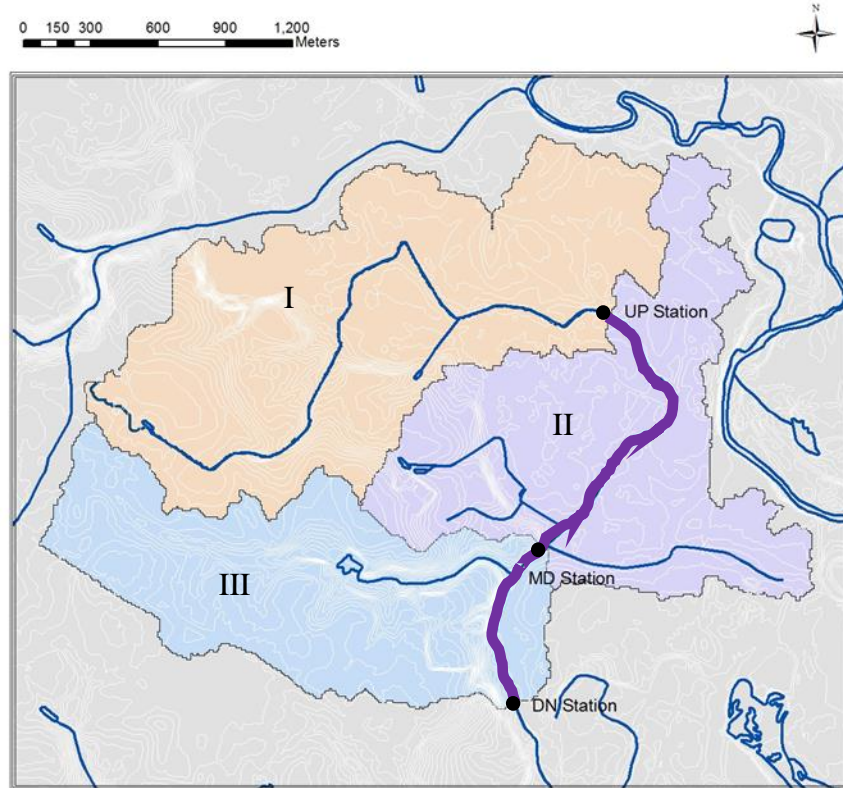


Figure 3.1

Three monitoring stations along the Claridge Canal in Goldsboro, North Carolina (I: Contributing watershed area for UP station; I and II: Contributing watershed area for MD station; I, II, and III: Contributing watershed area for DN station)

Flow measurements

Variable downstream control conditions in lowland coastal plain streams are common (Birgand et al., 2013) and rule out the use of the classical stable stage-discharge relationship. However, trapezoidal flumes (details in Etheridge et al., 2013 and Birgand, 2000) instrumented with Doppler flow meters (SonTek IQ Doppler meter, San Diego, CA, USA) are a good solution and were installed in the stream at the monitoring locations. The flume dimensions were measured by a total station after the installation of the flumes at the three

monitoring stations. Stage and stream velocity data were collected every 15 minutes from December 2013 to March 2015.

Instantaneous discharge (Q) is calculated as the product of cross-sectional average velocity (V) and cross-sectional area (A) (Equation 1).

$$Q = V \times A \quad \text{(Equation 1)}$$

At each measurement interval (15 min), the cross-sectional area (A) is calculated from the stage measurement provided by the SonTek IQ and the precisely known dimensions of the trapezoidal flumes. With the same times, the cross-sectional average velocity (V) is calculated from the velocity measurements provided by the SonTek IQ using the index velocity rating method (Morlock et al., 2002; Birgand, 2000; ISO 15769, 2010; further details in Chapter 2)

Water sample collection and measurements

Water quality at each station was measured at the same 15 min intervals using a UV-Vis spectrophotometer (spectro::lyser model, s::can), calibrated from laboratory analyses of samples taken by an automatic discrete sampler (ISCO 6712). The UV-Vis spectrophotometer measured the absorbance of light between 220 to 750 nm for 5 and 35 mm path lengths. The instruments provided turbidity (NTU), $\text{NO}_3\text{-N}$ (mg/L), DOC (mg/L), and total organic carbon (TOC; mg/L) concentration values every 15 minutes with the embedded Global Calibration from the manufacturer. The automatic discrete sampler took 900 ml discrete water samples every 12 hours at 12 am and 12 pm. Field-servicing occurred on biweekly intervals.

To lower the degree of fouling, the anti-fouling system developed by Etheridge et al. (2013) was applied, including the field visit cleaning procedures. It consists in minimizing the time of exposure of the optics to stream water by placing the instrument out of the water, and pump and purge water to the instrument, and rinse with tap water, using an automated Arduino controlled pumping system. All instruments were powered using 12V deep cycle marine batteries recharged by 120 W solar panels.

Laboratory analysis

During each field visit, the discrete water samples collected by the automatic discrete sampler were stored on ice and transported to the laboratory for analysis. The selections of the discrete samples for laboratory analysis depended on the initial water quality results from UV-Vis spectrophotometer and the flow events (e.g., the samples were preferentially selected when concentrations changed rapidly during flow events).

The initial 900 mL discrete samples were separated into several different volumes for analyses. 500 mL were transferred for TSS analysis (Standard Method 2540 D; Rice et al., 1997), while 150 mL were acidified with sulfuric acid for TKN (Standard Method 4500 N Org D; Rice et al., 2012) and TP analyses (Standard Method 4500 P F; Rice et al., 2012). The residual of the volume was filtered (pore size of 0.22 μm) (EMD Millipore Sterivex Sterile Pressure-Driven Devices, Darmstadt, Germany). Filtered solutions of 14 mL were transferred and acidified with sulfuric acid in 15 mL-centrifuge tubes for DOC to achieve pH 2 (Standard Method 5310 B; Greenberg et al., 2005) and TDN analysis (adapted by Standard Method 5310 B; Greenberg et al., 2005). Another 14 mL of filtered solutions without adding

sulfuric acid were transferred in 15 mL-centrifuge tubes for NO₃-N (The Cadmium Reduction Method; Eaton et al., 1995), NH₄-N (Salicylate Method; Eaton et al., 1995) and PO₄-P analysis (Ascorbic Acid Method; Eaton et al., 1995). NO₃-N, NH₄-N, TDN, PO₄-P, and DOC were analyzed at the Environmental and Agricultural Testing Service; TP and TKN were analyzed at the Center for Applied Aquatic Ecology; and TSS was analyzed at the Environmental Analysis Test Service Lab at North Carolina State University.

In addition, in order to evaluate degradation effects without adding the preservation agents into the unrefrigerated discrete samples in the field, a degradation study was applied. The details are available in Chapter 2. There were significant differences ($\alpha=0.05$) between the ‘fresh’ and ‘degraded’ samples for NO₃-N and NH₄-N at DN, and TKN and TP at the two stations in spring-summer. For these, only samples obtained within 48 hours of field visit were used in the calibration pool.

Calibration methods for concentrations from spectral data

As stated in Chapter 2, “PLSR as a regression model was used to correlate concentrations from the discrete samples to the spectral data (from UV-Vis spectrophotometers) measured at the same time. Then, the PLSR model was applied to predict 15 min concentrations from the 15-min spectral data. PLSR essentially decreases the hundreds of wavelengths of spectral data to a smaller number of principal component vectors to obtain highest correlation with water quality concentrations (Etheridge et al., 2013). This statistical technique is well suited for data in which the explanatory variables are highly auto correlated, as are absorbance values from sequential wavelengths (Mevik et al., 2011).”

The procedures for PLSR calibration are described in Chapter 2 using the pls package (Mevik et al., 2011) in the R software (R Core Team, 2016). Briefly, this package takes 90% of the points to create a calibration model and cross validates on the remaining 10%, and calculates indicators such as Root Mean Square Error of Prediction (RMSEP), percentage of variance of wavelengths being explained and R^2 for a given number of components. The model was run for 20 components initially. The optimum number of PLSR components for each analysis was chosen based on the two conditions. First, RMSEP values decreased dramatically as the increasing of number of components; then, RMSEP values became stable after the first turning point of the number of the component. Thus, the number of component related to the first transition point for RMSEP values was considered in the first condition. Second, the first number of component where the percentage of variance of wavelengths was higher than 99.95% was considered. At last, the minimum of the number of component obtained from the two conditions was determined for PLSR calibration. With PLSR calibrations, the 15-minutes continuous concentrations for $\text{NO}_3\text{-N}$, TDN, TKN, DOC, TP, and TSS were predicted from the spectral data and discrete sample results.

Besides, as reported in Chapter 2, previous research papers (Skarbøvik and Roseth, 2015; Ramos et al., 2015; and Gippel, G. J., 1995) indicated that there are high correlations between TSS concentrations and turbidity ($\text{TSS} = 0.46 \times \text{turbidity} + 8.95$, $R^2 = 0.8146$ in Skarbøvik and Roseth [2015], and $\text{TSS} = 2.493 \times \text{turbidity}$, $R^2 = 0.86$ in Ramos et al., [2015]). As a result, turbidity was used as a surrogate to predict the TSS concentrations as well. To predict continuous TSS concentrations from turbidity, the TSS concentrations from discrete samples corresponded to the turbidity results obtained from Global Calibration at the same

time were correlated with linear regression. Then, the continuous TSS concentrations results were calculated from the continuous turbidity results with the linear regression equation developed.

Uncertainties on concentrations and annual loads

Concentration uncertainties

Uncertainties on concentration values were estimated from the RMSE of the regression between predicted and lab measured concentrations.

Reference loads

The cumulative nutrient and material loads (L) is the integral over a given time (t) of instantaneous loads calculated as the product of solute concentration ($C(t)$) with flow rate ($Q(t)$; Equation 2). In reality, this integral can be approached by the summation of instantaneous 15-min loads calculated from the 15-min flow (Q_i) and concentration (C_i) data (Equation 3), where K is the unit adjustment factor and N is the number of 15 min intervals in t .

$$L = \int_0^t C(t)Q(t)dt \quad (\text{Equation 2})$$

$$L \approx K \sum_{i=1}^{i=N} C_i Q_i \quad (\text{Equation 3})$$

All loads calculated from calculated 15-min concentration data were calculated using Equation 3.

Resampling the existing calibration points

In order to evaluate the uncertainty associated with the use of UV-vis spectrophotometers, the existing calibration points were numerically resampled by using bootstrap, random and stratified sample subsets from the original dataset, and applied PLSR on these subsets, and predicted 15-min concentration data from the 15-min absorbance spectra. The computed loads were compared to the reference ones and expressed the differences in percentages.

Bootstrap sampling

Bootstrap sampling refers to random sampling with replacement from all the original existing calibration points. The sample size of the new datasets is identical with the number of original calibration points, and the bootstrap sampling in this research is referred to case bootstrap resampling. Bootstrap sampling was applied to NO₃-N, TDN, TKN, DOC, TP and TSS at both the UP and DN stations.

Random subset sampling

Random subset sampling refers to generating a new dataset by selecting a subset randomly without replacement from the original dataset. In this research, the samples sizes were chosen with subset sampling to be 52, 24 and 12 data points, so that the uncertainties would be comparable to those induced by weekly, biweekly, and monthly discrete sampling, respectively. The sample sizes with 52, 24 and 12 points were applied to NO₃-N, TDN, TKN,

DOC, TP and TSS at UP and DN stations. The sample sizes with 52 were not applied to TSS at DN because the maximum number of original calibration points was only 45.

Stratified sampling

In order to obtain higher quality of PLSR calibrations, Rieger et al. (2003) and Langergraber et al. (2006) suggested that the discrete samples be distributed equally over the given concentration range. Stratified sampling refers to separating the original dataset into mutually exclusive subgroups and using random sampling without replacement within each bin (or stratum). First, the concentrations range of the observed concentrations was calculated (Equation 4), where R is the concentration range, C_{\max} is the maximum concentration and C_{\min} is the minimum concentration.

$$R = C_{\max} - C_{\min} \quad (\text{Equation 4})$$

Then, the original data points were divided into m bins and the concentration ranges in each bin are: $(C_{\min}, C_{\min} + \frac{1}{m}R)$, $(C_{\min} + \frac{1}{m}R, C_{\min} + \frac{2}{m}R)$... $(C_{\min} + \frac{(m-1)}{m}R, C_{\max})$. At last, the calibration points were subset randomly without replacement from each bin. With stratified sampling, the uncertainties of annual loads estimation depending on calibration points distributed equally over the concentration range was evaluated. The stratified sampling was applied to $\text{NO}_3\text{-N}$ and TDN with two, three and five bins; DOC with two bins only at UP and DN, because of lack of enough samples for more bins. However, stratified sampling was not applied to TKN, TP, and TSS since there were not enough calibration points to make equally populated stratified bins.

Uncertainties estimation on annual loads as hydrological indicator with resampling

This research obtained 1000 different calibration point datasets for each sampling method. PLSR was applied to create a calibration for each of the datasets. The optimum number of components was selected based on the description in the Methods section. From each of these calibrations, the continuous concentrations were predicted and thus obtained 1000 load estimates for each of the parameters tested. In addition to the PLSR calibrations, 1000 TSS vs turbidity rating curves were created. For TSS, 1000 estimates of TSS loads using PLSR and 1000 estimates using turbidity as index data were obtained.

The uncertainties for annual loads were estimated as a percentage error to reference loads (Equation 5):

$$\text{Error percentage (\%)} = \frac{L_e - L_r}{L_r} \times 100\% \quad (\text{Equation 5})$$

Where L_r is the reference load using the continuous concentrations predicted from all existing original calibration points (for TSS, two reference load values for PLSR and turbidity based methods were obtained.) and where L_e is one of the 1000 estimated loads calculated as described above. A distribution of 1000 error percentages was obtained; thus, the average error (e_{avg}) and the median value (e_{50}) (both estimates of accuracy or bias) were extracted, as well as the 5th (e_5) and 95th (e_{95}) percentiles between which 90% of the total uncertainty was included, to express the range of uncertainties.

Uncertainties estimation on annual loads as hydrological indicator with infrequent sampling

For comparison purposes, the uncertainties were calculated expected on the annual loads that would have been induced by infrequent sampling. Many algorithms have been developed to estimate loads from infrequent concentration and continuous flow data (e.g., Phillips et al., 1999; Johnes, 2007; Birgand et al., 2010; Cassidy and Jordan, 2011). In this research, two algorithms were used: the flow-weighted concentration average estimator method and the linear interpolation method as they have been shown to perform best in coastal plain streams (Birgand et al., 2010).

For the first method, the annual flow weighted concentration average was estimated for a given sampling frequency from the summation of instantaneous loads obtained at the times of sampling divided by the summation of flow at the same times. This concentration was then multiplied by the flow volume calculated from continuous flow records. The first method is often referred to as the M5 method (Table 3.1; Phillips et al., 1999; Birgand et al., 2010). For the second method, 15 min concentrations were calculated from linear interpolation from discrete concentrations obtained at regular intervals. The second method is often referred to as the M6 method (Table 1; Phillips et al., 1999; Birgand et al., 2010).

Table 3.1

Methods applied to calculate the annual loads in this research (Adapted from Johnes, 2007; Birgand et al., 2010; Cassidy and Jordan, 2011)

Method Number	Equation	Description
M5	$Load = KV \frac{\sum_{i=1}^n C_i Q_i}{\sum_{i=1}^n Q_i}$	Product of the annual flow volume and the flow weighted average of the concentration (Littlewood, 1992).
M6	$Load = K \sum_{j=1}^{365} C_j^{int} Q_j$	Product of linear interpolation of concentrations and continuous flow rates (Q_j) (Moatar and Meybeck, 2005).
n	Number of samples	
K	Conversion factor accounts for units and intervals of sampling	
C_i	Instantaneous concentration measured at the time and day of the i th samples (mg L^{-1})	
Q_i	Instantaneous flow rate measured at the time and day of the i th samples ($\text{m}^3 \text{s}^{-1}$)	
Q_j	Continuous flow rate ($\text{m}^3 \text{s}^{-1}$)	
V	Annual cumulative flow volume ($\text{m}^3 \text{s}^{-1}$)	
C_{int}	Linearly interpolation concentration between the two consecutive samples	

To estimate uncertainties induced by infrequent sampling, the reference continuous concentrations were numerically resampled at the tested fixed intervals (weekly, biweekly and monthly). This research generated 1000 sets of fixed intervals discrete concentrations, for each of which the M5 and M6 loads were calculated. The error percentage between the estimated loads and the reference loads were calculated using Equation 5. The uncertainties induced by infrequent sampling were evaluated for $\text{NO}_3\text{-N}$, TDN, TKN, DOC, TP, and TSS at UP and DN.

Obtaining 12-month of the spectral data

During the 16-month monitoring period (from December 2013 to March 2015), human errors and equipment failure (e.g. power outage) caused distinct gaps in spectral data measured by the UV-Vis spectrophotometers. For the purpose of the uncertainty calculations, a synthetic dataset was created over a full hydrological year (as defined by USGS, the hydrological year in the U.S. is from October 1 for any given year to September 30 in the following year.) for each station. Fifteen-minute flow data were almost always available, so gap filling was applied mostly to concentration data. First, the missing spectral data periods were identified. Then, the available spectral data in previous/next year was searched that roughly corresponded to the same periods with similar storm events. Great care was taken to make sure that the flow and concentration peaks/troughs were fully synchronous. For example, data were missing from October 2013 to November 2013. As a result, the spectral data measured from October 2014 to November 2014 was used to patch the missing 2013 period. When no fitting concentration data were available, the concentration data were duplicated to best fit the flow events. In the end, there were very few duplications of instantaneous loads because most of the flow data were original.

3.3 Results and Discussion

Redundant potential in the annual spectral data

The composition of the synthetic spectral data at UP and DN stations are illustrated in Figure 3.2 and Figure 3.3, respectively. The two figures include the percentage of the original

data, the data patched from the same season/month in different years (e.g., the spectral data from October 2014 was used to fill in the missing period in October 2013.) and the duplicate data (e.g., the data from April was applied to adjacent period repeatedly).

Among the duplicated spectra added to patch missing data (36% of data at UP and 29% of data at DN), only 8% and 6% occurred during storm events, for UP and DN respectively, which are the critical periods for nutrient exports (Figure 3.2 and Figure 3.3). It is believed that the synthetic data created can be used as a realistic representation of flow and concentration dynamics that could have been recorded in these watersheds and therefore suitable datasets for uncertainty calculations.

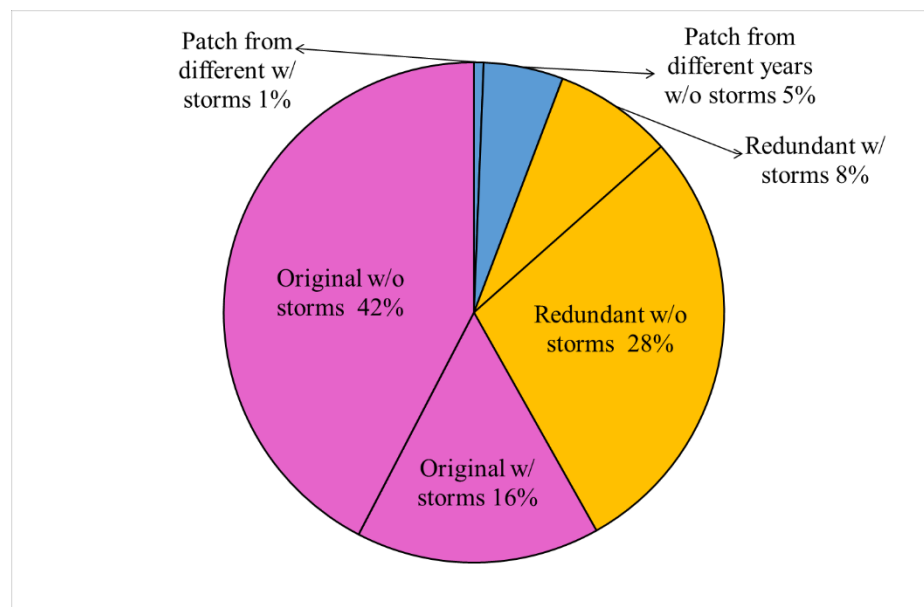


Figure 3.2

The source of annual spectral data including with (w/) and without (w/o) storm events presented in percentage at UP (Original: the initial spectral data; Patch from different years: the missing spectral data was filled from the same months in different years; Redundant: the missing spectral data was filled from different months).

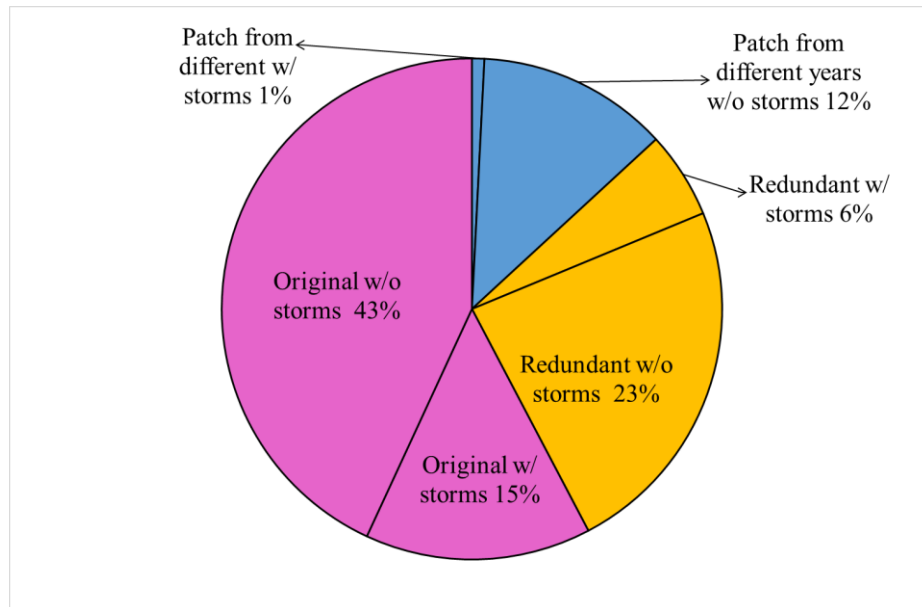


Figure 3.3

The source of annual spectral data including with (w/) and without (w/o) storm events presented in percentage at DN (Original: the initial spectral data; Patch from different years: the missing spectral data was filled from the same months in different years; Redundant: the missing spectral data was filled from different months).

Reference calibrations and loads

The laboratory results of discrete samples (including the number of samples and the range of observed concentrations) and annual reference loads for NO₃-N, TDN, TKN, DOC, TP, and TSS at UP and DN stations are summarized in Table 3.2. There are two values for TSS reference loads because both PLSR calibrations and turbidity predictions were applied to evaluate the TSS concentrations. For the simulations, the calibration pools were not separated into two calibration periods as in Chapter 2. The measured and predicted concentrations using PLSR calibrations with the original dataset for each water quality parameter at the two monitoring stations are reported in Figure 3.4 through Figure 3.6. The information of the

figures includes: the linear regression equation, r-squared values, selected number of components to predict the spectral data, number of observations (number of calibration points), and each calibration point was labeled with one identification number, which was corresponded to the specific time taken in the field.

The PLSR results for the reference calibrations using all available points are very comparable to those presented in Chapter 2, with the same level of significance as shown on the RMSE and NSE values (Table 3.2). The cumulative distribution functions plotted (from Figure 3.7 through Figure 3.11) for each parameter from the calibration pool show that concentrations are not equally distributed along their total range, and that the ratios between the smallest and highest concentrations can vary a lot. For each parameter, the concentrations most represented correspond to the most frequent, i.e., statistically outside hydrological events, and concentrations least represented correspond to the those associated with flow events. For $\text{NO}_3\text{-N}$ and TDN, the lower range concentrations are the least represented, as these occurred during events, while for DOC, TKN, TP, and TSS, the highest concentrations occurred during peaks and are least represented (Chapter 2). For $\text{NO}_3\text{-N}$, TDN, and DOC at UP and DN stations, the maximum concentrations are approximately five times those of the minimum concentrations, while for TP and TSS, the maximum to minimum concentration ratio reaches one hundred. Because of the skew in the distribution the full concentration range has little chance to be well represented in a random subsampling and this will have consequences on the expected uncertainties (details below).

Table 3.2

Summary of the laboratory analysis, PLSR predicted results and reference annual loads for NO₃-N, TDN, TKN, DOC TP, and TSS at UP and DN

	NO ₃ -N	TDN	TKN	DOC	TP	TSS
UP						
No. samples	289	289	276	249	274	138
Mean± Standard deviation (mg/L)	3.05±0.59	3.53±0.58	0.59±0.24	4.99±1.51	0.08±0.13	15.36±34.18
Observed Minimum (mg/L)	1.00	1.76	0.28	2.60	0.01	2.60
Observed Maximum (mg/L)	3.94	4.69	2.15	13.4	1.33	367.00
Predicted minimum (mg/L)	0.27	0.10	0.32	0.16	0.00	1.80 (PLSR) 1.45 (Turbidity)
Predicted maximum (mg/L)	0.93	4.48	9.30	14.13	3.58	943.80 (PLSR) 887.97 (Turbidity)
R ²	0.92	0.88	0.80	0.80	0.93	0.99 (PLSR) 0.99 (Turbidity)
RMSE	0.17	0.20	0.11	0.68	0.03	3.20 (PLSR) 3.16 (Turbidity)
NSE (% unsatif.)	0.92 (0%)	0.88 (0%)	0.80 (0%)	0.80 (2.2%)	0.93 (0%)	0.99 (0%) for both PLSR and Turbidity
Reference load (kg/ha)	12.96	15.30	3.5	26.80	0.73	138.56 (PLSR) 101.99 (Turbidity)

Table 3.2 Continued

	NO₃-N	TDN	TKN	DOC	TP	TSS
DN						
No. samples	195	192	181	218	180	45
Mean± Standard deviation (mg/L)	2.39±0.48	2.92±0.50	0.71±0.26	6.06±1.74	0.11±0.11	57.35±70.16
Minimum (mg/L)	0.953	1.62	0.28	3.7	0.02	3
Maximum (mg/L)	3.18	3.95	1.82	14.7	0.65	271
Predicted minimum (mg/L)	0.01	0.27	0.43	1.82	0.02	0.08 (PLSR) 1.39 (Turbidity)
Predicted maximum (mg/L)	3.32	4.07	2.21	13.89	1.38	434.88 (PLSR) 288.19 (Turbidity)
R ²	0.90	0.86	0.78	0.90	0.97	0.99 (PLSR) 0.99 (Turbidity)
RMSE	0.15	0.19	0.12	0.54	0.02	5.34 (PLSR) 5.49 (Turbidity)
NSE (% unsatif.)	0.90 (0%)	0.86 (0%)	0.78 (2.4%)	0.90 (0%)	0.97 (0%)	0.99 (0%) for both PLSR and Turbidity
Reference load (kg/ha)	10.53	13.42	5.18	36.86	1.21	243.28 (PLSR) 156.41 (Turbidity)

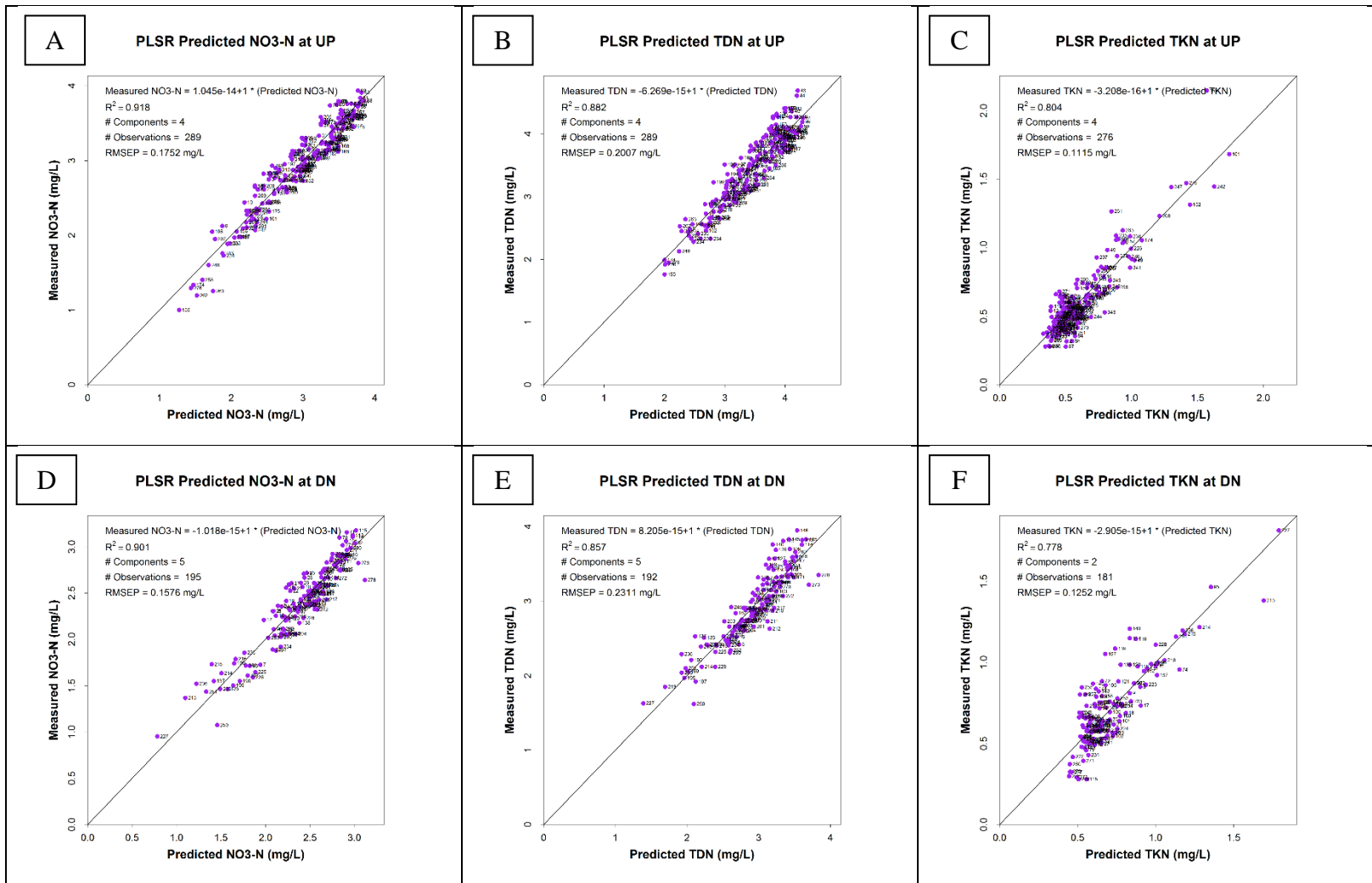


Figure 3.4: Regression relationship between measured and predicted NO₃-N (A and D), TDN (B and E), TKN (C and F) using PLSR calibration with original calibration points at UP (top row) and DN (bottom row).

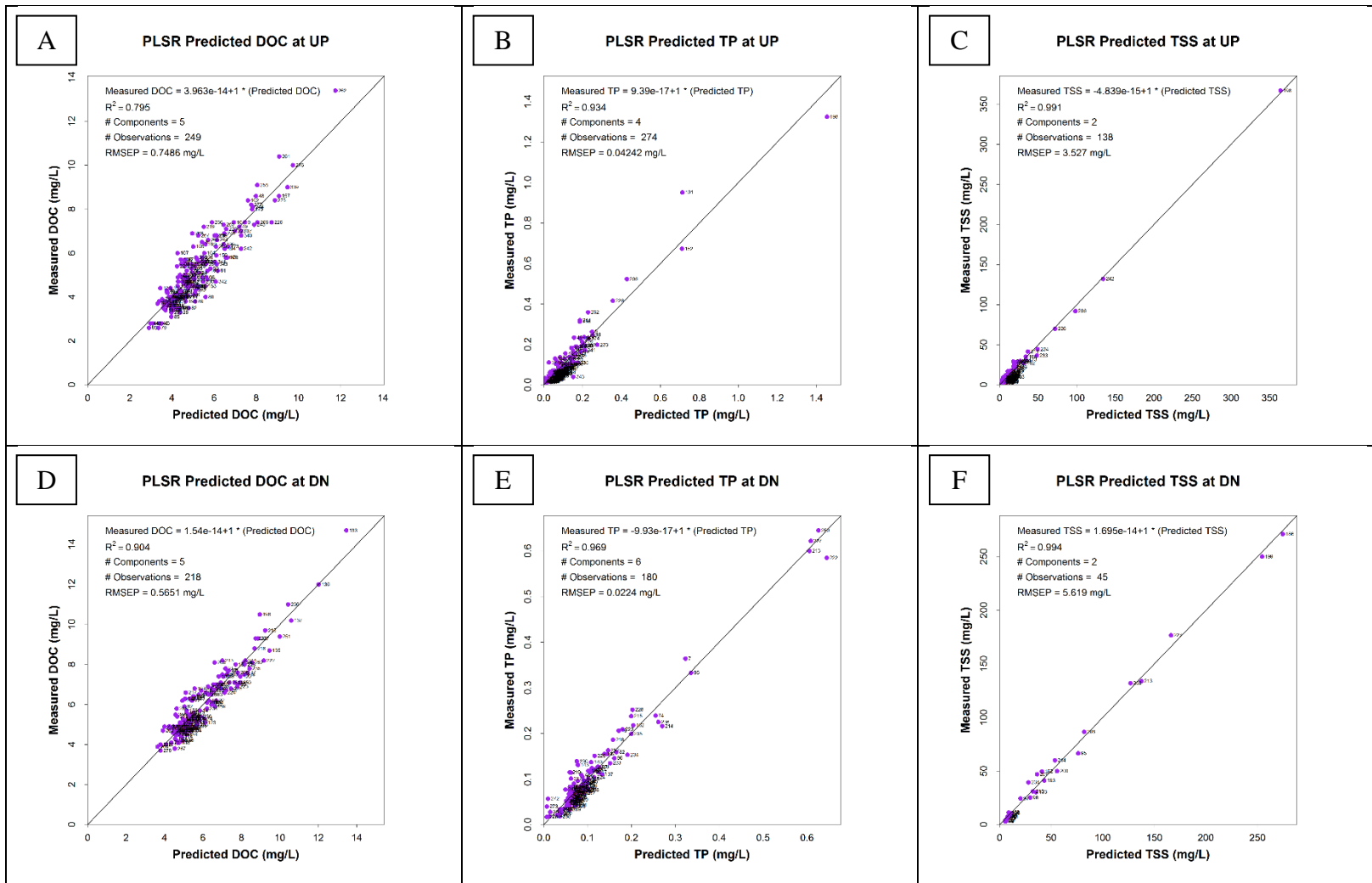


Figure 3.5: Regression relationship between measured and predicted DOC (A and D), TP (B and E), TSS (C and F) using PLSR calibration with original calibration points at UP (top row) and DN (bottom row).

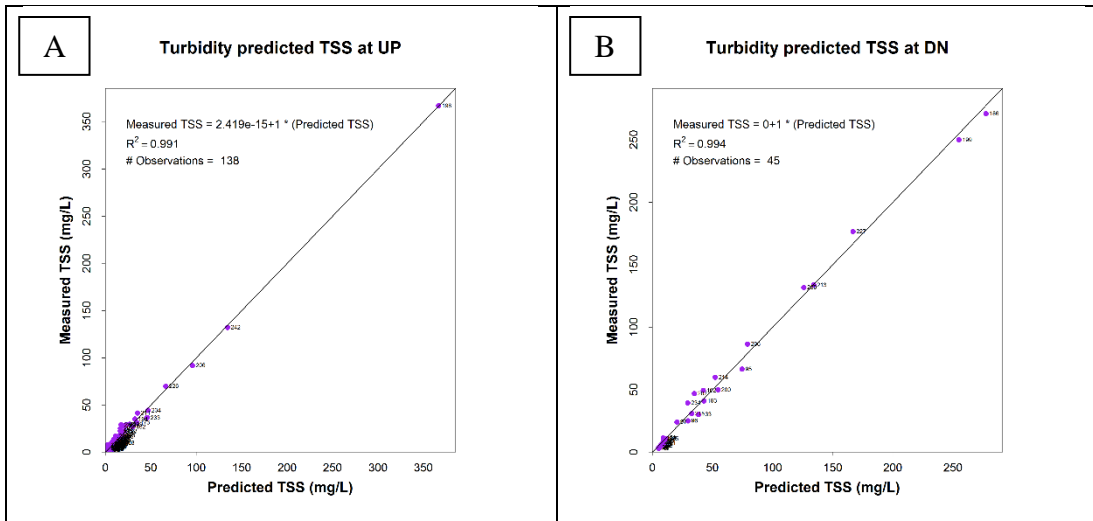


Figure 3.6: Regression relationship between measured and predicted TSS using Turbidity predictions with original calibration points at UP (A) and DN (B).

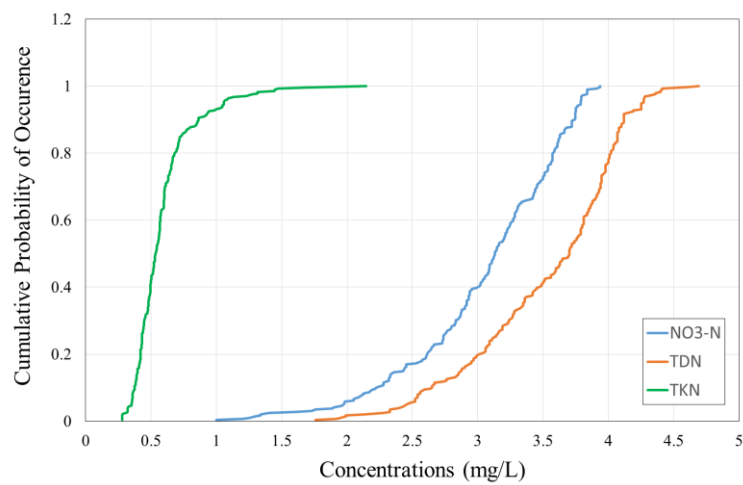


Figure 3.7
Cumulative probability of occurrence for NO₃-N, TDN and TKN concentrations at UP station

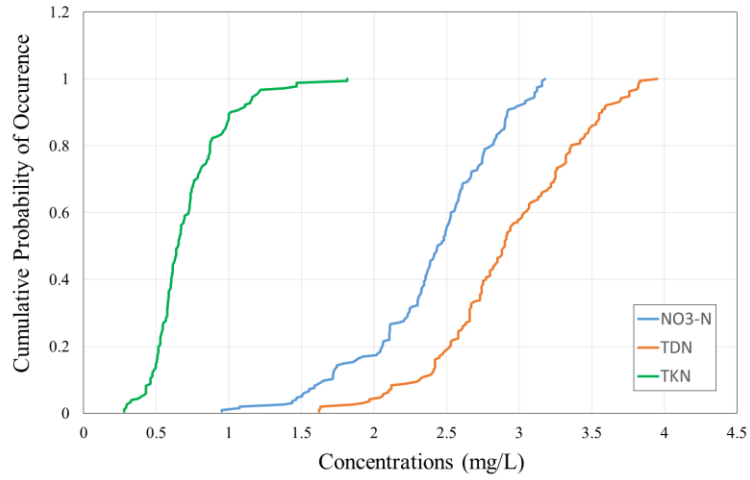


Figure 3.8

Cumulative probability of occurrence for NO₃-N, TDN and TKN concentrations at DN station

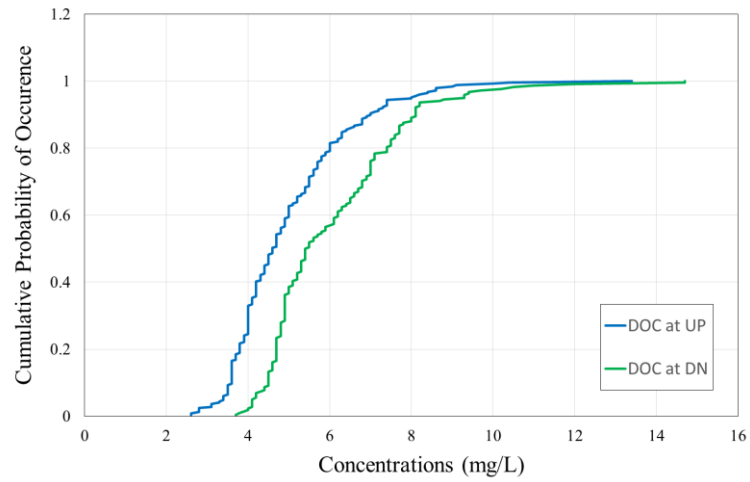


Figure 3.9

Cumulative probability of occurrence for DOC concentrations at UP and DN stations

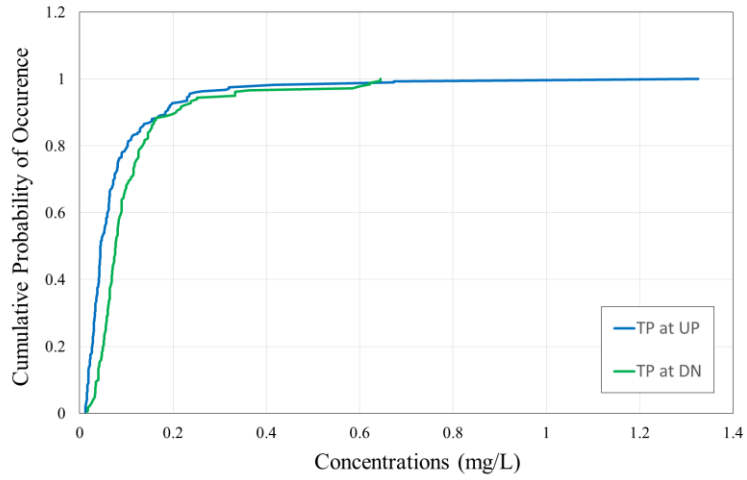


Figure 3.10

Cumulative probability of occurrence for TP concentrations at UP and DN stations

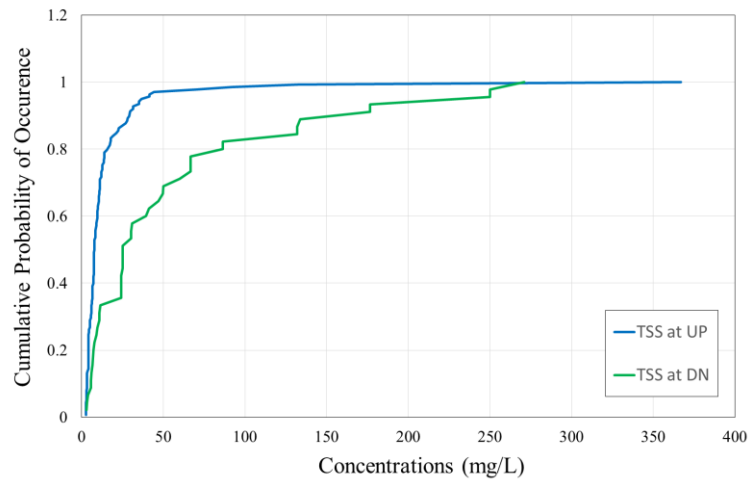


Figure 3.11

Cumulative probability of occurrence for TSS concentrations at UP and DN stations

Uncertainties estimations for three resampling methods and infrequent sampling

General results

For each of the subsampling method (bootstrap, random, stratified) and the infrequent sampling method (M5 and M6), the indicators of the uncertainties were calculated, i.e., e_{avg} , e_5 and e_{95} from the uncertainty distributions illustrated in Figure 3.12 below for nitrate and DOC for random and stratified sampling for 24 samples. All distribution histograms are available in Appendix B through Appendix E.

The indicators for all simulations for parameters tested are summarized in Table 3.3 to Table 3.9 below. For stratified sampling, the available samples were separated into 2 (2B), 3 (3B), and 5 (5B) ‘bins’ to cover the full range. Ideally, the more bins the more stratified the representation of the concentration range. But in many instances, the distribution of samples only allowed 2 bins (2B) to be tested.

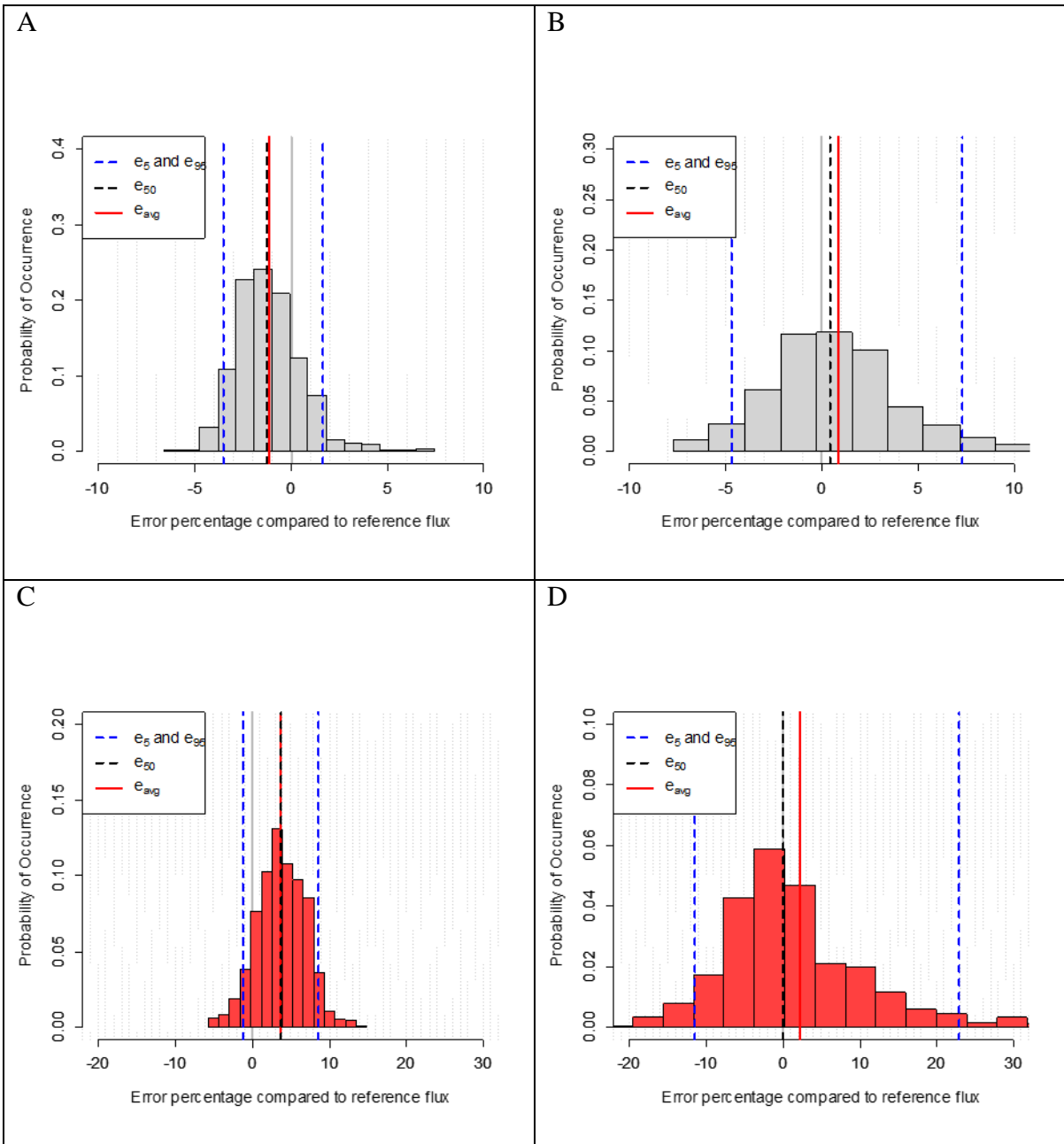


Figure 3.12: Distribution of uncertainties of annual loads for nitrate (top row; A and B) and DOC (bottom row; C and D) corresponding to 24 stratified (left column; A and C) and random (B and D) samples used to create the calibrations

Table 3.3

Uncertainty estimation for NO₃-N annual loads (e_{avg} and e_5 to e_{95} ; presented in the percentage as relative difference of the reference loads) for four sampling methods (bootstrap, random subset, stratified and infrequent sampling) with different number of samples and sampling intervals

Sample Method	UP		DN	
	e_{avg}	e_5 to e_{95}	e_{avg}	e_5 to e_{95}
Bootstrap	-0.1	-1.3 to +1.0	1.1	-1.2 to +3.8
Random Subset				
n = 12	1.2	-7.5 to +13.5	9.0	-8.8 to +41.2
n = 24	1.0	-4.5 to +7.6	3.0	-5.5 to +12.8
n = 52	0.4	-2.5 to +3.8	1.3	-4.1 to +7.0
Stratified – 2B				
n = 12	-0.5	-7.0 to +7.2	2.7	-5.9 to +13.2
n = 24	-0.8	-3.7 to +3.0	0.9	-4.6 to +7.2
n = 30	-0.6	-3.4 to +2.3	0.6	-4.4 to +5.7
n = 52	-1.0	-2.8 to +1.0	0.4	-2.3 to +3.0
Stratified – 3B				
n = 30	-1.1	-3.5 to +1.2	0.0	-3.7 to +3.3
Stratified – 5B				
n = 30	-1.2	-3.3 to +1.0	NA	NA
Infrequent Sampling – M5				
Monthly (n = 12)	8.9	-19.0 to +23.8	10.2	-21.4 to +30.4
Biweekly (n = 24)	4.7	-22.0 to +19.8	5.0	-28.2 to +24.1
Weekly (n = 52)	1.8	-15.4 to +12.2	2.1	-26.6 to +15.6
Infrequent Sampling – M6				
Monthly (n = 12)	14.0	+5.1 to +22.0	19.9	+6.0 to +30.8
Biweekly (n = 24)	13.6	+6.9 to +20.4	19.0	+9.7 to +27.3
Weekly (n = 52)	13.0	+8.2 to +16.5	17.6	+9.7 to +23.3

Table 3.4

Uncertainty estimation for TDN annual loads (e_{avg} and e_5 to e_{95} ; presented in the percentage as relative difference of the reference loads) for four sampling methods (bootstrap, random subset, stratified and infrequent sampling) with different number of samples and sampling intervals

Sample Method	UP		DN	
	e_{avg}	e_5 to e_{95}	e_{avg}	e_5 to e_{95}
Bootstrap	-0.1	-0.7 to +0.9	0.8	-1.4 to +3.1
Random Subset				
n = 12	3.8	-7.3 to +20.8	9.8	-10.0 to +49.0
n = 24	2.5	-2.8 to +11.5	4.0	-6.4 to +19.8
n = 52	1.0	-1.4 to +4.8	1.3	-4.1 to +6.4
Stratified – 2B				
n = 12	1.8	-6.5 to +15.5	8.0	-8.2 to +38.1
n = 24	0.3	-3.1 to +5.8	2.5	-5.8 to +14.3
n = 30	0.0	-2.7 to +3.5	2.0	-5.3 to +11.8
n = 52	-0.4	-2.0 to +1.3	1.0	-3.6 to +5.1
Stratified – 3B				
n = 30	-0.3	-2.5 to +2.2	2.0	-2.1 to +5.5
Stratified – 5B				
n = 30	-0.4	-2.0 to +1.5	2.0	-1.4 to +5.7
Infrequent Sampling – M5				
Monthly (n = 12)	6.8	-17.2 to +18.9	8.4	-19.8 to +24.0
Biweekly (n = 24)	3.5	-17.0 to +15.1	4.0	-22.7 to +18.8
Weekly (n = 52)	1.5	-11.9 to +10.0	1.7	-20.7 to +12.8
Infrequent Sampling – M6				
Monthly (n = 12)	10.0	+1.9 to +16.6	14.2	+4.1 to +24.5
Biweekly (n = 24)	10.0	+4.2 to +15.4	14.6	+7.0 to +21.6
Weekly (n = 52)	9.6	+5.5 to +12.5	13.5	+7.7 to +17.9

Table 3.5

Uncertainty estimation for TKN annual loads (e_{avg} and e_5 to e_{95} ; presented in the percentage as relative difference of the reference loads) for three sampling methods (bootstrap, random subset and infrequent sampling) with different number of samples and sampling intervals

Sample Method	UP		DN	
	e_{avg}	e_5 to e_{95}	e_{avg}	e_5 to e_{95}
Bootstrap	0.0	-3.5 to +3.6	1.0	-3.5 to +7.6
Random Subset				
n = 12	7.2	-20.8 to +56.4	24.0	-25.0 to +113.5
n = 24	2.0	-15.9 to +33.2	15.5	-11.2 to +68.0
n = 52	-0.5	-11.7 to +16.1	7.0	-7.0 to +33.5
Infrequent Sampling – M5				
Monthly (n = 12)	-14.1	-40.5 to +50.0	-12.0	-37.8 to +50.5
Biweekly (n = 24)	-8.5	-37.2 to +49.3	-7.0	-32.4 to +42.5
Weekly (n = 52)	-3.4	-28.0 to +58.0	-3.2	-23.5 to +33.5
Infrequent Sampling – M6				
Monthly (n = 12)	-31.4	-42.3 to -14.1	-30.0	-40.8 to -13.5
Biweekly (n = 24)	-29.0	-39.0 to -14.4	-28.0	-37.0 to -16.8
Weekly (n = 52)	-27.2	-35.4 to -12.8	-26.4	-32.8 to -15.9

Table 3.6

Uncertainty estimation for DOC annual loads (e_{avg} and e_5 to e_{95} ; presented in the percentage as relative difference of the reference loads) for four sampling methods (bootstrap, random subset, stratified and infrequent sampling) with different number of samples and sampling intervals

Sample Method	UP		DN	
	e_{avg}	e_5 to e_{95}	e_{avg}	e_5 to e_{95}
Bootstrap	-0.1	-3.0 to +2.5	-0.1	-2.2 to +2.1
Random Subset				
n = 12	9.0	-20.0 to +61.6	-0.6	-14.9 to +23.2
n = 24	2.2	-12.3 to +26.1	-1.6	-12.5 to +9.4
n = 52	-0.5	-6.8 to +7.3	-0.4	-6.7 to +5.0
Stratified – 2B				
n = 12	5.0	-7.7 to +16.8	4.9	-5.4 to +14.8
n = 24	3.9	-1.3 to +8.6	2.5	-0.1 to +5.2
Infrequent Sampling – M5				
Monthly (n = 12)	-10.2	-28.8 to +26.5	-6.5	-24.2 to +16.9
Biweekly (n = 24)	-6.0	-25.4 to +31.6	-2.6	-20.2 to +14.4
Weekly (n = 52)	-2.2	-15.5 to +20.5	-0.6	-14.3 to +19.3
Infrequent Sampling – M6				
Monthly (n = 12)	-22.5	-31.2 to -11.1	-16.7	-27.0 to -0.4
Biweekly (n = 24)	-19.2	-27.0 to -10.1	-14.1	-23.2 to -4.6
Weekly (n = 52)	-18.0	-23.3 to -11.8	-13.7	-18.7 to -7.2

Table 3.7

Uncertainty estimation for TP annual loads (e_{avg} and e_5 to e_{95} ; presented in the percentage as relative difference of the reference loads) for three sampling methods (bootstrap, random subset and infrequent sampling) with different number of samples and sampling intervals

Sample Method	UP		DN	
	e_{avg}	e_5 to e_{95}	e_{avg}	e_5 to e_{95}
Bootstrap	1.0	-6.5 to +13.8	0.7	-4.5 to +8.0
Random Subset				
n = 12	12.0	-33.0 to +67.8	4.9	-33.0 to +52.2
n = 24	10.0	-19.5 to +49.0	5.0	-11.0 to +32.4
n = 52	-5.6	-11.2 to +27.6	2.0	-7.8 to +17.0
Infrequent Sampling – M5				
Monthly (n = 12)	-26.0	-77.0 to +106.5	-26.0	-70.0 to +123.5
Biweekly (n = 24)	-16.0	-71.5 to +115.5	-17.0	-65.0 to +115.5
Weekly (n = 52)	-8.5	-57.0 to +112.0	-8.0	-55.0 to +87.0
Infrequent Sampling – M6				
Monthly (n = 12)	-57.0	-77.0 to -18.0	-57.0	-73.0 to -19.5
Biweekly (n = 24)	-55.0	-69.0 to -19.5	-54.0	-69.0 to -28.0
Weekly (n = 52)	-51.0	-67.0 to -15.0	-51.0	-64.0 to -24.5

Table 3.8

Uncertainty estimation for TSS annual loads with PLSR prediction (e_{avg} and e_5 to e_{95} ; presented in the percentage as relative difference of the reference loads) for three sampling methods (bootstrap, random subset and infrequent sampling) with different number of samples and sampling intervals

Sample Method	UP		DN	
	e_{avg}	e_5 to e_{95}	e_{avg}	e_5 to e_{95}
Bootstrap	-0.6	-4.9 to +2.3	-0.9	-4.3 to +3.1
Random Subset				
n = 12	-5.2	-34.1 to +15.0	0.8	-5.0 to +7.0
n = 24	-3.0	-17.2 to +7.9	-1.5	-4.4 to +1.6
n = 52	-1.5	-7.0 to +2.9	NA	NA
Infrequent Sampling – M5				
Monthly (n = 12)	-27.0	-76.5 to +133.0	-29.0	-82 to +180.0
Biweekly (n = 24)	-17.0	-73.5 to +153.0	-19.0	-79.5 to +156.5
Weekly (n = 52)	-10.0	-65.5 to +148.0	-9.5	-70 to +124.0
Infrequent Sampling – M6				
Monthly (n = 12)	-57.5	-78.0 to -5.5	-64.5	-83.0 to -17.5
Biweekly (n = 24)	-56.0	-74.5 to -12.0	-63.5	-81.5 to -30.0
Weekly (n = 52)	-52.5	-72.0 to -3.5	-59.5	-77.0 to -26.0

Table 3.9

Uncertainty estimation for TSS annual loads with Turbidity prediction (e_{avg} and e_5 to e_{95} ; presented in the percentage as relative difference of the reference loads) for three sampling methods (bootstrap, random subset and infrequent sampling) with different number of samples and sampling intervals

Sample Method	UP		DN	
	e_{avg}	e_5 to e_{95}	e_{avg}	e_5 to e_{95}
Bootstrap	0.0	-2.4 to +2.4	-0.1	-4.4 to +4.3
Random Subset				
n = 12	3.0	-13.6 to +25.1	-0.5	-7.5 to +7.4
n = 24	1.3	-7.4 to +13.6	-0.2	-4.4 to +3.8
n = 52	0.2	-3.8 to +4.9	NA	NA
Infrequent Sampling – M5				
Monthly (n = 12)	-27.0	-79.0 to +157.0	-29.5	-80.5 to +163.0
Biweekly (n = 24)	-17.0	-76.0 to +179.0	-17.5	-75.5 to +157.5
Weekly (n = 52)	-10.0	-70.5 to +136.0	-7.5	-69.0 to +127.0
Infrequent Sampling – M6				
Monthly (n = 12)	-61.0	-80.5 to -12.5	-61.0	-81.0 to -5.0
Biweekly (n = 24)	-59.0	-77.0 to -13.5	-60.0	-79.0 to -27.5
Weekly (n = 52)	-55.0	-74.0 to -14.0	-56.0	-74.0 to -25.0

Bootstrap sampling results for all parameters

Across all simulations for both stations and all parameters, the bootstrap resampling gave the smallest uncertainties, most of which within -3.5% to +3.5% (Table 3.3 to Table 3.9). This was expected as the number of calibration points was 5 to 30 times more numerous. The results demonstrated the smallest uncertainties for TDN (-0.7% to +0.9%) and the largest for TP (-6.5% to +13.8%). The uncertainty distributions with bootstrap sampling were symmetrical for all parameters at UP and DN stations and generally centered around 0,

except for TP at UP station, suggesting that the bias (e_{avg}) and median-bias (e_{50}) have the same trend.

The relatively large uncertainty for TP probably comes from the skewness of calibration points, as 90% of the points are within 15% of the total calibration range corresponding to the lowest concentrations at UP station (Figure 3.10). Even with bootstrap sampling, there were high probabilities for calibration points to be selected from the lower range (0.01 to 0.30 mg/L at UP). As a result, some of the bootstrap subsampling do not capture the high concentrations, which can generate higher uncertainties, particularly since the high concentrations occurred around flow peaks (Chapter 2). Consequently, the uncertainty range for estimating loads is larger for TP than TDN.

Much lower uncertainties from stratified compared to random sampling and infrequent sampling

For optical probes to be affordable and reliable, it is necessary to assess the number and distribution of calibration points that might be necessary. For most long-term monitoring stations, monthly sampling or 12 samples per year is the affordable number of samples. Regular interval sampling of 12 samples will tend to align more with the ‘random sampling’ scheme rather than the ‘stratified sampling’ scheme, which is a lot more complicated to obtain practically.

Similarly to what Rieger et al. (2003) and Langergraber et al. (2006) reported, it was found that uncertainties associated with stratified sampling are always better than those associated with random sampling, regardless of the number of calibration samples, the parameter, and the station (Table 3.3 to Table 3.9).

For TKN and DOC, the uncertainty associated with 12 or 24 random sampling for PLSR calibration are large and of the same order as those that would be induced with regular interval discrete sampling calculated using M5 and M6. For example, the PLSR calibration using 24 random samples for DOC at UP would generate -12.3% to +26.1%, while the uncertainty on the annual using no probe with the same number of samples every other week would be -25.4% to +31.6% (Table 3.6). For these parameters and using random sampling, having an expensive optical sensor does not provide sensible benefits.

For TP and TSS, discrete infrequent sampling generates much higher uncertainties, than the PLSR results. However, the uncertainties even with 52 samples can still be high using random sampling for TP at the upstream station (-11.2% to +27.6%).

With increasing number of samples (from 12 to 52), the bias associated with random sampling tends to converge toward zero. This is expected as this tends toward the reference calibration set. Two notable exception are TP at UP and TKN at DN, although the bias absolute values diminish, they are at -5.6% and +7%, respectively for 52 samples.

Interestingly, the bias associated with stratified sampling tends to converge towards negative numbers for nitrate and TDN and positive numbers for DOC and TKN, which reference sample distributions have more high and low concentrations, respectively. This suggests that the annual nitrate and TDN loads, and DOC and TKN loads, tend to be underestimated and overestimated, respectively, with a smaller stratified subset of sample for calibration. This could be due to an overrepresentation of the lower frequency concentrations in the stratified calibration subsets, and/or an overrepresentation of the higher frequency concentrations in the reference calibration set.

Because the biases, tend to stay relatively stable with stratified sampling, and because the skewness of regression residuals of the respectively lower and higher ranges (data not shown) of concentrations for nitrate and TDN, and DOC and TKN, it is concluded that the reference loads are likely systematically overestimating and underestimating, respectively, the actual loads. It is also concluded that the annual loads computed from stratified calibration sets are likely less biased than the reference loads.

More stratification is better

For nitrate and TDN, it was possible to test whether the number of bins or the stratification of the calibration samples improves prediction. Although this corresponds to a small improvement, it does seem that stratifying from 2 to 3 to 5 bins, does lower the overall uncertainties for these two parameters at the two stations, using 30 calibration samples. For example, the uncertainties for TDN at UP improved from -2.7% to +3.5% using two bins, to -2.5% to +2.2% using three bins, and to -2.0% to +1.5% using 5 bins (Table 3.4). The relatively small improvement might be due to the small uncertainties to start with for TDN and nitrate parameters.

Uncertainties and calibration robustness depend on parameters

Among all parameters, stations, and best estimation methods, uncertainties calculated on annual loads are lowest to highest in that order: nitrate, TDN (uncertainties very close to those of nitrate), DOC, TSS (both methods performing about the same), TKN and TP (Table 3.10).

Table 3.10

Summary of calculated uncertainties for all parameters, stations and method leading to lowest uncertainty

	Best method	UP	Best method	DN
Nitrate	Strat 52	-2.8 to +1.0	Strat 52	-2.3 to +3.0
TDN	Strat 52	-2.0 to +1.3	Strat 52	-3.6 to +5.1
TKN	Rand 52	-11.7 to +16.1	Rand 52	-7.0 to +33.5
DOC	Strat 24	-1.3 to +8.6	Strat 24	-0.1 to +5.2
TP	Rand 52	-11.2 to +27.6	Rand 52	-7.8 to +17.0
TSS (PLSR)	Rand 52	-7.0 to +2.9	NA	NA
TSS (turbidity)	Rand 52	-3.8 to +4.9	NA	NA

Not surprisingly, uncertainties on nitrate and TDN are very similar since TDN was predominantly composed by NO₃-N (50% to 90% for both stations) in the Claridge Canal based on the continuous concentrations. The improvement of the uncertainty from 12 to 24 stratified samples is a lot more pronounced with TDN and DOC than it is with nitrate (Table 3.3, Table 3.4, and Table 3.6), which suggests that with few samples, PLSR is able to better reproduce the relationship between absorbance and concentrations with nitrate, than it is with TDN or DOC. Nitrate is known to strongly absorb light between 190 nm to 250 nm (Crumpton et al. 1992; Suzuki and Kuroda 1987; Finch et al. 1998; Olsen, 2008), while TDN and DOC represent an ensemble of molecules of many different origins. There theoretically is a lesser correlation with identified wavelengths. Nonetheless, the uncertainties for DOC at

DN are of the same order of the ones for nitrate. For this station, PLSR was able to provide a more robust prediction of the DOC annual loads. This might be due to the intermittent addition of DOC from the Little River during very high flow events.

The much higher uncertainties for TKN and TP reported in Table 3.10 are due in large part to the fact that they report calibration with random sampling. The bootstrap results do show however, that for these two parameters, PLSR calibrations were the least robust (Table 3.5). This is somewhat expected as TKN represents a wide variety of both dissolved and particulate constituents and PLSR performance are not as good even with the reference calibration set (Table 3.2). The uncertainties associated with TP are of the same order of magnitude as those for TKN. For this parameter, it might be due to the large errors that can be induced by having or not, the high concentration values in the calibration dataset, because the R^2 for the reference set show higher prediction ability of PLSR for TP than for TKN. For these two parameters, it may be necessary to obtain more than 52 calibration samples across a better-stratified concentration range.

The low uncertainties reported for TSS are surprising with random subset sampling. The maximum to minimum concentration ratios show that they are comparable to those of TP, which suggests that the probability of misrepresenting the important highest values were similar. However, this result might be an artifact of the relatively small size of the original dataset to sample from (Table 3.2). It is possible that among the 1000 simulations, many subsets were in fact the same, reducing the apparent uncertainty range compared to TKN and TP (Table 3.5 and Table 3.7 to Table 3.9). The level of uncertainty appears to be the same for PLSR and turbidity predicted TSS concentrations, although the computed loads were vastly

overestimated using PLSR-based (+36% for UP and +55% for DN) compared to turbidity-based concentrations. This result confirms the findings of Chapter 2. For the TSS parameter, the major source of uncertainty is the extrapolation of concentrations beyond their calibration range. The use of the field spectrophotometer thus provided a lot more precise measurements than the M5 and M6 methods, but which accuracy remains unknown for this parameter because of unknown errors on TSS predictions beyond the calibration range.

The results from load estimations from common infrequent regular interval sampling show that the uncertainties are often one or more order of magnitude larger than with the spectrophotometer for 52 calibration samples per year. This confirms that spectrophotometers do lower uncertainties on nutrient loads compared to more standard infrequent sampling methods.

3.4 Conclusions

This manuscript is the first to report uncertainties on concentrations and annual loads using *in situ* spectrophotometers. The PLS rating approach allows the systematic exploration of the level of uncertainty expected on concentrations and loads. The strength of the PLSR ratings are very similar to those found in Chapter 2, which suggests that the synthetic dataset built was realistic and the gap filling method using data duplication in a small proportion of the times did not have obvious apparent consequences. As a result, it is believed that the results of this study are representative of those expected on the data collected between 2013 and 2015.

The first striking result is that the uncertainties are much lower using stratified sampling rather than random sampling. In other words, the first recommendation to obtain robust water quality rating curves is to obtain stratified concentrations in the calibration sample pool. The second striking result is that it is likely that even the robust, i.e., precise, calibrations obtained with 100+ samples, as the bootstrapping results suggest, might be inaccurate. Calibration might be biased towards overestimation for parameters exhibiting dilution effects during storms (such as nitrate and TDN in this research), and biased towards underestimation for parameters that exhibit concentration effects during storms, such as DOC, TP, and TSS. The third striking result is that a potential major source of uncertainty is the extrapolation of concentration predictions beyond the calibration range, as the results of the PLSR-based vs. turbidity-based results suggest.

Now, within the guidelines described above, it is possible to make other complementary observations. The results suggest that for nitrate (or TDN mostly made of nitrate) that is known to absorb light in a narrow UV range, very small uncertainties can be expected, i.e., within $\pm 2\%$ for 52 stratified samples. However, in these reactive watersheds 12 stratified samples to calibrate the instrument would yield uncertainties on annual loads within $\pm 7\%$, which is not small, although three times less than uncertainty using standard monthly sampling.

For DOC, which is also known to generally absorb light but which correspond to a large array of molecules, the uncertainty increase from -1% to $+9\%$ or a 10 percentage point spread, compared to a 6 percentage point spread for nitrate for 24 samples for calibration. It

is believed that the +4% bias corresponds to the systematic underestimation of the reference load, while it is believed that stratified sampling induces less bias.

For other parameters, such as TKN and TP, which are not known to absorb light and for which it is hypothesized that there is a co-variability of light absorbing constituents with concentrations to derive water quality rating curves, the uncertainties can be much higher than for nitrate and DOC. For these two, stratified sampling was unable to be tested from the sample pool which was obtained. Nonetheless, the uncertainties for 52 calibration points (randomly sampled) could yield uncertainties within a 30 to 40 percentage points, which is not too different from the equivalent 40 and 50 percentage points uncertainties induced from weekly regular interval discrete sampling. It thus seems that although the robust water quality rating curves could not be established for all parameter, one should expect large uncertainties on the annual loads for TKN and TP unless the number of calibration points be much more than 52, and that their concentrations be stratified. As a result, water quality rating curves might not be used as a routine practice for standard monitoring stations, and might remain an efficient research tool. In Chapter 2, it has been shown that it might be possible to obtain water quality rating curves for ammonium and phosphate. The small calibration pool did not allow exploring uncertainties with these parameters, but it is fair to say that the conclusions for TKN and TP also apply for these parameters too.

It is noted that the level of uncertainties computed with the M5 and M6 methods correspond to highly reactive watersheds, where uncertainties tend to be higher (e.g., Birgand et al., 2010). It is thus possible that the level of uncertainties on annual loads for all

parameters and all subsampling techniques are on the higher range and that smaller uncertainties might be expected for less reactive watersheds.

Finally, it is believed that the bootstrap and other subsampling techniques should be routinely used to estimate the uncertainty on computed annual loads when using *in situ* field spectrophotometers.

3.5 Acknowledgements

The funding for this research was supported by the North Carolina Department of Transportation, grant number 2013-37.

3.6 References

- Birgand F., Appelboom, T. W., Chescheir, G. M., Skaggs, R. W. 2011b. Estimating nitrogen, phosphorus, and carbon fluxes in forested and mixed-use watersheds of the lower coastal plain of North Carolina: uncertainties associated with infrequent sampling. *Trans. ASABE*, 54(6): 2099-2110.
- Birgand F., Faucheux, C., Gruau, G., Augeard, B., Moatar, F., Bordenave, P. 2010. Uncertainties in assessing annual nitrate load and concentration indicators: Part 1. Impact of sampling frequency and load estimation algorithms. *Trans. ASABE*, 53(2): 437-446.
- Birgand F., Faucheux, C., Gruau, G., Moatar, F., Meybeck, M. 2011a. Uncertainties in assessing annual nitrate loads and concentration indicators: Part 2. Deriving sampling frequency charts in Brittany, France. *Trans. ASABE*, 54(1): 93-104.
- Birgand, F. 2000. Quantification and modeling of in-stream processes in agricultural canals of the lower coastal plain. In: Ph.D. Dissertation. North Carolina State University, Raleigh, NC.

- Birgand, F., Aveni-Deforge, K., Smith, B., Maxwell, B., Horstman, M., Gerling, A. B., Carey, C. C. 2016. First report of a novel multiplexer pumping system coupled to a water quality probe to collect high temporal frequency *in situ* water chemistry measurements at multiple sites. *Limnol. Oceanogr. Methods*. doi:10.1002/lom3.10122.
- Birgand, F., Lellouche, G., Appelboom, T.W. 2013. Measuring flow in non-ideal conditions for short-term projects: Uncertainties associated with the use of stage-discharge rating curves. *J. Hydrol.*, 50(3): 186-195.
- Blaen, P. J., Khamis, K. Lloyd, C. E. M., Bradley, C., Hannah, D., Krause, S. 2016. Real-time monitoring of nutrients and dissolved organic matter in rivers: Capturing event dynamics, technological opportunities and future directions. *Science of The Total Environment*, 569–570: 647-660.
- Bowes, M. J., Jarvie, H. P., Halliday, S. J., Skeffington, R. A., Wade, A. J., Loewenthal, M., Gozzard, E., Newman, J. R., Palmer-Felgate, E. J. 2015. Characterising phosphorus and nitrate inputs to a rural river using high-frequency concentration–flow relationships. *Science of the Total Environment*, 511: 608-620.
- Cassidy, R. and Jordan, P. 2011. Limitations of instantaneous water quality sampling in surface-water catchments: comparison with near-continuous phosphorus time-series data. *J Hydrol*, 405:18-193.
- Crumpton, W. G., Isenhardt, T. M., Mitchell, P. D. 1992. Nitrate and organic N analyses with second-derivative spectroscopy. *Limnol. Oceanogr.*, 37: 907-913.
- Eaton, A. D., Clesceri, L. S., Greensberg, A. E. 1995. Standard methods for the examination of water and wastewater, 19th ed. American Public Health Association.
- Etheridge, J. R., 2013. Quantifying the water quality benefits of a constructed brackish marsh and tidal stream system using continuous water quality and flow monitoring. In: Ph.D. Dissertation. North Carolina State University, Raleigh, NC.

- Etheridge, J. R., Birgand, F., Burchell, M. R. 2015. Quantifying nutrient and suspended solids fluxes in a constructed tidal marsh following rainfall: The value of capturing the rapid changes in flow and concentrations. *Ecological Engineering*, 78: 41-52.
- Etheridge, J. R., Birgand, F., Osborne, J. A., Osburn, C. L., Burchell, M. R., Irving, J. 2014. Using *in situ* ultraviolet–visual spectroscopy to measure nitrogen, carbon, phosphorus, and suspended solids concentrations at a high frequency in a brackish tidal marsh. *Limnol. Oceanogr. Methods*, 12: 10-22.
- Fichot, C. G. and Benner, R. 2011. A novel method to estimate DOC concentrations from CDOM absorption coefficients in coastal waters. *Geophys. Res. Lett.* 38: L03610 doi:10.1029/2010GL046152.
- Finch, M. S., Hydes, D. J., Clayson, C. H., Weigl, B., Dakin, J., Gwilliam, P. 1998. A low power ultra violet spectrophotometer for measurement of nitrate in seawater: introduction, calibration and initial sea trials. *Anal. Chim. Acta.* 377: 167-177.
- Flemming, H.-C. 2011. Microbial biofouling: Unsolved problems, insufficient approaches, and possible solutions. In: H.C. Flemming, J. Wingender, and U. Szewzyk, editors, *Biofilm highlights*. Springer, New York. 81–109.
- Gippel, G. J. 1995. Potential of turbidity monitoring for measuring the transport of suspended solids in streams. *Hydrol Process.*, 9: 83-97.
- Glasgow, H. B., Burkholder, J. M., Reed, R. E., Lewitus, A. J., Kleinman, J. E. 2004. Real-time remote monitoring of water quality: a review of current applications, and advancements in sensor, telemetry, and computing technologies. *J Exp Mar Biol Ecol.*, 200: 409-448.
- Grayson, R. P. and Holder, J. 2016. Improved automation of dissolved organic carbon sampling for organic-rich surface waters. *Science of the Total Environment*, 543: 44-51.

- Greenberg, A. E., Clesceri, L. S., Eaton, A. D. 2005. Standard methods for the examination of water and wastewater, 25th ed. American Public Health Association; American Water Works Association; Water Environment Federation. American Public Health Association, Washington, D.C.
- Halliday, S. J., Skeffington, R. A., Wade, A. J., Bowes, M. J., Gozzard, E., Newman, J. R., Loewenthal, M., Palmer-Felgate, E. J., Jarvie, J. P. 2015. High-frequency water quality monitoring in an urban catchment: hydrochemical dynamics, primary production and implications for the Water Framework Directive. *Hydrological Process*, 29: 3388-3407.
- ISO 15769. 2010. Hydrometry - Guidelines for the application of acoustic velocity meters using the Doppler and echo correlation methods.
- Johnes, P. J. 2007. Uncertainties in annual riverine phosphorus load estimation: Impact of load estimation methodology, sampling frequency, baseflow index and catchment population density. *Journal of Hydrology*, 332: 241-258.
- Langergraber, G., Fleischmann, N., Hofstädter, F. 2003. A multivariate calibration procedure for UV/VIS spectrometric quantification of organic matter and nitrate in wastewater. *Water Sci. Technol.*, 47(2): 63-71.
- Lepot, M., Torres, A., Hofer, T., Caradot, N., Gruber, G., Aubin, J.-B., Bertrand-Krajewski, J.-L. 2016. Calibration of UV/Vis spectrophotometers: A review and comparison of different methods to estimate TSS and total and dissolved COD concentrations in sewers, WWTPs and rivers. *Water Research*, 101:519-534.
- Mevik, B., Wehrens, R., Liland, K. H. 2015. pls: Partial least squares and principal component regression. R package 2.4-3. <http://CRAN.R-project.org/package=pls>.
- Moatar, F. and Meybeck, M. 2007. Riverine fluxes of pollutants: Towards predictions of uncertainties by flux duration indicators. *Comptes Rendu Geosci.*, 339(6): 367-382.

- Moatar, F., and Meybeck, M. 2005. Compared performances of different algorithms for estimating annual nutrient loads discharged by the eutrophic River Loire. *Hydrol. Proc.*, 19: 429-444.
- Morlock, S. E., Nguyen, H. T., Ross, J. H. 2002. Feasibility of Acoustic Doppler Velocity Meters for the Production of Discharge Records from US Geological Survey Streamflow-Gaging Stations. US Geological Survey. Water-Resources Investigations Report 01-4157.
- Olsen, K. K. 2008. Multiple wavelength ultraviolet determinations of nitrate concentration, method comparisons from the Preakness Brook monitoring project, October 2005 to October 2006. *Water Air Soil Poll.* 187: 195-202.
- Phillips, J. M., Webb, B. W., Walling, D. E., Leeks, G. J. L. 1999. Estimating the suspended sediment loads of rivers in the LOIS study area using infrequent samples. *Hydrol. Proc.*, 13: 1035-1050.
- R Core Team. 2016. R: A language and environment for Statistical Computing. <http://www.R-project.org>.
- Ramos, T. B., Gonçalves, M. C., Branco, M. A., Brito, D., Rodrigues, S., Sánchez-Pérez, J.-M., Sauvage, S., Prazeres, Â., Martins, J. C., Fernandes, M. L., Pires, F. P. 2015, Sediment and nutrient dynamics during storm events in the Enxoé temporary river, southern Portugal. *Catena*, 127: 177-190.
- Rice, E. W., Baird, R. B., Eaton, A. D., Clesceri, L. S. 1997. Standard methods for the examination of water and wastewater: 2540 Solids, 22nd ed. American Public Health Association; American Water Works Association; Water Environment Federation. American Public Health Association, Washington, D.C.
- Rice, E. W., Baird, R. B., Eaton, A. D., Clesceri, L. S. 2012. Standard methods for the examination of water and wastewater, 22nd ed. American Public Health Association; American Water Works Association; Water Environment Federation. American Public Health Association, Washington, D.C.

- Rieger, L., Langergraber, G., Siegrist, H. 2006. Uncertainties of spectral *in situ* measurements in wastewater using different calibration approaches. *Water Sci. Technol.*, 53: 187-198.
- Rochelle-Newall, E. and Fisher, T. 2002. Chromophoric dissolved organic matter and dissolved organic carbon in Chesapeake Bay. *Mar. Chem.*, 77: 23-41.
- Rode, M., Angelstein, S. H. N., Anis, M. R., Borchardt, D., Weitere, M. 2016 Continuous instream assimilatory nitrate uptake from high frequency sensor measurements, *Environ. Sci. Technol.*, 50: 5685–5694.
- Saraceno, J. F., Pellerin, B. A., Downing, B. D., Boss, E., Bachand, P. A., Bergamaschi, B. A. 2009. High-frequency *in situ* optical measurements during a storm event: Assessing relationships between dissolved organic matter, sediment concentrations, and hydrologic processes. *J. Geophys. Res.* 114: G00F09, doi:10.1029/2009JG000989.
- Skarbøvik, E. and Roseth, R. 2015. Use of sensor data for turbidity, pH and conductivity as an alternative to conventional water quality monitoring in four Norwegian case studies. *Acta Agriculturae Scandinavica, Section B- Soil & Plant Science*, 65(1): 63-73.
- Suzuki, N. and Kuroda, R. 1987. Direct simultaneous determination of nitrate and nitrite by ultraviolet second-derivative spectrophotometry. *Analyst* 112:1077-1079.
- Torres, A. and Bertrand-Krajewski, J.-L. 2008. Partial Least Squares local calibration of a UV–visible spectrometer used for *in situ* measurements of COD and TSS concentrations in urban drainage systems. *Water Sci. Technol.*, 57: 581-588.
- United States Geological Survey, "Explanations for the National Water Conditions", http://water.usgs.gov/nwc/explain_data.html
- Whelan, A., and Regan, F. 2006. Antifouling strategies for marine and riverine sensors. *J. Environ. Monit.*, 8: 880-886.

Chapter 4: High resolution hydrochemical dynamics to reveal biogeochemical processes in an agricultural coastal plain watershed

4.1 Introduction

It had been advocated in the first two chapters on the importance of capturing high frequency water quality data to reduce uncertainty on nutrient and material loads, as a necessary means to have chance to measure the water quality effects of a stream restoration. It had been proposed the concept of water quality rating curves to quantify important parameters of the N, P, C and material fluxes (Chapter 2) and estimated the uncertainties associated with the method (Chapter 3). The massive installation of continuous water quality sensors and their assessments (e.g., this study; Etheridge et al., 2015, Blanco et al., 2010; Bowes et al., 2015; Halliday et al., 2014; Pellerin et al., 2014) opens the possibility to study nutrient export dynamics at an unprecedented resolution and possibly unveil misunderstood processes within watersheds.

Because concentrations change dramatically, and a disproportionately high amount of material is exported in streams during and after rainfall events in a relatively short proportion of the time, it is essential to understand the water quality dynamics during events. The potential transport of nutrients to streams is determined by the availability and source of nutrients, the transport mechanisms, and the distance from the source to the monitoring stations (Bowes et al., 2015, 2009, and 2005).

Within the last 15 years, there has been an increasing number of articles in the literature that have explored the information about watershed and in-stream processes embedded in the

high-resolution water quality data, particularly during storm events (e.g., Bowes et al., 2009; Carey et al., 2014; House and Warwick, 1998; Kronvang et al., 1997; Lawler et al., 2006; Lloyd et al., 2016b; Ramos et al., 2015a, 2015b). From the early work, there seems to be two main concentration patterns. Concentrations tend to exhibit either a ‘dilution effect’ or a ‘concentration effect’, i.e., that chemographs exhibit ‘troughs’ and ‘peaks’ during flow peaks, respectively.

In addition to the two concentration patterns, there has been a particular interest in the hysteresis patterns of the C-Q relationship during events to estimate the origins of nutrients and the nutrient transport pathways in watersheds (e.g., Williams, 1989; Lefrançois et al., 2007; Butturini et al., 2008; Blanco et al., 2010; Cerro et al., 2014; Outram et al., 2014; Bieroza and Heathwaite, 2015; Bowes et al., 2015; Fovet et al., 2015; Lloyd et al., 2016b). Two main hysteresis patterns for C-Q relationship have been observed. First, a clockwise loop where the nutrient concentrations are higher in the rising limb than in the falling limb of the hydrograph. It indicates a rapid transport of nutrients from their sources to the monitoring station. Second, an anti-clockwise loop where the nutrient concentrations are lower in the rising limb than in the falling limb of the hydrograph. Nutrients are transported more slowly to the monitoring point (Bowes et al., 2015). To better quantify hysteresis, Lawler et al. (2006) and Lloyd et al. (2016a) have established hysteresis indices (HI) to evaluate the trajectory directions (‘dilution’ vs ‘concentration’ effects) and quantify magnitudes of hysteresis loops.

Most the studies reported patterns observed in upland watersheds where organic rich riparian zone soils intercept much of the surface and subsurface flow lines, and where surface runoff can play an important role in flow generation. Much of the ‘dilution effect’ observed for nitrate in agriculture-dominated watersheds is often attributed to dilution from surface runoff (Blanco et al., 2010; Bowes et al., 2015). However, dilution effects have been observed at the outlet of drains where surface runoff cannot explain nitrate concentration dilutions during events (Arlot, 1999). The concentration effect observed with dissolved organic carbon (DOC) and the clockwise loops can be explained in part by the overwhelming role played by the riparian zone (e.g., Thomas et al., 2016). Flat artificially drained watersheds of the coastal plain become particularly interesting because the majority of the flow is due to subsurface drainage and little surface runoff is expected, and water is carried in artificial open ditches in very shallow thalweg that have no riparian vegetation. In other words, the conditions are quite different from those in upland watersheds.

To obtain a bigger picture on the nutrient export trends over longer than event periods, it is hypothesized that cumulative loads are robust indicators to detect trends that the analyses at the event scale cannot reveal.

Objectives

The general objective of this research is to use high frequency flow, nitrate, and DOC water quality data to reveal soil and in-stream processes that might be particular to coastal plain watersheds. Thus, the first objective is to use cumulative load indicators to detect the seasonal trends in the generation and export of nitrate and DOC in these watersheds. The

second is to classify the relationships and use existing tools quantifying the hysteresis loops between nutrient concentrations ($\text{NO}_3\text{-N}$ and DOC) and discharge during storm events to reveal soil and in-stream processes in these watersheds. The third is to report peculiar patterns of water exchanges that might occur within the floodplain between the main river and secondary artificial streams.

4.2 Methods

Site description

In an effort to quantify the water quality benefits of a stream restoration (details in previous chapters), three monitoring stations were installed in the Claridge Canal at the Western edge of the floodplain of the Little River floodplain near Goldsboro, North Carolina (35.42° N, 78.02° W; Figure 4.1, details in Appendix A.1). The studied reach is equipped with three monitoring stations referred to as the Upstream Station (UP), the Middle Stream Station (MD, located 1,390 m from UP), and the Downstream Station (DN, located 807 m from MD).

Nearly 60% of the total drainage area at the downstream station (573 ha) is agriculture, about 15% is in forest/shrubs, 10% is suburban areas, 7% are wetlands, and less than 3% are impervious surfaces (Table 4.2). In the watershed, upstream of the UP station (subwatershed I – 236 ha; Figure 4.1), 60% of the area that corresponds to the flat floodplain area where artificial subsurface drainage dominates, is located closest to the monitoring station. About 40%, which corresponds to the plateau area elevated about 0.6 m above the floodplain, is

located furthest from the monitoring station. Over 80% of subwatershed II and III areas correspond to the floodplain and the plateau areas, respectively. Along the main stem of the Claridge canal, four main tributaries (labeled as A, B, C, and D) can be identified and the lengths are consigned in Table 4.1. Of particular interest, during very high flow events, tributary C connects the Claridge Canal to the Little River, resulting in water movement from the river to the canal.

The majority of the area is covered with sandy soils (USDA, 2009; Table 4.2), although four hydraulic soil groups are present. Group A: soils (less than 10% clay, and more than 90% sand; loamy sand; sandy loam) have low runoff potential and high infiltration rates when thoroughly wetted. Group B: soils (10%~ 20% clay, and 50%~ 90% sand; silt loam, silt) have moderately low runoff and moderate infiltration rates when thoroughly wetted. Group C: soils (20%~ 40% clay, and less than 50% sand; sandy clay loam; clay loam) have moderately high runoff potential and low filtration rates when thoroughly wetted. Group D: soils (greater than 40% clay, and less than 50% sand; silty clay loam; silty clay) have high runoff potential when thoroughly wetted and have high shrink-swell potential. Table 4.2 shows that the majority of the area corresponds to Group A (112.31 ha, 19.6%) and Group B (362.14 ha, 63.2%) at DN, suggesting a high potential for infiltration during rainfall events.

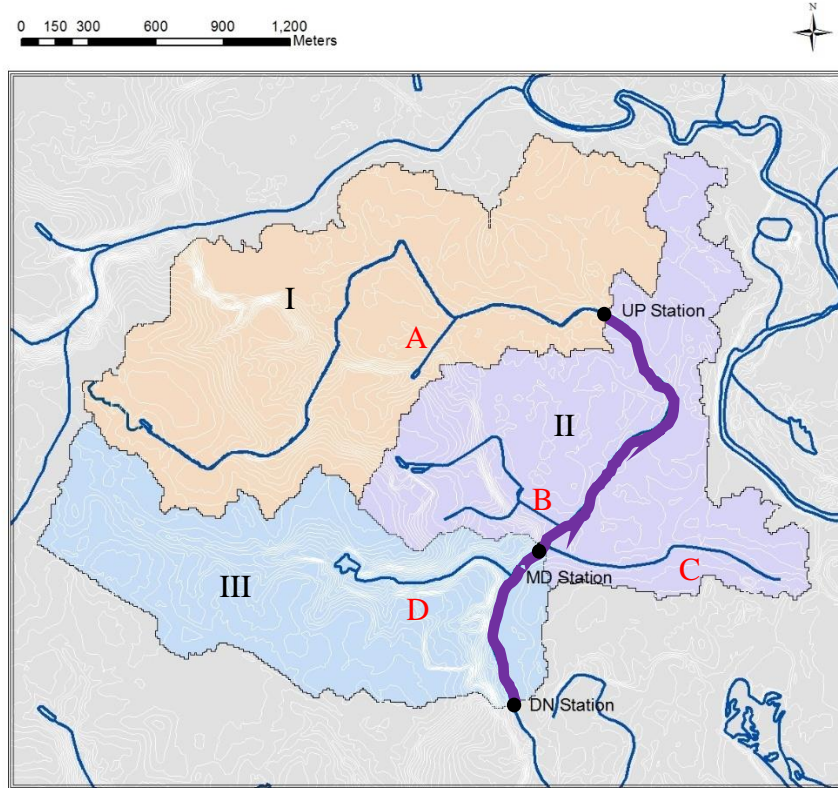


Figure 4.1

Three monitoring stations along the Clairidge Canal in Goldsboro, North Carolina (I: Contributing watershed area for UP station; I and II: Contributing watershed area for MD station; I, II, and III: Contributing watershed area for DN station)

Table 4.1

The length of tributaries in the Clairidge Canal

Tributary	Total length of tributary (m)
A	399
B	1783.32
C	1149.21
D	1119.23

(Note: Data from Wayne County, NC website (<http://www.waynegov.com/235/GIS-Data-Download>).

Table 4.2**Vegetation cover, land use, and soil properties in the studied watersheds**

Station	UP		MD		DN	
Watershed area (ha)	236		414		573	
	Percentage of area (%)	Area (ha)	Percentage of area (%)	Area (ha)	Percentage of area (%)	Area (ha)
Classification of vegetation cover and land use						
Cultivated crops and hay	56.98	134.47	57.28	237.12	57.32	328.45
Forest	12.05	28.43	16.00	66.25	13.67	78.34
Shrub or scrub	2.43	5.73	1.38	5.73	1.00	5.73
Wetland	10.57	24.94	8.28	34.28	6.70	38.40
Developed land	4.66	11.00	4.53	18.75	9.56	54.78
Impervious area	0.78	1.84	0.99	4.10	2.54	14.55
Others	12.54	29.59	11.54	47.78	9.21	52.75
Hydrologic soil classification						
Group A	23.4	55.22	17.9	74.11	19.6	112.31
Group B	56.6	133.58	67.5	279.45	63.2	362.14
Group C	12.5	29.50	10.2	42.23	10.7	61.31
Group D	7.34	17.32	4.18	17.31	6.16	35.30

(Note: Data from USGS website http://streamstatsags.cr.usgs.gov/v3_beta/viewer.htm?stabbr=NC).

Flow measurement

Because the coastal plain streams are low gradient, there tends to be variable control downstream conditions. As a result, stage measurements alone are insufficient to evaluate discharge (Birgand et al., 2013). To solve this problem, Doppler velocity meters (SonTek IQ

Doppler meter, San Diego, CA, USA) were installed in wooden trapezoidal flumes at the three monitoring stations and measured the stage and velocity every 15 minutes in the stream. The discharge or flow rate (Q) was calculated as the product of cross-sectional average velocity (V) and cross-sectional area (A) (Equation 1). The cross-sectional area (A) was calculated with stage and the known dimensions of the trapezoidal flume.

$$Q = V \times A \quad (\text{Equation 1})$$

The cross-sectional average velocity (V) was calculated with the application of the index velocity rating method (Morlock et al., 2002; Birgand et al., 2005; ISO 15769, 2010; details in Chapter 2)

Water samples collections and measurements

Water quality was collected from December 2013 to March 2015 at the three monitoring stations. A UV-Vis spectrophotometer (spectro::lyser model, s::can) was installed which collected light absorbance and water quality data every 15 minutes. To limit biological and chemical fouling, the instrument was removed from the water and used an Arduino controlled pumping system to pump and purge stream water to and from the instrument. The optics were consecutively rinsed with tap waters (details in Chapter 2). An automatic discrete sampler (ISCO 6712) took samples every 12 hours at 12 am and 12 pm at each station. During each biweekly field-servicing visit, hydrology and water quality data were downloaded, the optics of the instruments carefully scrubbed and cleaned with HCl (details in Chapter 2).

Laboratory analysis

During each field visit, the discrete water samples were stored on ice, filtered at 0.22 μm for dissolved parameters, and delivered to the laboratory for analysis. The selections of the discrete samples for laboratory analysis depended on the initial water quality results from UV-Vis spectrophotometer and the flow events (e.g., the samples were selected when the water quality changed quickly during the rainfall events).

The discrete water samples were analyzed for $\text{NO}_3\text{-N}$ (The Cadmium Reduction Method, [Eaton et al., 1995]) and DOC (Standard Method 5310 B, [Greenberg et al., 2005]). $\text{NO}_3\text{-N}$, and DOC were analyzed at the Environmental and Agricultural Testing Service at North Carolina State University. The discrete sample results were applied to correlate the UV-Vis absorbance spectra data; then, ultimately applied to predict continuous $\text{NO}_3\text{-N}$ and DOC data 15 minutes with the PLSR calibration (details in Chapter 2).

Cumulative loads, annual and seasonal flow-weighted concentration calculations

Double-mass curves have been used for decades in hydrology to detect land use or treatment effects in watersheds (e.g., Searcy and Hardison, 1960). Double-mass curves traditionally consist in plotting cumulative flow volumes for two watersheds against one another for a period of record. If something has affected the behavior of one of the watersheds, then the slope of this curve will change. Several authors have proposed to apply the same principle by plotting cumulative loads as a function of cumulative volume within the same watershed (e.g., Arlot, 1999; Brown et al., 2013). Over seasonal or annual scales,

these authors have observed that three behaviors seem to exist that correspond to specific processes.

For a particular watershed, a generally linear curve, i.e., that the exports increase over several consecutive events at a constant trend with flow volume, suggests that the source of the nutrient or material is essentially infinite compared to the leaching/transport mechanisms in the watershed and/or that the export processes remain unchanged. Gradual downward or asymptotic inflections in the curves, suggest that the source of nutrient or material is limited compared to the leaching/transport mechanisms and that, over time, it takes more water to export the same amount of nutrients or material. Sudden upward/downward inflections in the curves, suggest however, that either the sources have suddenly, i.e., over few mm of cumulative flow volume, become more/less abundant, and/or that the export processes suddenly changed. The slope of the linear trends over apparently homogeneous phases corresponds to the flow-weighted average concentration values.

For analysis, the flow-weighted average concentrations were calculated over the entire period of record. It was visually identified homogeneous periods over which the double-mass curves exhibited the patterns described above and over each period. Then, flow-weighted concentrations were compared to the overall trend to detect seasonal trends. Most of the analysis will focus on the UP station, because of its relative homogeneity, and because there are known potential nutrient point sources contributing to MD (hog lagoon) and to DN (sweet potatoes and watermelon processing plant random discharges).

The general method to calculate the cumulative load (L) is to integrate instantaneous loads as the product of solute concentration (C(t)) and discharge (Q(t)) over a certain time (t) (Equation 2). With high frequency data, a very close estimate is the summation over 15-min interval measurements, of instantaneous loads, calculated from 15-min concentrations (C_i) and flow rate (Q_i) data (Equation 3), where K is the unit adjustment factor and N is the number of 15-min intervals in t.

$$L = \int_0^t C(t)Q(t)dt \quad (\text{Equation 2})$$

$$L \approx K \sum_{i=1}^{i=N} C_i Q_i \quad (\text{Equation 3})$$

Hysteresis index (HI) calculation for concentration and flow rate and statistical analysis

To quantify and evaluate the nutrient concentration-discharge (C-Q) relationship during storm events, this research applied the hysteresis index (HI) method established by Lloyd et al. (2016a) and Lawler et al. (2006) to estimate the event scale dynamics and replace them within seasonal variations at the three stations.

The hysteresis index (HI) was calculated with the following procedures for each storm event (Lloyd et al., 2016a):

First, the observed nutrient concentration (C_i) and flow rate (Q_i) at timestep *i* with 15-min measurements were normalized by the maximum concentration (C_{max}) and minimum concentration (C_{min}); and maximum flow rate (Q_{max}) and minimum flow rate (Q_{min}), respectively (Equation 4 and Equation 5).

$$C_{i,normalized} = \frac{C_i - C_{min}}{C_{max} - C_{min}} \quad (\text{Equation 4})$$

$$Q_{i,normalized} = \frac{Q_i - Q_{min}}{Q_{max} - Q_{min}} \quad (\text{Equation 5})$$

As shown in Figure 4.2, the normalized flow rate was separated into several sections with the 5 % increase of normalized flow rate (e.g., $Q_{5\%}$, $Q_{10\%}$... $Q_{90\%}$, $Q_{95\%}$). The 5% increase for normalized flow rate was suggested by Lloyd et al., (2016a) to obtain robust hysteresis index results for most storms with different sizes and shapes. Then, this research evaluated the calculated concentrations with linear interpolation between two observed points for the rising limb ($C_{j,RL}$) and the falling limb ($C_{j,FL}$) corresponding to each normalized flow rate. The hysteresis index (HI_j) for each normalized flow rate with an increase of 5% interval was calculated using Equation 6.

$$HI_j = C_{j,RL} - C_{j,FL} \quad (\text{Equation 6})$$

At last, the final hysteresis index (HI) that represented the storm was calculated by averaging all HI_j related to each normalized flow rate. The HI ranges between -1 and 1, where the positive value represents clockwise direction; the negative value represents anti-clockwise direction. In addition, the HI value represents the magnitude of difference for normalized concentrations corresponding to the rising and falling limbs.

In addition to HI, a slope indicator was calculated, of the ‘dilution’ and ‘concentration’ effects using Equation 7 to Equation 9. C_s and C_b are the nutrient concentrations at the peak discharge and base flow, respectively. C_{max} and C_{min} represent the highest and lowest concentrations observed during the event. The slope by subtracting normalized C_b from

normalized C_s was calculated (Equation 9). The slope indicator ranges between -1 and 1. The positive values refer to a concentration effect, and the negative values refer to a dilution effect. The magnitude of slope indicates the amount of difference between normalized C_b and normalized C_s during the storm event.

$$C_{s,normalized} = \frac{C_s - C_{min}}{C_{max} - C_{min}} \quad (\text{Equation 7})$$

$$C_{b,normalized} = \frac{C_b - C_{min}}{C_{max} - C_{min}} \quad (\text{Equation 8})$$

$$Slope = C_{s,normalized} - C_{b,normalized} \quad (\text{Equation 9})$$

It has been verified that the HI final results follow a normal distribution using the Shapiro-Wilk Normality Test at the $p=0.05$ level. As a result, analysis of variance (ANOVA) was applied to compare the differences of HI values and evaluate the seasonal and spatial effects in the Claridge Canal. In addition, when the ANOVA results indicated a significant difference, Tukey's honest significance test was applied to detect the difference among the groups.

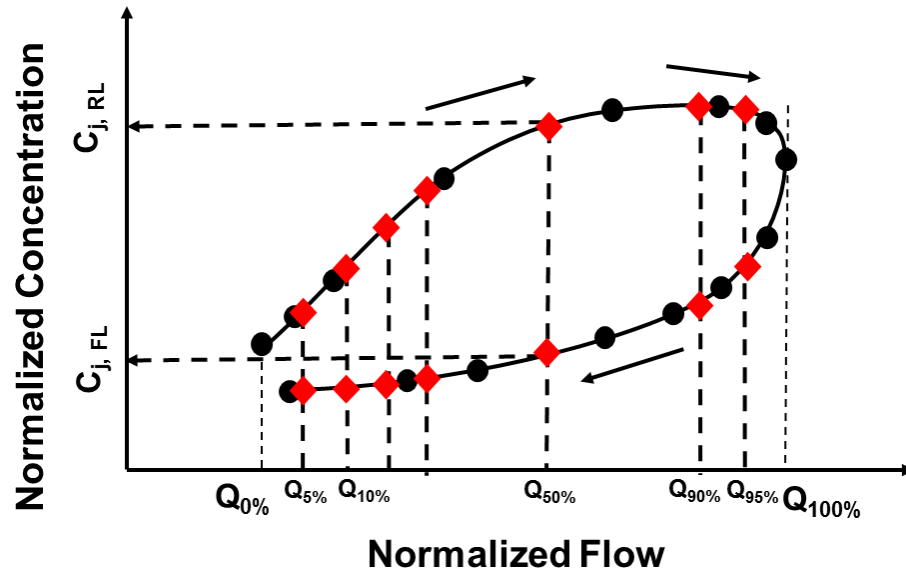


Figure 4.2

Example of the C vs Q relationship during an event (not to scale) to demonstrate the calculation for hysteresis index for a clockwise loop (Black circle: The normalized observed concentrations $[C_i, normalized]$ as a function of normalized flow rate $[Q_i, normalized]$, red diamond: the calculated concentrations with the linear interpolation between two observed points for the rising limb $[C_j, RL]$ and the falling limb $[C_j, FL]$)

4.3 Results and Discussion

Typical coastal plain concentration and load levels

At all stations, nitrate concentrations were typical and similar to the first or second order agricultural watersheds of the coastal plain (e.g., Birgand et al., 2010), with most concentrations (70%) between 2.8 and 3.5 mg/L (Chapter 2) and an annual load between 12 and 15 kg N/ha/yr. The computed $\text{NO}_3\text{-N}$ cumulative loads were 19.60 kg/ha (15.4 kg/ha/yr),

15.57 kg/ha (12.3 kg/ha/yr), and 16.53 kg/ha (13.0 kg/ha/yr) at UP, MD and DN, respectively (Figure 4.3).

Most DOC concentrations ranged between 3.5 and 7 mg/L in baseflow condition (Chapter 2). The DOC cumulative loads were 38.4 (30.2 kg/ha/yr), 59.0 (46.4 kg/ha/yr), and 58.3 kg/ha (45.9 kg/ha/yr) at UP, MD and DN, respectively (Figure 4.4). The DOC annual load at UP is very close to the 28 kg/ha/yr previously reported in the lower coastal plain (Birgand, 2000). However, the loads at MD and DN are surprisingly 50% higher, suggesting that a major source of DOC existed between UP and MD (further discussion below).

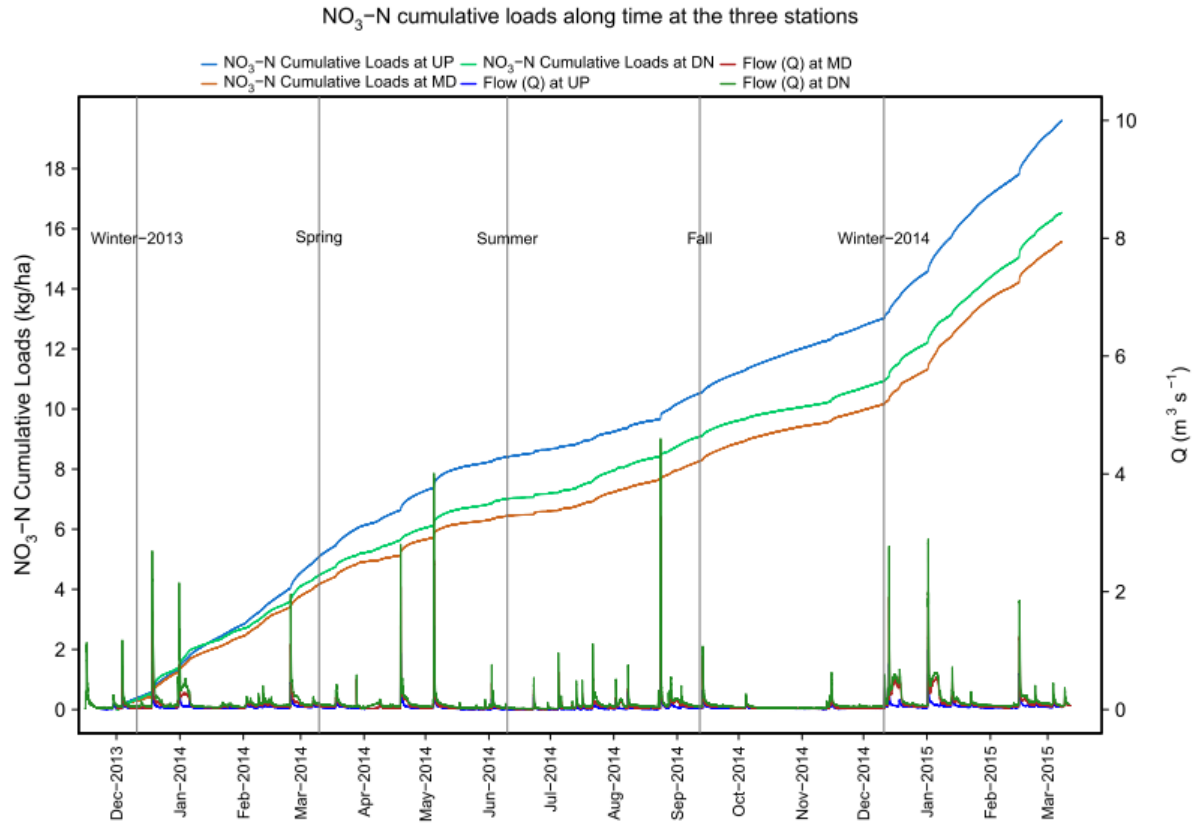


Figure 4.3

NO₃-N Cumulative loads (kg/ha) over entire monitoring period (2013-12-12 to 2015-03-18) at all stations in the Claridge Canal

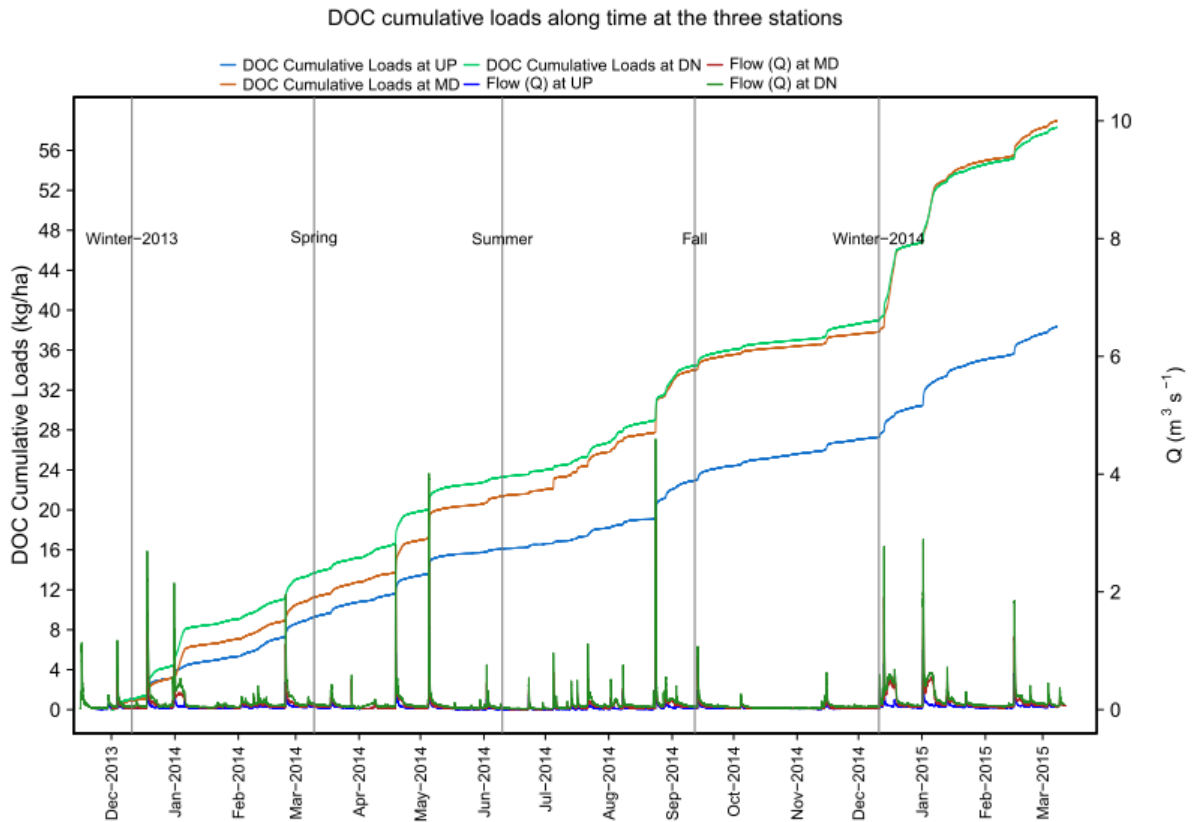


Figure 4.4

DOC Cumulative loads (kg/ha) over entire monitoring period (2013-12-12 to 2015-03-18) at all stations in the Claridge Canal

General dilution and concentration effects during storm events in the Claridge Canal

Regardless of the seasons and of the storm intensity, the $\text{NO}_3\text{-N}$ concentrations exhibited a clear ‘dilution effect’, while the DOC exhibited a clear ‘concentration effect’ at UP (Figure 4.5 and Figure 4.6).

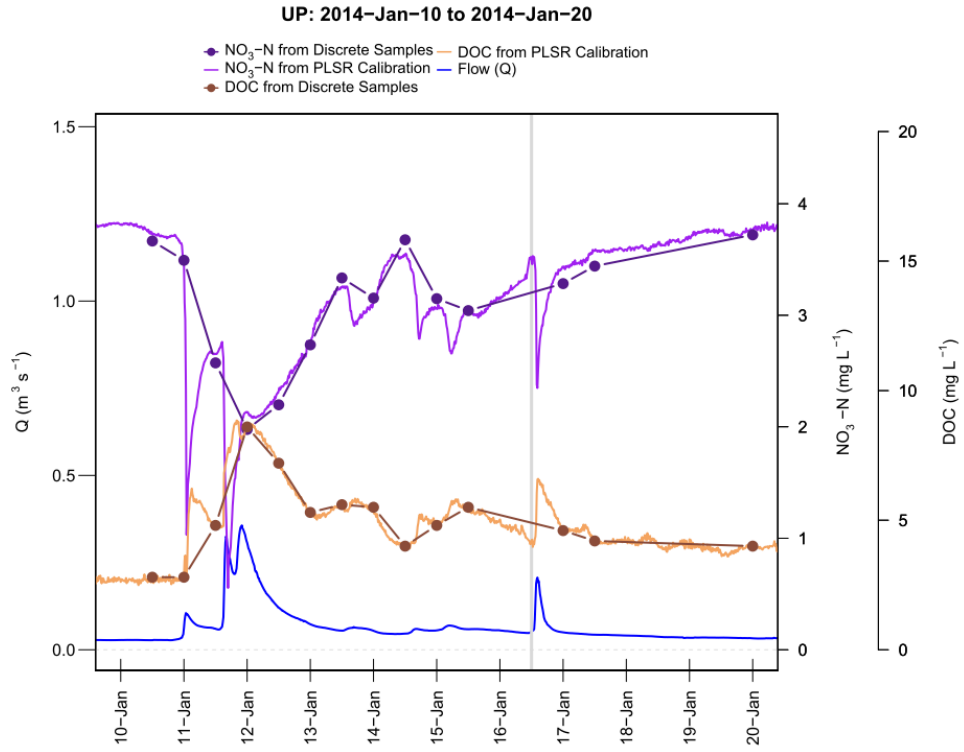


Figure 4.5

Continuous and discrete NO₃-N and DOC with flow rate from January 10 to January 20 at UP in winter 2014

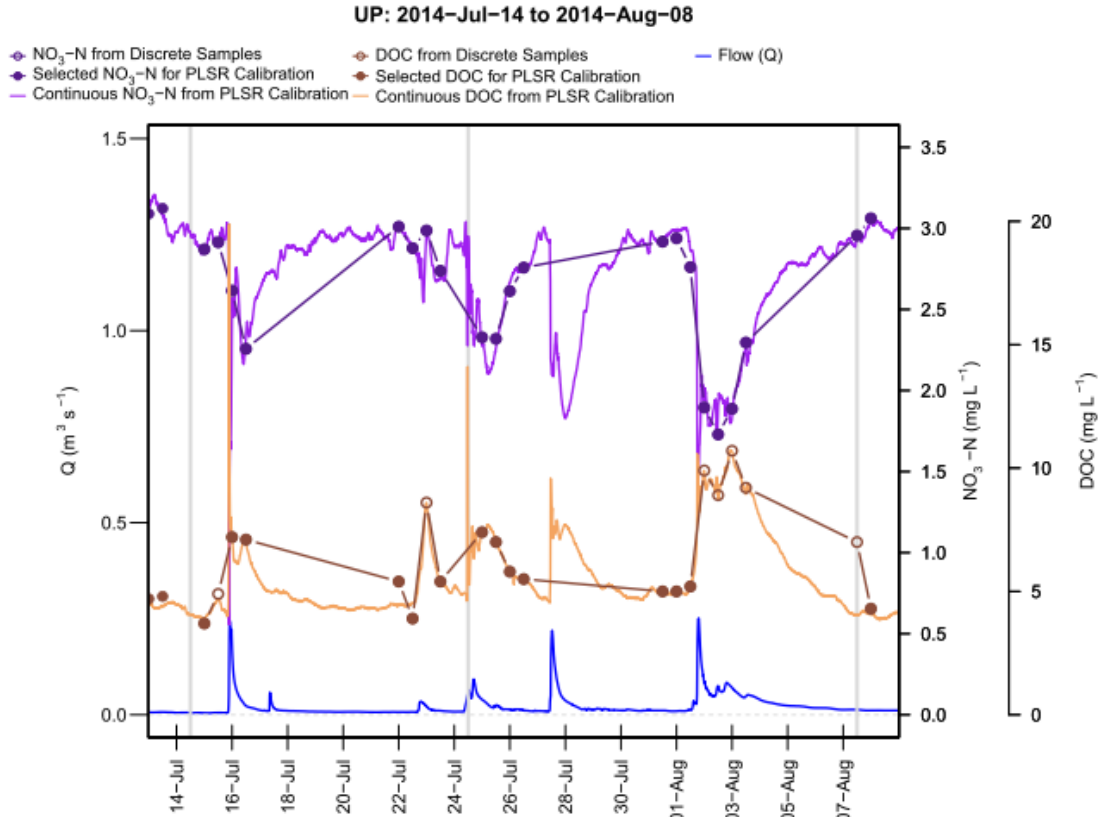


Figure 4.6

Continuous and discrete NO₃-N and DOC with flow rate from July 14 to August 08 at UP in summer 2014

During the low flow summer period, the DOC chemograph exhibited a peculiar 2-3 concentration peak pattern. At the onset of each event, there was a very short-lived DOC concentration peak, followed by one or two saw tooth concentration trough/peak (particularly obvious on the July 28 event in Figure 4.6). At the same time, the nitrate chemograph exhibited a mirror image chemograph with an obvious and deeper last concentration trough (particularly obvious on the July 28 event in Figure 4.6). The last concentration saw tooth DOC peak was always in synchrony with the last nitrate trough. The last DOC/nitrate

peak/troughs occurred 4-8 hours after the flow peak, suggesting a longer travel time from a rather homogeneous area.

It is hypothesized that this may correspond to the spatial dichotomy between the plateau vs the floodplain area of subwatershed I. Water from the intensely farmed artificially drained area in the floodplain arrives at UP earlier and is generally more concentrated than the water from the less intensely farmed land on the plateau that has on average twice the distance to travel to UP. The splitting of the chemographs does not appear during winter, probably because the differences in concentrations may be small, and if they still exist, the water from the floodplain mixing from that of the plateau likely blurs the differences.

The initial short-lived summer DOC peaks (less than one hour) occurred during the rising limb of the hydrographs. These likely correspond to DOC-rich (2-3 times the baseflow concentration, due to in-stream sediment diagenetic processes) and nitrate-poor (sediment denitrification/and or plant uptake) stream water present in the channel storage exchange zones prior to rainfall events, that was 'pushed' by the arrival of new water generated by the rain (Birgand, 2000; Ramos et al., 2015a, 2015b).

While the time lag between the concentration nitrate troughs and DOC peaks in summer can be attributed to the spatial distance for water to reach the UP station, the nitrate troughs in winter appear to be in very close synchrony with the flow peaks. At the same time, the DOC peaks continue to lag behind the flow peaks, suggesting two different spatial locations for the generation of nitrate-poor and DOC-rich waters during events. The causes for the consistent nitrate troughs and DOC peaks and the differences in lags cannot be explained by

the classical surface runoff dilution hypothesis and riparian zone interception in these watersheds. The results from the hysteresis analysis shed more light on the possible processes at play.

Hysteresis index analyses confirm differences in lags between flow and concentration peaks and troughs

As suggested by Bowes et al. (2015), a storm event was selected when flow increased over than 40%. There were 51 storm events observed during the entire monitoring period, and the HI values with the trajectory directions for NO₃-N and DOC in different seasons at the three stations were summarized in Table 4.3. Some continuous concentration data were not applicable due to the failure of monitoring equipment, so there are several missing HI values. The number of available rainfall events are 37, 29, and 38 at UP, MD, and DN, respectively. To compare the seasonal effects for the concentrations-flow rate relationship during the storm events, all available HI results were used in Table 4.3 and analyzed with ANOVA.

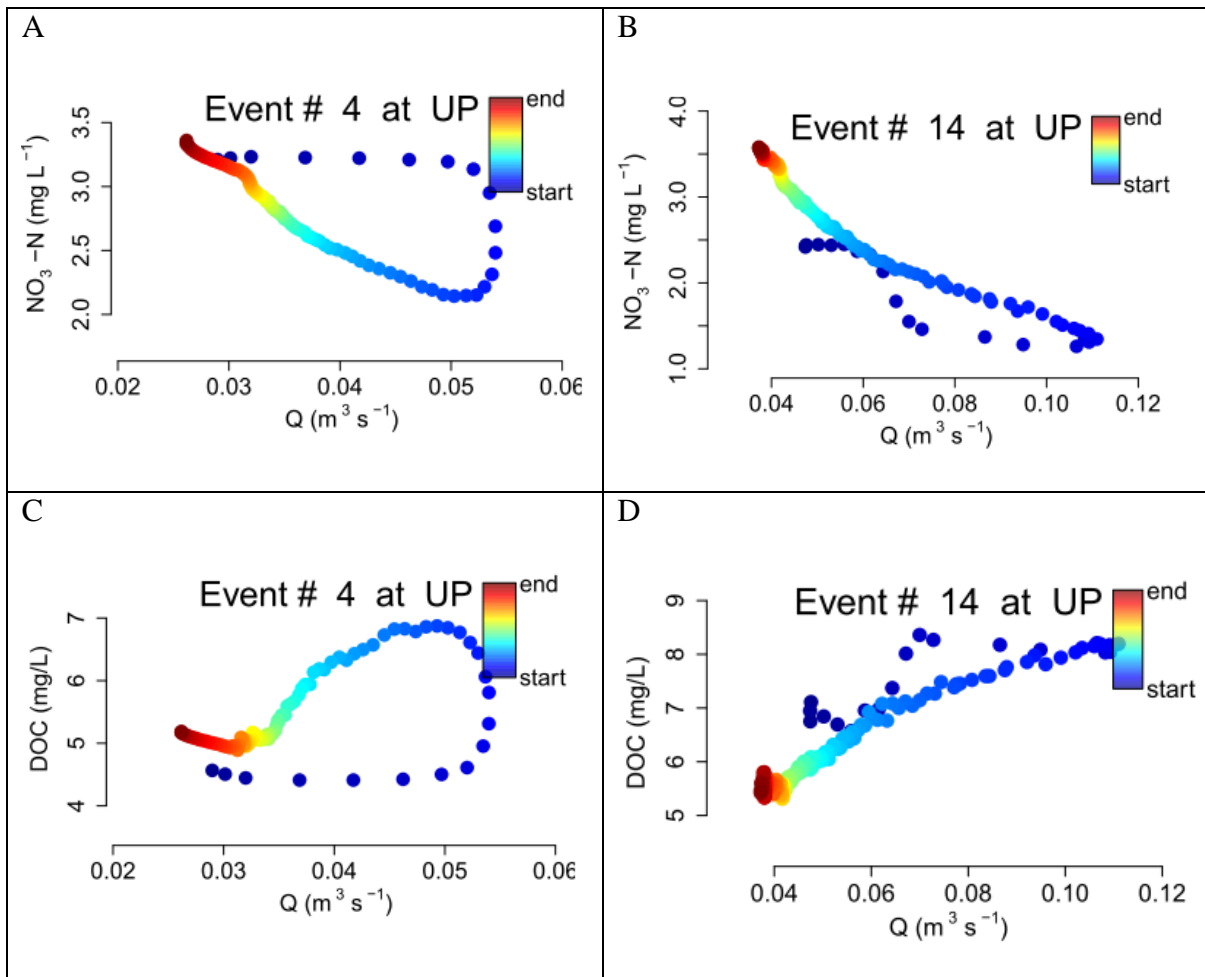


Figure 4.7

Hysteresis patterns observed for nitrate (A and B) and DOC (C and D) showing clockwise (A and D) and anticlockwise patterns (B and C) for events #4 (2013-12-17) and #14 (2014-02-25) at the UP station

Typical hysteresis patterns observed are illustrated in Figure 4.7. Event #4 that occurred in late December 2013 shows the classical patterns of clockwise and dilution effect for nitrate and anticlockwise and concentration effect for DOC. Robust HI and slope indicators can be calculated from these. However, in many events where saw tooth concentration patterns were

represented by the HI indicator chosen. As a result, HI values for nitrate and DOC do not show any particular trend in summer (Figure 4.8). However, the HI values calculated for winter and spring show significant differences for nitrate and DOC (p -value < 0.05) at UP. The HI values for DOC are negative and their absolute values higher than those of nitrate. The average negative HI values for DOC, corresponding to anticlockwise pattern suggest that the DOC peaks generally lag behind the flow peaks in winter, suggesting that water generating the rising limb and the peak is less concentrated than the falling limb. The positive average HI value for nitrate in winter suggests that water generating the rising limb of the hydrograph is very diluted in nitrate. In winter, the absolute HI values for nitrate are significantly lower than those of DOC ($p = 0.00029$). This suggests that the processes leading to the nitrate dilution effect and those for the DOC concentration effects are not the same (further discussion below).

Table 4.3

Summary of Hysteresis Indices and trajectory directions (C: Clockwise, AC: Anti-Clockwise) for observed storm events for NO₃-N and DOC in the Claridge Canal (NA: concentration data not applicable; the storm with bold font and star symbol is used for estimating the spatial effects)

Storm number	Peak Date	Season	UP				MD				DN			
			NO ₃ -N		DOC		NO ₃ -N		DOC		NO ₃ -N		DOC	
			HI	Trajectory	HI	Trajectory	HI	Trajectory	HI	Trajectory	HI	Trajectory	HI	Trajectory
1	2013-12-10	Winter	NA		NA		NA		NA		-0.339	AC	-0.220	AC
2	2013-12-14	Winter	NA		NA		NA		NA		-0.242	AC	-0.272	AC
3	2013-12-16	Winter	NA		NA		NA		NA		-0.514	AC	0.639	C
4	2013-12-17	Winter	0.576	C	-0.684	AC	0.655	C	-0.163	AC	0.107	C	0.015	C
5	2013-12-24	Winter	0.036	C	-0.237	AC	NA		NA		-0.149	AC	-0.362	AC
6	2013-12-29	Winter	NA		NA		NA				NA		NA	
7	2014-01-11	Winter	0.437	C	-0.584	AC	0.139	C	0.360	C	-0.020	AC	-0.262	AC
8	2014-01-11	Winter	-0.271	AC	-0.161	AC	0.455	C	-0.129	AC	0.139	C	-0.544	AC
9	2014-01-16	Winter	0.327	C	-0.641	AC	-0.147	AC	0.231	C	NA		NA	
10	2014-02-13	Winter	-0.040	AC	-0.173	AC	NA		NA		NA		NA	
11	2014-02-15	Winter	0.160	C	-0.301	AC	NA		NA		-0.118	AC	-0.463	AC
12	2014-02-19	Winter	-0.044	AC	-0.377	AC	NA		NA		-0.329	AC	-0.367	AC
13	2014-02-21	Winter	NA		NA		NA		NA		-0.080	AC	-0.363	AC
14	2014-02-25	Winter	-0.147	AC	0.152	C	-0.003	AC	0.146	C	0.315	C	-0.079	AC
15	2014-03-07	Winter	-0.040	AC	-0.255	AC	0.154	C	-0.208	AC	-0.318	AC	-0.137	AC

Table 4.3 Continued

Storm number	Peak Date	Season	UP				MD				DN			
			NO ₃ -N		DOC		NO ₃ -N		DOC		NO ₃ -N		DOC	
			HI	Trajectory	HI	Trajectory	HI	Trajectory	HI	Trajectory	HI	Trajectory	HI	Trajectory
16	2014-03-18	Winter	NA		NA		0.110	C	-0.344	AC	-0.246	AC	-0.284	AC
17	2014-03-29	Spring	0.144	C	-0.200	AC	0.546	C	-0.510	AC	0.613	C	-0.551	AC
18	2014-04-19	Spring	0.276	C	-0.243	AC	NA		NA		-0.406	AC	0.423	C
19	2014-04-29	Spring	0.007	C	0.199	C	0.437	C	-0.589	AC	0.197	C	-0.041	AC
20	2014-04-30	Spring	0.090	C	-0.108	AC	-0.032	AC	0.163	C	0.081	C	-0.024	AC
21	2014-05-16	Spring	0.135	C	-0.219	AC	0.583	C	0.378	C	0.055	C	-0.505	AC
22	2014-06-13	Spring	0.426	C	0.122	C	-0.549	AC	0.703	C	-0.103	AC	-0.337	AC
23	2014-06-13	Spring	-0.029	AC	0.160	C	-0.381	AC	-0.041	AC	0.314	C	0.041	C
24	2014-07-03	Summer	-0.029	AC	0.064	C	NA		NA		NA		NA	
25	2014-07-10	Summer	-0.502	AC	-0.248	AC	-0.268	AC	0.248	C	-0.045	AC	-0.129	AC
26	2014-07-15	Summer	-0.383	AC	0.370	C	0.005	C	-0.338	AC	-0.352	AC	0.057	C
27	2014-07-17	Summer	-0.048	AC	0.055	C	-0.397	AC	0.387	C	0.288	C	-0.172	AC
28	2014-07-22	Summer	-0.114	AC	-0.471	AC	0.008	C	0.027	C	0.707	C	-0.785	AC
29	2014-07-24	Summer	0.338	C	-0.083	AC	-0.068	AC	0.220	C	0.019	C	-0.186	AC
30	2014-07-27	Summer	0.112	C	0.177	C	0.177	C	0.151	C	0.352	C	-0.196	AC
31	2014-08-10	Summer	-0.112	AC	0.027	C	0.232	C	0.232	C	0.001	C	-0.366	AC
32	2014-08-12	Summer	0.069	C	0.086	C	-0.033	AC	0.325	C	0.002	C	-0.182	AC
33	2014-08-18	Summer	0.095	C	-0.055	AC	0.042	C	-0.446	AC	0.040	C	-0.504	AC
34	2014-09-02	Summer	-0.061	AC	-0.169	AC	NA		NA		NA		NA	

Table 4.3 Continued

Storm number	Peak Date	Season	UP				MD				DN			
			NO ₃ -N		DOC		NO ₃ -N		DOC		NO ₃ -N		DOC	
			HI	Trajectory	HI	Trajectory	HI	Trajectory	HI	Trajectory	HI	Trajectory	HI	Trajectory
35	2014-09-03	Summer	-0.147	AC	0.091	C	NA		NA		NA		NA	
36	2014-09-08	Summer	0.149	C	0.158	C	0.368	C	-0.083	AC	0.300	C	-0.299	AC
37	2014-09-14	Summer	0.561	C	-0.482	AC	-0.041	AC	0.083	C	NA		NA	
38	2014-09-24	Fall	-0.202	AC	0.004	C	NA		NA		-0.172	AC	-0.606	AC
39	2014-10-15	Fall	NA		NA		-0.033	AC	-0.581	AC	-0.084	AC	-0.430	AC
40	2014-11-24	Fall	NA		NA		NA		NA		-0.359	AC	0.244	C
41	2014-11-25	Fall	NA		NA		NA		NA		-0.302	AC	-0.148	AC
42	2014-11-26	Fall	NA		NA		-0.101	AC	0.046	C	0.048	C	-0.347	AC
43	2014-12-22	Winter	0.090	C	-0.389	AC	NA		NA		0.013	C	-0.488	AC
44	2014-12-24	Winter	-0.190	AC	-0.419	AC	NA		NA		0.058	C	-0.410	AC
45	2014-12-29	Winter	NA		NA		NA		NA		NA		NA	
46	2015-01-12	Winter	-0.057	AC	-0.265	AC	NA		NA		NA		NA	
47	2015-01-24	Winter	0.025	C	-0.068	AC	NA		NA		NA		NA	
48	2015-02-02	Winter	NA		NA		NA		NA		NA		NA	
49	2015-02-26	Winter	NA		NA		0.688	C	0.037	C	NA		NA	
50	2015-03-05	Winter	NA		NA		0.144	C	-0.149	AC	NA		NA	
51	2015-03-14	Winter	0.245	C	-0.290	AC	0.110	C	-0.421	AC	0.063	C	-0.468	AC

Proposed mechanisms to explain event scale concentration patterns

The systematic nitrate dilution pattern slightly out of phase with the DOC concentration pattern cannot be explained by surface runoff alone, which would not explain the DOC concentration effect, or the leaching of the nonexistent riparian zone. A possible unifying explanation for the observed patterns may be associated with the unique hydrological functioning of these flat artificially drained systems.

As stated in Dobbs (2017): “Drainage hydraulics and numerical solutions of the Richard’s equation tell us that the shape of the water table, directly following rainfall is not elliptical, but tends to be deformed at the near stream zone, where the hydraulic gradient is steeper.” Therefore, a large portion of the flow volume is disproportioned which leaches through the near-ditch soil profile (Paris, 2004; deformed water table illustrated as time 2 in Figure 4.9).

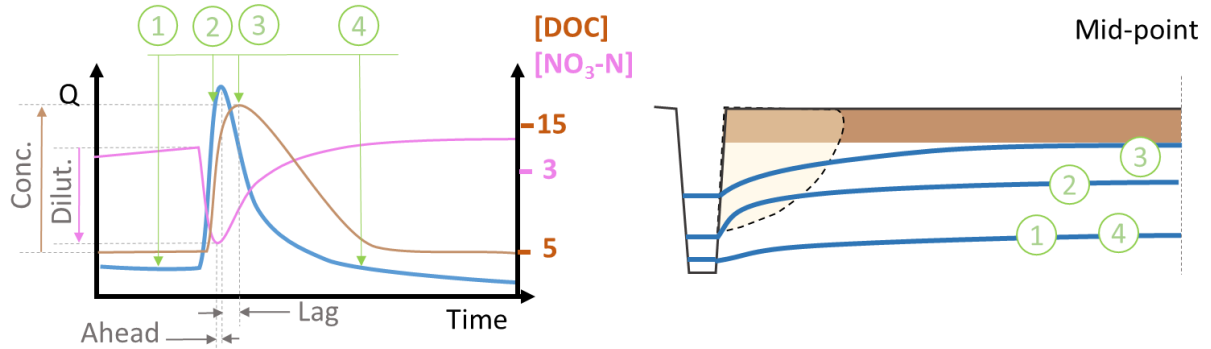


Figure 4.9

Hypothetical hydraulic and nutrient export functioning in the artificially drained soils of the coastal plain during an event (Left: nitrate: pink line; DOC: brown line; flow: blue line. Right: water table: dark blue lines; organic horizon of soil: brown; near stream zone: beige. Number in green circles represent the change of the water table in order during a storm event)

Dobbs (2017) also addressed that: “This zone of the soil, because of the water table drawn down near the ditch, tends to be relatively drier than the rest of the soil profile, and undergoes more organic matter mineralization. This zone being drier and being more leached, in relative terms, with higher volumes than the rest of the soil profile, is expected to contain over time less leachable material, including DOC and NO₃-N.”

This hypothesis implies that before an event, when the water table is below the organically rich soil horizon, the nitrate concentrations are at 3-4 mg/L in the soil and in the stream, resulting from the N-enriched soils associated with fertilizing crops (Figure 4.9, time 1).

At the onset of an event, as the water table rises in the soil, its shape is no longer elliptical and is deformed and the rising limb of the hydrograph corresponds to water that has

disproportionally leached this area (Figure 4.9, time 2). The combined short residence time of water in this near stream zone and the relatively nutrient poor for reasons invoked above, explain nitrate trough at this time. The DOC concentrations increase as water leaching through the near stream zone has the potential to entrain DOC at concentrations higher than the pre-event groundwater concentration. The exact timing of the beginning of the nitrate concentrations decreasing determines the clockwise vs anticlockwise pattern (Figure 4.9; 'ahead' vs 'lag'). The relative low absolute values (most between 0 to 0.2) of the HI for nitrate in winter, and switch between positive and negative values supports the hypothesis.

The increasing DOC concentrations in the rising limb of the hydrograph and beyond the flow peak, implies that this water has resided in an organically rich area of the soil, enough to lead to higher than baseflow DOC concentrations. It is hypothesized that this corresponds to the rise of the water table within the organic horizon of the soil (Figure 4.9; time 3), and flow lines become horizontal increasing chances for water to leach DOC. The arrival of this water is delayed compared to the one leaching the near stream zone, explaining the lag between the DOC and flow peaks.

As water table drops, water leaches a less organic soil horizon, which explains the falling limb of the DOC chemograph towards time 4 in Figure 4.9. The slow rise of the nitrate concentrations suggests that the nitrogen mineralization/nitrification process in the soil that nourish the elevated baseflow nitrate concentrations are slower than the DOC leaching capacity.

Previous authors have reported clockwise patterns with dilution effects (e.g., Borah et al., 2003; Kato et al., 2009) and have indicated nitrate was dominantly transported by surface runoff during storm events and mobilized rapidly in the stream (Butturini et al., 2006; Blanco et al., 2010; Bowes et al., 2015; Lloyd et al., 2016b). These conclusions do not seem to apply well to the coastal plain watershed conditions. The low HI absolute values found even when positive (clockwise pattern) suggest small hysteresis pattern in the watershed.

The same and other authors, have concluded in their conditions that the anti-clockwise pattern with dilution effects during events generally corresponded to when nitrate was mainly exported from the groundwater and subsurface runoff, resulting in a delay mechanism in falling limb (Blanco et al., 2010; Cerro et al., 2014; Lloyd et al., 2016b; Outram et al., 2014). The subsurface source and delivery of DOC have been also documented in anticlockwise patterns (Cerro et al., 2014; Lambert et al., 2013; Morel et al., 2009; Ramos et al., 2015b).

Odd DOC concentration and load patterns at the MD reveal exchanges with the Little River

The 50% increase in the DOC load at the MD compared to the UP is intriguing. Several times during the monitoring period, ‘humps’ in the hydrograph were observed, i.e., a secondary low and long flow peak following the more classical short and high peak. It was discovered that during high flow events, the Little River could connect to the Claridge Canal through a ditch (tributary C in Figure 4.1) temporarily bringing large extra flow through the MD station. Because of the large difference in watershed size, the time to peak in the Little River is 20 hours to several days delayed compared to the Claridge canal.

Figure 4.10 and Figure 4.11 illustrated the storm events during August 11 to August 22, 2014, at UP and DN. There was the notable discharge hump at DN but not at UP. The discharge hump was accompanied with a nitrate trough and a large DOC peak. It is believed the combined large flow volumes containing high DOC concentrations are the reasons for the large DOC loads at MD and DN compared to those at UP.

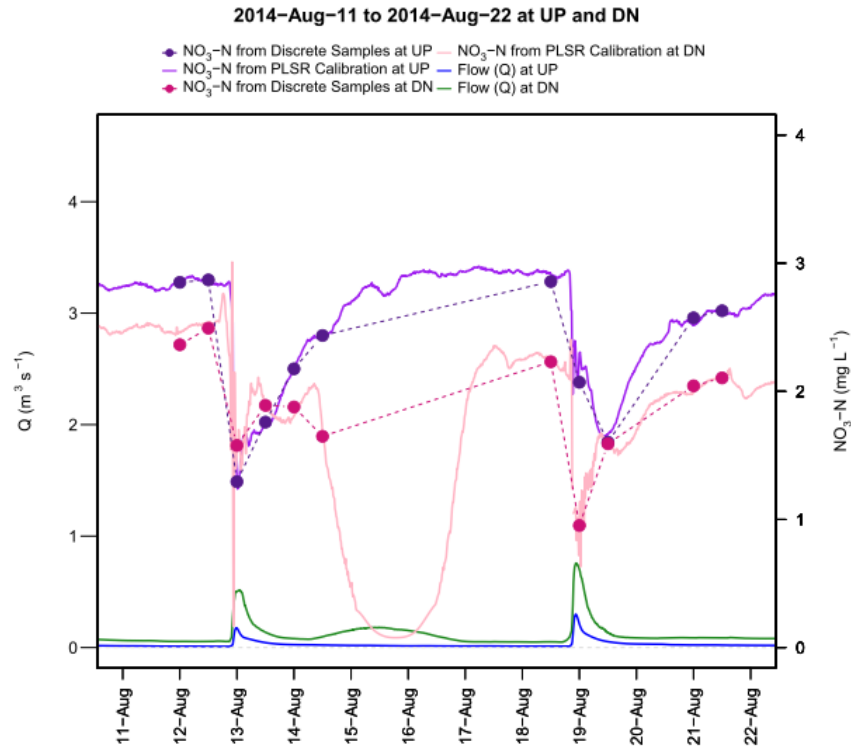


Figure 4.10

Continuous and discrete of $\text{NO}_3\text{-N}$ with flow rate from August 11 to August 22 in 2014 at UP and DN

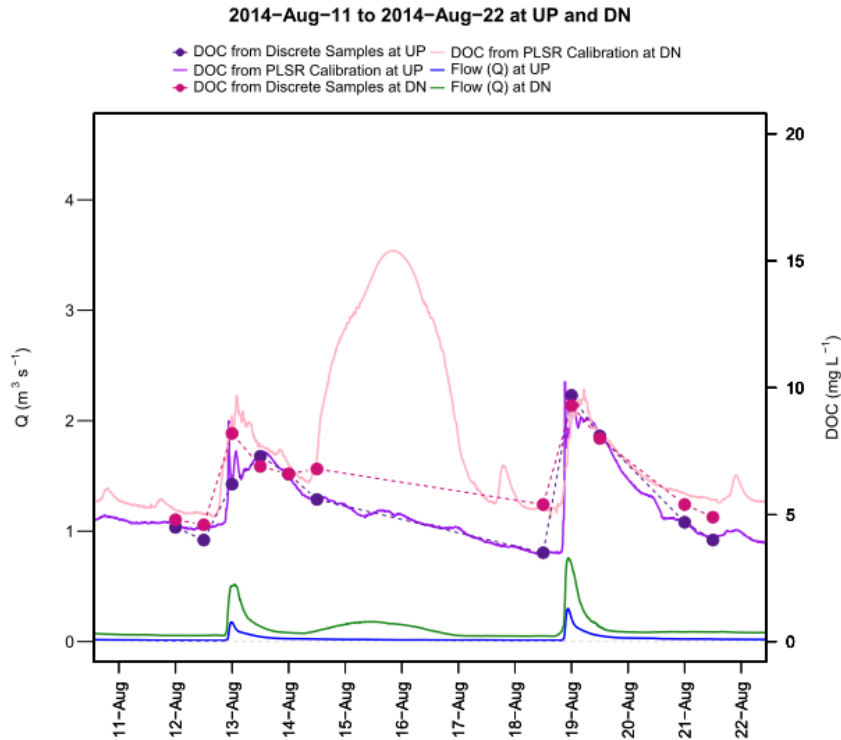


Figure 4.11

Continuous and discrete of DOC with flow rate from August 11 to August 22 in 2014 at UP and DN

Double-mass curves reveal season scale dynamics drivers for NO₃-N and DOC exports

The double-mass curves, i.e., cumulative loads as a function of cumulative volumes, for NO₃-N and DOC at UP station are illustrated in Figure 4.12. The entire monitoring period was separated into five homogeneous main phases based on the transitions of slopes, which were visually identified (Figure 4.12). Within each phase, the double-mass curves ‘undulate’ because of the concentration and dilution effects described earlier during multiple storms, but undulate around a steady trend. Each phase corresponds to a visually clearly identifiable trend.

Phase 1 was defined between winter and early spring (0 ~ 220 mm); Phase 2 between early spring and late summer (220 ~ 344 mm); Phase 3 between late summer and early fall (344 ~ 406 mm); Phase 4 between early fall and early winter (406 ~ 538 mm); and Phase 5 after early winter (538 ~ 674 mm).

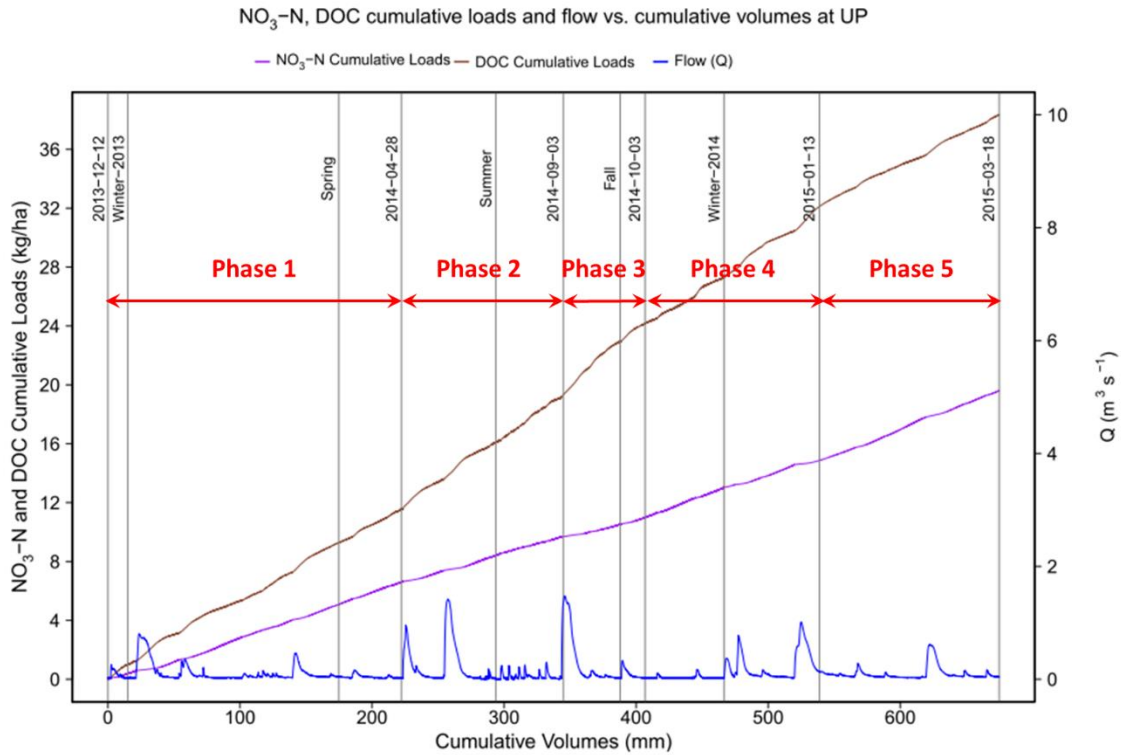


Figure 4.12

Cumulative loads (kg/ha) of NO₃-N and DOC as a function of cumulative flow volumes over entire monitoring period (2013-12-12 to 2015-03-18) with 5 phases at UP station (The vertical lines labeled as season represented the beginning date of the certain season.)

The flow-weighted concentrations of NO₃-N and DOC for five phases and overall monitoring period were calculated and reported in Table 4.4. For each phase, the differences of the flow-weighted concentrations from the overall trend were calculated. Figure 4.13 illustrates the percentage difference of each phase compared to the overall monitoring period.

Table 4.4
Flow-weighted concentrations of NO₃-N and DOC (mg/L) for different phases during entire monitoring period (2013-12-12 to 2015-03-18) at UP station

	Overall	Phase 1	Phase 2	Phase 3	Phase 4	Phase 5
NO₃-N	2.90	2.97	2.52	2.11	2.93	3.48
DOC	5.68	5.19	6.35	7.81	6.02	4.58

Compared to the overall flow-weighted concentration in the entire monitoring period, the flow-weighted concentration for nitrate decreased from Phase 1 to Phase 3, and increased from Phase 3 to Phase 5 (Figure 4.13). The factors possibly affecting the amount of nutrient export in the stream include the interactions of rainfall, vegetation cover, soil characteristics and land use (Blanco et al., 2010). Furthermore, the different temporal behaviors of dissolved nitrogen dynamics were likely affected by soil nitrogen condition, storm/rainfall features, runoff properties, and antecedent moisture (Webb and Walling, 1985) and groundwater effects (Blanco et al., 2010).

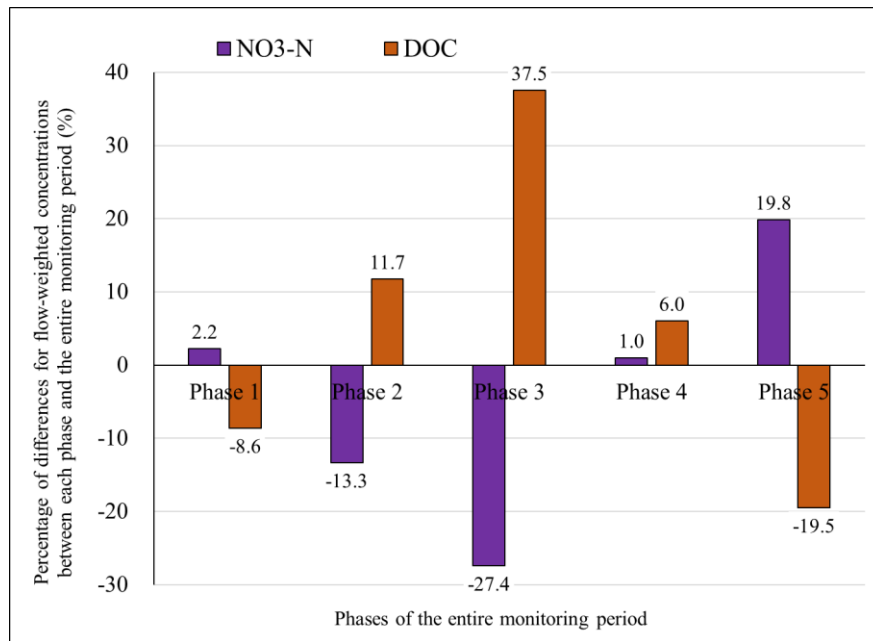


Figure 4.13

Percentage of differences for flow-weighted concentrations between each phase and the entire monitoring period (2013-12-12 to 2015-03-18) for NO₃-N and DOC at UP station (0% represents there is no difference for flow-weighted concentration between each phase and the entire monitoring period)

The decreasing of the flow-weighted concentrations for nitrate in Phase 2 and Phase 3 could be explained by crop and in-stream algae/macrophytes uptake, and soil/sediment denitrification from early spring to summer. In addition, drier soil condition, low water table and less groundwater contribution could explain lower nitrate export from the watershed into the stream during summer in Phase 3. These seasonal patterns for the variations of nitrate dynamics were observed by Blanco et al. (2010) in a coastal agricultural watershed as well.

The large relative increase of DOC concentrations during Phase 3 suggests that the main source of DOC at this time of the year cannot be the soils (low water table) and has to be the

sediment diagenetic processes (Birgand, 2000; Ramos et al., 2015b; Aubert et al., 2013). The very short-lived DOC peaks at the beginning of the summer events lead to the same conclusion. This also suggests that in-stream retention of nitrate during summer played an important role (Birgand, 2000; Ramos et al., 2015b).

After the dry conditions in summer, rewetting of the soil during the fall events started a new upward trend in nitrate concentrations. This trend was further reinforced in Phase 5, where the flow-weighted concentrations were the highest, probably due to the high water table level in the soils which make for more efficient nitrate leaching mechanisms and likely increased the rate of nitrification and mineralization of organic nitrogen (Outram et al., 2014).

Compared to $\text{NO}_3\text{-N}$, DOC had opposite pattern that the flow-weighted concentrations increased from Phase 1 to Phase 3, and decreased from Phase 3 to Phase 5 (Figure 4.13). The increasing of the flow-weighted concentrations for DOC in Phase 2 and Phase 3 could be attributed to the microbial activities degrading organic matter in the soil profile (Lambert et al., 2013) and sediment diagenetic mechanisms, both of which were favored by increased temperatures.

Diminishing temperatures and relatively dry soil profiles in the fall could explain, the declining of the microbial activities generating DOC in the soil in the watershed, and the declining DOC concentrations in Phase 4 and Phase 5 during fall and winter in the stream. The previous research (Kalbitz et al., 2000; Stedmon et al., 2006; Tipping et al., 1999) also reported that DOC concentrations varied seasonally and were lower in winter than summer.

From what has been discussed above, DOC concentrations differed in temporal scale were affected by the alterations in DOC sources including DOC reservoirs and water flow paths (Hood et al., 2006; Inamdar et al., 2006; Lambert et al., 2013; McGlynn and McDonnell, 2003; Pacific et al., 2010; Sanderman et al., 2009); as a result, a decrease of DOC concentrations was observed in wet season (fall and winter) in the Claridge Canal.

4.4 Conclusions

In this research, nitrate and DOC were measured on a continuous basis with the application of UV-Vis spectrophotometers to capture the nutrient dynamics in an agricultural coastal plain stream. During the entire monitoring period, the continuous hydro-chemo graphs indicated it had dilution effects for nitrate in most of storm events and concentration effects for DOC for all the storm events in the Claridge Canal. The factors affected nitrate and DOC transport during the rainfall events include soil hydraulic properties of the catchment (e.g., soil moisture, the availability of nitrate and DOC in soil profiles, the level of the water table), surface flow, subsurface flow, land type (Bowes et al., 2015; Cerro et al., 2014; Ramos et al., 2015a, 2015b).

To quantify the relationship between nutrients concentrations and flow rate and analyze the sources of nutrients, this research calculated hysteresis index and classified the trajectory of concentrations and discharge during the storm events. Based on continuous chemographs and HI results, seasonal differences affected the nitrate and DOC dynamics. In summer, the spatial distance of nitrate and DOC sources caused the time lag between nitrate troughs and DOC peaks. In winter, nitrate troughs almost synchronized with flow peak; however, DOC

peaks continued a lag after flow peak during the rainfall events. Thus, the sources of nitrate and DOC were transported from different locations, and the significant difference for the absolute HI values between nitrate and DOC in winter supported the observation.

For nitrate, the hysteresis patterns were either clockwise or anti-clockwise at the three stations. Thus, it showed the availability of nitrate sources, the flow path of surface runoff and groundwater, leaching process tended to vary between each event in the Claridge Canal.

For DOC, most of HI values are negative confirmed by the anti-clockwise patterns. The sources of DOC came from terrestrial plants, litter, and organic matter in soil (Cerro et al., 2014; Ramos et al., 2015b; Stedmon et al., 2006; Thurman, 1985), and the flow path influenced the transport of DOC (Cerro et al., 2014; Lambert et al., 2013; Morel et al., 2009; Ramos et al., 2015b). During the rainfall events, less mobile DOC was transferred with delay of arrival in the stream caused the anti-clockwise hysteresis pattern in the Claridge Canal.

The cumulative loads and flow-weighted concentrations demonstrated seasonal variations affecting the export of nitrate and DOC. With a higher denitrification rate, crop uptake from nitrate, and increased of microbial activity in soil, the stream transported the least amount of nitrate but the highest amount of DOC during summer. However, the increase of leaching process for nitrate and the decreasing of microbial ability elevated nitrate transport and reduced DOC export during winter.

This suggested only high frequency monitoring could detect the sudden and subtle variations of nitrate and DOC in the flashy agricultural watershed, e.g., the Claridge Canal. With the continuous hydrology and water quality data, this research is able to provide

comprehensive methods to illustrate the stream solutes dynamics of seasonal and spatial effects.

4.5 Acknowledgements

The funding for this research was supported by the North Carolina Department of Transportation, grant number 2013-37.

4.6 References

- Arlot, M.P., 1999. Nitrate in water – drainage as actor, or drainage as witness? Learning experience from both a hydrology and hydraulic approach. Unpublished PhD diss. Paris, France University of Paris VI. (in French)
- Aubert, A. H., Gascuel-Oudou, C., Gruau, G., Akkal, N., Faucheux, M., Fauvel, Y., Grimaldi, C., Hamon, Y., Jaffrézic, A., Lecoq-Boutnik, M., Molénat, J., Petitjean, P., Ruiz, L., Merot, P. 2013. Solute transport dynamics in small, shallow groundwater-dominated agricultural catchments: insights from a high-frequency, multisolute 10 yr-long monitoring study. *Hydrology and Earth System Sciences*, 17(4): 1379–1391.
- Bieroza, M. Z. and Heathwaite, A. L. 2015. Seasonal variation in phosphorus concentration–discharge hysteresis inferred from high-frequency *in situ* monitoring. *Journal of Hydrology*, 524: 333–347.
- Birgand F., Faucheux, C., Gruau, G., Augeard, B., Moatar, F., Bordenave, P. 2010. Uncertainties in assessing annual nitrate load and concentration indicators: Part 1. Impact of sampling frequency and load estimation algorithms. *Trans. ASABE*, 53(2):437-446.

- Birgand, F. 2000. Quantification and modeling of in-stream processes in agricultural canals of the lower coastal plain. In: Ph.D. Dissertation. North Carolina State University, Raleigh, NC.
- Birgand, F., Benoist, J.-C., Novince, E., Gilliet, N., Saint-Cast, P., Le Saos, E. 2005. Guide d'application de la technique du Doppler continu pour une section calibrée en bois, *Ingénierie-EAT*, 41: 77-82.
- Birgand, F., Lellouche, G., Appelboom, T. W. 2013. Measuring flow in non-ideal conditions for short-term projects: Uncertainties associated with the use of stage-discharge rating curves. *Journal of Hydrology*, 503: 186–195.
- Blanco, A. C., Nadaoka, K., Yamamoto, T., Kinjo, K. 2010. Dynamic evolution of nutrient discharge under stormflow and baseflow conditions in a coastal agricultural watershed in Ishigaki Island, Okinawa, Japan. *Hydrological Processes*, 24(18): 2601–2616.
- Borah, D. K., Bera, M., Shaw, S. 2003. Water, sediment, nutrient, and pesticide measurements in an agricultural watershed in Illinois during storm events. *Transactions of the ASAE*, 46(3): 657–674.
- Bowes, M. J., House, W. A., Hodgkinson, R. A., Leach, D. V. 2005. Phosphorus-discharge hysteresis during storm events along a river catchment: The River Swale, UK. *Water Res.* 39: 751-762.
- Bowes, M. J., Jarvie, H. P., Halliday, S. J., Skeffington, R. A., Wade, A. J., Loewenthal, M., Gozzard, E., Newman, J. R., Palmer-Felgate, E. J. 2015. Characterising phosphorus and nitrate inputs to a rural river using high-frequency concentration–flow relationships. *Science of the Total Environment*, 511: 608-620.
- Bowes, M. J., Smith, J. T., Neal, C. 2009. The value of high-resolution nutrient monitoring: a case study of the River Frome, Dorset, UK. *J. Hydrol.*, 378: 82-96.

- Brown, R. A., Birgand, F., Hunt, W. F. 2013. Analysis of consecutive events for nutrient and sediment treatment in field-monitored bioretention cells. *Water, Air, & Soil Pollution*, 224(6). <https://doi.org/10.1007/s11270-013-1581-6>.
- Butturini, A., Alvarez, M., Bernal, S., Vazquez, E., Sabater, F. 2008. Diversity and temporal sequences of forms of DOC and NO₃-discharge responses in an intermittent stream: predictable or random succession? *J. Geophys. Res.*, 113: G03016.
- Butturini, A., Gallart, F., Latron, J., Vazquez, E., Sabater, F. 2006. Cross-site comparison of variability of DOC and nitrate C–Q hysteresis during the autumn–winter period in three Mediterranean headwater streams: a synthetic approach. *Biogeochemistry*, 77: 327-349.
- Carey, R. O., Wollheim, W. M., Mulukutla, G. K., Mineau, M. M. 2014. Characterizing storm-event nitrate fluxes in a fifth order suburbanizing watershed using *in situ* sensors. *Environmental Science & Technology*, 48(14), 7756–7765. <https://doi.org/10.1021/es500252j>
- Cerro, I., Sanchez-Perez, J. M., Ruiz-Romera, E., Antigüedad, I. 2014. Variability of particulate (SS, POC) and dissolved (DOC, NO₃) matter during storm events in the Alegria agricultural watershed: the importance of storm events in agricultural watersheds. *Hydrological Processes*, 28(5): 2855–2867.
- Dobbs, N. A., 2017. Hydrology and Water Quality Dynamics in Coastal Plain and Upland Watersheds with Loblolly Pine (*Pinus taeda*) and Switchgrass (*Panicum virgatum*) Intercropping in the southeastern United States. In: Ph.D. Dissertation. North Carolina State University, Raleigh, NC.
- Eaton, A. D., Clesceri, L. S., Greensberg, A. E. 1995. Standard methods for the examination of water and wastewater, 19th ed. American Public Health Association.

- Etheridge, J. R., 2013. Quantifying the water quality benefits of a constructed brackish marsh and tidal stream system using continuous water quality and flow monitoring. In: Ph.D. Dissertation. North Carolina State University, Raleigh, NC.
- Etheridge, J. R., Birgand, F., Burchell, M. R. 2015. Quantifying nutrient and suspended solids fluxes in a constructed tidal marsh following rainfall: The value of capturing the rapid changes in flow and concentrations. *Ecological Engineering*, 78: 41-52.
- Fovet, O., Ruiz, L., Hrachowitz, M., Fauchaux, M., Gascuel-Oudou, C. 2015. Hydrological hysteresis and its value for assessing process consistency in catchment conceptual models. *Hydrology and Earth System Sciences*, 19(1): 105–123.
- Greenberg, A. E., Clesceri, L. S., Eaton, A. D. 2005. Standard methods for the examination of water and wastewater, 25th ed. American Public Health Association; American Water Works Association; Water Environment Federation. American Public Health Association, Washington, D.C.
- Halliday, S. J., Skeffington, R. A., Bowes, M. J., Gozzard, E., Newman, J., Loewenthal, M., Palmer-Felgate, E. J., Jarvie, H. P., Wade, A. J. 2014. The water quality of the river Enborne, UK: observations from high-frequency monitoring in a rural, lowland river system. *Water*, 6(1): 150–180.
- Hood, E., Gooseff, M. N., Johnson, S. L. 2006. Changes in the character of stream water dissolved organic carbon during flushing in three small watersheds, Oregon. *Journal of Geophysical Research*, 111(G1). <https://doi.org/10.1029/2005JG000082>.
- House, W. A., and Warwick, M. S. 1998. Hysteresis of the solute concentration/discharge relationship in rivers during storms. *Water Research*, 32(8): 2279–2290.
- Inamdar, S. P., O’Leary, N., Mitchell, M. J., Riley, J. T. 2006. The impact of storm events on solute exports from a glaciated forested watershed in western New York, USA. *Hydrological Processes*, 20(16): 3423–3439.

ISO 15769. 2010. Hydrometry - Guidelines for the application of acoustic velocity meters using the Doppler and echo correlation methods.

Kalbitz, K., Solinger, S., Park, J. H., Michalzik, B., Matzner, E. 2000. Controls on the dynamics of dissolved organic matter in soils: A review. *Soil Science*, 165(4): 277–304.

Kato, T., Kuroda, H., Nakasone, H. 2009. Runoff characteristics of nutrients from an agricultural watershed with intensive livestock production. *Journal of Hydrology*, 368(1–4): 79–87.

Kronvang, B., Laubel, A., Grant, R. 1997. Suspended sediment and particulate phosphorus transport and delivery pathways in an Arable Catchment, Gelbæk Stream, Denmark. *Hydrological Processes*, 11(6): 627–642.

Lambert, T., Pierson-Wickmann, A.-C., Gruau, G., Jaffrezic, A., Petitjean, P., Thibault, J.-N., Jeanneau, L. 2013. Hydrologically driven seasonal changes in the sources and production mechanisms of dissolved organic carbon in a small lowland catchment. *Water Resources Research*, 49(9): 5792–5803.

Lawler, D. M., Petts, G. E., Foster, I. D. L., Harper, S. 2006. Turbidity dynamics during spring storm events in an urban headwater river system: The Upper Tame, West Midlands, UK. *Science of The Total Environment*, 360(1–3): 109–126.

Lefrançois, J., Grimaldi, C., Gascuel-Oudou, C., Gilliet, N. 2007. Suspended sediment and discharge relationships to identify bank degradation as a main sediment source on small agricultural catchments. *Hydrological Processes*, 21(21): 2923–2933.

Lloyd, C. E. M., Freer, J. E., Johns, P. J., Collins, A. L. 2016a. Technical Note: Testing an improved index for analysing storm discharge–concentration hysteresis. *Hydrology and Earth System Sciences*, 20(2): 625–632.

- Lloyd, C. E. M., Freer, J. E., Johnes, P. J., Collins, A. L. 2016b. Using hysteresis analysis of high-resolution water quality monitoring data, including uncertainty, to infer controls on nutrient and sediment transfer in catchments. *Science of The Total Environment*, 543: 388–404.
- McGlynn, B. L. and McDonnell, J. J. 2003. Role of discrete landscape units in controlling catchment dissolved organic carbon dynamics: catchment doc export. *Water Resources Research*, 39(4). <https://doi.org/10.1029/2002WR001525>.
- Morel, B., Durand, P., Jaffrezic, A., Gruau, G., Molenat, J. 2009. Sources of dissolved organic carbon during stormflow in a headwater agricultural catchment. *Hydrological Processes*, 23(20): 2888–2901.
- Morlock, S. E., Nguyen, H. T., Ross, J. H. 2002. Feasibility of acoustic doppler velocity meters for the production of discharge records from US Geological Survey Streamflow-Gaging Stations. US Geological Survey. *Water-Resources Investigations Report 01-4157*.
- Natural Resources Conservation Service, United States Department of Agriculture. 2009. *National Engineering Handbook Hydrology Chapter 7: Hydrologic soil groups*.
- Outram, F. N., Lloyd, C. E. M., Jonczyk, J., Benskin, C. M. H., Grant, F., Perks, M. T., Deasy, C., Burke, S. P., Collins, A.L., Freer, J., Haygarth, P. M., Hiscock, K. M., Johnes, P. J., Lovett, A. L., 2014. High-frequency monitoring of nitrogen and phosphorus response in three rural catchments to the end of the 2011–2012 drought in England. *Hydrology and Earth System Sciences*, 18(9): 3429–3448.
- Pacific, V. J., Jencso, K. G., McGlynn, B. L. 2010. Variable flushing mechanisms and landscape structure control stream DOC export during snowmelt in a set of nested catchments. *Biogeochemistry*, 99(1–3): 193–211.

- Paris, T. 2004. Study of the transfer of water and solutes in artificially drained high water table soils. Ph.D. Dissertation. Ecole Nationale du Génie Rural et des Eaux et Forêts, Paris.
- Pellerin, B. A., Bergamaschi, B. A., Gilliom, R. J., Crawford, C. G., Saraceno, J., Frederick, C. P., Downing, B. D., Murphy, J. C. 2014. Mississippi River nitrate loads from high frequency sensor measurements and regression-based load estimation. *Environmental Science & Technology*, 48(21): 12612–12619.
- Ramos, T. B., Gonçalves, M. C., Branco, M. A., Brito, D., Rodrigues, S., Sánchez-Pérez, J.-M., Sauvage, S., Prazeres, Â., Martins, J. C., Fernandes, M. L., Pires, F. P. 2015a, Sediment and nutrient dynamics during storm events in the Enxoé temporary river, southern Portugal. *Catena*, 127: 177-190.
- Ramos, T. B., Rodrigues, S., Branco, M. A., Prazeres, A., Brito, D., Gonçalves, M. C., Martins, J. C., Fernandes, M. L., Pires, F. P. 2015b. Temporal variability of soil organic carbon transport in the Enxoe agricultural watershed. *Environmental Earth Sciences*, 73(10): 6663–6676.
- Sanderman, J., Lohse, K. A., Baldock, J. A., Amundson, R. 2009. Linking soils and streams: Sources and chemistry of dissolved organic matter in a small coastal watershed: Chemistry of dissolved organic matter. *Water Resources Research*, 45(3).
<https://doi.org/10.1029/2008WR006977>
- Searcy, J. K., and C. H. Hardison. 1960. Double-mass curves. USGS Water Supply Paper 1541-B. Washington, D.C.: U.S. Geological Survey.
- Stedmon, C. A., Markager, S., Sondergaard, M., Vang, T., Laubel, A., Borch, N. H., Windelin, A. 2006. Dissolved organic matter (DOM) export to a temperate estuary: Seasonal variations and implications of land use. *Estuaries and Coasts*, 29(3): 388–400.
- StreamStats from USGS. http://streamstatsags.cr.usgs.gov/v3_beta/viewer.htm?stabbr=NC

Thomas, Z., B. W. Abbott, O. Troccaz, J. Baudry, G. Pinay 2016, Proximate and ultimate controls on carbon and nutrient dynamics of small agricultural catchments, *Biogeosciences*,13(6): 1863–1875.

Thurman, E. M. 1985. Transport, origin and source of dissolved organic carbon. In *Organic Geochemistry of Natural Waters*. Springer Netherlands. 67–85.
https://doi.org/10.1007/978-94-009-5095-5_3.

Tipping, E., Woof, C., Rigg, E., Harrison, A. F., Ineson, P., Taylor, K., Benham, D., Poskitt, J., Rowland, A. P., Bol, R., Harkness, D. D. 1999. Climatic influences on the leaching of dissolved organic matter from upland UK moorland soils, investigated by a field manipulation experiment. *Environment International*, 25(1): 83–95.

Wayne County, NC website (<http://www.waynegov.com/235/GIS-Data-Download>)

Webb, B. W. and Walling, D. E. 1985. Nitrate behaviour in streamflow from a grassland catchment in Devon, UK. *Water Research*, 19(8): 1005–1016.

Williams, G. P. 1989. Sediment concentration versus water discharge during single hydrologic events in rivers. *Journal of Hydrology*, 111(1): 89–106.

Chapter 5: General Conclusion

The context of this research is the quantification of water quality benefits of stream restoration. This information is needed to associate nutrient credits to this practice. To fill this void in the literature, North Carolina Department of Transportation (NC DOT), North Carolina Forest Service (NCFS) and North Carolina State University (NCSU) have collaborated to conduct this pilot study.

Until now, there has not been any clear evidence that stream restoration can provide water quality benefits (e.g., Bernhardt et al., 2005; Craig et al., 2008; Alexander and Allan, 2006; Castillo et al., 2016; Daigneault et al., 2017; Eshleman and Sabo, 2016), much less accepted numbers on the water quality benefits. The reasons for this might be that the benefits are too small to be measurable, and/or that the uncertainties on the quantification methods were just too large to detect benefits. It has been shown that the uncertainties on robust indicators, annual cumulative loads, can easily reach 20 to 40% using standard weekly or biweekly sampling methods (Chapter 3), leaving little chance to quantify with any confidence water quality improvement of the same or lower magnitude. This reason alone could explain the reasons for the lack of recognized water quality benefits. One chance to dramatically reduce the uncertainties on measuring loads, and therefore on the bulk water quality effect, is to obtain concentration values at a pace that can capture the dynamics of the rapid concentration changes with flow.

Because water quality benefits largely depend on residence time (e.g. Craig et al., 2008), it is likely that the water quality improvements in restored streams are inherently small. The

residence time was estimated in the 2,200 m stream to be around 5 hours during April base flow conditions (Appendix H on tracer study). When the differences for nitrate cumulative loads were compared between Upstream (19.60 kg/ha) and Downstream (16.53 kg/ha) stations, 16% of nitrate was retained in the Claridge Canal during 16 months in pre-restoration period. In constructed wetlands with long water residence times of day, the removal efficiencies have been measured to reach up to 97%, 32%, 25%, and 53% for nitrate, TDN, ammonium, and soluble active phosphorous, respectively (Ardón et al., 2010). The advent of new water quality sensors is able to measure concentration at frequency on par with those of flow or stage sensors, opens the possibility to reduce uncertainty to much lower levels, and should the water quality effects be much higher than the measurement uncertainties, to quantify these benefits.

Continuous hydrology and water quality monitoring were applied in the Claridge Canal which was restored in Goldsboro, North Carolina. This thesis is thus a methodological piece of work at its core. It first required to test whether new optical based sensors could even be used in the low gradient streams of the coastal plain of North Carolina. In particular, it was very interesting to show that (1) one can apply *in situ* ultraviolet-visual (UV-Vis) spectrophotometers and create water quality rating curves using Partial Least Squares Regression (PLSR) to measure water quality parameters ($\text{NO}_3\text{-N}$, $\text{NH}_4\text{-N}$, TDN, TKN, DOC, $\text{PO}_4\text{-P}$, TP and TSS); (2) one can quantify the uncertainties on measuring the cumulative loads associated with the data generated by UV-Vis spectrophotometers and provide guidelines for robust sampling strategies. Once these two methodological approaches were

done, it became possible to learn about the local biogeochemical functioning of these watersheds and (3) characterize the nutrient dynamics from the high frequency water quality information with hysteresis analysis during the storm events and nutrient exports in seasonal scales in the lowland coastal plain watershed.

Ability to create water quality rating curves for UV-Vis spectrophotometers

UV-Vis spectrophotometers were used to create water quality rating curves to obtain concentration data on a high frequency basis to calculate robust N, P, C, and material fluxes. The PLSR rating seems to be more robust than the algorithms embedded in the instruments for the Claridge Canal. The results demonstrated that it was possible to construct robust water quality rating curves to measure nitrate, TDN, TKN, DOC, and TP, using the absorbance data as index data and Partial Least Squares Regression (PLSR) as a rating method in an agricultural stream of the coastal plain of North Carolina. The results also indicated that this method did not work well for $\text{NH}_4\text{-N}$ and $\text{PO}_4\text{-P}$, although it is possible that optimal calibration point pools were not obtained. Extrapolating beyond the calibration range is inherently risky and may result in errors, and in the case of parameters that exhibit concentration changes during events, large overestimation was observed for TSS prediction by using PLSR. For predicting TSS, it is suggested to use the more conservative turbidity based method. To obtain fully continuous nutrient flux data, it is necessary to provide methods to fill the gaps. This research demonstrated that acceptable methods were developed to fill missing flow and concentration data.

Reduce errors on measuring loads with using UV-Vis spectrophotometers and the most robust sampling method for affordable number of calibration points

This research is the first to report uncertainties on concentrations and annual loads using *in situ* spectrophotometers. The existing calibration points were numerically resampled by using bootstrap, random and stratified sample subsets from the original dataset, and applied PLSR on these subsets to estimate the uncertainties on annual loads. From the bootstrap resampling results, continuous monitoring with the application of UV-Vis spectrophotometers can reduce errors on measuring loads, e.g., within $\pm 5\%$ measuring error for nitrate, TDN, TKN, DOC and TSS; and approximately $\pm 10\%$ for TP.

The uncertainties are much lower using stratified sampling rather than random sampling. It is likely that even the robust, i.e., precise, calibrations obtained with over 100 samples, as the bootstrapping results suggest, might be inaccurate. Indeed, we have shown that an over-representation of concentrations stratification, or lack thereof, of the calibration concentration pool, tends to bias load values towards the load values for which the calibration concentrations are overrepresented. Calibration might be biased towards overestimation for parameters exhibiting dilution effects during storms (such as nitrate and TDN), and biased towards underestimation for parameters that exhibit concentration effects during storms, such as DOC, TP, and TSS in this research.

The results suggested that for nitrate (or TDN mostly made of nitrate) that is known to absorb light in a narrow UV range, very small uncertainties can be expected, i.e., within $\pm 2\%$ for 52 stratified samples. For DOC, which is also known to generally absorb light but which

correspond to a large array of molecules, the uncertainty increase from -1% to +9% or a 10-percentage point spread, compared to a 6-percentage point spread for nitrate for 24 samples for calibration. For other parameters, such as TKN and TP, which are not known to absorb light, it is hypothesized that there is a co-variability of light absorbing constituents with concentrations to derive water quality rating curves, the uncertainties can be much higher than for nitrate and DOC.

The level of uncertainties computed with the flow-weighted concentration average estimator method (M5) and the linear interpolation method (M6) correspond to highly reactive watersheds, where uncertainties tend to be higher (e.g., Birgand et al., 2010). It is thus possible that the level of uncertainties on annual loads for all parameters and all subsampling techniques are on the higher range and that smaller uncertainties might be expected for less reactive watersheds. This research suggested the bootstrap and other subsampling techniques should be routinely used to estimate the uncertainty on computed annual loads when using *in situ* field spectrophotometers.

The results thus show that the level of uncertainty on the annual load cumulative indicator is indeed largely reduced compared to the infrequent sampling methods that have been applied in past stream restoration monitoring. Now, the monitoring design and methods involved a lot of time and resources. It is interesting to evaluate the relative effort that this type of monitoring would represent in the whole stream restoration costs.

Costs comparisons between continuous monitoring and stream restoration projects

From 1990, the United States has invested at least \$1 billion every year in stream restoration projects (Bernhardt et al., 2005; Fischenich, 2011). In addition, there were 1,345 stream restoration projects implemented from 1970 to 2004 with \$444 million investment in the Upper Midwest, USA (Michigan, Ohio, Wisconsin; Alexander and Allan, 2006). Water quality management is one of the top priorities in stream restoration, and \$60 million was invested (median cost of \$234,500). Only 33% of water quality management projects were monitored in the Upper Midwest, with higher expense projects having more opportunities to be monitored (Alexander and Allan, 2006). Due to the lack of monitoring, evaluations of the stream restoration project-caused improvements have been inhibited; thus, establishing standardization of monitoring is essential (Alexander and Allan, 2006). The same authors (Alexander and Allan, 2007) interviewed the staff in 39 projects among 1,345 stream restoration projects in Upper Midwest, USA. The results indicated that the “lack of people power or staff time” was the most common reason projects were not monitored.

The costs for stream restoration projects were mostly affected by the type and size of the watersheds (Bonham and Stephenson, 2004). Table 5.1 summarizes the costs analysis with linear foot for several stream restoration projects. The construction costs (\$30-\$70/ft.) for the different projects are comparable except for the project in Long Creek, Bessemer City, North Carolina. In addition, the total costs for stream restoration projects during 2016-2017 reported by NC Division of Mitigation Services (NCDMS) is \$391/ft.

Based on the estimated budget from the research proposal (Birgand, 2013), the total fees for continuous monitoring in pre-restoration period in three years (2013-2016) were about \$353,000 for the Claridge Canal with 2,200 m in length. Thus, the continuous monitoring fees in the Claridge Canal were \$16.23/ft., including \$5.53/ft. (34%) for personnel, and \$10.7/ft. (66%) for field supplies/material, monitoring equipment, and transportation. When comparing the continuous monitoring costs for the Claridge Canal and the total costs for stream restoration estimated by NCDMS, the continuous monitoring costs is 4% of the total costs for stream restoration. Thus, it is fair to say that the costs for pre-restoration continuous monitoring represented a small proportion of the overall project. The post-restoration costs increase this percentage to about 10% (Birgand, personal communication).

Table 5.1 Costs analysis for the stream restoration projects (Unit: \$/ft.)

Description	Pre-construction	Site Acquisition	Construction	Post-Construction	Total Costs	Restoration Goal	References
Small Stream (<3,001 ft.)	26.14	5.65	68.35	18.81	118.96	Reduce the impacts by surface coal mining in the Southern Appalachian Region	Bonham and Stephenson (2004)
Medium Stream (3,001 – 10,000 ft.)	21.25	4.21	57.28	10.01	92.74		
Large stream (>10,000 ft.)	13.04	-	45.82	6.37	65.22		
Long Creek, Bessemer City, NC	-	-	13.33	-	-	Improve stability and habitat	Jennings et al. (2005)
Kentucky Creek, Newland, NC	-	-	33.33	-	-		
East Prong Roaring River, Stone Mountain State Park, NC	-	-	60	-	-		
Little Garvin Creek, Clemson, NC	-	-	50	-	-		
Stream restoration fees in North Carolina (NC) during 2016-2017	-	-	-	-	391	-	The website from NC Division of Mitigation Services

-: data not applicable

Biogeochemical process in an agricultural coastal plain watershed

Nitrate and DOC were measured on a continuous basis with the application of UV-Vis spectrophotometers to capture the nutrient dynamics in the Claridge Canal. During the entire monitoring period, the continuous hydro-chemo graphs indicated it had dilution effects for nitrate in most of storm events and concentration effects for DOC for all the storm events in the Claridge Canal.

Based on continuous chemographs and hysteresis index results, seasonal differences affected the nitrate and DOC dynamics. In summer, the spatial distance of nitrate and DOC

sources caused the time lag between nitrate troughs and DOC peaks. In winter, nitrate troughs almost synchronized with flow peak; however, DOC peaks continued a lag after flow peak during the rainfall events. Thus, the sources of nitrate and DOC were transported from different locations, and the significant difference for the absolute hysteresis index values between nitrate and DOC in winter supported the observation.

The cumulative loads and flow-weighted concentrations demonstrated seasonal variations affecting the export of nitrate and DOC. With a higher denitrification rate, crop uptake from nitrate, and increased of microbial activity and soil diagenetic mechanism, the stream transported the least amount of nitrate but the highest amount of DOC during summer. However, the increase of leaching process for nitrate and the decreasing of microbial ability elevated nitrate transport and reduced DOC export during winter.

The results suggested high frequency monitoring could detect the sudden and subtle variations of nitrate and DOC in storm events and seasonal scales in the flashy agricultural watershed, e.g., the Claridge Canal. With the continuous hydrology and water quality data which can be inferred soil and instream export mechanisms unique to coastal plain watersheds.

Comparisons of nutrient dynamics between lowland coastal plain watershed and other watersheds

The nutrient dynamics are affected by soil properties (e.g., soil hydraulic, soil types, and antecedent moisture), drainage characteristics, rainfall features, runoff characteristics, groundwater effects; sources and availability of nutrients, vegetation cover, and land use in

watersheds (Blanco et al., 2010; Bowes et al., 2015; Cerro et al., 2014; Ramos et al., 2015a, 2015b; Stedmon et al., 2006; Webb and Walling, 1985).

Table 5.2 summarized nitrate and DOC dynamics in several watersheds (including this research) with different types of land use. Comparing residential and agricultural watersheds, forested watershed had the minimal export of nitrate (lowest nitrate concentrations) because the lack of anthropogenic nitrate inputs reduced the sources of nitrate (Poor and McDonnell, 2007). Seasonal effects for nitrate are similar for agricultural watersheds (including upland and lowland streams) and nitrate concentrations decreased in spring and summer, and increased in fall and winter (this research, Oak Creek Watershed and Alegria watershed).

The range of DOC concentrations (Table 5.2) were similar in agricultural watersheds (including upland and lowland streams); however, the nitrate concentrations were apparently lower in the Claridge Canal than the other three watersheds (Kervidy-Naizin catchment, Alegria watershed, and the Enxoé catchment). The high nitrate concentrations were due to the application of numerous fertilizers and the species of planted crops in Kervidy-Naizin catchment, Alegria watershed, and the Enxoé catchment. In addition, DOC loads in upland streams were obviously lower than those of lowland stream; thus, the availability DOC sources are lesser than in lowland streams (Alegria watershed and the Enxoé catchment).

In Table 5.2, nitrate concentrations were either diluted or concentrated, and DOC concentrations were concentrated in all watersheds except for the Enxoé catchment during storm events. Comparing subsurface flow, DOC concentrations were lower in surface runoff during the rainfall events in the Enxoé river (Ramos et al., 2015b). In addition, it was

reported that the transport mechanisms for nitrate and DOC were different in the watersheds (Aubert et al., 2013; Cerro et al., 2014; Ramos et al., 2015a, 2015b; this research).

In summary, compared with other watersheds (Table 5.2), the exports of nitrate and DOC loads were relatively lower and higher, respectively, in the coastal agricultural plain watershed (this research). In this research, the watershed showed some unique soil and in-stream mechanisms and indicate different dynamics and sources for nitrate and DOC in the Claridge Canal.

Table 5.2 Summary of nitrate and DOC dynamics for the Claridge Canal and other research

Site	Land use Area (ha)	Nitrate concentrations (mg/L)	DOC concentrations (mg/L)	Dilution/concentration effects during storm events	Nitrate loads (kg/ha/year)	DOC loads (kg/ha/year)	References
The Claridge Canal, NC, USA	Agricultural (lowland) UP: 236 MD: 474 DN: 573	2.8-3.5 (baseflow condition)	3.5-7 (baseflow condition)	Nitrate: dilution DOC: concentration	UP: 15.4 MD: 12.3 DN: 13.0	UP: 30.2 MD: 46.4 DN: 45.9	This research
Oak Creek Watershed, Oregon, USA	Agricultural (lowland) 52.2	Spring: 0.02-0.2 Fall: 0.6-1.1 Winter: 0.09-0.17 (baseflow condition)	-	Dilution in fall and winter Concentration in spring	-	-	Poor and McDonnell (2007)
	Residential (lowland) 42.9	0.6-0.29 (baseflow condition)	-	Concentration	-	-	
	Forested (upland) 49.5	0.005-0.06 (baseflow condition)	-	Concentration	-	-	
Ishigaki Island, Okinawa, Japan	Agricultural (lowland) 1082	3 (baseflow condition)	-	Dilution	20.4	-	Blanco et al. (2010)
Kervidy-Naizin catchment, western France	Agricultural (lowland) 482	16.9 (mean)	4.4 (mean)	Nitrate: dilution DOC: concentration	-	-	Aubert et al. (2013)
Alegria watershed, Ebro river basin, northern Spain	Agricultural (upland) 11300	30-35 (baseflow condition)	4.45 (mean)	Nitrate: dilution DOC: concentration	37.3	3.94	Cerro et al. (2014)
The Enxoé catchment, Alentejo region, Southern Portugal	Agricultural (upland dominated) 6080	0-27.8 (during entire monitoring period)	10.27 (mean)	Nitrate: concentration in fall and dilution in spring DOC: dilution	45.5	7.3	Ramos et al. (2015a; 2015b)

-: data not applicable

5.2 References

- Alexander, G. G. and Allan, J. D. 2006. Stream restoration in the Upper Midwest, USA. *Restoration Ecology*, 14(4): 595–604.
- Alexander, G. G. and Allan, J. D. 2007. Ecological success in stream restoration: case studies from the Midwestern United States. *Environmental Management*, 40(2): 245–255.
- Ardón, M., Morse, J. L., Doyle, M. W., Bernhardt, E. S. 2010. The water quality consequences of restoring wetland hydrology to a large agricultural watershed in the Southeastern Coastal Plain. *Ecosystems*, 13(7): 1060–1078.
- Aubert, A. H., Gascuel-Oudou, C., Gruau, G., Akkal, N., Faucheux, M., Fauvel, Y., Grimaldi, C., Hamon, Y., Jaffr'ezic, A., Lecoq-Boutnik, M., Mol'énat, J., Petitjean, P., Ruiz, L., Merot, P. 2013. Solute transport dynamics in small, shallow groundwater-dominated agricultural catchments: insights from a high-frequency, multisolute 10 yr-long monitoring study. *Hydrology and Earth System Sciences*, 17(4): 1379–1391.
- Bernhardt, E. S., Palmer, M. A., Allan, J. D., Alexander, G., Barnas, K., Brooks, S., Carr, J., Clayton, S., Dahm, C., Follstad-Shah, J., Galat, D., Gloss, S., Goodwin, P., Hart, D., Hassett, B., Jenkinson, R., Katz, S., Kondolf, G. M., Lake, P. S., Lave, R., Meyer, J. L., O'Donnell, T. K., Pagano, L., Powell, B., Sudduth, E. 2005. Synthesizing U.S. river restoration efforts. *Science*, 308: 636-637.
- Birgand F., Faucheux, C., Gruau, G., Augéard, B., Moatar, F., Bordenave, P. 2010. Uncertainties in assessing annual nitrate load and concentration indicators: Part 1. Impact of sampling frequency and load estimation algorithms. *Trans. ASABE*, 53(2): 437-446.
- Birgand, F. 2013. Intensive Monitoring of Nutrient and Material Load in Claridge Nursery Stream “The Canal” pre-, during and post construction of Highway 70 Bypass in Wayne County, NC. NCDOT Research Proposal.

- Blanco, A. C., Nadaoka, K., Yamamoto, T., Kinjo, K. 2010. Dynamic evolution of nutrient discharge under stormflow and baseflow conditions in a coastal agricultural watershed in Ishigaki Island, Okinawa, Japan. *Hydrological Processes*, 24(18): 2601–2616.
- Bonham, J. and Stephenson, K. 2004. A cost analysis of stream compensatory mitigation projects in the Southern Appalachian Region. The American Society of Agricultural Engineers, Self-Sustaining Solutions for Streams, Watersheds, and Wetlands Conference, St. Paul Minnesota, September 12-15, 2004.
- Bowes, M. J., Jarvie, H. P., Halliday, S. J., Skeffington, R. A., Wade, A. J., Loewenthal, M., Gozzard, E., Newman, J. R., Palmer-Felgate, E. J. 2015. Characterizing phosphorus and nitrate inputs to a rural river using high-frequency concentration–flow relationships. *Science of the Total Environment*, 511: 608-620.
- Castillo, D., Kaplan, D., Mossa, J. 2016. A synthesis of stream restoration efforts in Florida (USA): Florida Stream Restoration. *River Research and Applications*, 32(7): 1555–1565.
- Cerro, I., Sanchez-Perez, J. M., Ruiz-Romera, E., Antigüedad, I. 2014. Variability of particulate (SS, POC) and dissolved (DOC, NO₃) matter during storm events in the Alegria agricultural watershed: The importance of storm events in agricultural watersheds. *Hydrological Processes*, 28(5): 2855–2867.
- Craig, L. S., Palmer, M. A., Richardson, D. C., Filoso, S., Bernhardt, E. S., Bledsoe, B. P., Doyle, M. W., Groffman, P. M., Hassett, B. A., Kaushal, S. S., Mayer, P. M., Smith, S. M. 2008. Stream restoration strategies for reducing river nitrogen loads. *Frontiers in Ecology and the Environment*, 6(10): 529–538.
- Daigneault, A. J., Eppink, F. V., Lee, W. G. 2017. A national riparian restoration programme in New Zealand: Is it value for money? *Journal of Environmental Management*, 187: 166–177.

Eshleman, K. N. and Sabo, R. D. 2016. Declining nitrate-N yields in the Upper Potomac River Basin: What is really driving progress under the Chesapeake Bay restoration? *Atmospheric Environment*, 146: 280–289.

Fischenich, J. C. 2011. Stream restoration benefits. *Stream Restoration in Dynamic Fluvial Systems: Scientific Approaches, Analyses, and Tools Geophysical Monograph Series 194*, Published in 2011 by the American Geophysical Union.

<https://deq.nc.gov/about/divisions/mitigation-services/dms-customers/fee-schedules>

Jennings, G., Clinton, D., Bidelspach, D., Penrose, D., Shaffer, M., Rozzell, L., Hall, K., Bass, K., Doll, B., Zink, J., Calabria, J., Foster, S. (2005). *Stream Restoration Lessons Learned in North Carolina*.
<http://srwqis.tamu.edu/media/1731/greg%20jennings%20ky%20stream%20oct05.pdf>.

Poor, C. J. and McDonnell, J. J. 2007. The effects of land use on stream nitrate dynamics. *Journal of Hydrology*, 332(1–2): 54–68.

Ramos, T. B., Gonçalves, M. C., Branco, M. A., Brito, D., Rodrigues, S., Sánchez-Pérez, J.-M., Sauvage, S., Prazeres, Â., Martins, J. C., Fernandes, M. L., Pires, F. P. 2015a, Sediment and nutrient dynamics during storm events in the Enxoé temporary river, southern Portugal. *Catena*, 127: 177-190.

Ramos, T. B., Rodrigues, S., Branco, M. A., Prazeres, A., Brito, D., Gonçalves, M. C., Martins, J. C., Fernandes, M. L., Pires, F. P. 2015b. Temporal variability of soil organic carbon transport in the Enxoé agricultural watershed. *Environmental Earth Sciences*, 73(10): 6663–6676.

Stedmon, C. A., Markager, S., Sondergaard, M., Vang, T., Laubel, A., Borch, N. H., Windelin, A. 2006. Dissolved organic matter (DOM) export to a temperate estuary: Seasonal variations and implications of land use. *Estuaries and Coasts*, 29(3): 388–400.

Webb, B. W. and Walling, D. E. 1985. Nitrate behaviour in streamflow from a grassland catchment in Devon, UK. *Water Research*, 19(8): 1005–1016.

APPENDICES

Appendix A:

A.1 The GIS sources for Figure 1.1

Figure 1.1 was produced by ESRI'S ArcGIS (<http://www.esri.com/>). The shape files for three monitoring stations were downloaded from USGS website (http://streamstatsags.cr.usgs.gov/v3_beta/viewer.htm?stabbr=NC); the contours file and hydrology file were obtained from Wayne County, NC website (<http://www.waynegov.com/page/214>).

Appendix B: Uncertainties estimations for annual loads for different stream solutes with bootstrap sampling

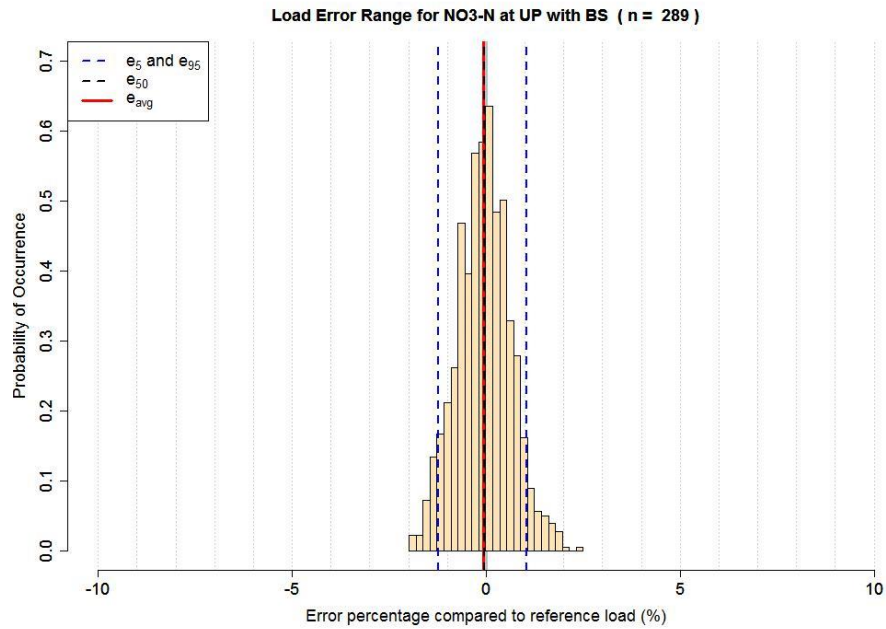


Figure B.1

Distribution of uncertainties estimation presented in the percentage as relative difference of reference annual load expressed as histogram for NO₃-N (uncertainties with the bias [e_{avg} , red solid line or e_{50} , black dash line] and precision [e_5 and e_{95} , blue dash lines, are precision limits of 5th and 95th percentiles, respectively) with bootstrap (BS) sampling at UP.

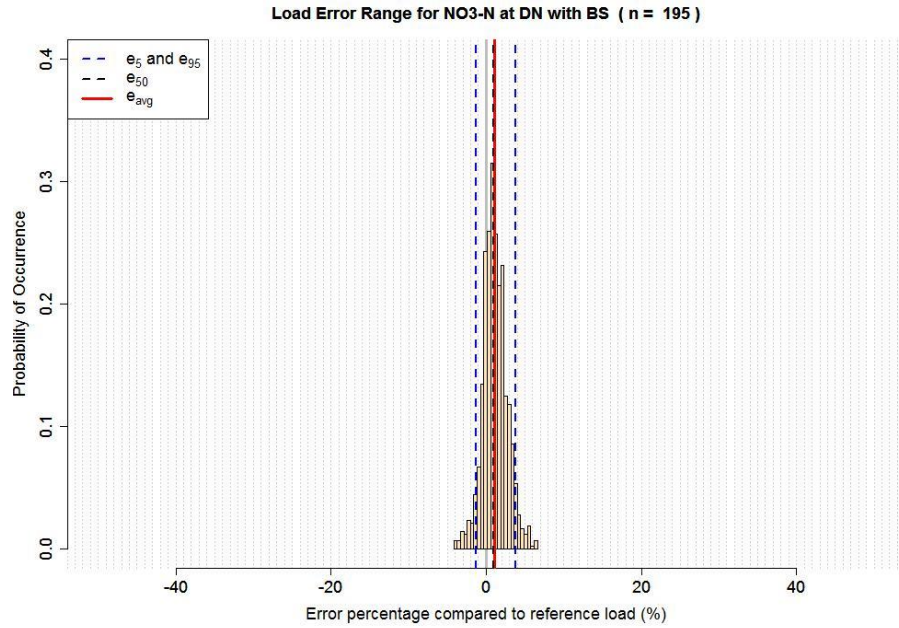


Figure B.2

Distribution of uncertainties estimation presented in the percentage as relative difference of reference annual load expressed as histogram for NO₃-N (uncertainties with the bias [e_{avg} , red solid line or e_{50} , black dash line] and precision [e_5 and e_{95} , blue dash lines, are precision limits of 5th and 95th percentiles, respectively) with bootstrap (BS) sampling at DN.

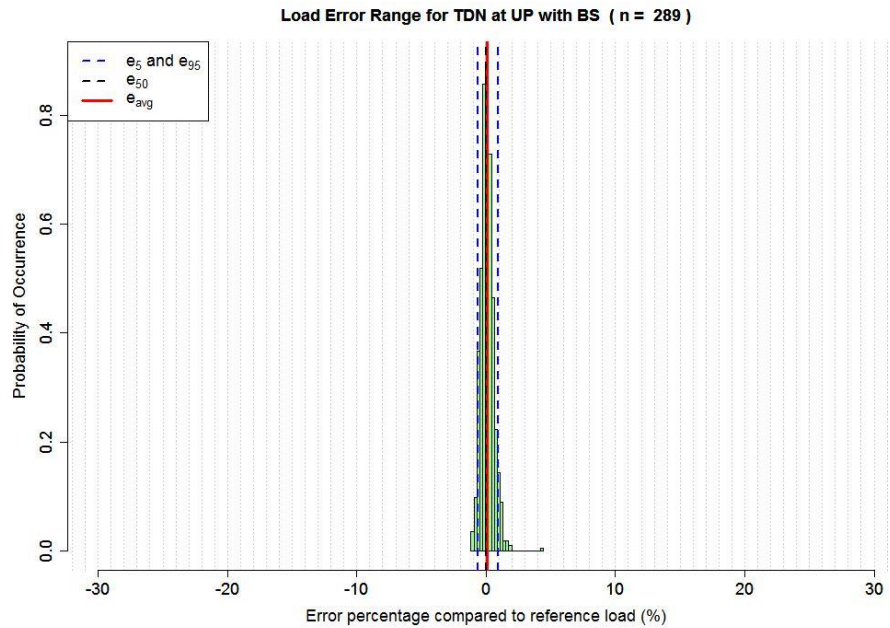


Figure B.3

Distribution of uncertainties estimation presented in the percentage as relative difference of reference annual load expressed as histogram for TDN (uncertainties with the bias [e_{avg} , red solid line or e_{50} , black dash line] and precision [e_5 and e_{95} , blue dash lines, are precision limits of 5th and 95th percentiles, respectively) with bootstrap (BS) sampling at UP.

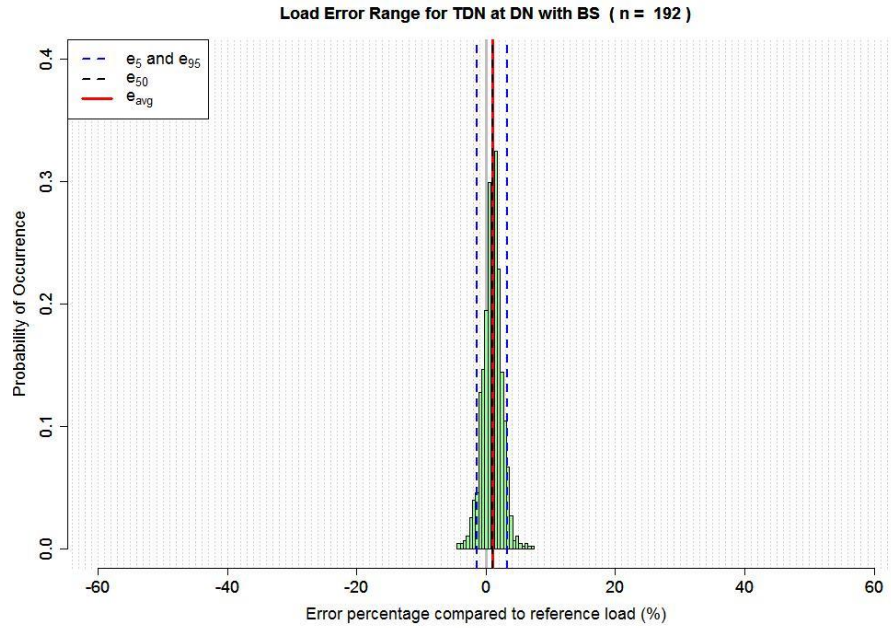


Figure B.4

Distribution of uncertainties estimation presented in the percentage as relative difference of reference annual load expressed as histogram for TDN (uncertainties with the bias [e_{avg} , red solid line or e_{50} , black dash line] and precision [e_5 and e_{95} , blue dash lines, are precision limits of 5th and 95th percentiles, respectively) with bootstrap (BS) sampling at TDN.

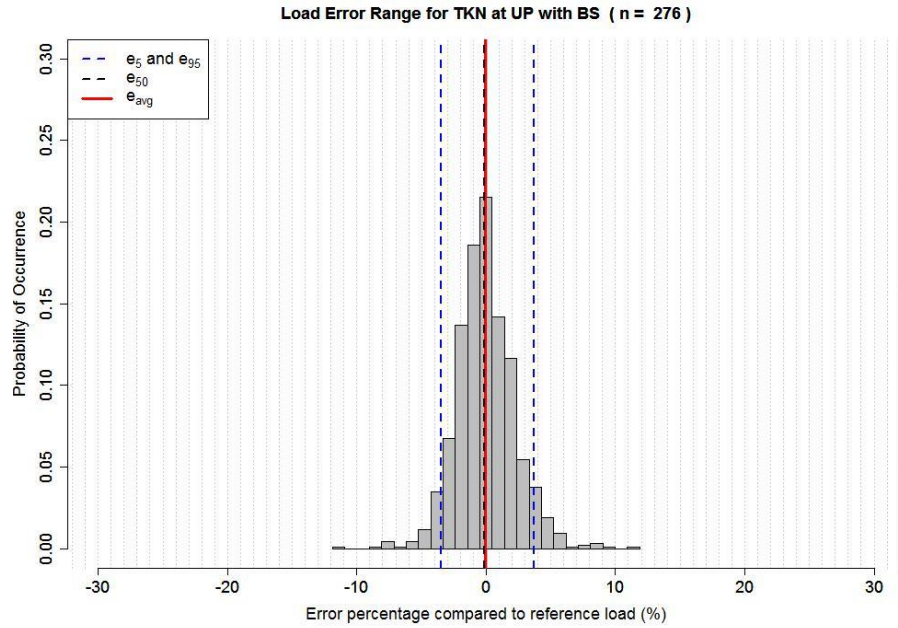


Figure B.5

Distribution of uncertainties estimation presented in the percentage as relative difference of reference annual load expressed as histogram for TKN (uncertainties with the bias [e_{avg} , red solid line or e_{50} , black dash line] and precision [e_5 and e_{95} , blue dash lines, are precision limits of 5th and 95th percentiles, respectively) with bootstrap (BS) sampling at UP.

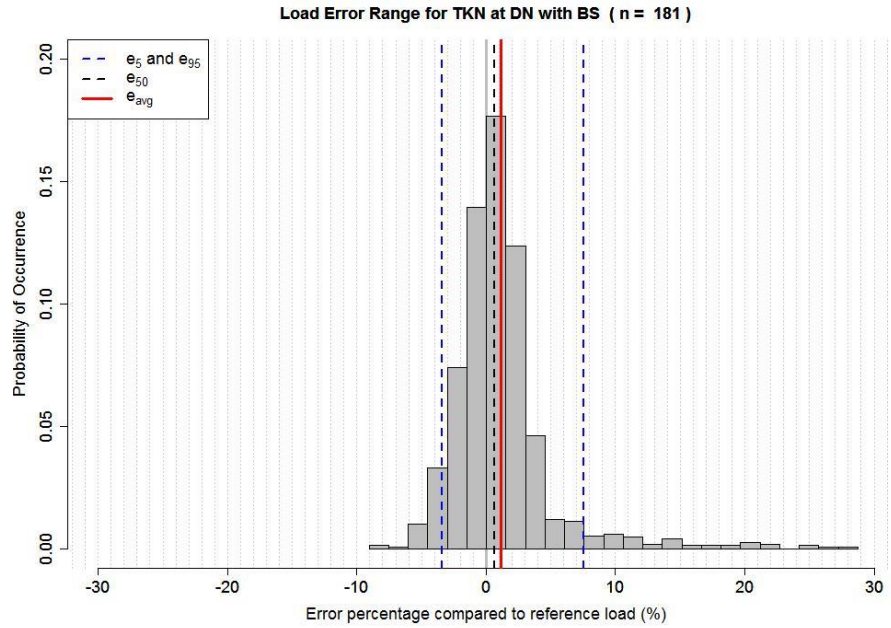


Figure B.6

Distribution of uncertainties estimation presented in the percentage as relative difference of reference annual load expressed as histogram for TKN (uncertainties with the bias [e_{avg} , red solid line or e_{50} , black dash line] and precision [e_5 and e_{95} , blue dash lines, are precision limits of 5th and 95th percentiles, respectively) with bootstrap (BS) sampling at DN.

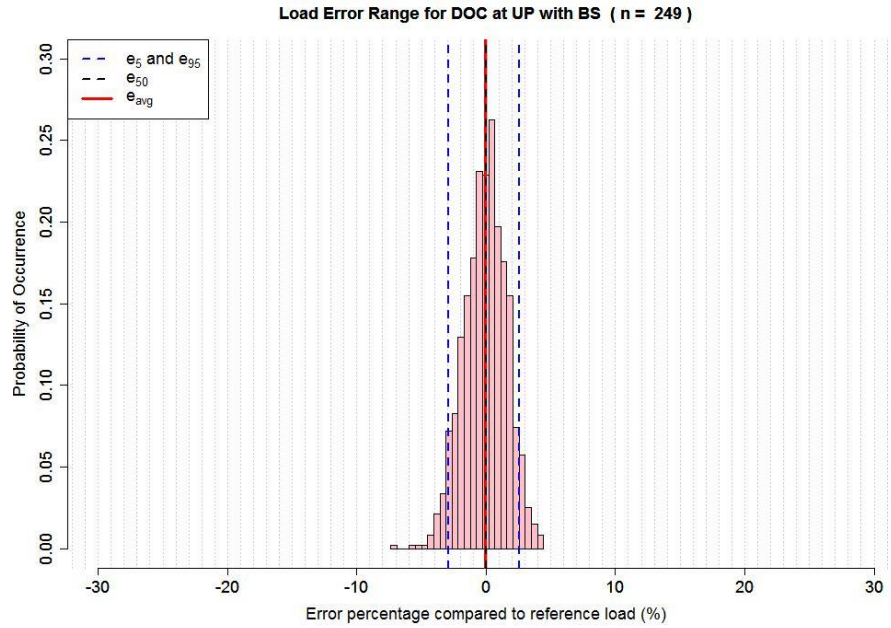


Figure B.7

Distribution of uncertainties estimation presented in the percentage as relative difference of reference annual load expressed as histogram for DOC (uncertainties with the bias [e_{avg} , red solid line or e_{50} , black dash line] and precision [e_5 and e_{95} , blue dash lines, are precision limits of 5th and 95th percentiles, respectively) with bootstrap (BS) sampling at UP..

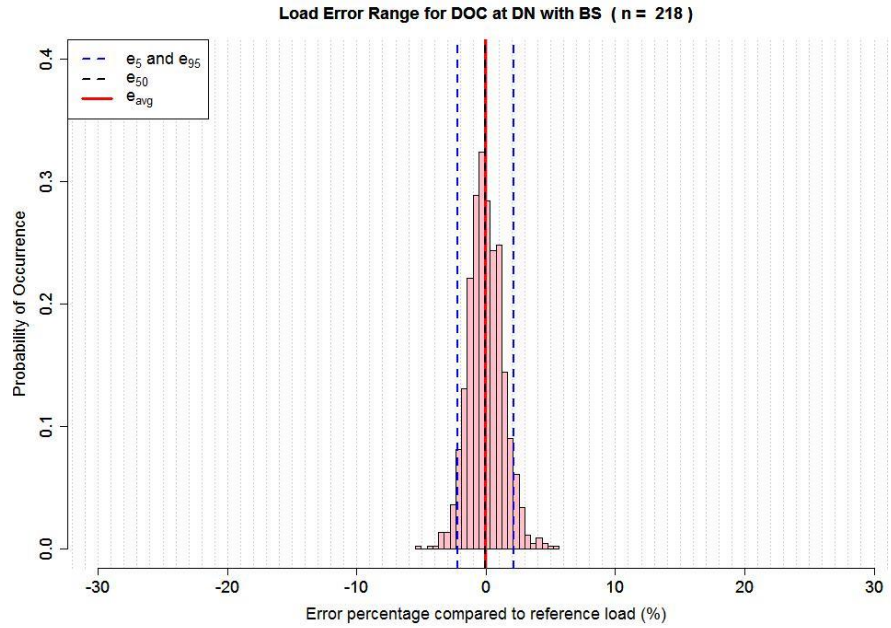


Figure B.8

Distribution of uncertainties estimation presented in the percentage as relative difference of reference annual load expressed as histogram for DOC (uncertainties with the bias [e_{avg} , red solid line or e_{50} , black dash line] and precision [e_5 and e_{95} , blue dash lines, are precision limits of 5th and 95th percentiles, respectively) with bootstrap (BS) sampling at DN.

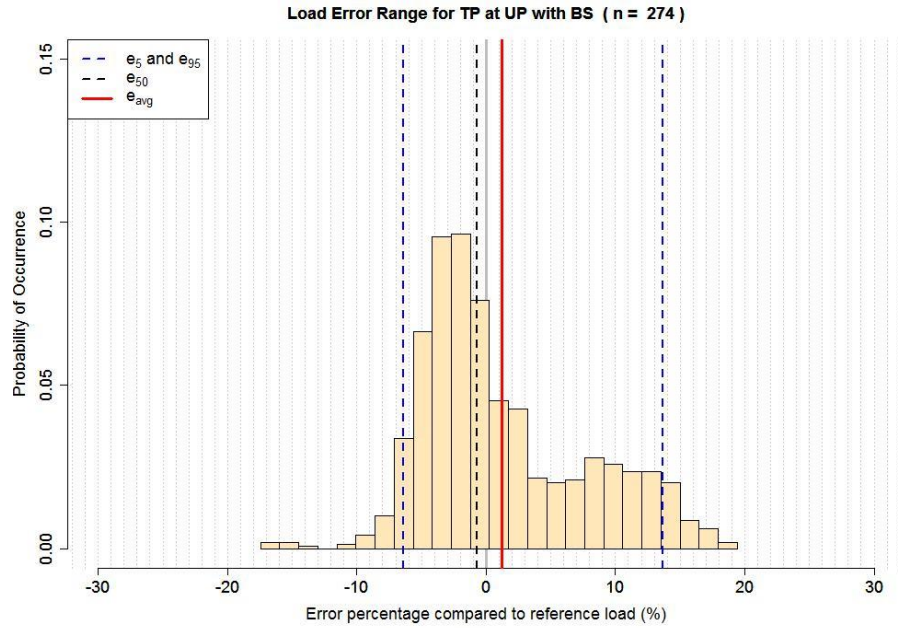


Figure B.9

Distribution of uncertainties estimation presented in the percentage as relative difference of reference annual load expressed as histogram for TP (uncertainties with the bias [e_{avg} , red solid line or e_{50} , black dash line] and precision [e_5 and e_{95} , blue dash lines, are precision limits of 5th and 95th percentiles, respectively) with bootstrap (BS) sampling at UP.

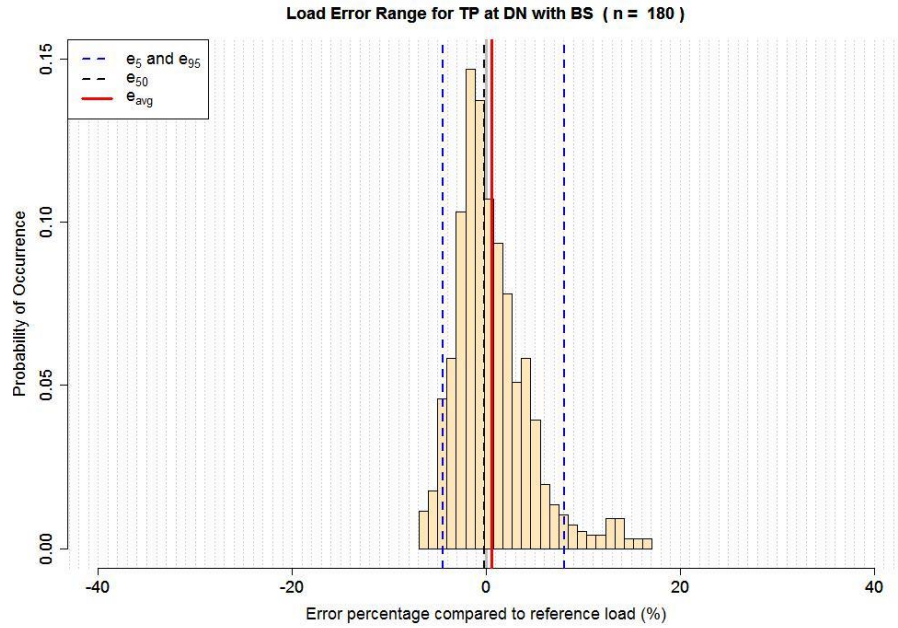


Figure B.10

Distribution of uncertainties estimation presented in the percentage as relative difference of reference annual load expressed as histogram for TP (uncertainties with the bias [e_{avg} , red solid line or e_{50} , black dash line] and precision [e_5 and e_{95} , blue dash lines, are precision limits of 5th and 95th percentiles, respectively) with bootstrap (BS) sampling at DN.

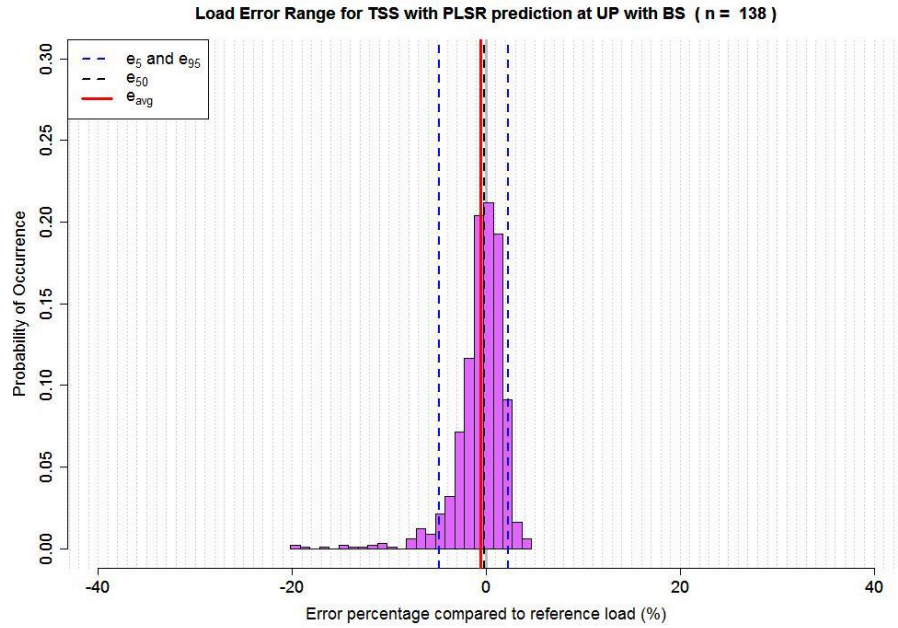


Figure B.11

Distribution of uncertainties estimation presented in the percentage as relative difference of reference annual load expressed as histogram for TSS with PLSR prediction (uncertainties with the bias [e_{avg} , red solid line or e_{50} , black dash line] and precision [e_5 and e_{95} , blue dash lines, are precision limits of 5th and 95th percentiles, respectively) with bootstrap (BS) sampling at UP.

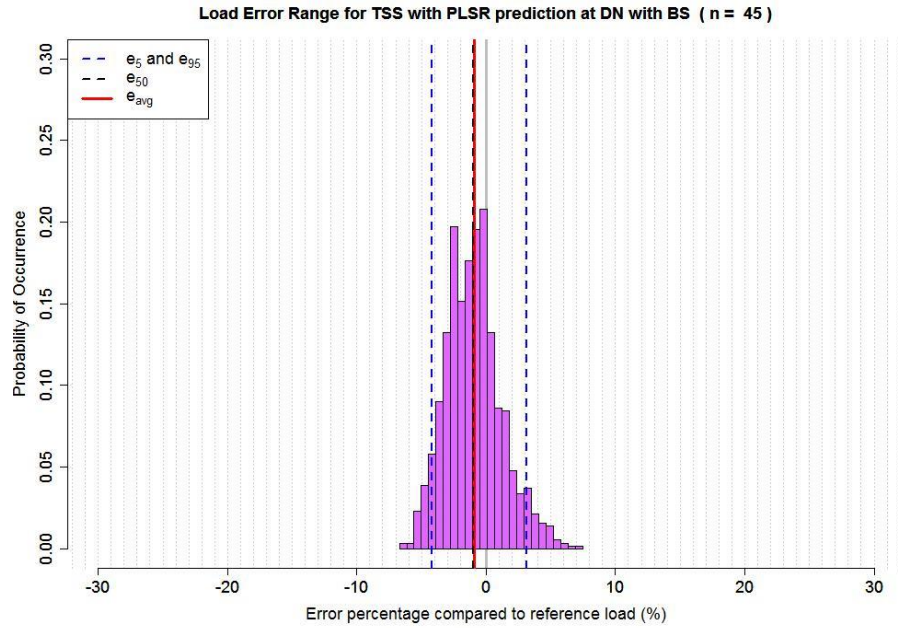


Figure B.12

Distribution of uncertainties estimation presented in the percentage as relative difference of reference annual load expressed as histogram for TSS with PLSR prediction (uncertainties with the bias [e_{avg} , red solid line or e_{50} , black dash line] and precision [e_5 and e_{95} , blue dash lines, are precision limits of 5th and 95th percentiles, respectively) with bootstrap (BS) sampling at DN.

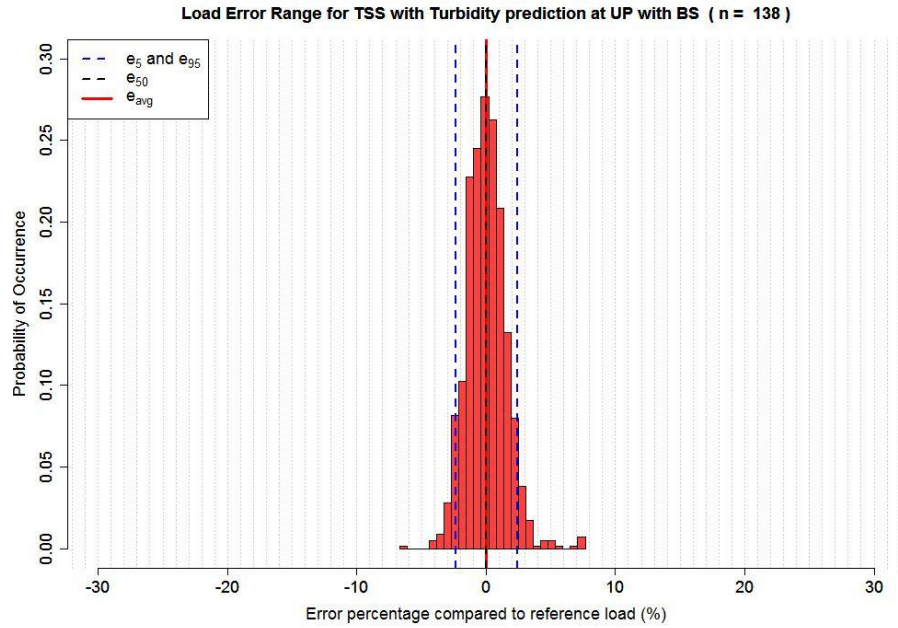


Figure B.13 Distribution of uncertainties estimation presented in the percentage as relative difference of reference annual load expressed as histogram for TSS with Turbidity prediction (uncertainties with the bias [e_{avg} , red solid line or e_{50} , black dash line] and precision [e_5 and e_{95} , blue dash lines, are precision limits of 5th and 95th percentiles, respectively) with bootstrap (BS) sampling at UP.

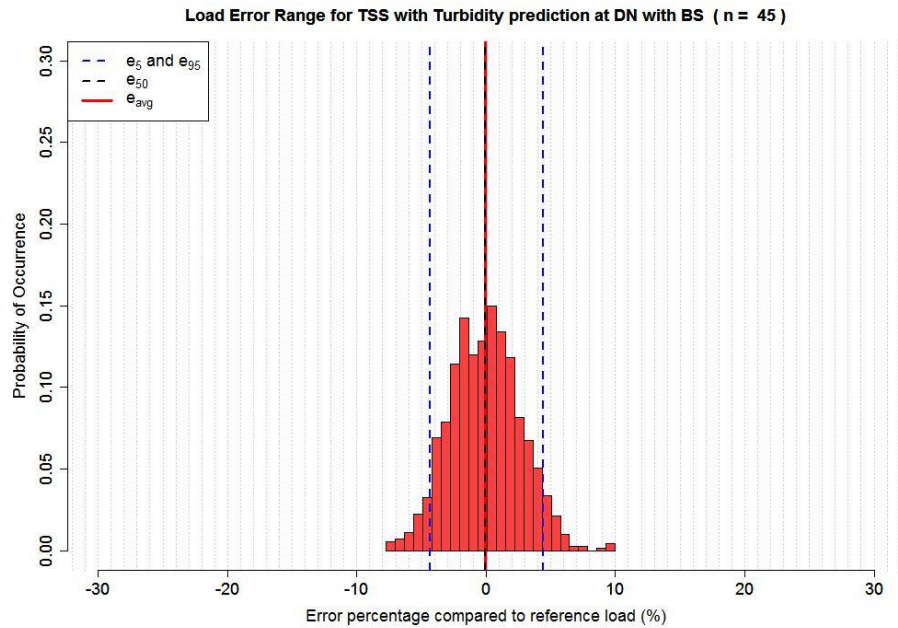


Figure B.14

Distribution of uncertainties estimation presented in the percentage as relative difference of reference annual load expressed as histogram for TSS with Turbidity prediction (uncertainties with the bias [e_{avg} , red solid line or e_{50} , black dash line] and precision [e_5 and e_{95} , blue dash lines, are precision limits of 5th and 95th percentiles, respectively) with bootstrap (BS) sampling at DN.

Appendix C: Uncertainties estimations for annual loads for different stream solutes with random subset sampling

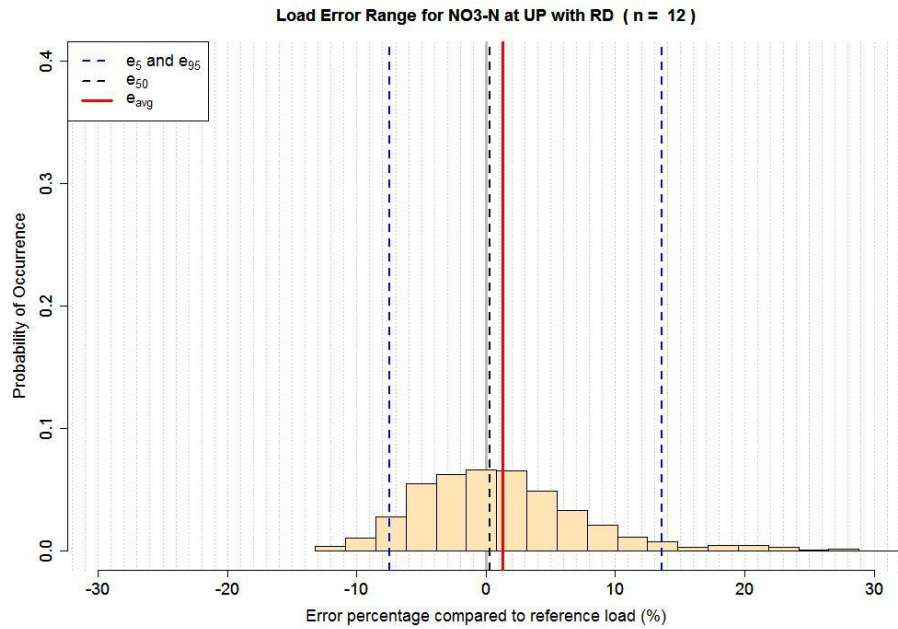


Figure C.1

Distribution of uncertainties estimation presented in the percentage as relative difference of reference annual load expressed as histogram for NO₃-N (uncertainties with the bias [e_{avg} , red solid line or e_{50} , black dash line] and precision [e_5 and e_{95} , blue dash lines, are precision limits of 5th and 95th percentiles, respectively) with random (RD) subset sampling (n = 12) at UP.

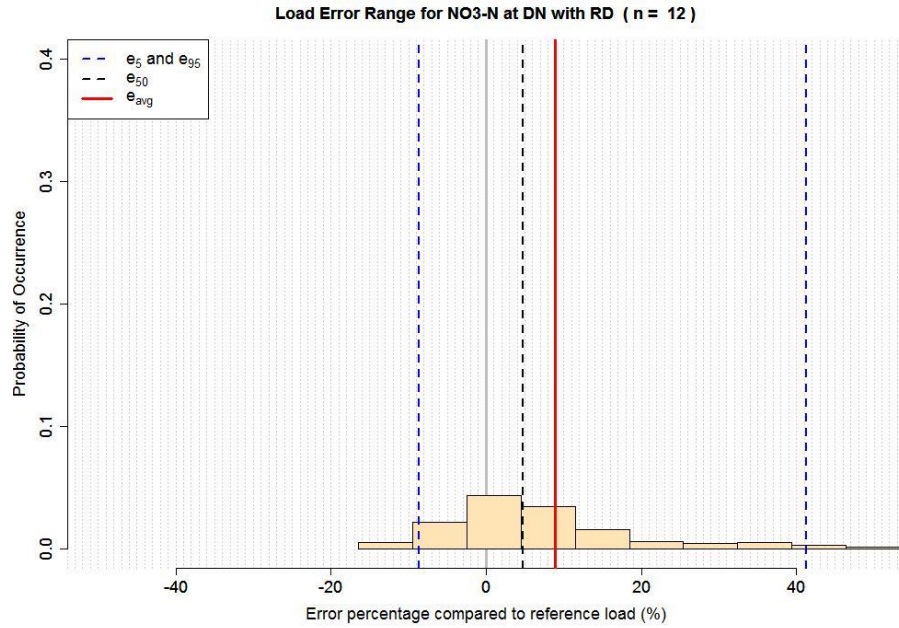


Figure C.2

Distribution of uncertainties estimation presented in the percentage as relative difference of reference annual load expressed as histogram for NO₃-N (uncertainties with the bias [e_{avg} , red solid line or e_{50} , black dash line] and precision [e_5 and e_{95} , blue dash lines, are precision limits of 5th and 95th percentiles, respectively) with random (RD) subset sampling (n = 12) at DN.

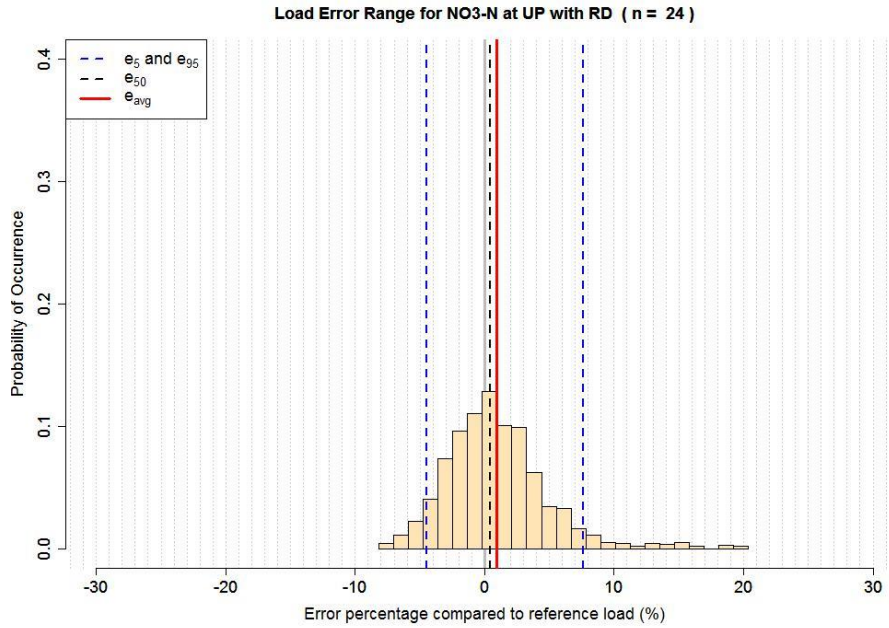


Figure C.3

Distribution of uncertainties estimation presented in the percentage as relative difference of reference annual load expressed as histogram for NO₃-N (uncertainties with the bias [e_{avg} , red solid line or e_{50} , black dash line] and precision [e_5 and e_{95} , blue dash lines, are precision limits of 5th and 95th percentiles, respectively) with random (RD) subset sampling (n = 24) at UP.

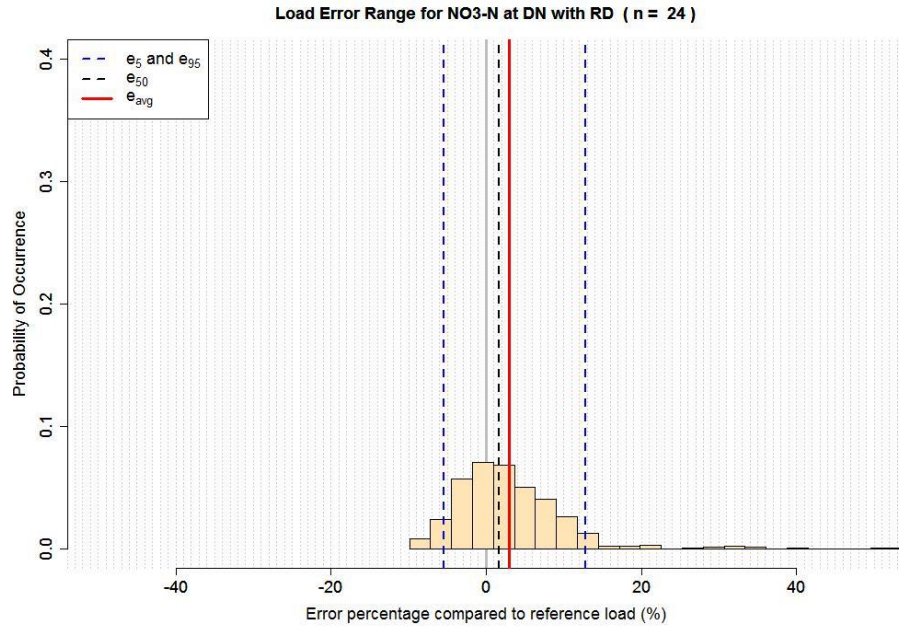


Figure C.4

Distribution of uncertainties estimation presented in the percentage as relative difference of reference annual load expressed as histogram for NO₃-N (uncertainties with the bias [e_{avg} , red solid line or e_{50} , black dash line] and precision [e_5 and e_{95} , blue dash lines, are precision limits of 5th and 95th percentiles, respectively) with random (RD) subset sampling (n = 24) at DN.

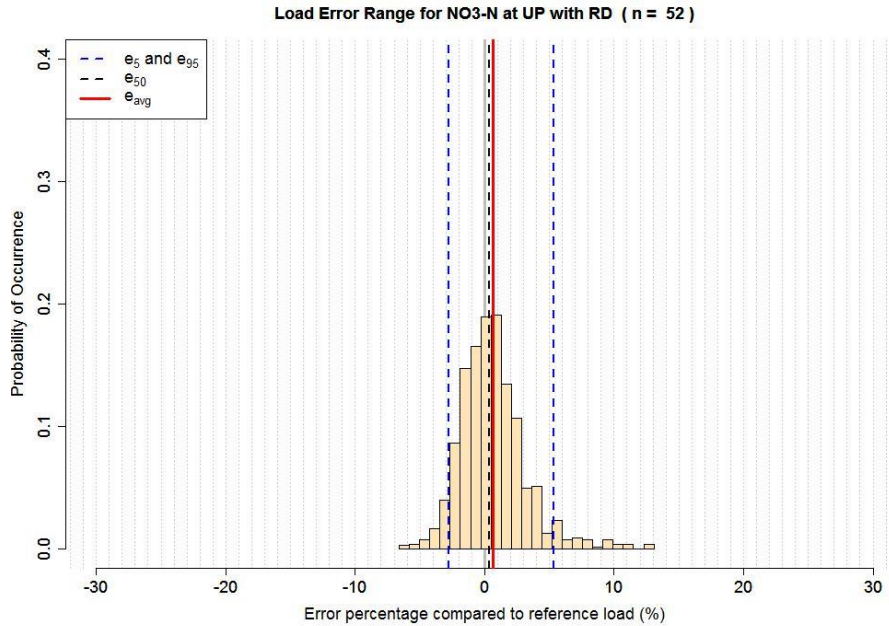


Figure C.5

Distribution of uncertainties estimation presented in the percentage as relative difference of reference annual load expressed as histogram for NO₃-N (uncertainties with the bias [e_{avg} , red solid line or e_{50} , black dash line] and precision [e_5 and e_{95} , blue dash lines, are precision limits of 5th and 95th percentiles, respectively) with random (RD) subset sampling (n = 52) at UP.

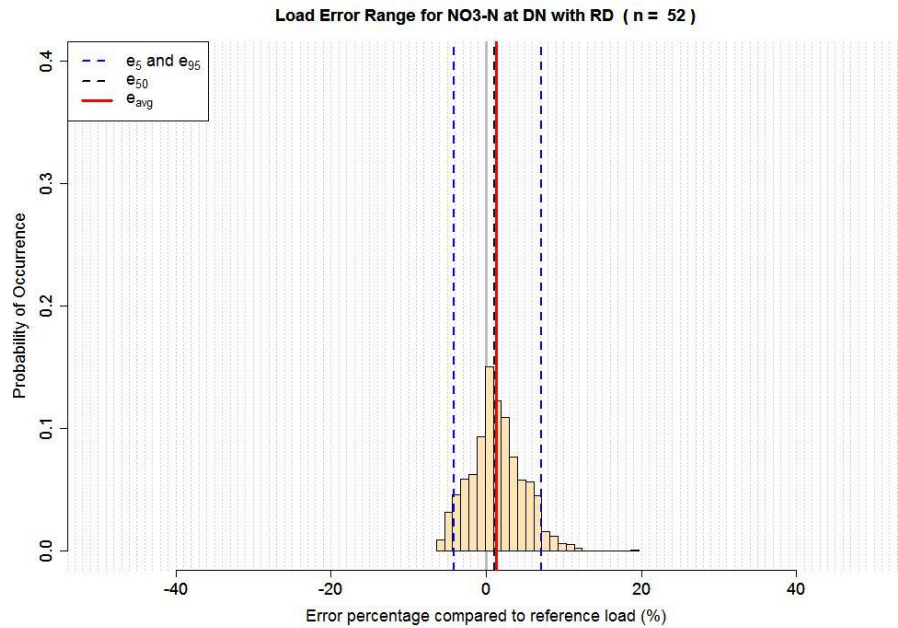


Figure C.6

Distribution of uncertainties estimation presented in the percentage as relative difference of reference annual load expressed as histogram for NO₃-N (uncertainties with the bias [e_{avg} , red solid line or e_{50} , black dash line] and precision [e_5 and e_{95} , blue dash lines, are precision limits of 5th and 95th percentiles, respectively) with random (RD) subset sampling (n = 52) at DN.

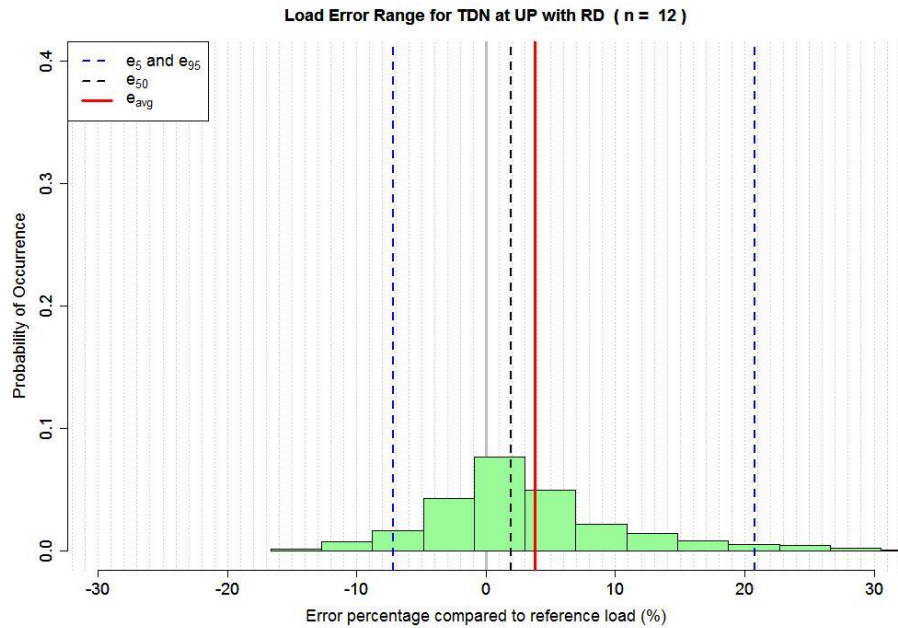


Figure C.7

Distribution of uncertainties estimation presented in the percentage as relative difference of reference annual load expressed as histogram for TDN (uncertainties with the bias [e_{avg} , red solid line or e_{50} , black dash line] and precision [e_5 and e_{95} , blue dash lines, are precision limits of 5th and 95th percentiles, respectively) with random (RD) subset sampling ($n = 12$) at UP.

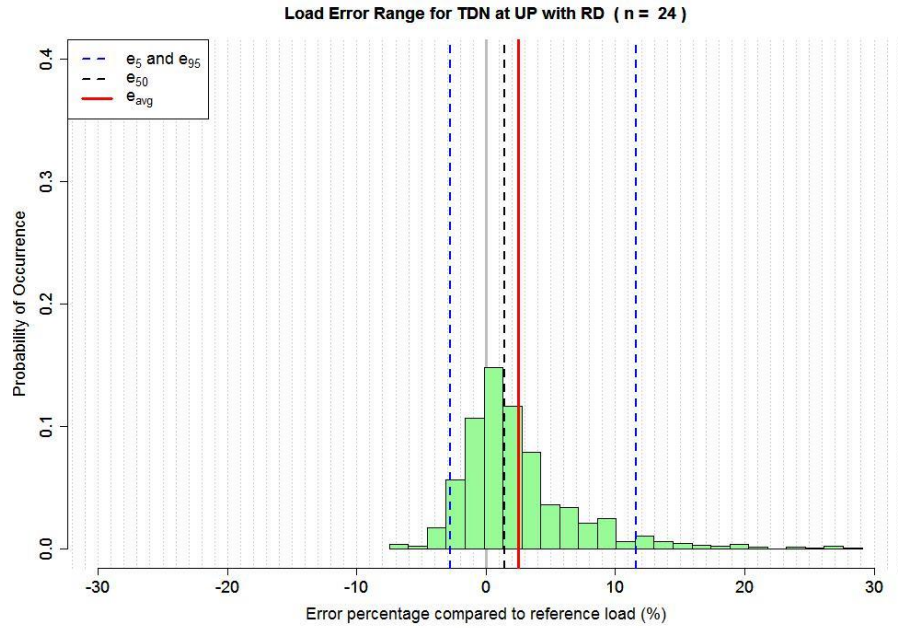


Figure C.8

Distribution of uncertainties estimation presented in the percentage as relative difference of reference annual load expressed as histogram for TDN (uncertainties with the bias [e_{avg} , red solid line or e_{50} , black dash line] and precision [e_5 and e_{95} , blue dash lines, are precision limits of 5th and 95th percentiles, respectively) with random (RD) subset sampling ($n = 24$) at UP.

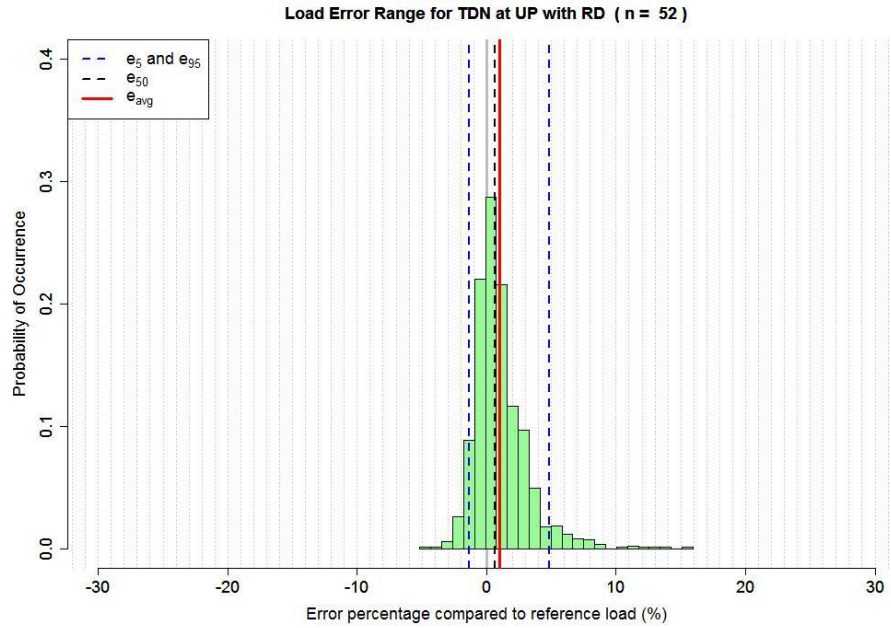


Figure C.9

Distribution of uncertainties estimation presented in the percentage as relative difference of reference annual load expressed as histogram for TDN (uncertainties with the bias [e_{avg} , red solid line or e_{50} , black dash line] and precision [e_5 and e_{95} , blue dash lines, are precision limits of 5th and 95th percentiles, respectively) with random (RD) subset sampling ($n = 52$) at UP.

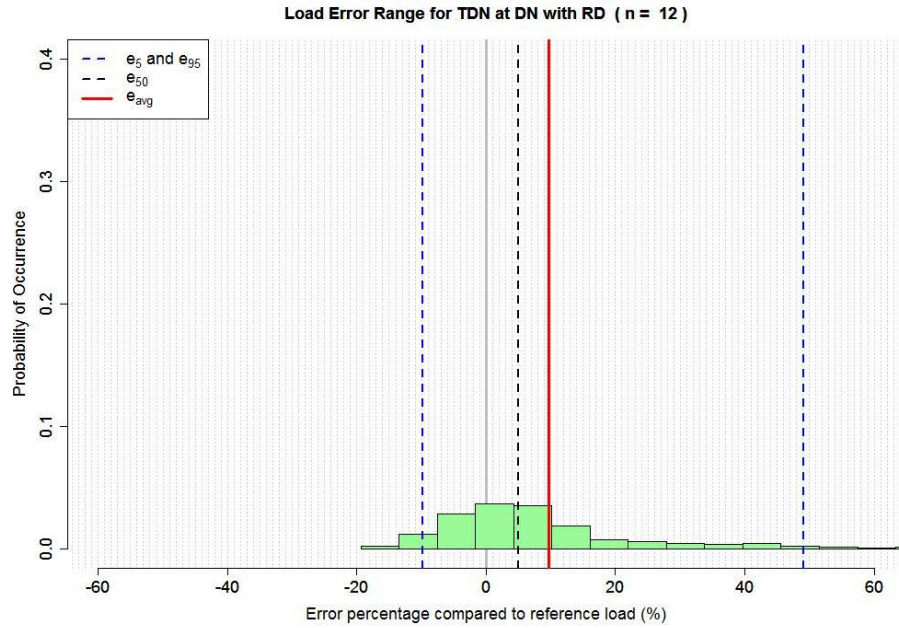


Figure C.10

Distribution of uncertainties estimation presented in the percentage as relative difference of reference annual load expressed as histogram for TDN (uncertainties with the bias [e_{avg} , red solid line or e_{50} , black dash line] and precision [e_5 and e_{95} , blue dash lines, are precision limits of 5th and 95th percentiles, respectively) with random (RD) subset sampling ($n = 12$) at DN.

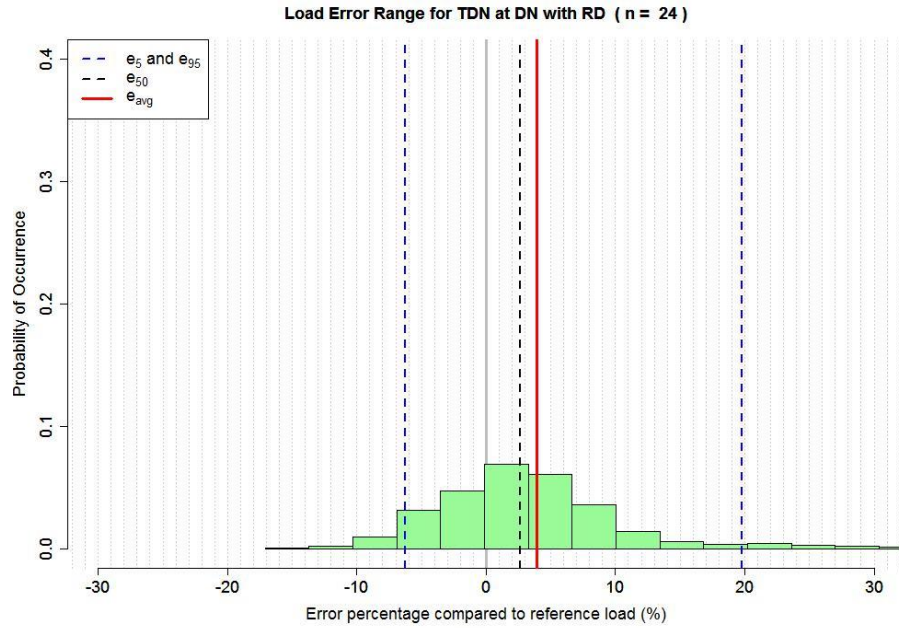


Figure C.11

Distribution of uncertainties estimation presented in the percentage as relative difference of reference annual load expressed as histogram for TDN (uncertainties with the bias [e_{avg} , red solid line or e_{50} , black dash line] and precision [e_5 and e_{95} , blue dash lines, are precision limits of 5th and 95th percentiles, respectively) with random (RD) subset sampling ($n = 24$) at DN.

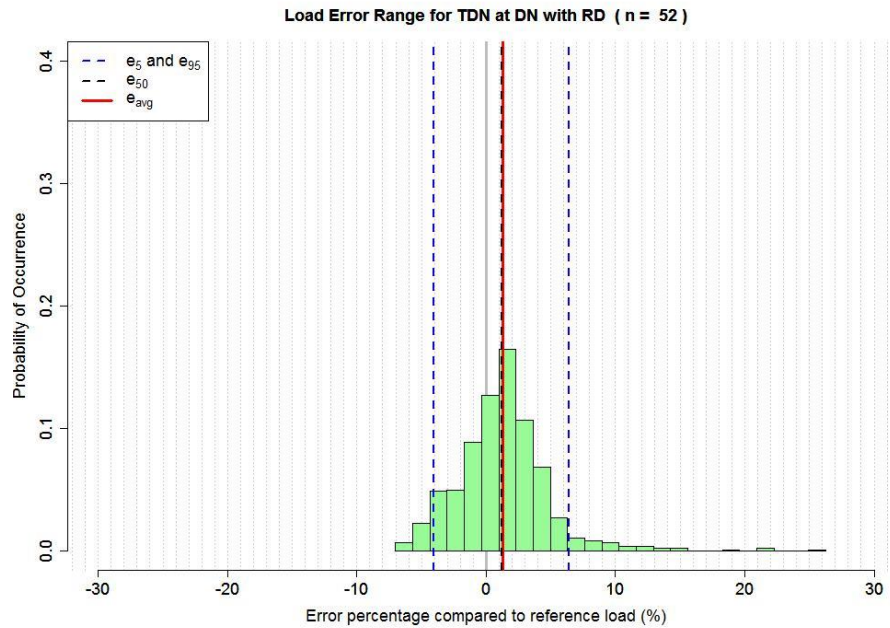


Figure C.12

Distribution of uncertainties estimation presented in the percentage as relative difference of reference annual load expressed as histogram for TDN (uncertainties with the bias [e_{avg} , red solid line or e_{50} , black dash line] and precision [e_5 and e_{95} , blue dash lines, are precision limits of 5th and 95th percentiles, respectively) with random (RD) subset sampling ($n = 52$) at DN.

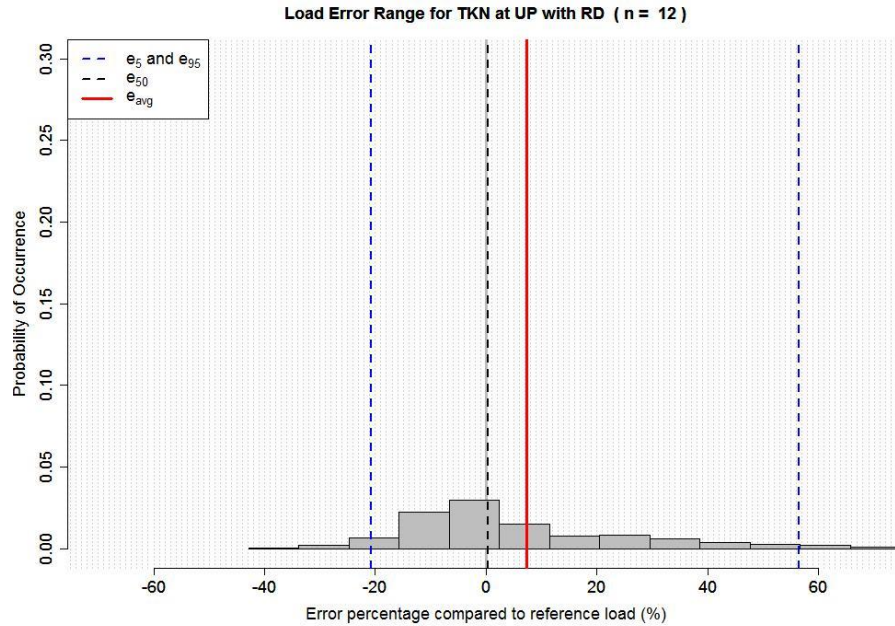


Figure C.13

Distribution of uncertainties estimation presented in the percentage as relative difference of reference annual load expressed as histogram for TKN (uncertainties with the bias [e_{avg} , red solid line or e_{50} , black dash line] and precision [e_5 and e_{95} , blue dash lines, are precision limits of 5th and 95th percentiles, respectively) with random (RD) subset sampling ($n = 12$) at UP.

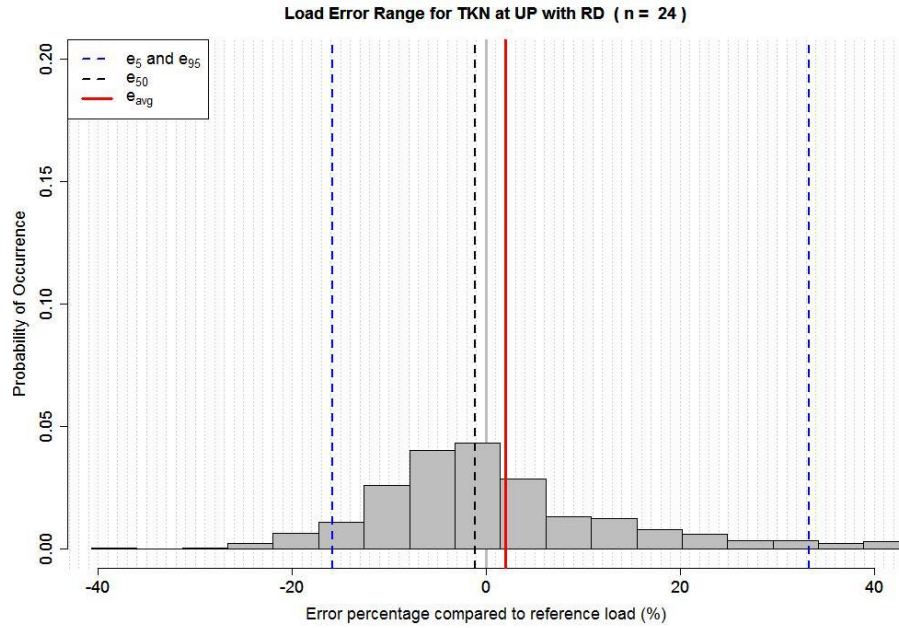


Figure C.14

Distribution of uncertainties estimation presented in the percentage as relative difference of reference annual load expressed as histogram for TKN (uncertainties with the bias [e_{avg} , red solid line or e_{50} , black dash line] and precision [e_5 and e_{95} , blue dash lines, are precision limits of 5th and 95th percentiles, respectively) with random (RD) subset sampling (n = 24) at UP.

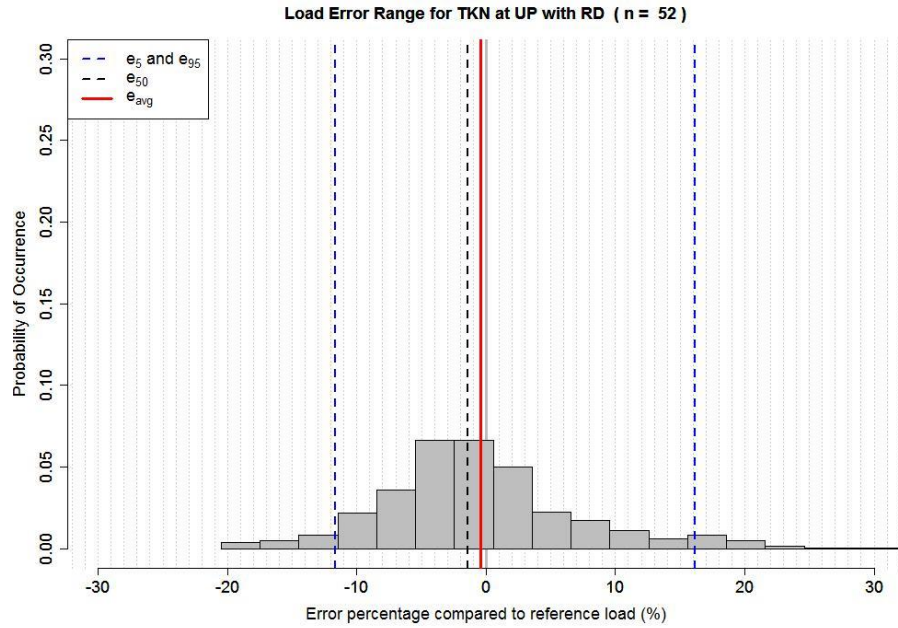


Figure C.15

Distribution of uncertainties estimation presented in the percentage as relative difference of reference annual load expressed as histogram for TKN (uncertainties with the bias [e_{avg} , red solid line or e_{50} , black dash line] and precision [e_5 and e_{95} , blue dash lines, are precision limits of 5th and 95th percentiles, respectively) with random (RD) subset sampling ($n = 52$) at UP.

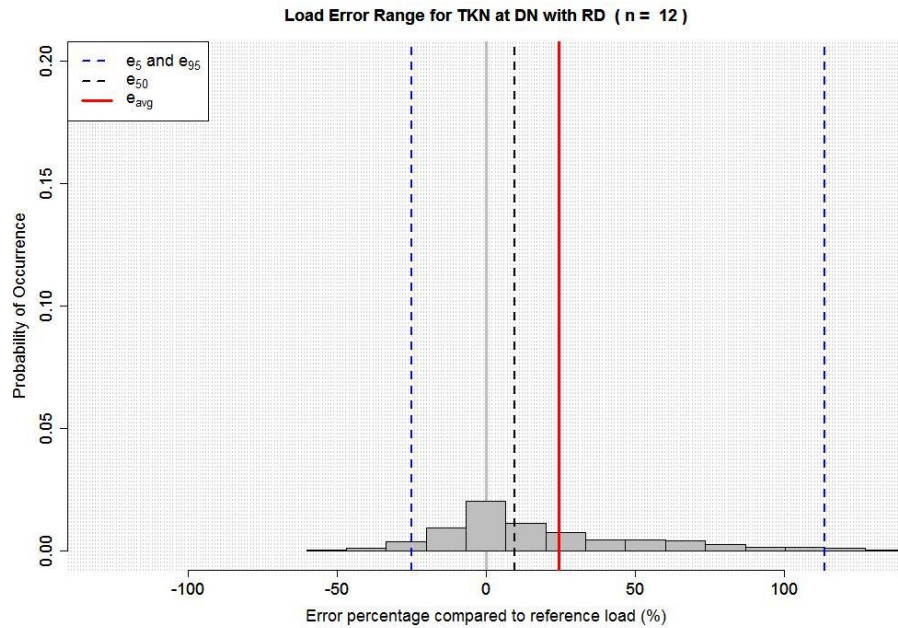


Figure C.16

Distribution of uncertainties estimation presented in the percentage as relative difference of reference annual load expressed as histogram for TKN (uncertainties with the bias [e_{avg} , red solid line or e_{50} , black dash line] and precision [e_5 and e_{95} , blue dash lines, are precision limits of 5th and 95th percentiles, respectively) with random (RD) subset sampling (n = 12) at DN.

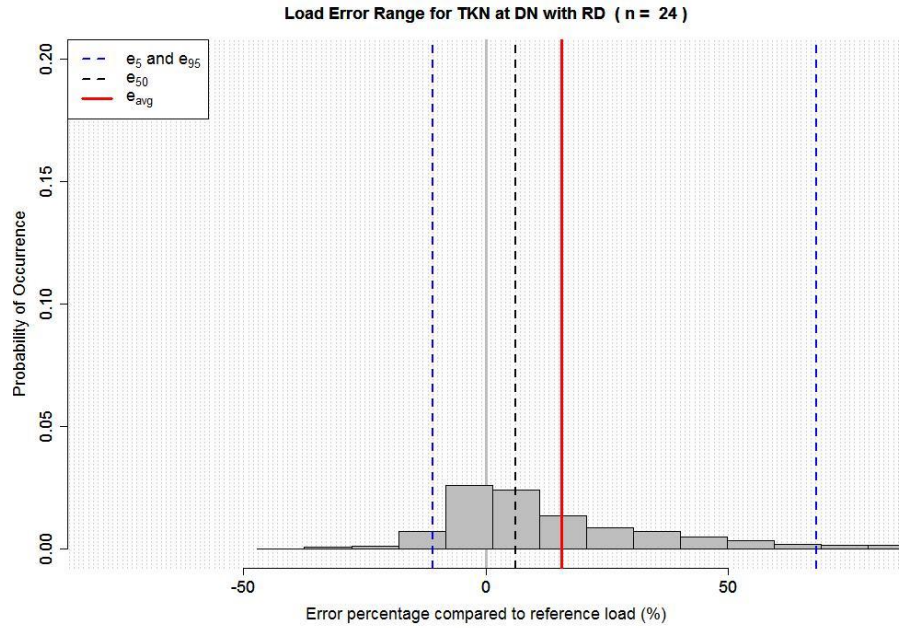


Figure C.17

Distribution of uncertainties estimation presented in the percentage as relative difference of reference annual load expressed as histogram for TKN (uncertainties with the bias [e_{avg} , red solid line or e_{50} , black dash line] and precision [e_5 and e_{95} , blue dash lines, are precision limits of 5th and 95th percentiles, respectively) with random (RD) subset sampling (n = 24) at DN.

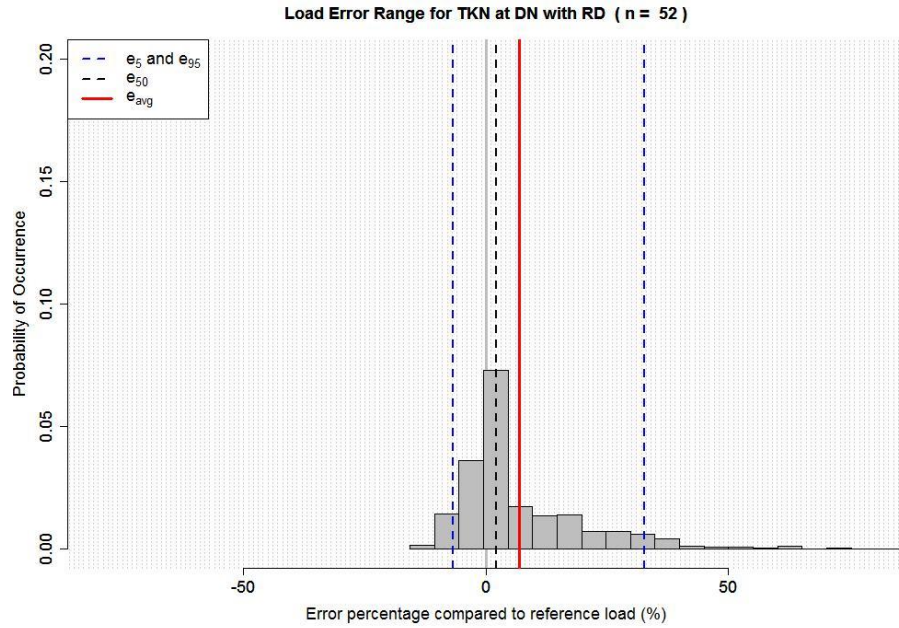


Figure C.18

Distribution of uncertainties estimation presented in the percentage as relative difference of reference annual load expressed as histogram for TKN (uncertainties with the bias [e_{avg} , red solid line or e_{50} , black dash line] and precision [e_5 and e_{95} , blue dash lines, are precision limits of 5th and 95th percentiles, respectively) with random (RD) subset sampling ($n = 52$) at DN.

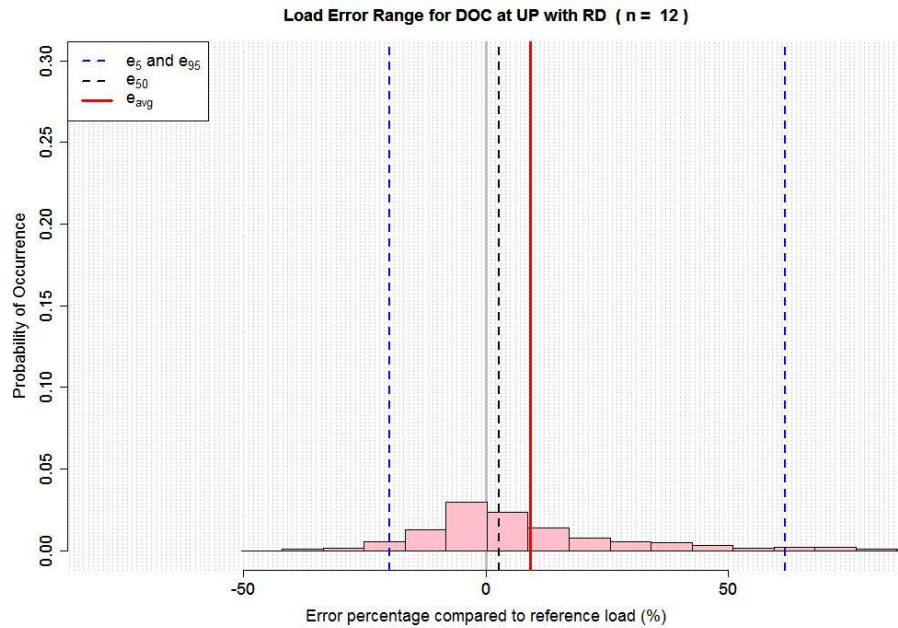


Figure C.19

Distribution of uncertainties estimation presented in the percentage as relative difference of reference annual load expressed as histogram for DOC (uncertainties with the bias [e_{avg} , red solid line or e_{50} , black dash line] and precision [e_5 and e_{95} , blue dash lines, are precision limits of 5th and 95th percentiles, respectively) with random (RD) subset sampling (n = 12) at UP.

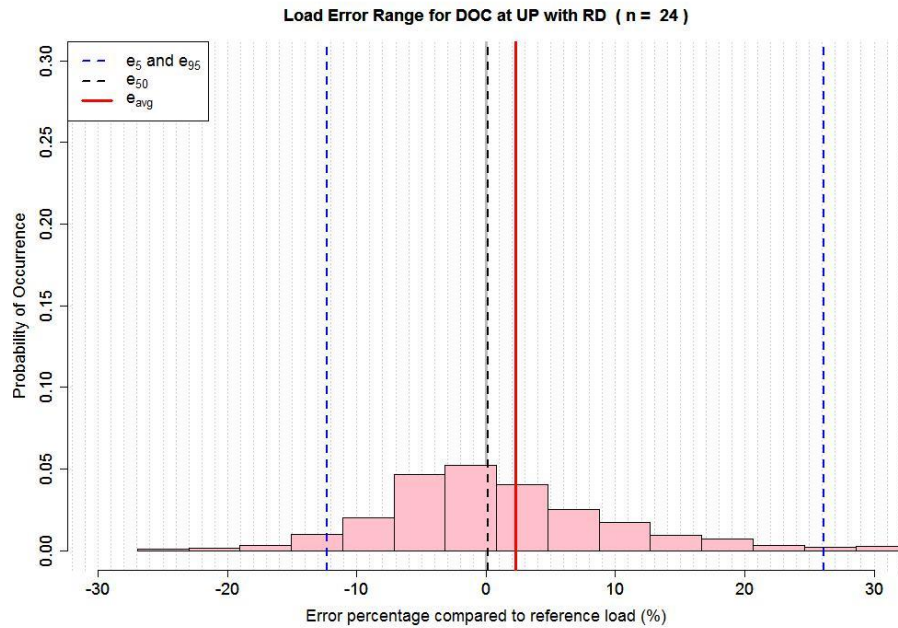


Figure C.20

Distribution of uncertainties estimation presented in the percentage as relative difference of reference annual load expressed as histogram for DOC (uncertainties with the bias [e_{avg} , red solid line or e_{50} , black dash line] and precision [e_5 and e_{95} , blue dash lines, are precision limits of 5th and 95th percentiles, respectively) with random (RD) subset sampling (n = 24) at UP.

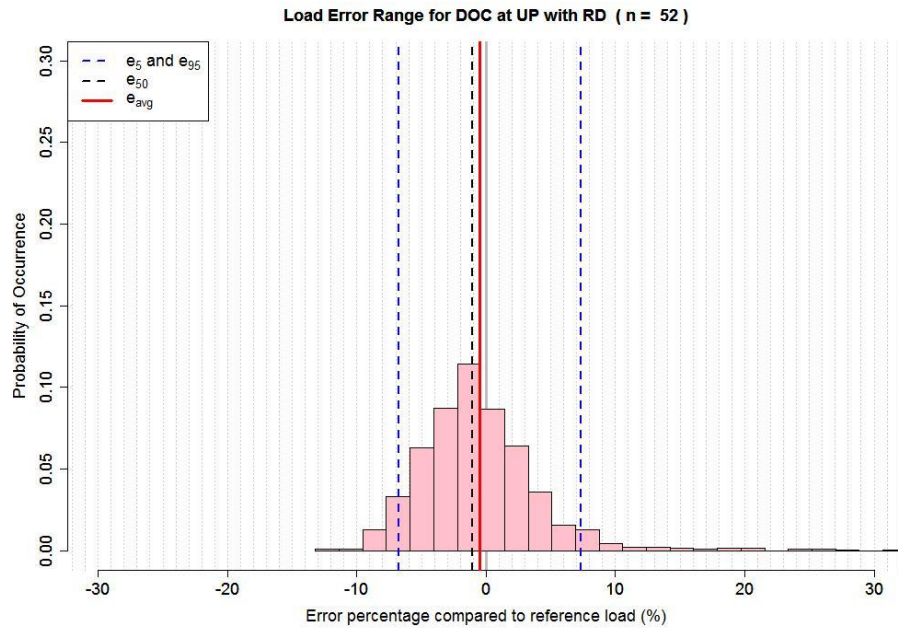


Figure C.21

Distribution of uncertainties estimation presented in the percentage as relative difference of reference annual load expressed as histogram for DOC (uncertainties with the bias [e_{avg} , red solid line or e_{50} , black dash line] and precision [e_5 and e_{95} , blue dash lines, are precision limits of 5th and 95th percentiles, respectively) with random (RD) subset sampling (n = 52) at UP.

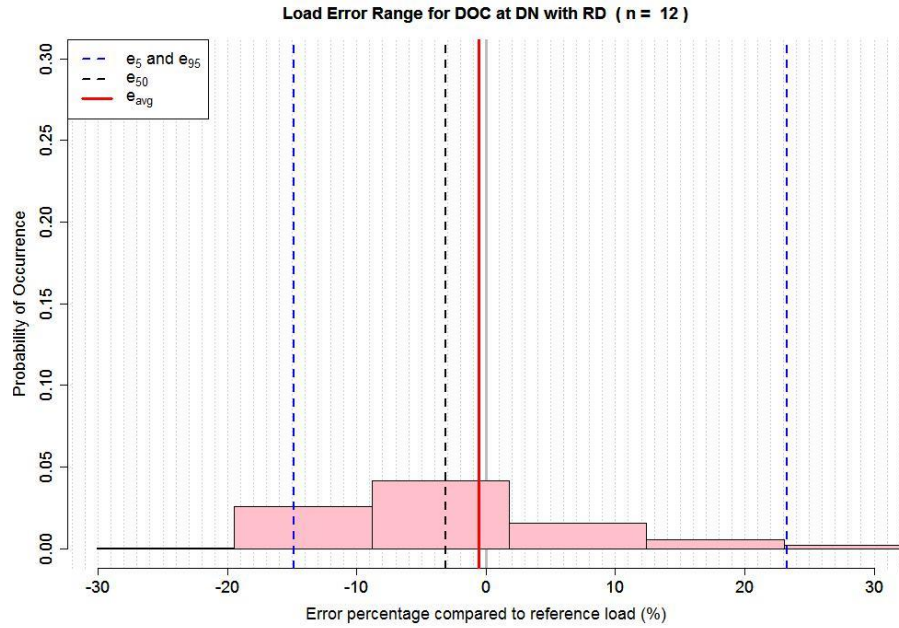


Figure C.22

Distribution of uncertainties estimation presented in the percentage as relative difference of reference annual load expressed as histogram for DOC (uncertainties with the bias [e_{avg} , red solid line or e_{50} , black dash line] and precision [e_5 and e_{95} , blue dash lines, are precision limits of 5th and 95th percentiles, respectively) with random (RD) subset sampling (n = 12) at DN.

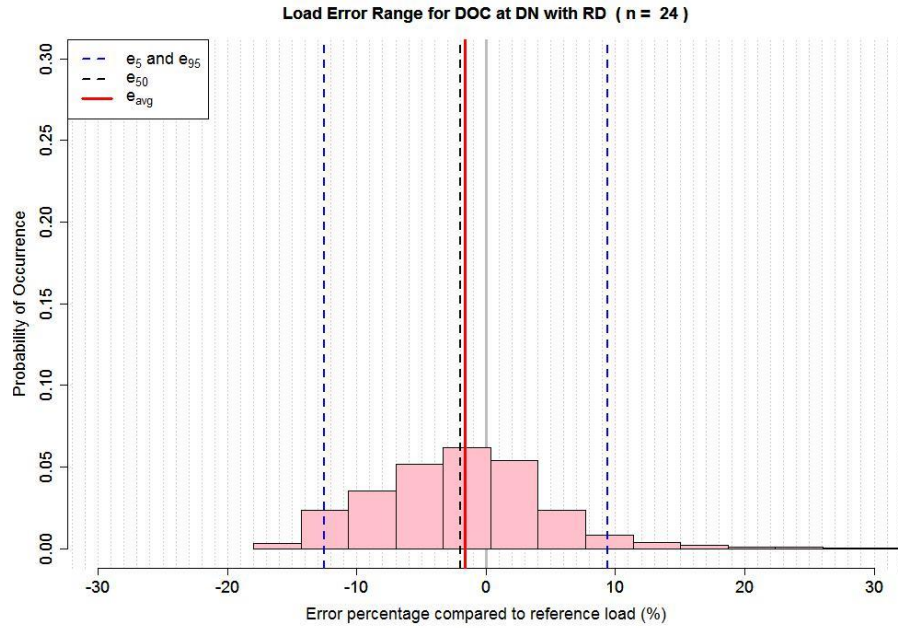


Figure C.23

Distribution of uncertainties estimation presented in the percentage as relative difference of reference annual load expressed as histogram for DOC (uncertainties with the bias [e_{avg} , red solid line or e_{50} , black dash line] and precision [e_5 and e_{95} , blue dash lines, are precision limits of 5th and 95th percentiles, respectively) with random (RD) subset sampling (n = 24) at DN.

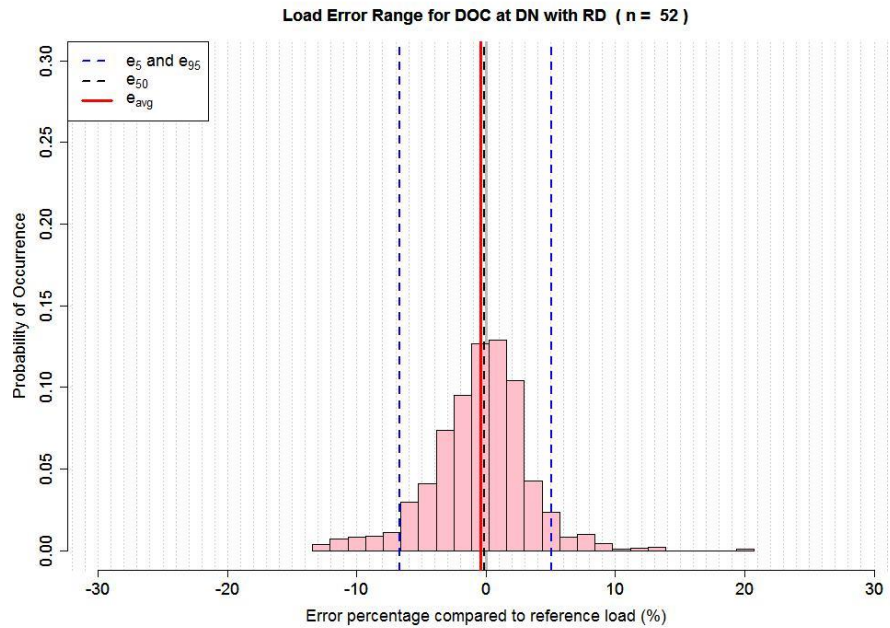


Figure C.24

Distribution of uncertainties estimation presented in the percentage as relative difference of reference annual load expressed as histogram for DOC (uncertainties with the bias [e_{avg} , red solid line or e_{50} , black dash line] and precision [e_5 and e_{95} , blue dash lines, are precision limits of 5th and 95th percentiles, respectively) with random (RD) subset sampling ($n = 52$) at DN.

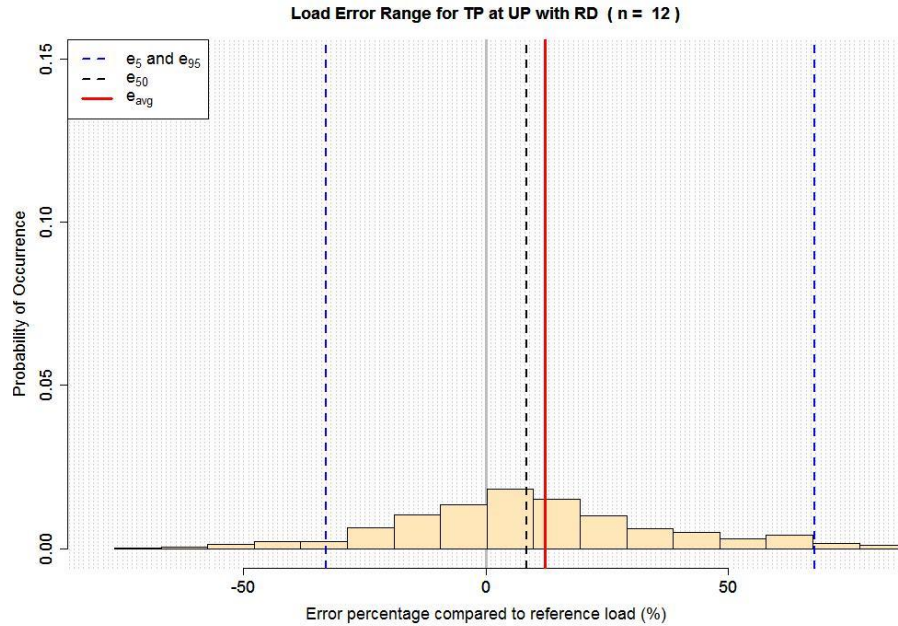


Figure C.25

Distribution of uncertainties estimation presented in the percentage as relative difference of reference annual load expressed as histogram for TP (uncertainties with the bias [e_{avg} , red solid line or e_{50} , black dash line] and precision [e_5 and e_{95} , blue dash lines, are precision limits of 5th and 95th percentiles, respectively) with random (RD) subset sampling (n = 12) at UP.

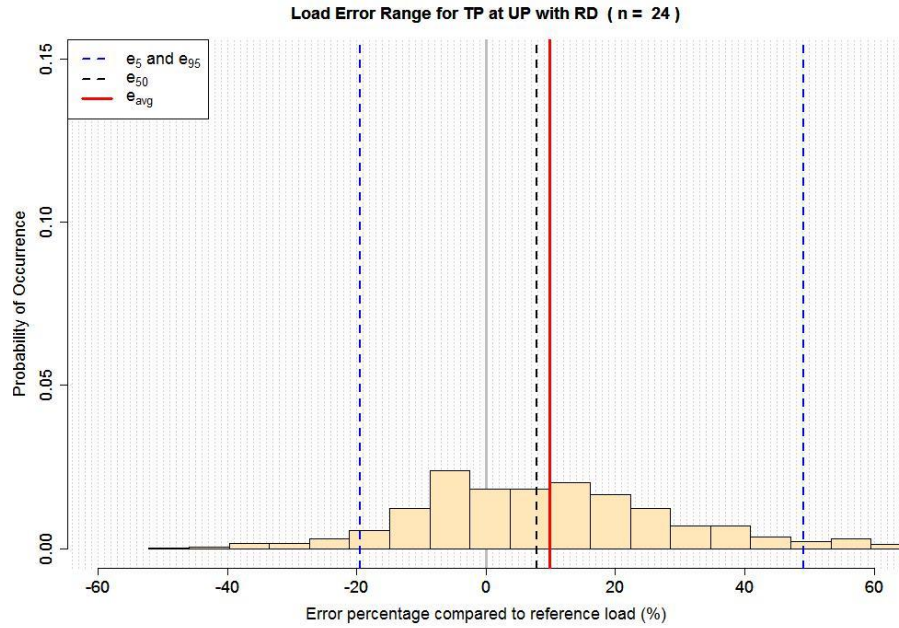


Figure C.26

Distribution of uncertainties estimation presented in the percentage as relative difference of reference annual load expressed as histogram for TP (uncertainties with the bias [e_{avg} , red solid line or e_{50} , black dash line] and precision [e_5 and e_{95} , blue dash lines, are precision limits of 5th and 95th percentiles, respectively) with random (RD) subset sampling ($n = 24$) at UP.

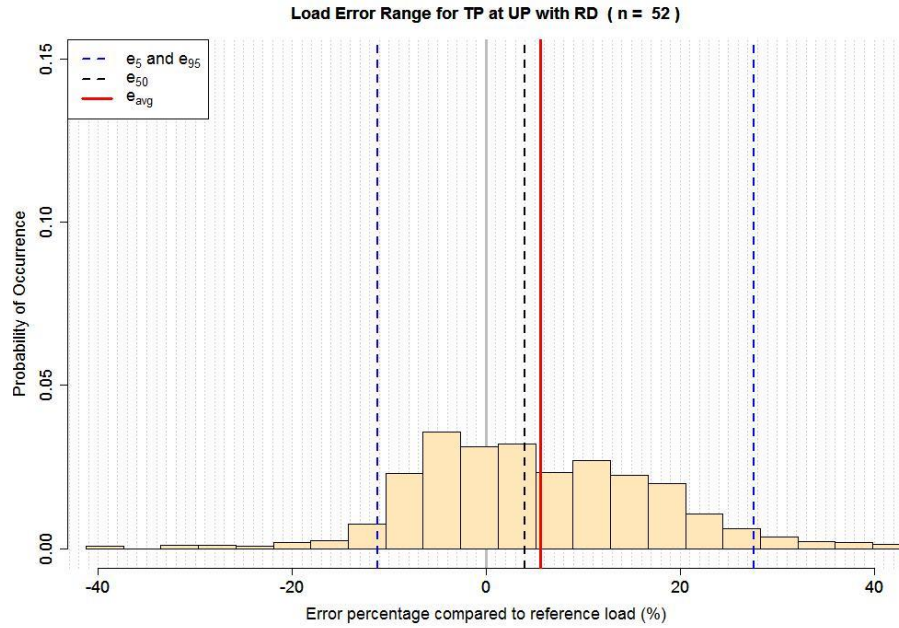


Figure C.27

Distribution of uncertainties estimation presented in the percentage as relative difference of reference annual load expressed as histogram for TP (uncertainties with the bias [e_{avg} , red solid line or e_{50} , black dash line] and precision [e_5 and e_{95} , blue dash lines, are precision limits of 5th and 95th percentiles, respectively) with random (RD) subset sampling ($n = 52$) at UP.

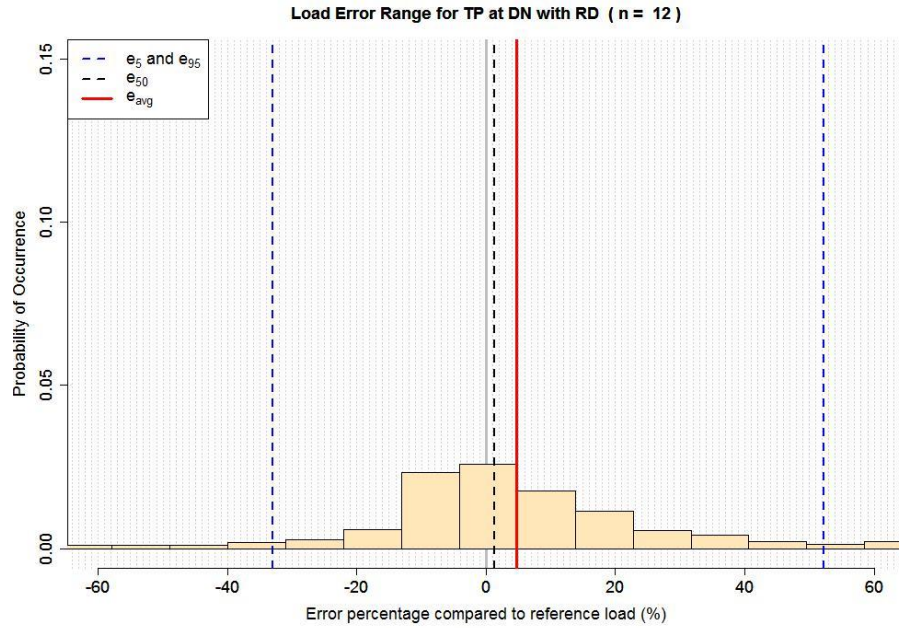


Figure C.28

Distribution of uncertainties estimation presented in the percentage as relative difference of reference annual load expressed as histogram for TP (uncertainties with the bias [e_{avg} , red solid line or e_{50} , black dash line] and precision [e_5 and e_{95} , blue dash lines, are precision limits of 5th and 95th percentiles, respectively) with random (RD) subset sampling (n = 12) at DN.

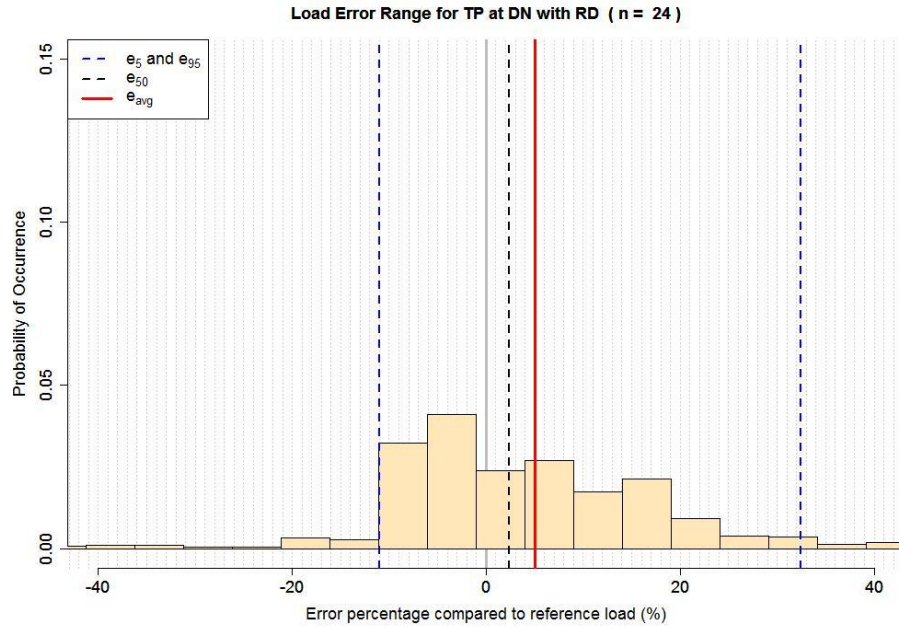


Figure C.29

Distribution of uncertainties estimation presented in the percentage as relative difference of reference annual load expressed as histogram for TP (uncertainties with the bias [e_{avg} , red solid line or e_{50} , black dash line] and precision [e_5 and e_{95} , blue dash lines, are precision limits of 5th and 95th percentiles, respectively) with random (RD) subset sampling ($n = 24$) at DN.

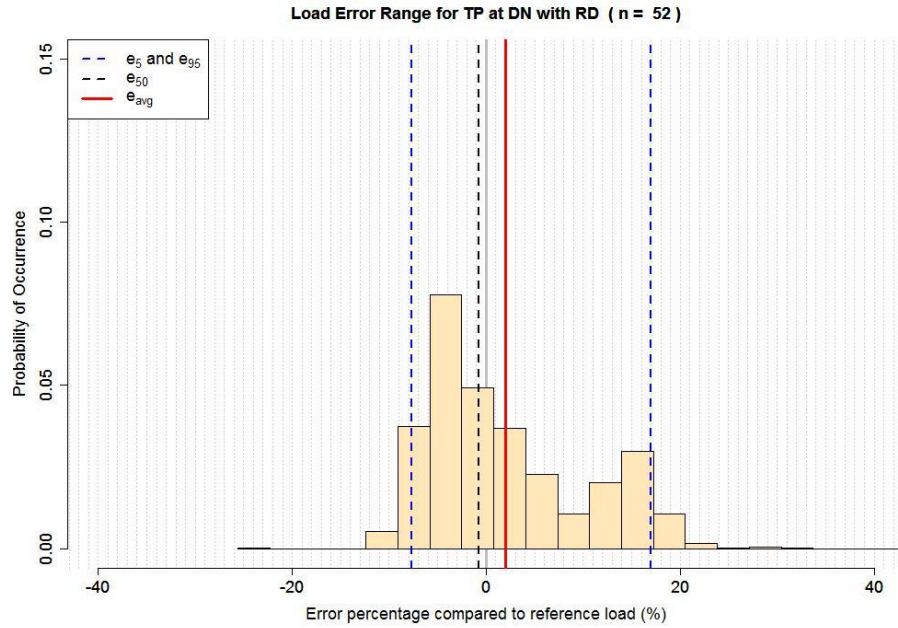


Figure C.30

Distribution of uncertainties estimation presented in the percentage as relative difference of reference annual load expressed as histogram for TP (uncertainties with the bias [e_{avg} , red solid line or e_{50} , black dash line] and precision [e_5 and e_{95} , blue dash lines, are precision limits of 5th and 95th percentiles, respectively) with random (RD) subset sampling (n = 52) at DN.

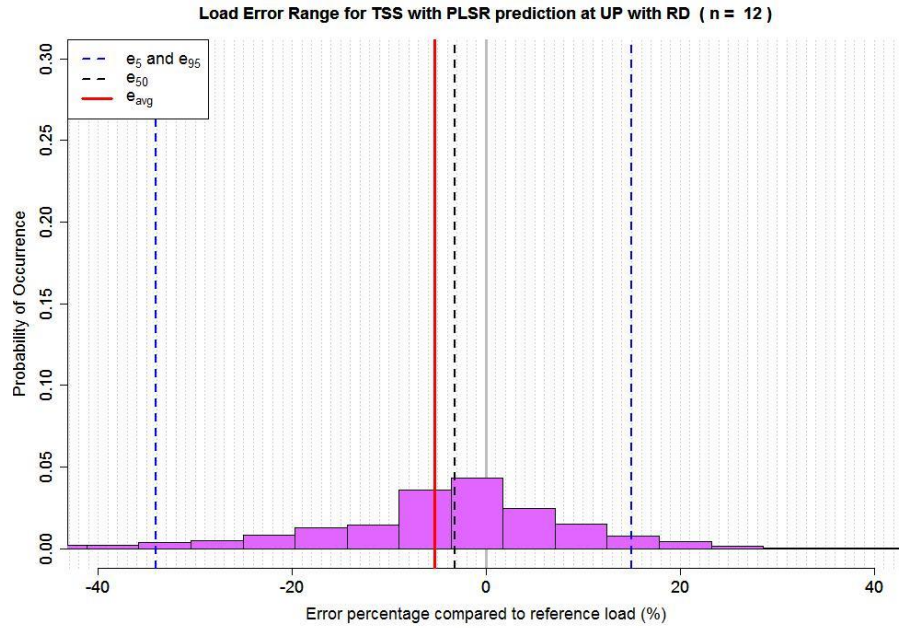


Figure C.31

Distribution of uncertainties estimation presented in the percentage as relative difference of reference annual load expressed as histogram for TSS with PLSR prediction (uncertainties with the bias [e_{avg} , red solid line or e_{50} , black dash line] and precision [e_5 and e_{95} , blue dash lines, are precision limits of 5th and 95th percentiles, respectively) with random (RD) subset sampling (n = 12) at UP.

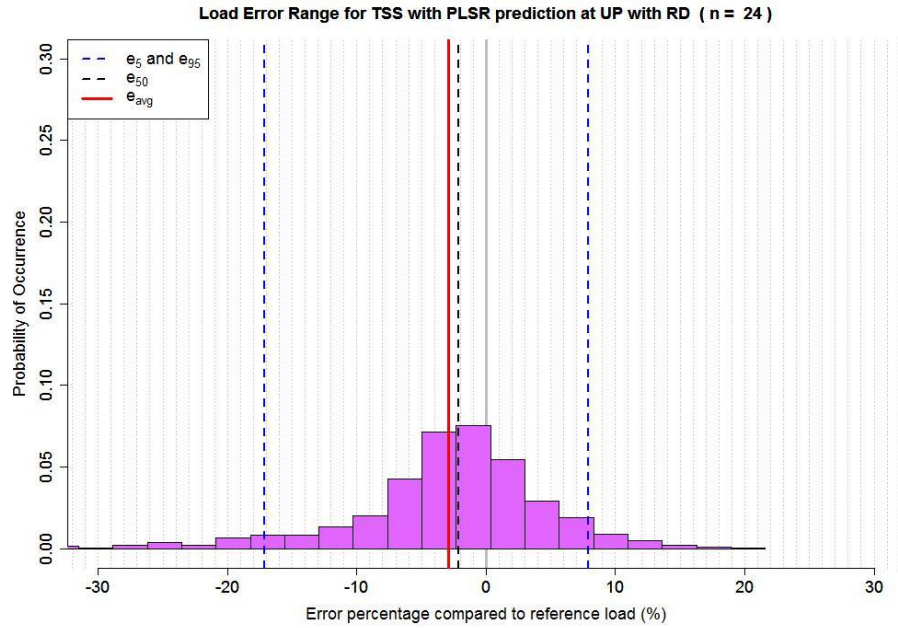


Figure C.32

Distribution of uncertainties estimation presented in the percentage as relative difference of reference annual load expressed as histogram for TSS with PLSR prediction (uncertainties with the bias [e_{avg} , red solid line or e_{50} , black dash line] and precision [e_5 and e_{95} , blue dash lines, are precision limits of 5th and 95th percentiles, respectively) with random (RD) subset sampling (n = 24) at UP.

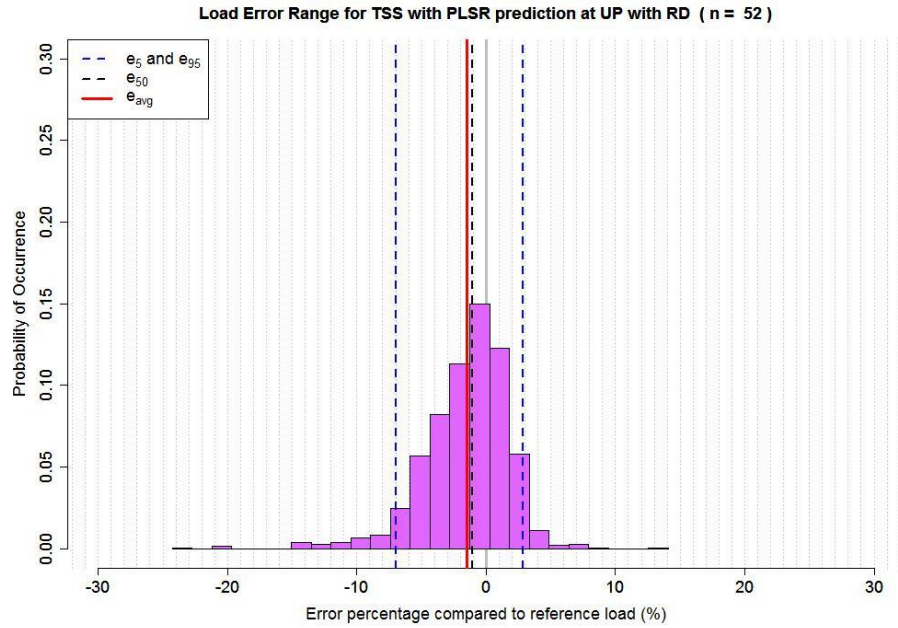


Figure C.33

Distribution of uncertainties estimation presented in the percentage as relative difference of reference annual load expressed as histogram for TSS with PLSR prediction (uncertainties with the bias [e_{avg} , red solid line or e_{50} , black dash line] and precision [e_5 and e_{95} , blue dash lines, are precision limits of 5th and 95th percentiles, respectively) with random (RD) subset sampling (n = 52) at UP.

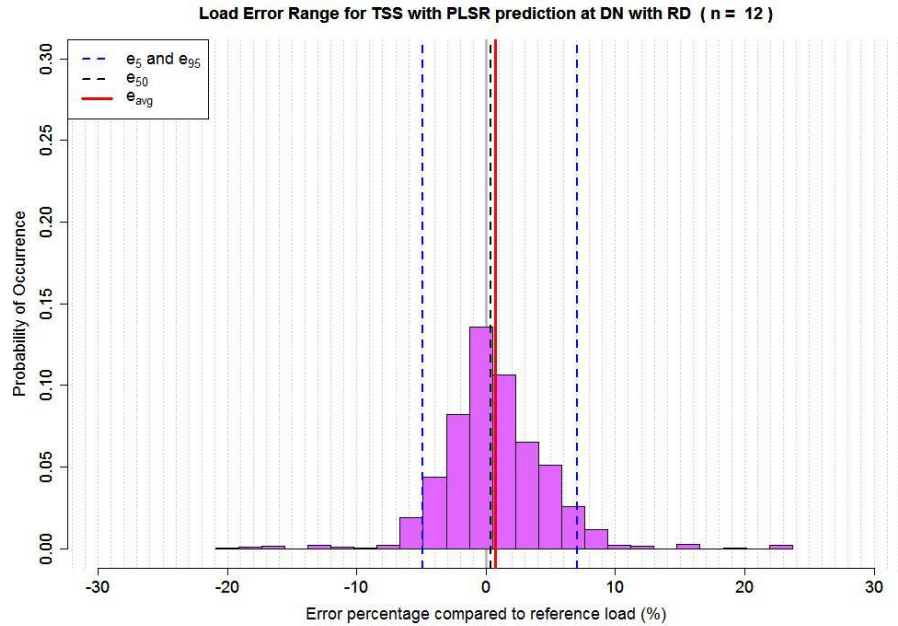


Figure C.34

Distribution of uncertainties estimation presented in the percentage as relative difference of reference annual load expressed as histogram for TSS with PLSR prediction (uncertainties with the bias [e_{avg} , red solid line or e_{50} , black dash line] and precision [e_5 and e_{95} , blue dash lines, are precision limits of 5th and 95th percentiles, respectively) with random (RD) subset sampling (n = 12) at DN.

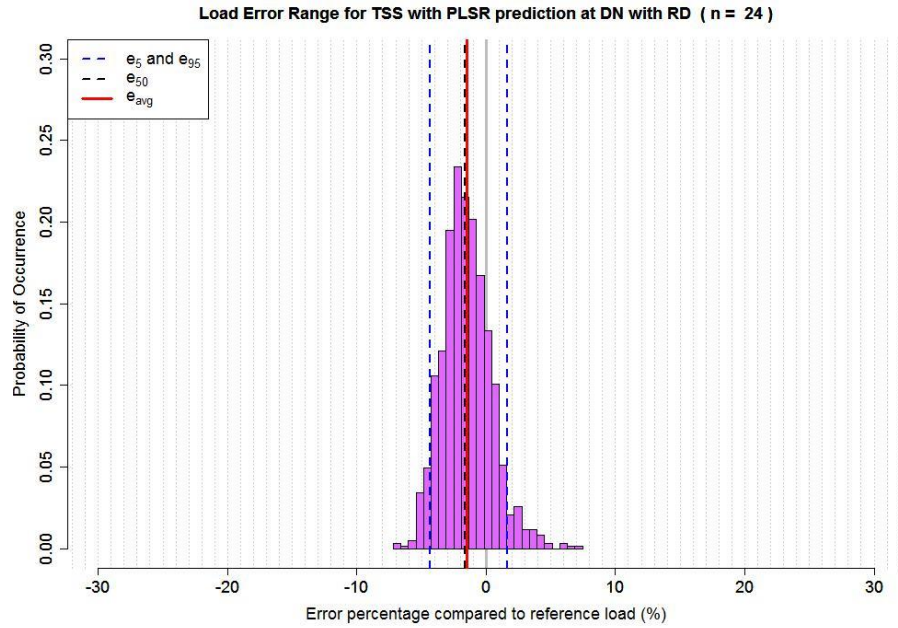


Figure C.35

Distribution of uncertainties estimation presented in the percentage as relative difference of reference annual load expressed as histogram for TSS with PLSR prediction (uncertainties with the bias [e_{avg} , red solid line or e_{50} , black dash line] and precision [e_5 and e_{95} , blue dash lines, are precision limits of 5th and 95th percentiles, respectively) with random (RD) subset sampling (n = 24) at DN.

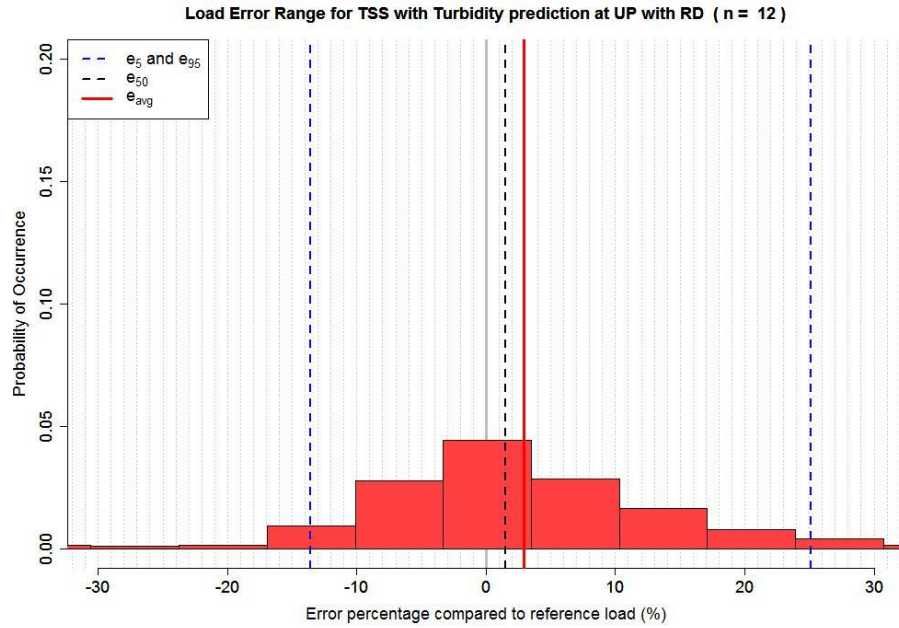


Figure C.36

Distribution of uncertainties estimation presented in the percentage as relative difference of reference annual load expressed as histogram for TSS with Turbidity prediction (uncertainties with the bias [e_{avg} , red solid line or e_{50} , black dash line] and precision [e_5 and e_{95} , blue dash lines, are precision limits of 5th and 95th percentiles, respectively) with random (RD) subset sampling (n = 12) at UP.

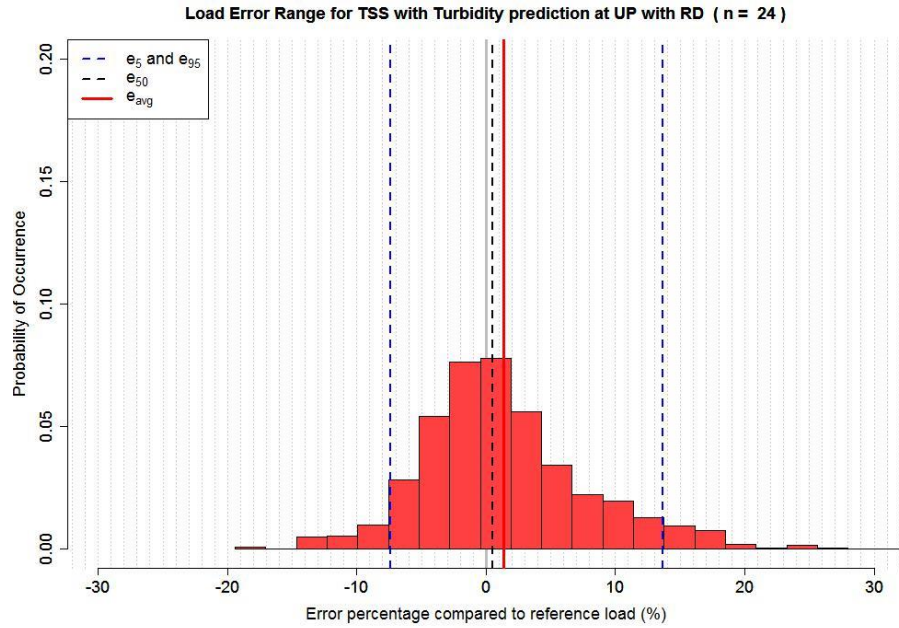


Figure C.37

Distribution of uncertainties estimation presented in the percentage as relative difference of reference annual load expressed as histogram for TSS with Turbidity prediction (uncertainties with the bias [e_{avg} , red solid line or e_{50} , black dash line] and precision [e_5 and e_{95} , blue dash lines, are precision limits of 5th and 95th percentiles, respectively) with random (RD) subset sampling (n = 24) at UP.

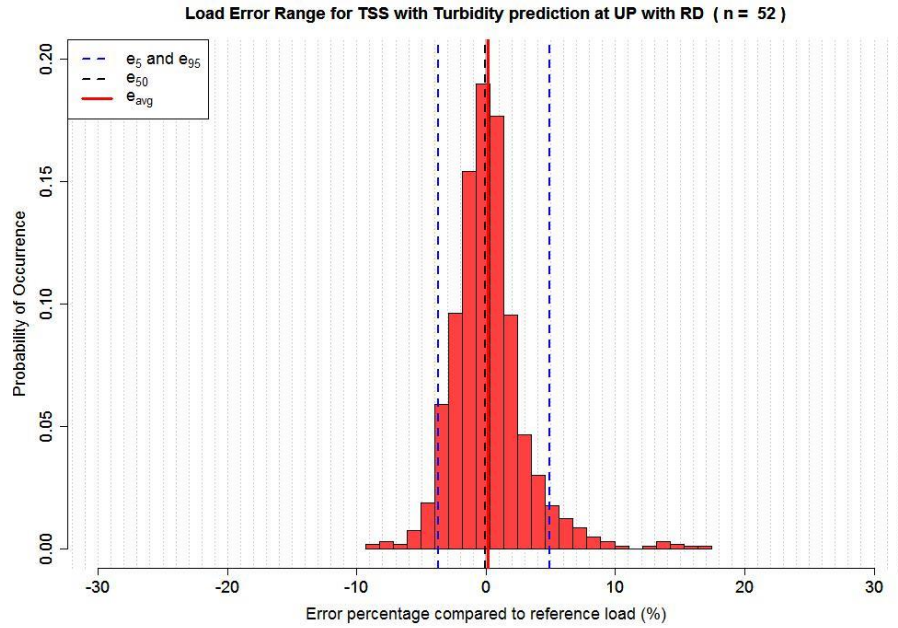


Figure C.38

Distribution of uncertainties estimation presented in the percentage as relative difference of reference annual load expressed as histogram for TSS with Turbidity prediction (uncertainties with the bias [e_{avg} , red solid line or e_{50} , black dash line] and precision [e_5 and e_{95} , blue dash lines, are precision limits of 5th and 95th percentiles, respectively) with random (RD) subset sampling (n = 52) at UP.

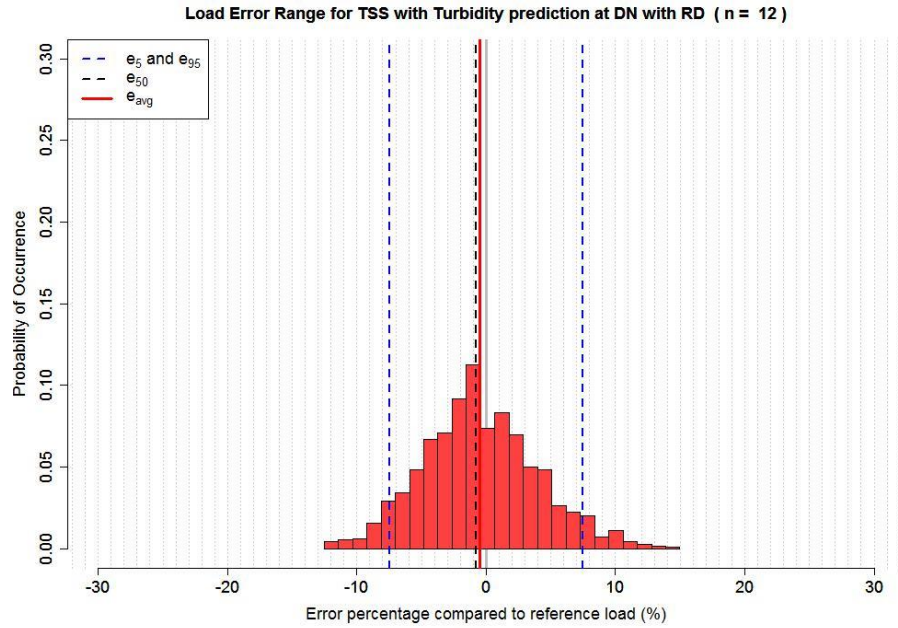


Figure C.39

Distribution of uncertainties estimation presented in the percentage as relative difference of reference annual load expressed as histogram for TSS with Turbidity prediction (uncertainties with the bias [e_{avg} , red solid line or e_{50} , black dash line] and precision [e_5 and e_{95} , blue dash lines, are precision limits of 5th and 95th percentiles, respectively) with random (RD) subset sampling (n = 12) at DN.

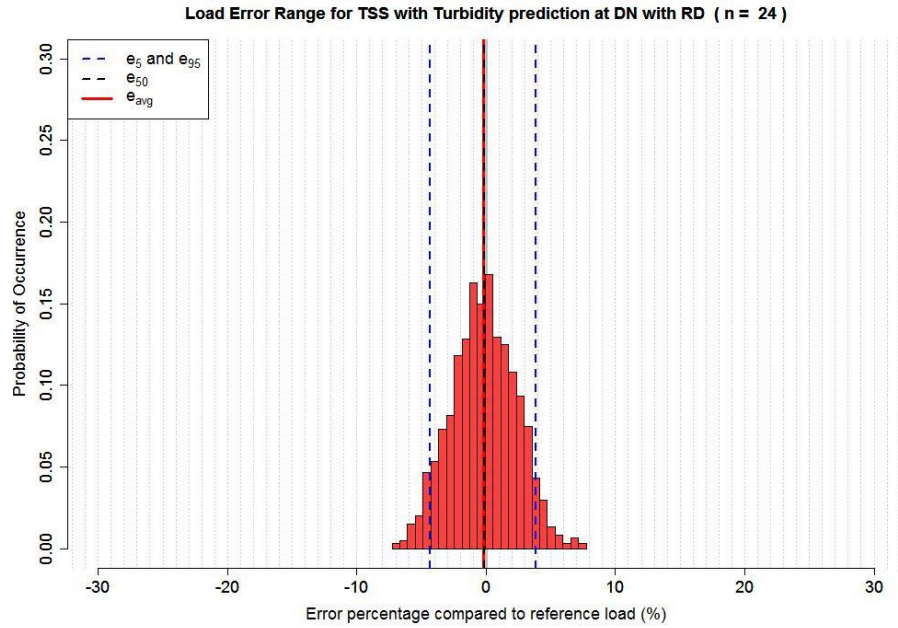


Figure C.40

Distribution of uncertainties estimation presented in the percentage as relative difference of reference annual load expressed as histogram for TSS with Turbidity prediction (uncertainties with the bias [e_{avg} , red solid line or e_{50} , black dash line] and precision [e_5 and e_{95} , blue dash lines, are precision limits of 5th and 95th percentiles, respectively) with random (RD) subset sampling (n = 24) at DN.

Appendix D: Uncertainties estimations for annual loads for different stream solutes with stratified sampling

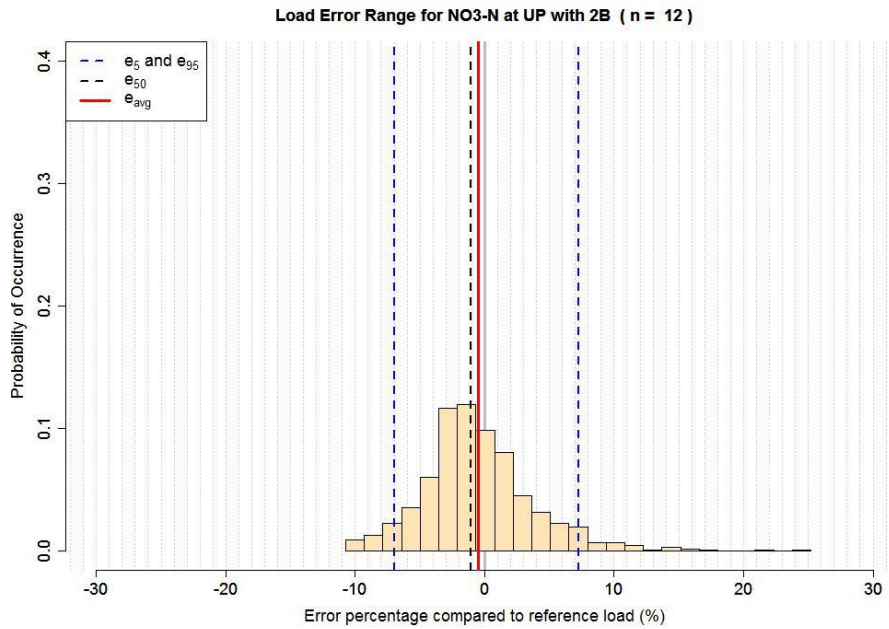


Figure D.1

Distribution of uncertainties estimation presented in the percentage as relative difference of reference annual load expressed as histogram for NO₃-N (uncertainties with the bias [e_{avg} , red solid line or e_{50} , black dash line] and precision [e_5 and e_{95} , blue dash lines, are precision limits of 5th and 95th percentiles, respectively) with stratified sampling (2B, n = 12) at UP.

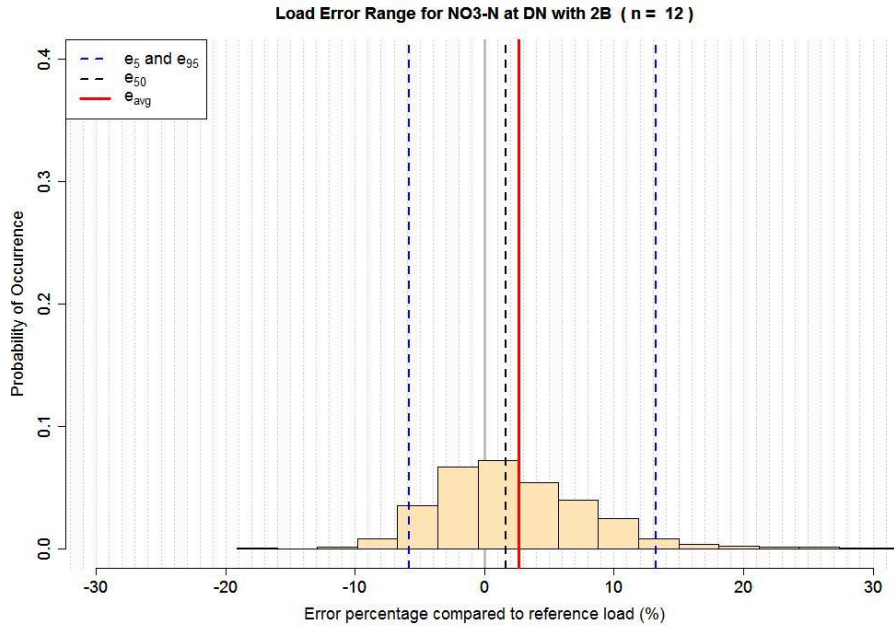


Figure D.2

Distribution of uncertainties estimation presented in the percentage as relative difference of reference annual load expressed as histogram for NO₃-N (uncertainties with the bias [e_{avg} , red solid line or e_{50} , black dash line] and precision [e_5 and e_{95} , blue dash lines, are precision limits of 5th and 95th percentiles, respectively) with stratified sampling (2B, n = 12) at DN.

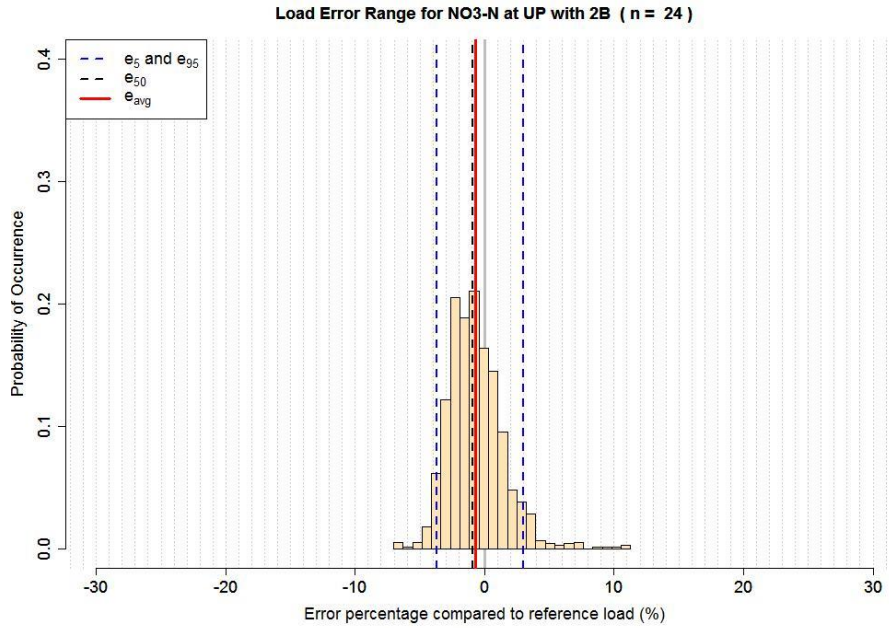


Figure D.3

Distribution of uncertainties estimation presented in the percentage as relative difference of reference annual load expressed as histogram for NO₃-N (uncertainties with the bias [e_{avg} , red solid line or e_{50} , black dash line] and precision [e_5 and e_{95} , blue dash lines, are precision limits of 5th and 95th percentiles, respectively) with stratified sampling (2B, n = 24) at UP.

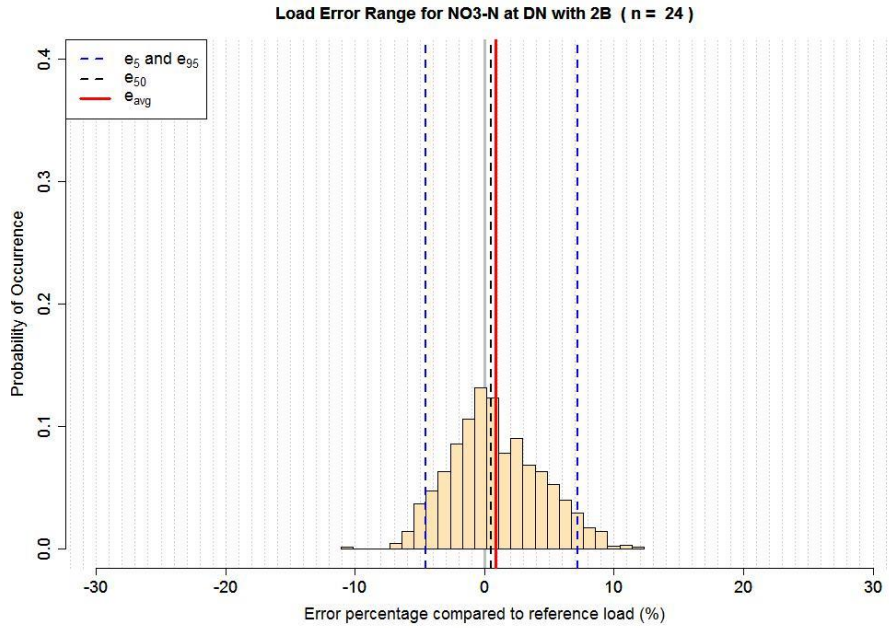


Figure D.4

Distribution of uncertainties estimation presented in the percentage as relative difference of reference annual load expressed as histogram for NO₃-N (uncertainties with the bias [e_{avg} , red solid line or e_{50} , black dash line] and precision [e_5 and e_{95} , blue dash lines, are precision limits of 5th and 95th percentiles, respectively) with stratified sampling (2B, n = 24) at DN.

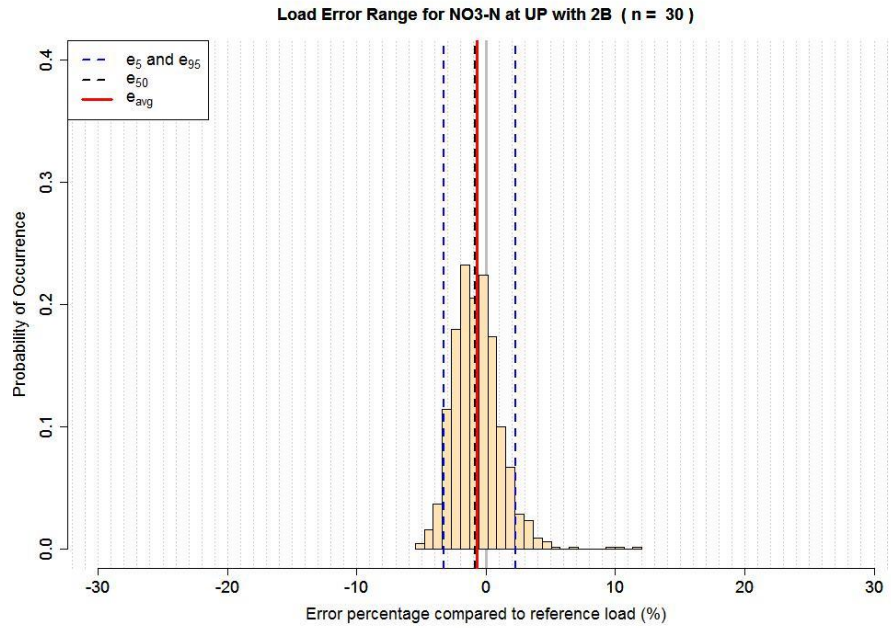


Figure D.5

Distribution of uncertainties estimation presented in the percentage as relative difference of reference annual load expressed as histogram for NO₃-N (uncertainties with the bias [e_{avg} , red solid line or e_{50} , black dash line] and precision [e_5 and e_{95} , blue dash lines, are precision limits of 5th and 95th percentiles, respectively) with stratified sampling (2B, n = 30) at UP.

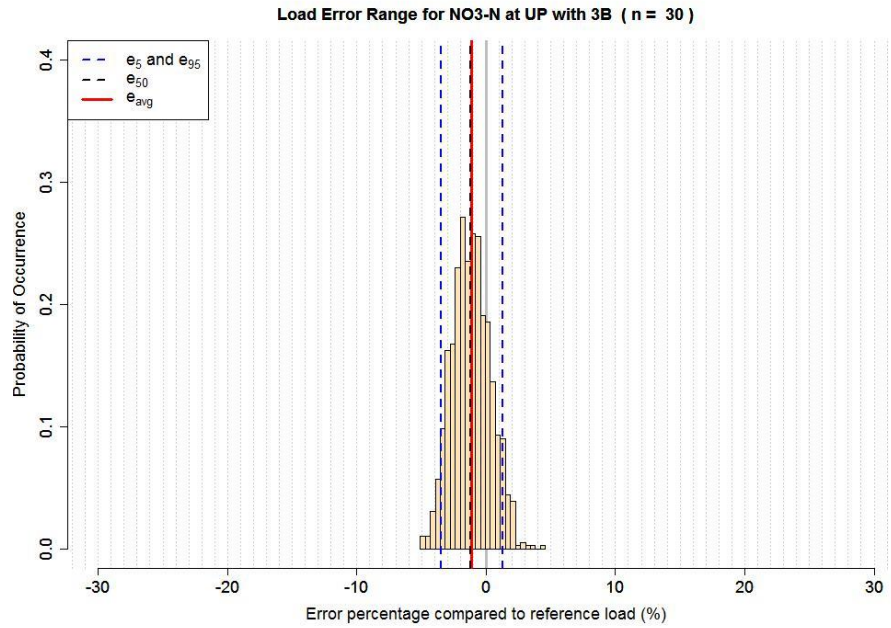


Figure D.6

Distribution of uncertainties estimation presented in the percentage as relative difference of reference annual load expressed as histogram for NO₃-N (uncertainties with the bias [e_{avg} , red solid line or e_{50} , black dash line] and precision [e_5 and e_{95} , blue dash lines, are precision limits of 5th and 95th percentiles, respectively) with stratified sampling (3B, n = 30) at UP.

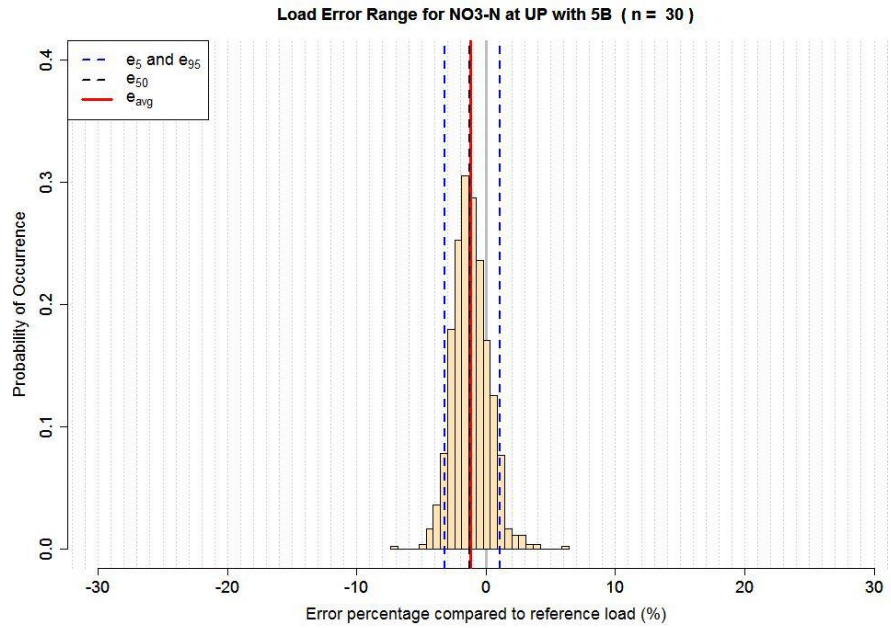


Figure D.7

Distribution of uncertainties estimation presented in the percentage as relative difference of reference annual load expressed as histogram for NO₃-N (uncertainties with the bias [e_{avg}, red solid line or e₅₀, black dash line] and precision [e₅ and e₉₅, blue dash lines, are precision limits of 5th and 95th percentiles, respectively) with stratified sampling (5B, n = 30) at UP.

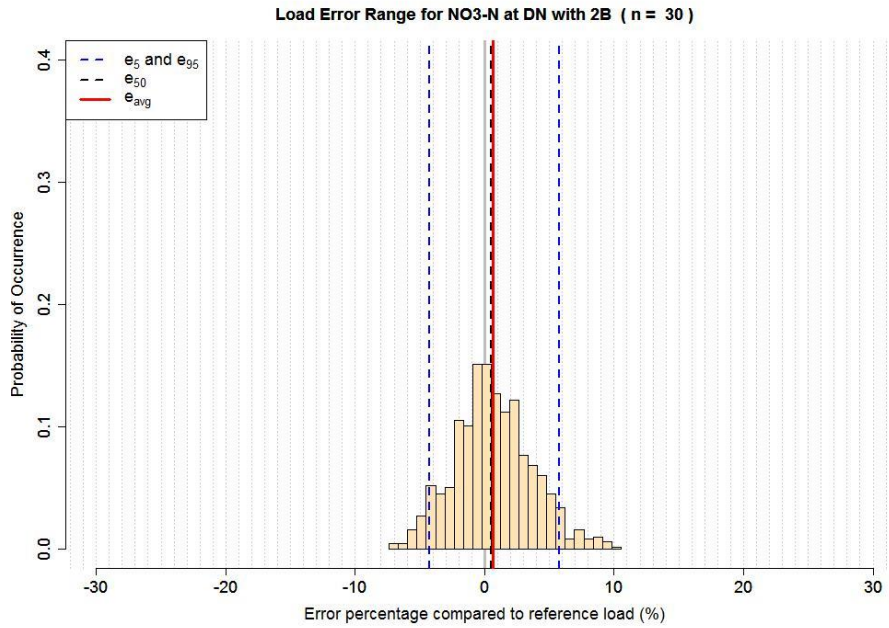


Figure D.8

Distribution of uncertainties estimation presented in the percentage as relative difference of reference annual load expressed as histogram for NO₃-N (uncertainties with the bias [e_{avg}, red solid line or e₅₀, black dash line] and precision [e₅ and e₉₅, blue dash lines, are precision limits of 5th and 95th percentiles, respectively) with stratified sampling (2B, n = 30) at DN.

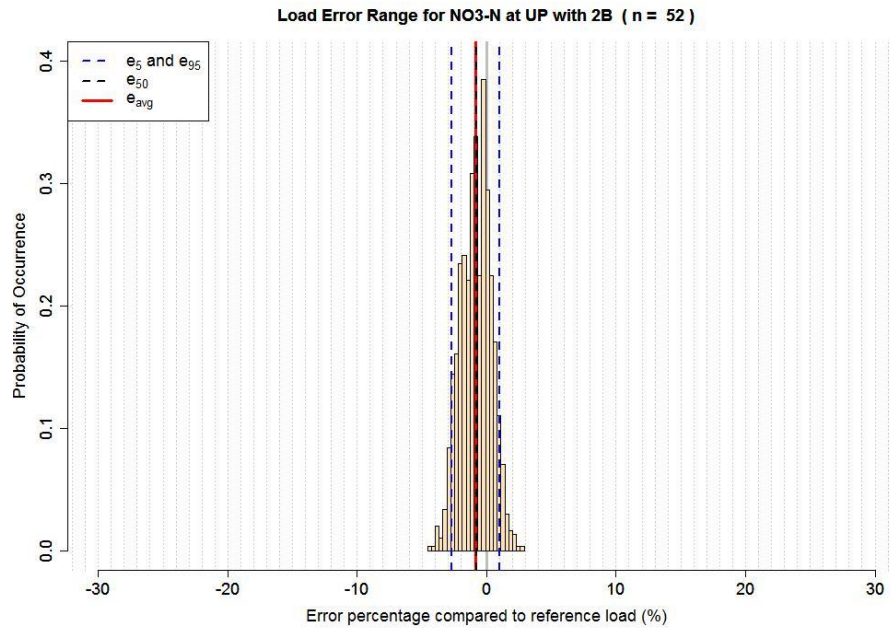


Figure D.9

Distribution of uncertainties estimation presented in the percentage as relative difference of reference annual load expressed as histogram for NO₃-N (uncertainties with the bias [e_{avg} , red solid line or e_{50} , black dash line] and precision [e_5 and e_{95} , blue dash lines, are precision limits of 5th and 95th percentiles, respectively) with stratified sampling (2B, n = 52) at UP.

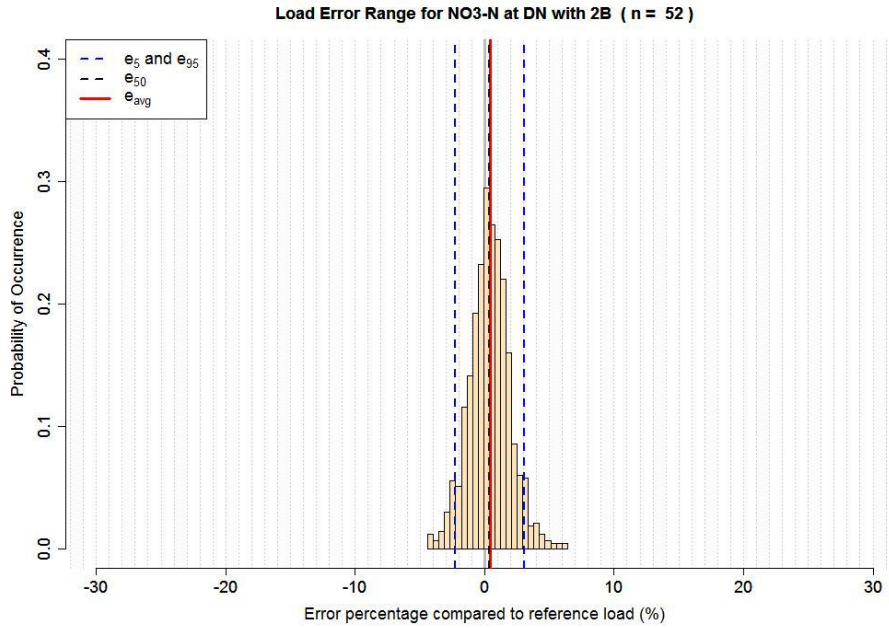


Figure D.10

Distribution of uncertainties estimation presented in the percentage as relative difference of reference annual load expressed as histogram for NO₃-N (uncertainties with the bias [e_{avg} , red solid line or e_{50} , black dash line] and precision [e_5 and e_{95} , blue dash lines, are precision limits of 5th and 95th percentiles, respectively) with stratified sampling (2B, n = 52) at DN.

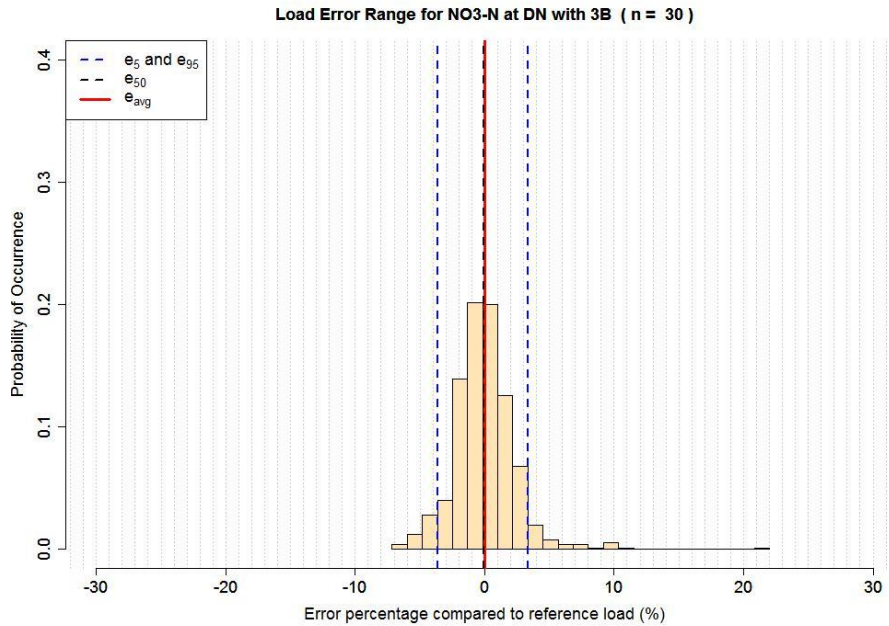


Figure D.11

Distribution of uncertainties estimation presented in the percentage as relative difference of reference annual load expressed as histogram for NO₃-N (uncertainties with the bias [e_{avg} , red solid line or e_{50} , black dash line] and precision [e_5 and e_{95} , blue dash lines, are precision limits of 5th and 95th percentiles, respectively) with stratified sampling (3B, n = 30) at DN.

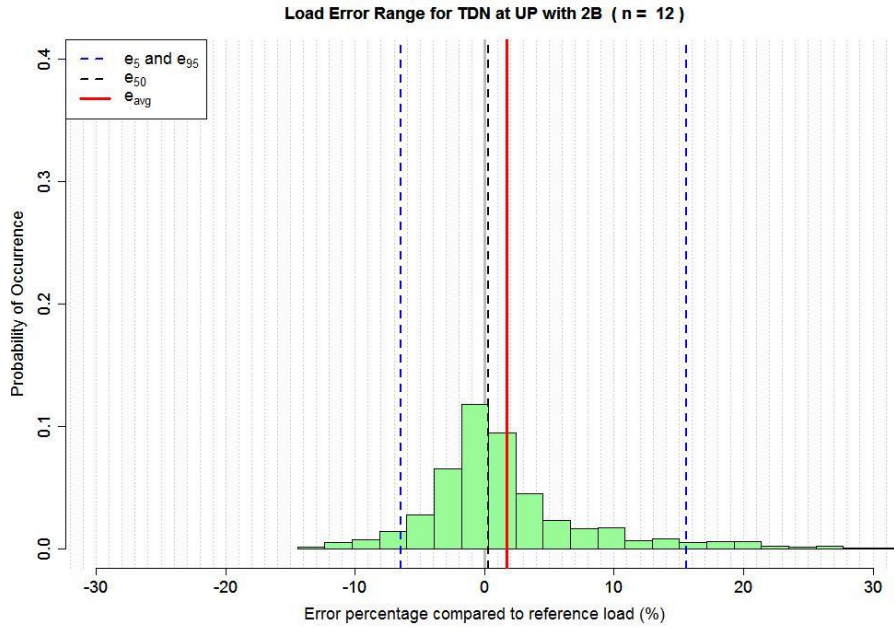


Figure D.12

Distribution of uncertainties estimation presented in the percentage as relative difference of reference annual load expressed as histogram for TDN (uncertainties with the bias [e_{avg} , red solid line or e_{50} , black dash line] and precision [e_5 and e_{95} , blue dash lines, are precision limits of 5th and 95th percentiles, respectively) with stratified sampling (2B, n = 12) at UP.

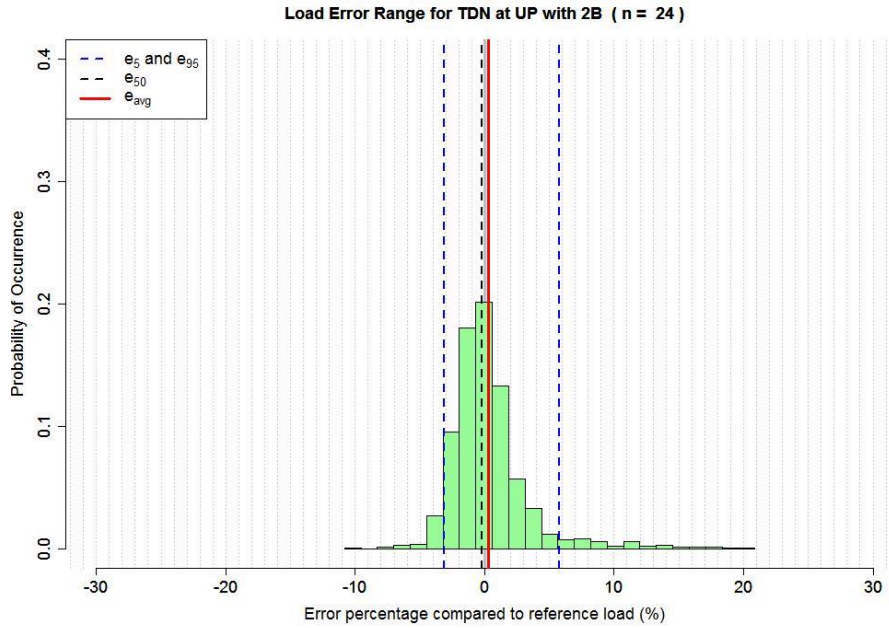


Figure D.13

Distribution of uncertainties estimation presented in the percentage as relative difference of reference annual load expressed as histogram for TDN (uncertainties with the bias [e_{avg} , red solid line or e_{50} , black dash line] and precision [e_5 and e_{95} , blue dash lines, are precision limits of 5th and 95th percentiles, respectively) with stratified sampling (2B, $n = 24$) at UP.

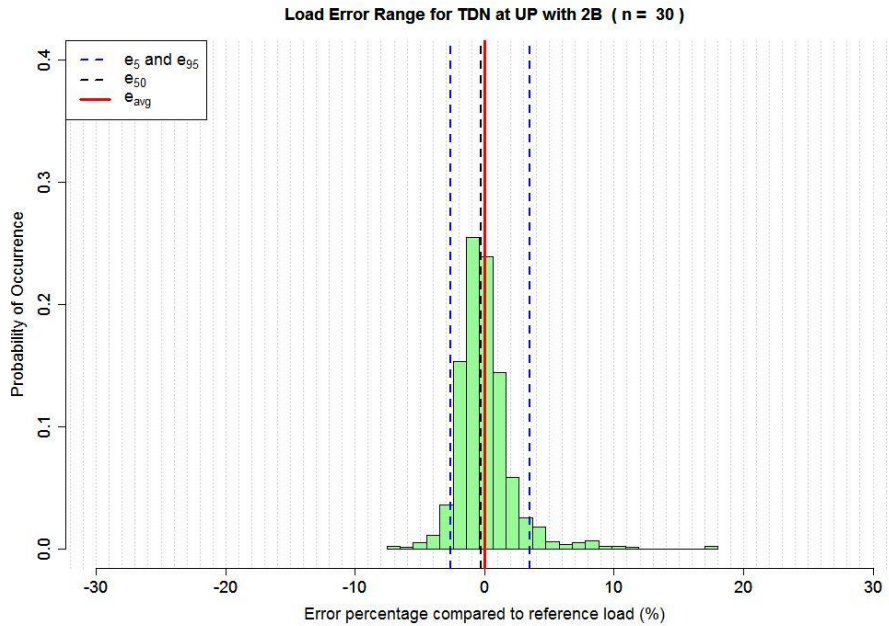


Figure D.14

Distribution of uncertainties estimation presented in the percentage as relative difference of reference annual load expressed as histogram for TDN (uncertainties with the bias [e_{avg} , red solid line or e_{50} , black dash line] and precision [e_5 and e_{95} , blue dash lines, are precision limits of 5th and 95th percentiles, respectively) with stratified sampling (2B, n = 30) at UP.

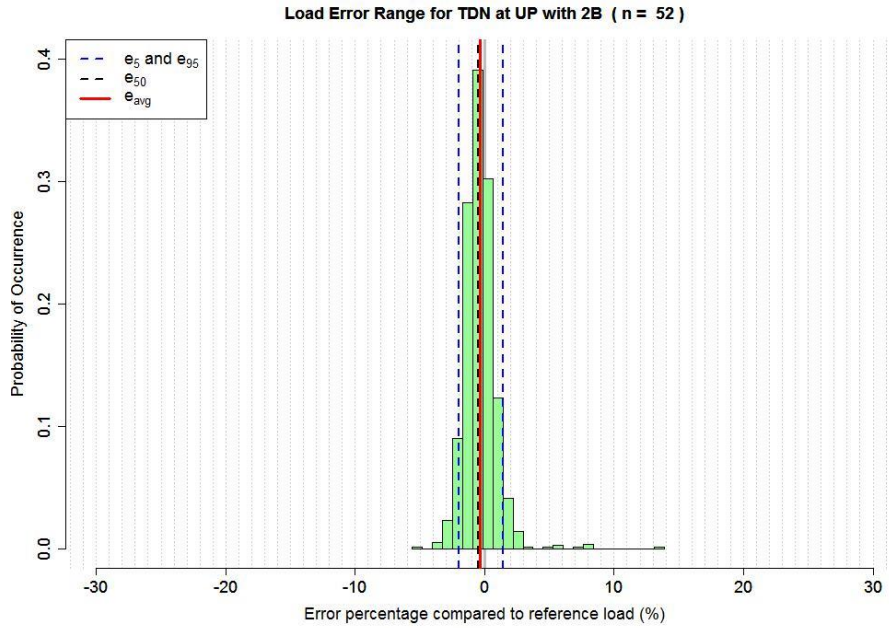


Figure D.15

Distribution of uncertainties estimation presented in the percentage as relative difference of reference annual load expressed as histogram for TDN (uncertainties with the bias [e_{avg} , red solid line or e_{50} , black dash line] and precision [e_5 and e_{95} , blue dash lines, are precision limits of 5th and 95th percentiles, respectively) with stratified sampling (2B, $n = 52$) at UP.

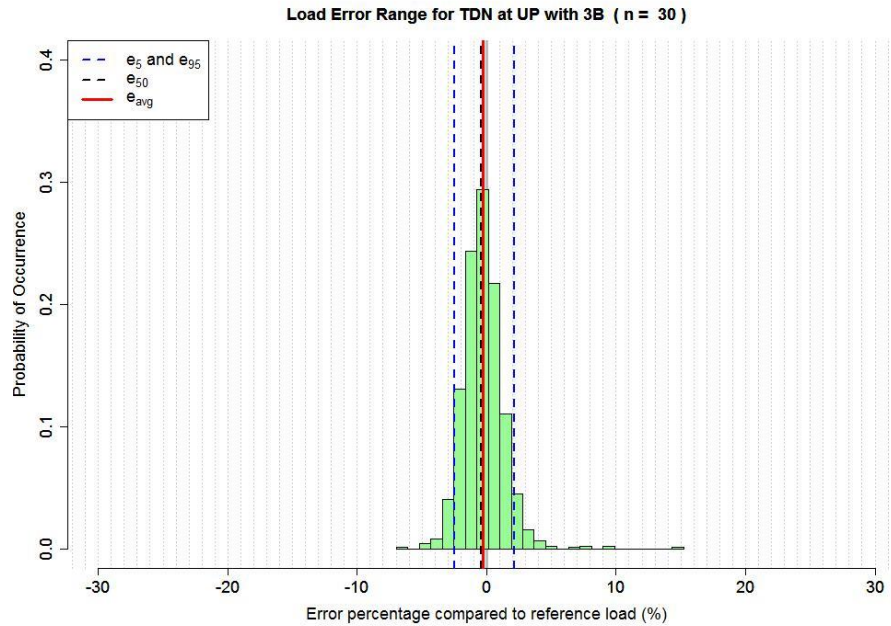


Figure D.16

Distribution of uncertainties estimation presented in the percentage as relative difference of reference annual load expressed as histogram for TDN (uncertainties with the bias [e_{avg} , red solid line or e_{50} , black dash line] and precision [e_5 and e_{95} , blue dash lines, are precision limits of 5th and 95th percentiles, respectively) with stratified sampling (3B, n = 30) at UP.

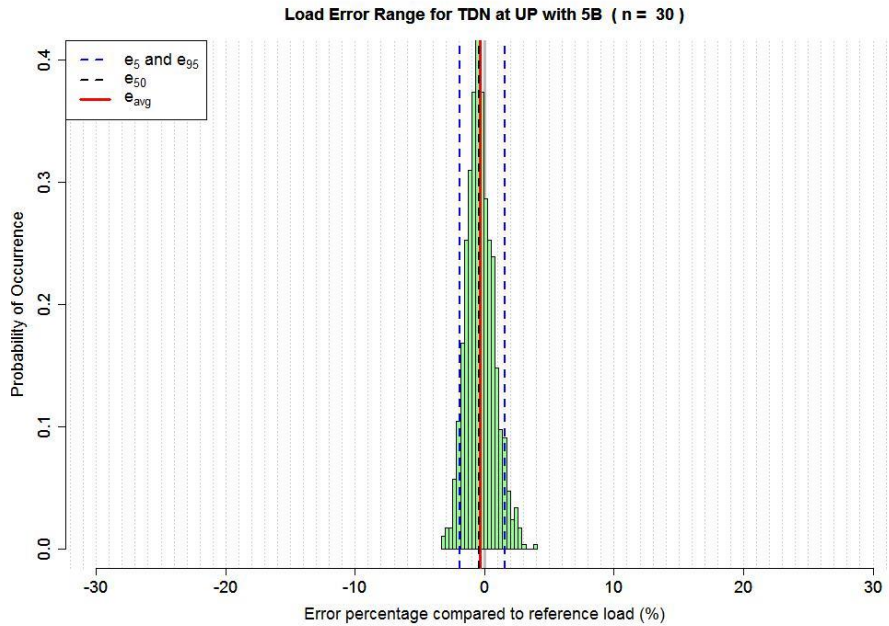


Figure D.17

Distribution of uncertainties estimation presented in the percentage as relative difference of reference annual load expressed as histogram for TDN (uncertainties with the bias [e_{avg} , red solid line or e_{50} , black dash line] and precision [e_5 and e_{95} , blue dash lines, are precision limits of 5th and 95th percentiles, respectively) with stratified sampling (5B, n = 30) at UP.

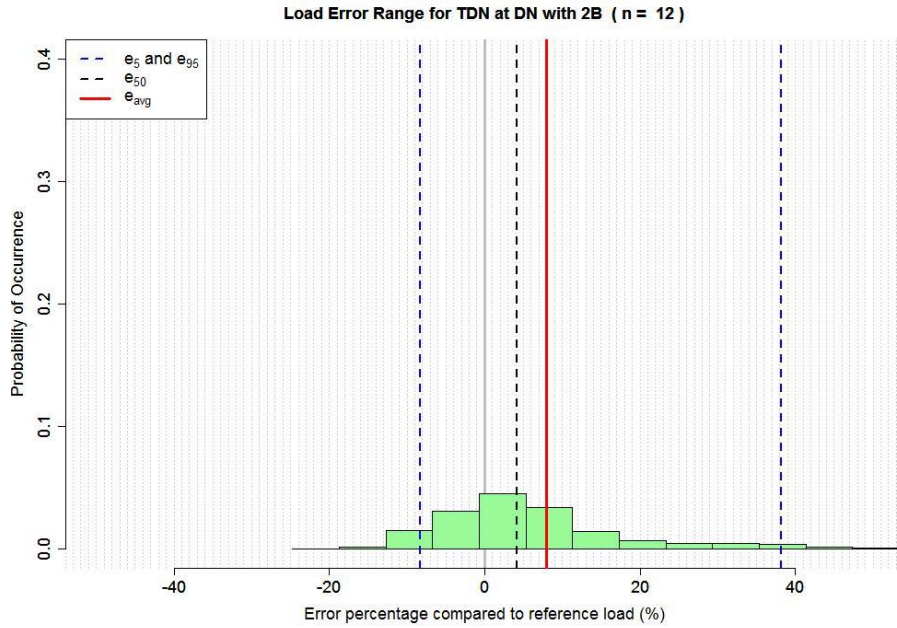


Figure D.18

Distribution of uncertainties estimation presented in the percentage as relative difference of reference annual load expressed as histogram for TDN (uncertainties with the bias [e_{avg} , red solid line or e_{50} , black dash line] and precision [e_5 and e_{95} , blue dash lines, are precision limits of 5th and 95th percentiles, respectively) with stratified sampling (2B, n = 12) at DN.

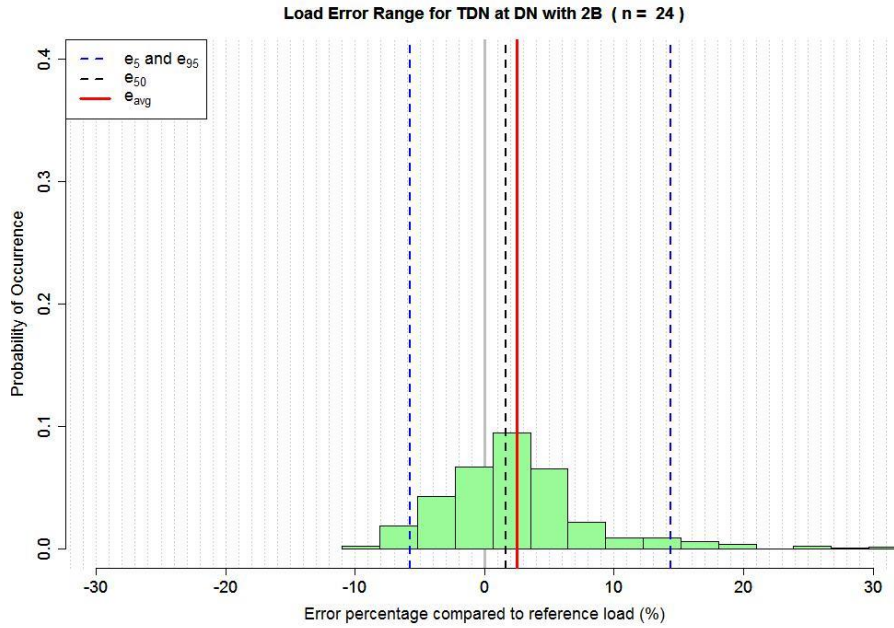


Figure D.19

Distribution of uncertainties estimation presented in the percentage as relative difference of reference annual load expressed as histogram for TDN (uncertainties with the bias [e_{avg} , red solid line or e_{50} , black dash line] and precision [e_5 and e_{95} , blue dash lines, are precision limits of 5th and 95th percentiles, respectively) with stratified sampling (2B, n = 24) at DN.

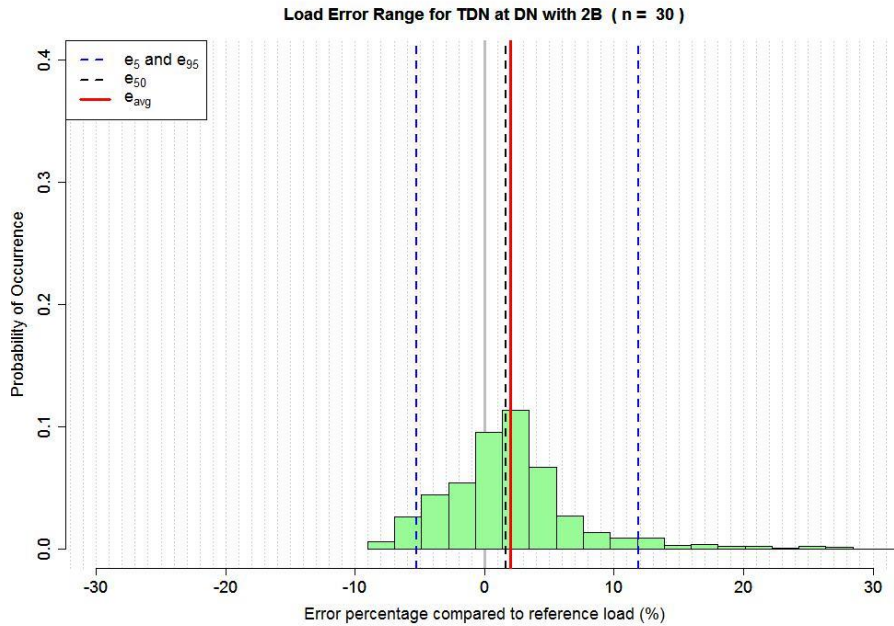


Figure D.20

Distribution of uncertainties estimation presented in the percentage as relative difference of reference annual load expressed as histogram for TDN (uncertainties with the bias [e_{avg} , red solid line or e_{50} , black dash line] and precision [e_5 and e_{95} , blue dash lines, are precision limits of 5th and 95th percentiles, respectively) with stratified sampling (2B, n = 30) at DN.

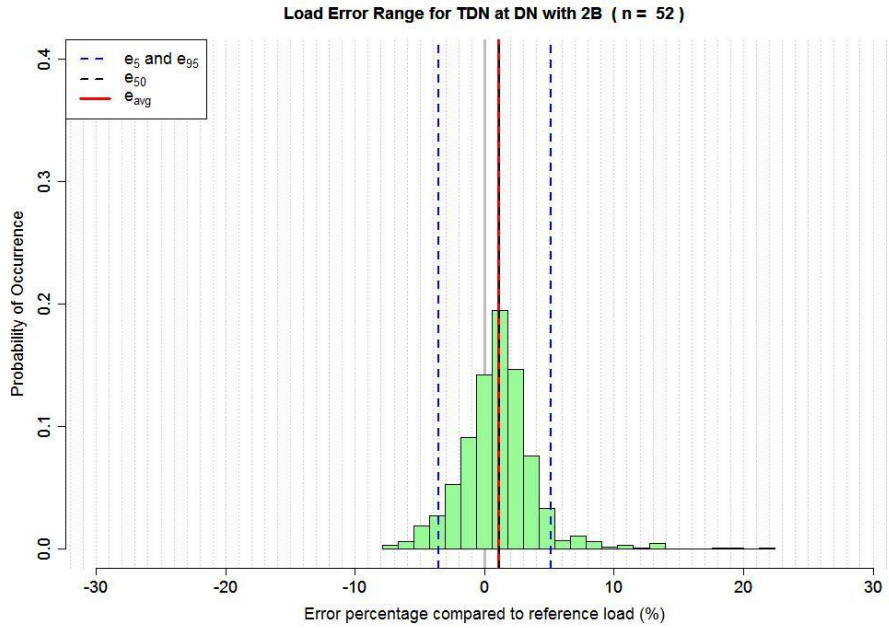


Figure D.21

Distribution of uncertainties estimation presented in the percentage as relative difference of reference annual load expressed as histogram for TDN (uncertainties with the bias [e_{avg} , red solid line or e_{50} , black dash line] and precision [e_5 and e_{95} , blue dash lines, are precision limits of 5th and 95th percentiles, respectively) with stratified sampling (2B, $n = 52$) at DN.

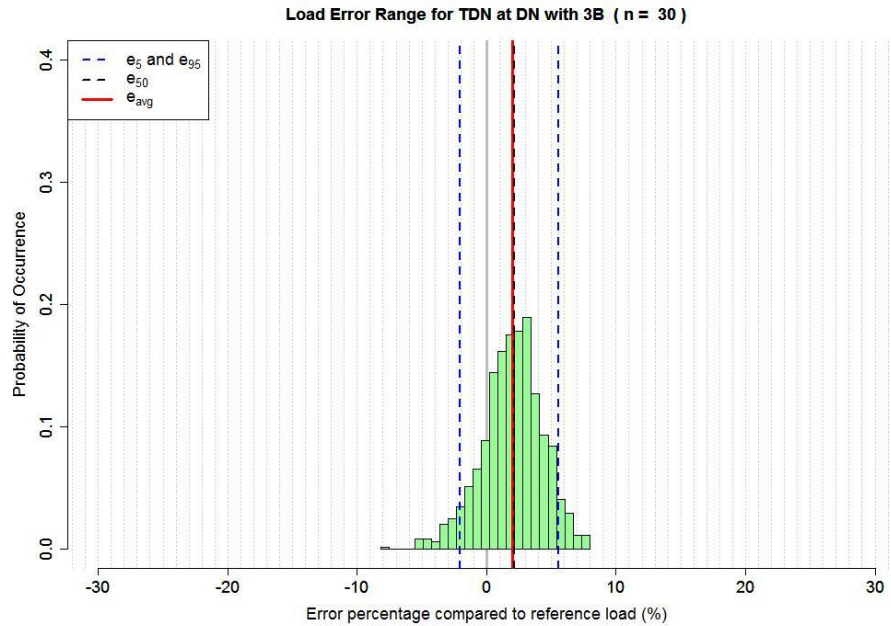


Figure D.22

Distribution of uncertainties estimation presented in the percentage as relative difference of reference annual load expressed as histogram for TDN (uncertainties with the bias [e_{avg} , red solid line or e_{50} , black dash line] and precision [e_5 and e_{95} , blue dash lines, are precision limits of 5th and 95th percentiles, respectively) with stratified sampling (3B, n = 30) at DN.

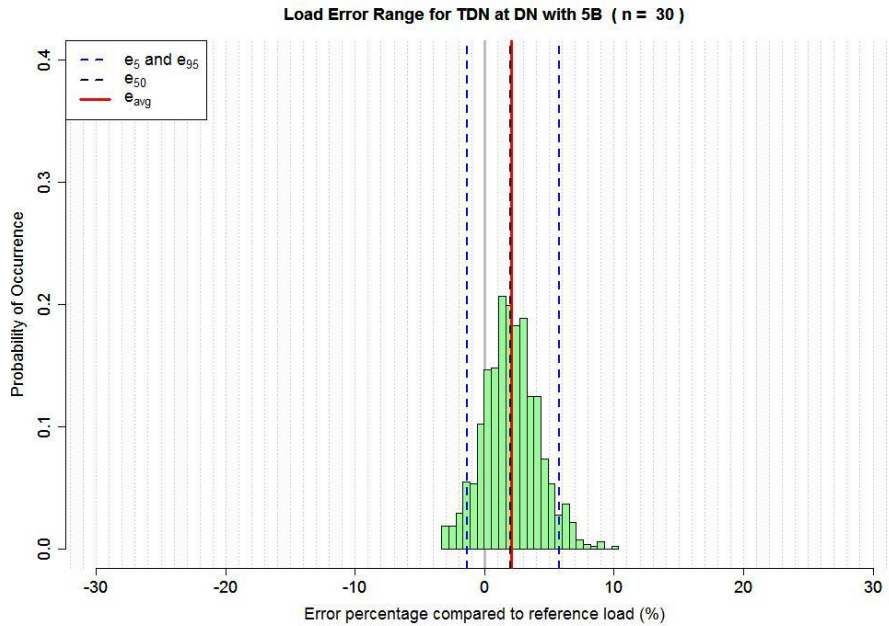


Figure D.23

Distribution of uncertainties estimation presented in the percentage as relative difference of reference annual load expressed as histogram for TDN (uncertainties with the bias [e_{avg} , red solid line or e_{50} , black dash line] and precision [e_5 and e_{95} , blue dash lines, are precision limits of 5th and 95th percentiles, respectively) with stratified sampling (5B, n = 30) at DN.

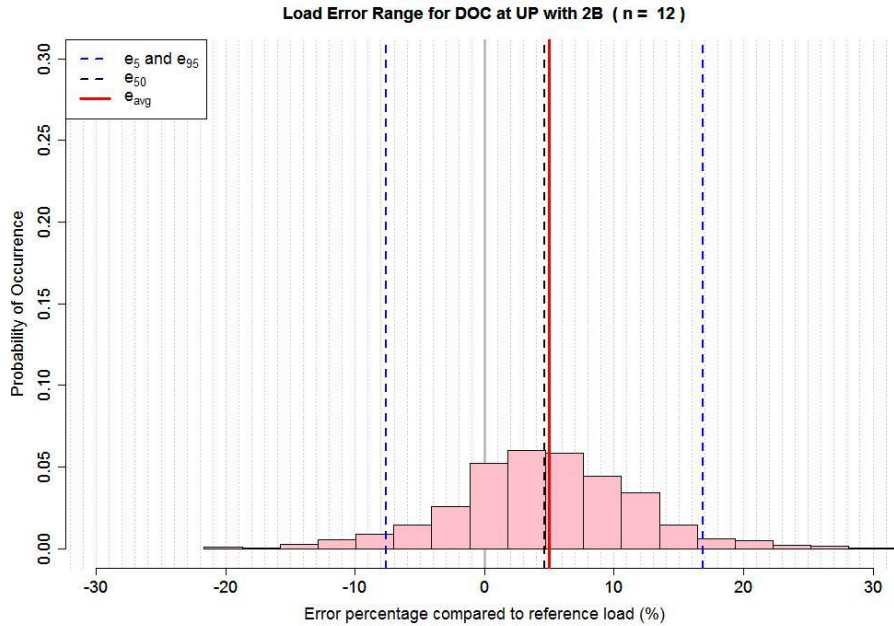


Figure D.24

Distribution of uncertainties estimation presented in the percentage as relative difference of reference annual load expressed as histogram for DOC (uncertainties with the bias [e_{avg} , red solid line or e_{50} , black dash line] and precision [e_5 and e_{95} , blue dash lines, are precision limits of 5th and 95th percentiles, respectively) with stratified sampling (2B, $n = 12$) at UP.

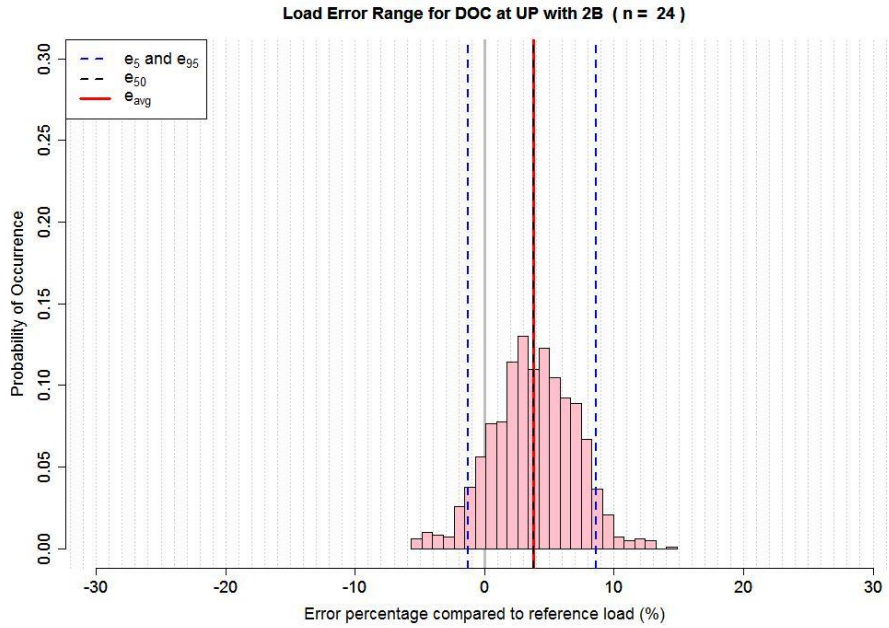


Figure D.25

Distribution of uncertainties estimation presented in the percentage as relative difference of reference annual load expressed as histogram for DOC (uncertainties with the bias [e_{avg} , red solid line or e_{50} , black dash line] and precision [e_5 and e_{95} , blue dash lines, are precision limits of 5th and 95th percentiles, respectively) with stratified sampling (2B, $n = 24$) at UP.

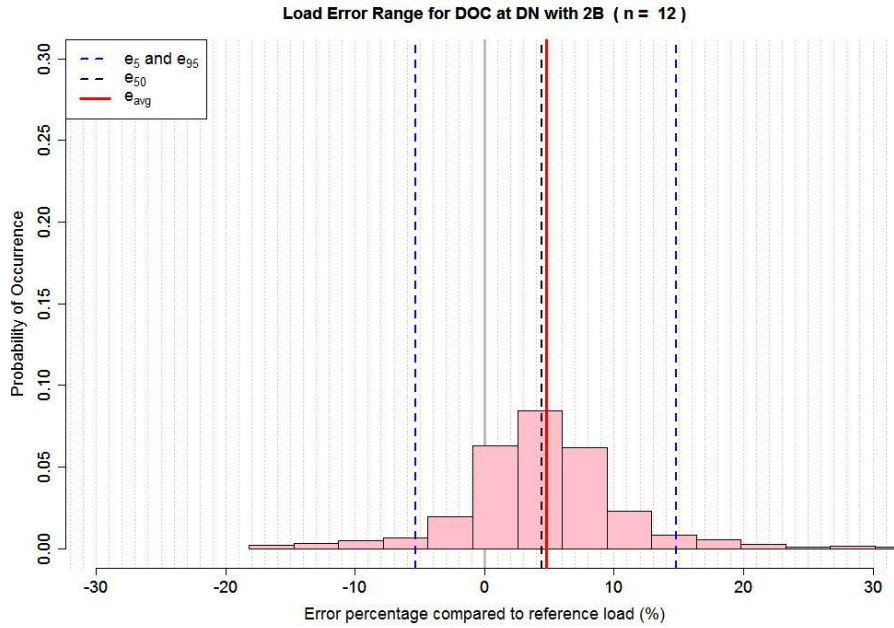


Figure D.26

Distribution of uncertainties estimation presented in the percentage as relative difference of reference annual load expressed as histogram for DOC (uncertainties with the bias [e_{avg} , red solid line or e_{50} , black dash line] and precision [e_5 and e_{95} , blue dash lines, are precision limits of 5th and 95th percentiles, respectively) with stratified sampling (2B, $n = 12$) at DN.

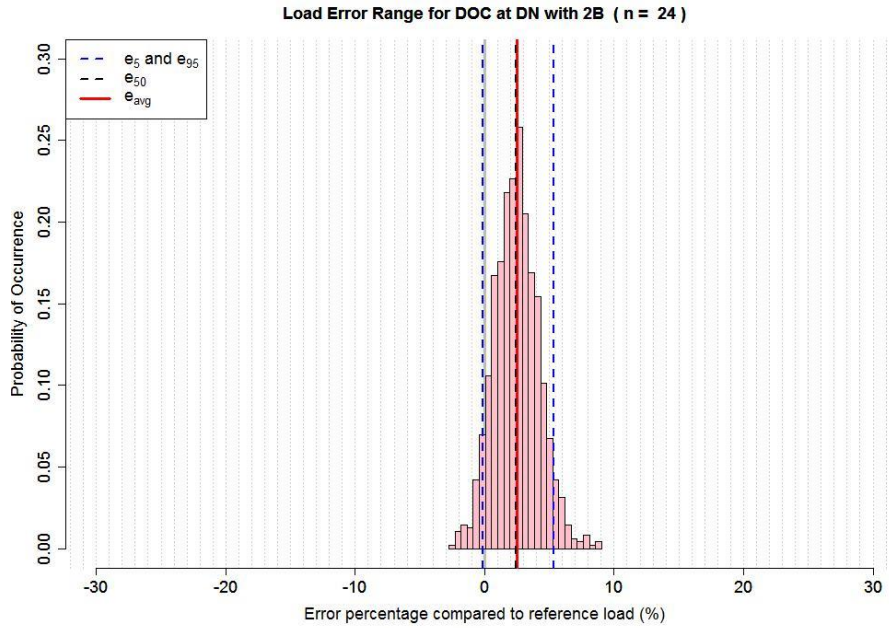


Figure D.27

Distribution of uncertainties estimation presented in the percentage as relative difference of reference annual load expressed as histogram for DOC (uncertainties with the bias [e_{avg} , red solid line or e_{50} , black dash line] and precision [e_5 and e_{95} , blue dash lines, are precision limits of 5th and 95th percentiles, respectively) with stratified sampling (2B, $n = 24$) at DN.

Appendix E: Uncertainties estimations for annual loads for different stream solutes with infrequent sampling

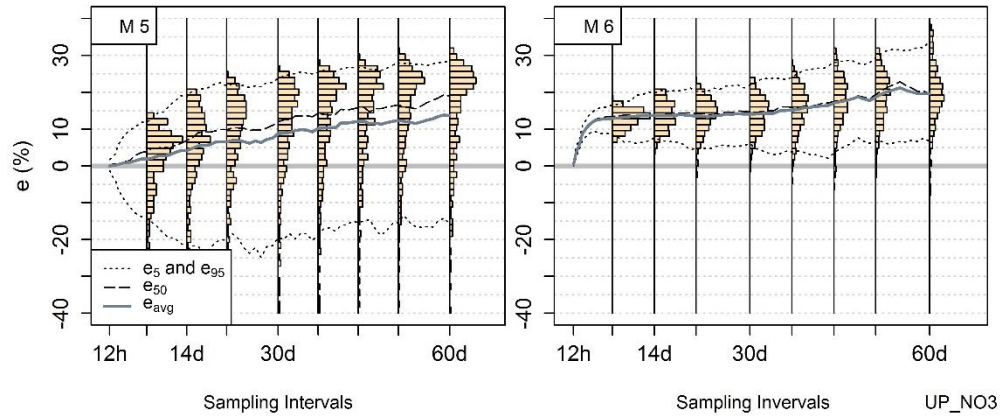


Figure E.1

Comparison of uncertainties (e %) with the bias (e_{avg} or e_{50}) and precision (e_5 and e_{95} are precision limits of 5th and 95th percentiles, respectively) for $\text{NO}_3\text{-N}$ load estimations as the function of sampling intervals with the algorithms (M5 and M6) at UP

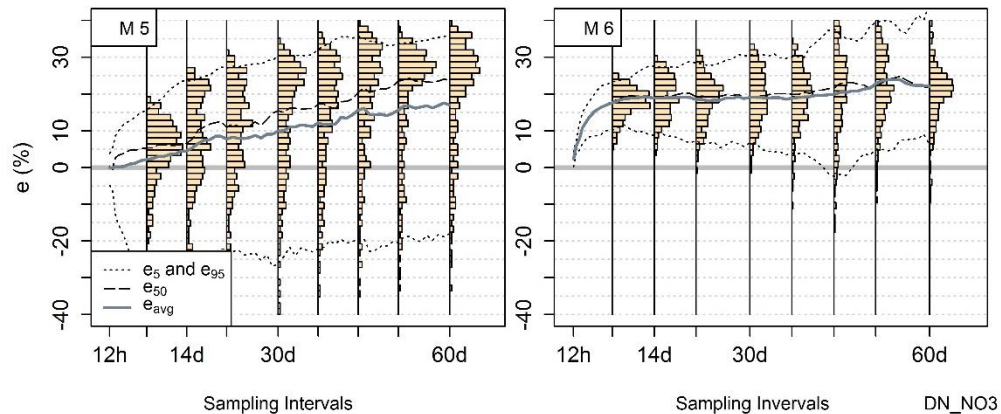


Figure E.2

Comparison of uncertainties (e %) with the bias (e_{avg} or e_{50}) and precision (e_5 and e_{95} are precision limits of 5th and 95th percentiles, respectively) for $\text{NO}_3\text{-N}$ load estimations as the function of sampling intervals with the algorithms (M5 and M6) at DN

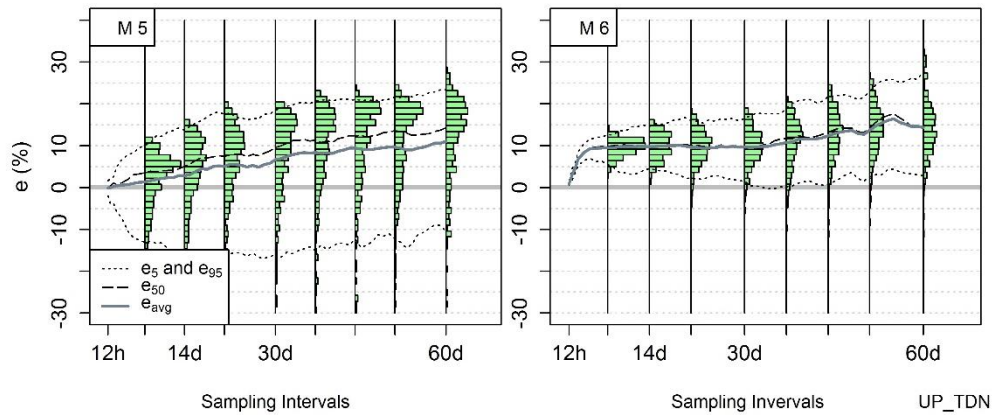


Figure E.3

Comparison of uncertainties (e %) with the bias (e_{avg} or e_{50}) and precision (e_5 and e_{95} are precision limits of 5th and 95th percentiles, respectively) for TDN load estimations as the function of sampling intervals with the algorithms (M5 and M6) at UP

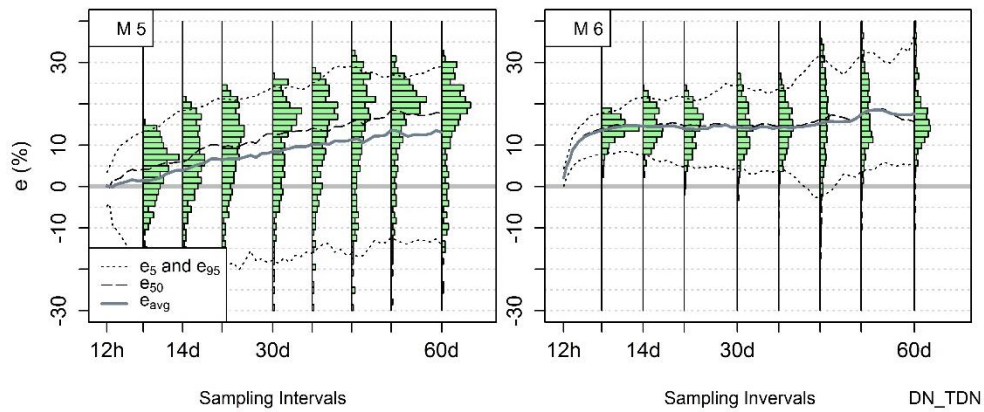


Figure E.4

Comparison of uncertainties (e %) with the bias (e_{avg} or e_{50}) and precision (e_5 and e_{95} are precision limits of 5th and 95th percentiles, respectively) for TDN load estimations as the function of sampling intervals with the algorithms (M5 and M6) at DN

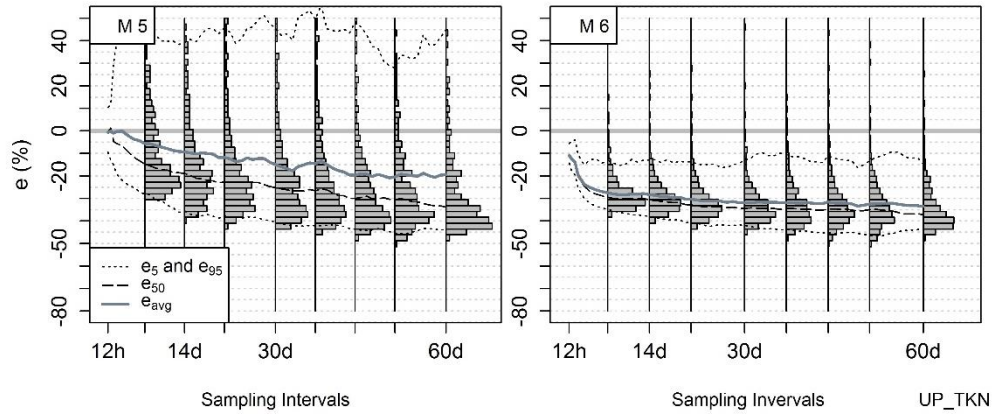


Figure E.5

Comparison of uncertainties (e %) with the bias (e_{avg} or e_{50}) and precision (e_5 and e_{95} are precision limits of 5th and 95th percentiles, respectively) for TKN load estimations as the function of sampling intervals with the algorithms (M5 and M6) at UP

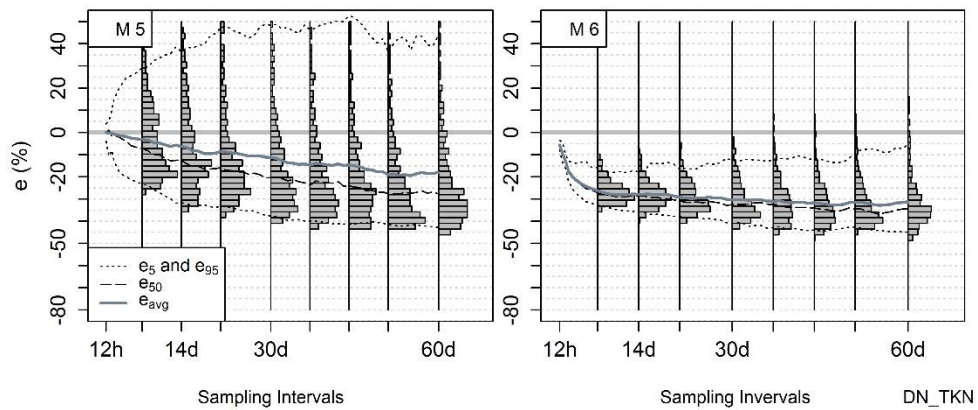


Figure E.6

Comparison of uncertainties (e %) with the bias (e_{avg} or e_{50}) and precision (e_5 and e_{95} are precision limits of 5th and 95th percentiles, respectively) for TKN load estimations as the function of sampling intervals with the algorithms (M5 and M6) at DN

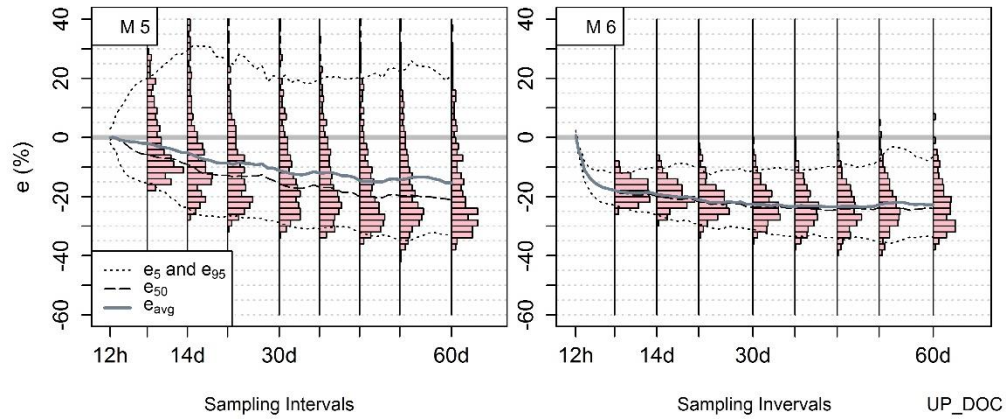


Figure E.7

Comparison of uncertainties (e %) with the bias (e_{avg} or e_{50}) and precision (e_5 and e_{95} are precision limits of 5th and 95th percentiles, respectively) for DOC load estimations as the function of sampling intervals with the algorithms (M5 and M6) at UP

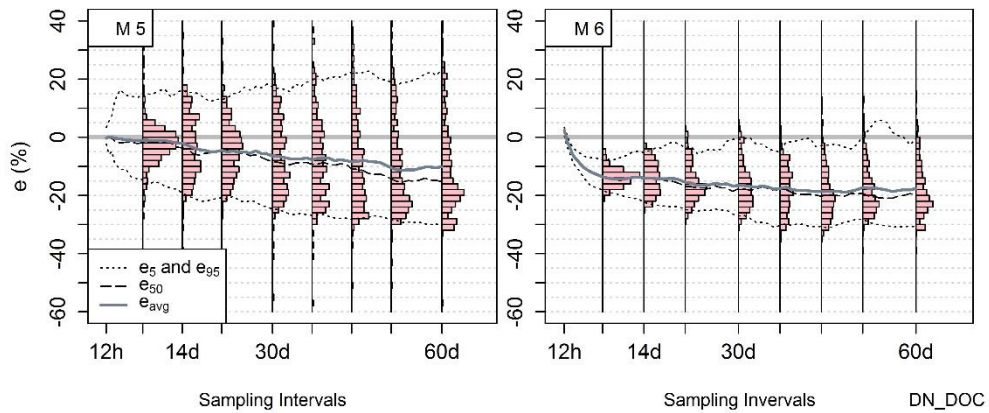


Figure E.8

Comparison of uncertainties (e %) with the bias (e_{avg} or e_{50}) and precision (e_5 and e_{95} are precision limits of 5th and 95th percentiles, respectively) for DOC load estimations as the function of sampling intervals with the algorithms (M5 and M6) at DN

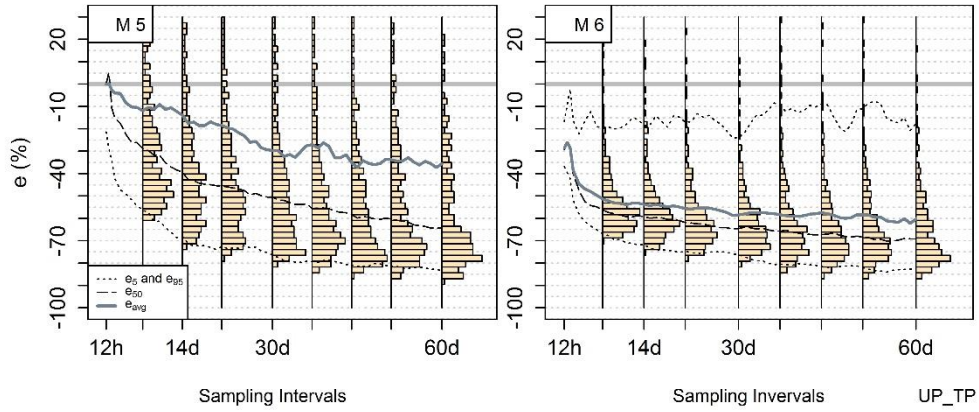


Figure E.9

Comparison of uncertainties (e %) with the bias (e_{avg} or e_{50}) and precision (e_5 and e_{95} are precision limits of 5th and 95th percentiles, respectively) for TP load estimations as the function of sampling intervals with the algorithms (M5 and M6) at UP

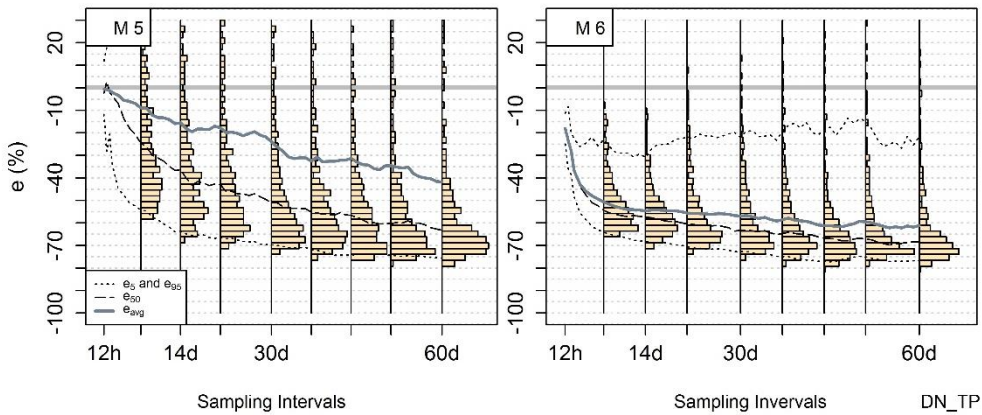


Figure E.10

Comparison of uncertainties (e %) with the bias (e_{avg} or e_{50}) and precision (e_5 and e_{95} are precision limits of 5th and 95th percentiles, respectively) for TP load estimations as the function of sampling intervals with the algorithms (M5 and M6) at DN

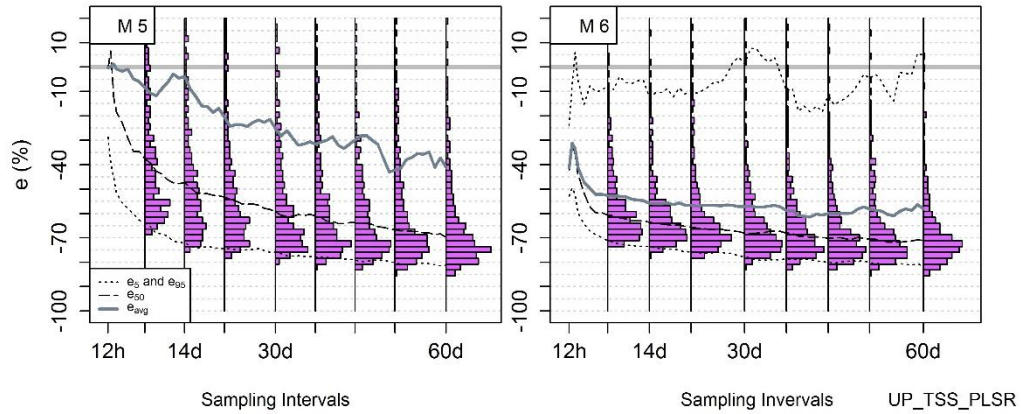


Figure E.11

Comparison of uncertainties (e %) with the bias (e_{avg} or e_{50}) and precision (e_5 and e_{95} are precision limits of 5th and 95th percentiles, respectively) for TSS load estimations as the function of sampling intervals with the algorithms (M5 and M6) with PLSR prediction at UP

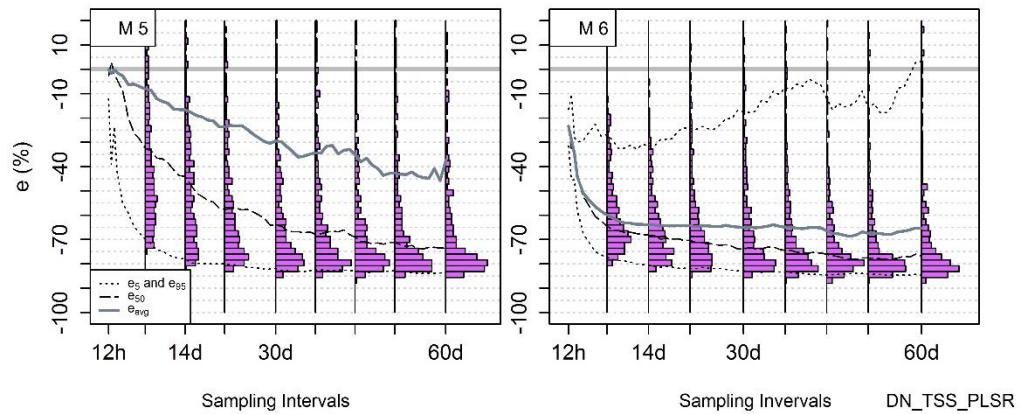


Figure E.12

Comparison of uncertainties (e %) with the bias (e_{avg} or e_{50}) and precision (e_5 and e_{95} are precision limits of 5th and 95th percentiles, respectively) for TSS load estimations as the function of sampling intervals with the algorithms (M5 and M6) with PLSR prediction at DN

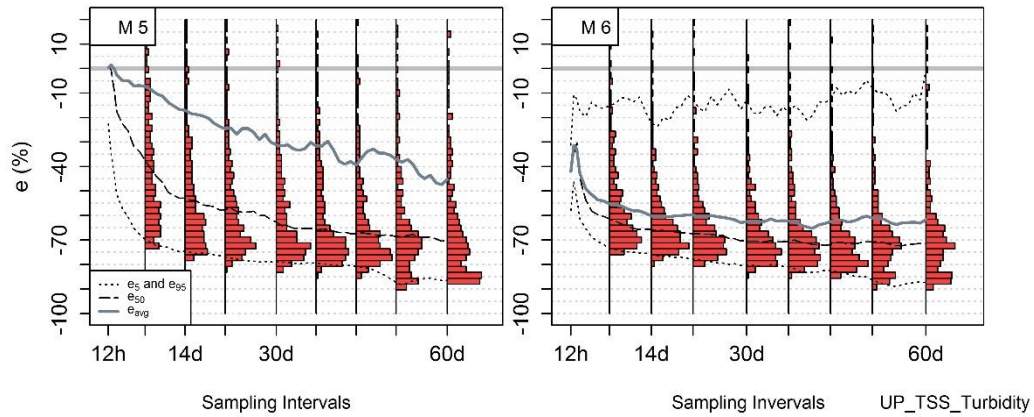


Figure E.13

Comparison of uncertainties (e %) with the bias (e_{avg} or e_{50}) and precision (e_5 and e_{95} are precision limits of 5th and 95th percentiles, respectively) for TSS load estimations as the function of sampling intervals with the algorithms (M5 and M6) with Turbidity prediction at UP

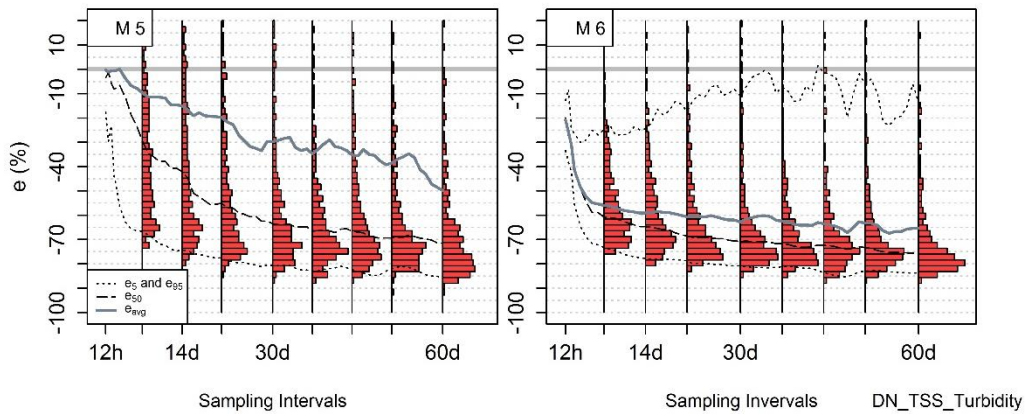


Figure E.14

Comparison of uncertainties (e %) with the bias (e_{avg} or e_{50}) and precision (e_5 and e_{95} are precision limits of 5th and 95th percentiles, respectively) for TSS load estimations as the function of sampling intervals with the algorithms (M5 and M6) with Turbidity prediction at DN

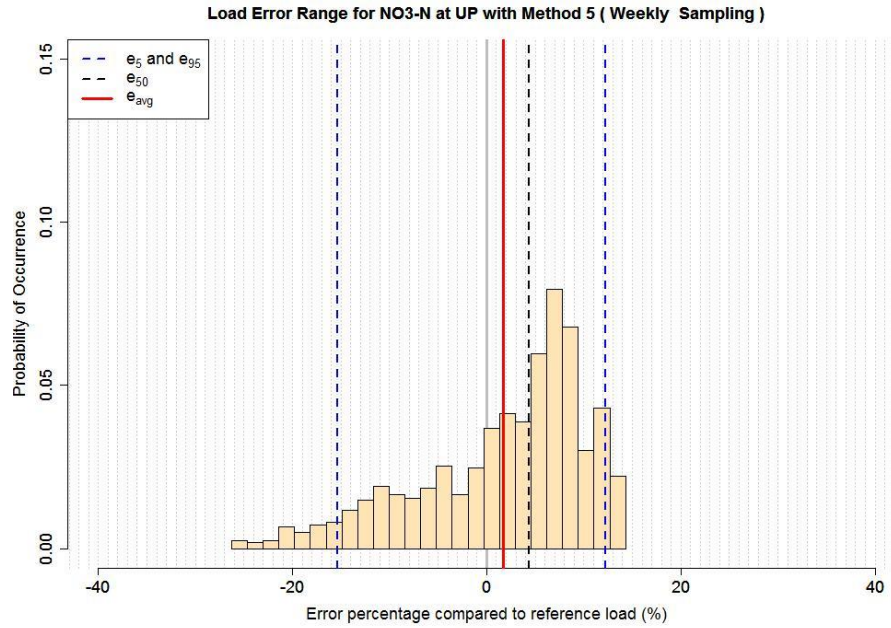


Figure E.15

Distribution of uncertainties estimation presented in the percentage as relative difference of reference annual load expressed as histogram for NO₃-N (uncertainties with the bias [e_{avg} , red solid line or e_{50} , black dash line] and precision [e_5 and e_{95} , blue dash lines, are precision limits of 5th and 95th percentiles, respectively) with infrequent sampling (M5, weekly) at UP.

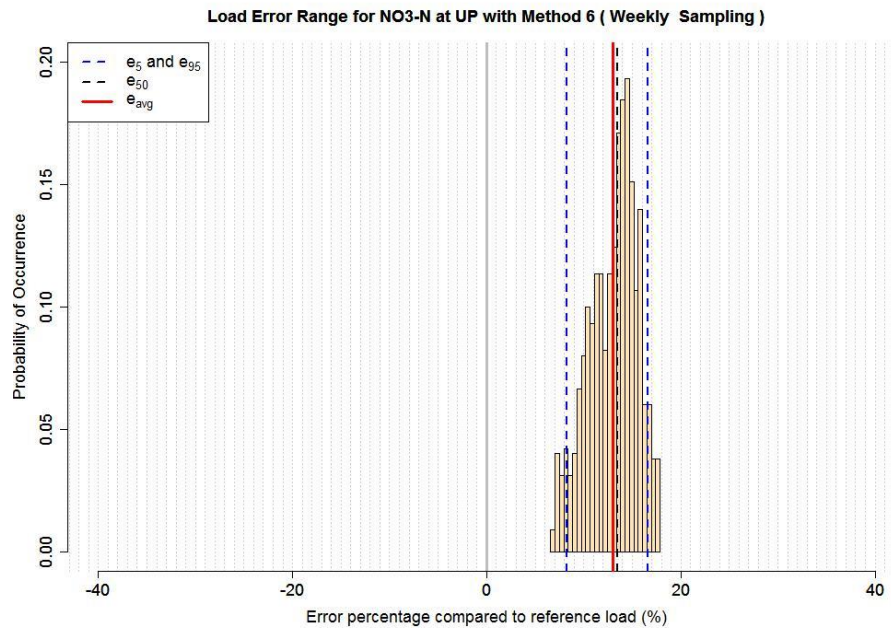


Figure E.16

Distribution of uncertainties estimation presented in the percentage as relative difference of reference annual load expressed as histogram for NO₃-N (uncertainties with the bias [e_{avg} , red solid line or e_{50} , black dash line] and precision [e_5 and e_{95} , blue dash lines, are precision limits of 5th and 95th percentiles, respectively) with infrequent sampling (M6, weekly) at UP.

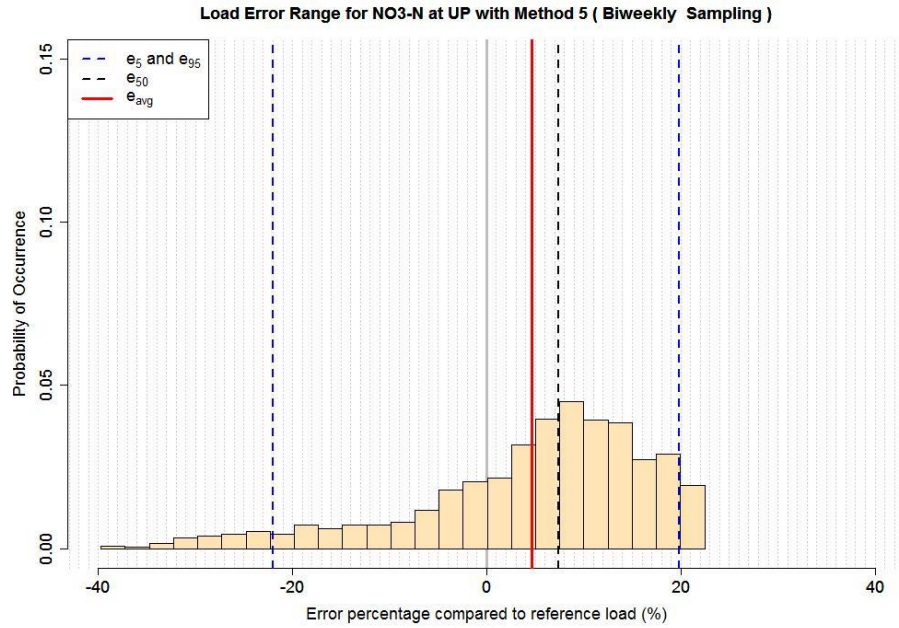


Figure E.17

Distribution of uncertainties estimation presented in the percentage as relative difference of reference annual load expressed as histogram for NO₃-N (uncertainties with the bias [e_{avg} , red solid line or e_{50} , black dash line] and precision [e_5 and e_{95} , blue dash lines, are precision limits of 5th and 95th percentiles, respectively) with infrequent sampling (M5, biweekly) at UP.

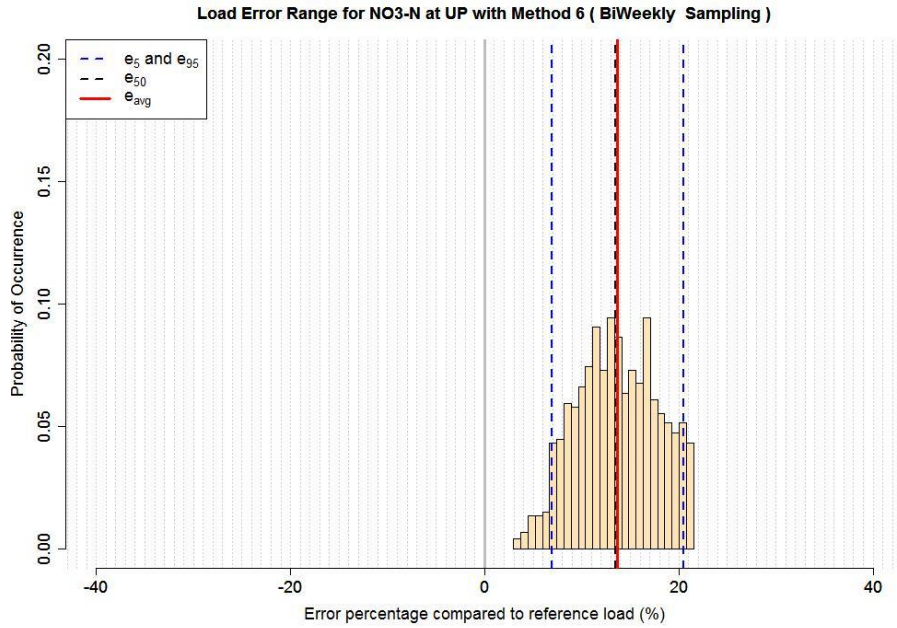


Figure E.18

Distribution of uncertainties estimation presented in the percentage as relative difference of reference annual load expressed as histogram for NO₃-N (uncertainties with the bias [e_{avg} , red solid line or e_{50} , black dash line] and precision [e_5 and e_{95} , blue dash lines, are precision limits of 5th and 95th percentiles, respectively) with infrequent sampling (M6, biweekly) at UP.

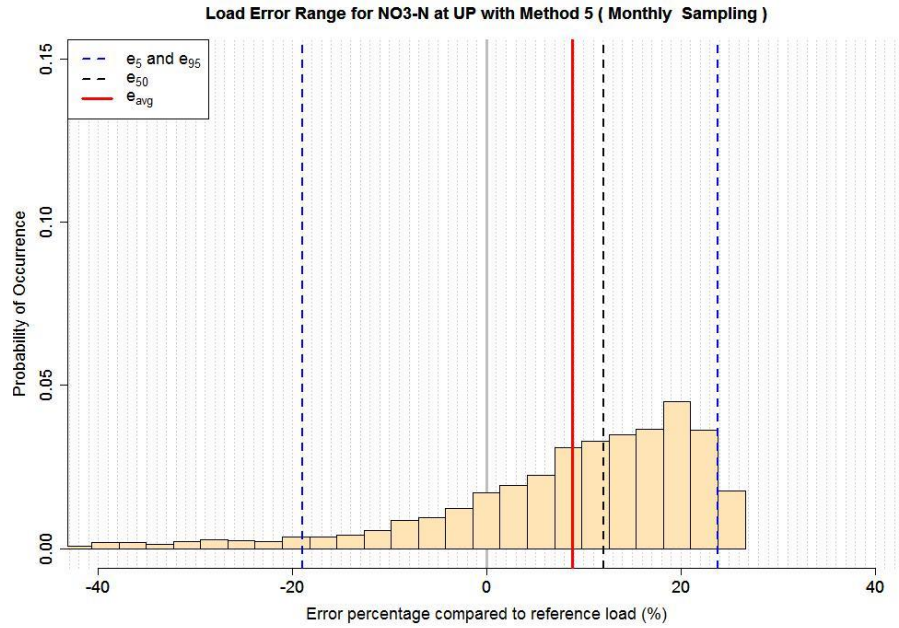


Figure E.19

Distribution of uncertainties estimation presented in the percentage as relative difference of reference annual load expressed as histogram for NO₃-N (uncertainties with the bias [e_{avg} , red solid line or e_{50} , black dash line] and precision [e_5 and e_{95} , blue dash lines, are precision limits of 5th and 95th percentiles, respectively) with infrequent sampling (M5, monthly) at UP.

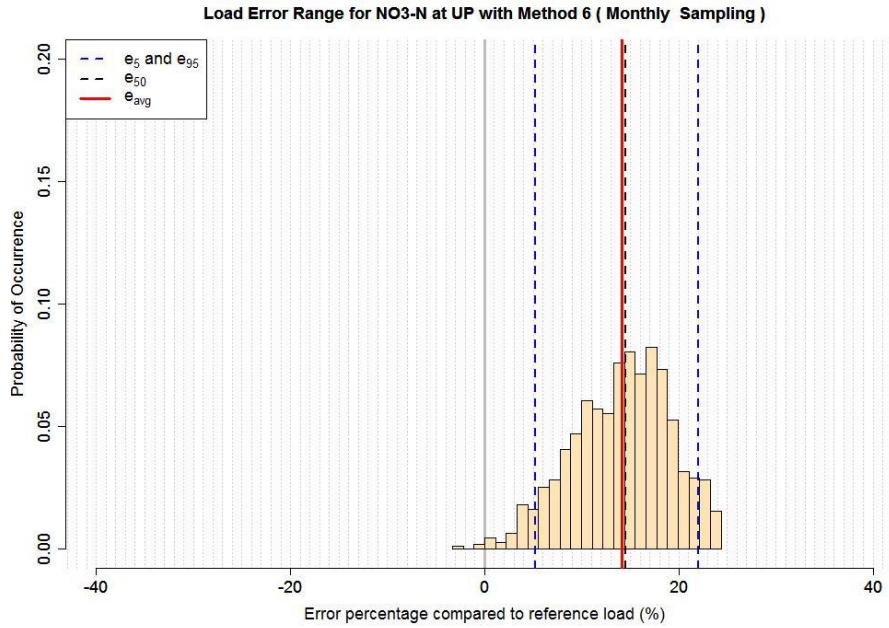


Figure E.20

Distribution of uncertainties estimation presented in the percentage as relative difference of reference annual load expressed as histogram for NO₃-N (uncertainties with the bias [e_{avg} , red solid line or e_{50} , black dash line] and precision [e_5 and e_{95} , blue dash lines, are precision limits of 5th and 95th percentiles, respectively) with infrequent sampling (M6, monthly) at UP.

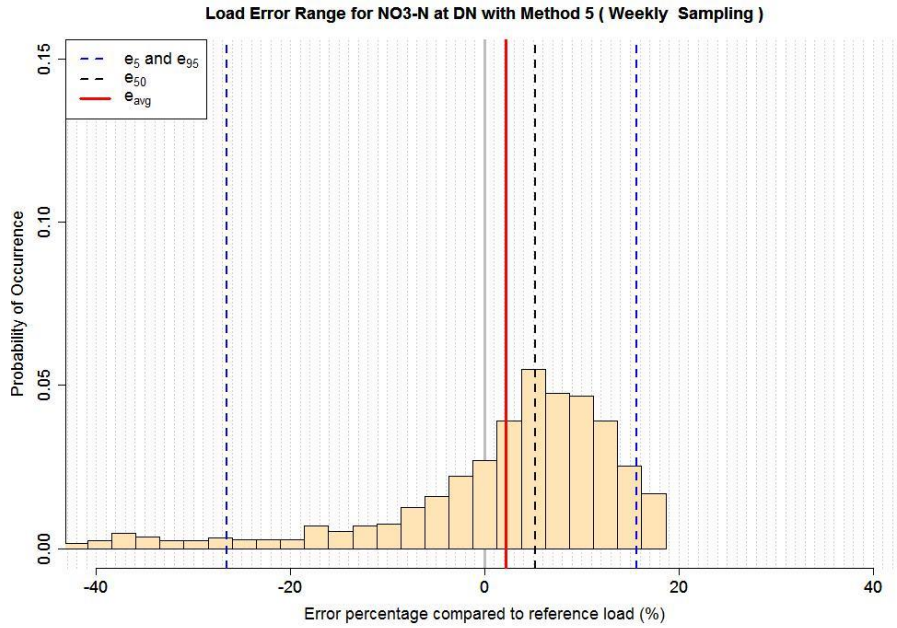


Figure E.21

Distribution of uncertainties estimation presented in the percentage as relative difference of reference annual load expressed as histogram for NO₃-N (uncertainties with the bias [e_{avg} , red solid line or e_{50} , black dash line] and precision [e_5 and e_{95} , blue dash lines, are precision limits of 5th and 95th percentiles, respectively) with infrequent sampling (M5, weekly) at DN.

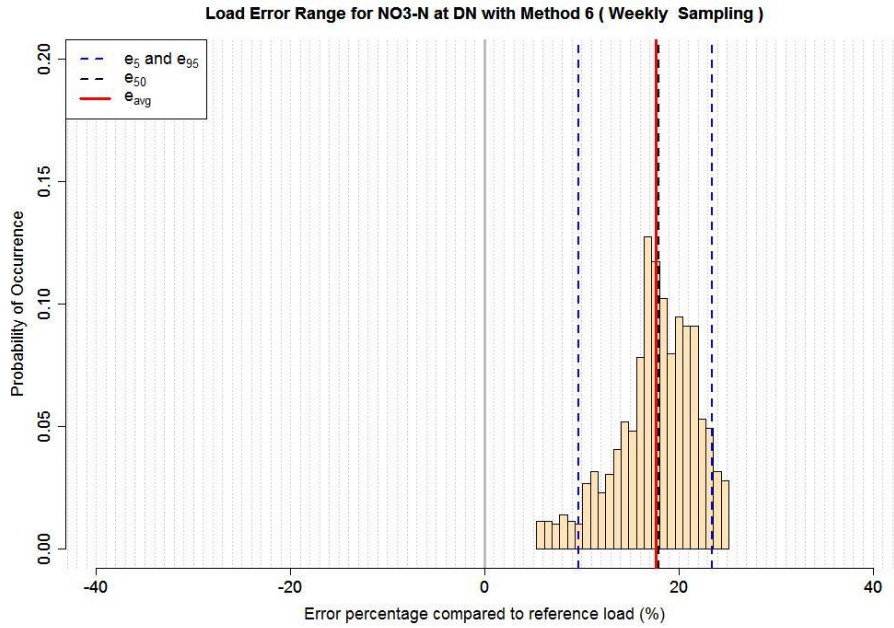


Figure E.22

Distribution of uncertainties estimation presented in the percentage as relative difference of reference annual load expressed as histogram for NO₃-N (uncertainties with the bias [e_{avg} , red solid line or e_{50} , black dash line] and precision [e_5 and e_{95} , blue dash lines, are precision limits of 5th and 95th percentiles, respectively) with infrequent sampling (M6, weekly) at DN.

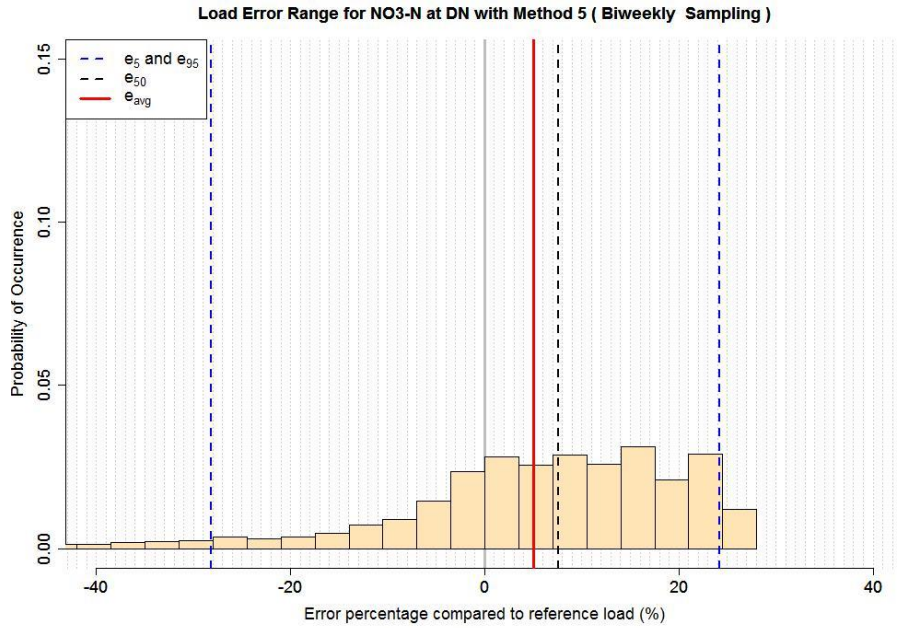


Figure E.23

Distribution of uncertainties estimation presented in the percentage as relative difference of reference annual load expressed as histogram for NO₃-N (uncertainties with the bias [e_{avg} , red solid line or e_{50} , black dash line] and precision [e_5 and e_{95} , blue dash lines, are precision limits of 5th and 95th percentiles, respectively) with infrequent sampling (M5, biweekly) at DN.

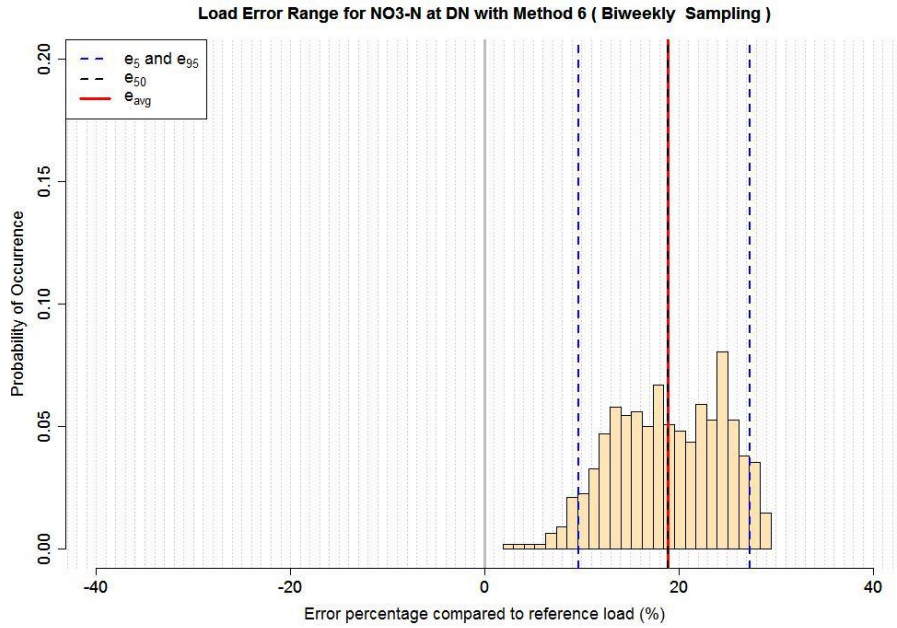


Figure E.24

Distribution of uncertainties estimation presented in the percentage as relative difference of reference annual load expressed as histogram for NO₃-N (uncertainties with the bias [e_{avg} , red solid line or e_{50} , black dash line] and precision [e_5 and e_{95} , blue dash lines, are precision limits of 5th and 95th percentiles, respectively) with infrequent sampling (M6, biweekly) at DN.

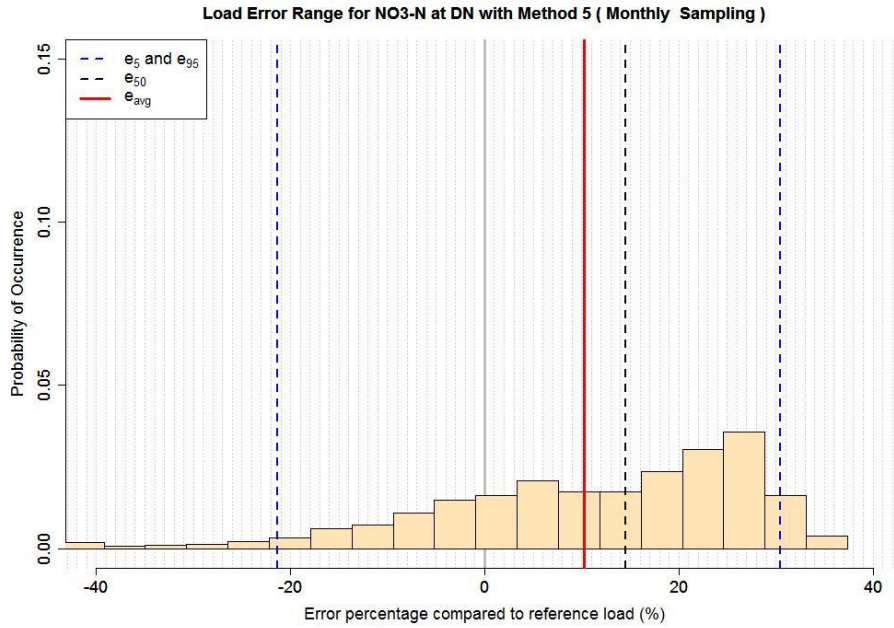


Figure E.25

Distribution of uncertainties estimation presented in the percentage as relative difference of reference annual load expressed as histogram for NO₃-N (uncertainties with the bias [e_{avg} , red solid line or e_{50} , black dash line] and precision [e_5 and e_{95} , blue dash lines, are precision limits of 5th and 95th percentiles, respectively) with infrequent sampling (M5, monthly) at DN.

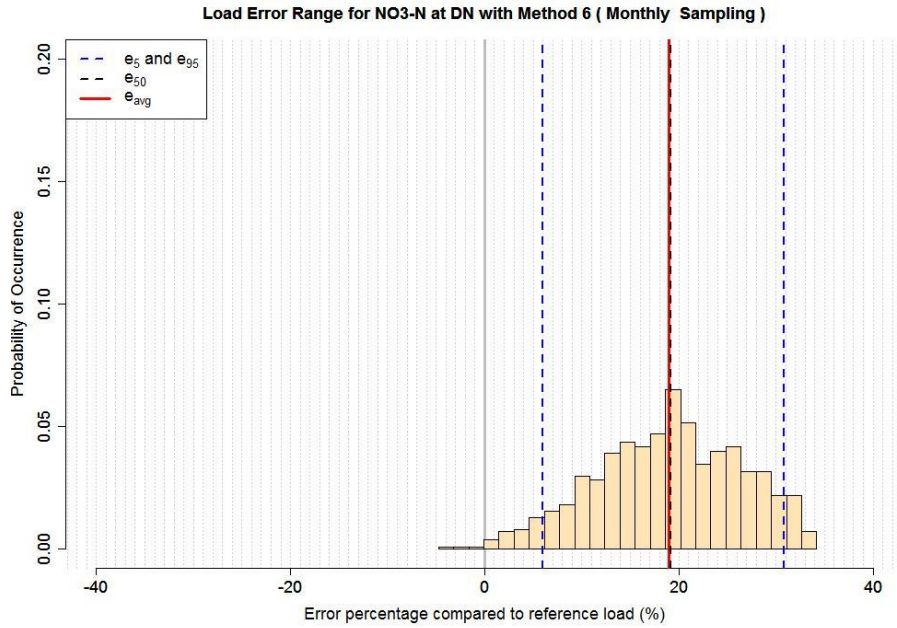


Figure E.26

Distribution of uncertainties estimation presented in the percentage as relative difference of reference annual load expressed as histogram for NO₃-N (uncertainties with the bias [e_{avg} , red solid line or e_{50} , black dash line] and precision [e_5 and e_{95} , blue dash lines, are precision limits of 5th and 95th percentiles, respectively) with infrequent sampling (M6, monthly) at DN.

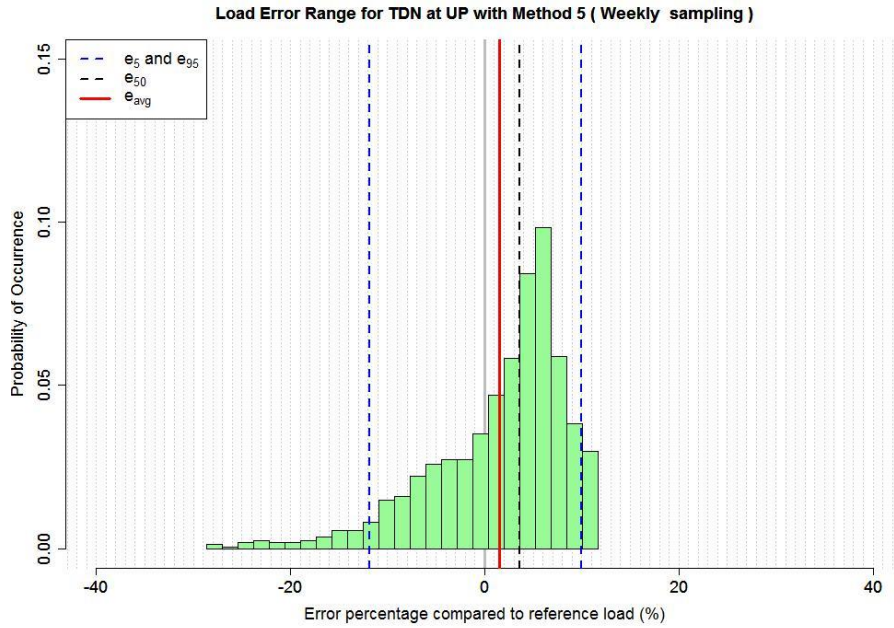


Figure E.27

Distribution of uncertainties estimation presented in the percentage as relative difference of reference annual load expressed as histogram for TDN (uncertainties with the bias [e_{avg} , red solid line or e_{50} , black dash line] and precision [e_5 and e_{95} , blue dash lines, are precision limits of 5th and 95th percentiles, respectively) with infrequent sampling (M5, weekly) at UP.

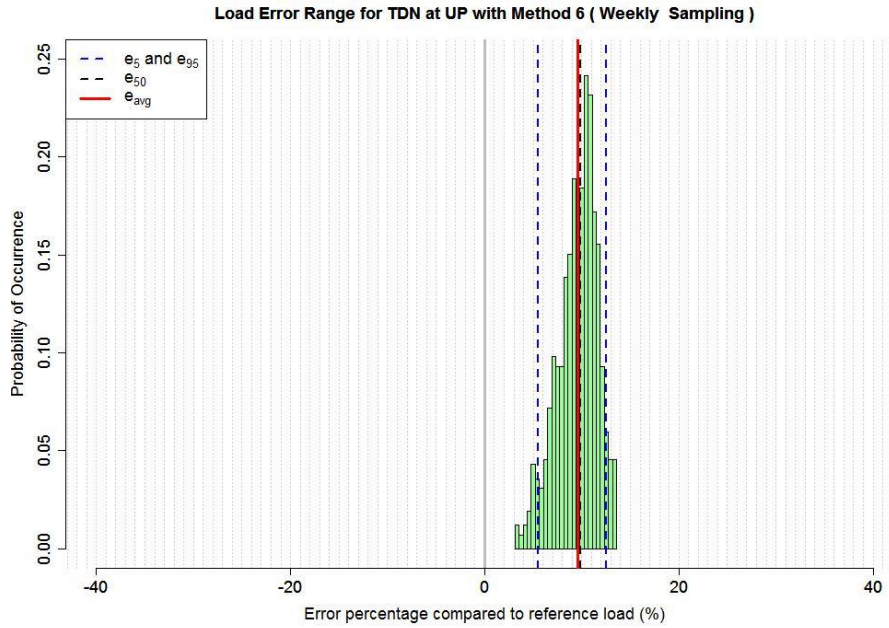


Figure E.28

Distribution of uncertainties estimation presented in the percentage as relative difference of reference annual load expressed as histogram for TDN (uncertainties with the bias [e_{avg} , red solid line or e_{50} , black dash line] and precision [e_5 and e_{95} , blue dash lines, are precision limits of 5th and 95th percentiles, respectively) with infrequent sampling (M6, weekly) at UP.

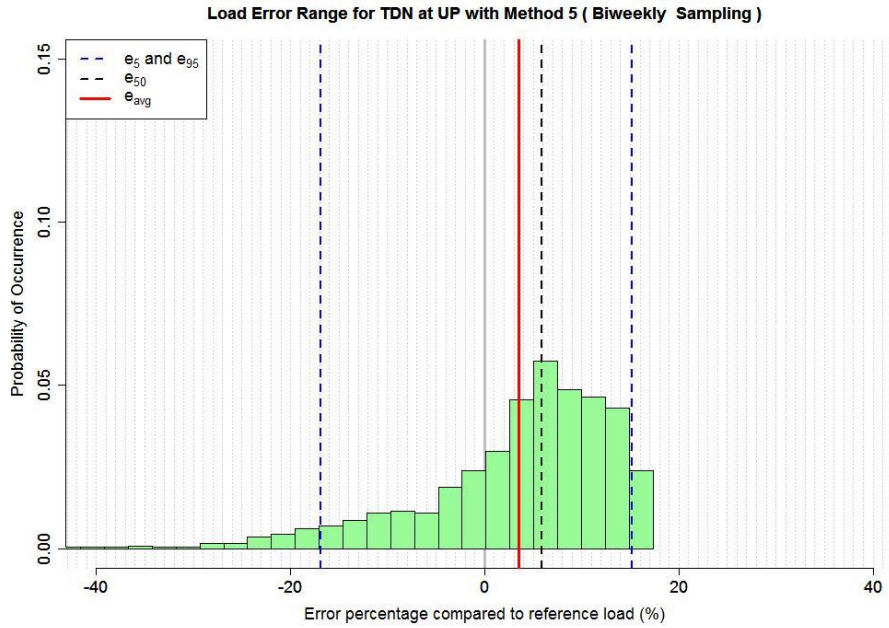


Figure E.29

Distribution of uncertainties estimation presented in the percentage as relative difference of reference annual load expressed as histogram for TDN (uncertainties with the bias [e_{avg} , red solid line or e_{50} , black dash line] and precision [e_5 and e_{95} , blue dash lines, are precision limits of 5th and 95th percentiles, respectively) with infrequent sampling (M5, biweekly) at UP.

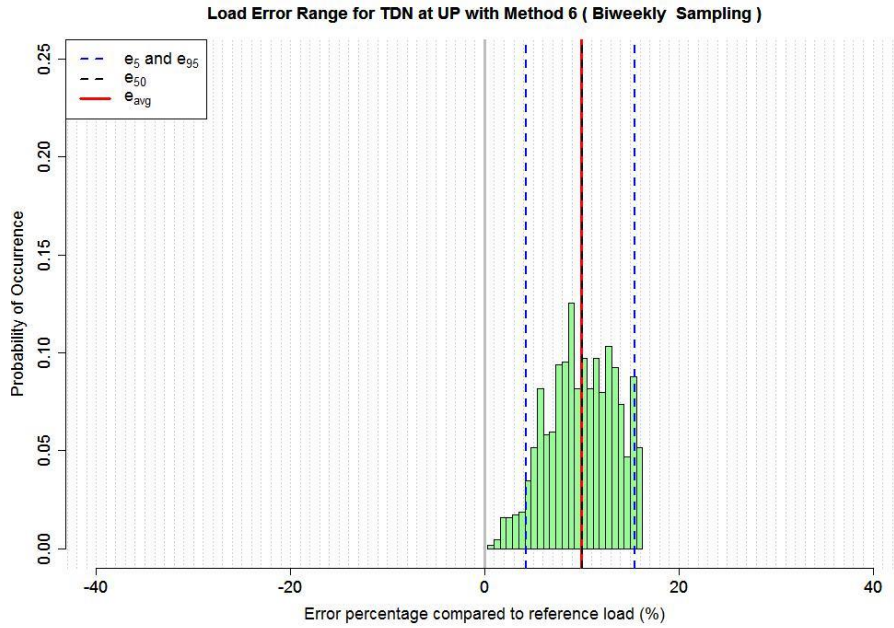


Figure E.30

Distribution of uncertainties estimation presented in the percentage as relative difference of reference annual load expressed as histogram for TDN (uncertainties with the bias [e_{avg} , red solid line or e_{50} , black dash line] and precision [e_5 and e_{95} , blue dash lines, are precision limits of 5th and 95th percentiles, respectively) with infrequent sampling (M6, biweekly) at UP.

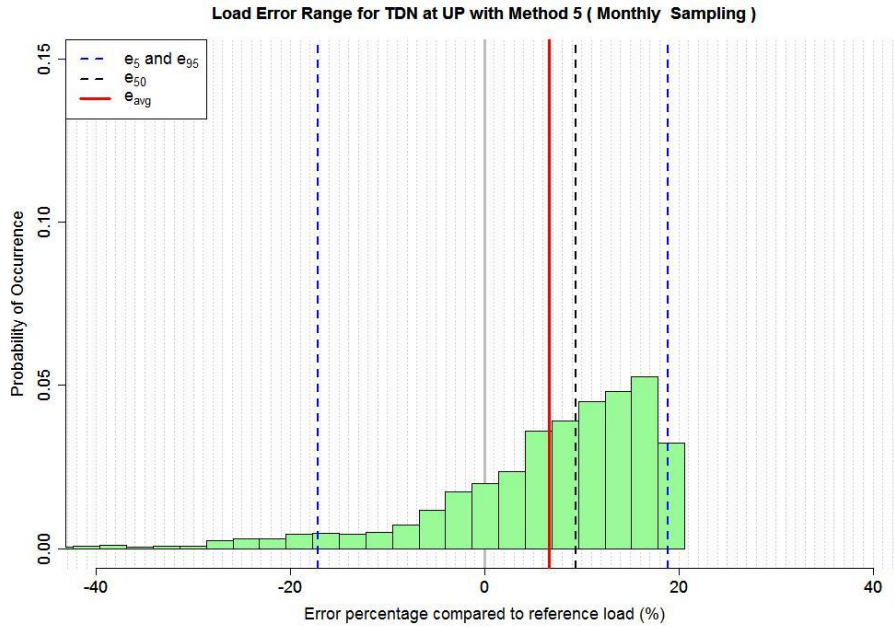


Figure E.31

Distribution of uncertainties estimation presented in the percentage as relative difference of reference annual load expressed as histogram for TDN (uncertainties with the bias [e_{avg} , red solid line or e_{50} , black dash line] and precision [e_5 and e_{95} , blue dash lines, are precision limits of 5th and 95th percentiles, respectively) with infrequent sampling (M5, monthly) at UP.

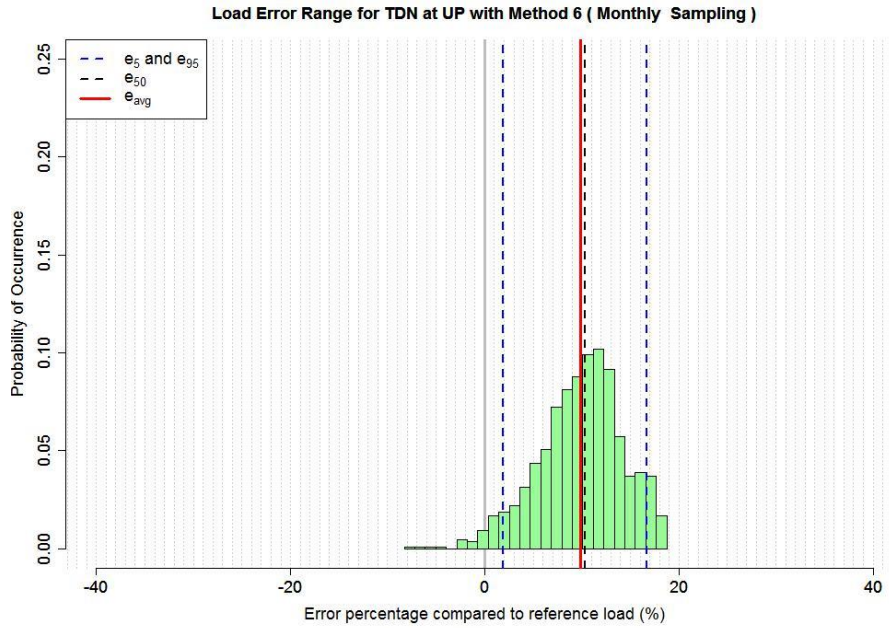


Figure E.32

Distribution of uncertainties estimation presented in the percentage as relative difference of reference annual load expressed as histogram for TDN (uncertainties with the bias [e_{avg} , red solid line or e_{50} , black dash line] and precision [e_5 and e_{95} , blue dash lines, are precision limits of 5th and 95th percentiles, respectively) with infrequent sampling (M6, monthly) at UP.

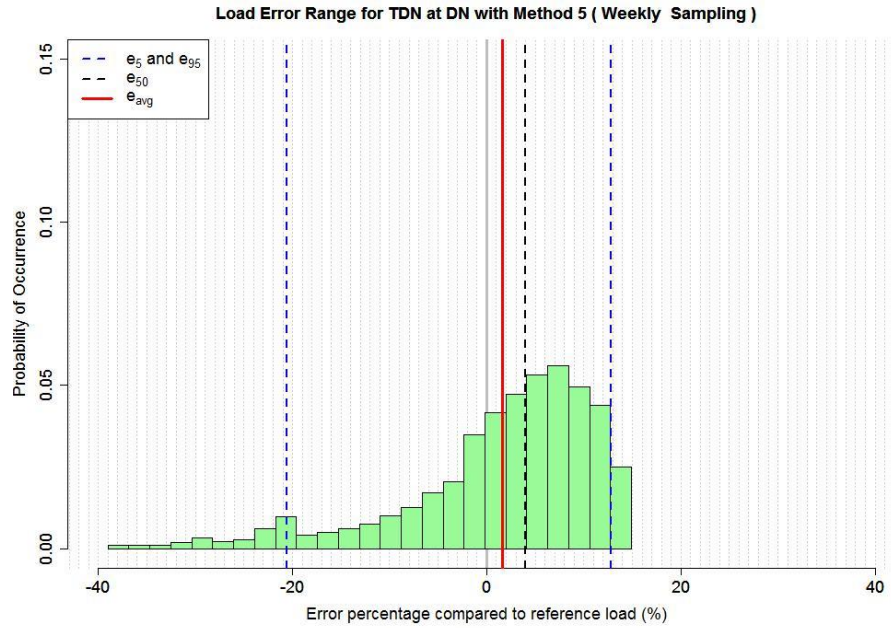


Figure E.33

Distribution of uncertainties estimation presented in the percentage as relative difference of reference annual load expressed as histogram for TDN (uncertainties with the bias [e_{avg} , red solid line or e_{50} , black dash line] and precision [e_5 and e_{95} , blue dash lines, are precision limits of 5th and 95th percentiles, respectively) with infrequent sampling (M5, weekly) at DN.

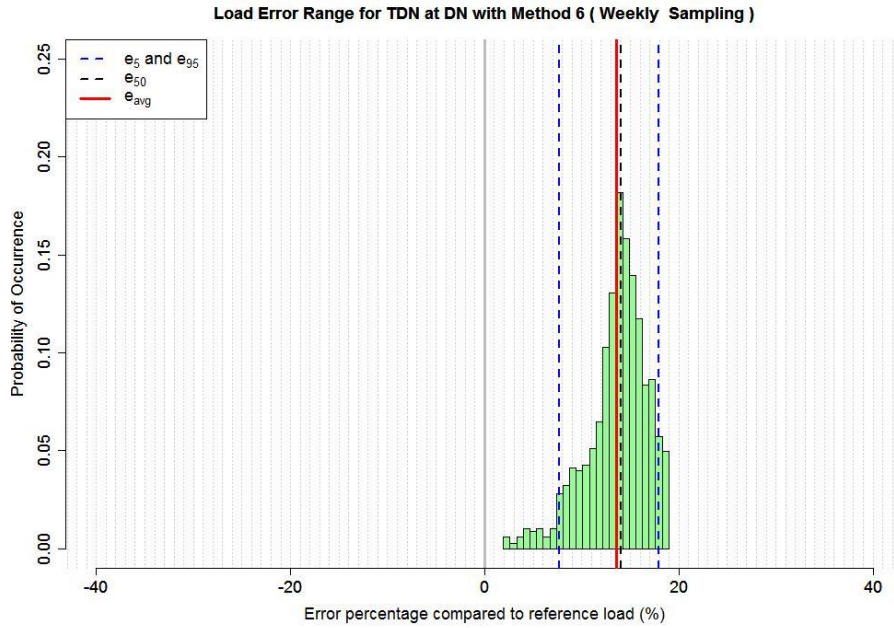


Figure E.34

Distribution of uncertainties estimation presented in the percentage as relative difference of reference annual load expressed as histogram for TDN (uncertainties with the bias [e_{avg} , red solid line or e_{50} , black dash line] and precision [e_5 and e_{95} , blue dash lines, are precision limits of 5th and 95th percentiles, respectively) with infrequent sampling (M6, weekly) at DN.

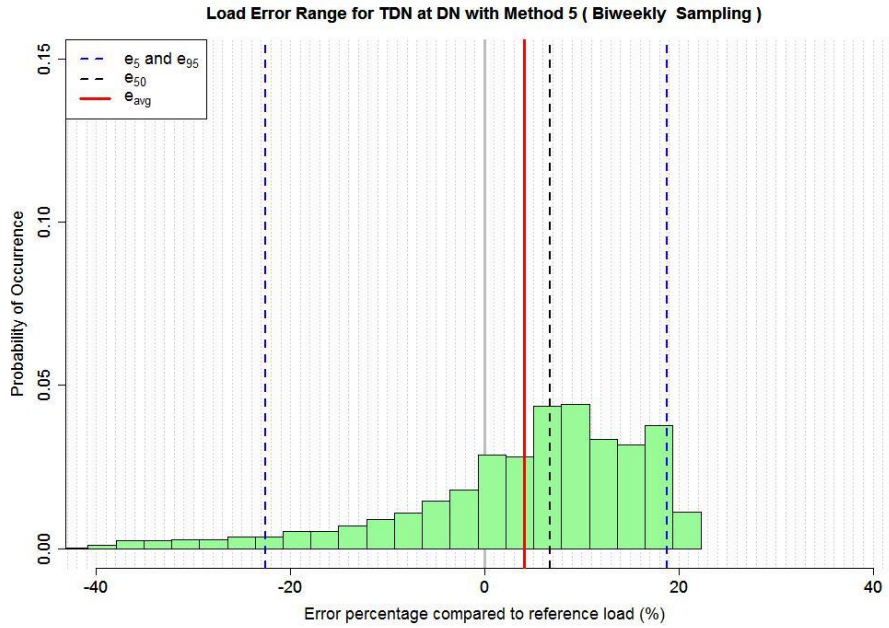


Figure E.35

Distribution of uncertainties estimation presented in the percentage as relative difference of reference annual load expressed as histogram for TDN (uncertainties with the bias [e_{avg} , red solid line or e_{50} , black dash line] and precision [e_5 and e_{95} , blue dash lines, are precision limits of 5th and 95th percentiles, respectively) with infrequent sampling (M5, biweekly) at DN.

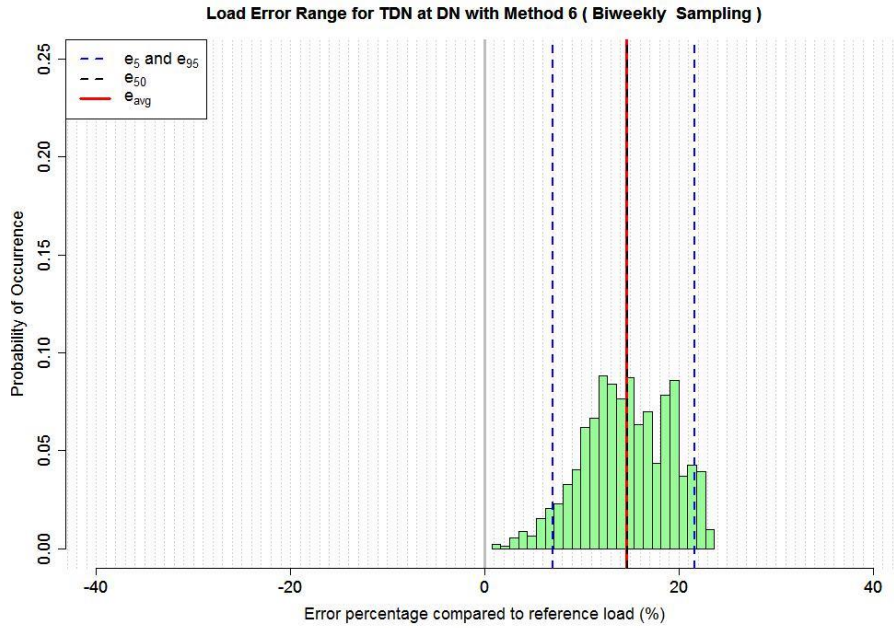


Figure E.36

Distribution of uncertainties estimation presented in the percentage as relative difference of reference annual load expressed as histogram for TDN (uncertainties with the bias [e_{avg} , red solid line or e_{50} , black dash line] and precision [e_5 and e_{95} , blue dash lines, are precision limits of 5th and 95th percentiles, respectively) with infrequent sampling (M6, biweekly) at DN.

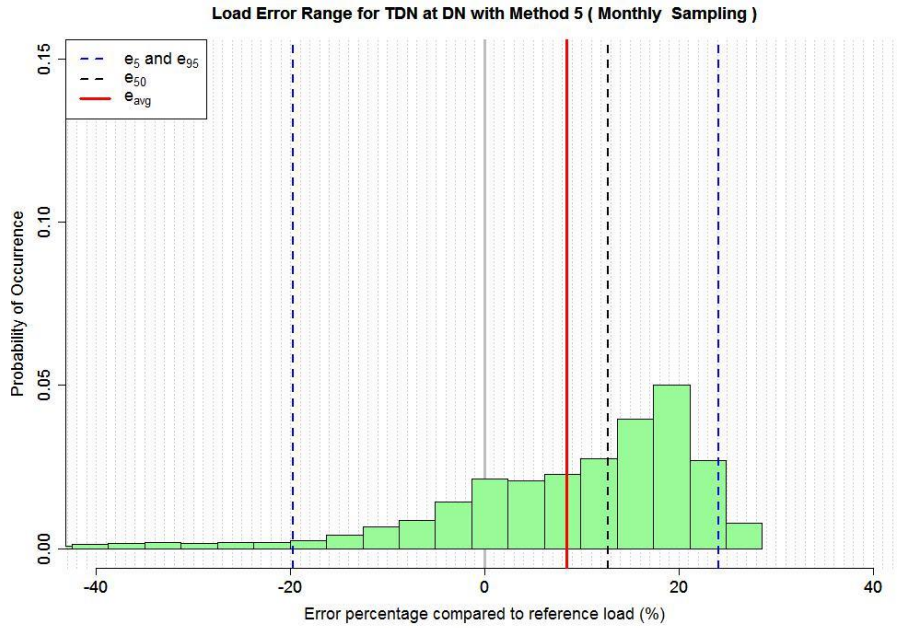


Figure E.37

Distribution of uncertainties estimation presented in the percentage as relative difference of reference annual load expressed as histogram for TDN (uncertainties with the bias [e_{avg} , red solid line or e_{50} , black dash line] and precision [e_5 and e_{95} , blue dash lines, are precision limits of 5th and 95th percentiles, respectively) with infrequent sampling (M5, monthly) at DN.

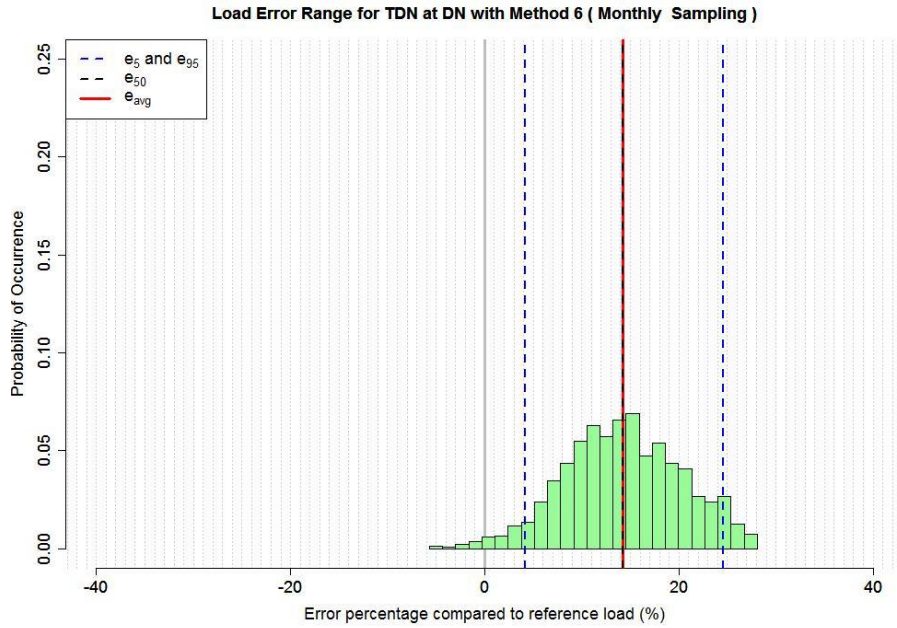


Figure E.38

Distribution of uncertainties estimation presented in the percentage as relative difference of reference annual load expressed as histogram for TDN (uncertainties with the bias [e_{avg} , red solid line or e_{50} , black dash line] and precision [e_5 and e_{95} , blue dash lines, are precision limits of 5th and 95th percentiles, respectively) with infrequent sampling (M6, monthly) at DN.

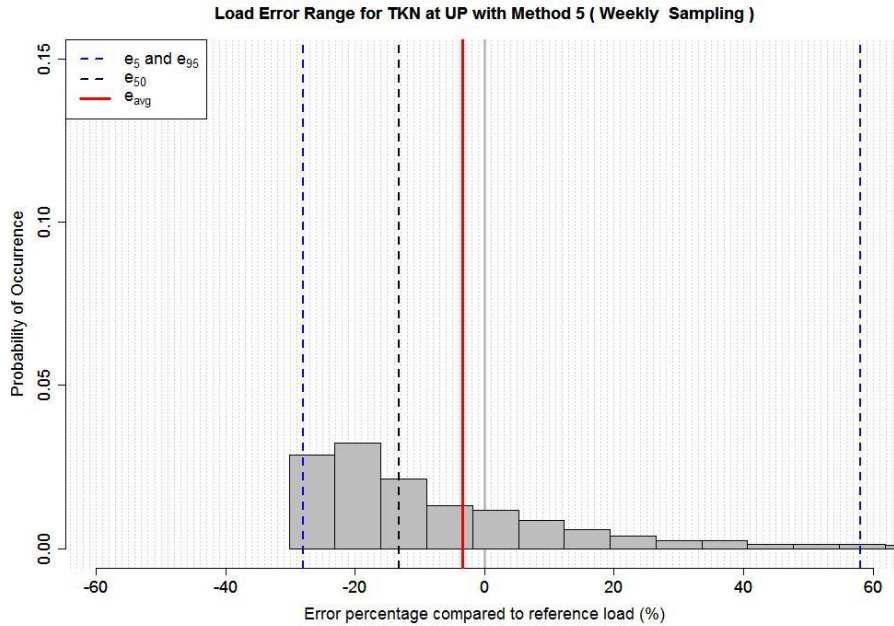


Figure E.39

Distribution of uncertainties estimation presented in the percentage as relative difference of reference annual load expressed as histogram for TKN (uncertainties with the bias [e_{avg} , red solid line or e_{50} , black dash line] and precision [e_5 and e_{95} , blue dash lines, are precision limits of 5th and 95th percentiles, respectively) with infrequent sampling (M5, weekly) at UP.

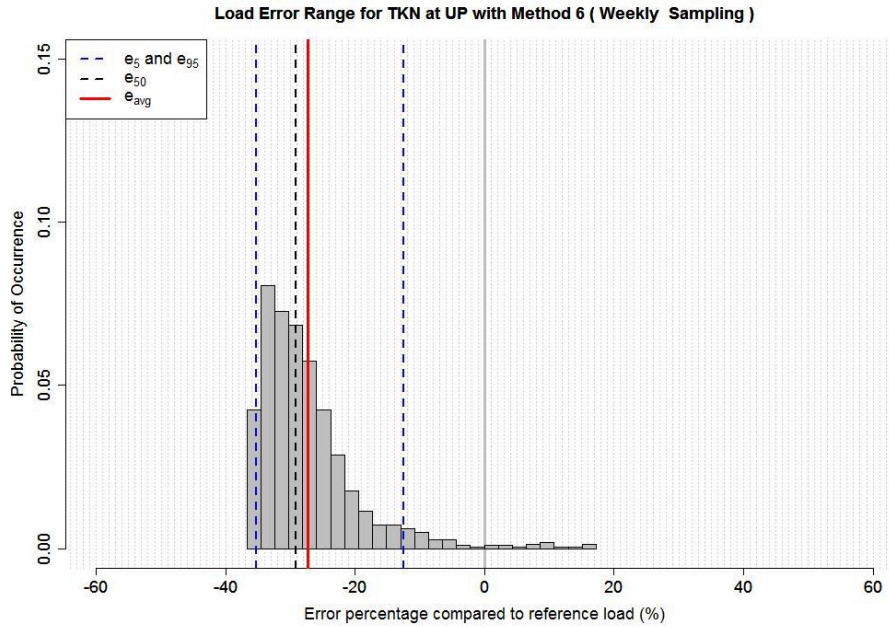


Figure E.40

Distribution of uncertainties estimation presented in the percentage as relative difference of reference annual load expressed as histogram for TKN (uncertainties with the bias [e_{avg} , red solid line or e_{50} , black dash line] and precision [e_5 and e_{95} , blue dash lines, are precision limits of 5th and 95th percentiles, respectively) with infrequent sampling (M6, weekly) at UP.

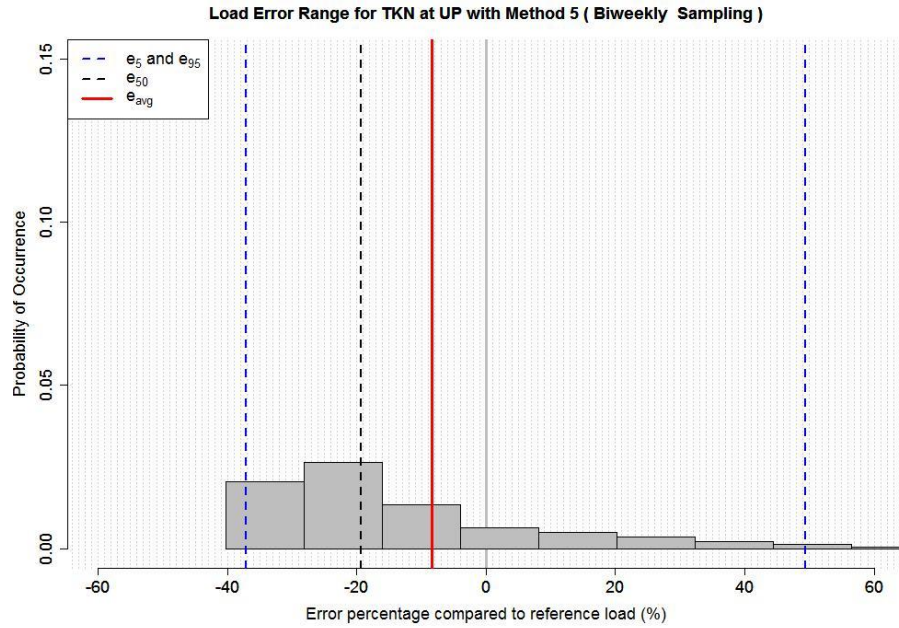


Figure E.41

Distribution of uncertainties estimation presented in the percentage as relative difference of reference annual load expressed as histogram for TKN (uncertainties with the bias [e_{avg} , red solid line or e_{50} , black dash line] and precision [e_5 and e_{95} , blue dash lines, are precision limits of 5th and 95th percentiles, respectively) with infrequent sampling (M5, biweekly) at UP.

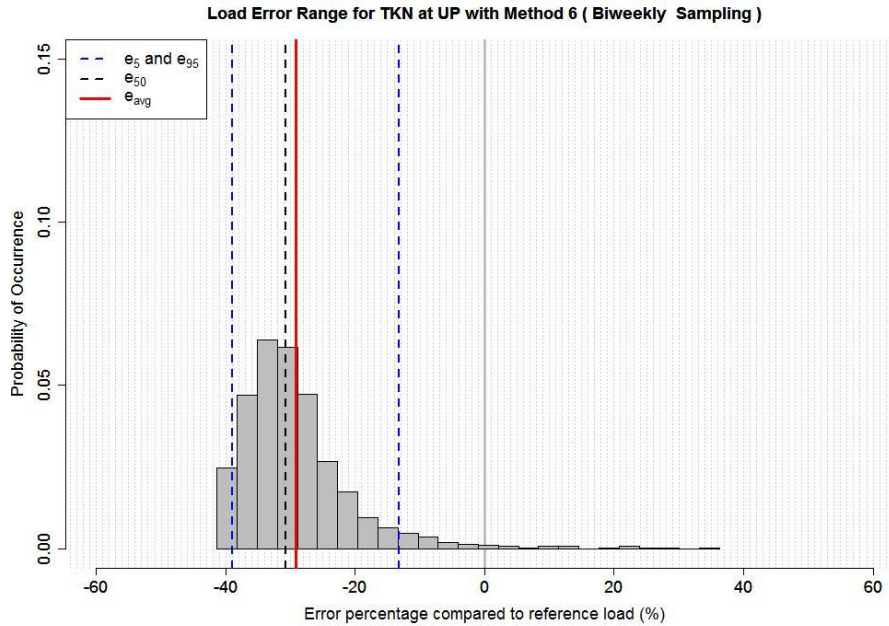


Figure E.42

Distribution of uncertainties estimation presented in the percentage as relative difference of reference annual load expressed as histogram for TKN (uncertainties with the bias [e_{avg} , red solid line or e_{50} , black dash line] and precision [e_5 and e_{95} , blue dash lines, are precision limits of 5th and 95th percentiles, respectively) with infrequent sampling (M6, biweekly) at UP.

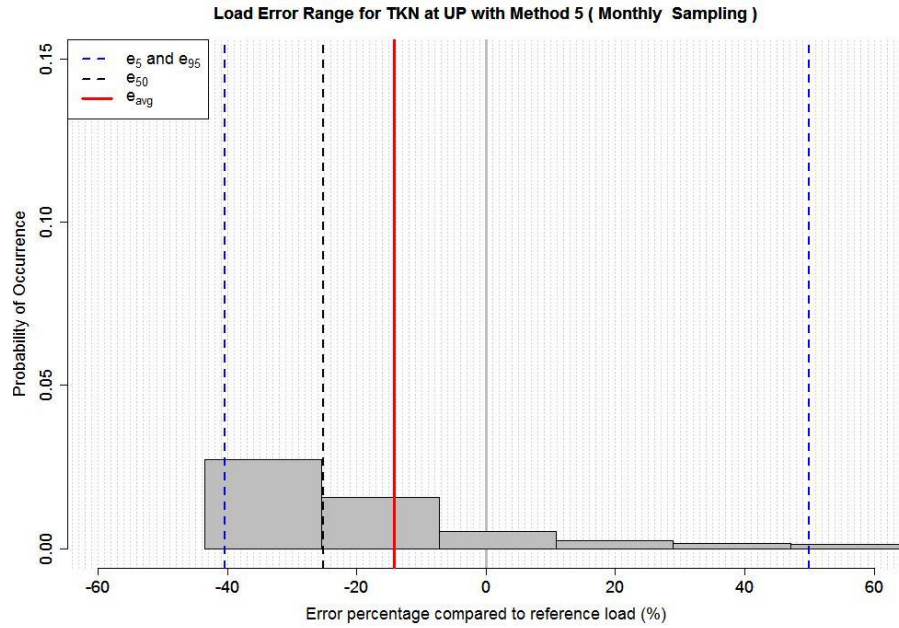


Figure E.43

Distribution of uncertainties estimation presented in the percentage as relative difference of reference annual load expressed as histogram for TKN (uncertainties with the bias [e_{avg} , red solid line or e_{50} , black dash line] and precision [e_5 and e_{95} , blue dash lines, are precision limits of 5th and 95th percentiles, respectively) with infrequent sampling (M5, monthly) at UP.

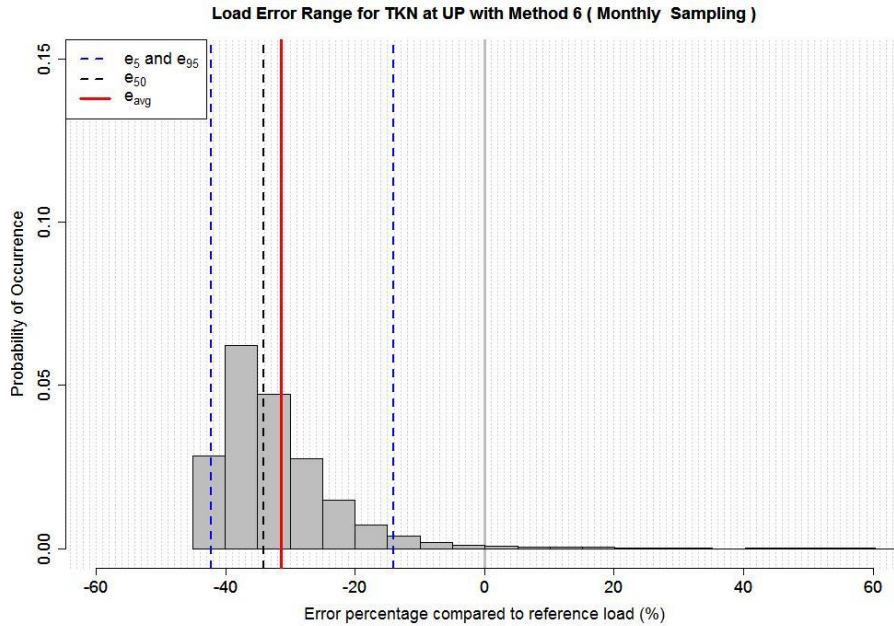


Figure E.44

Distribution of uncertainties estimation presented in the percentage as relative difference of reference annual load expressed as histogram for TKN (uncertainties with the bias [e_{avg} , red solid line or e_{50} , black dash line] and precision [e_5 and e_{95} , blue dash lines, are precision limits of 5th and 95th percentiles, respectively) with infrequent sampling (M6, monthly) at UP.

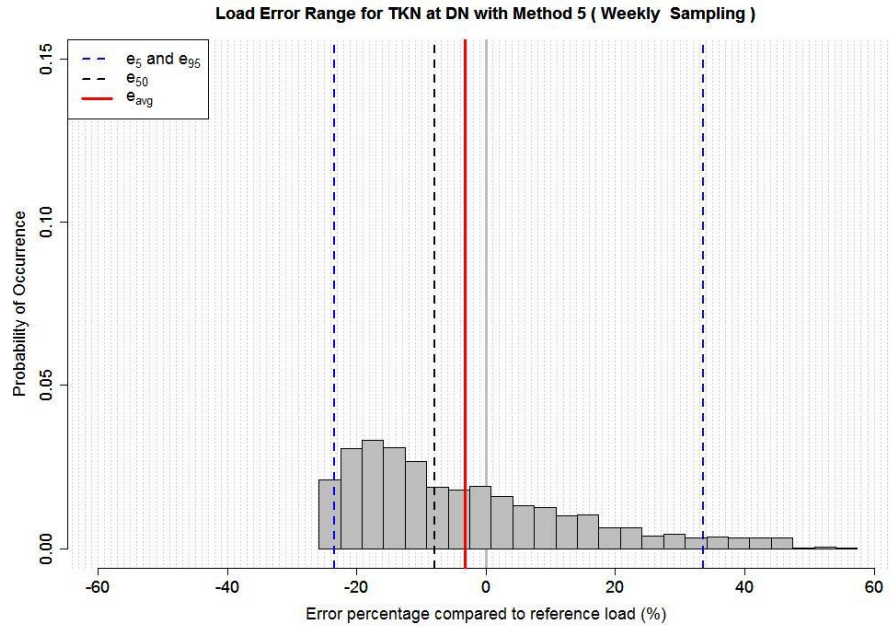


Figure E.45

Distribution of uncertainties estimation presented in the percentage as relative difference of reference annual load expressed as histogram for TKN (uncertainties with the bias [e_{avg} , red solid line or e_{50} , black dash line] and precision [e_5 and e_{95} , blue dash lines, are precision limits of 5th and 95th percentiles, respectively) with infrequent sampling (M5, weekly) at DN.

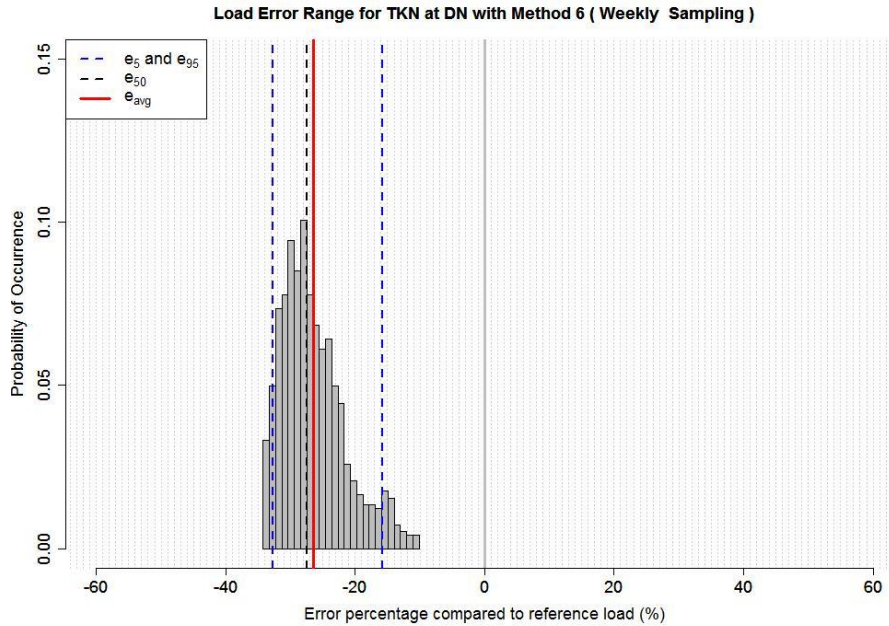


Figure E.46

Distribution of uncertainties estimation presented in the percentage as relative difference of reference annual load expressed as histogram for TKN (uncertainties with the bias [e_{avg} , red solid line or e_{50} , black dash line] and precision [e_5 and e_{95} , blue dash lines, are precision limits of 5th and 95th percentiles, respectively) with infrequent sampling (M6, weekly) at DN.

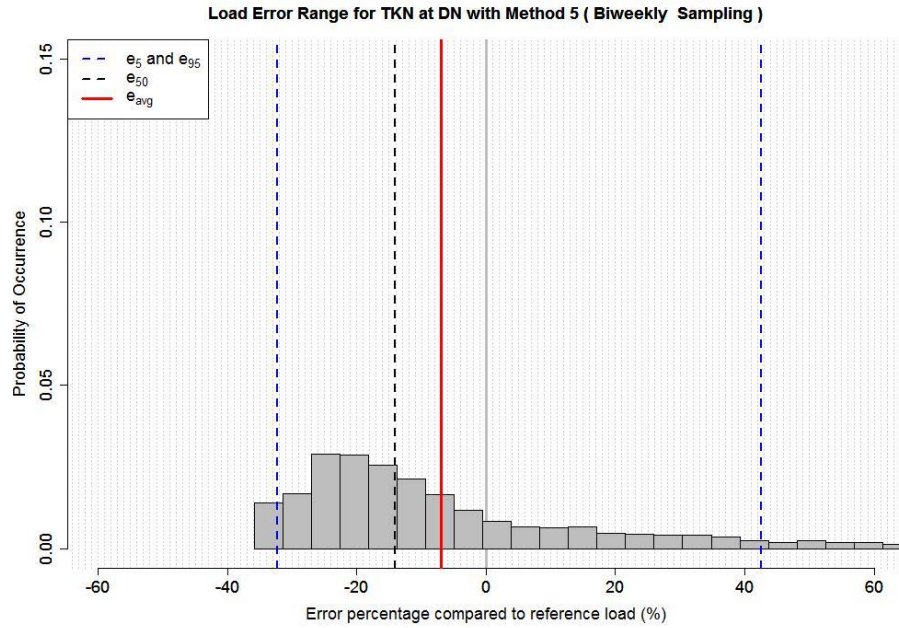


Figure E.47

Distribution of uncertainties estimation presented in the percentage as relative difference of reference annual load expressed as histogram for TKN (uncertainties with the bias [e_{avg} , red solid line or e_{50} , black dash line] and precision [e_5 and e_{95} , blue dash lines, are precision limits of 5th and 95th percentiles, respectively) with infrequent sampling (M5, biweekly) at DN.

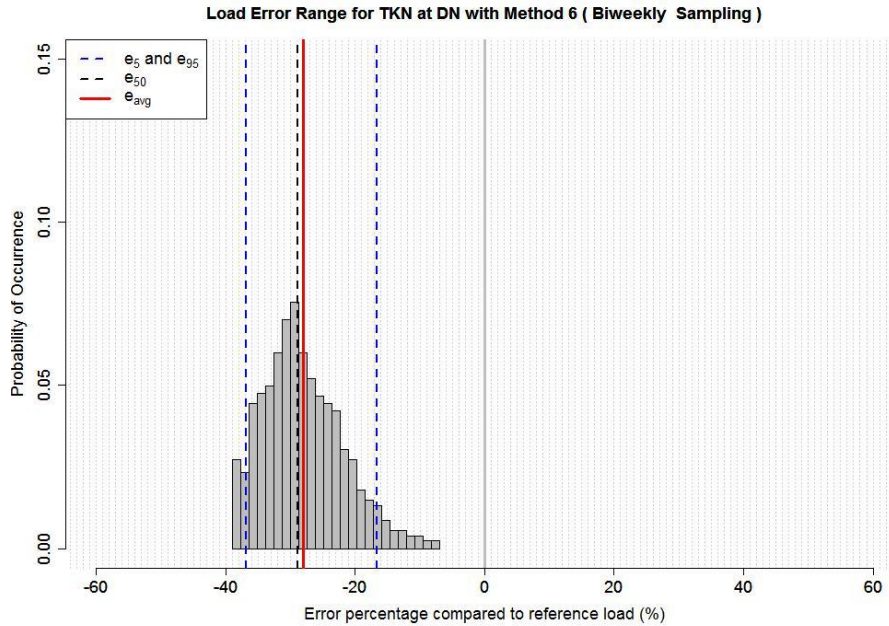


Figure E.48

Distribution of uncertainties estimation presented in the percentage as relative difference of reference annual load expressed as histogram for TKN (uncertainties with the bias [e_{avg} , red solid line or e_{50} , black dash line] and precision [e_5 and e_{95} , blue dash lines, are precision limits of 5th and 95th percentiles, respectively) with infrequent sampling (M6, biweekly) at DN.

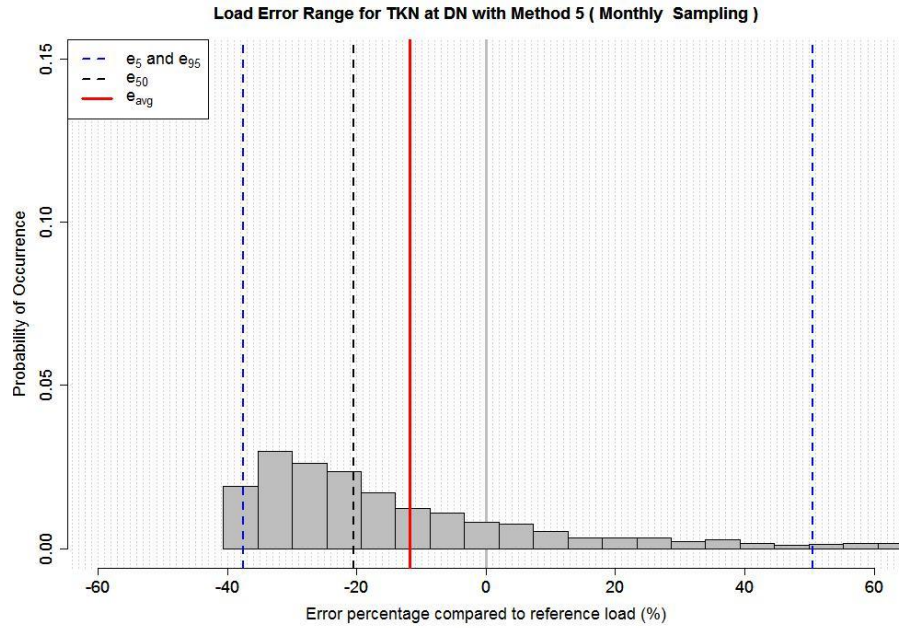


Figure E.49

Distribution of uncertainties estimation presented in the percentage as relative difference of reference annual load expressed as histogram for TKN (uncertainties with the bias [e_{avg} , red solid line or e_{50} , black dash line] and precision [e_5 and e_{95} , blue dash lines, are precision limits of 5th and 95th percentiles, respectively) with infrequent sampling (M5, monthly) at DN.

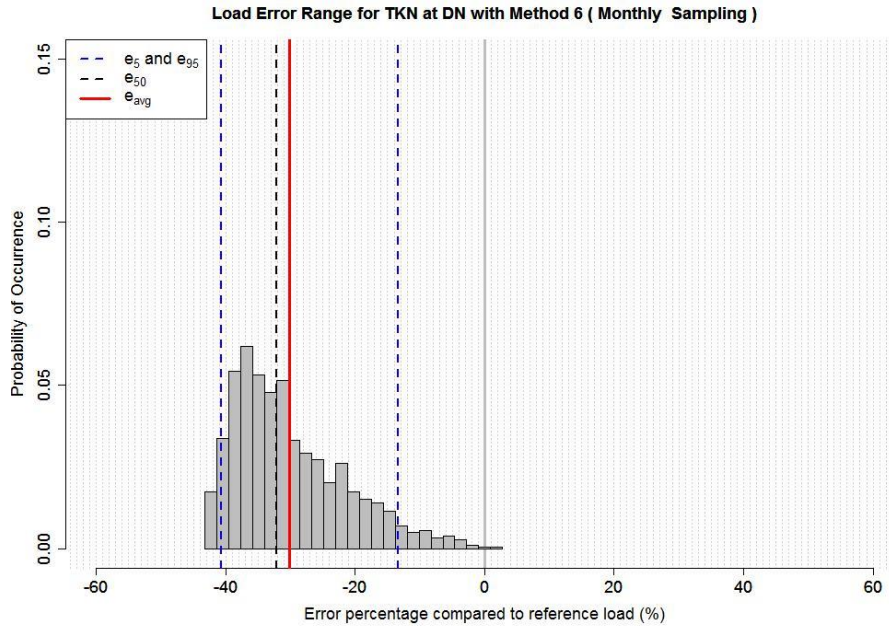


Figure E.50

Distribution of uncertainties estimation presented in the percentage as relative difference of reference annual load expressed as histogram for TKN (uncertainties with the bias [e_{avg} , red solid line or e_{50} , black dash line] and precision [e_5 and e_{95} , blue dash lines, are precision limits of 5th and 95th percentiles, respectively) with infrequent sampling (M6, monthly) at DN.

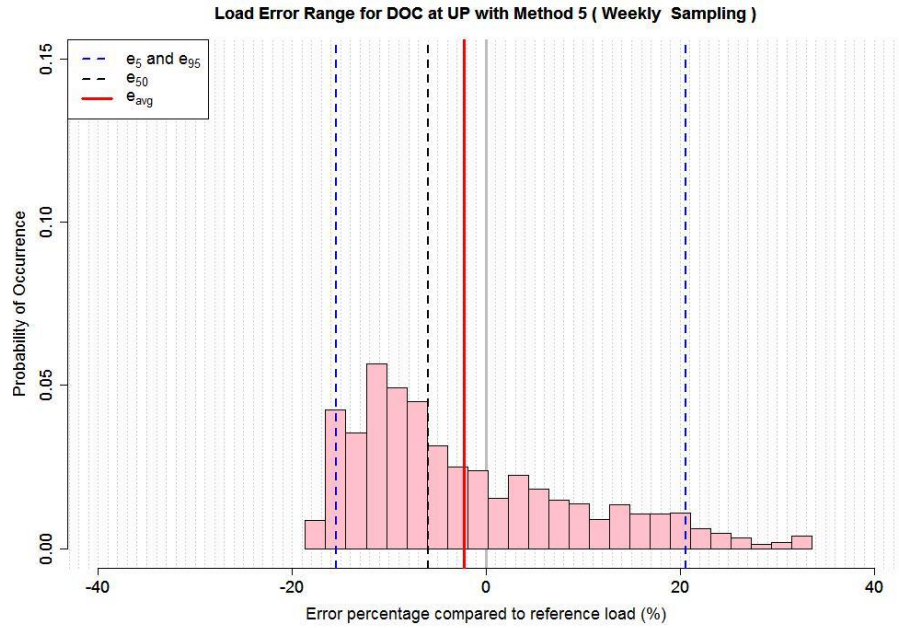


Figure E.51

Distribution of uncertainties estimation presented in the percentage as relative difference of reference annual load expressed as histogram for DOC (uncertainties with the bias [e_{avg} , red solid line or e_{50} , black dash line] and precision [e_5 and e_{95} , blue dash lines, are precision limits of 5th and 95th percentiles, respectively) with infrequent sampling (M5, weekly) at UP.

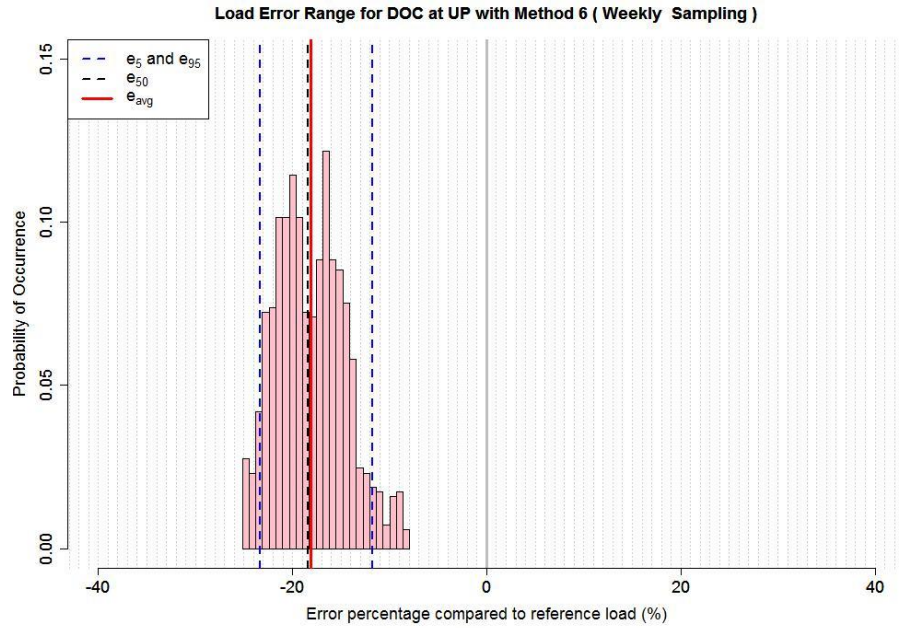


Figure E.52

Distribution of uncertainties estimation presented in the percentage as relative difference of reference annual load expressed as histogram for DOC (uncertainties with the bias [e_{avg} , red solid line or e_{50} , black dash line] and precision [e_5 and e_{95} , blue dash lines, are precision limits of 5th and 95th percentiles, respectively) with infrequent sampling (M6, weekly) at UP.

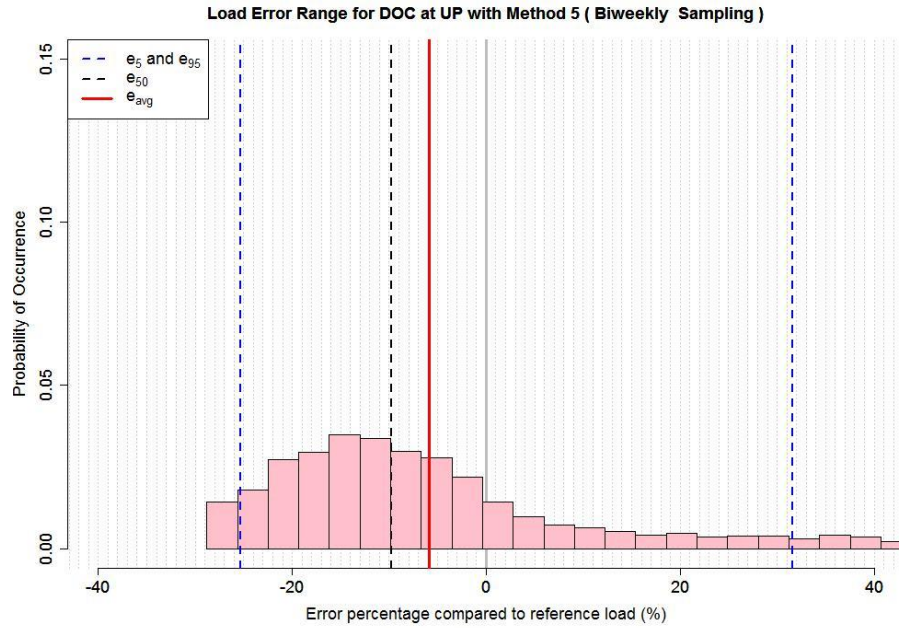


Figure E.53

Distribution of uncertainties estimation presented in the percentage as relative difference of reference annual load expressed as histogram for DOC (uncertainties with the bias [e_{avg} , red solid line or e_{50} , black dash line] and precision [e_5 and e_{95} , blue dash lines, are precision limits of 5th and 95th percentiles, respectively) with infrequent sampling (M5, biweekly) at UP.

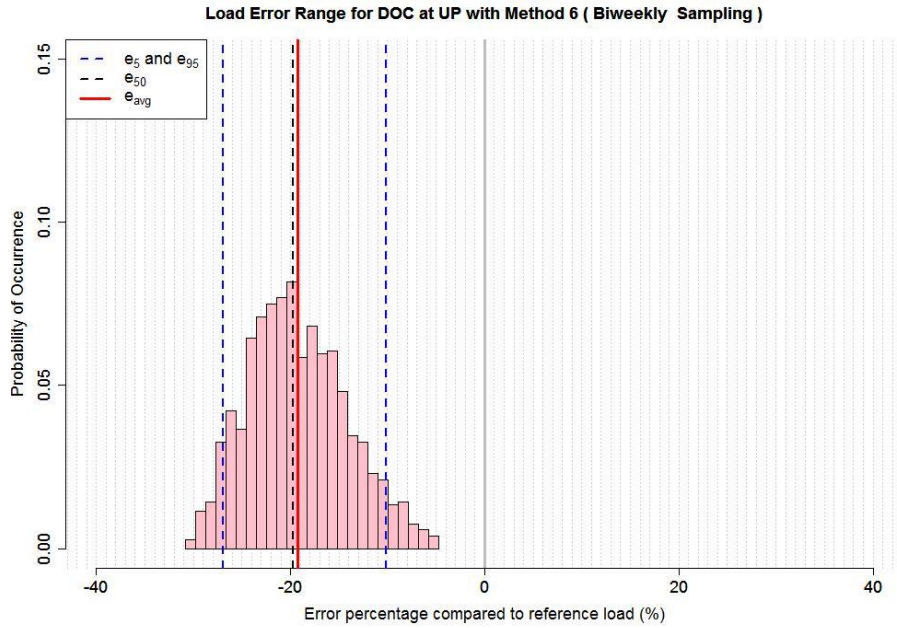


Figure E.54

Distribution of uncertainties estimation presented in the percentage as relative difference of reference annual load expressed as histogram for DOC (uncertainties with the bias [e_{avg} , red solid line or e_{50} , black dash line] and precision [e_5 and e_{95} , blue dash lines, are precision limits of 5th and 95th percentiles, respectively) with infrequent sampling (M6, biweekly) at UP.

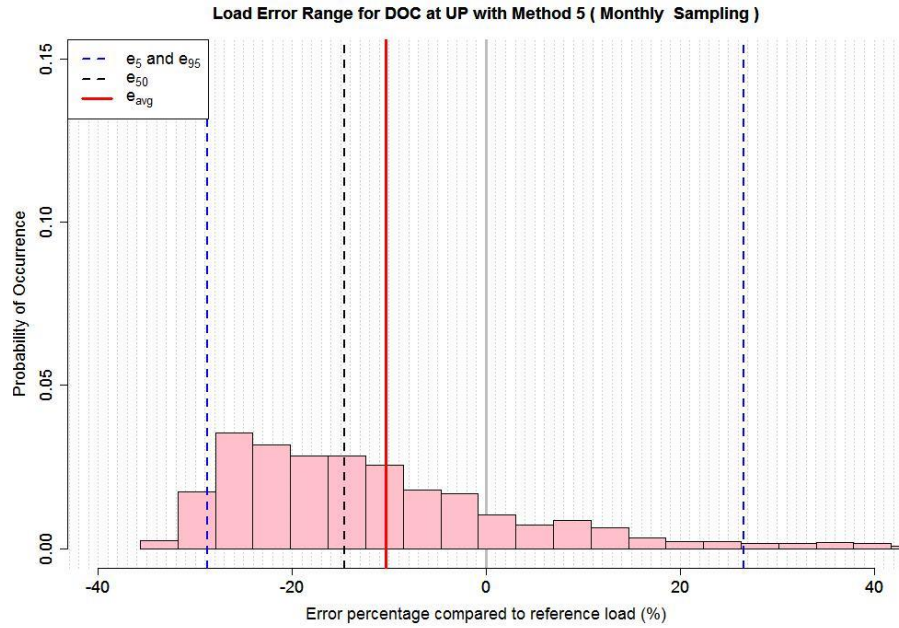


Figure E.55

Distribution of uncertainties estimation presented in the percentage as relative difference of reference annual load expressed as histogram for DOC (uncertainties with the bias [e_{avg} , red solid line or e_{50} , black dash line] and precision [e_5 and e_{95} , blue dash lines, are precision limits of 5th and 95th percentiles, respectively) with infrequent sampling (M5, monthly) at UP.

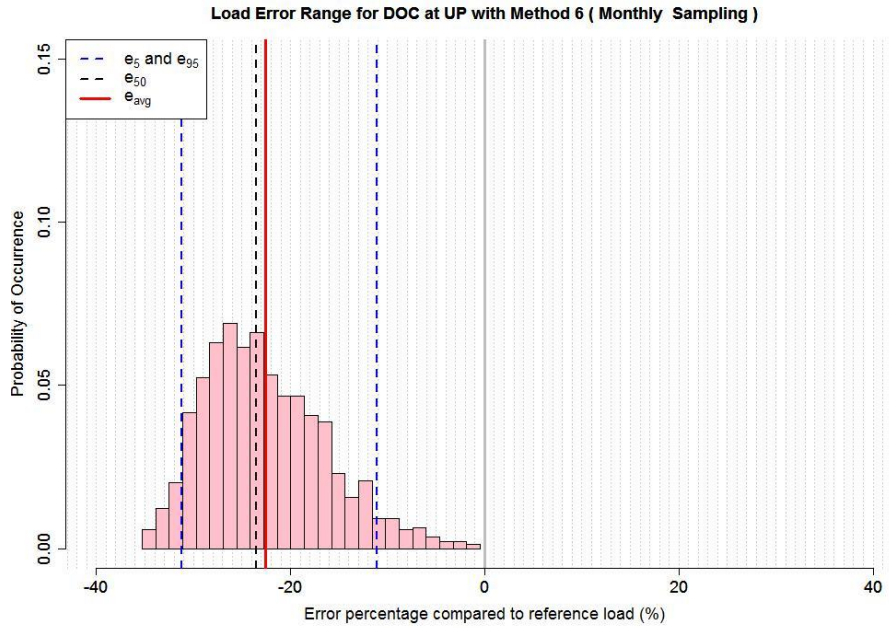


Figure E.56

Distribution of uncertainties estimation presented in the percentage as relative difference of reference annual load expressed as histogram for DOC (uncertainties with the bias [e_{avg} , red solid line or e_{50} , black dash line] and precision [e_5 and e_{95} , blue dash lines, are precision limits of 5th and 95th percentiles, respectively) with infrequent sampling (M6, monthly) at UP.

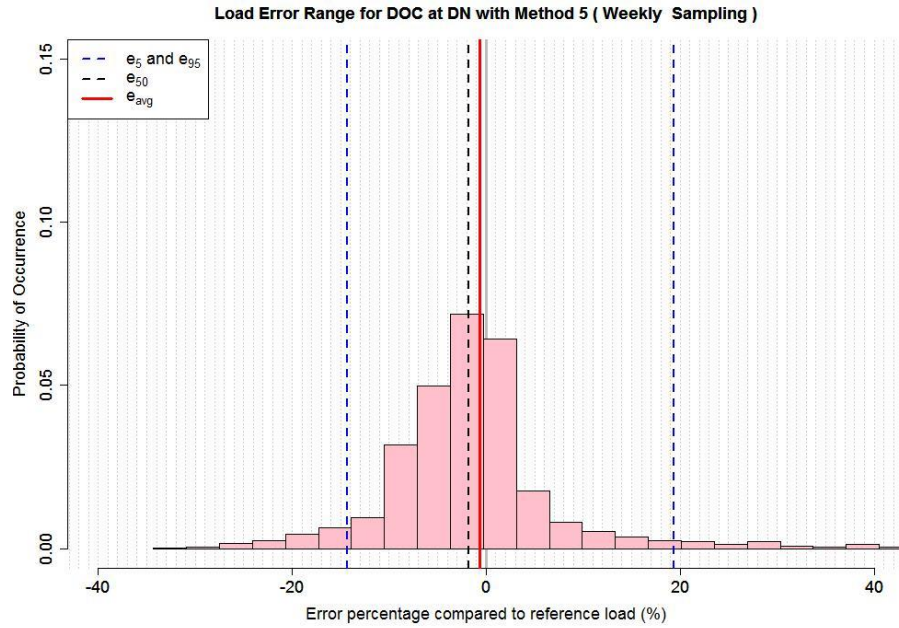


Figure E.57

Distribution of uncertainties estimation presented in the percentage as relative difference of reference annual load expressed as histogram for DOC (uncertainties with the bias [e_{avg} , red solid line or e_{50} , black dash line] and precision [e_5 and e_{95} , blue dash lines, are precision limits of 5th and 95th percentiles, respectively) with infrequent sampling (M5, weekly) at DN.

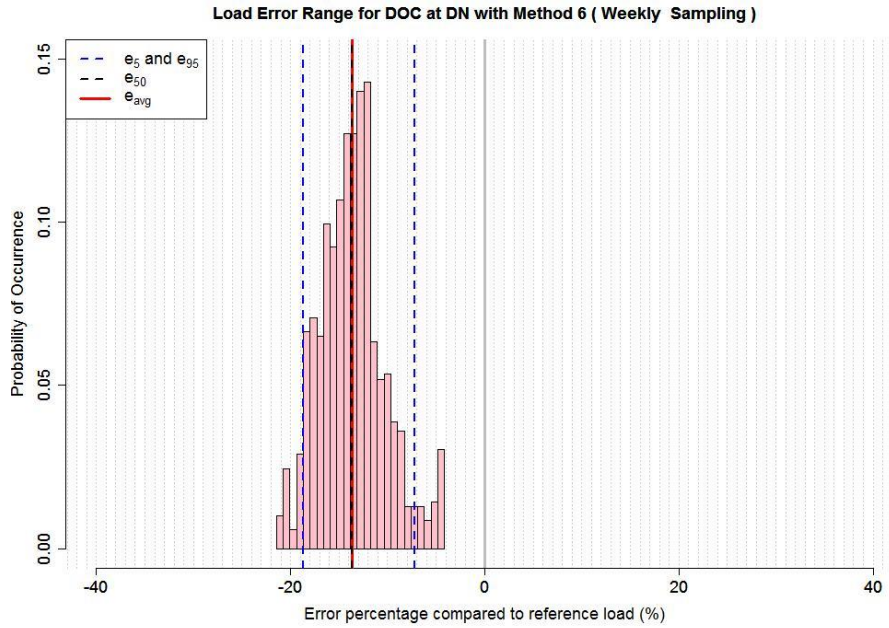


Figure E.58

Distribution of uncertainties estimation presented in the percentage as relative difference of reference annual load expressed as histogram for DOC (uncertainties with the bias [e_{avg} , red solid line or e_{50} , black dash line] and precision [e_5 and e_{95} , blue dash lines, are precision limits of 5th and 95th percentiles, respectively) with infrequent sampling (M6, weekly) at DN.

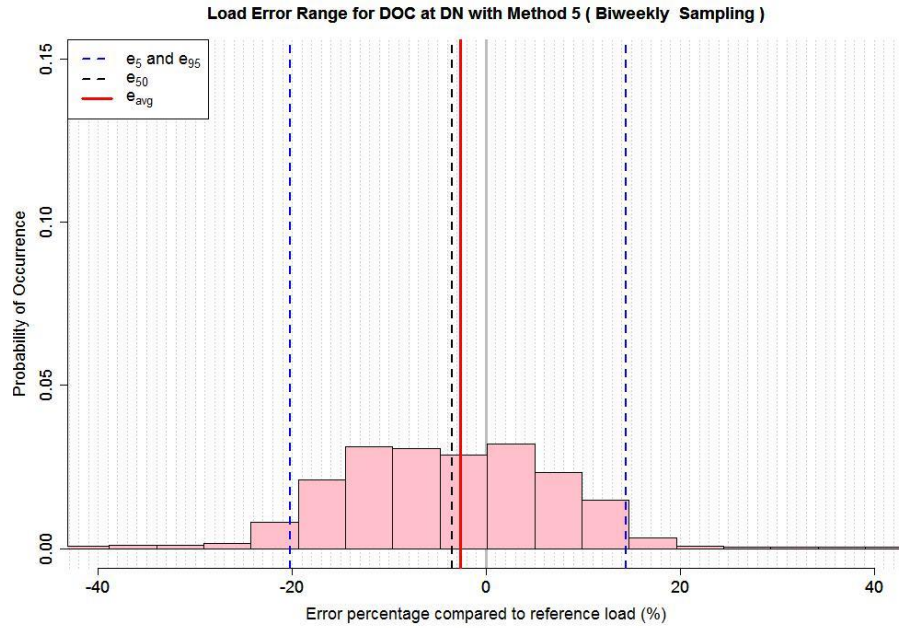


Figure E.59

Distribution of uncertainties estimation presented in the percentage as relative difference of reference annual load expressed as histogram for DOC (uncertainties with the bias [e_{avg} , red solid line or e_{50} , black dash line] and precision [e_5 and e_{95} , blue dash lines, are precision limits of 5th and 95th percentiles, respectively) with infrequent sampling (M5, biweekly) at DN.

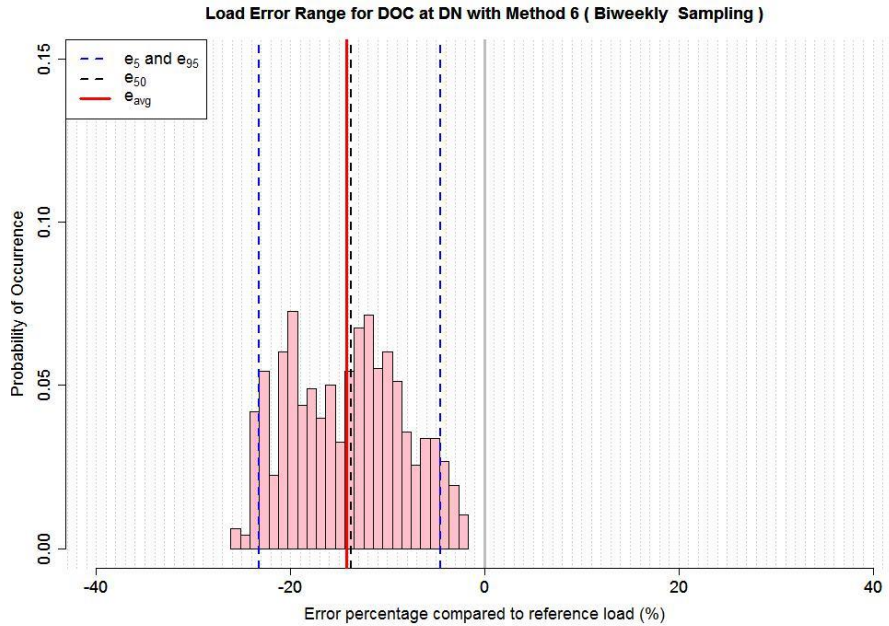


Figure E.60

Distribution of uncertainties estimation presented in the percentage as relative difference of reference annual load expressed as histogram for DOC (uncertainties with the bias [e_{avg} , red solid line or e_{50} , black dash line] and precision [e_5 and e_{95} , blue dash lines, are precision limits of 5th and 95th percentiles, respectively) with infrequent sampling (M6, biweekly) at DN.

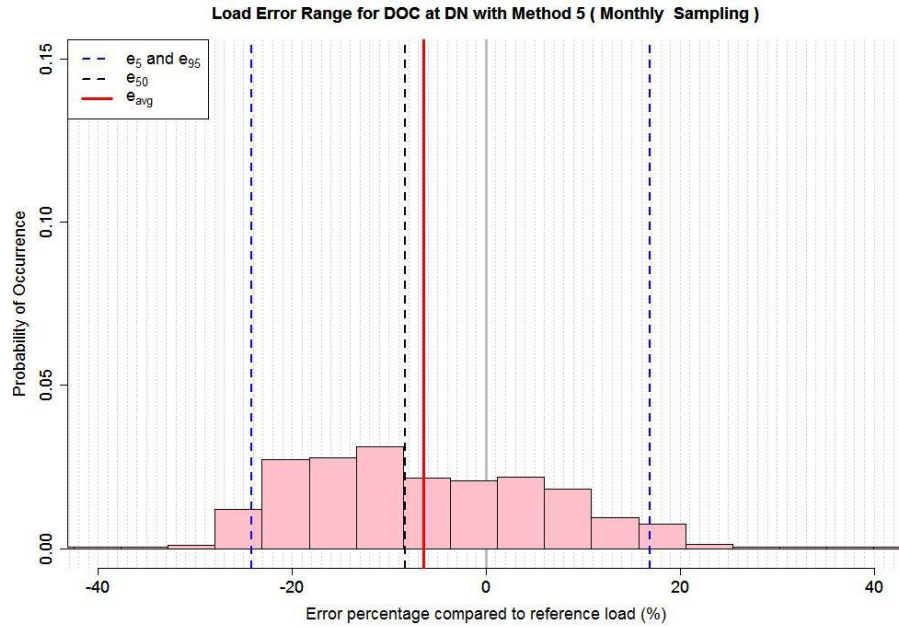


Figure E.61

Distribution of uncertainties estimation presented in the percentage as relative difference of reference annual load expressed as histogram for DOC (uncertainties with the bias [e_{avg} , red solid line or e_{50} , black dash line] and precision [e_5 and e_{95} , blue dash lines, are precision limits of 5th and 95th percentiles, respectively) with infrequent sampling (M5, monthly) at DN.

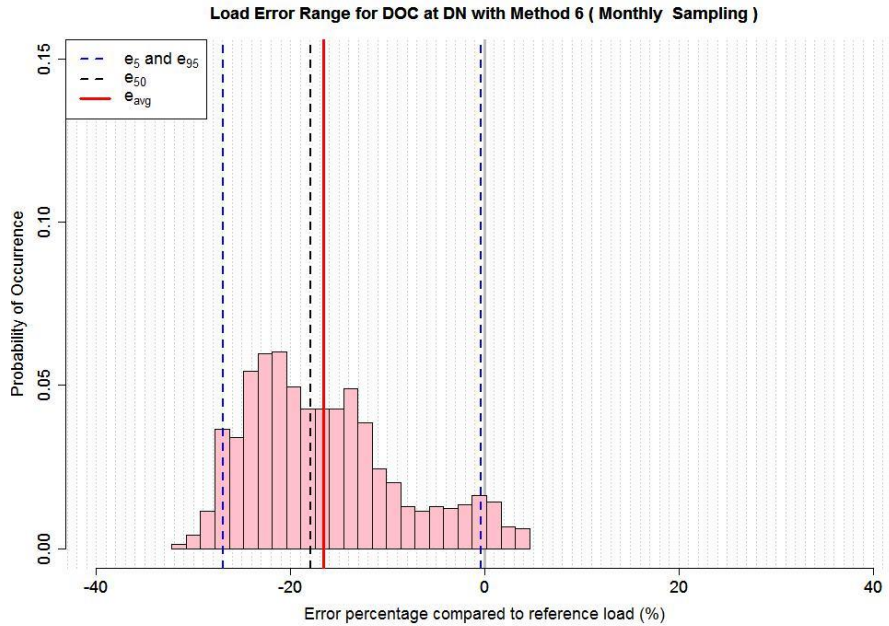


Figure E.62

Distribution of uncertainties estimation presented in the percentage as relative difference of reference annual load expressed as histogram for DOC (uncertainties with the bias [e_{avg} , red solid line or e_{50} , black dash line] and precision [e_5 and e_{95} , blue dash lines, are precision limits of 5th and 95th percentiles, respectively) with infrequent sampling (M6, monthly) at DN.

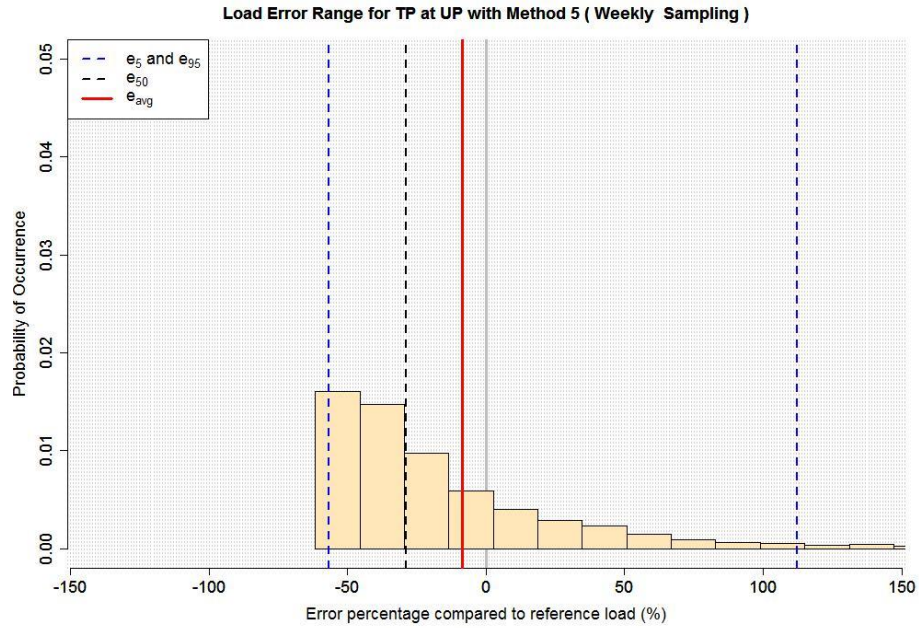


Figure E.63

Distribution of uncertainties estimation presented in the percentage as relative difference of reference annual load expressed as histogram for TP (uncertainties with the bias [e_{avg} , red solid line or e_{50} , black dash line] and precision [e_5 and e_{95} , blue dash lines, are precision limits of 5th and 95th percentiles, respectively) with infrequent sampling (M5, weekly) at UP.

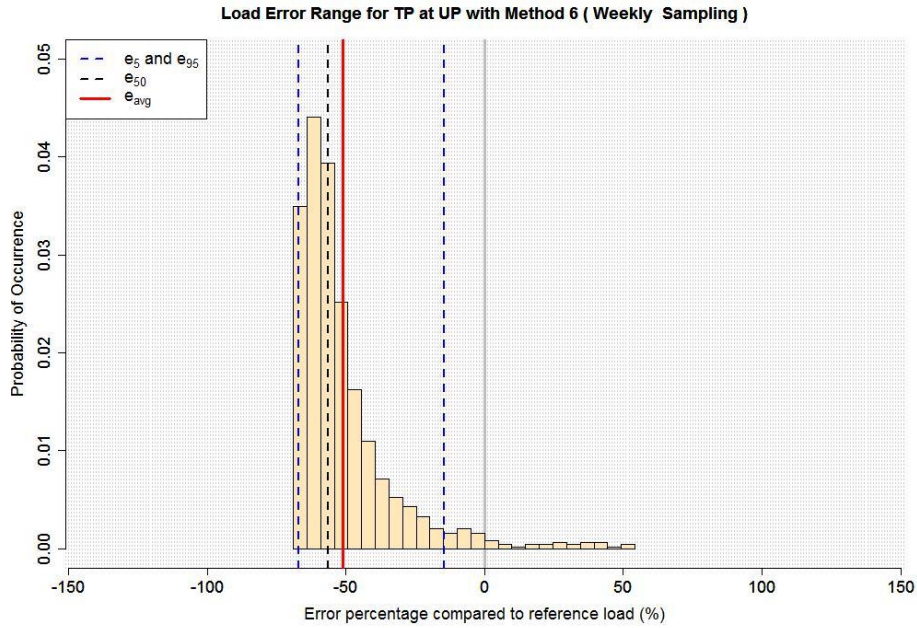


Figure E.64

Distribution of uncertainties estimation presented in the percentage as relative difference of reference annual load expressed as histogram for TP (uncertainties with the bias [e_{avg} , red solid line or e_{50} , black dash line] and precision [e_5 and e_{95} , blue dash lines, are precision limits of 5th and 95th percentiles, respectively) with infrequent sampling (M6, weekly) at UP.



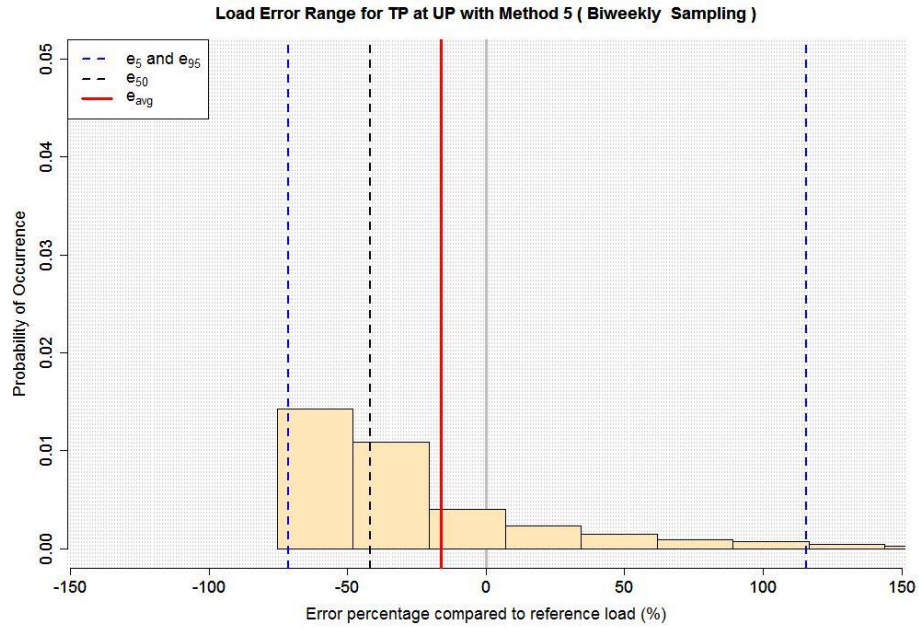


Figure E.65

Distribution of uncertainties estimation presented in the percentage as relative difference of reference annual load expressed as histogram for TP (uncertainties with the bias [e_{avg} , red solid line or e_{50} , black dash line] and precision [e_5 and e_{95} , blue dash lines, are precision limits of 5th and 95th percentiles, respectively) with infrequent sampling (M5, biweekly) at UP.

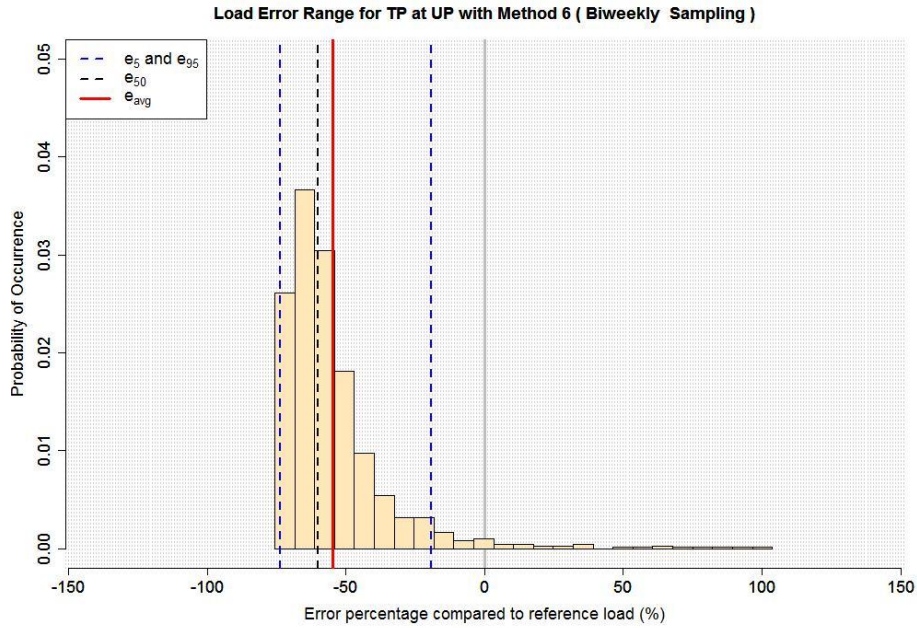


Figure E.66

Distribution of uncertainties estimation presented in the percentage as relative difference of reference annual load expressed as histogram for TP (uncertainties with the bias [e_{avg} , red solid line or e_{50} , black dash line] and precision [e_5 and e_{95} , blue dash lines, are precision limits of 5th and 95th percentiles, respectively) with infrequent sampling (M6, biweekly) at UP.

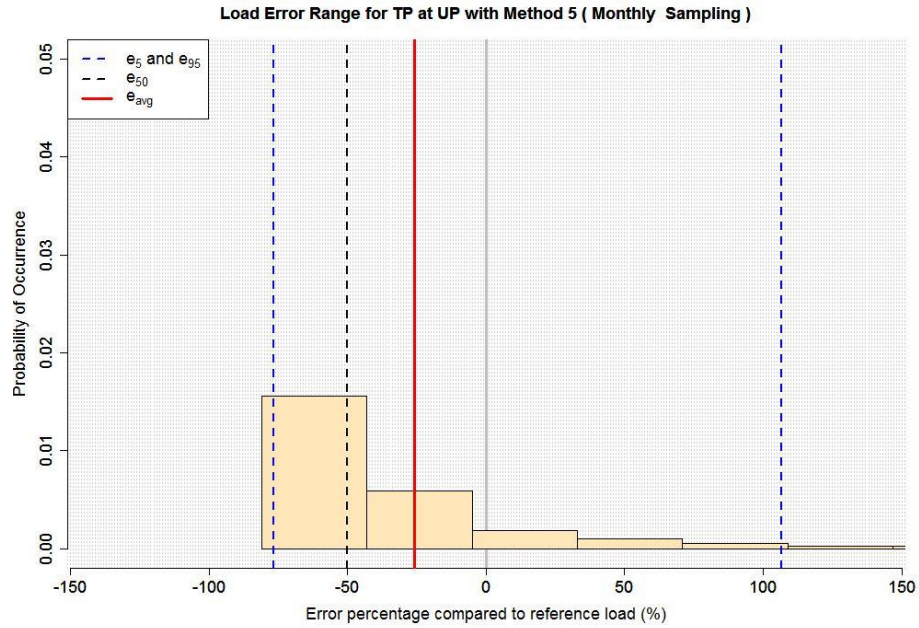


Figure E.67

Distribution of uncertainties estimation presented in the percentage as relative difference of reference annual load expressed as histogram for TP (uncertainties with the bias [e_{avg} , red solid line or e_{50} , black dash line] and precision [e_5 and e_{95} , blue dash lines, are precision limits of 5th and 95th percentiles, respectively) with infrequent sampling (M5, monthly) at UP.

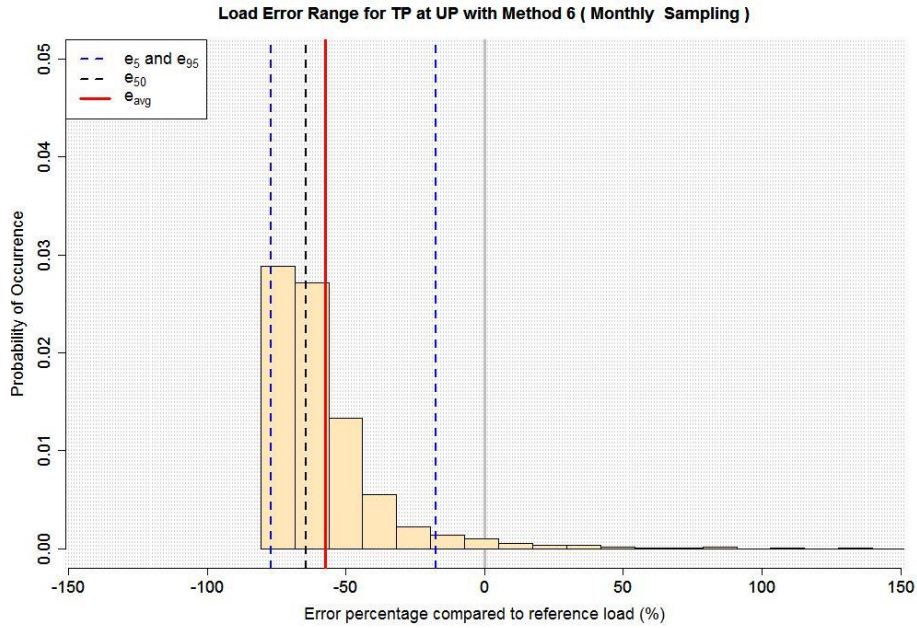


Figure E.68

Distribution of uncertainties estimation presented in the percentage as relative difference of reference annual load expressed as histogram for TP (uncertainties with the bias [e_{avg} , red solid line or e_{50} , black dash line] and precision [e_5 and e_{95} , blue dash lines, are precision limits of 5th and 95th percentiles, respectively) with infrequent sampling (M6, monthly) at UP.

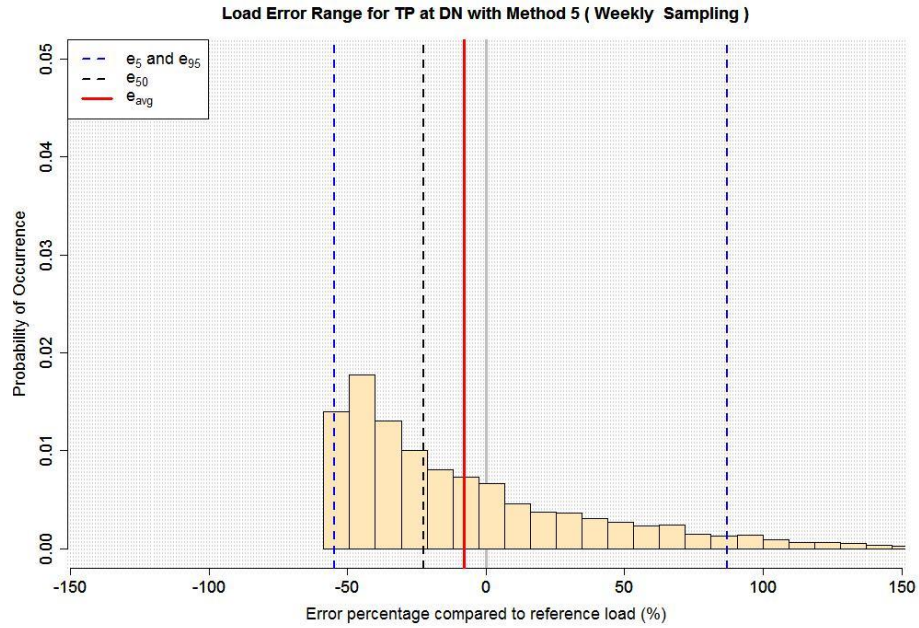


Figure E.69

Distribution of uncertainties estimation presented in the percentage as relative difference of reference annual load expressed as histogram for TP (uncertainties with the bias [e_{avg} , red solid line or e_{50} , black dash line] and precision [e_5 and e_{95} , blue dash lines, are precision limits of 5th and 95th percentiles, respectively) with infrequent sampling (M5, weekly) at DN.

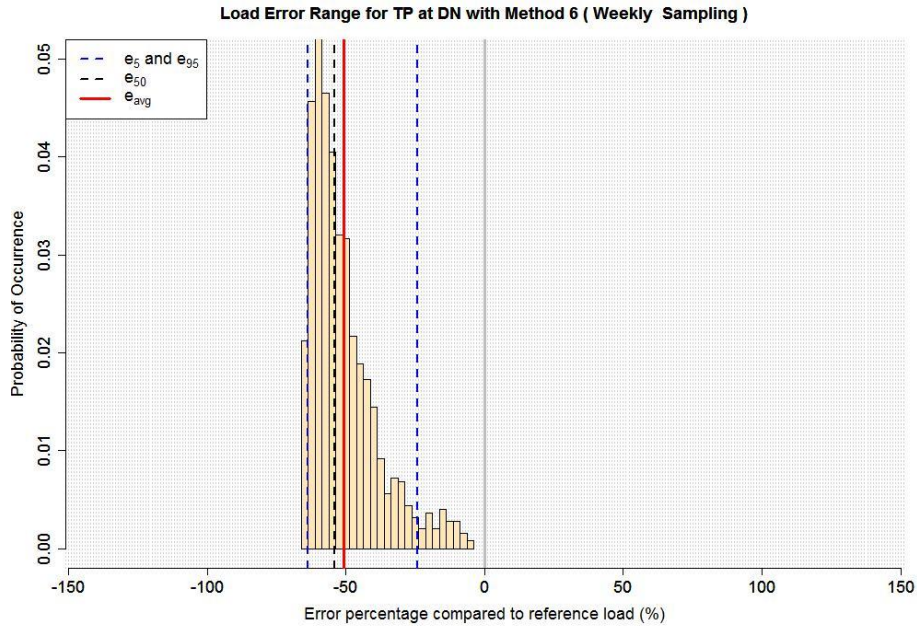


Figure E.70

Distribution of uncertainties estimation presented in the percentage as relative difference of reference annual load expressed as histogram for TP (uncertainties with the bias [e_{avg} , red solid line or e_{50} , black dash line] and precision [e_5 and e_{95} , blue dash lines, are precision limits of 5th and 95th percentiles, respectively) with infrequent sampling (M6, weekly) at DN.

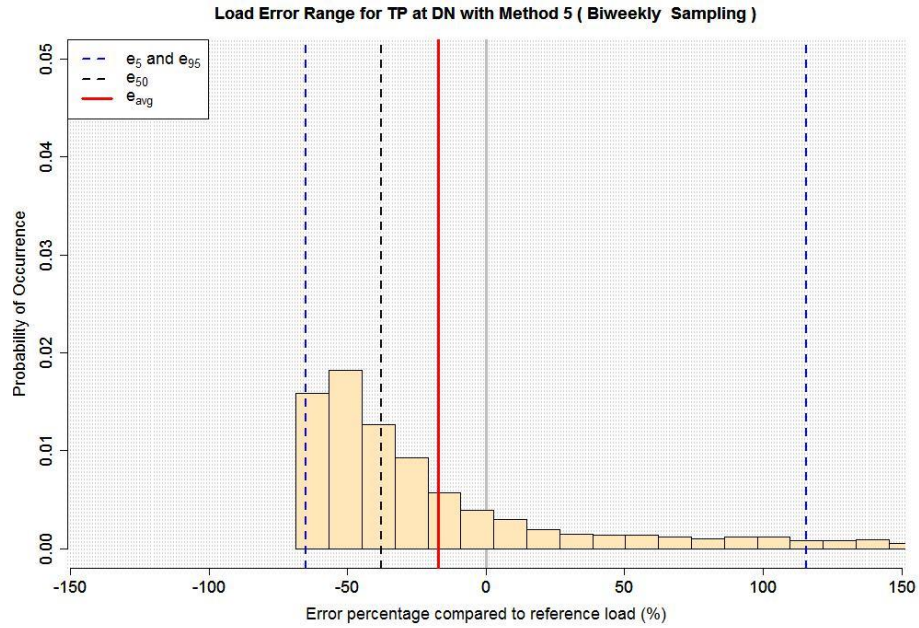


Figure E.71

Distribution of uncertainties estimation presented in the percentage as relative difference of reference annual load expressed as histogram for TP (uncertainties with the bias [e_{avg} , red solid line or e_{50} , black dash line] and precision [e_5 and e_{95} , blue dash lines, are precision limits of 5th and 95th percentiles, respectively) with infrequent sampling (M5, biweekly) at DN.

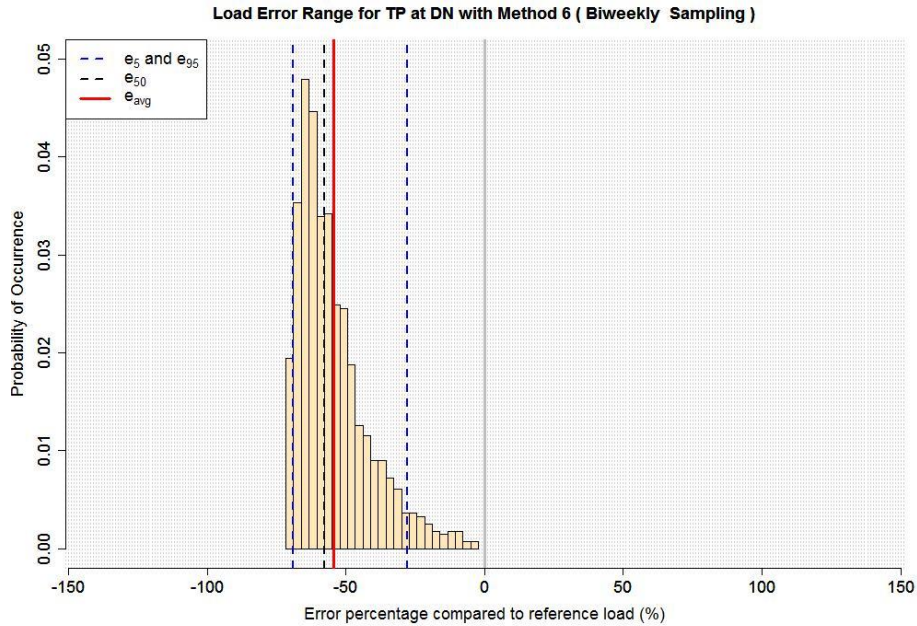


Figure E.72

Distribution of uncertainties estimation presented in the percentage as relative difference of reference annual load expressed as histogram for TP (uncertainties with the bias [e_{avg} , red solid line or e_{50} , black dash line] and precision [e_5 and e_{95} , blue dash lines, are precision limits of 5th and 95th percentiles, respectively) with infrequent sampling (M6, biweekly) at DN.

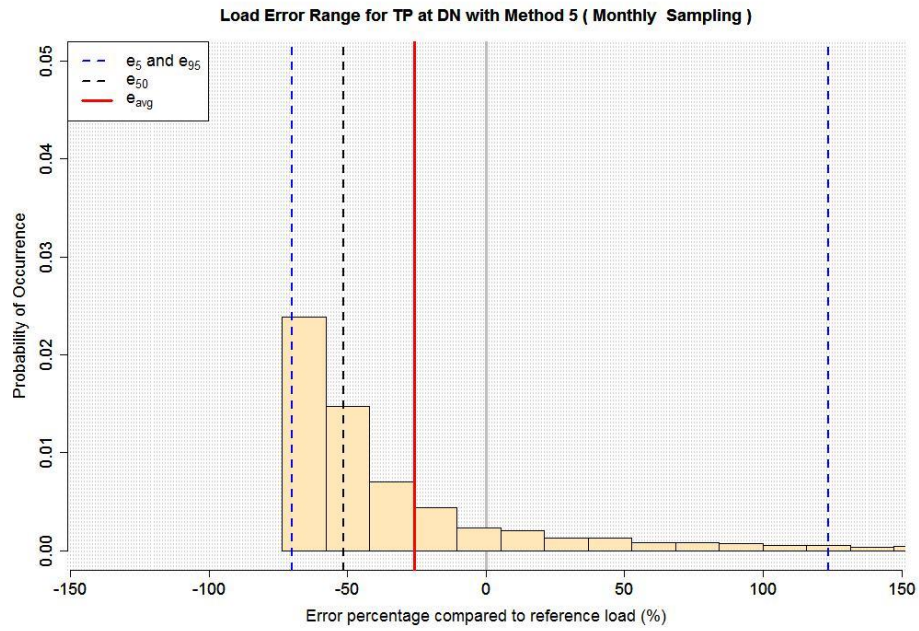


Figure E.73

Distribution of uncertainties estimation presented in the percentage as relative difference of reference annual load expressed as histogram for TP (uncertainties with the bias [e_{avg} , red solid line or e_{50} , black dash line] and precision [e_5 and e_{95} , blue dash lines, are precision limits of 5th and 95th percentiles, respectively) with infrequent sampling (M5, monthly) at DN.

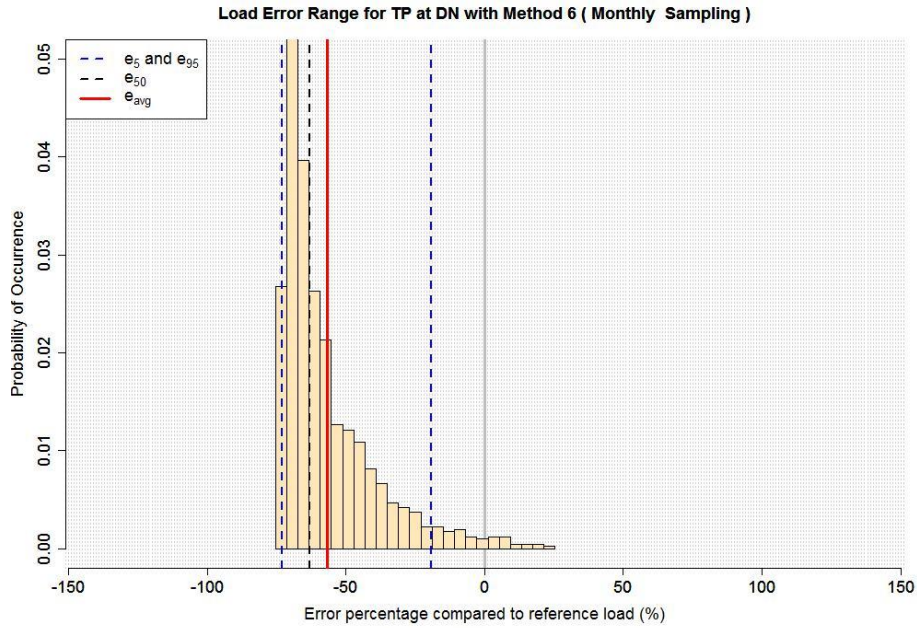


Figure E.74

Distribution of uncertainties estimation presented in the percentage as relative difference of reference annual load expressed as histogram for TP (uncertainties with the bias [e_{avg} , red solid line or e_{50} , black dash line] and precision [e_5 and e_{95} , blue dash lines, are precision limits of 5th and 95th percentiles, respectively) with infrequent sampling (M6, monthly) at DN.

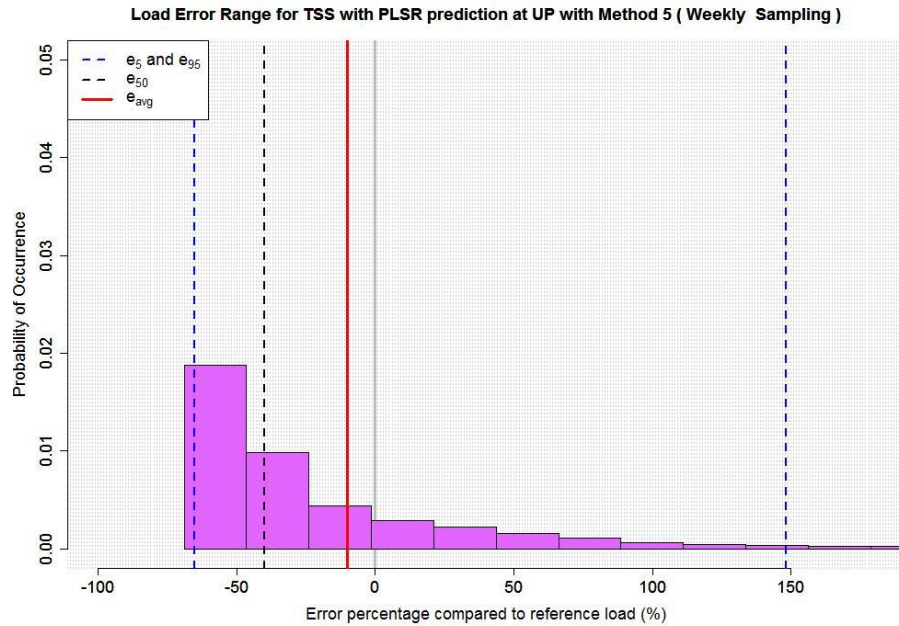


Figure E.75

Distribution of uncertainties estimation presented in the percentage as relative difference of reference annual load expressed as histogram for TSS with PLSR prediction (uncertainties with the bias [e_{avg} , red solid line or e_{50} , black dash line] and precision [e_5 and e_{95} , blue dash lines, are precision limits of 5th and 95th percentiles, respectively) with infrequent sampling (M5, weekly) at UP.

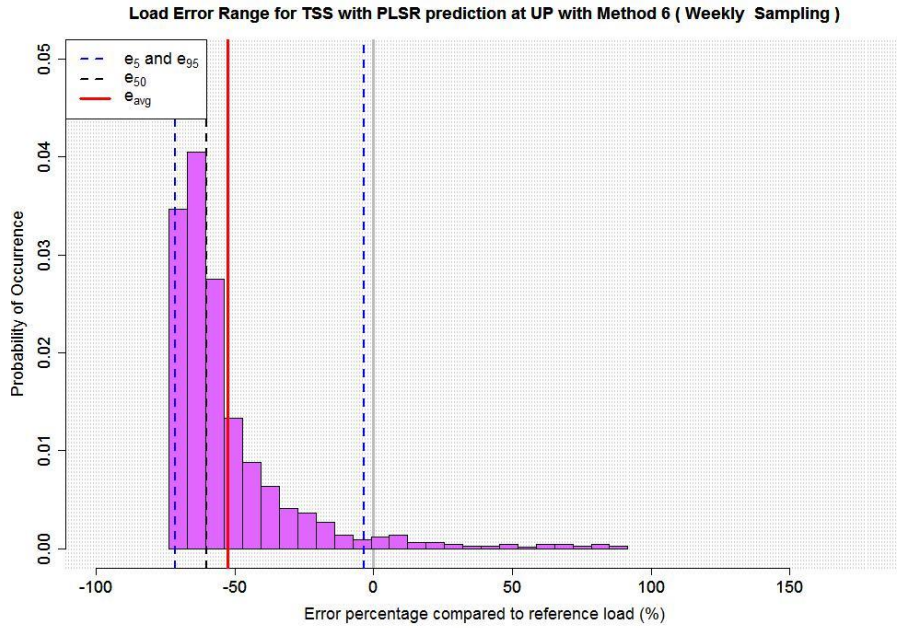


Figure E.76

Distribution of uncertainties estimation presented in the percentage as relative difference of reference annual load expressed as histogram for TSS with PLSR prediction (uncertainties with the bias [e_{avg} , red solid line or e_{50} , black dash line] and precision [e_5 and e_{95} , blue dash lines, are precision limits of 5th and 95th percentiles, respectively) with infrequent sampling (M6, weekly) at UP.

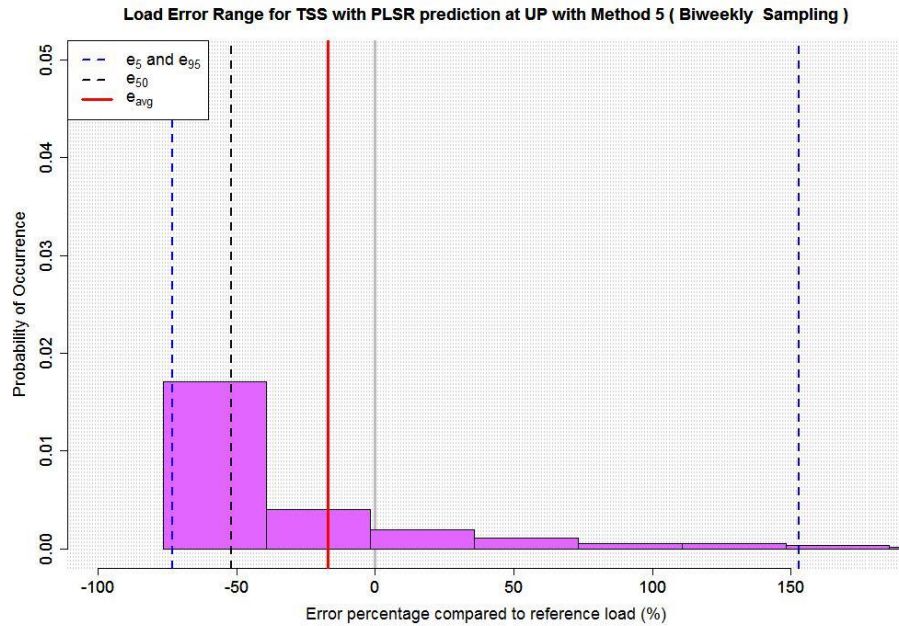


Figure E.77

Distribution of uncertainties estimation presented in the percentage as relative difference of reference annual load expressed as histogram for TSS with PLSR prediction (uncertainties with the bias [e_{avg} , red solid line or e_{50} , black dash line] and precision [e_5 and e_{95} , blue dash lines, are precision limits of 5th and 95th percentiles, respectively) with infrequent sampling (M5, biweekly) at UP.

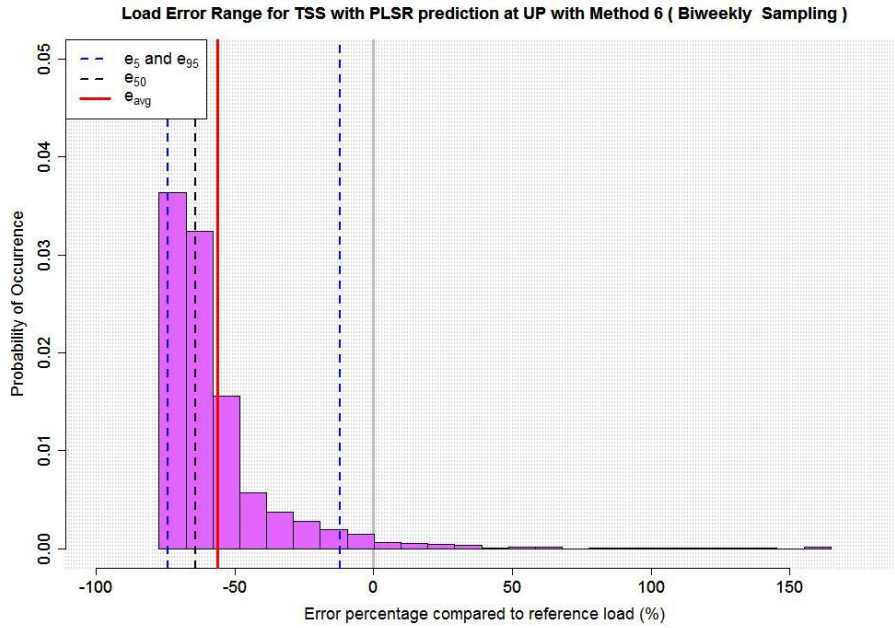


Figure E.78

Distribution of uncertainties estimation presented in the percentage as relative difference of reference annual load expressed as histogram for TSS with PLSR prediction (uncertainties with the bias [e_{avg} , red solid line or e_{50} , black dash line] and precision [e_5 and e_{95} , blue dash lines, are precision limits of 5th and 95th percentiles, respectively) with infrequent sampling (M6, biweekly) at UP.

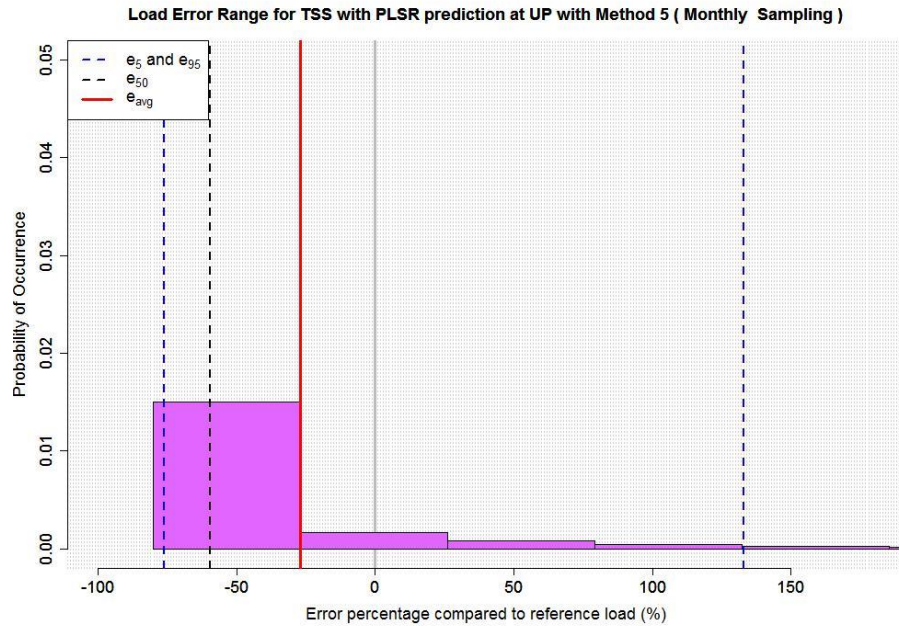


Figure E.79

Distribution of uncertainties estimation presented in the percentage as relative difference of reference annual load expressed as histogram for TSS with PLSR prediction (uncertainties with the bias [e_{avg} , red solid line or e_{50} , black dash line] and precision [e_5 and e_{95} , blue dash lines, are precision limits of 5th and 95th percentiles, respectively) with infrequent sampling (M5, monthly) at UP.

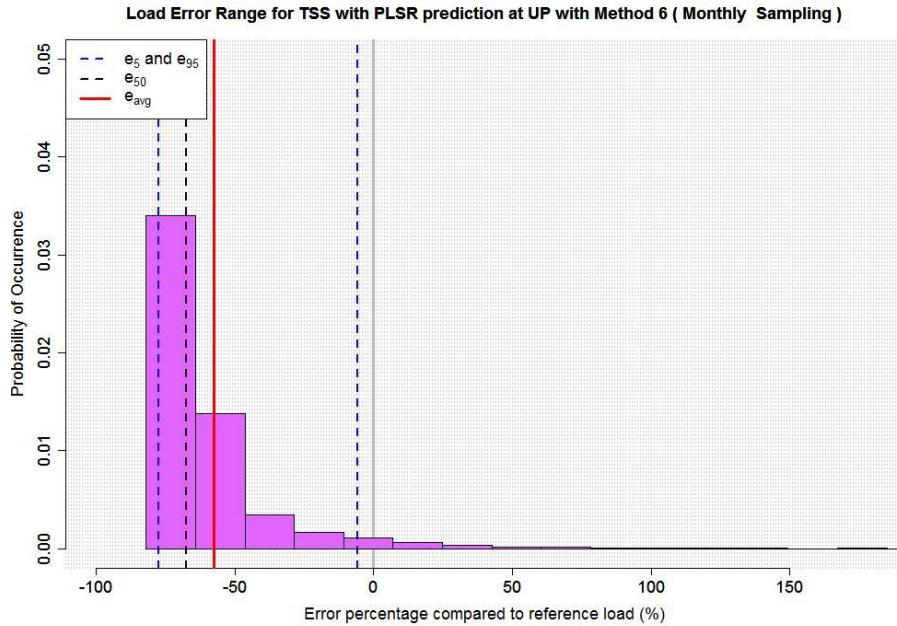


Figure E.80

Distribution of uncertainties estimation presented in the percentage as relative difference of reference annual load expressed as histogram for TSS with PLSR prediction (uncertainties with the bias [e_{avg} , red solid line or e_{50} , black dash line] and precision [e_5 and e_{95} , blue dash lines, are precision limits of 5th and 95th percentiles, respectively) with infrequent sampling (M6, monthly) at UP.

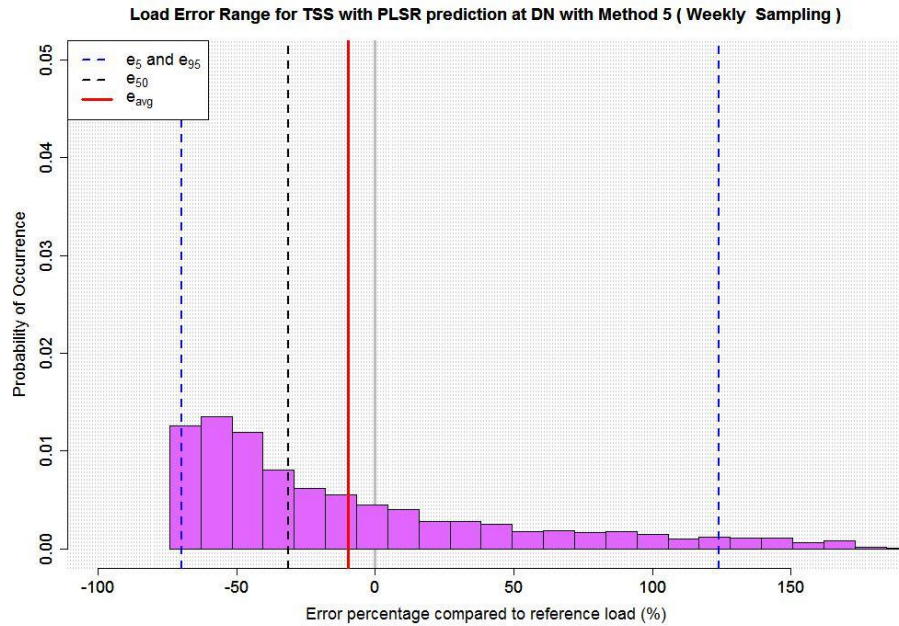


Figure E.81

Distribution of uncertainties estimation presented in the percentage as relative difference of reference annual load expressed as histogram for TSS with PLSR prediction (uncertainties with the bias [e_{avg} , red solid line or e_{50} , black dash line] and precision [e_5 and e_{95} , blue dash lines, are precision limits of 5th and 95th percentiles, respectively) with infrequent sampling (M5, weekly) at DN.

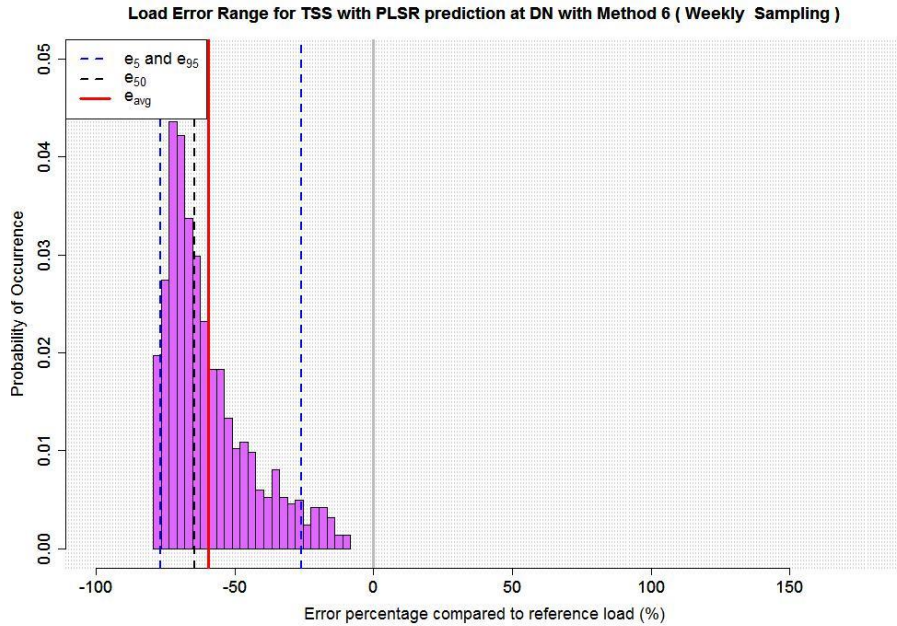


Figure E.82

Distribution of uncertainties estimation presented in the percentage as relative difference of reference annual load expressed as histogram for TSS with PLSR prediction (uncertainties with the bias [e_{avg} , red solid line or e_{50} , black dash line] and precision [e_5 and e_{95} , blue dash lines, are precision limits of 5th and 95th percentiles, respectively) with infrequent sampling (M6, weekly) at DN.

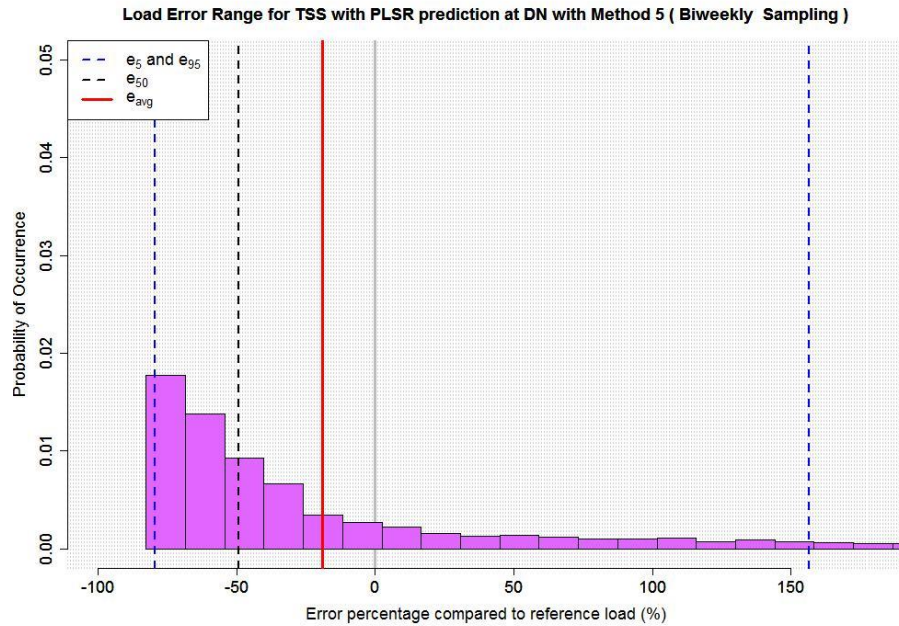


Figure E.83

Distribution of uncertainties estimation presented in the percentage as relative difference of reference annual load expressed as histogram for TSS with PLSR prediction (uncertainties with the bias [e_{avg} , red solid line or e_{50} , black dash line] and precision [e_5 and e_{95} , blue dash lines, are precision limits of 5th and 95th percentiles, respectively) with infrequent sampling (M5, biweekly) at DN.

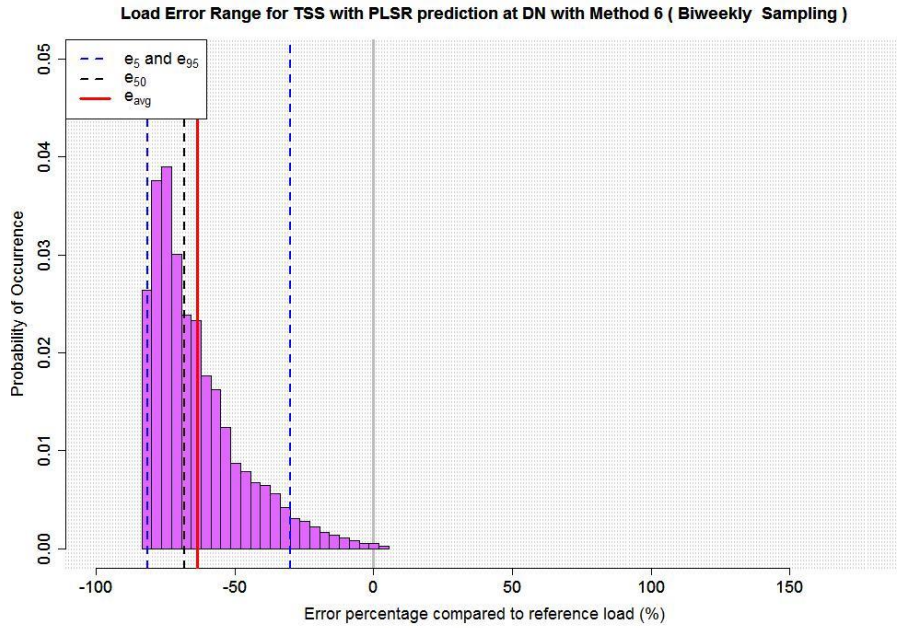


Figure E.84

Distribution of uncertainties estimation presented in the percentage as relative difference of reference annual load expressed as histogram for TSS with PLSR prediction (uncertainties with the bias [e_{avg} , red solid line or e_{50} , black dash line] and precision [e_5 and e_{95} , blue dash lines, are precision limits of 5th and 95th percentiles, respectively) with infrequent sampling (M6, biweekly) at DN.

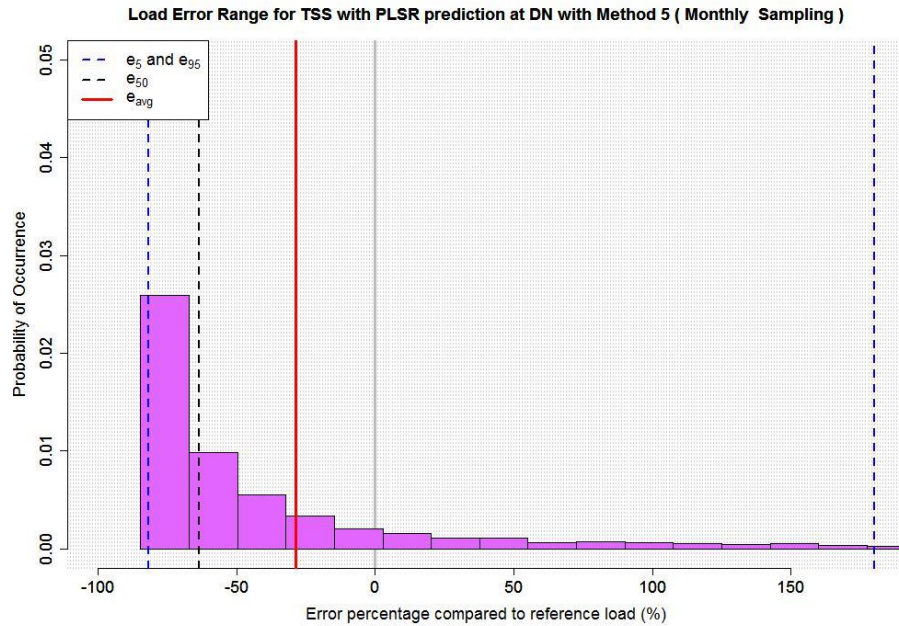


Figure E.85

Distribution of uncertainties estimation presented in the percentage as relative difference of reference annual load expressed as histogram for TSS with PLSR prediction (uncertainties with the bias [e_{avg} , red solid line or e_{50} , black dash line] and precision [e_5 and e_{95} , blue dash lines, are precision limits of 5th and 95th percentiles, respectively) with infrequent sampling (M5, monthly) at DN.

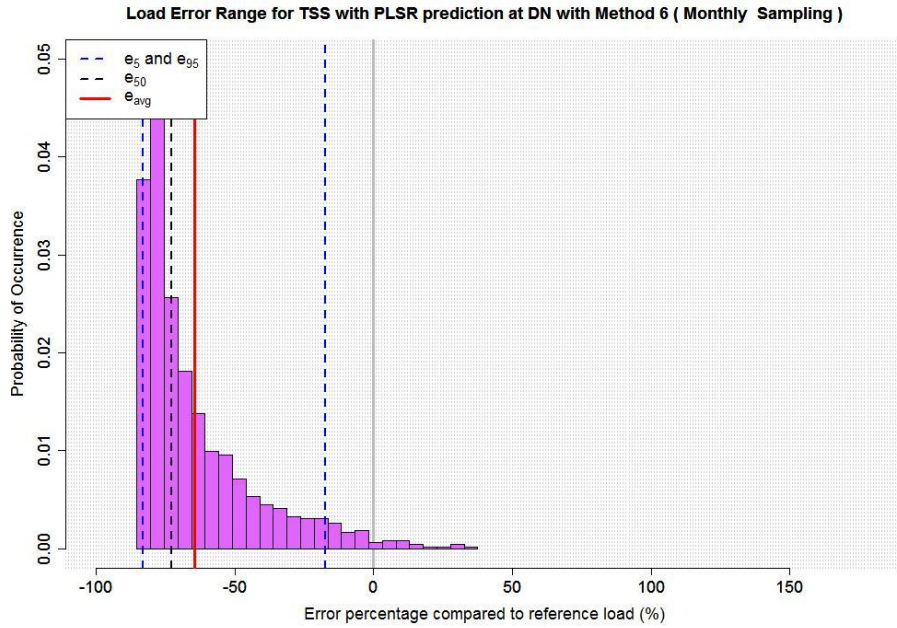


Figure E.86

Distribution of uncertainties estimation presented in the percentage as relative difference of reference annual load expressed as histogram for TSS with PLSR prediction (uncertainties with the bias [e_{avg} , red solid line or e_{50} , black dash line] and precision [e_5 and e_{95} , blue dash lines, are precision limits of 5th and 95th percentiles, respectively) with infrequent sampling (M6, monthly) at DN.

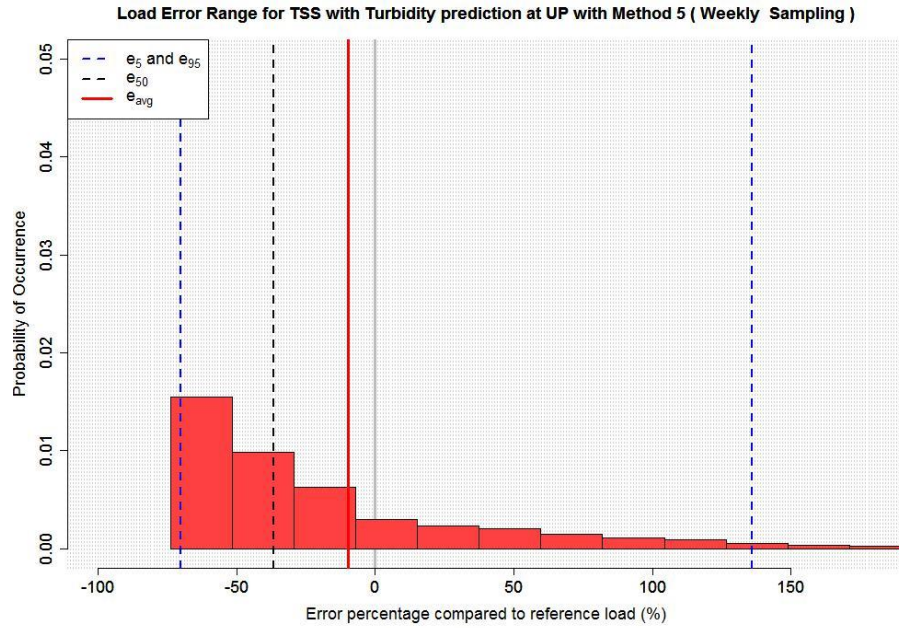


Figure E.87

Distribution of uncertainties estimation presented in the percentage as relative difference of reference annual load expressed as histogram for TSS with Turbidity prediction (uncertainties with the bias [e_{avg} , red solid line or e_{50} , black dash line] and precision [e_5 and e_{95} , blue dash lines, are precision limits of 5th and 95th percentiles, respectively) with infrequent sampling (M5, weekly) at UP.

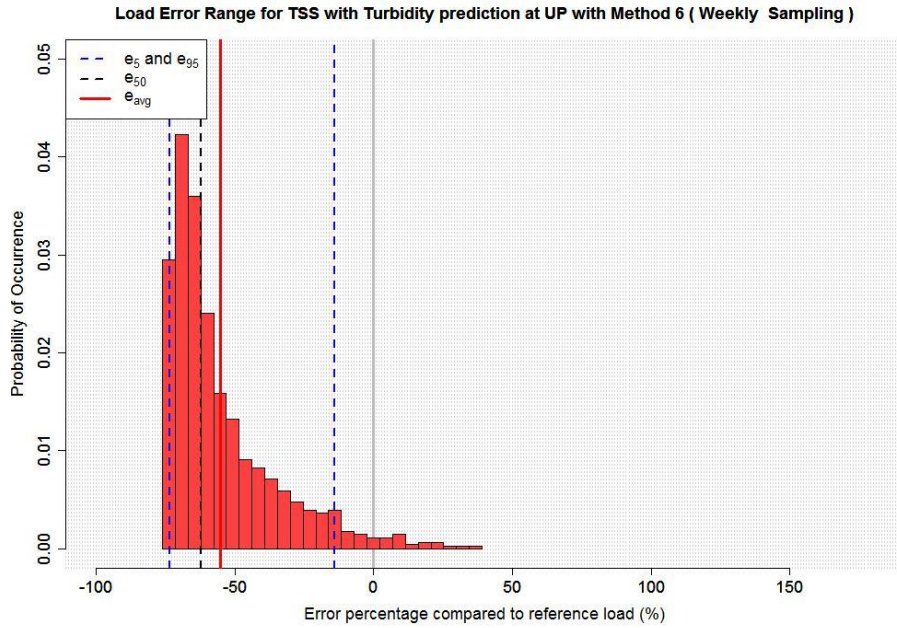


Figure E.88

Distribution of uncertainties estimation presented in the percentage as relative difference of reference annual load expressed as histogram for TSS with Turbidity prediction (uncertainties with the bias [e_{avg} , red solid line or e_{50} , black dash line] and precision [e_5 and e_{95} , blue dash lines, are precision limits of 5th and 95th percentiles, respectively) with infrequent sampling (M6, weekly) at UP.

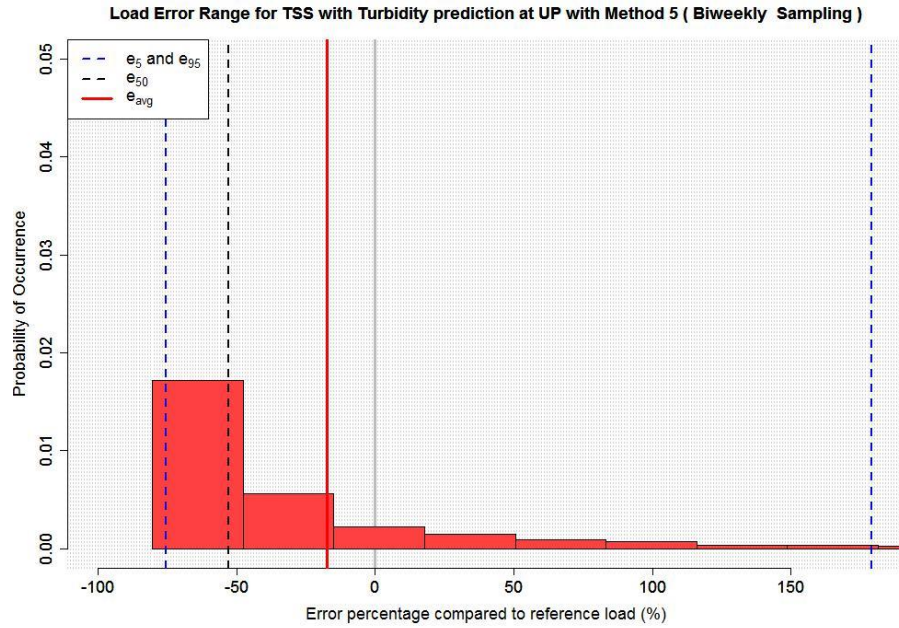


Figure E.89

Distribution of uncertainties estimation presented in the percentage as relative difference of reference annual load expressed as histogram for TSS with Turbidity prediction (uncertainties with the bias [e_{avg} , red solid line or e_{50} , black dash line] and precision [e_5 and e_{95} , blue dash lines, are precision limits of 5th and 95th percentiles, respectively) with infrequent sampling (M5, biweekly) at UP.

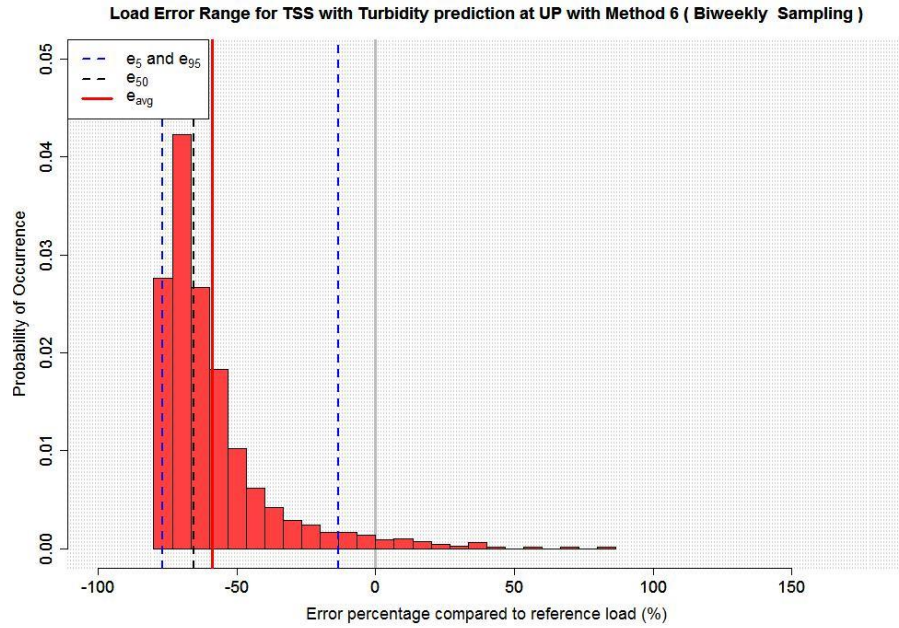


Figure E.90

Distribution of uncertainties estimation presented in the percentage as relative difference of reference annual load expressed as histogram for TSS with Turbidity prediction (uncertainties with the bias [e_{avg} , red solid line or e_{50} , black dash line] and precision [e_5 and e_{95} , blue dash lines, are precision limits of 5th and 95th percentiles, respectively) with infrequent sampling (M6, biweekly) at UP.

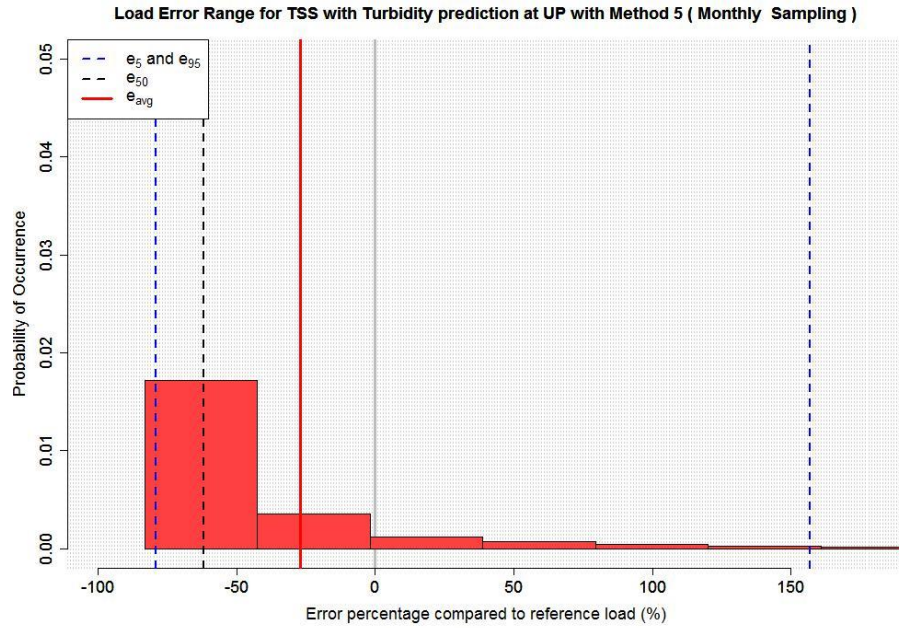


Figure E.91

Distribution of uncertainties estimation presented in the percentage as relative difference of reference annual load expressed as histogram for TSS with Turbidity prediction (uncertainties with the bias [e_{avg} , red solid line or e_{50} , black dash line] and precision [e_5 and e_{95} , blue dash lines, are precision limits of 5th and 95th percentiles, respectively) with infrequent sampling (M5, monthly) at UP.

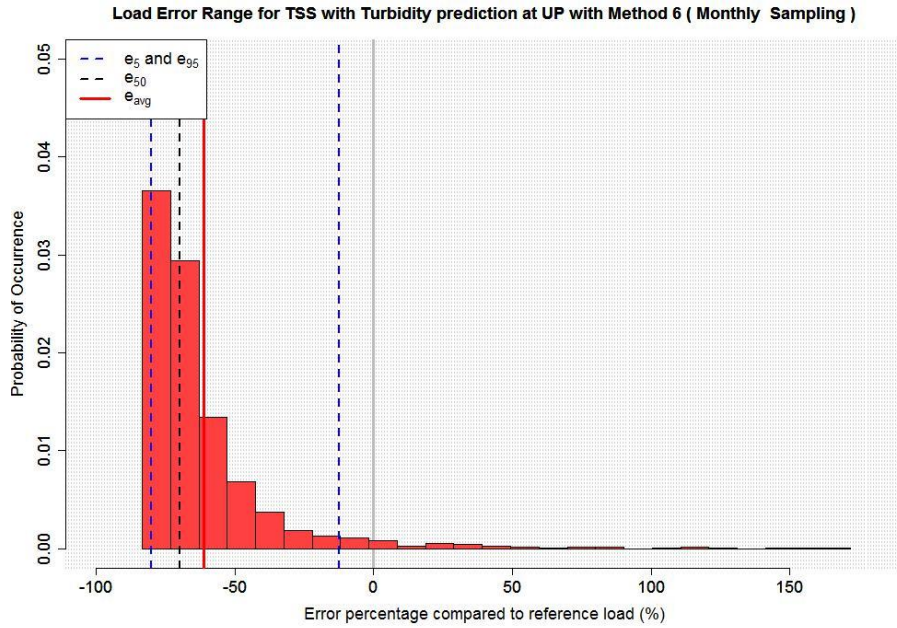


Figure E.92

Distribution of uncertainties estimation presented in the percentage as relative difference of reference annual load expressed as histogram for TSS with Turbidity prediction (uncertainties with the bias [e_{avg} , red solid line or e_{50} , black dash line] and precision [e_5 and e_{95} , blue dash lines, are precision limits of 5th and 95th percentiles, respectively) with infrequent sampling (M6, monthly) at UP.

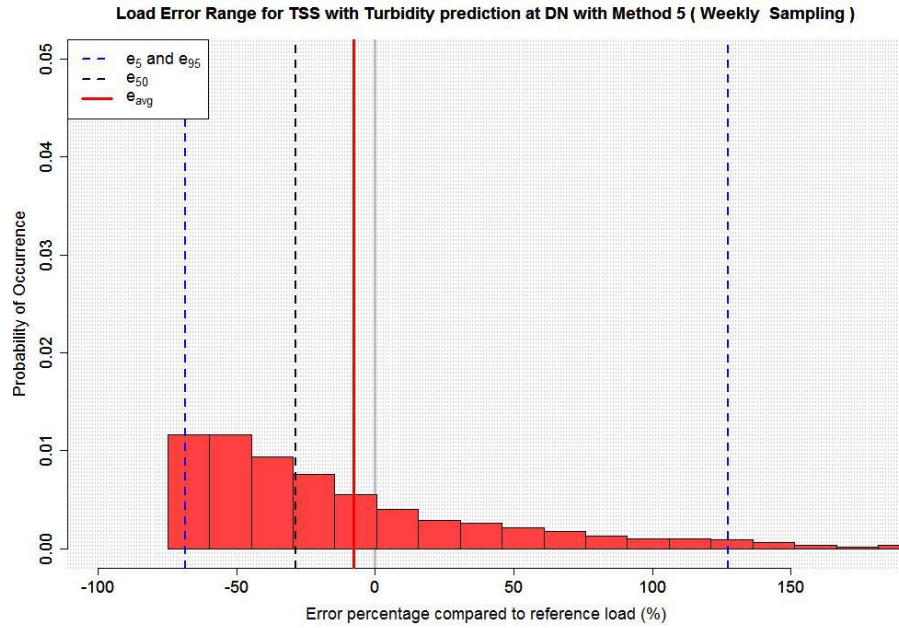


Figure E.93

Distribution of uncertainties estimation presented in the percentage as relative difference of reference annual load expressed as histogram for TSS with Turbidity prediction (uncertainties with the bias [e_{avg} , red solid line or e_{50} , black dash line] and precision [e_5 and e_{95} , blue dash lines, are precision limits of 5th and 95th percentiles, respectively) with infrequent sampling (M5, weekly) at DN.

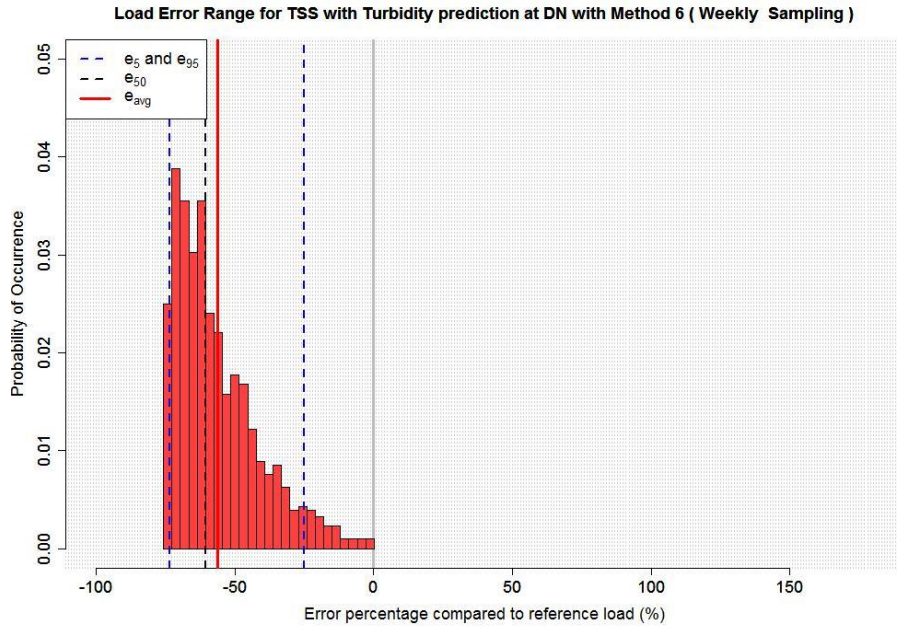


Figure E.94

Distribution of uncertainties estimation presented in the percentage as relative difference of reference annual load expressed as histogram for TSS with Turbidity prediction (uncertainties with the bias [e_{avg} , red solid line or e_{50} , black dash line] and precision [e_5 and e_{95} , blue dash lines, are precision limits of 5th and 95th percentiles, respectively) with infrequent sampling (M6, weekly) at DN.

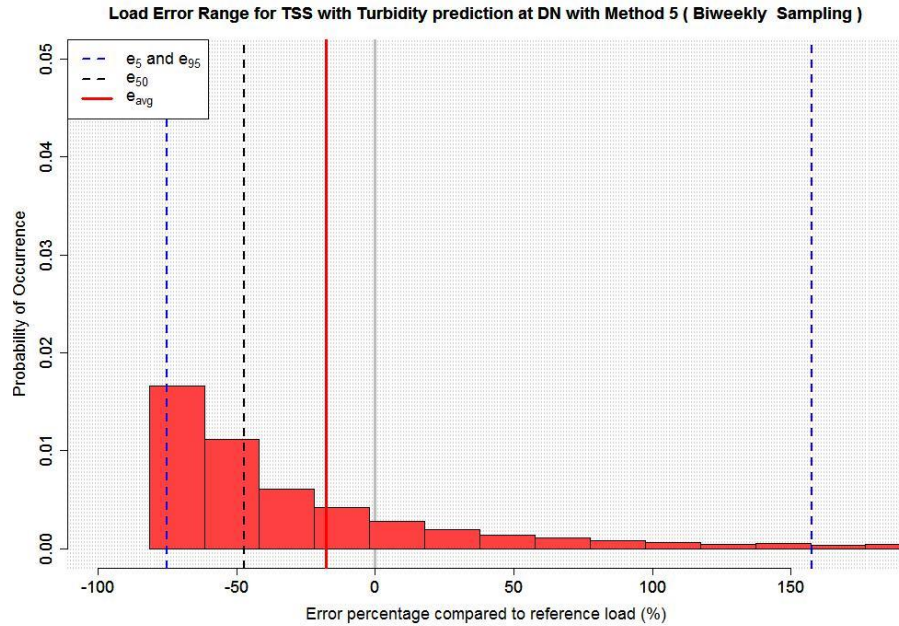


Figure E.95

Distribution of uncertainties estimation presented in the percentage as relative difference of reference annual load expressed as histogram for TSS with Turbidity prediction (uncertainties with the bias [e_{avg} , red solid line or e_{50} , black dash line] and precision [e_5 and e_{95} , blue dash lines, are precision limits of 5th and 95th percentiles, respectively) with infrequent sampling (M5, biweekly) at DN.

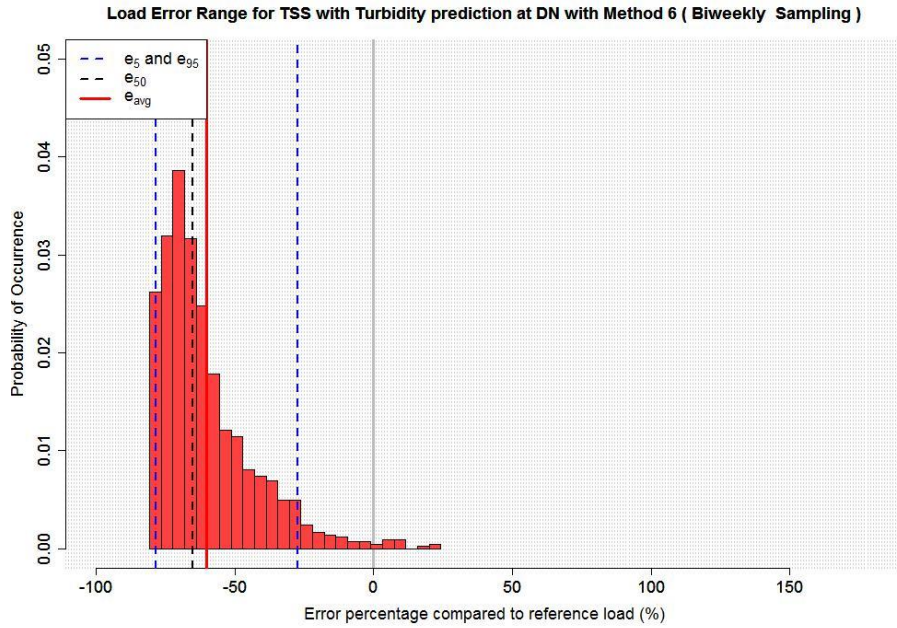


Figure E.96

Distribution of uncertainties estimation presented in the percentage as relative difference of reference annual load expressed as histogram for TSS with Turbidity prediction (uncertainties with the bias [e_{avg} , red solid line or e_{50} , black dash line] and precision [e_5 and e_{95} , blue dash lines, are precision limits of 5th and 95th percentiles, respectively) with infrequent sampling (M6, biweekly) at DN.

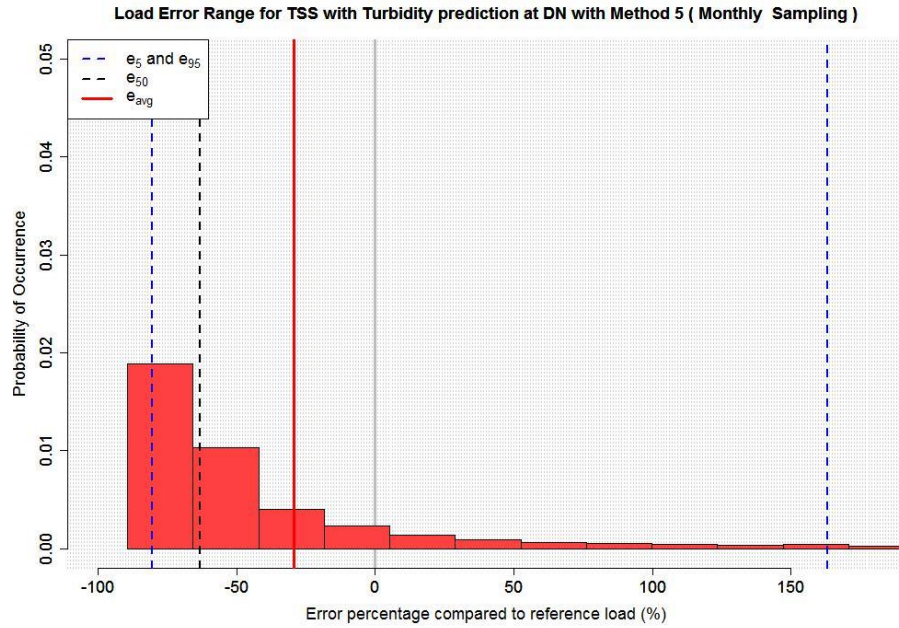


Figure E.97

Distribution of uncertainties estimation presented in the percentage as relative difference of reference annual load expressed as histogram for TSS with Turbidity prediction (uncertainties with the bias [e_{avg} , red solid line or e_{50} , black dash line] and precision [e_5 and e_{95} , blue dash lines, are precision limits of 5th and 95th percentiles, respectively) with infrequent sampling (M5, monthly) at DN.

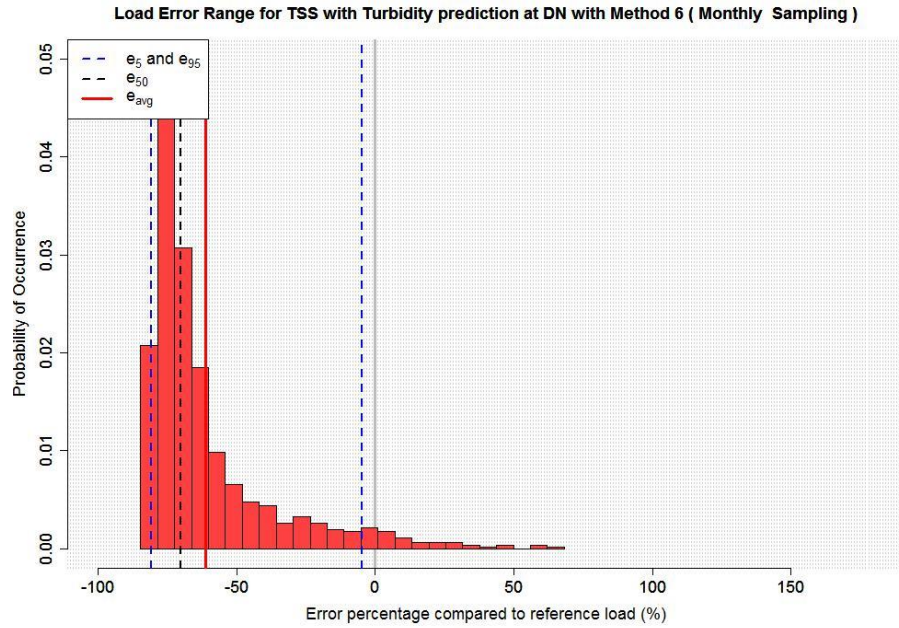


Figure E.98

Distribution of uncertainties estimation presented in the percentage as relative difference of reference annual load expressed as histogram for TSS with Turbidity prediction (uncertainties with the bias [e_{avg} , red solid line or e_{50} , black dash line] and precision [e_5 and e_{95} , blue dash lines, are precision limits of 5th and 95th percentiles, respectively) with infrequent sampling (M6, monthly) at DN.

Appendix F: Hysteresis Graphs for NO₃-N and DOC

F.1 Hysteresis plots at UP station

Figure F.1 Hysteresis plots for NO₃-N at UP

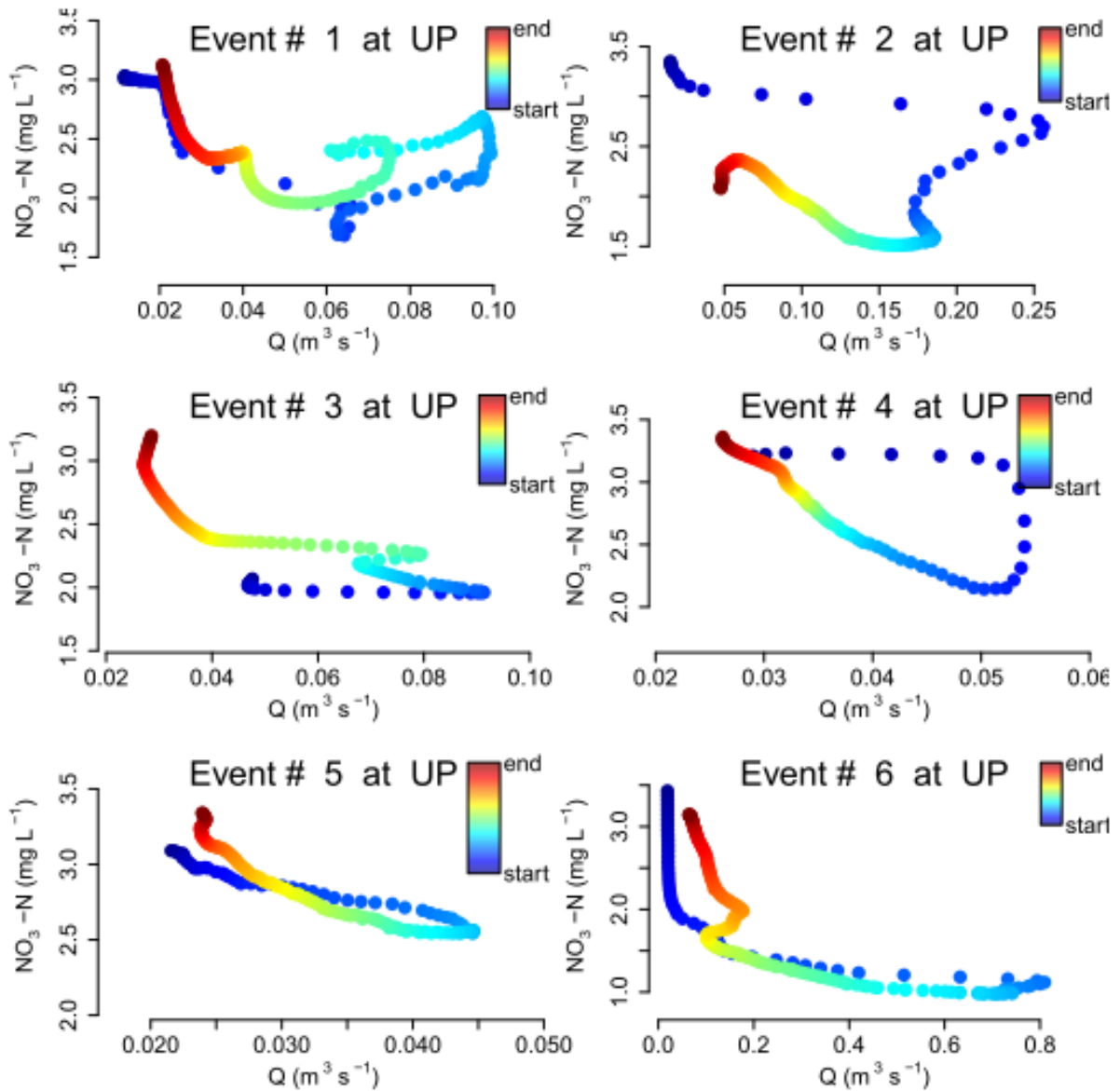


Figure F.1 Continued

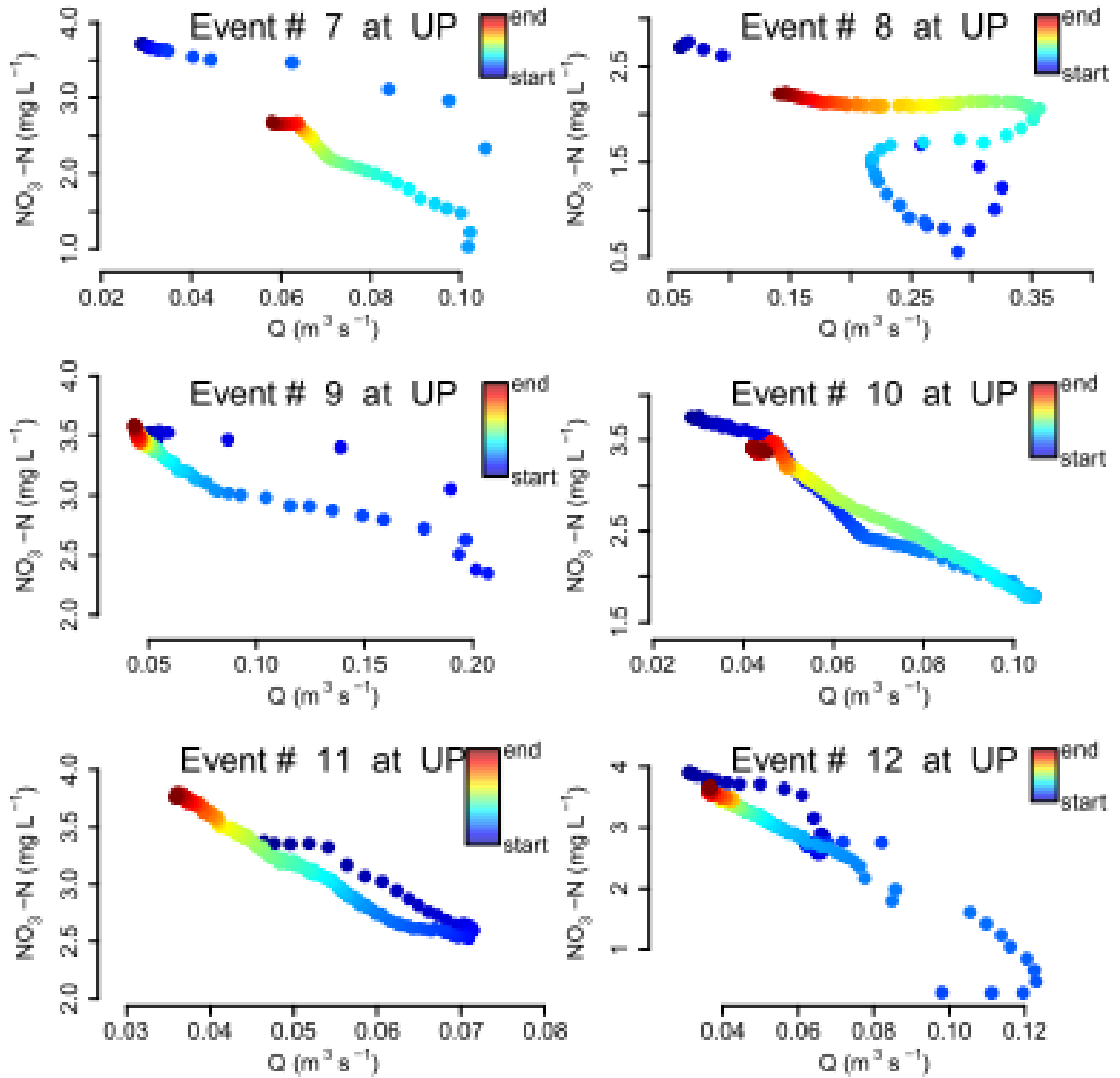


Figure F.1 Continued

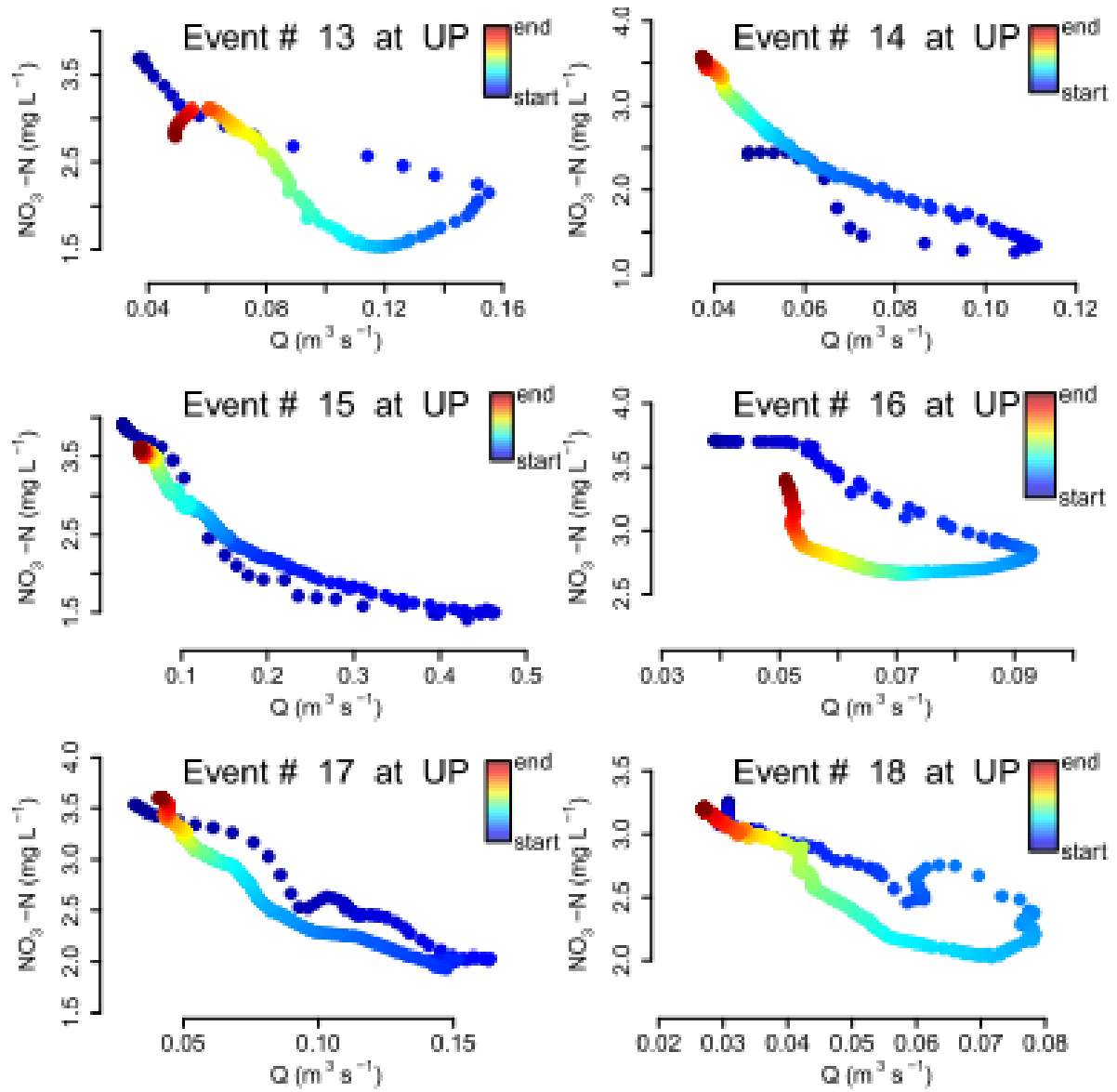


Figure F.1 Continued

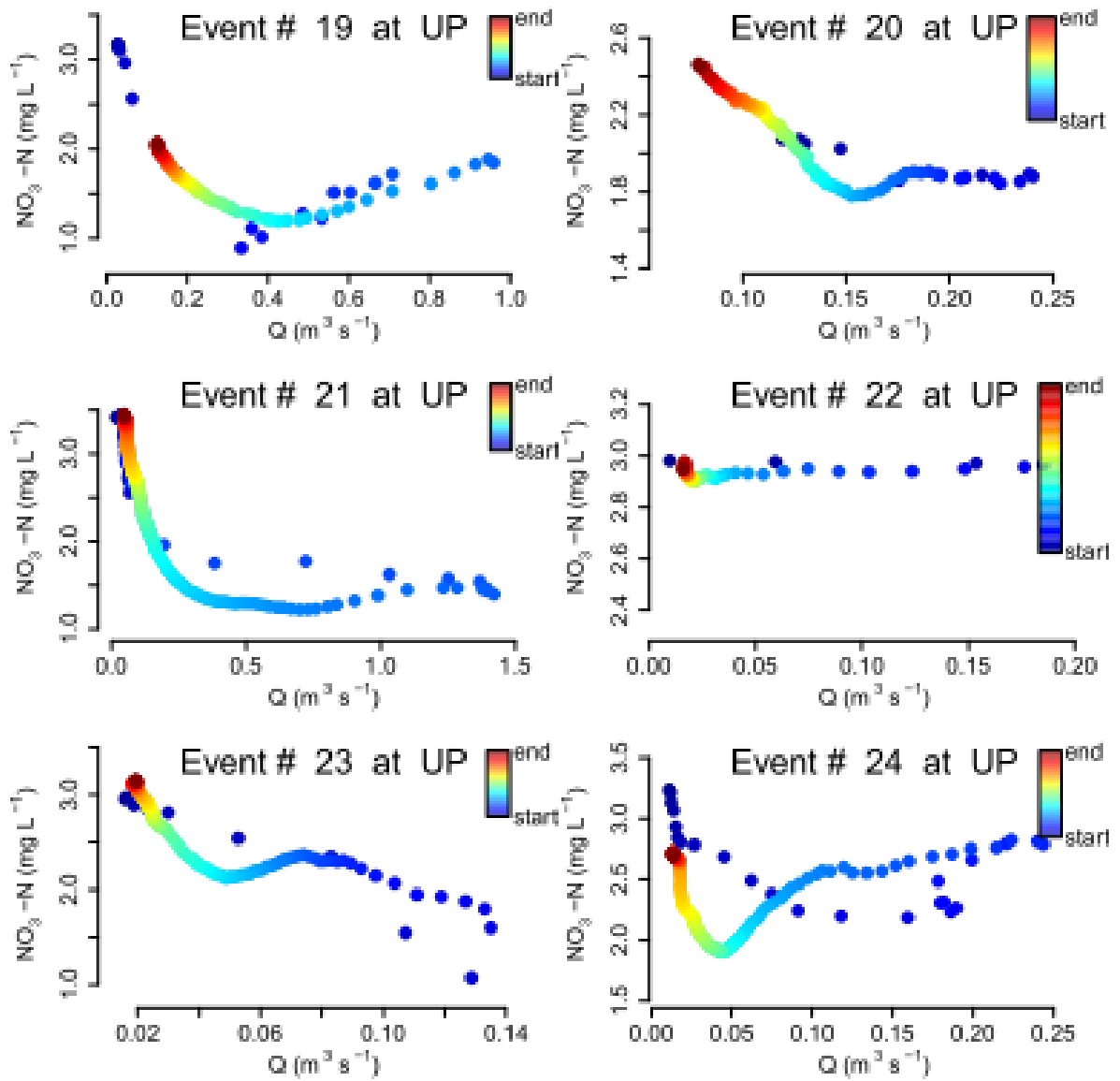


Figure F.1 Continued

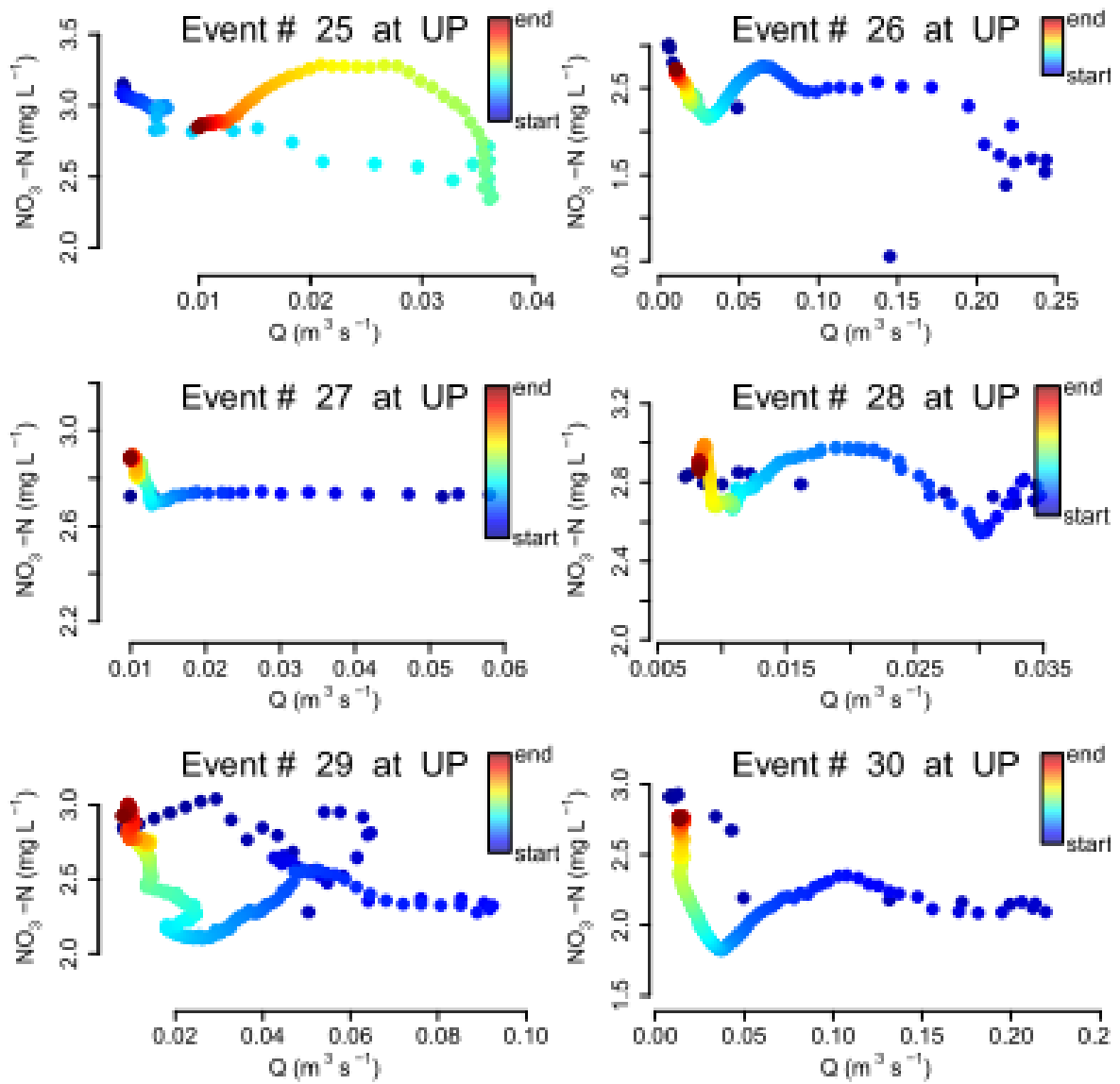


Figure F.1 Continued

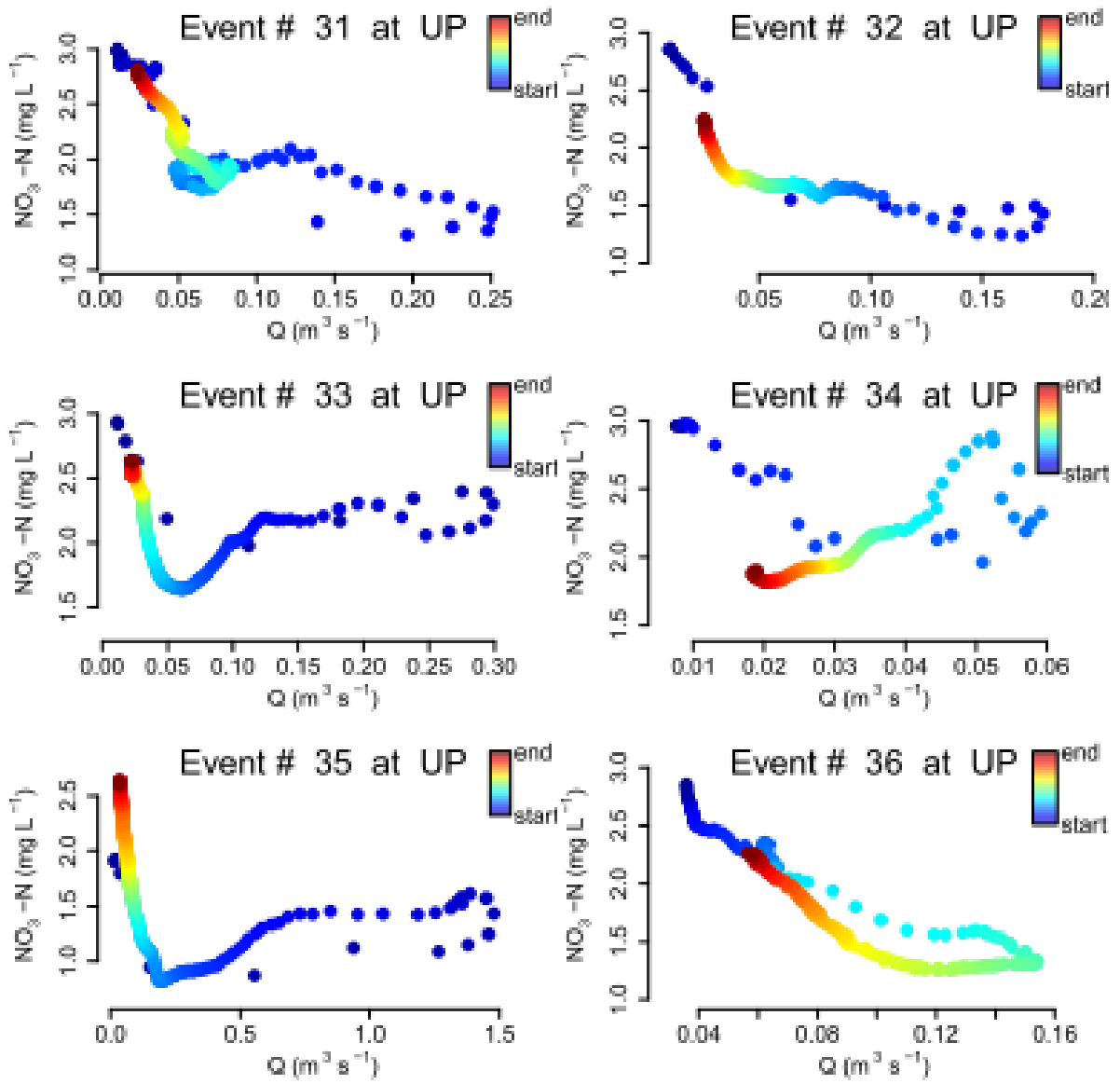


Figure F.1 Continued

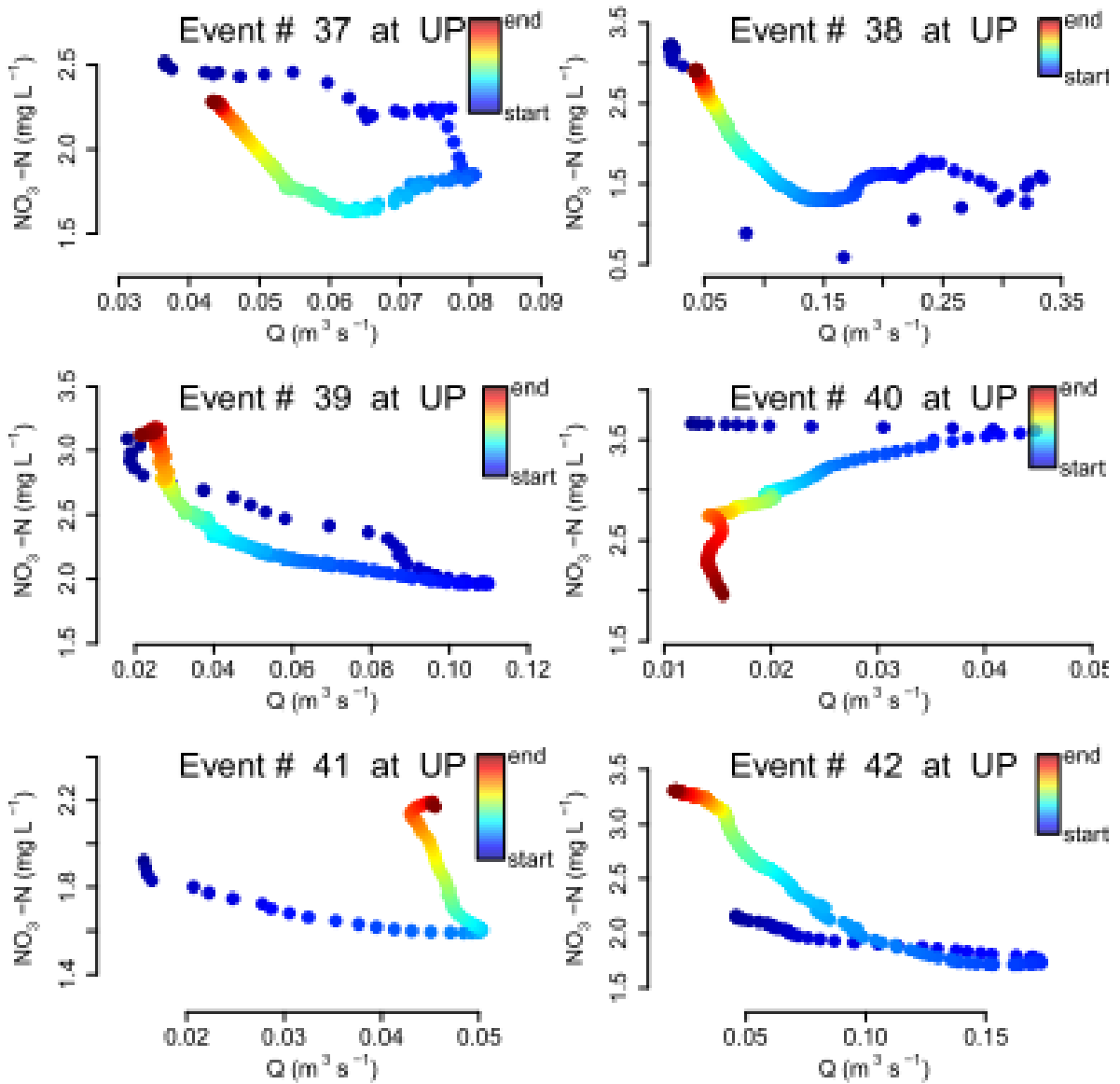


Figure F.1 Continued

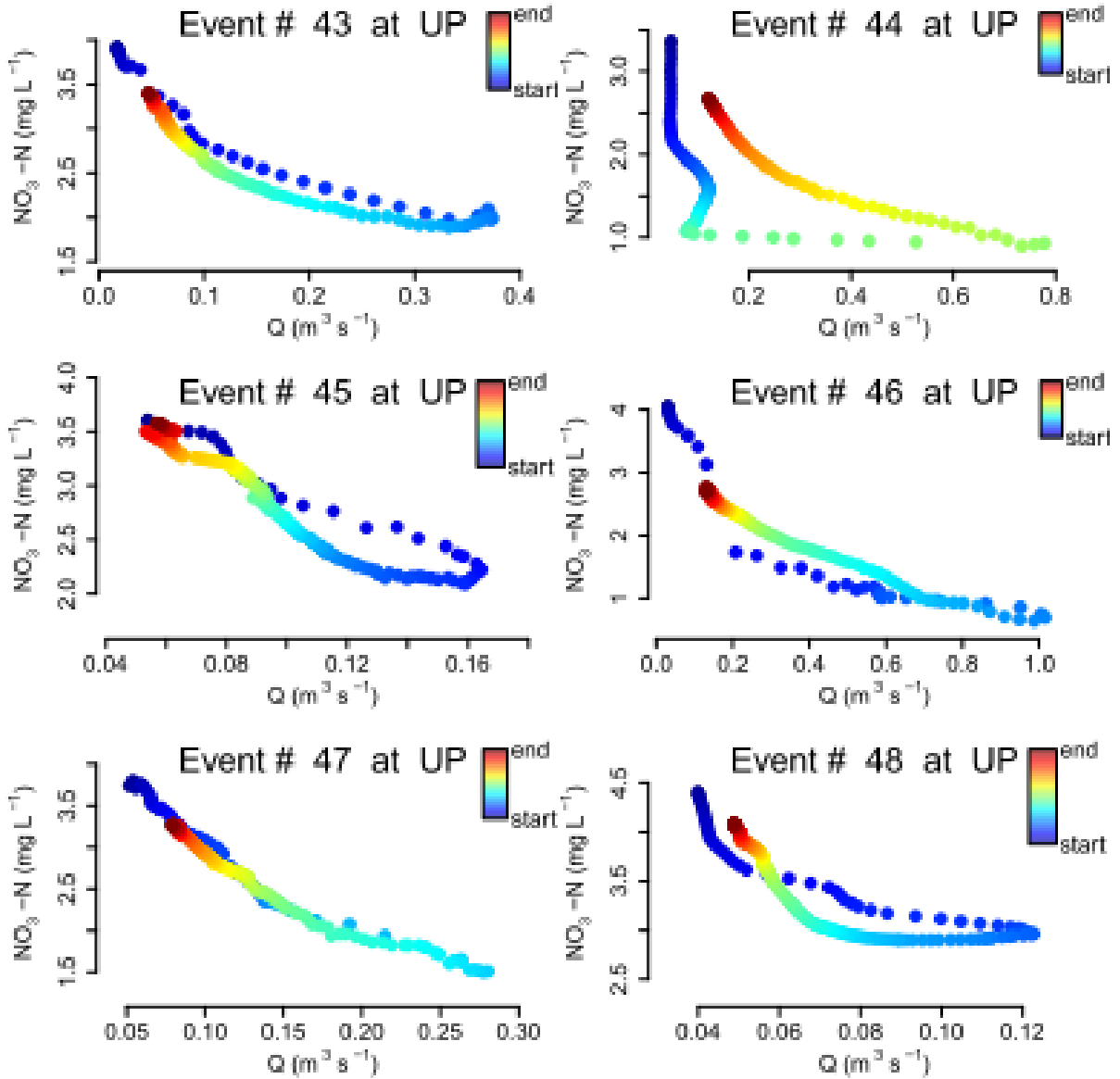


Figure F.1 Continued

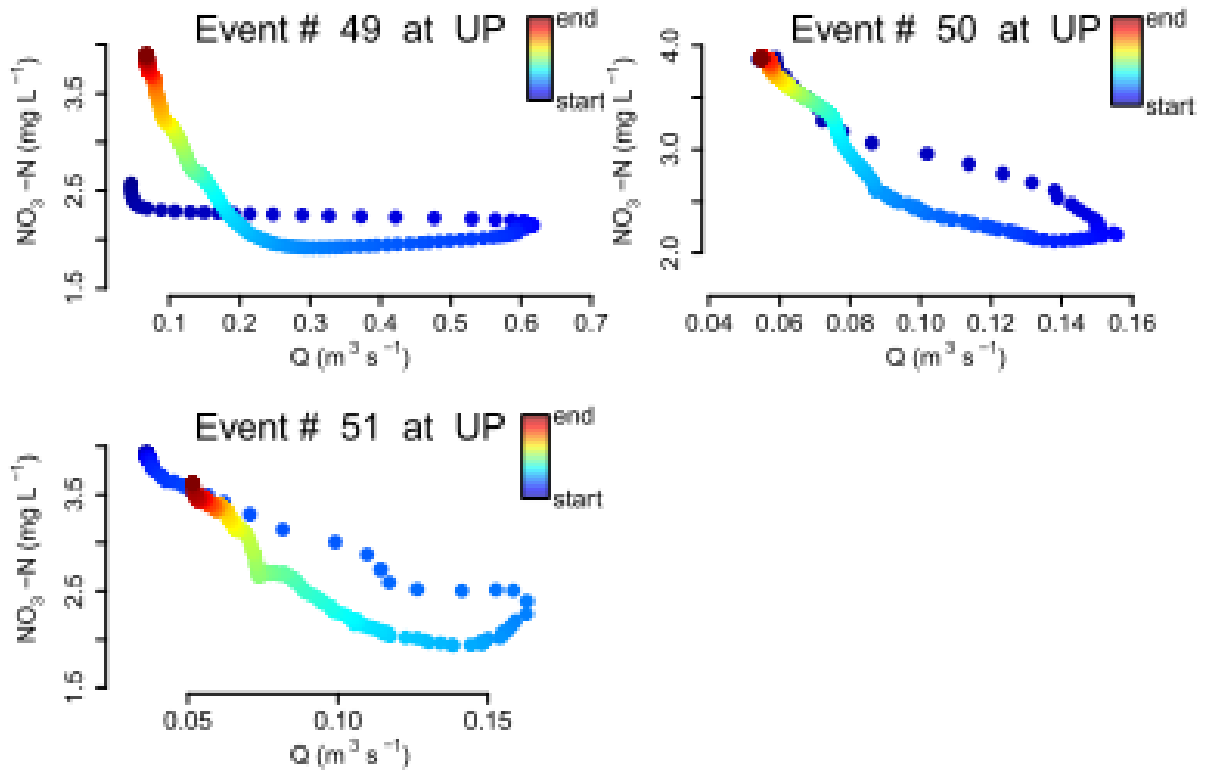


Figure F.2 Hysteresis plots for DOC at UP

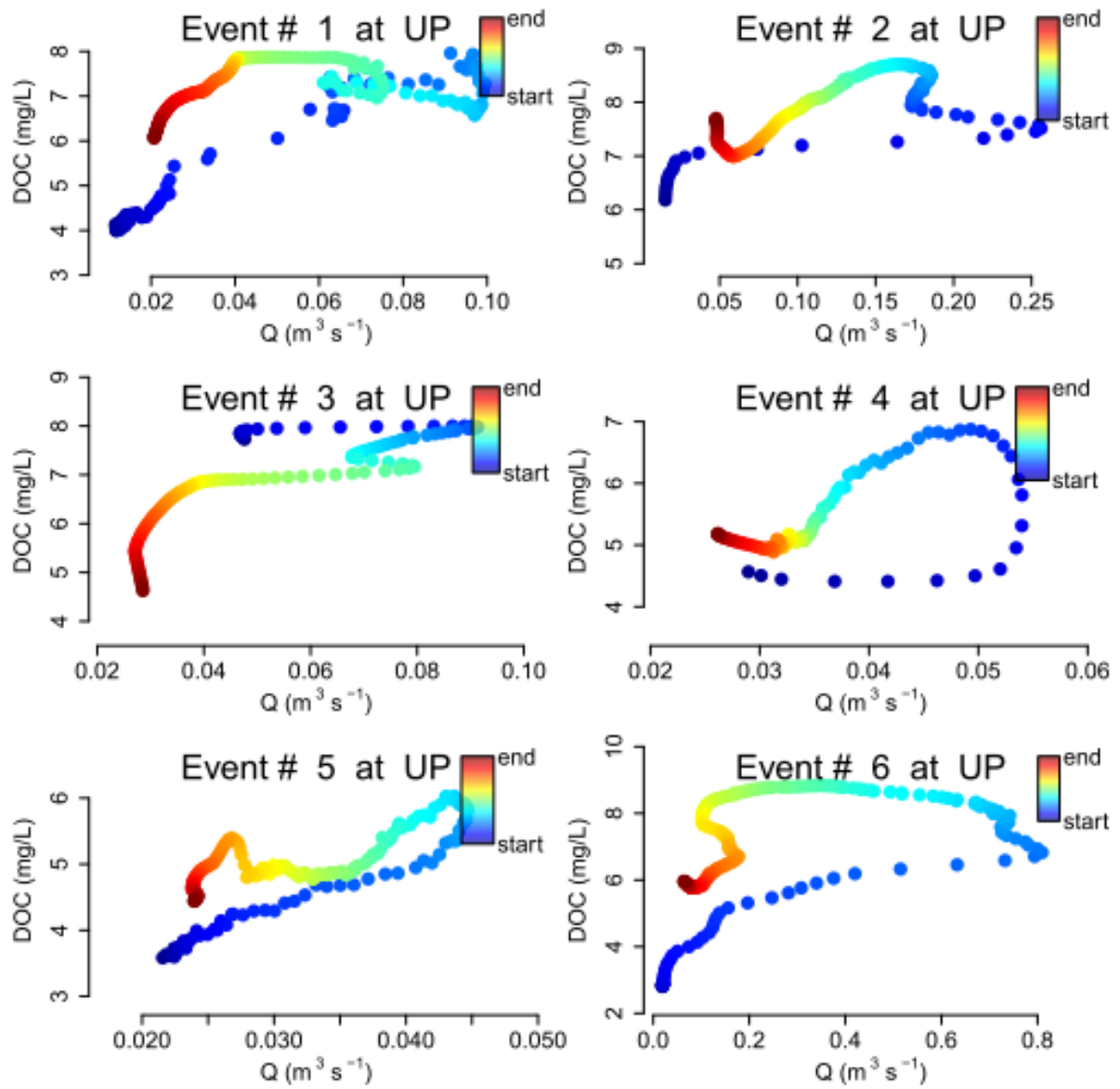


Figure F.2 Continued

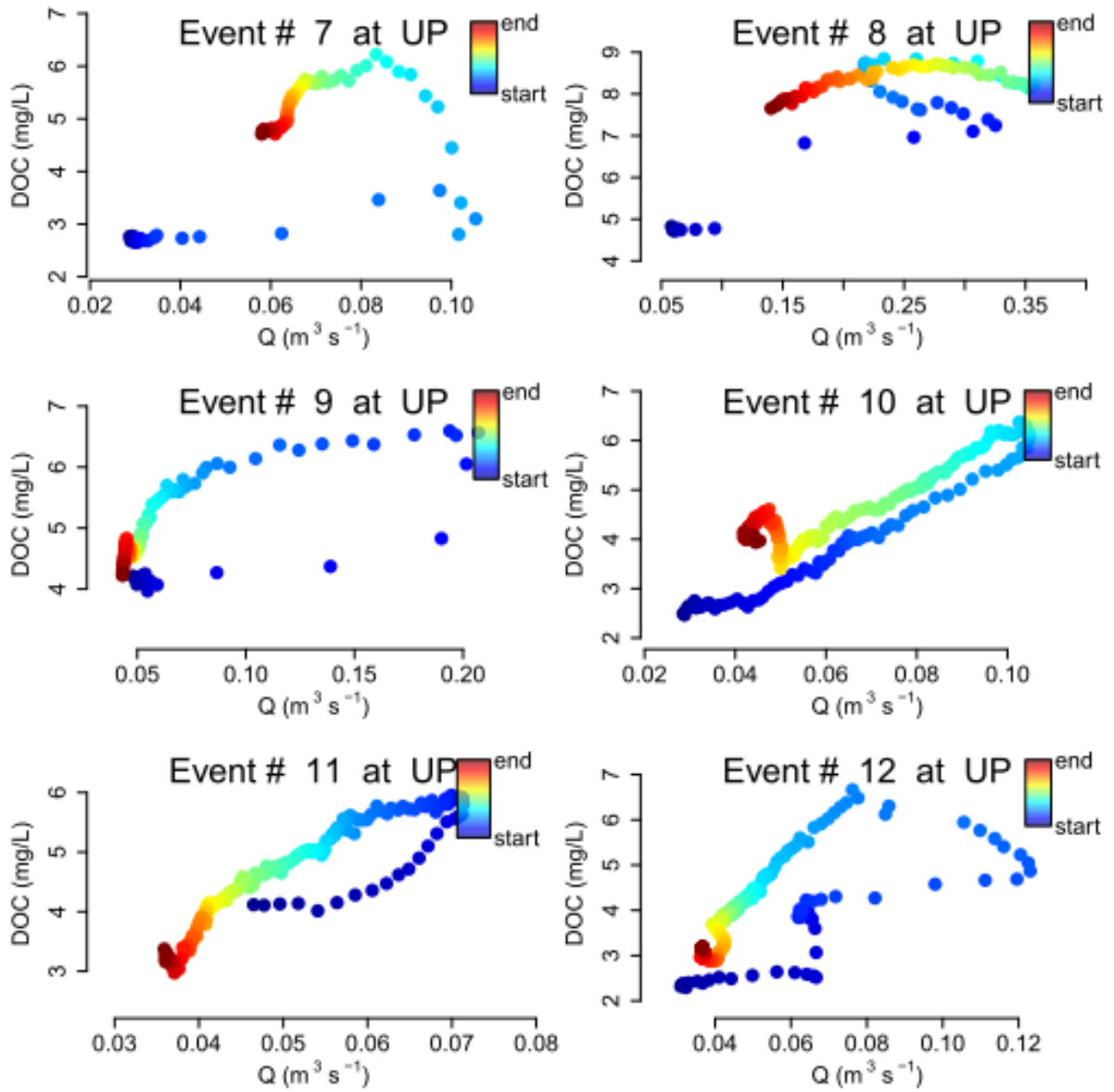


Figure F.2 Continued

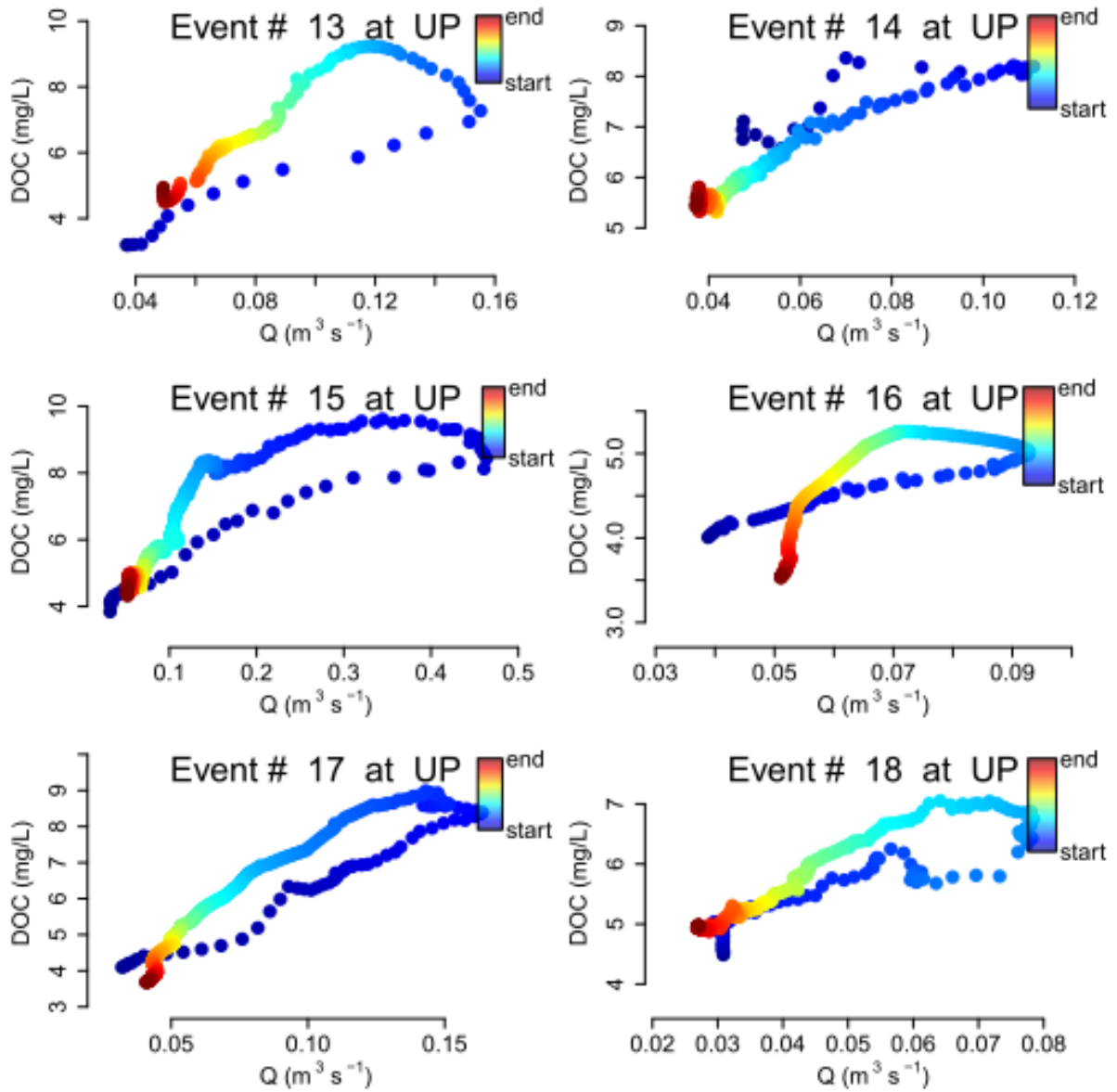


Figure F.2 Continued

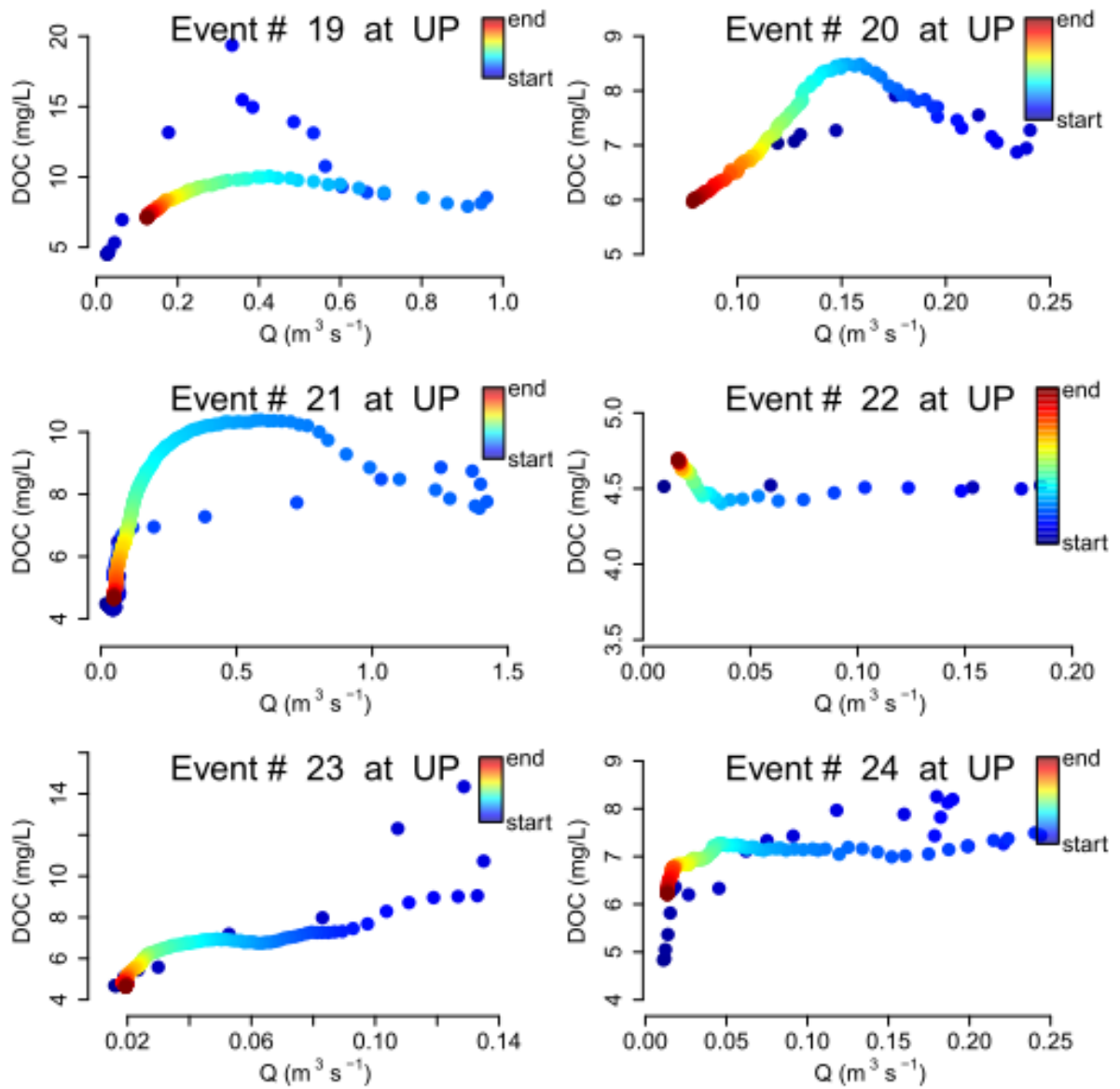


Figure F.2 Continued

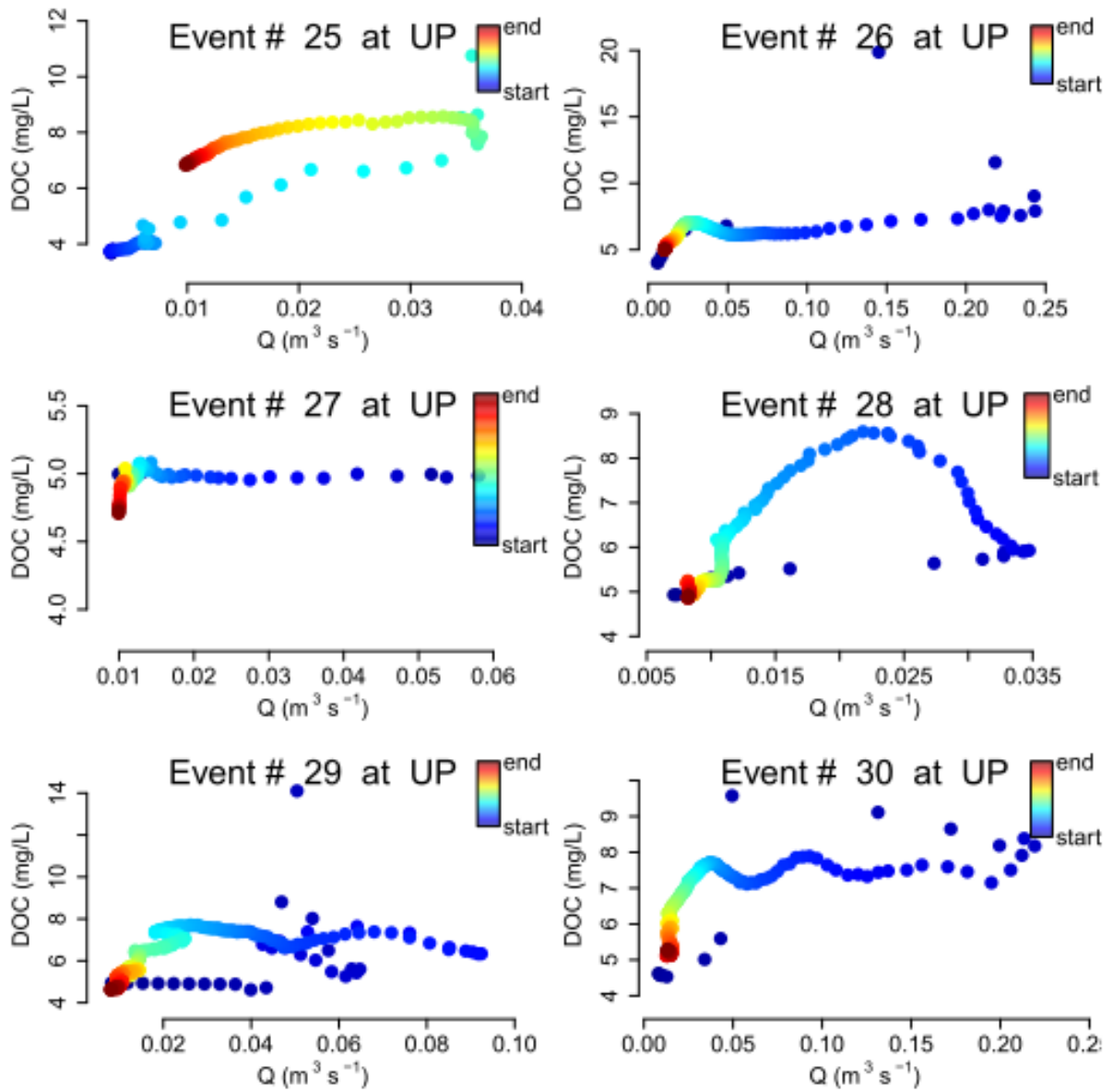


Figure F.2 Continued

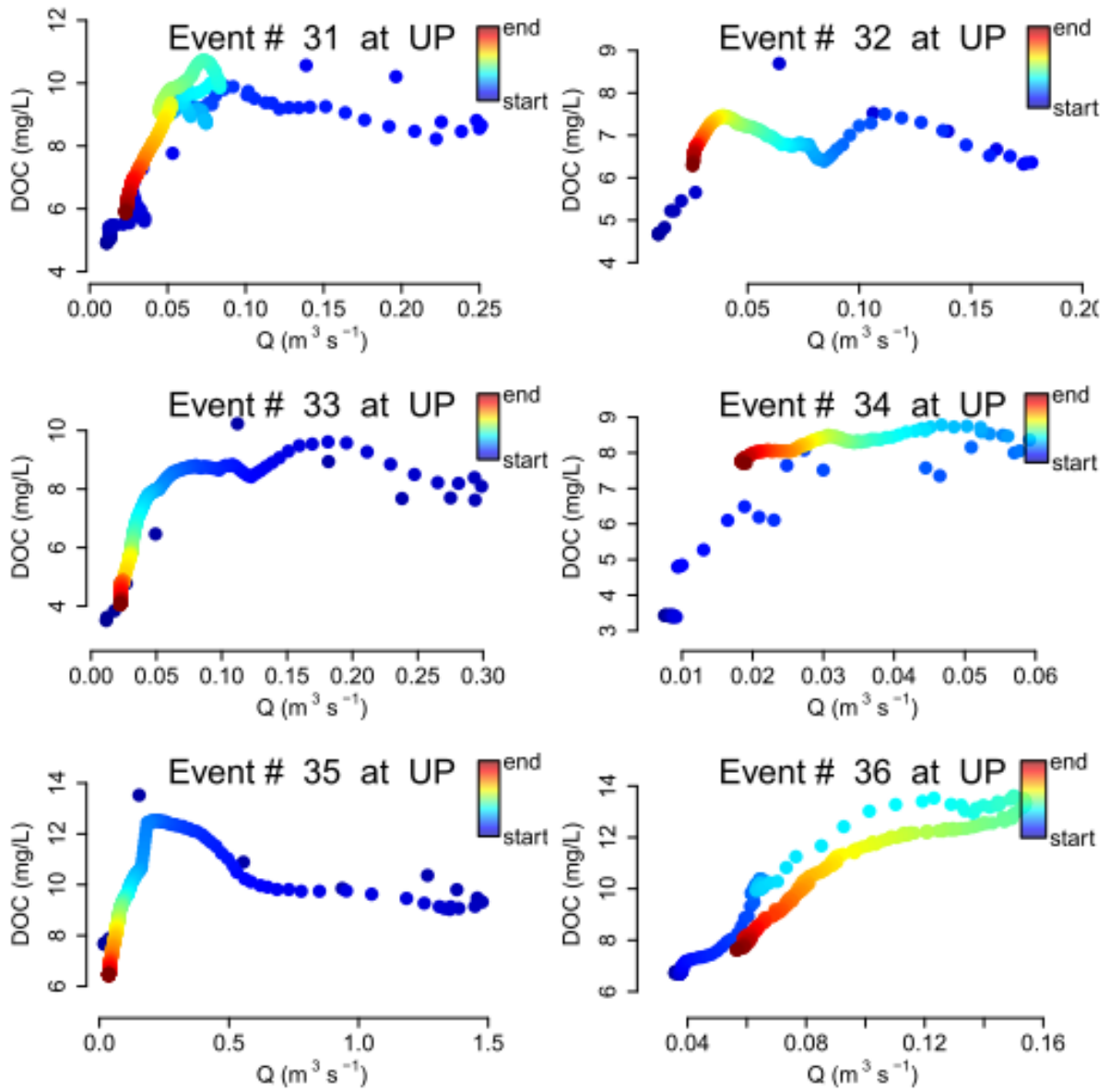


Figure F.2 Continued

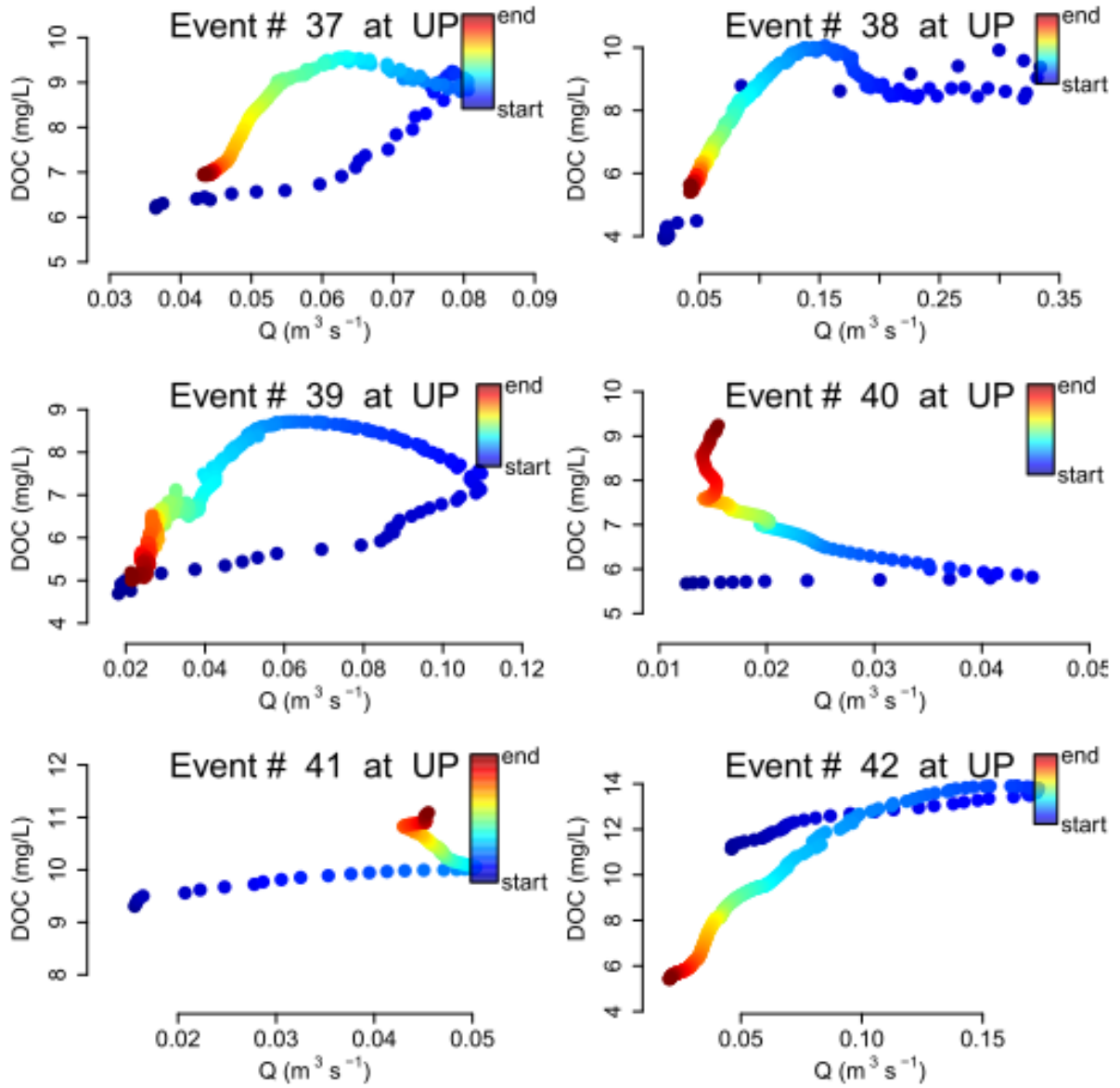


Figure F.2 Continued

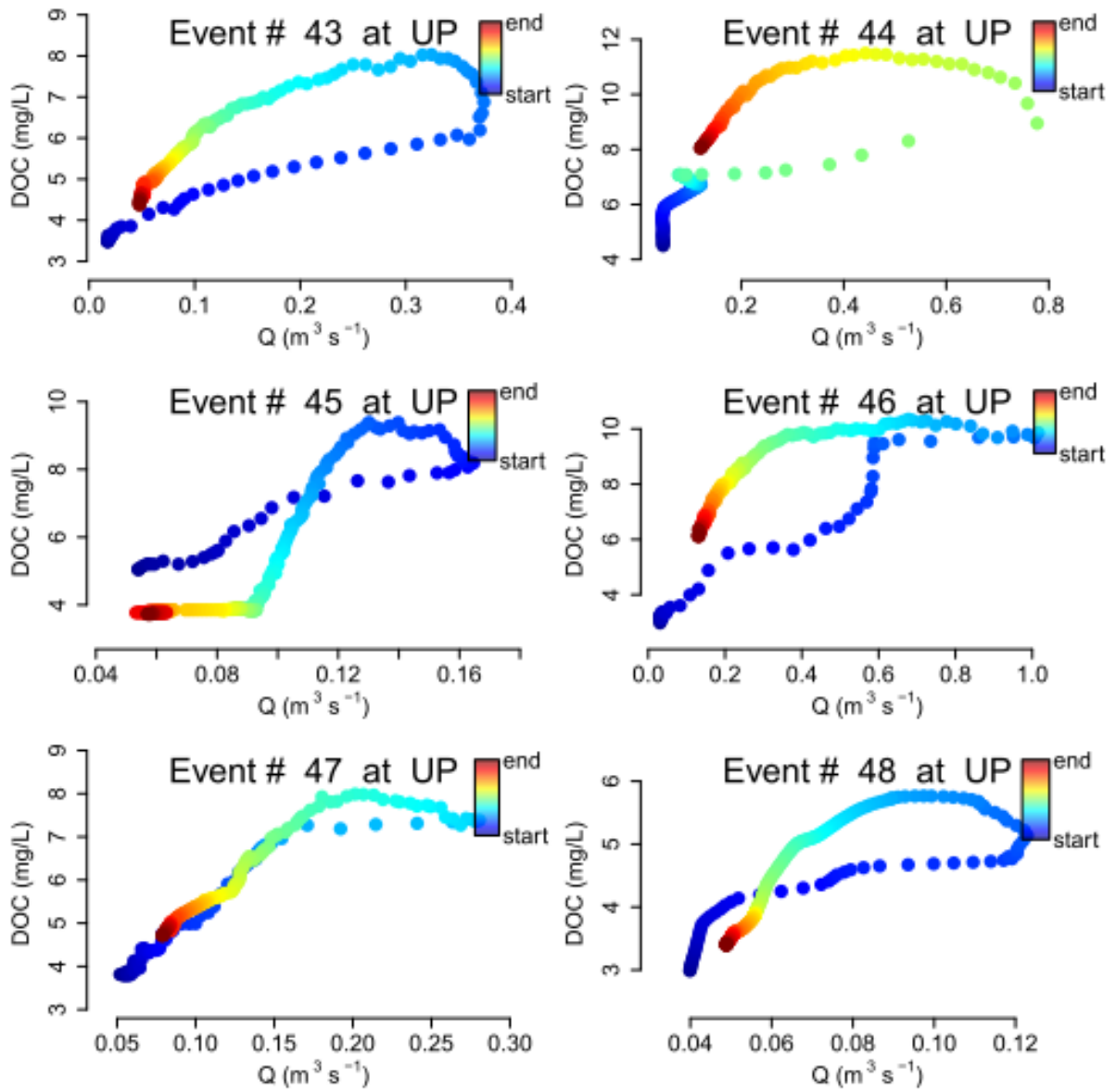
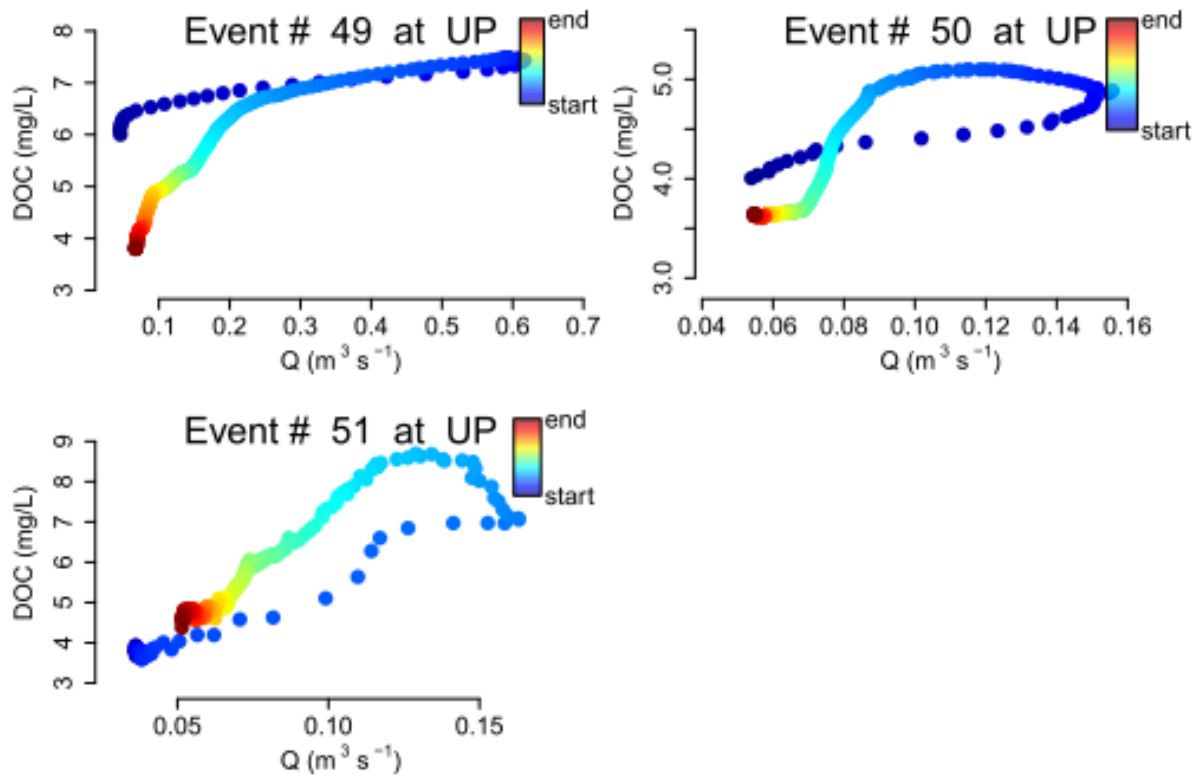


Figure F.2 Continued



F.2 Hysteresis plots at MD station

Figure F.3 Hysteresis plots for $\text{NO}_3\text{-N}$ at MD

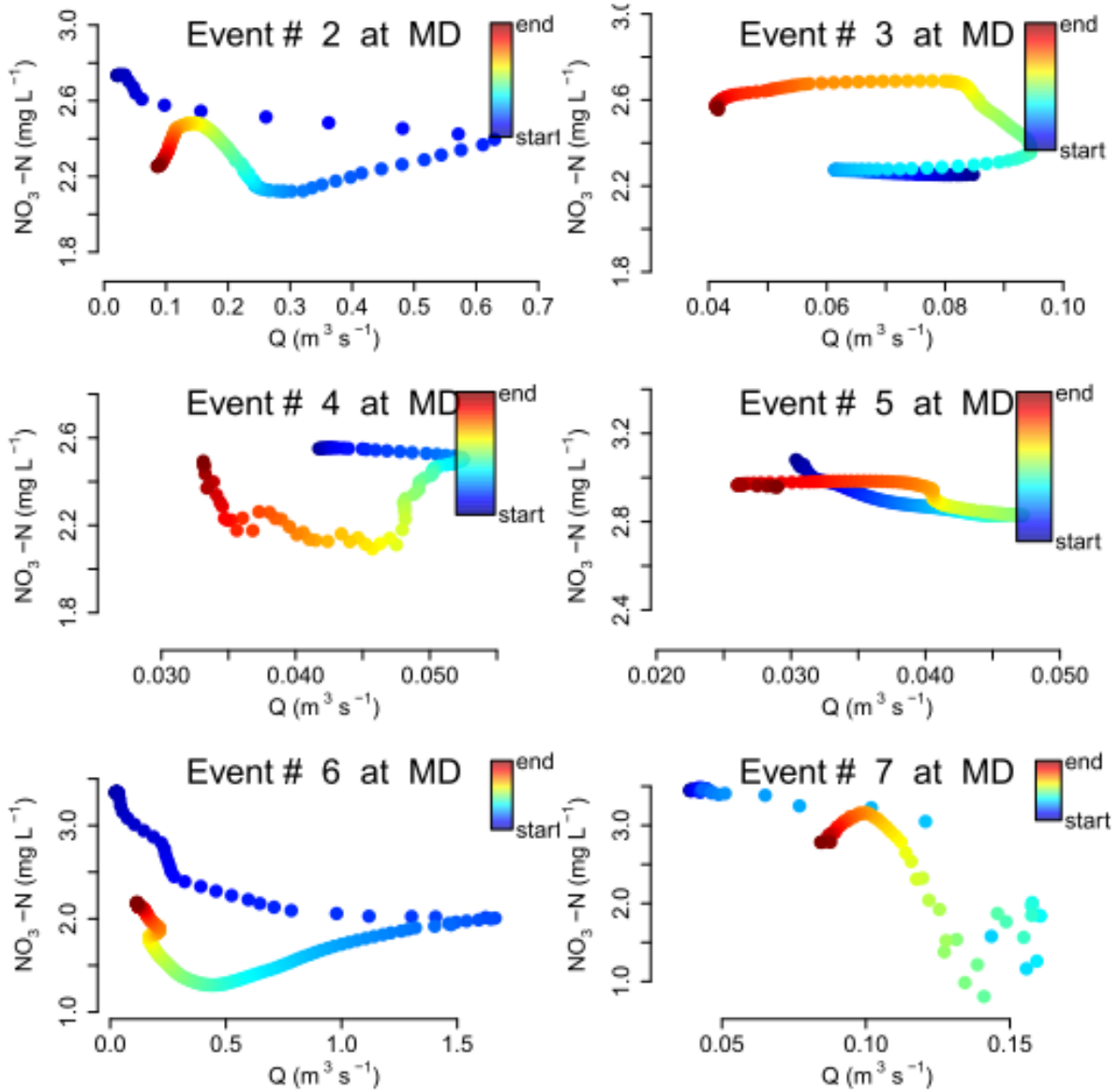


Figure F.3 Continued

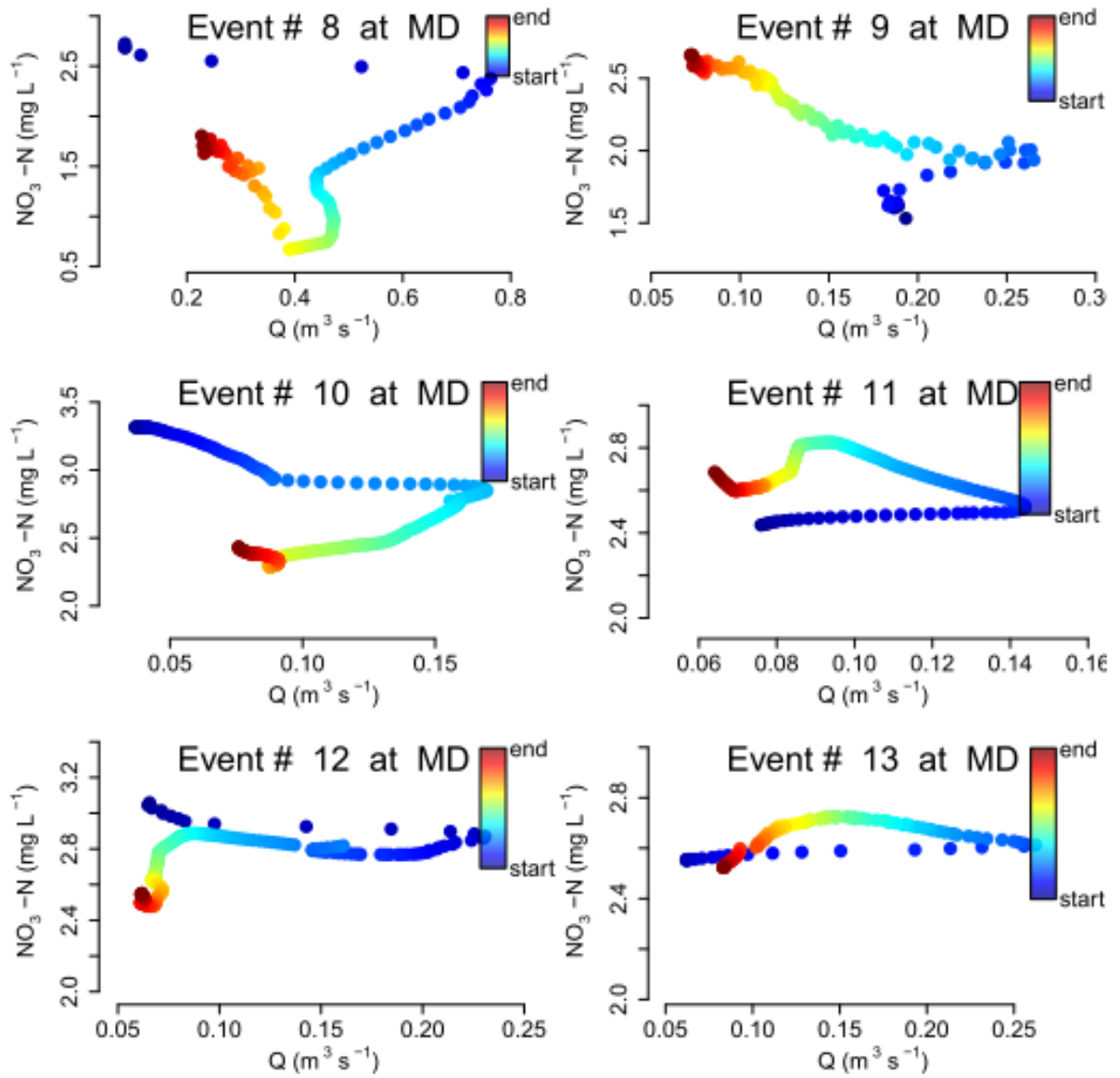


Figure F.3 Continued

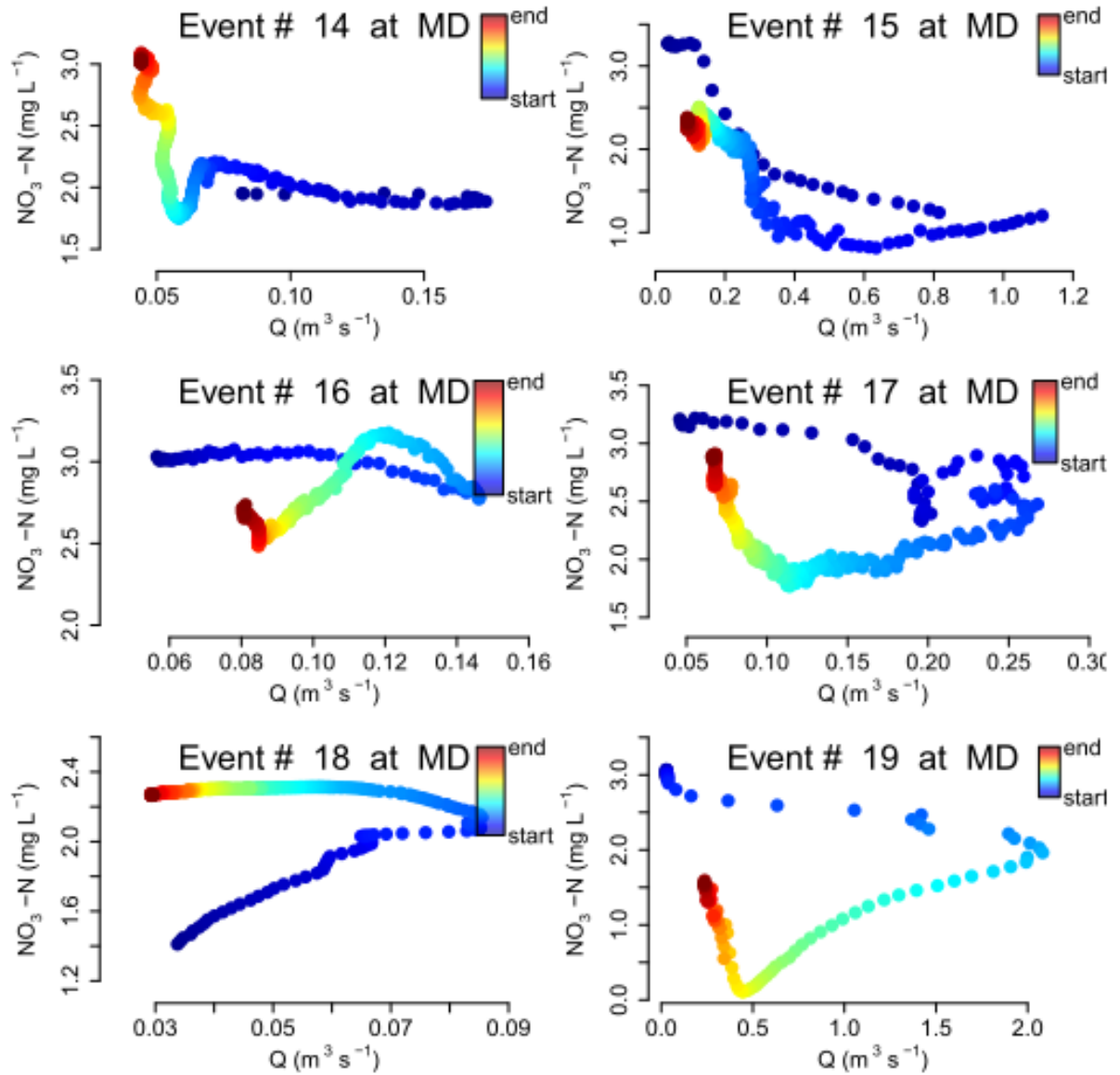


Figure F.3 Continued

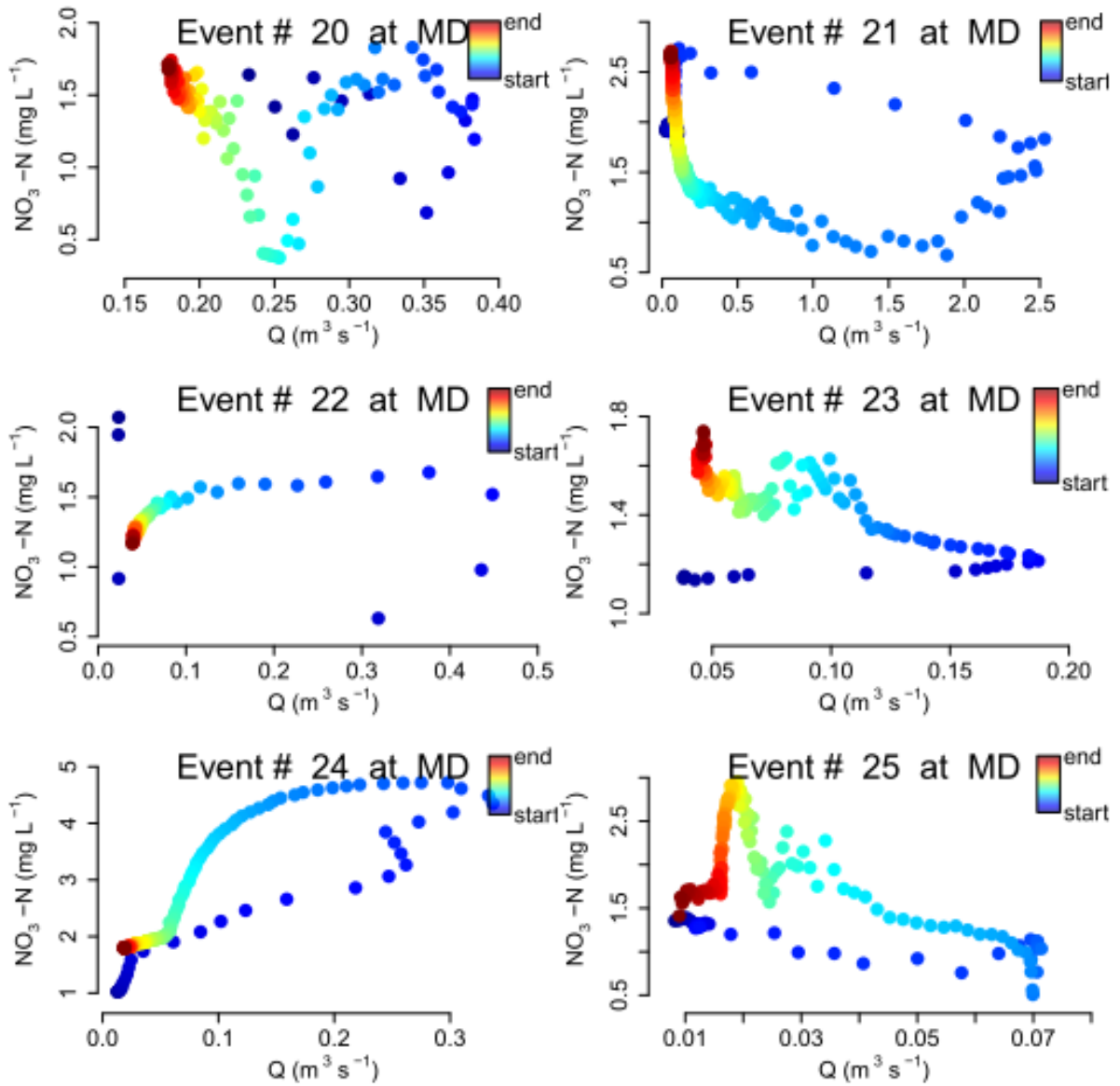


Figure F.3 Continued

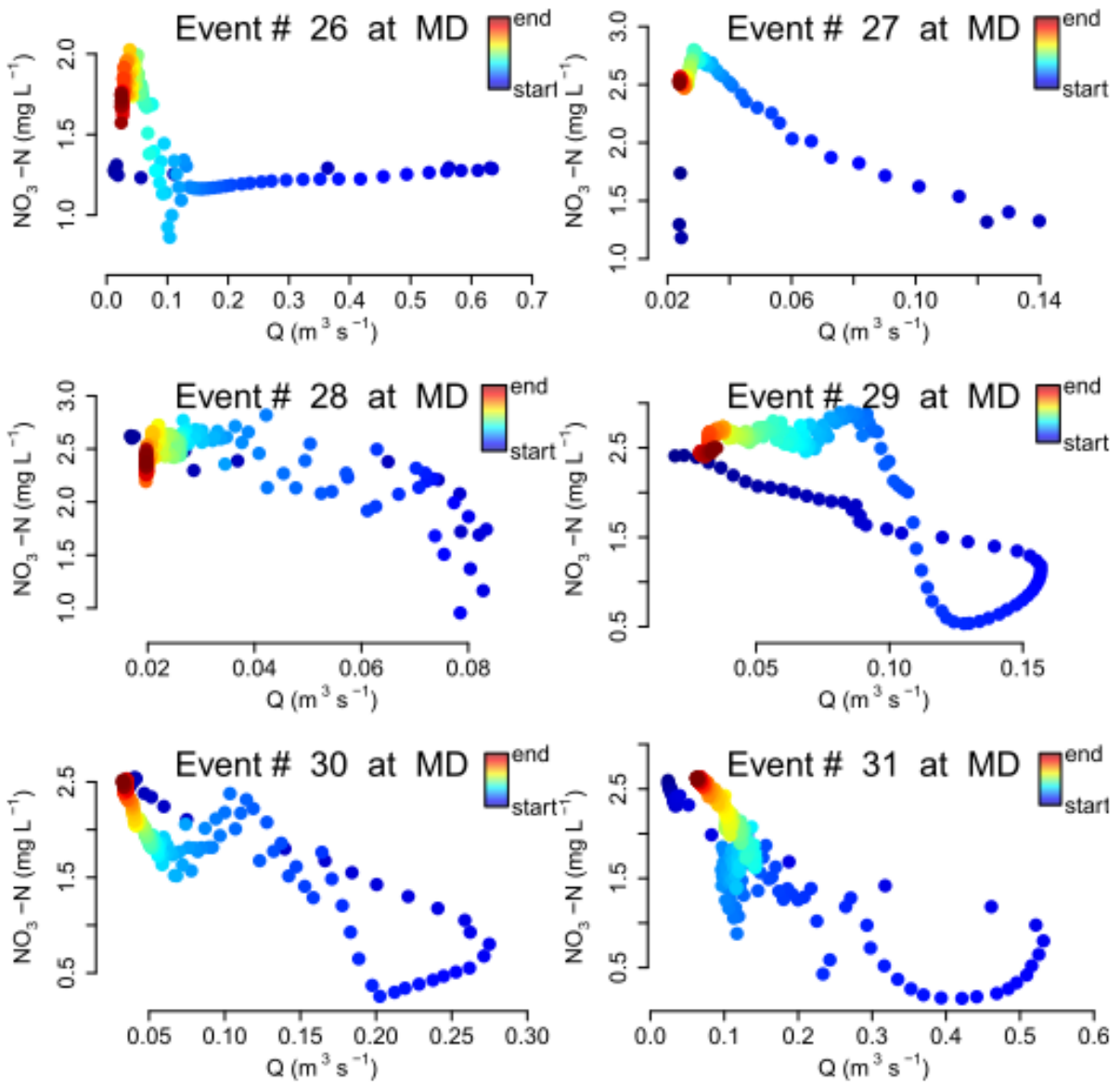


Figure F.3 Continued

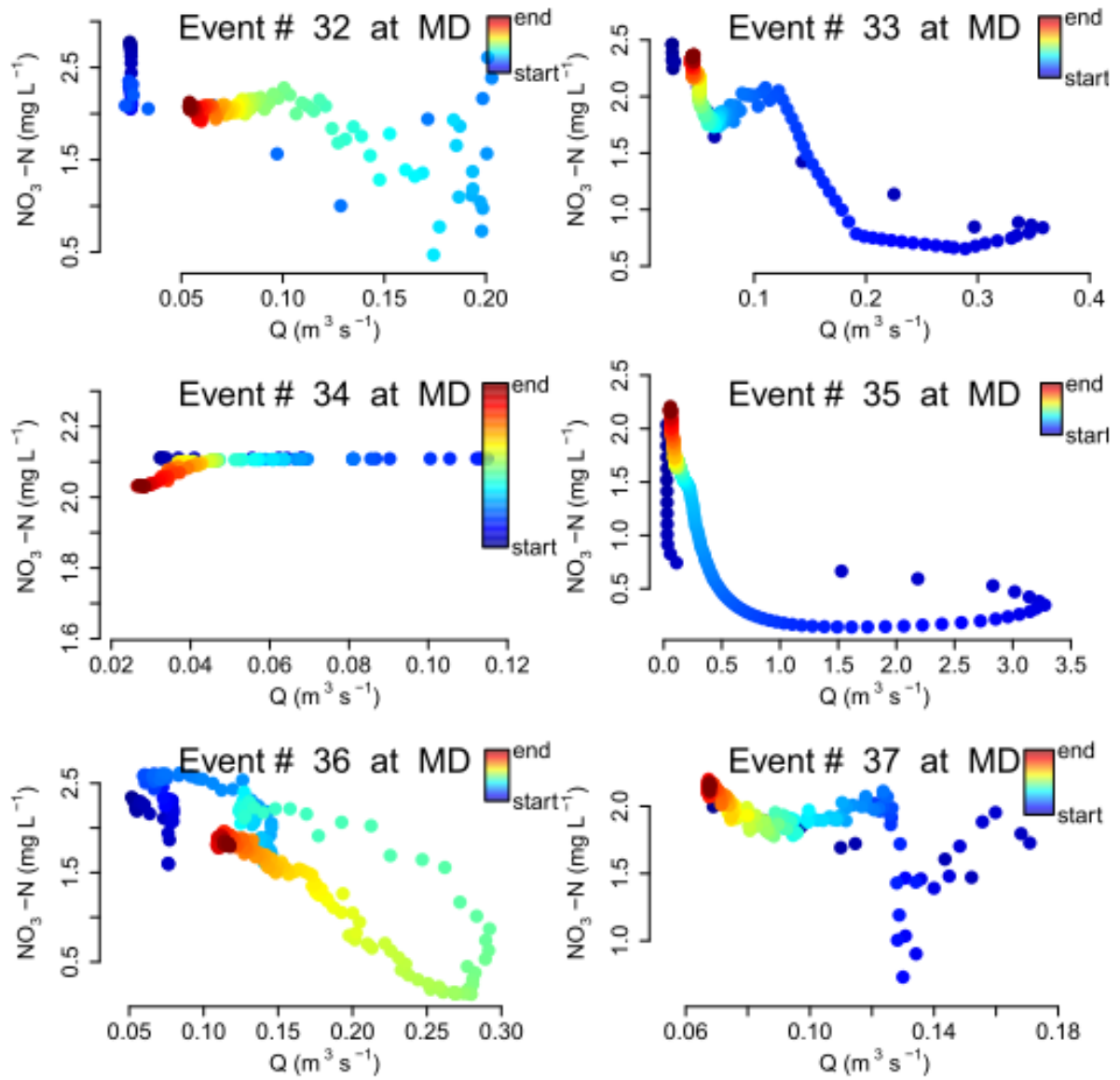


Figure F.3 Continued

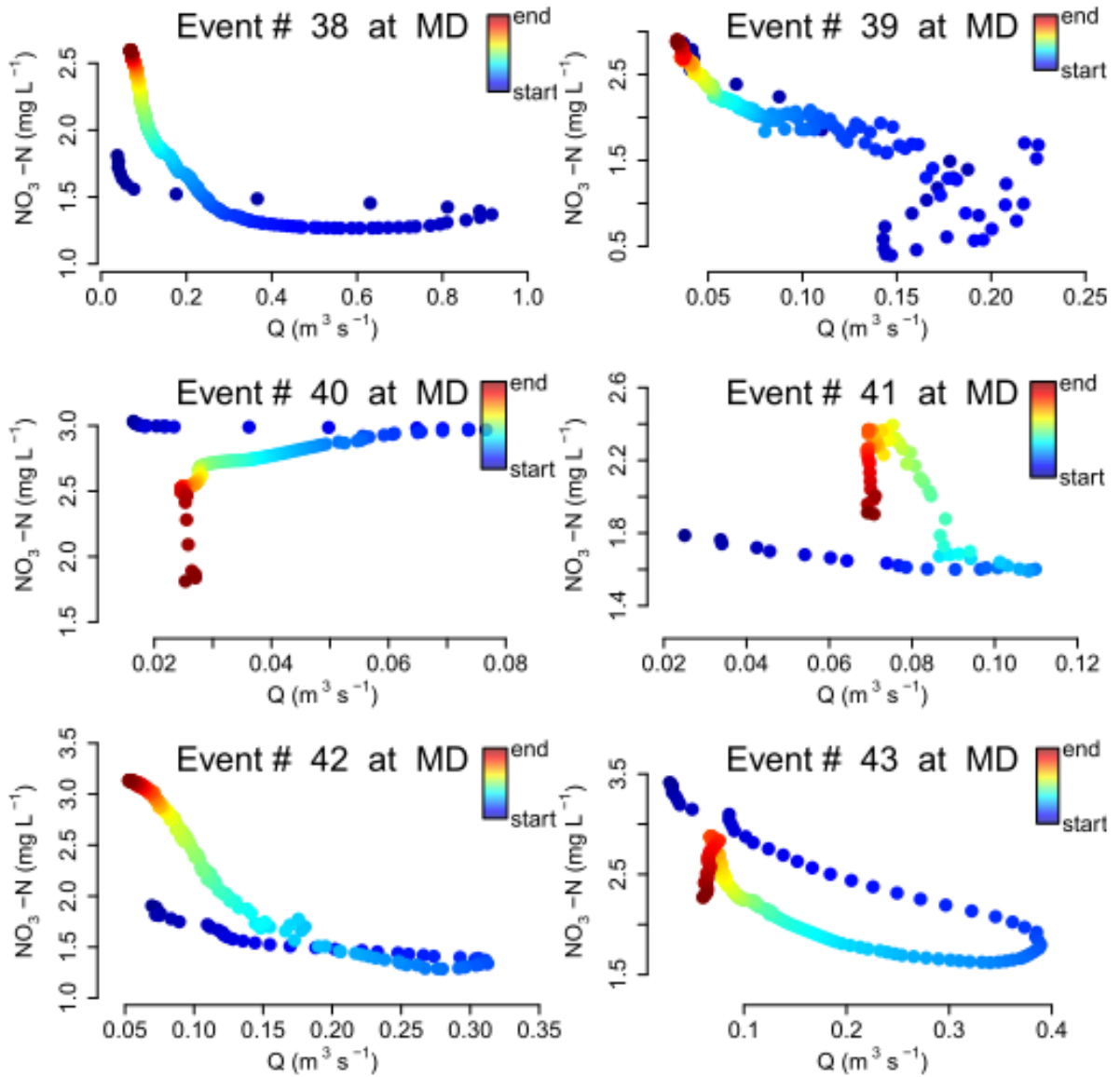


Figure F.3 Continued

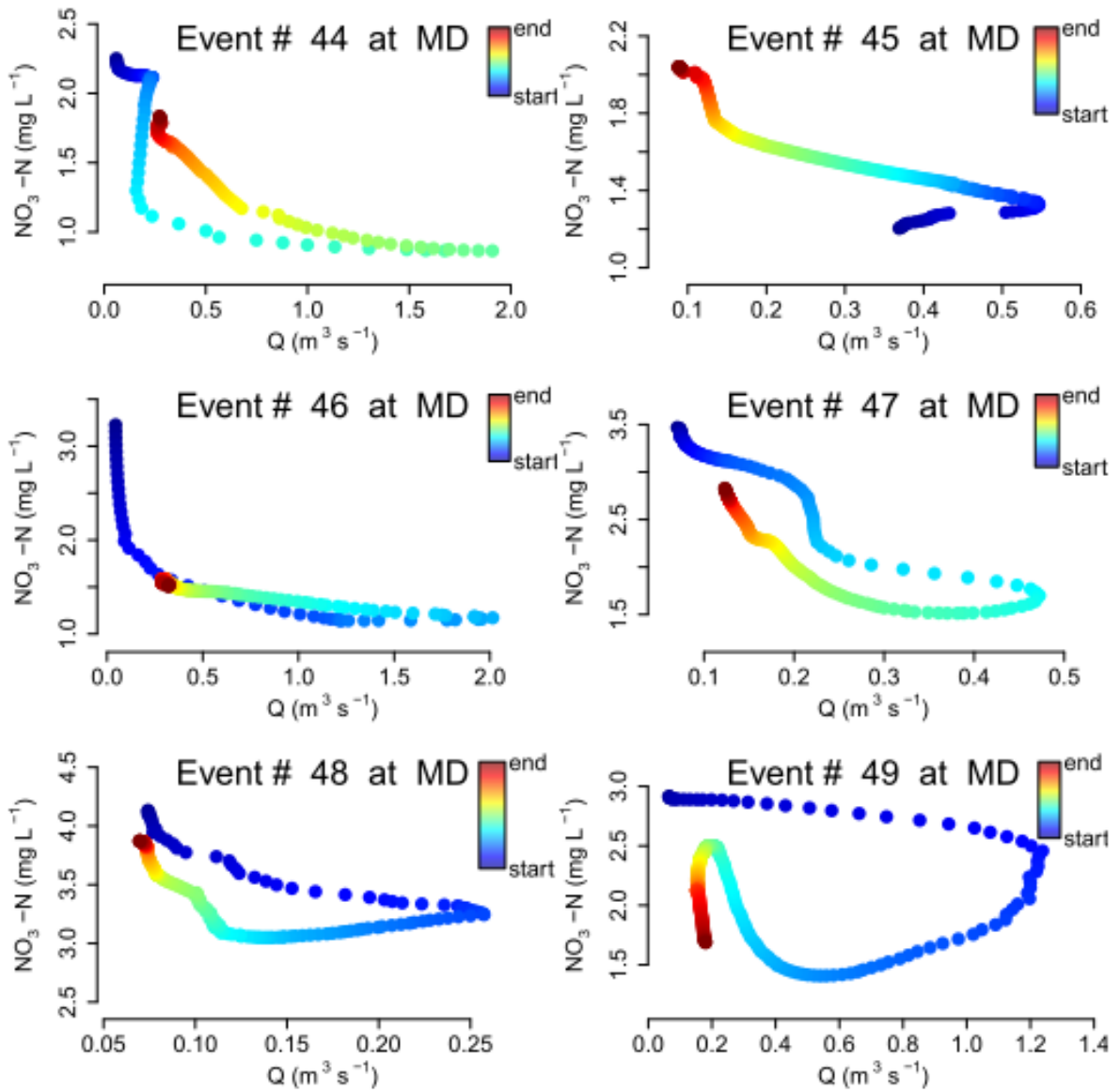


Figure F.3 Continued

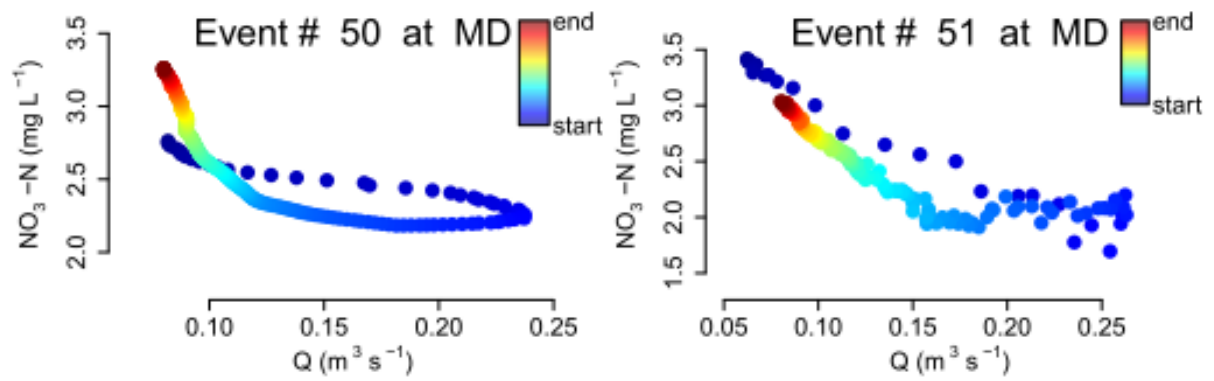


Figure F.4 Hysteresis plots for DOC at MD

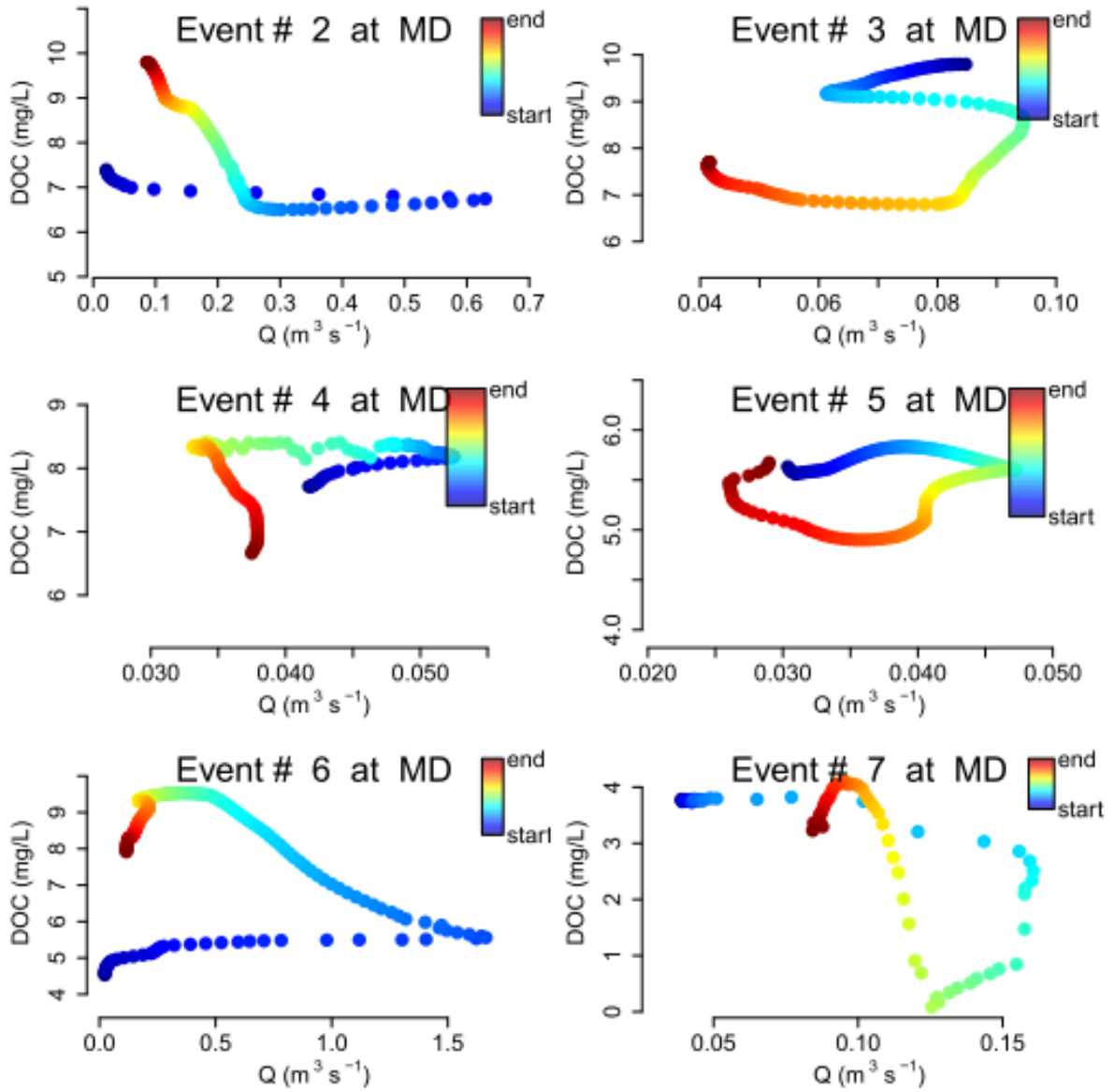


Figure F.4 Continued

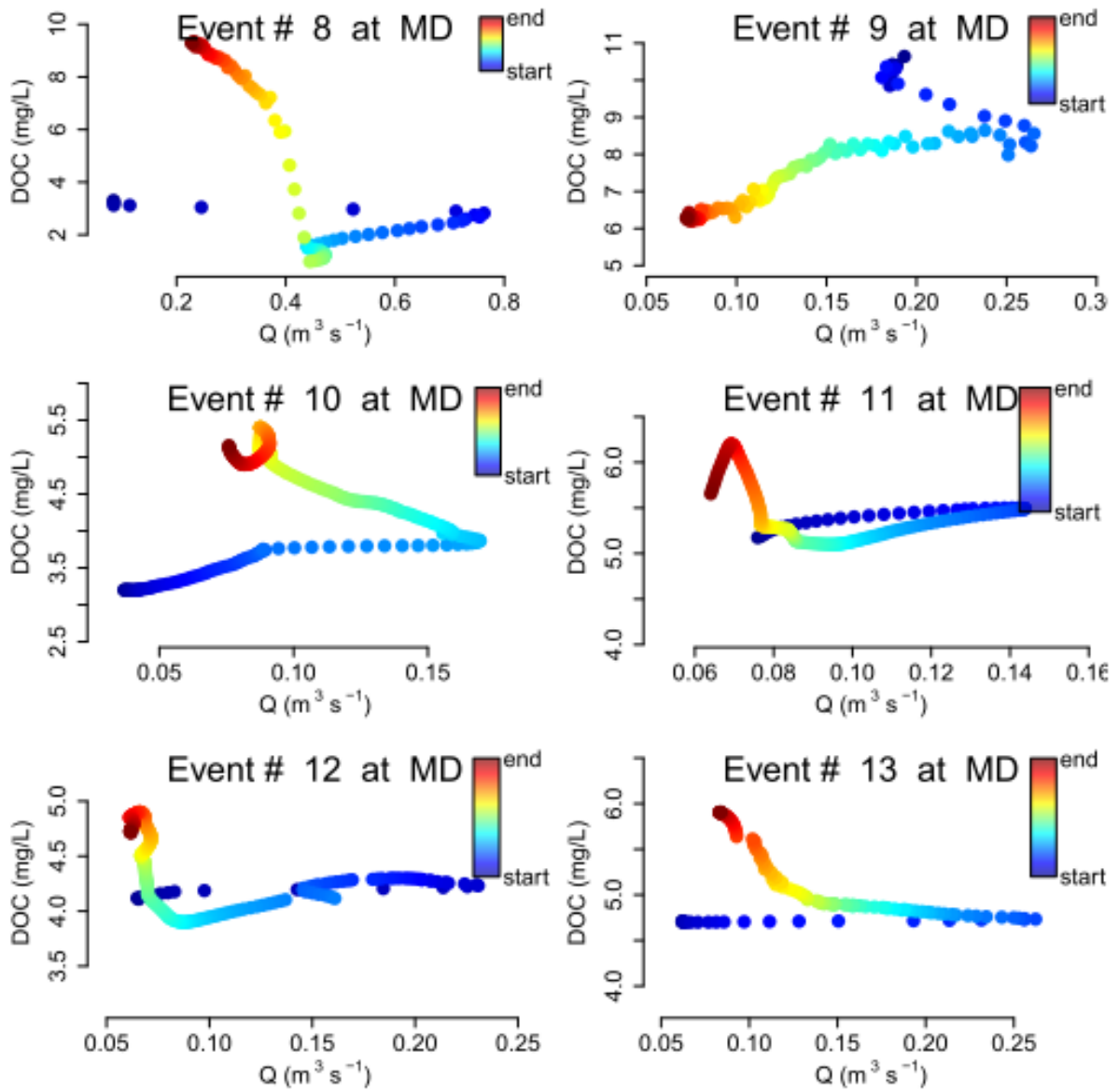


Figure F.4 Continued

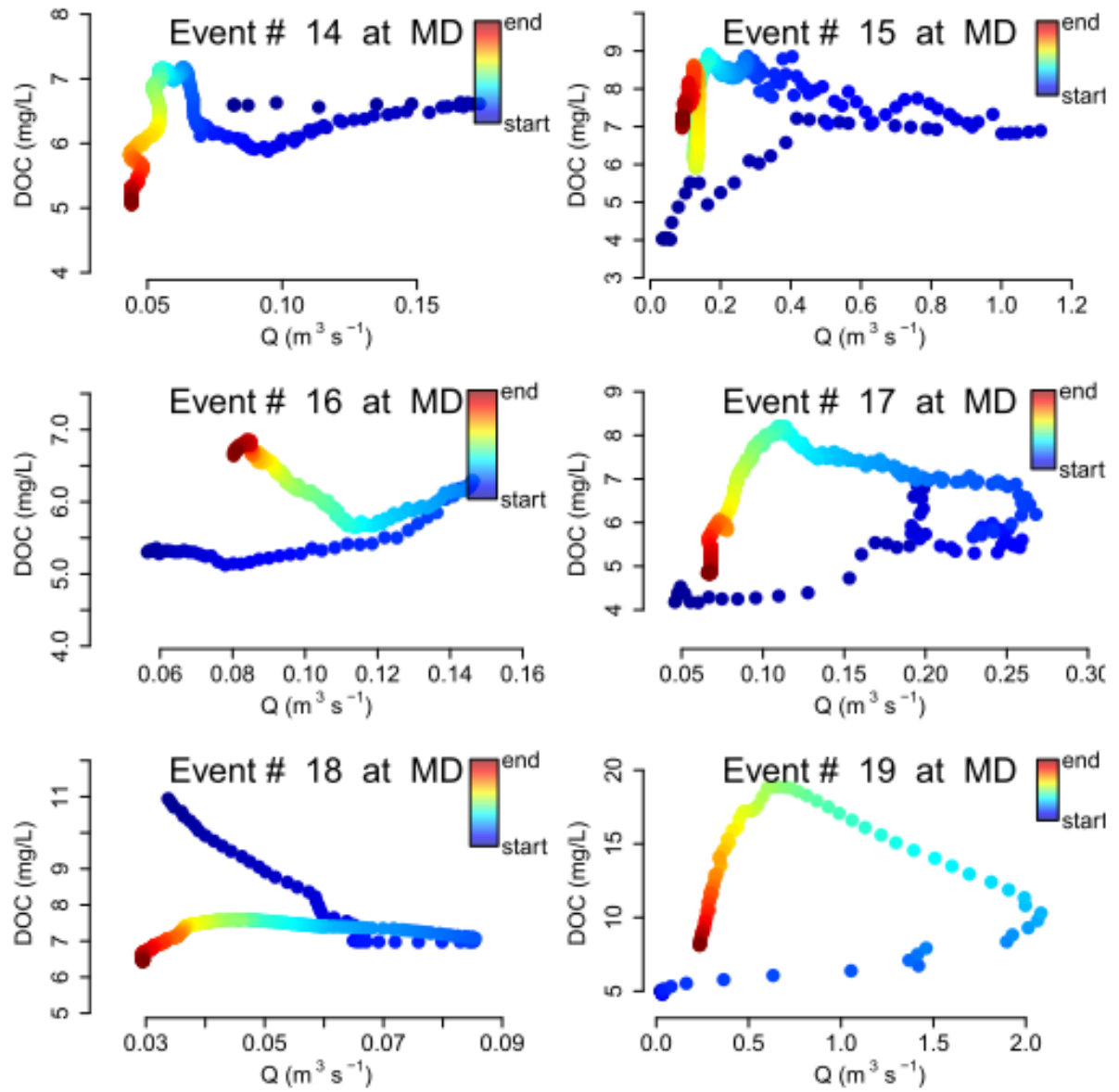


Figure F.4 Continued

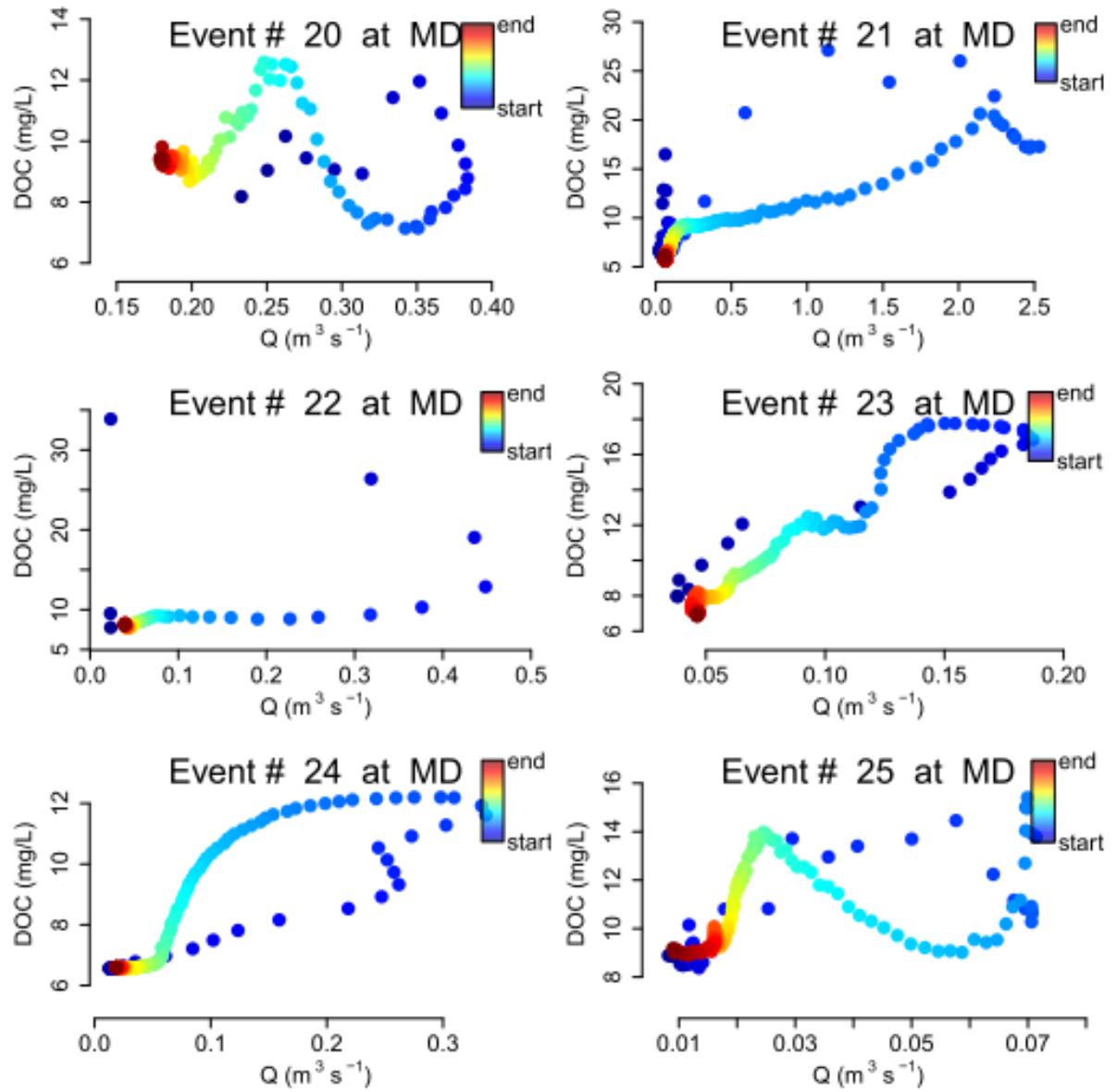


Figure F.4 Continued

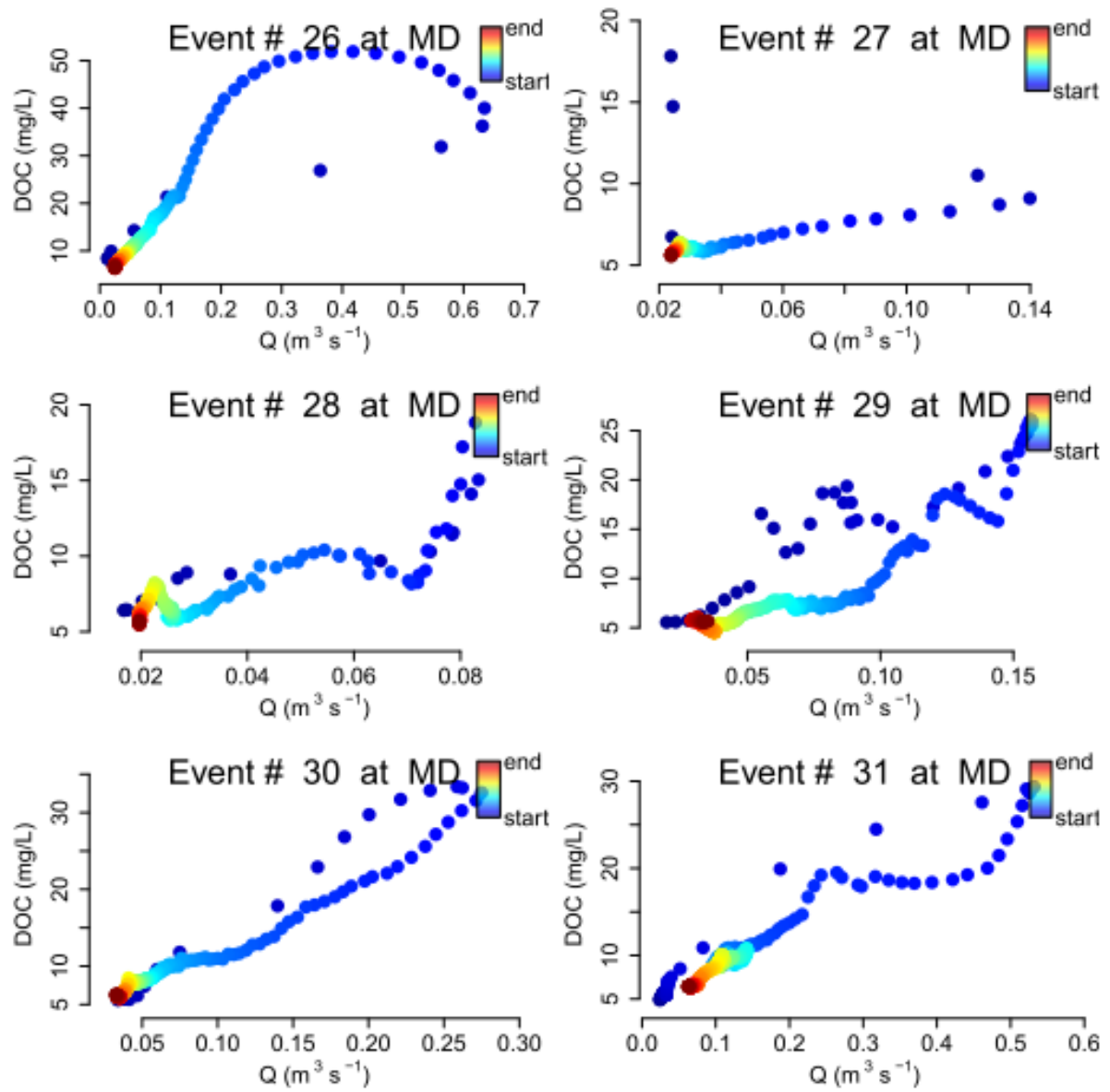


Figure F.4 Continued

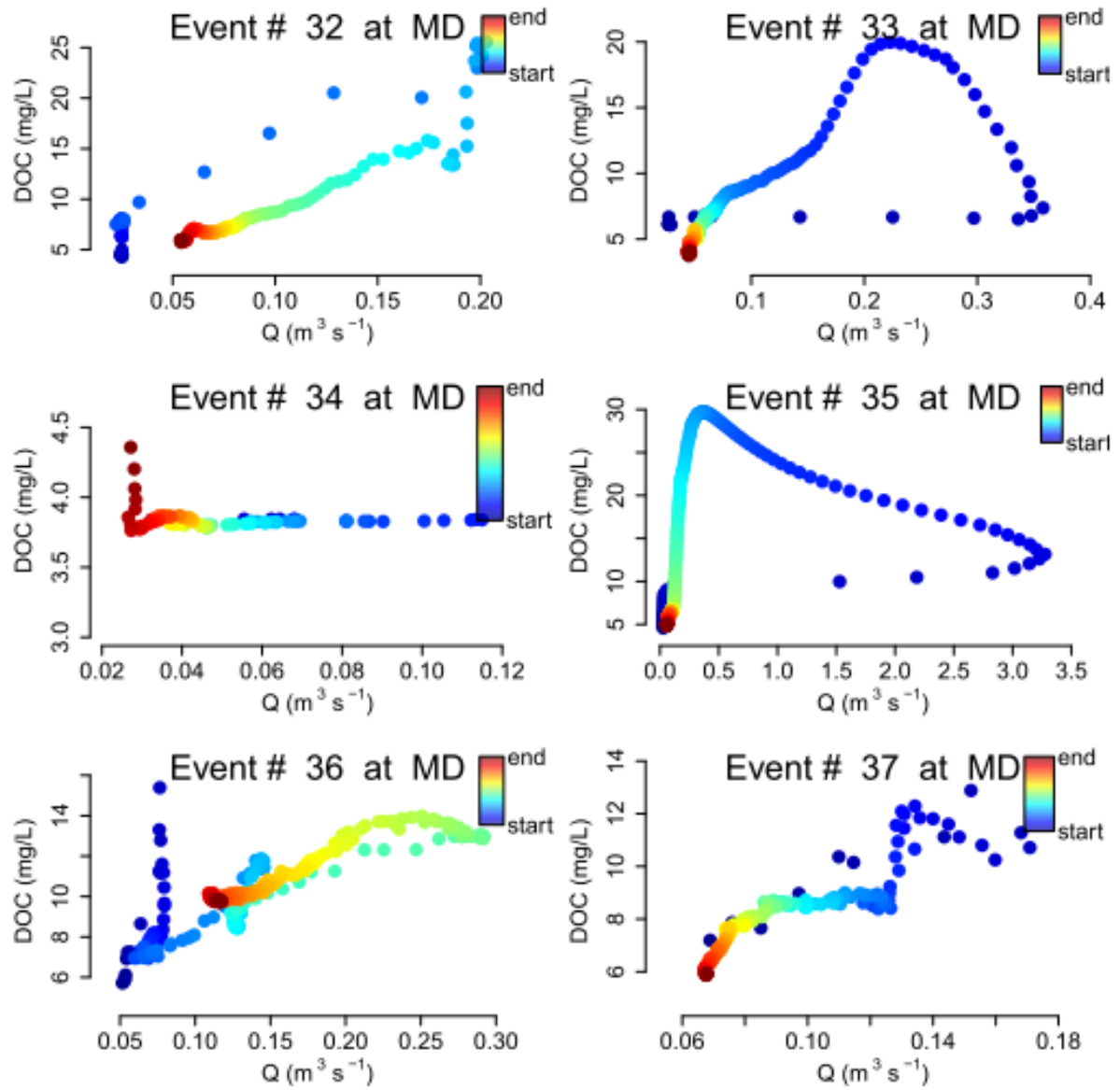


Figure F.4 Continued

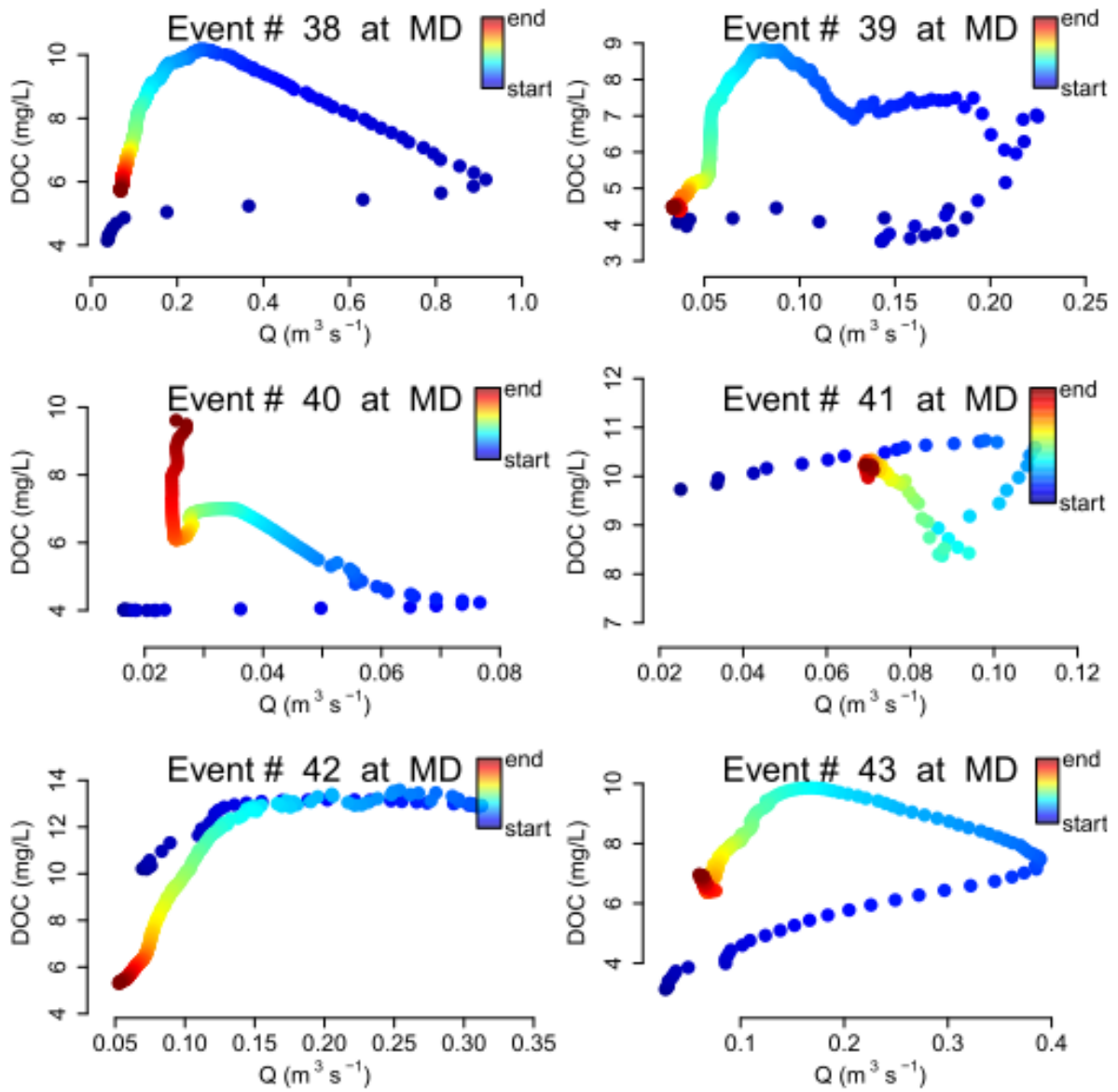


Figure F.4 Continued

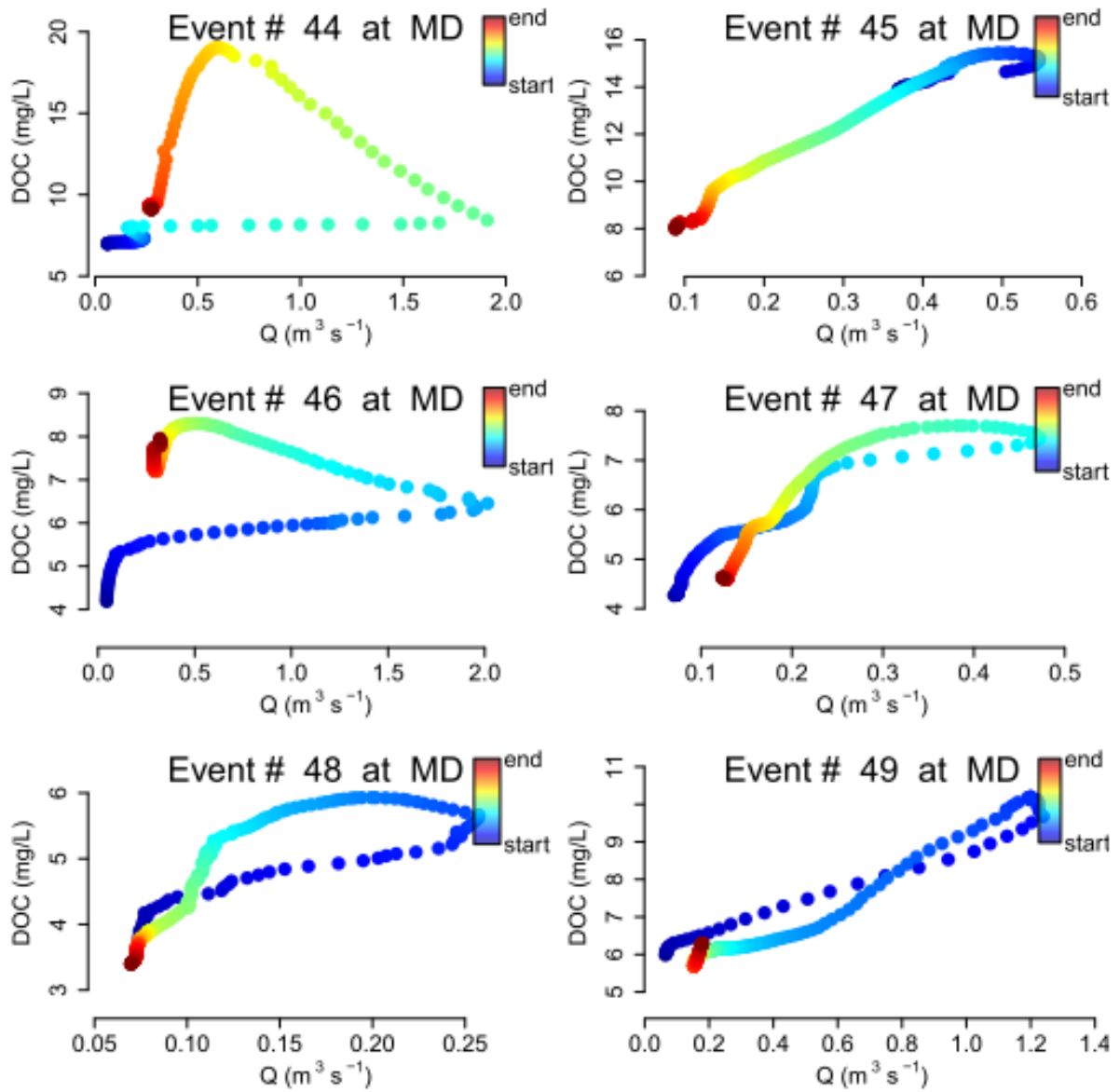
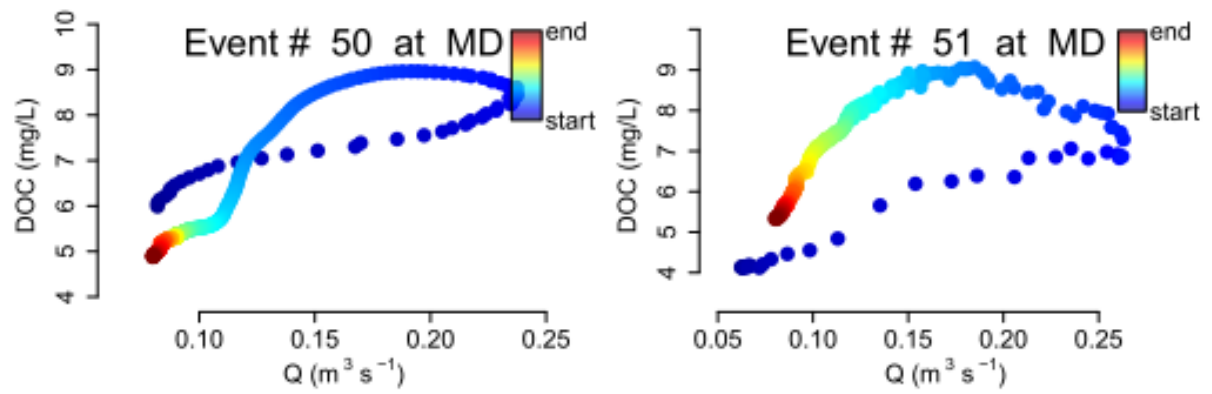


Figure F.4 Continued



F.3 Hysteresis plots at DN station

Figure F.5 Hysteresis plots for $\text{NO}_3\text{-N}$ at DN

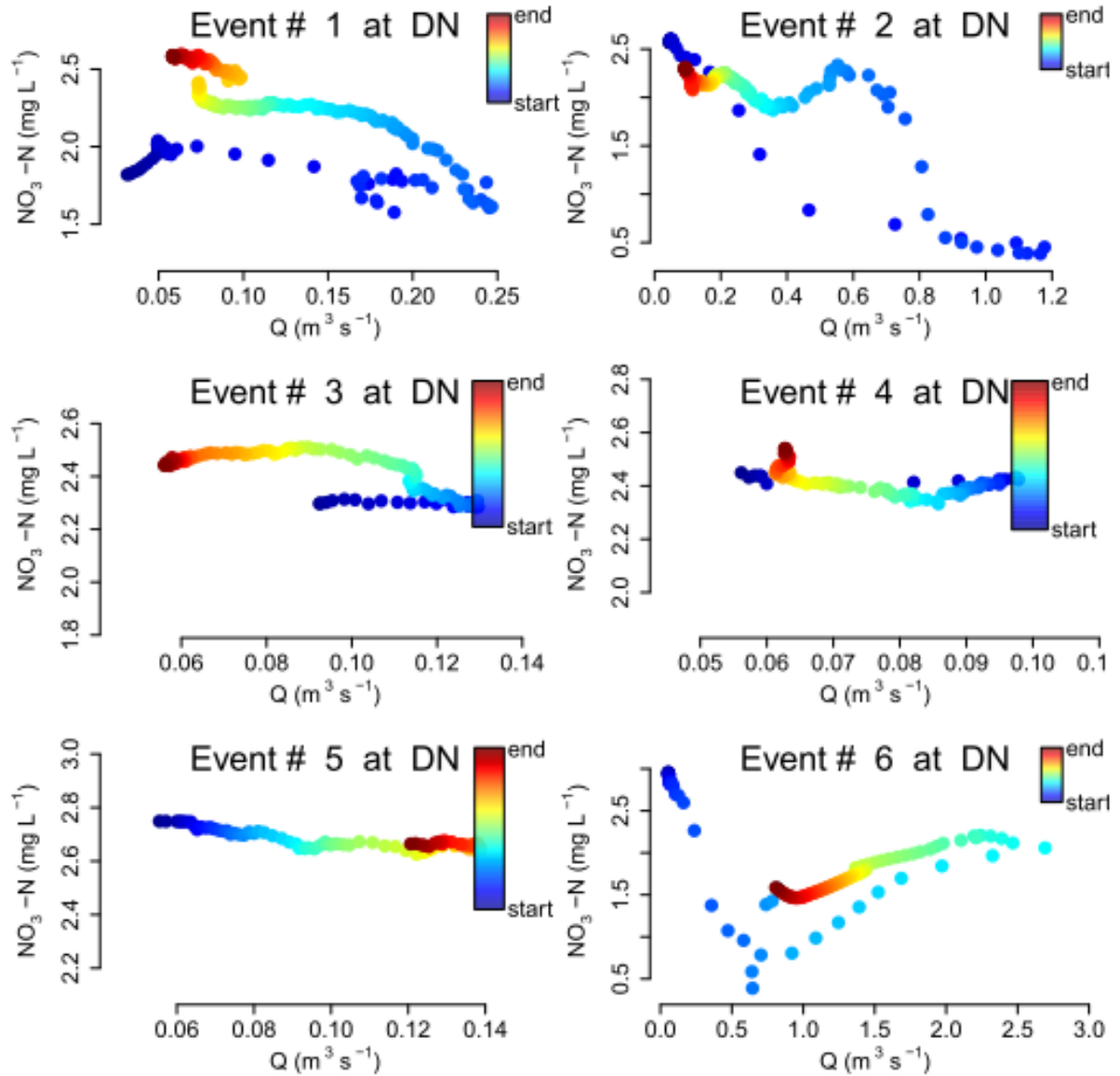


Figure F.5 Continued

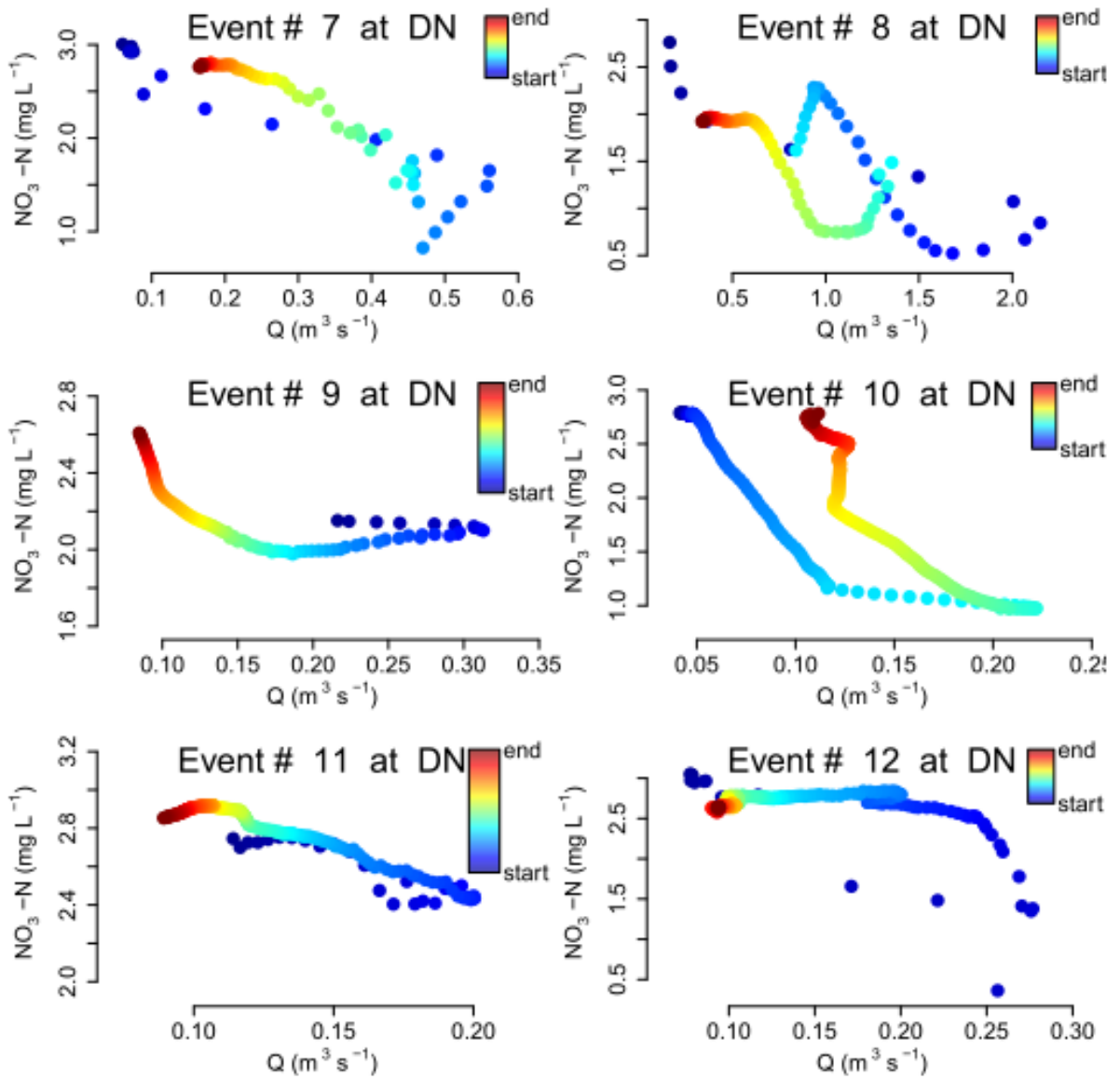


Figure F.5 Continued

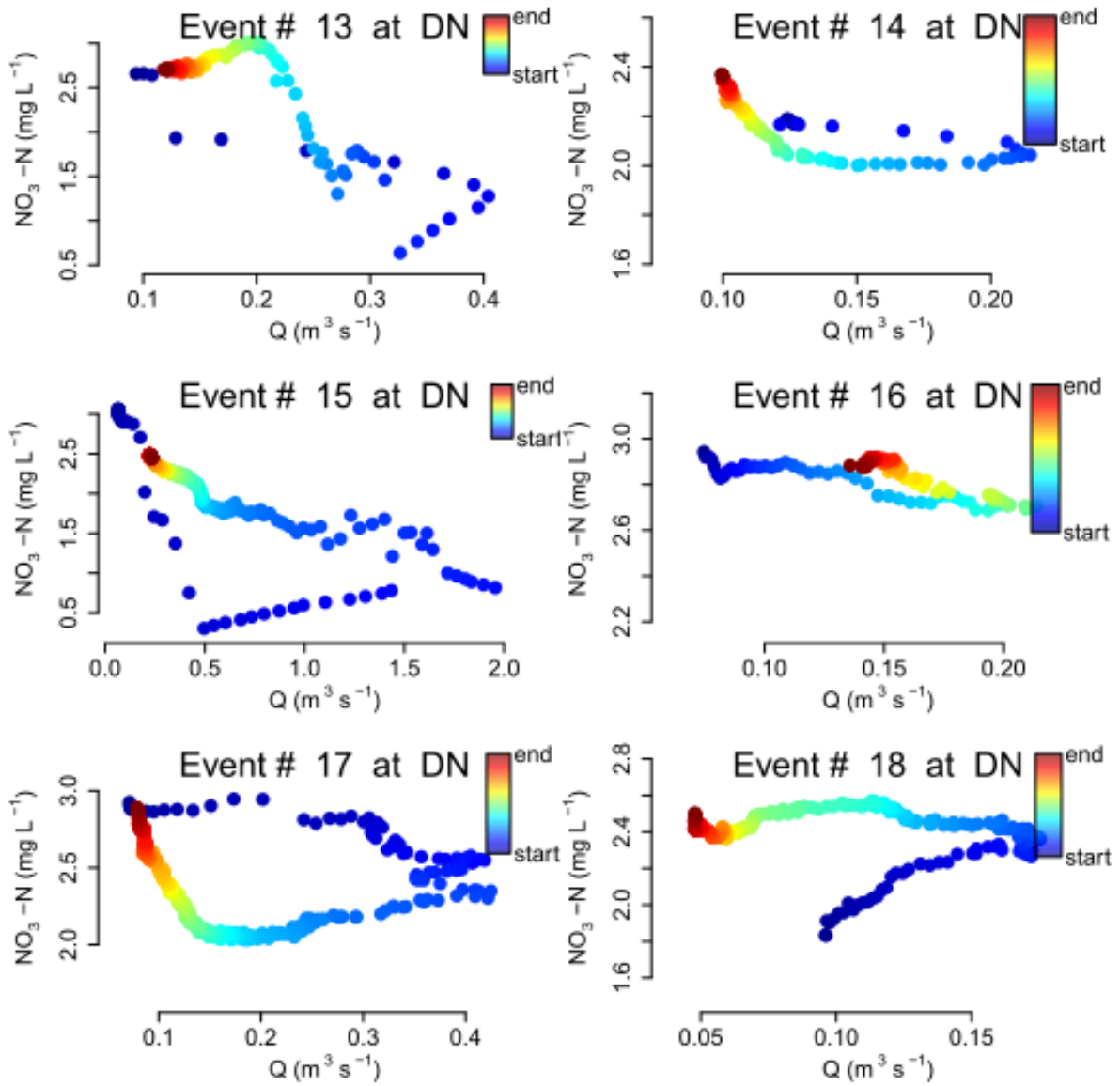


Figure F.5 Continued

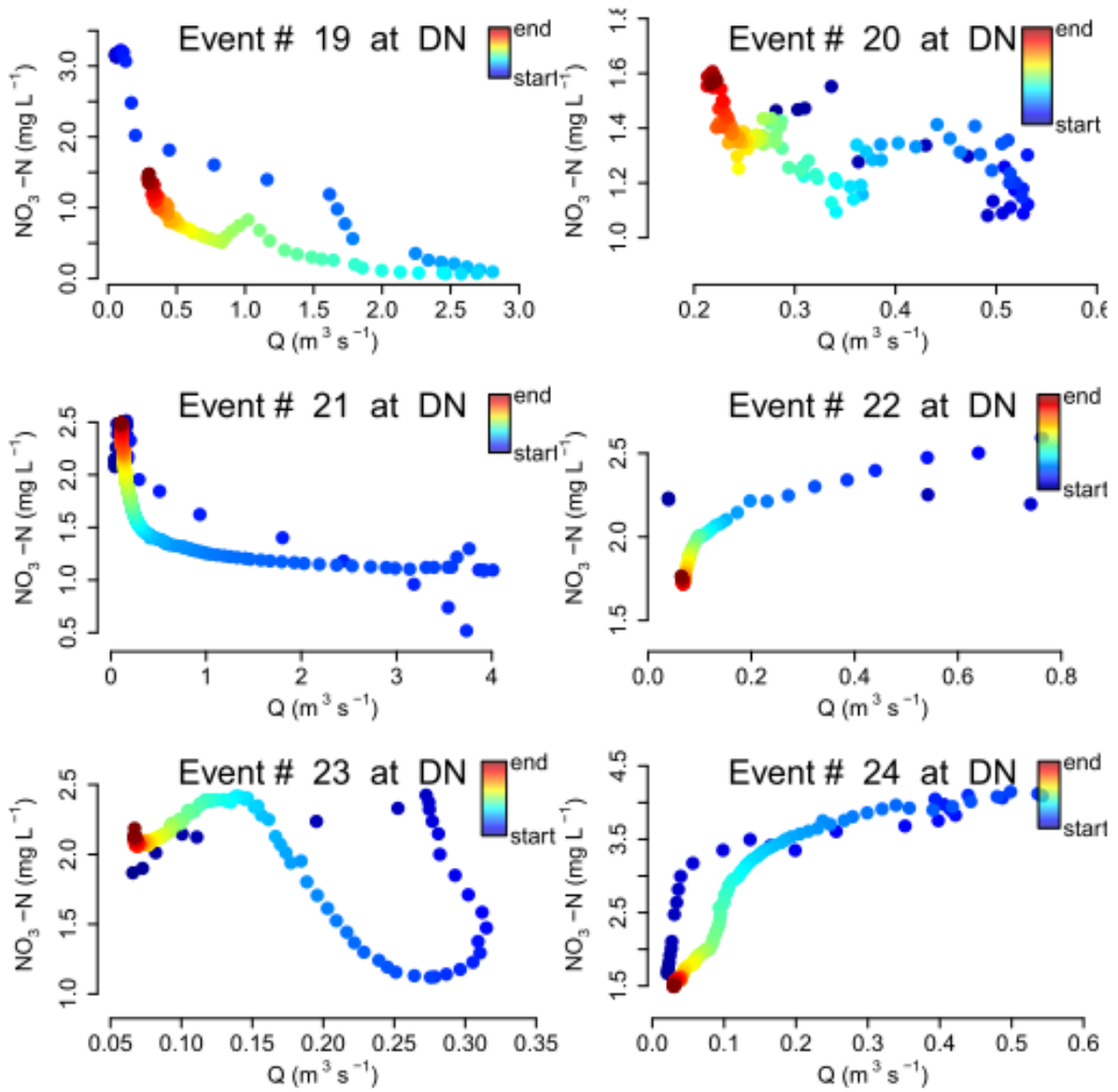


Figure F.5 Continued

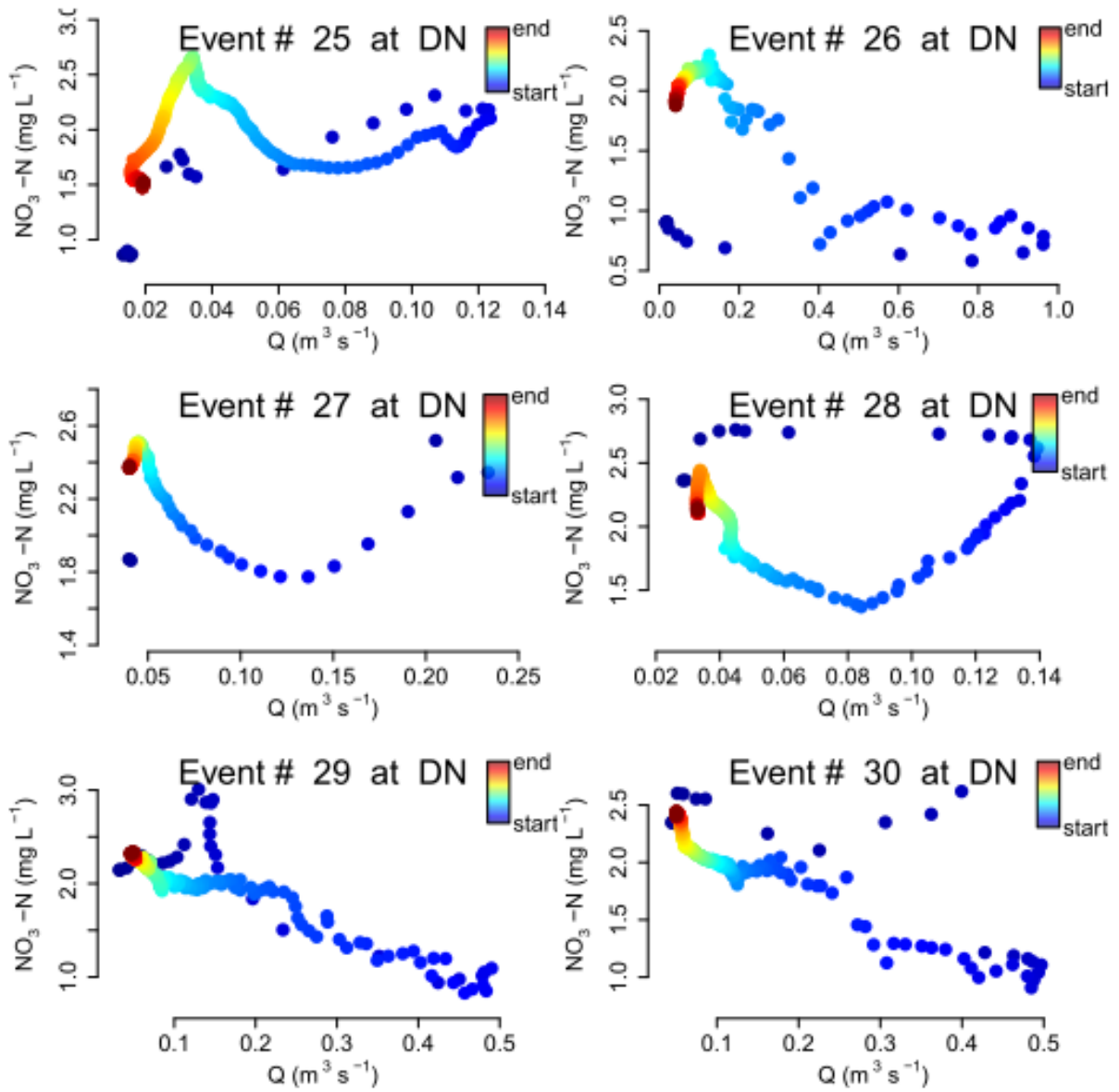


Figure F.5 Continued

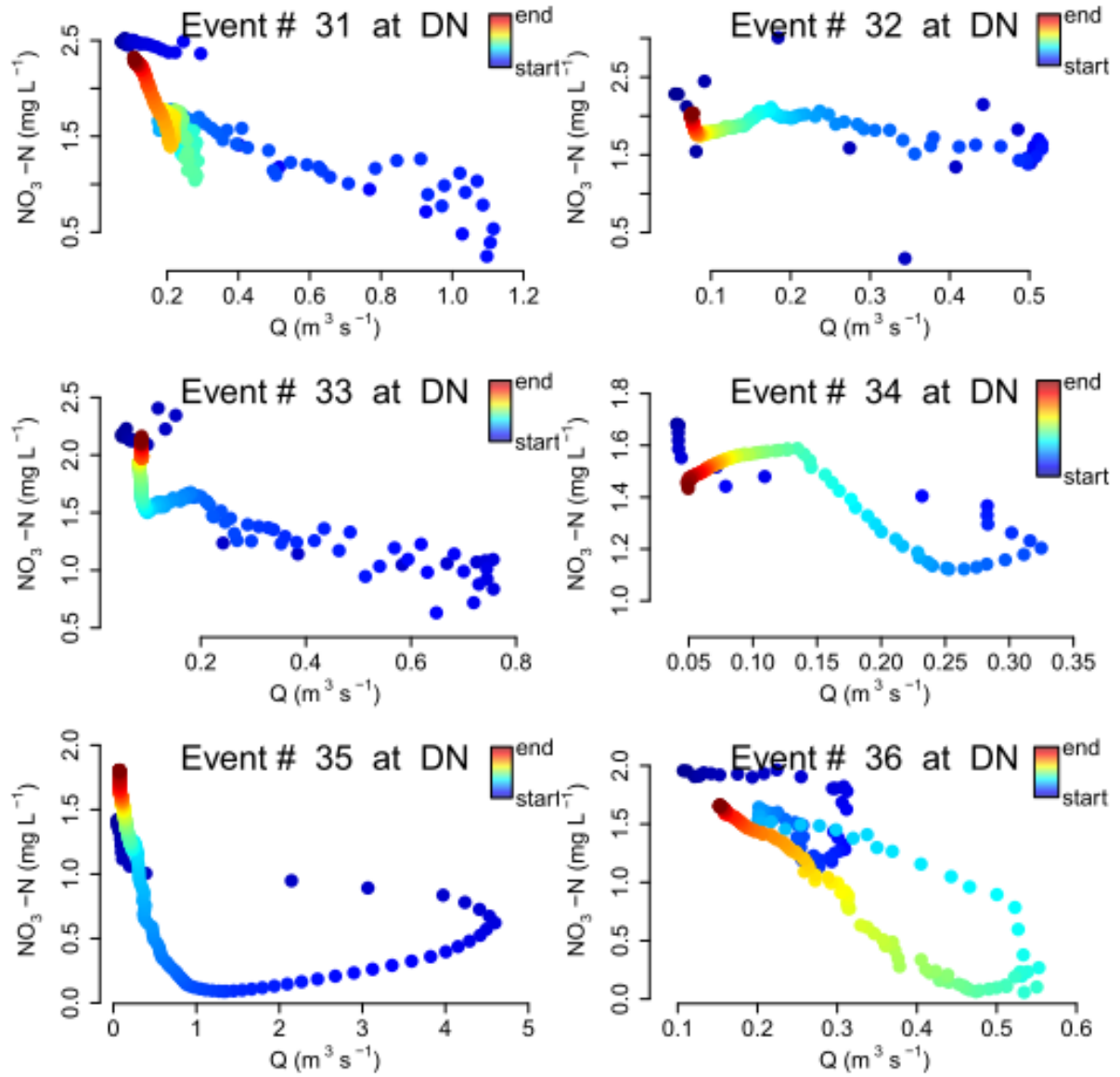


Figure F.5 Continued

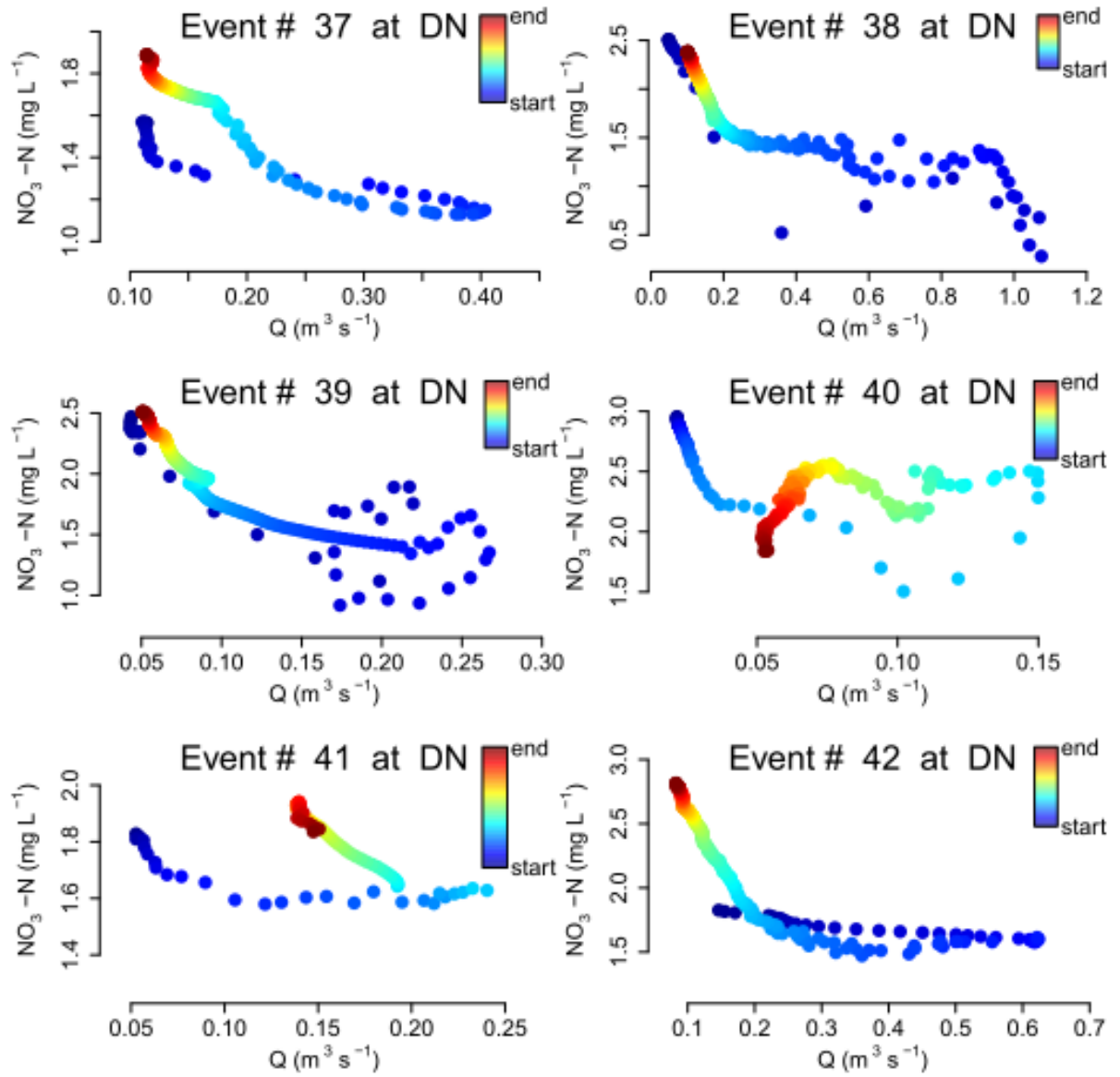


Figure F.5 Continued

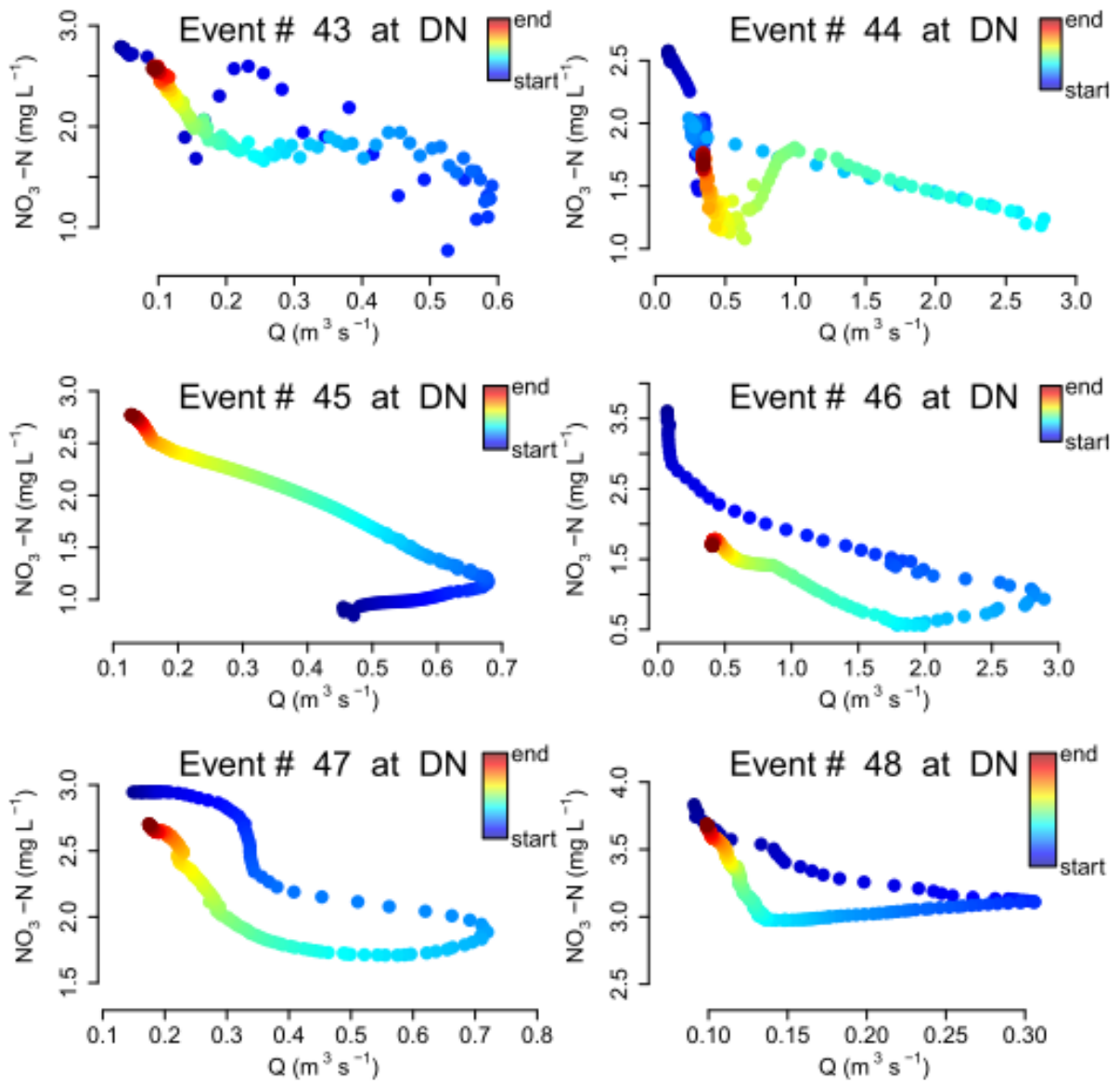


Figure F.5 Continued

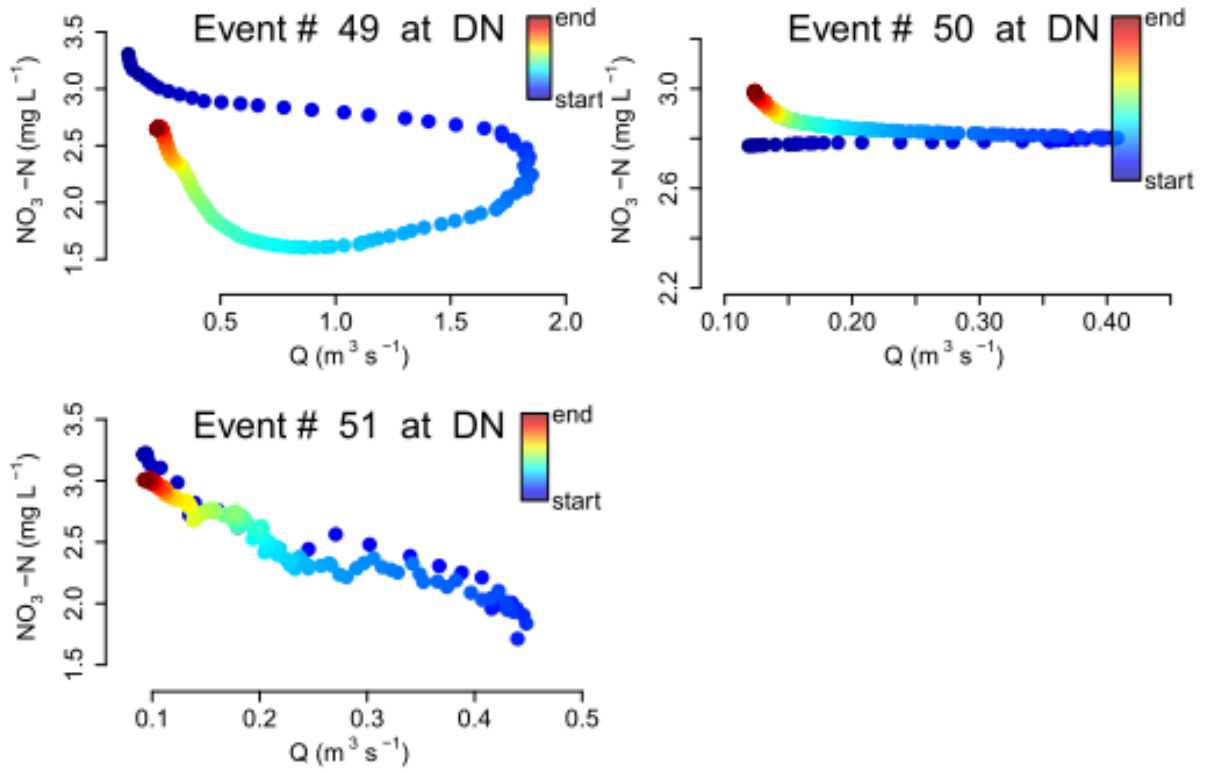


Figure F.6 Hysteresis plots for DOC at DN

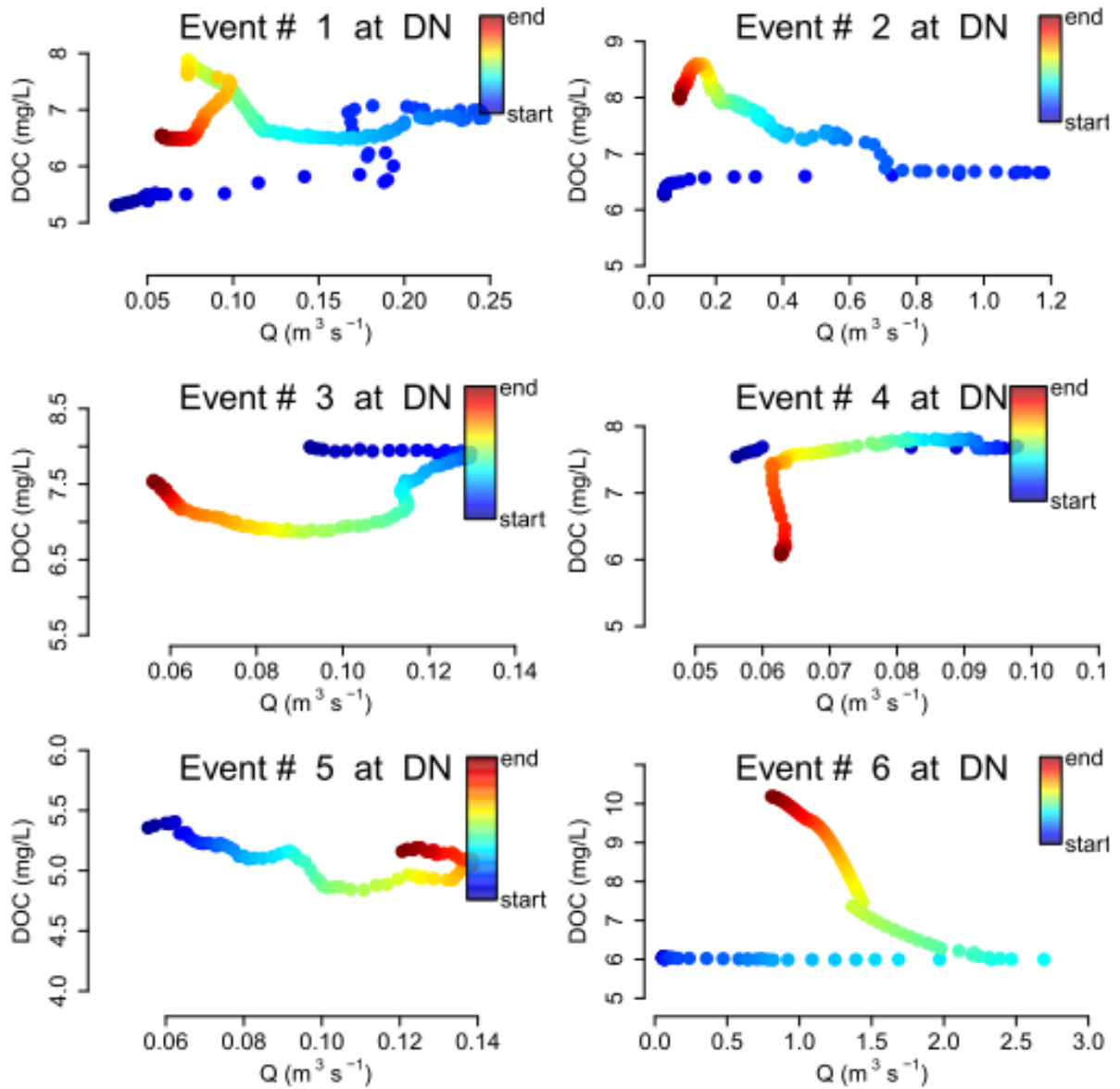


Figure F.6 Continued

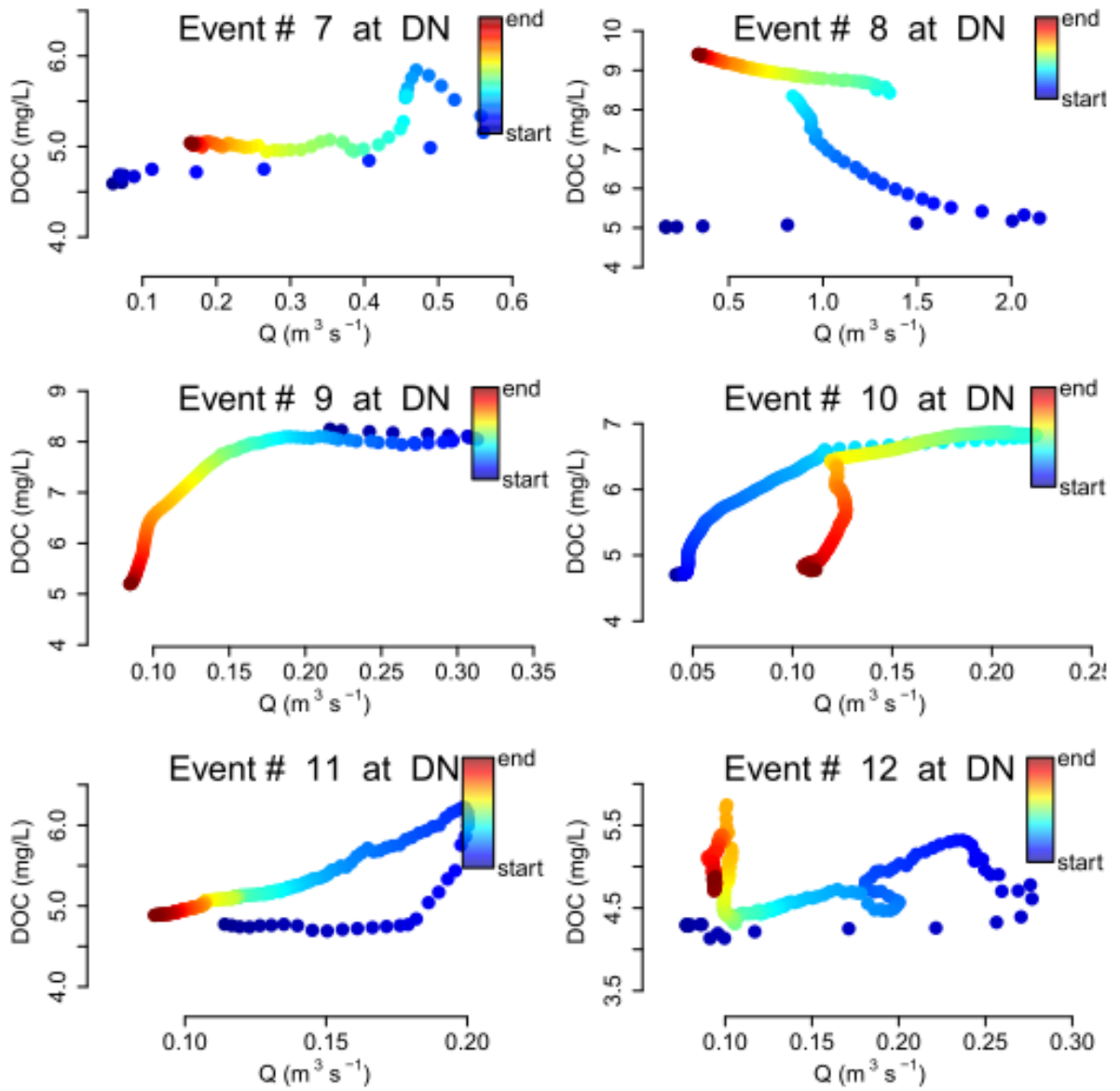


Figure F.6 Continued

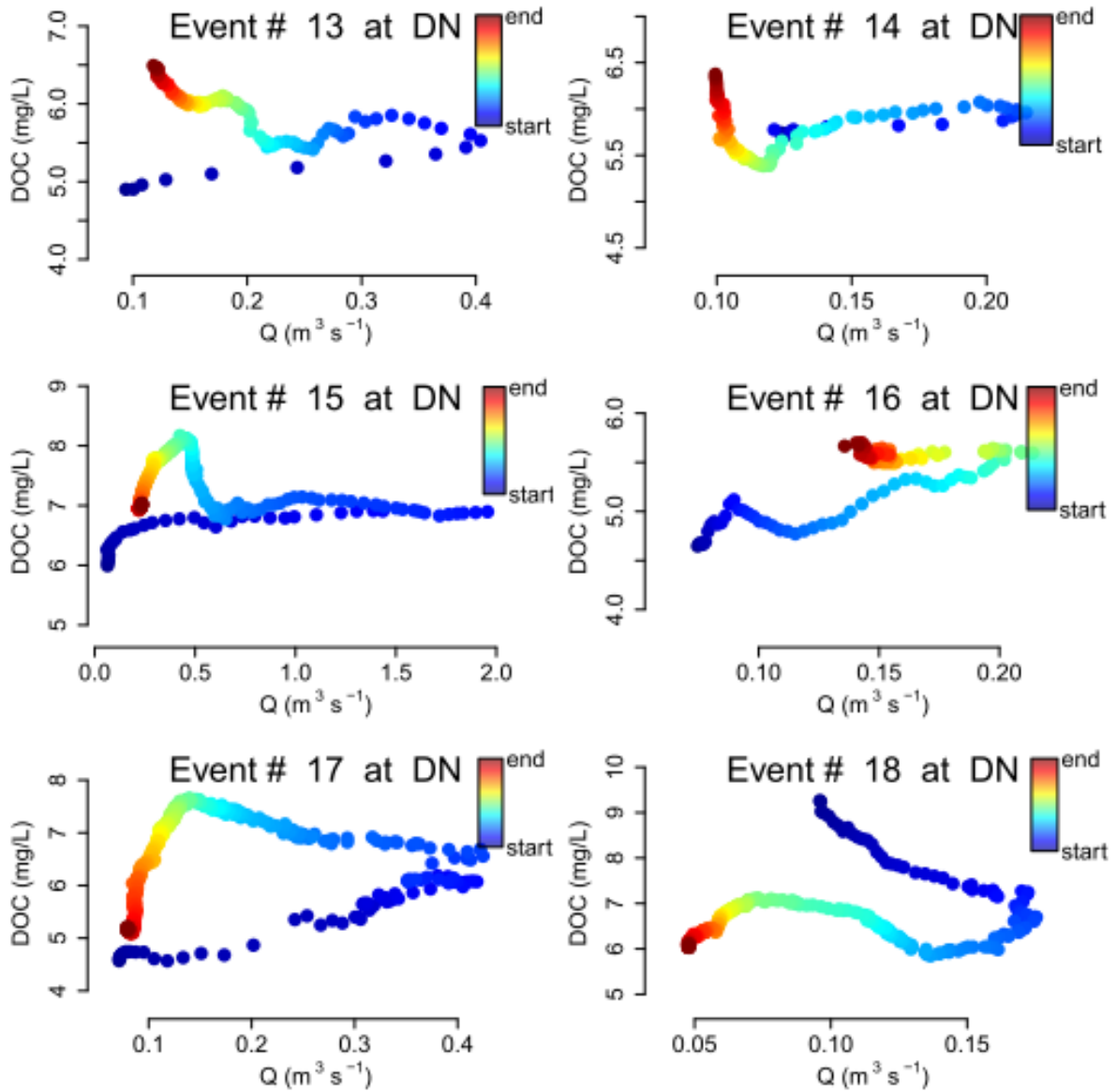


Figure F.6 Continued

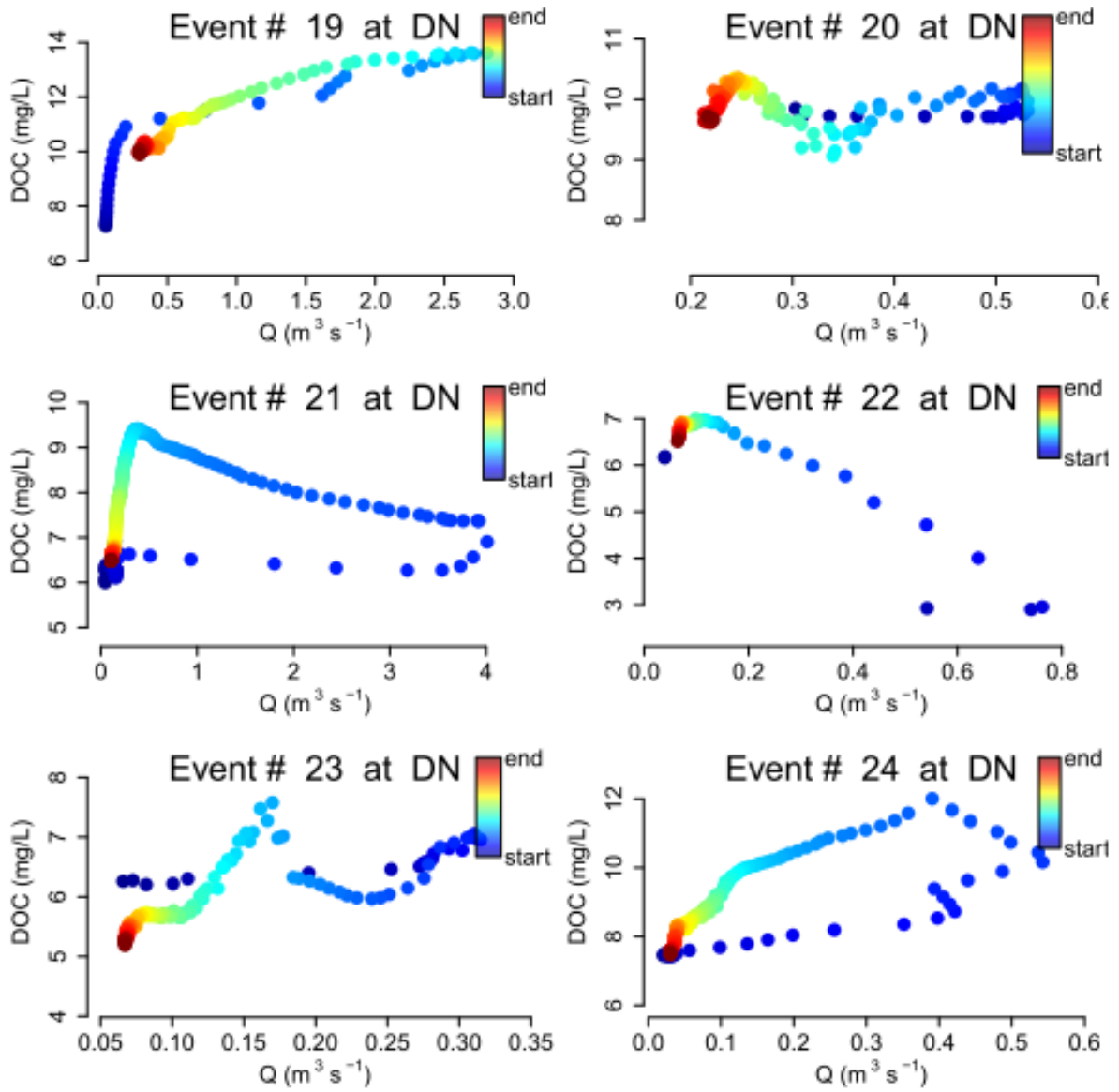


Figure F.6 Continued

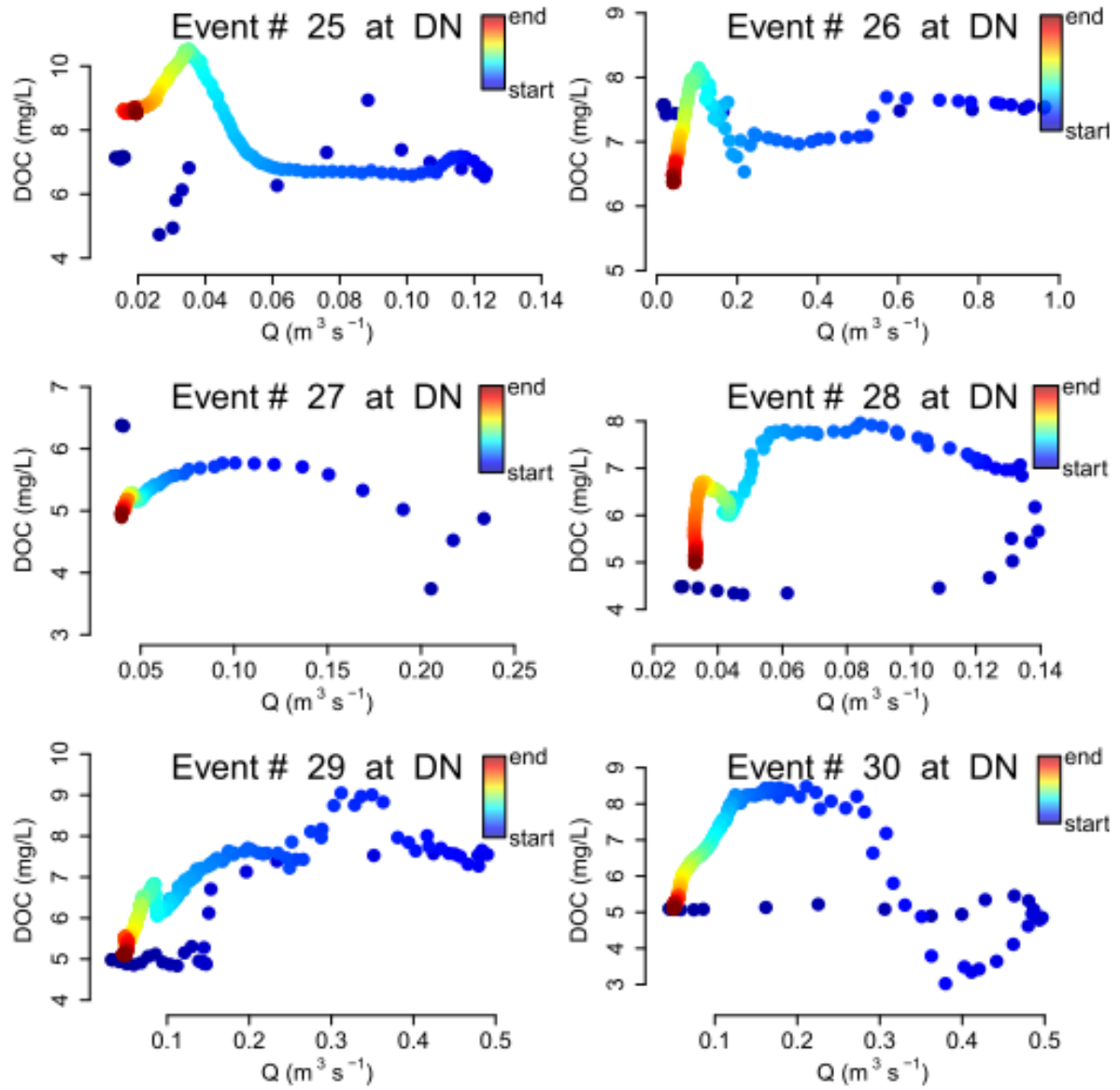


Figure F.6 Continued

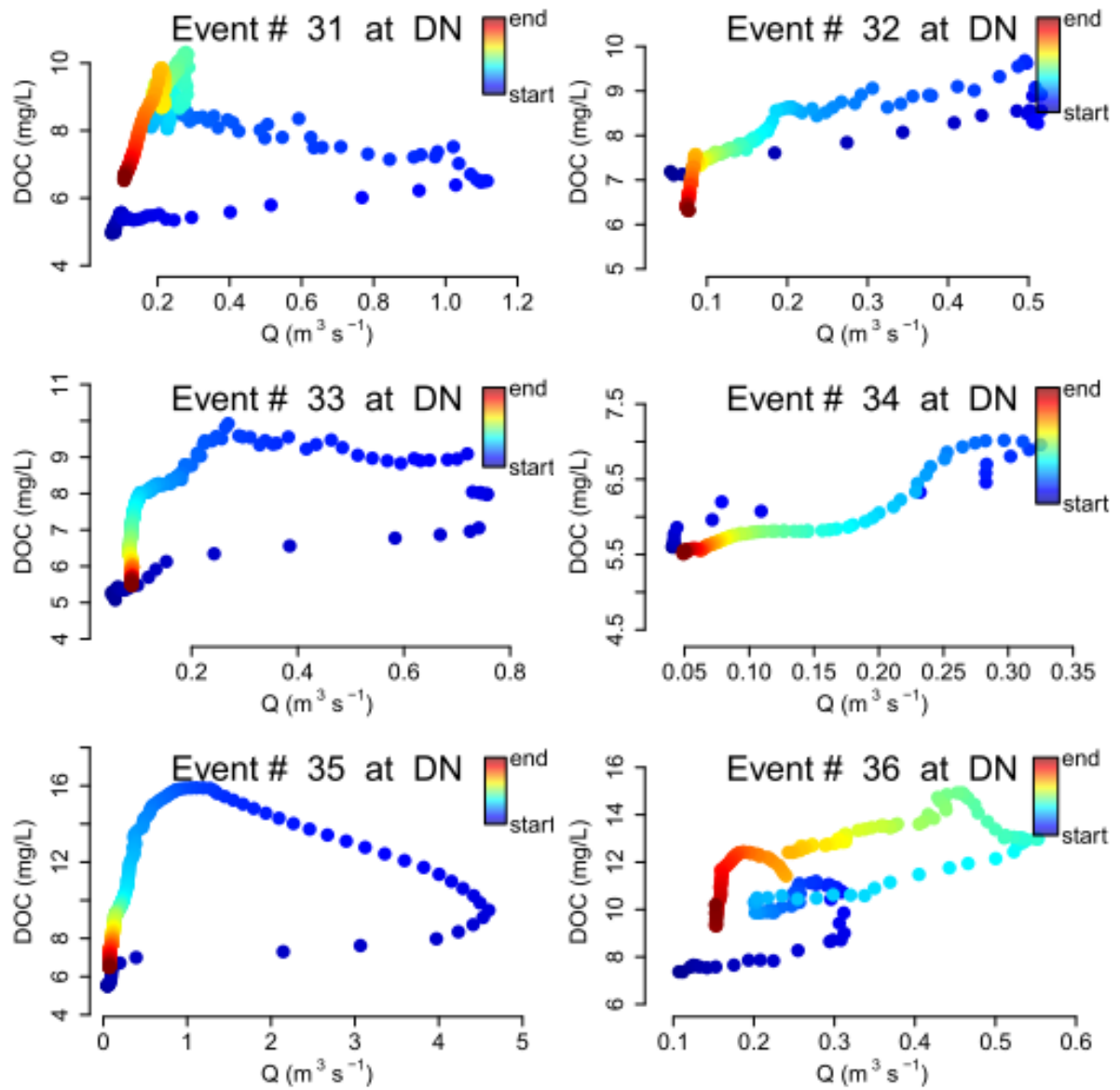


Figure F.6 Continued

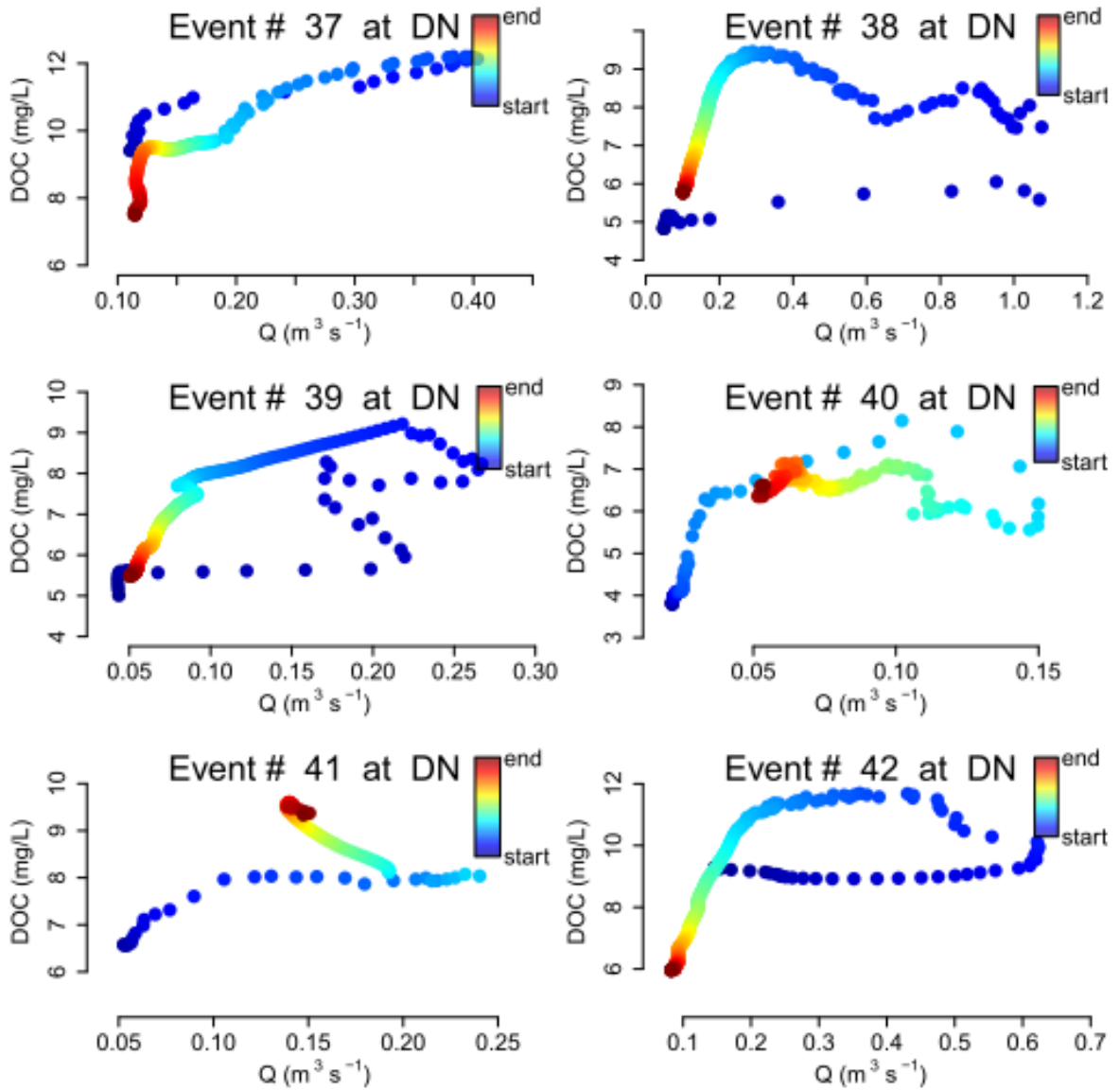


Figure F.6 Continued

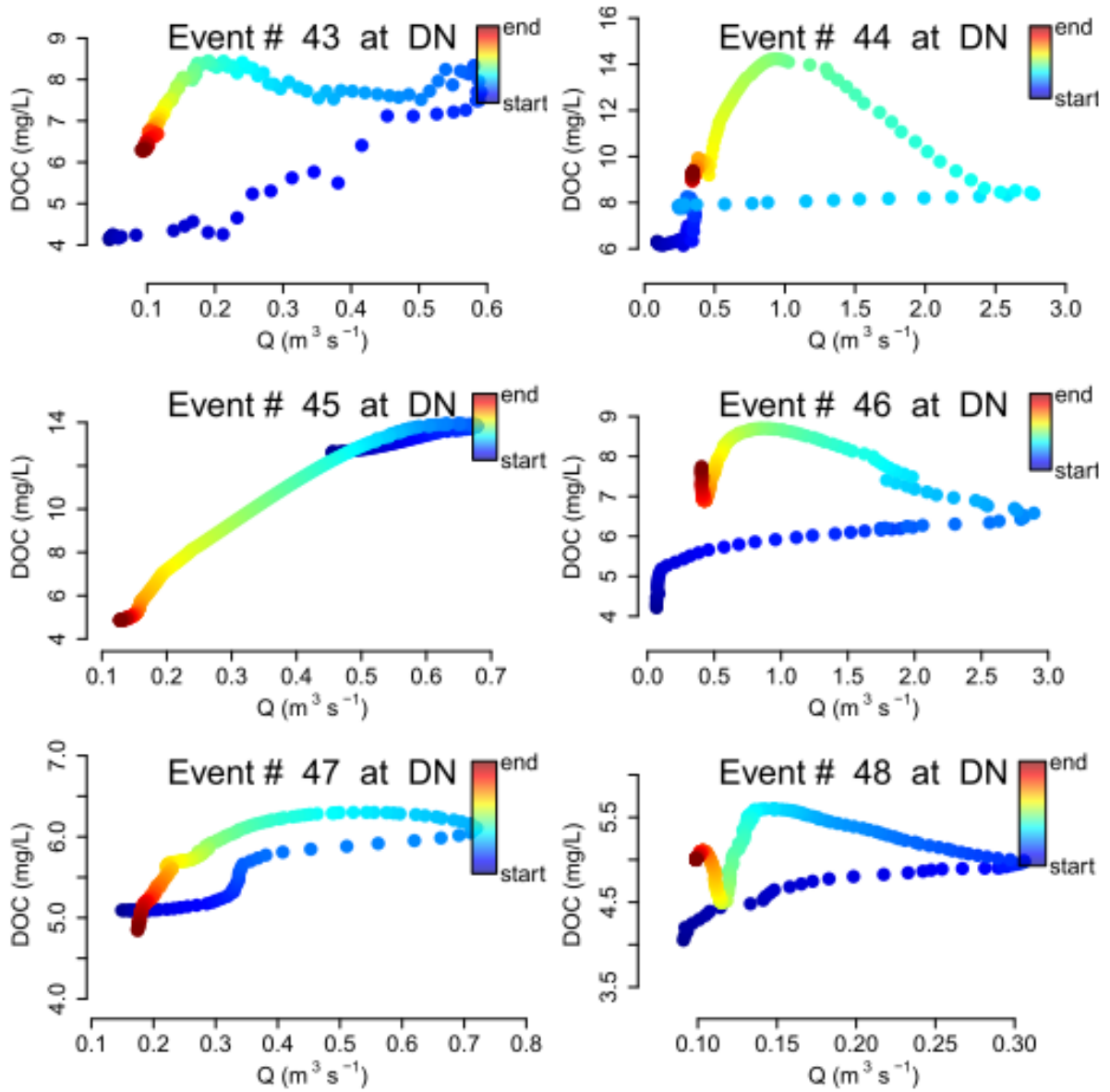
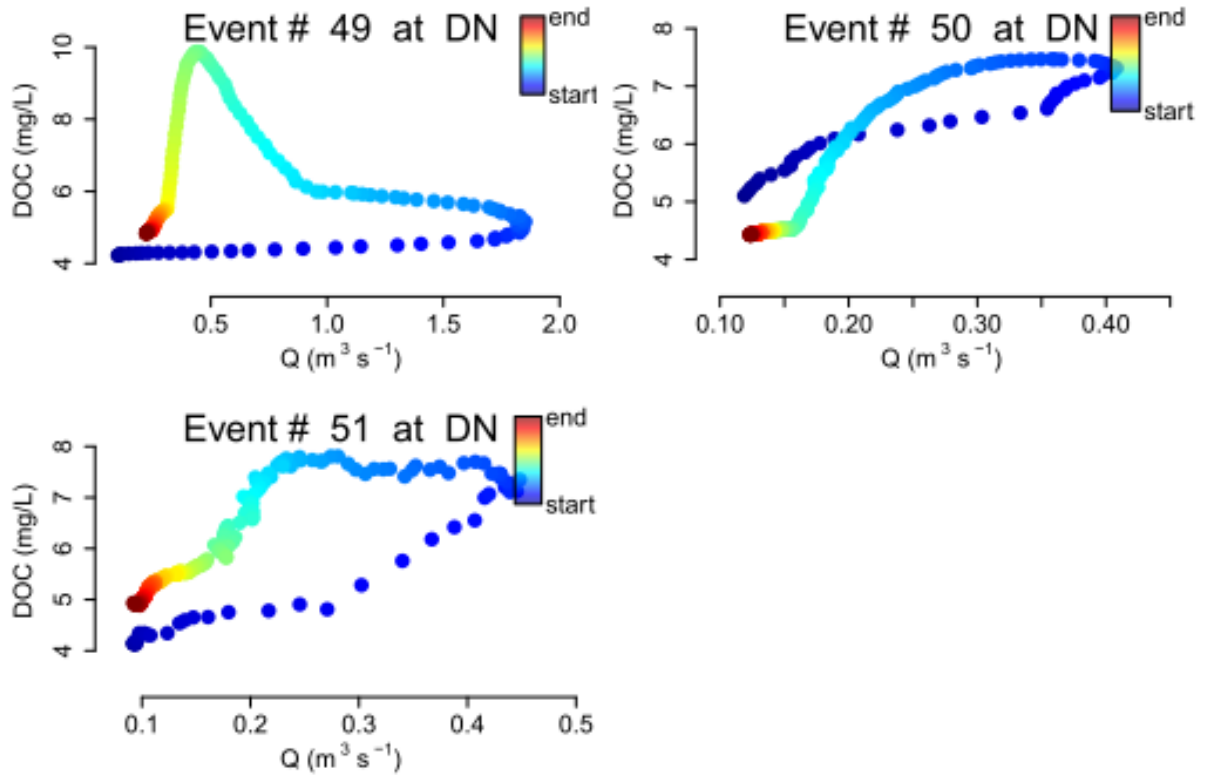


Figure F.6 Continued



Appendix G: Summary of Hysteresis Index

Table G.1

Summary of number of storm events with trajectory direction (C: Clockwise, AC: Anti-Clockwise) for NO₃-N and DOC in different seasons in the Claridge Canal

Station	Spring			Summer			Fall			Winter		
	Total Events	C	AC									
NO₃-N												
UP	7	6	1	14	6	8	1	0	1	15	8	7
MD	6	3	3	11	6	5	2	0	2	10	8	2
DN	7	5	2	10	8	2	5	1	4	16	6	10
DOC												
UP	7	3	4	14	8	6	1	0	1	15	1	14
MD	6	3	3	11	8	3	2	1	1	10	4	6
DN	7	2	5	10	1	9	5	1	4	16	2	14

Table G.2

Summary of number of mutual storm events with trajectory direction (C: Clockwise, AC: Anti-Clockwise) for NO₃-N and DOC at the three stations in the Claridge Canal (n = 22 for each station)

Station	NO ₃ -N		DOC	
	C	AC	C	AC
UP	13	9	10	12
MD	14	8	12	10
DN	17	5	3	19

Appendix H: Tracer Experiment

H.1 Introduction

A tracer experiment is a general experiment to evaluate nutrients dynamics (including nutrient transport and exchanges), internal hydraulic functioning and hyporheic zone in streams. A tracer study involves the injection of certain concentrations of conservative or non-conservative solutes at a known constant rate into the stream for a certain time period and the measurement of the variations of the solutes concentration after injection at the downstream direction of the injection place; thus, the processes of advection, dispersion, lateral inflow and transient storage in the stream are able to be estimated (Stream Solute Workshop, 1990; Wagner, and Harvey, 1997). Different solutes were applied in previous research. Bencala et al. (1984) used chloride, lithium, potassium, strontium and sodium to evaluate the interactions between the solutes and streambed sediment in a mountain stream; Bukaveckas (2007) injected salt (NaCl) as a conservative tracer, nitrate and phosphate as non-conservative tracers in a channelized stream to measure transient storage and nutrient uptake.

H.2 Methods

Site Description

An agricultural coastal plain stream, the Claridge Canal (35.42° N, 78.02° W), was restored from July of 2015 to 2016 to mitigate the effects of highway (Highway 70 Bypass) construction in Goldsboro, North Carolina (NC). In order to determine lateral contribution,

transient storage, and $\text{NO}_3\text{-N}$ dynamics in the stream before the restoration period, the tracer study was implemented in the stream from March 23 to March 26 in 2015. The injection site was A with nine monitoring stations, B-J (Figure H.1), installed at the downstream direction of A to measure water quality in situ, collect discrete samples for laboratory analysis, and obtain flow rate measurements along the stream.



Figure H.1

The injection site and 9 monitoring stations for tracer study along the Claridge Canal in Goldsboro, North Carolina

Stream Tracer Experiment

The tracer solution was composed of KBr and KNO₃, and was injected by a piston pump controlled by an Arduino microprocessor with 70 mL/min over 20 hours at injection site A (Figure H.1). The detailed descriptions of the equipment for water quality sampling and flow rate measurement at injection site (A) and the nine monitoring stations (B-J) (Figure H.1) are listed in Table H.1.

Table H.1.

The installment of monitoring equipment at the injection site and nine monitoring stations

Station Name	Equipment of water quality sampling and flow rate measurement	
	Continuous water quality and flow rate monitoring <i>in situ</i>	Discrete water quality sampling for lab analysis
A (Injection Site)	YSI probe measured conductivity every 2 mins	
B(Upstream Station)	UV-Vis spectrophotometer (spectro::lyser model, s::can) measured NO ₃ -N every 4 mins, Multi-parameter sonde (Eureka Manta 2) measured conductivity every 5 mins, Flow meter (Sontek-IQ Standard) measured velocity every 5 mins	Automatic discrete sampler (ISCO 6712) for laboratory analysis for Br and NO ₃ -N
C	UV-Vis spectrophotometer (spectro::lyser model, s::can) measured NO ₃ -N every 4 mins, YSI probe measured conductivity every 2 mins	Automatic discrete sampler (ISCO 6712) for laboratory analysis for Br and NO ₃ -N
D	YSI probe measured conductivity every 2 mins	
E	UV-Vis spectrophotometer (spectro::lyser model, s::can) measured NO ₃ -N every 4 mins, YSI probe measured conductivity every 2 mins	Automatic discrete sampler (ISCO 6712) for laboratory analysis for Br and NO ₃ -N
F	YSI probe measured conductivity every 2 mins	
G	UV-Vis spectrophotometer (spectro::lyser model, s::can) measured NO ₃ -N every 4 mins, YSI probe measured conductivity every 2 mins	Automatic discrete sampler (ISCO 6712) for laboratory analysis for Br and NO ₃ -N
H	YSI probe measured conductivity every 2 mins	
I (Middle Stream Station)	UV-Vis spectrophotometer (spectro::lyser model, s::can) measured NO ₃ -N every 4 mins, Multi-parameter sonde (Eureka Manta 2) measured conductivity every 5 mins, Flow meter (Sontek-IQ Standard) measured velocity every 5 mins	Automatic discrete sampler (ISCO 6712) for laboratory analysis for Br and NO ₃ -N
J	YSI probe measured conductivity every 2 mins	

H.3 Preliminary Results and Data Analysis

Figure H.2 shows the breakthrough curves for $\text{NO}_3\text{-N}$ at Stations B, C, E, G, and I at the Claridge Canal before restoration period. From Figure H.2, the continuous concentration data was from UV-Vis spectrophotometer manufacturer calibration (raw data), however it was required to calibrate with PLSR calibrations since the values were offset from the concentration measured from discrete samples.

The nutrient uptake parameters (S_w (uptake length), V_f (uptake velocity), U (areal uptake rate)) at Station C were calculated with the information of $\text{NO}_3\text{-N}$ breakthrough curves (Figure H.2) at Station B and Station C in the Clardige Canal. The distance of stream length from Station B to Station C is 147 m. The values for S_w (uptake length), U (areal uptake rate), V_f (uptake velocity), and stream order at Station C are listed in Table H.2. The uptake values (except for V_f) at Station C were lower than the mean values which were addressed in Table H.2 from Ensign et al. (2006) with the stream order 2.

Figure H.3, Figure H.4, and Figure H.5 were the relationship for S_w , V_f , and U to $\text{NO}_3\text{-N}$, and S_w and V_f had similar patterns with Covino et al., (2010). With the application of the TASCC, it provides more set for nutrient uptake values instead of one set of values estimated from traditional methods (plateau method and BTC-integrated method), thus, it can reduce the error for estimating the nutrient uptake mechanisms. In addition, the authors (Covino et al., 2010) suggested the TASCC can be applied in plateau condition as well.

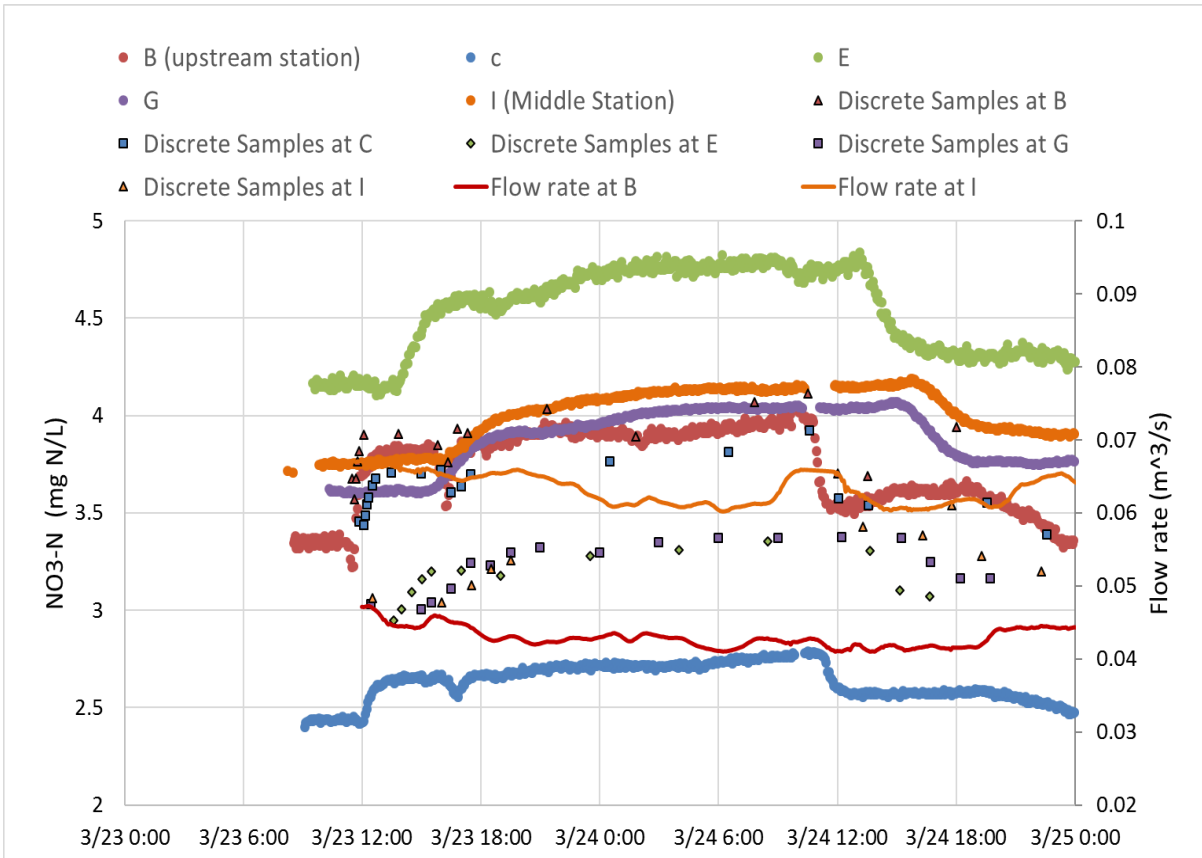


Figure H.2

The concentration of NO₃-N breakthrough curves (continuous results: raw data from UV-Vis spectrophotometer manufacturer calibration, discrete results: laboratory analysis) at Station B, C, E, G, and I at the Claridge Canal before restoration period

Table H.2

Nutrient uptake parameters at Station C in the Claridge Canal

S_w (m)	U ($\mu\text{g m}^{-2} \text{min}^{-1}$)	V_f (mm min^{-1})	Stream order
135.0	23.72	6.30	2

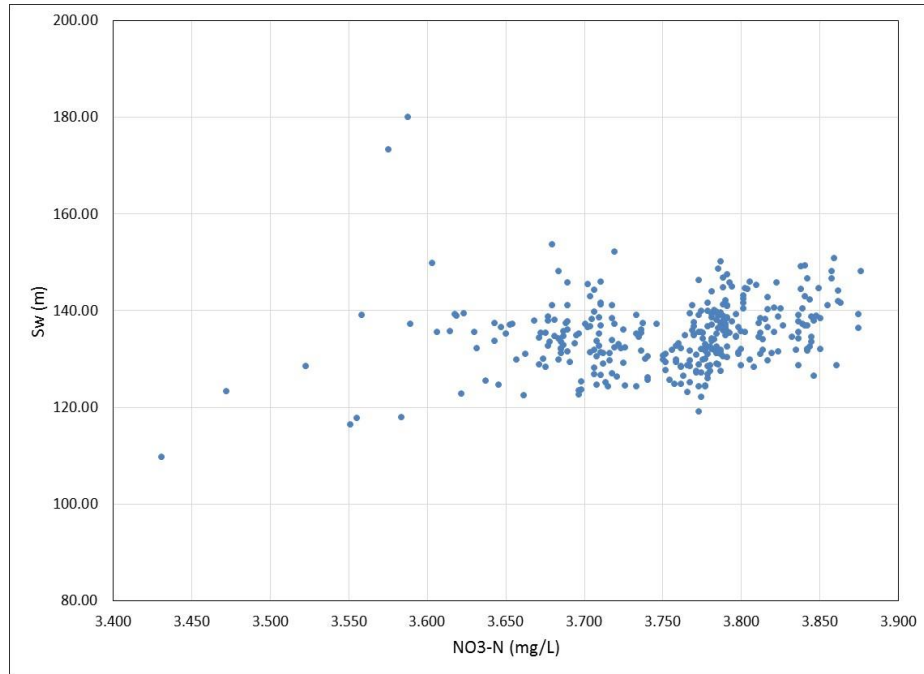


Figure H.3

The relationship for S_w and NO_3-N

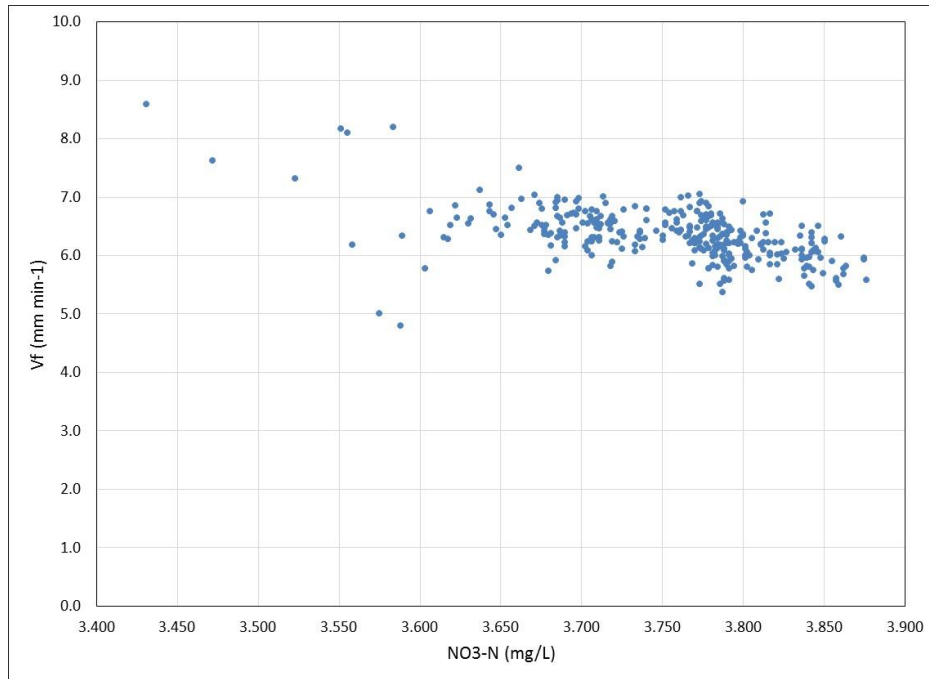


Figure H.4

The relationship for V_F and NO_3-N

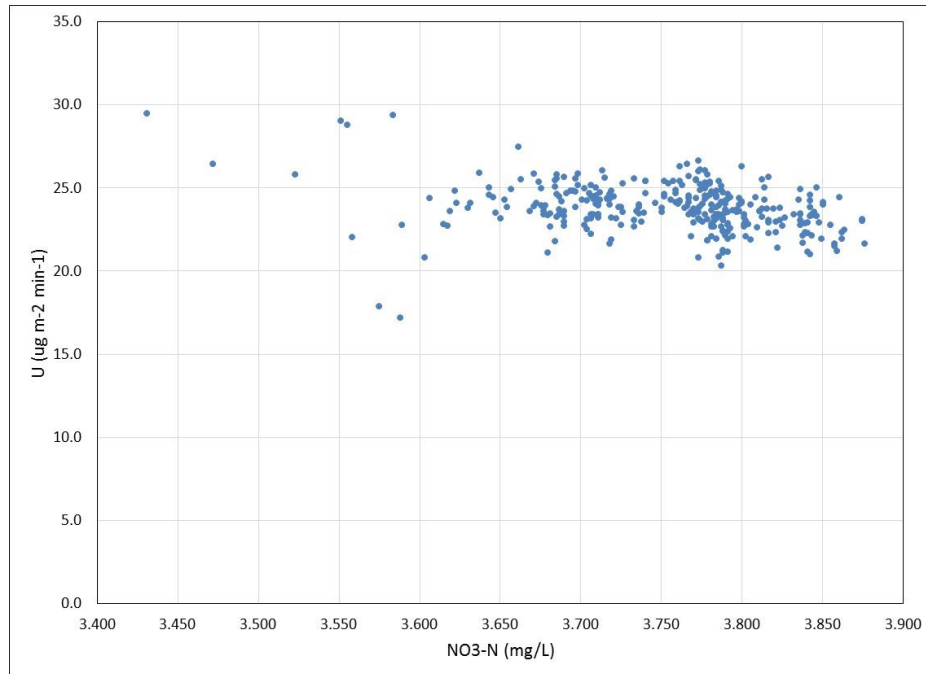


Figure H.5

The relationship for U and NO₃-N

H.4 References

- Bencala, K. E., Kennedy, V. C., Zellweger, G. W., Jackman A. P., Avanzino, R. J. 1984. Interactions of solutes and streambed sediment. 1. An experimental analysis of cation and anion transport in a mountain stream. *Water Resources Research*, 20: 1797-1803.
- Bukaveckas, P. A. 2007, Effects of channel restoration on water velocity, transient storage, and nutrient uptake in a channelized stream. *Environ. Sci. Technol.*, 41 (5): 1570-1576.
- Covino, T. P., McGlynn, B. L., McNamara, R. A. 2010. Tracer Additions for Spiraling Curve Characterization (TASCC): Quantifying stream nutrient uptake kinetics from ambient to saturation. *Limnol. Oceanogr.: Methods* 8: 484–498.

Ensign, S. C. and Doyle, M. W. 2006 Nutrient spiraling in streams and river networks, JOURNAL OF GEOPHYSICAL RESEARCH, VOL. 111, G04009, doi:10.1029/2005JG000114.

Stream Solute Workshop. 1990. Concepts and methods for assessing solute dynamics in stream ecosystems. Journal of the North American Benthological Society, 9(2): 95–119.

Wagner, B. J. and Harvey, J. W. 1997. Experimental design for estimating parameters of rate-limited mass transfer: analysis of stream tracer studies. Water Resources Research, 33(7): 1731-1741.

Appendix I: Extracellular coenzyme activity experiment

I.1 Introduction

Basic theory of EEA

Sinsabaugh et al. (2009) defined coenzymes as “all enzymes located outside the confines of intact cell membranes regardless of whether such enzymes enter the environment by secretion or lysis.” In most research, organic carbon (C), nitrogen (N) and phosphorus (P) are the most commonly studied environmental nutrient sources degraded by coenzyme catalysis (Sinsabaugh and Follstad Shah, 2012). The role of extracellular coenzyme is to decompose the large organic matter compounds into simpler compounds that microorganisms can utilize easily from the environment, thus, the low-molecular mass products which are able to be consumed by microorganisms directly are produced with extracellular coenzyme activity (EEA) (Sinsabaugh and Follstad Shah, 2012).

The four coenzymes (β -D-glucosidase [GLU, BG], Leucine-aminopeptidase [LAP], β -N-Acetyl glucosaminidase [NAG], and Alkaline phosphatase [AP]) were evaluated in the Claridge Canal since the four coenzymes were also commonly measured EEA in previous research (e.g., Sinsabaugh et al. 2009, 2010). In addition, the production of the four coenzymes has the relationship in response to nutrients (C, N, and P) limitation by microorganisms. GLU (BG) is the indicator of carbon demand, NAG and LAP are the indicators for nitrogen demand, and AP is the indicator of phosphorus demand (e.g., AP activity had the inverse relationship with the bioavailability of environmental phosphorus

(Sinsabaugh et al., 2012). As a result, by quantifying the EEA for the four ecoenzymes, it can provide the information of nutrient demand for microorganisms.

Objectives

The objective is to address the patterns and relationships between EEA as ecological indicators for four ecoenzymes (β -D-glucosidase [GLU, BG], Leucine-aminopeptidase [LAP], β -N-Acetyl glucosaminidase [NAG], and Alkaline phosphatase [AP]) and nutrients (nitrate [NO₃-N], dissolved organic carbon [DOC, total phosphorous [TP]) and estimate the ecosystem function in the agricultural coastal plain stream before the restoration period.

I.2 Methods

Site Description

The details for site description were addressed in Chapter 2. The composition of substrate at three stations are described as following: (1) upstream station (UP): there is approximately 10 cm of organic material on top of sand; (2) middle stream station (MD): there is over 30 cm of organic muck on sand; and (3) downstream station (DN): most of substrate is sand (Birgand, 2013). The bottom width at UP, MD, and DN were 2.5, 3.0, 4.5 m, respectively.

Water Quality Sampling and Measurements

The water quality results from one of the two grab water quality samples which was labeled as “Fresh” will be applied to correlate and analyze the relationship between nutrients and EEA. The reason for using the “Fresh” grab sample is that the water quality sample was

collected at the same time that the EEA sediment samples were collected. The details for the water quality sampling and measurements were addressed in Chapter 2.

EEA Sampling and Experiment

The EEA samples were collected from October 2014 to March 2015, and the samples were collected from the top 5 cm of the sediments at three stations. The number of samples collected were 3, 4, and 4 samples at UP, MD, DN, respectively at one cross-section, 1-2 m from the downstream direction of the flume. Since the bottom of width at MD and DN was wider than at UP, one more sample was collected at MD and DN. The sediment samples were stored with ice and transported to the refrigerator with -80 °C in the laboratory until being analyzed.

Laboratory analysis for EEA

The general concept (Figure I.1) of an EEA experiment for laboratory analysis to quantify the activity of ecoenzymes is as follows: Extracellular ecoenzymes are bound to the fluorescent model substrate; then, with the catalytic mechanism from ecoenzymes, the breakdown of the fluorescent model substrate releases the fluorescent product; thus, the fluorescence or absorbance is able to be measured by using a microplate reader (Synergy Mx, Biotek). The four ecoenzymes (β -D-glucosidase [GLU, BG], Leucine-aminopeptidase [LAP], β -N-Acetyl glucosaminidase [NAG], and Alkaline phosphatase [AP]) which were also commonly measured EEA in previous research (e.g., Sinsabaugh et al. 2009; and Harbott and Grace, 2005), the fluorescent model substrates, and the biological function of the ecoenzymes in this research are listed in Table I.1.

The general process to measure EEA in sediment is to mix the sample with the relative fluorescent model substrate solution in a buffer medium and measure the emission of fluorescent production over a period of time (The details of pretreatments for sediment samples and fluorescent model substrate solution are similar with Oviedo-Vargas (2013) and Harbott and Grace (2005). For EEA experiment, the units are nanomoles (nmol) or micromoles (μmol) for the fluorescent product (MUB or AMC); thus, the ultimate units are represented as nmol (or μmol) g^{-1} of dry weight of sediment hr^{-1} ($\text{nmol g}^{-1} \text{DW h}^{-1}$ or $\mu\text{mol g}^{-1} \text{DW h}^{-1}$), and nmol (or μmol) g^{-1} of organic matter hr^{-1} ($\text{nmol g}^{-1} \text{OM h}^{-1}$ or $\mu\text{mol g}^{-1} \text{OM h}^{-1}$) to indicate how much fluorescent model substrate breakdown by ecoenzymes occurs over time.

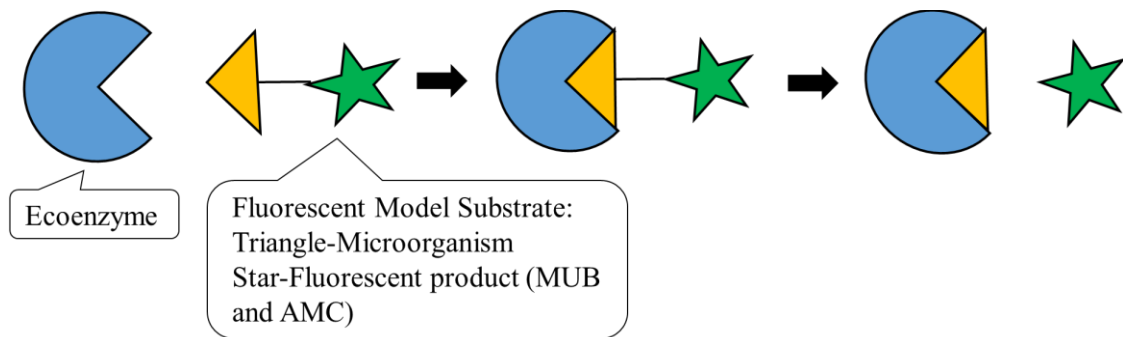


Figure I.1

The concept of EEA experiment for laboratory analysis

Table I.1**Ecoenzymes, relative fluorescent model substrate, and biological function in this study**

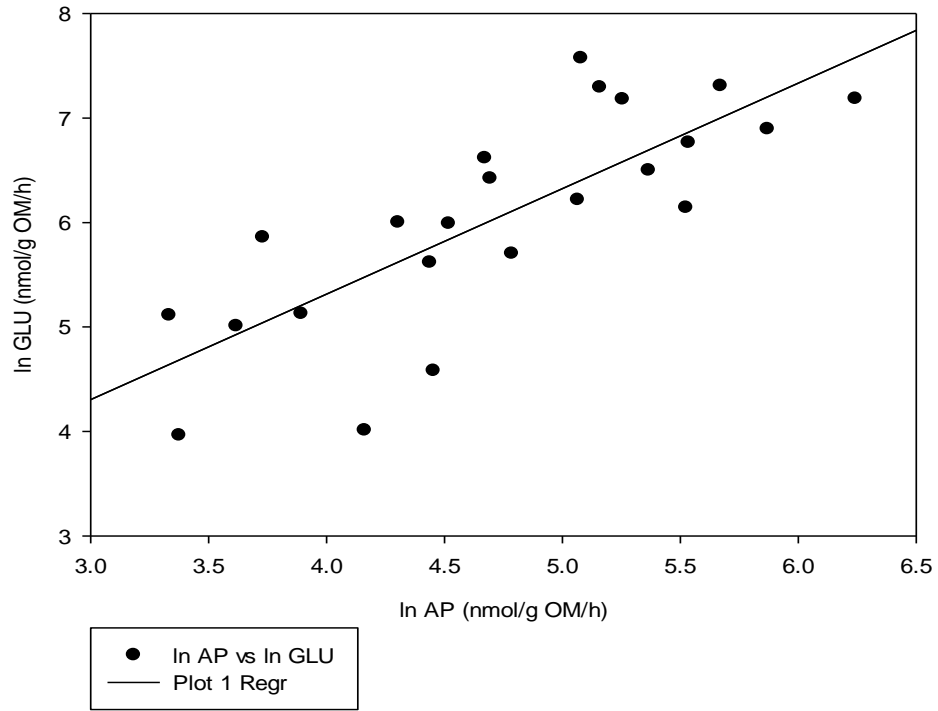
Ecoenzyme	Fluorescent Model substrate	Biological function (Sinsabaugh et al.,2009)
β -1,4-D-glucosidase (GLU, BG)	MUB- β -D-glucose	Cellulose degradation: Hydrolysis of glucose from cellobiose
Leucine-aminopeptidase (LAP)	L-Leucine-AMC	Proteolysis: Hydrolysis of leucine from polypeptides
β -1,4-N-Acetyl glucosaminidase (NAG)	MUB- N-acetyl- β -D-glucosaminide	Chitin and peptidoglycan degradation: Hydrolysis of glucosamine from chitobiose
Alkaline phosphatase (AP)	MUB-Phosphate	Hydrolysis of phosphate from phosphosaccharides and phospholipids

*The fluorescent product: MUB= 4-methylumbelliferone; AMC=4-aminomethylcoumarine

I.3 Preliminary Results and Data Analysis

Figure I.2 shows the preliminary results for the relationship between GLU and AP, and the linear regression equation is: $(\ln \text{GLU}) = (1.010 * \ln \text{AP}) + 1.275$. The linear regression equation for freshwater sediments is $(\ln \text{GLU}) = ([0.946 \pm 0.030] * \ln \text{AP}) + (1.02 \pm 0.29)$ in Sinsabaugh and Follstad Shah (2012). When the regression equation in Figure B.2 (in this research) was compared with Sinsabaugh and Follstad Shah (2012), it indicated that EEA existed in the sediments and it had a similar tendency with previous research.

Relationship between ln GLU and ln AP



Linear Regression
 $\ln \text{GLU nmol/g OM/h} = 1.275 + (1.010 * \ln \text{AP nmol/g OM/h})$
 N = 23
 R = 0.783 Rsqr = 0.613 Adj Rsqr = 0.595
 Standard Error of Estimate = 0.662

	Coefficient	Std. Error	t	P
Constant	1.275	0.839	1.520	0.143
ln AP nmol/g OM/h	1.010	0.175	5.768	<0.001

Figure I.2

Preliminary results for the relationship between ln GLU and ln AP

The ratios of EEA in the Claridge Canal

Figure I.3, Figure I.4, and Figure I.5 demonstrated the relationships for four coenzymes as indicators for C, N, P acquisition. The slope for the linear regression was 0.8416 in Figure

I.3, thus, it indicated the acquisitions for C: P was close to 1:1 for microorganism in the Claridge Canal. In addition, Sinsabaugh et al. (2008) had similar C: P ratio in soil. The p-value for the slope as statistically significant relationship for $\ln(\text{BG})$ vs. $\ln(\text{NAG} + \text{LAP})$ is 0.154 (Figure I.4), therefore, the linear regression for C: N was not statistically significant. The reason was addressed as following: the EEA for NAG and LAP were really low and the EEA for NAG and LAP could not even be detected in some sediments samples in the Claridge Canal. In Figure I.5, the regression equation was $\text{C: N} = 0.8732 (\text{C: P}) + 1.1119$, and it had similar slope with Sinsabaugh et al. (2008), however, the p-value for the slope as statistically significant relationship was 0.151 in the Claridge Canal. As a result, the acquisition for C and P is more robust than the acquisition for C and N for microorganism in the Claridge Canal.

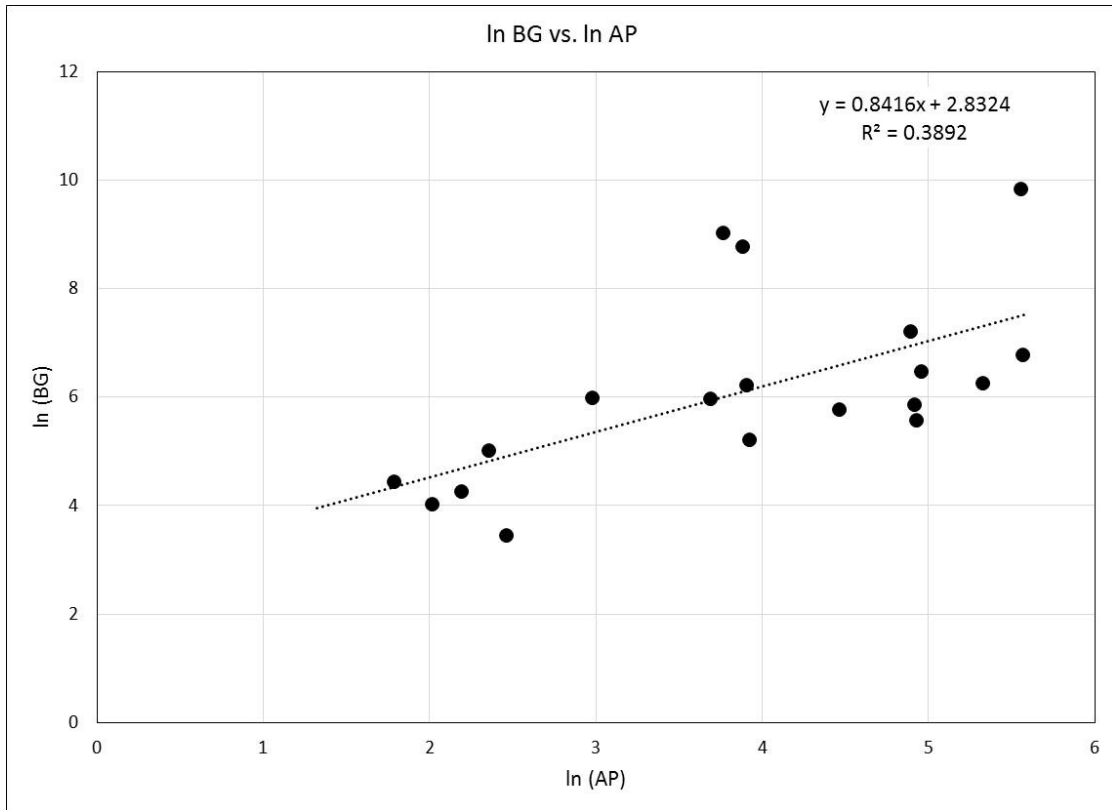


Figure I.3

Ecoenzymes activities for ln(BG) and ln(AP) as an indicator of C: P acquisition

(Note: 1. The EEA unit is $\text{nmol h}^{-1} \text{g SOM}^{-1}$ which is the same unit with Sinsabaugh et al., (2008).

2. The p-value for the slope as statistically significant relationship is $0.004309 < 0.05$ for the linear regression.)

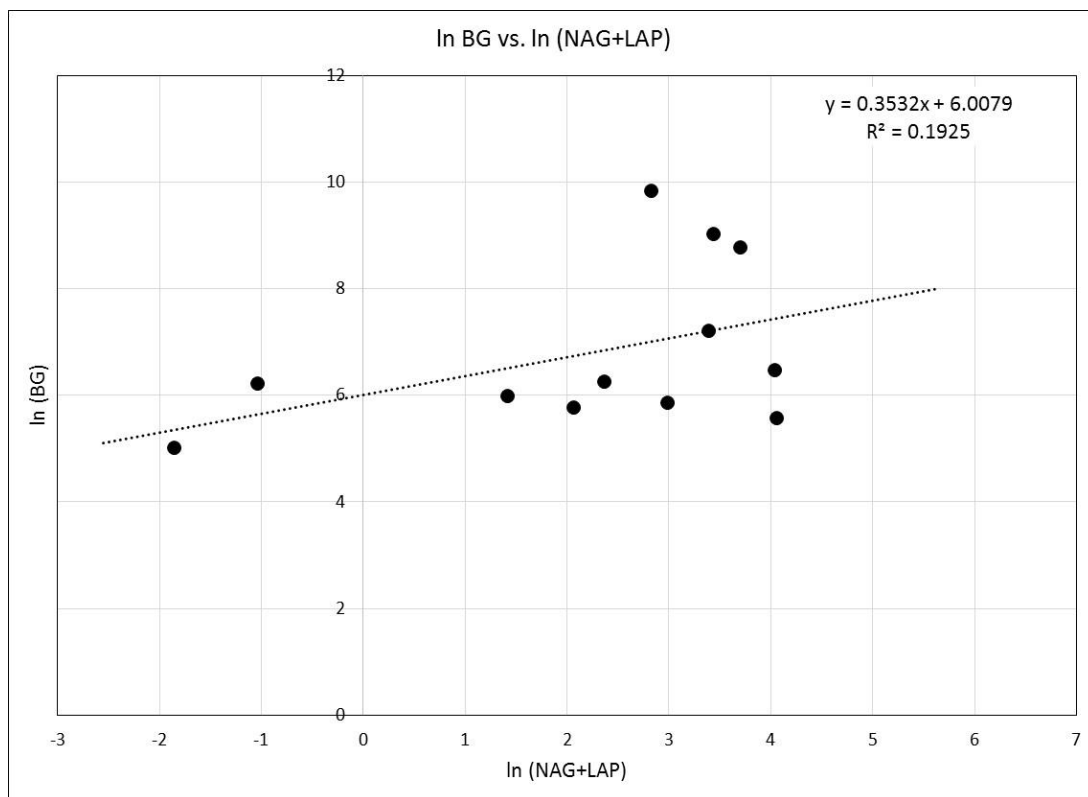


Figure I.4

Ecoenzymes activities for ln(BG) and ln(NAG+LAP) as an indicator of C: N acquisition

(Note: 1. The EEA unit is $\text{nmol h}^{-1} \text{g SOM}^{-1}$ which is the same unit with Sinsabaugh et al., (2008).

2. The p-value for the slope as statistically significant relationship is $0.154 > 0.05$ for the linear regression.)

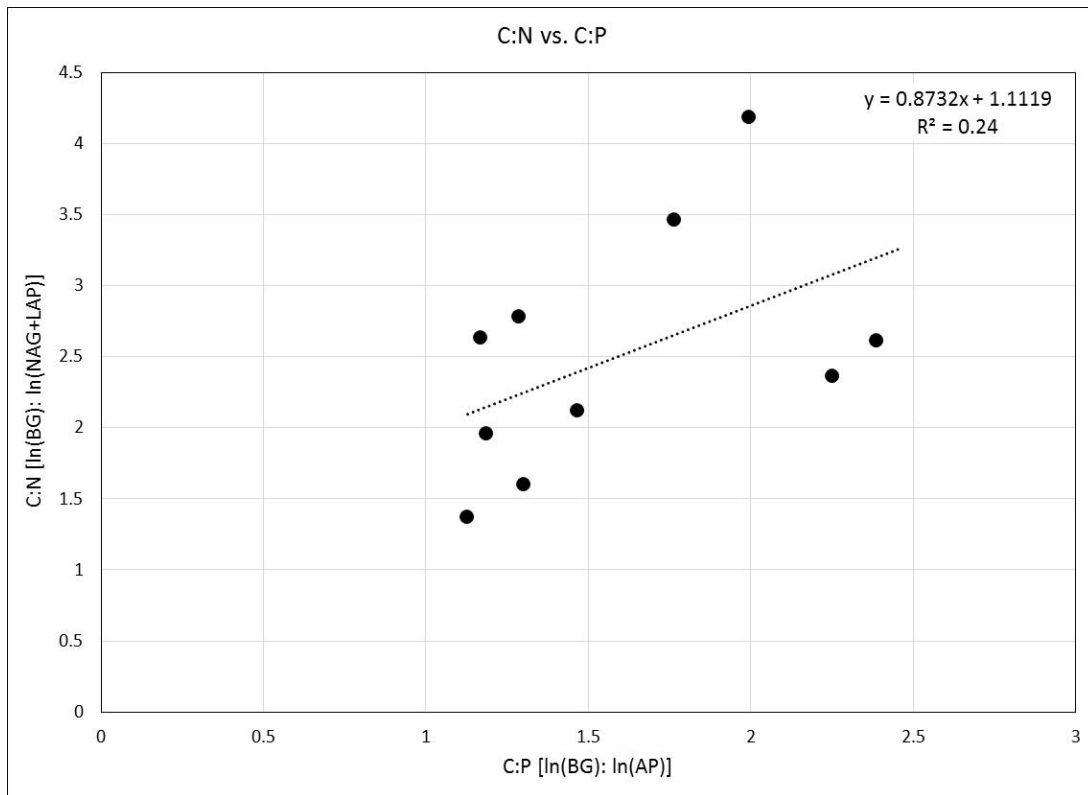


Figure I.5

The relationship for ecezymes activities for the ratio of ln(BG): ln(NAG+LAP), as an indicator of C: N acquisition and the ratio of ln(BG): ln(AP) as an indicator of C: P acquisition.

(Note: The p-value for the slope as statistically significant relationship is $0.151 > 0.05$ for the linear regression.)

I.4 References

Birgand, F. 2013. Intensive Monitoring of Nutrient and Material Load in Claridge Nursery Stream “The Canal” pre-, during and post construction of Highway 70 Bypass in Wayne County, NC, DOT Proposal.

Harbott, E. L. and Grace, M. R. 2005. Extracellular enzyme response to bioavailability of dissolved organic C in streams of varying catchment urbanization. *Journal of the North American Benthological Society*, 24: 588-601.

Oviedo-Vargas, D. 2013. Dissolved organic matter and coupled biogeochemical cycles in streams and rivers, In: Ph.D. Dissertation. Indiana University.

Sinsabaugh R. L., Horn, D. J. V., Follstad Shah, J. J., Findlay, S. 2010. Ecoenzymatic Stoichiometry in Relation to Productivity for Freshwater Biofilm and Plankton Communities. *Microb Ecol.*, 60: 885-893.

Sinsabaugh R. L., Lauber, C. L., Weintraub, M. N., Ahmed, B., Allison, S.D., et al. 2008. Stoichiometry of soil enzyme activity at global scale. *Ecol. Lett.* 11: 1252-64.

Sinsabaugh, R. L. and Follstad Shah, J. J. 2012. Ecoenzymatic Stoichiometry and Ecological Theory. *Annu. Rev. Ecol. Evol. Syst.*,43: 313-343.

Sinsabaugh, R. L., Hill, B. H., Follstad Shah, J. J. 2009. Ecoenzymatic stoichiometry of microbial organic nutrient acquisition in soil and sediment. *Nature*, 462:795-98.